



Alharthi, Abdulrahman (2014) *Hydrogen and carbon nanostructure formation from methane cracking over iron and zeolite based catalysts*. PhD thesis.

<http://theses.gla.ac.uk/5309/>

Copyright and moral rights for this work are retained by the author

A copy can be downloaded for personal non-commercial research or study, without prior permission or charge

This work cannot be reproduced or quoted extensively from without first obtaining permission in writing from the author

The content must not be changed in any way or sold commercially in any format or medium without the formal permission of the author

When referring to this work, full bibliographic details including the author, title, awarding institution and date of the thesis must be given

Enlighten:Theses  
<http://theses.gla.ac.uk/>  
theses@ gla.ac.uk

**Hydrogen and Carbon Nanostructure  
Formation from Methane Cracking over Iron  
and Zeolite Based Catalysts**



**University  
of Glasgow**

**Abdulrahman Alharthi**

**A thesis submitted in fulfilment of the  
requirements for the degree of Doctor of  
Philosophy**

**School of Chemistry  
College of Science and Engineering  
April 2014**

## Abstract

The production of hydrogen by the catalytic cracking of methane was investigated. An extensive study was undertaken on two categories of materials, namely iron-containing wastes and prepared catalysts, which include palladium-based catalysts, nickel-based catalysts and a copper-based catalyst. Three types of iron-containing waste materials were examined as pre-catalysts. The iron waste samples comprised a biogenic sample from a local Landfill site; waste residue sample from an old local nail works site and Red Mud. The resulting waste iron catalysts are environmentally benign and may be “thrown away” following use. The biogenic sample presented an unusual tubular morphology resulting from its biogenesis. All these materials possessed significant peak activity for hydrogen production at 800 °C. Significant carbon deposition occurred on these samples. Calcination of biogenic and waste residue samples at 900 °C enhanced performance. Carbon was deposited in the form of carbon filaments on the waste residue sample. The addition of Pd promoted the biogenic sample’s activity but poisoned the waste residue sample. Cracking of methane over palladium-containing zeolite catalysts has also been studied. Pd/H-ZSM-5 exhibited the highest peak hydrogen formation rate at 750 °C and the highest amount of carbon was produced at 900 °C. The addition of Ni, Co, Cu and Fe dopants did not improve performance. The effect of support type (H-ZSM-5,  $\gamma$ -Al<sub>2</sub>O<sub>3</sub> and SiO<sub>2</sub>) on the Pd catalyst performance was also investigated, with  $\gamma$ -Al<sub>2</sub>O<sub>3</sub> producing the best activity. All post-reaction Pd catalysts showed the formation of carbon filaments. On comparing the catalytic activity of Pd/H-ZSM-5, Ni/H-ZSM-5 and Cu/H-ZSM-5, it was found that Pd/H-ZSM-5 catalyst possessed the highest activity, while Ni/H-ZSM-5 and Cu/H-ZSM-5 catalysts showed lower activity and similarity to each other in behaviour. Carbon filaments were formed over Pd/H-ZSM-5 and Cu/H-ZSM-5 but did not form over Ni/H-ZSM-5. It was observed that the carbon filaments only grow at higher Ni-loading on the zeolite. The catalytic activities of Ni on different supports were evaluated and SiO<sub>2</sub> was found to be the most effective support.

## Contents

<b>1. Introduction</b> .....	<b>1</b>
1.1. General introduction.....	1
1.2. Hydrogen production.....	3
1.2.1 Hydrogen production from methane.....	4
1.2.2 Steam methane reforming (SMR).....	4
1.2.3 Partial oxidation of methane (POM).....	5
1.2.4 Autothermal reforming of methane (ATR).....	5
1.2.5 Direct cracking of methane.....	5
1.3. Carbon deposition.....	11
1.3.1 Carbon nanotubes (CNTs).....	12
1.3.2 Carbon nanofibres (CNFs).....	17
1.3.3 Carbon nano-onions.....	20
1.4. Biogenic iron oxide.....	22
1.5. Zeolites.....	25
1.5.1 Zeolite Structure and properties.....	26
1.5.2 H-ZSM-5.....	28
1.5.3 Catalysis by zeolites.....	29
1.6. Objectives.....	31
<b>2. Experimental</b> .....	<b>32</b>
2.1. Introduction.....	32
2.2. Waste materials containing iron as catalysts.....	32
2.2.1 Landfill and Factory samples.....	32
2.2.2 Red Mud sample (RM).....	34
2.2.3 Modification of Landfill and Factory sample.....	34
2.3. Catalyst preparation.....	35
2.3.1 Preparation of Pd/H-ZSM-5 catalyst and its doping.....	35
2.3.2 Preparation of Pd/H-ZSM-5 catalyst by different precursors.....	36
2.3.3 Preparation of Pd based catalyst on non-zeolite supports.....	37
2.3.4 Preparation of Cu/H-ZSM-5, Ni/H-ZSM-5 with different Ni loadings and doping Ni/H-ZSM-5 with Pd.....	37
2.3.5 Preparation of Ni based catalyst on non-zeolite supports.....	38
2.3.6 Synthesis of 2-line ferrihydrite.....	38
2.4. Catalytic testing.....	39
2.4.1 Gas calibrations.....	40
2.4.2 Catalytic testing procedure.....	40
2.4.3 Manipulation of GC Data.....	41
2.5. Characterisation of the catalyst.....	41
2.5.1 X-ray powder diffraction (XRD).....	41
2.5.2 Hot stage X-ray powder diffraction (XRD).....	41
2.5.3 Thermal gravimetric analysis (TGA).....	42
2.5.4 Elemental analysis (CHN).....	42
2.5.5 N <sub>2</sub> -physisorption.....	42
2.5.6 Raman Spectroscopy.....	42
2.5.7 Scanning Electron Microscopy (SEM).....	43
2.5.8 High resolution transmission Electron Microscopy (HRTEM).....	43
2.5.9 Inductively coupled plasma optical emission spectroscopy (ICP-OES).....	43
2.5.10 Fourier Transform Infrared spectroscopy (FTIR).....	44
2.5.11 NMR spectroscopy.....	44
<b>Results</b> .....	<b>45</b>
<b>3. Waste iron oxides as catalysts for hydrogen production via direct cracking of methane</b> .....	<b>45</b>

3.1.	General introduction .....	45
3.2.	Results and discussion .....	47
3.2.1.	Characterisation of raw Red Mud, Landfill and Factory samples .....	47
3.2.1.1.	XRD patterns .....	47
3.2.1.2.	ICP analysis of raw Landfill, Factory and Red Mud samples .....	49
3.2.1.3.	CHN analysis of raw Landfill, Factory and Red Mud samples .....	50
3.2.1.4.	SEM, EDX spectroscopy and HRTEM analysis of the raw Landfill, Factory and Red Mud samples .....	51
3.2.1.5.	BET surface area measurements .....	54
3.3.	Reaction data .....	55
3.3.1.	Characterisation of post-reaction for the Landfill, Factory and Red Mud samples 61	
3.3.1.1.	XRD patterns .....	61
3.3.1.2.	Post-reaction CHN and TGA analysis .....	63
3.3.1.3.	Post-reaction BET surface area measurements .....	66
3.3.1.4.	Post-reaction SEM and HRTEM images .....	67
3.4.	Effect of reaction temperature on methane cracking over the Landfill sample ....	71
3.4.1.	Reaction data .....	71
3.4.2.	XRD studies .....	73
3.4.3.	CHN and TGA analysis .....	74
3.4.4.	SEM and HRTEM images .....	76
3.4.5.	BET surface area .....	80
3.5.	Direct cracking of methane over synthesised 2-line ferrihydrite for hydrogen production .....	81
3.5.1.	Introduction .....	81
3.5.2.	Results and discussion .....	82
3.5.2.1.	Reaction data .....	82
3.5.2.2.	XRD studies .....	84
3.5.2.3.	Post-reaction CHN and TGA analysis .....	85
3.5.2.4.	BET surface area measurements .....	86
3.5.2.5.	SEM images .....	86
3.5.3.	<i>In situ</i> XRD studies and the reaction pathway over the Landfill sample .....	87
3.6.	Summary .....	91
<b>4.</b>	<b>Modification of Landfill and Factory samples for hydrogen production from direct cracking of methane .....</b>	<b>93</b>
4.1.	Introduction .....	93
4.2.	Results and discussion- Effect of calcination temperature on Landfill and Factory samples 94	
4.2.1.	Characterisation of calcined Landfill and Factory samples .....	94
4.2.2.	Reaction data .....	102
4.2.3.	Characterisation of post-reaction calcined Landfill and Factory samples ...	108
4.3.	Effect of acid treatment on Landfill and Factory samples .....	122
4.3.1.	Introduction .....	122
4.3.2.	Reaction data .....	122
4.3.3.	ICP analysis of Landfill and Factory samples treated with HCl .....	124
4.3.4.	XRD patterns .....	125
4.3.5.	CHN and TGA analysis .....	127
4.3.6.	BET surface area measurements .....	129
4.3.7.	SEM images .....	130
4.4.	Effect of palladium dopant on the Landfill and Factory samples .....	132
4.4.1.	Introduction .....	132
4.4.2.	Reaction data .....	132

4.4.3	XRD patterns.....	138
4.4.4	CHN and TGA analysis .....	140
4.4.5	BET surface area measurements.....	142
4.4.6	SEM images .....	144
4.5.	Summary .....	146
<b>5.</b>	<b>Cracking of methane over Pd based catalysts for the production of hydrogen and carbon nanostructures .....</b>	<b>150</b>
5.1.	Introduction .....	150
5.2.	Effects of reaction temperature on direct cracking of methane over 0.4 wt% Pd/H-ZSM-5 catalyst .....	151
5.2.1	Introduction .....	151
5.3.	Results and discussion.....	151
5.3.1	Reaction data.....	151
5.3.2	XRD patterns.....	153
5.3.3	Post-reaction carbon and TGA analysis.....	153
5.3.4	Post-reaction SEM and HRTEM images .....	156
5.3.5	Raman spectroscopy.....	163
5.4.	Effect of feed gas flow rate on direct cracking of methane over 0.4 wt% Pd/H-ZSM-5 catalyst .....	165
5.4.1	Introduction .....	165
5.4.2	Reaction data.....	165
5.4.3	XRD patterns.....	166
5.4.4	Post-reaction CHN and TGA analysis .....	167
5.4.5	Post-reaction SEM images .....	169
5.4.6	Raman spectroscopy.....	171
5.5.	Effects of dopants on the activity of 0.4 wt% Pd/H-ZSM-5 catalyst for direct cracking of methane .....	172
5.5.1	Introduction .....	172
5.5.2	Reaction data.....	173
5.5.3	XRD patterns.....	176
5.5.4	Post-reaction CHN and TGA analysis .....	178
5.5.5	Post-reaction SEM images .....	181
5.6.	The effect of palladium precursor on the activity of 0.4 wt% Pd/H-ZSM-5 catalyst for direct cracking of methane .....	184
5.6.1	Introduction .....	184
5.6.2	Reaction data.....	185
5.6.3	XRD patterns.....	187
5.6.4	Post-reaction CHN and TGA analysis .....	189
5.6.5	Post-reaction SEM images .....	192
5.6.6	Raman spectroscopy.....	194
5.7.	Effect of support on the activity of palladium catalysts for direct cracking of methane .....	195
5.7.1	Introduction .....	195
5.7.2	Reaction data.....	197
5.7.3	XRD patterns.....	199
5.7.4	Post-reaction CHN and TGA analysis .....	200
5.7.5	Post-reaction SEM images .....	202
5.7.6	Raman spectroscopy.....	204
5.8.	Summary .....	206
<b>6.</b>	<b>Cracking of methane over Ni- and Cu-based catalysts for the production of hydrogen and carbon nanostructures .....</b>	<b>209</b>
6.1.	Introduction .....	209

6.2.	Direct catalytic cracking of methane over 0.4 wt% Ni/HZSM-5, 0.4 wt% Pd/HZSM-5 and Pd-Ni/HZSM-5 catalysts for hydrogen and carbon production: comparative study .....	211
6.2.1	Introduction .....	211
6.2.2	Reaction data .....	211
6.2.3	XRD patterns .....	214
6.2.4	Post-reaction CHN and TGA analyses .....	214
6.2.5	Post-reaction SEM images .....	216
6.3.	Effects of reaction temperature on the direct cracking of methane over the 0.4 wt% Ni/H-ZSM-5 catalyst .....	219
6.3.1	Introduction .....	219
6.3.2	Reaction data .....	219
6.3.3	XRD patterns .....	220
6.3.4	Post-reaction CHN and TGA analyses .....	221
6.3.5	Post-reaction SEM images .....	224
6.4.	Effect of nickel loading on the direct cracking of methane over the Ni/H-ZSM-5 catalyst .....	226
6.4.1	Introduction .....	226
6.4.2	Reaction data .....	227
6.4.3	XRD patterns .....	228
6.4.4	Post-reaction CHN and TGA analyses .....	230
6.4.5	Post-reaction SEM images .....	232
6.5.	Effect of support on the activity of nickel catalysts for the direct cracking of methane .....	233
6.5.1	Introduction .....	233
6.5.2	Reaction data .....	234
6.5.3	XRD patterns .....	237
6.5.4	Post-reaction CHN and TGA analyses .....	239
6.5.5	Post-reaction SEM images .....	241
6.6.	Direct catalytic cracking of methane over 0.4 wt% Cu/HZSM-5 catalyst for hydrogen and carbon production .....	244
6.6.1	Introduction .....	244
6.6.2	Reaction data .....	244
6.6.3	XRD patterns .....	245
6.6.4	Post-reaction CHN and TGA analyses .....	246
6.6.5	Post-reaction SEM images .....	248
6.7.	Summary .....	249
<b>7.</b>	<b>Conclusions and Future work .....</b>	<b>252</b>
7.1.	Future work .....	257
<b>8.</b>	<b>Appendix .....</b>	<b>258</b>
8.1.	Appendix 1 .....	258
8.2.	Appendix 2 .....	259
	<b>References .....</b>	<b>270</b>

## List of figures

<b>Figure 1-1</b> Diagrammatic representation of an individual PEM fuel cell [10].	2
<b>Figure 1-2</b> Diagrammatic representation of the bulk of literature, preferred reaction temperature range for thermal catalytic cracking of methane reaction. Catalysts: 1 – Ni-based, 2 – Fe-based, 3 – carbon-based, 4 – summary of data related to Co, Ni, Fe, Pd, Pt, Cr, Ru, Mo, W catalysts, 5 – non-catalytic cracking [36].	7
<b>Figure 1-3</b> Two theoretical models for crystallite growth due to sintering by (A) atomic migration or (B) crystallite migration [67].	9
<b>Figure 1-4</b> Theoretical model of fouling, crystallite encapsulation and pore plugging of a supported metal catalyst due to carbon deposition [67].	10
<b>Figure 1-5</b> TEM image of the post-reaction Ni/HZSM-5 catalyst applied to methane decomposition at 700 °C [71].	11
<b>Figure 1-6</b> Schematic representation of an amorphous carbon structure (A) [79], and a graphitic carbon structure (B) [80].	12
<b>Figure 1-7</b> Schematic diagrams of single-wall carbon nanotube (SWCNTs) and multi-wall carbon nanotube (MWCNTs) structures [98].	13
<b>Figure 1-8</b> HRTEM images for the carbon materials deposited on the Fe/MgO catalysts at 800 °C [99].	14
<b>Figure 1-9</b> Schematic representation of the two main growth mechanisms of carbon nanotubes [73].	15
<b>Figure 1-10</b> SEM image for the post-reaction 70 wt % Ni/SiO <sub>2</sub> catalyst after reaction at 500 °C, bright spots represent the Ni metal particles located at the tip of the filaments [40].	16
<b>Figure 1-11</b> SEM image for the post-reaction Ni-Si material at 700 °C, conical-shaped metallic nanoparticles are encapsulated at the base ends of the CNTs, as marked with arrows [110].	16
<b>Figure 1-12</b> HRTEM images of CNFs (stacked form), A) a single CNF at low magnification and B) at high magnification (arrows and lines in image (B) represent the direction of fibre axis and graphene layer of carbon nanofibres, respectively [114]). C) Schematic representation that shows the arrangement of graphite layers to the axis of fibre [111].	17
<b>Figure 1-13</b> TEM images of CNFs (herringbone form), (A) and (B) show single CNFs with different angles between the graphite layers [112], C) schematic representation that shows the arrangement of graphite layers with a specific angle to the axis of fibre [115].	18
<b>Figure 1-14</b> Schematic representation of the growth mechanisms of carbon nanofibres (A) and carbon nanotubes (B) [103].	19
<b>Figure 1-15</b> TEM images of bamboo-structured carbon nanotubes observed after methane decomposition over 10 wt % Cu/MgO and 5 wt % Mo/MgO at 850 °C for 1 h, A) low magnification and B) high magnification [116], C) schematic diagram of the growth model of a bamboo tube with a Ni-based catalyst [117].	19
<b>Figure 1-16</b> HRTEM images of the carbon onions formed from methane decomposition over Ni/Al catalyst, (A) HRTEM image of the carbon nano-onions with nickel particle encapsulated, (B) HRTEM image of carbon nano-onions with hollow cores [92].	21

- Figure 1-17** Schematic representation of the growth mechanism of onion-like carbon nanosphere formation, (A) the carbon nano-onion with metal particle filled core, (B) the carbon nano-onion with an empty core [92]. .....22
- Figure 1-18** Scanning electron micrographs demonstrating two morphologies of biogenic iron oxide. A) L shows the shape of hollow micro-tubes or sheaths associated with *Leptothrix ochracea*, G illustrates the shape of twisted stalks with *Gallionella ferruginea* [137], B) hollow micro tubes, sheaths, associated with *Leptothrix ochracea* [138]......24
- Figure 1-19** photographs for some sites of the accumulations of biogenic iron oxide, which are formed by *Leptothrix ochracea* [147]. .....25
- Figure 1-20** Structures of four selected zeolites (from top to bottom: faujasite or zeolites X, Y; zeolite ZSM-12; zeolite ZSM-5 or silicalite-1; zeolite Theta-1 or ZSM-22) and their micropore systems and dimensions [148]. .....27
- Figure 1-21** Scheme for the thermal interconversion of Brønsted to Lewis acid sites in a zeolite framework [150]. .....28
- Figure 1-22** Schematic representation of coke distribution in zeolite [160]. .....30
- Figure 2-1** The site in the River Allander from where the Landfill sample was obtained. .33
- Figure 2-2** The site in the Lennoxton Nail Works from where the Factory sample was obtained. ....33
- Figure 2-3** Schematic representation of the reactor system. ....39
- Figure 3-1** Powder X-ray diffraction pattern of the raw Landfill sample which is consistent with the 2-line ferrihydrite structure  $\text{Fe}_5\text{HO}_8 \cdot 4\text{H}_2\text{O}$ . ....48
- Figure 3-2** Powder X-ray diffraction pattern of the raw Factory samples. 1: quartz ( $\text{SiO}_2$ ) 33-1161; 2: haematite ( $\text{Fe}_2\text{O}_3$ ) 33-0664; 3: clinoferrosilite ( $\text{FeSiO}_3$ ) 17-0548; 4: silicon oxide ( $\text{SiO}_2$ ) 43-0596; 5: aluminium oxide ( $\text{Al}_2\text{O}_3$ ) 31-0026; 6: iron oxide phosphate ( $\text{Fe}_9\text{O}_8\text{PO}_4$ ) 38-0031. ....48
- Figure 3-3** Powder X-ray diffraction patterns of the raw RM samples. 1: goethite ( $\text{FeOOH}$ ) 17-0536; 2: haematite ( $\text{Fe}_2\text{O}_3$ ) 13-0534; 3: gibbsite ( $\text{Al}(\text{OH})_3$ ) 29-0041; 4: quartz ( $\alpha\text{-SiO}_2$ ) 05-0490. ....48
- Figure 3-4** SEM images of (A) raw Landfill sample, (B) a scanned image of the raw Landfill sample to reveal the inner and outer diameters of the tubes, (C) raw Factory sample and (D) raw RM sample. ....52
- Figure 3-5** SEM images and EDX analysis for the raw Landfill sample. (A) SEM images indicated by a square for the tubular shape. (B) EDX analysis for the selected spot indicated by the square in the SEM image (A). (C) SEM image that is indicated by a square for the non-tubular shape. (D) EDX analysis for the selected spot indicated by a square in the SEM image (C). ....53
- Figure 3-6** HRTEM images of raw Landfill and Factory samples. (A) Low magnification image of the raw Landfill sample, (B) high magnification image of the raw Landfill sample, the sheath surface, (C) low magnification image of the raw Factory sample and (D) high magnification image of the raw Factory sample. ....54
- Figure 3-7** Hydrogen formation rates as a function of TOS for  $\text{CH}_4$  cracking over the Landfill, Factory and RM samples in the temperature programme from 600 to 800 °C. The  $\text{CH}_4/\text{N}_2$  flow rate was 12 mL/min and 0.4 g sample mass. ....56

- Figure 3-8** CO formation rates as a function of TOS for CH<sub>4</sub> cracking over the Landfill and Factory samples in the temperature programme from 600 to 800 °C. The CH<sub>4</sub>/N<sub>2</sub> flow rate was 12 mL/min and 0.4 g sample mass.....58
- Figure 3-9** CO<sub>2</sub> formation rates as a function of TOS for CH<sub>4</sub> cracking over the Landfill and Factory samples in the temperature programme from 600 to 800 °C. The CH<sub>4</sub>/N<sub>2</sub> flow rate was 12 mL/min and 0.4 g sample mass.....59
- Figure 3-10** The side product on the walls of the reactor in the temperature range of 600 to 650 °C. ....60
- Figure 3-11** The results of spectral analysis for the side product. (A) The FTIR spectrum, (B) the <sup>1</sup>H NMR spectrum and (C) the <sup>13</sup>C NMR spectrum. ....60
- Figure 3-12** X-ray pattern for post-reaction Landfill sample. 1: iron (Fe) 06-0696; 2: cohenite (Fe<sub>3</sub>C) 34-0001; 3: iron (Fe) 31-0619; 4: graphite-3R 26-1079.....62
- Figure 3-13** X-ray pattern for post-reaction Factory sample. 1: iron oxide (FeO) 39-1088; 2: iron carbide (Fe<sub>3</sub>C) 03-0989; 3: cohenite (Fe<sub>3</sub>C) 35-0772; 4: giniite (FeFe<sub>4</sub>(PO<sub>4</sub>)<sub>4</sub>(OH)<sub>2</sub>·2H<sub>2</sub>O; 5: graphite (C) 23-0064; 6: quartz (SiO<sub>2</sub>) 33-1161.....62
- Figure 3-14** X-ray pattern for post-reaction RM sample. 1: iron (Fe) 06-0696; 2: iron carbide (Fe<sub>3</sub>C) 03-0989; 3: quartz (SiO<sub>2</sub>) 04-0359; 4: graphite (C) 25-0284 .....63
- Figure 3-15** TGA profiles for the post-reaction Landfill, Factory and RM samples. ....65
- Figure 3-16** TGA profiles for the post-reaction Landfill, Factory and RM samples .....66
- Figure 3-17** SEM images of the post-reaction Landfill, Factory and RM sample. (A) The post-reaction Landfill sample shows the formation of carbon filaments, indicated by arrows, (B) the post-reaction Landfill sample shows the remnants of the tubular morphology in the sample, (C) the post-reaction Factory sample and (D) the post-reaction RM sample shows the presence of carbon filaments. ....68
- Figure 3-18** TEM images of the post-reaction Landfill sample. (A) The post-reaction Landfill sample shows that the formation of chain-like carbon fibres and iron metal could be found at the centre of the carbon fibres (B) and (C) onion-like carbon nanospheres. ....69
- Figure 3-19** TEM images of the post-reaction Factory sample. A and B depict the sintering, aggregation of metals and encapsulation of carbon. ....70
- Figure 3-20** H<sub>2</sub> formation rate as a function of TOS for cracking of CH<sub>4</sub> over the Landfill sample at different temperatures. (A) At 600 °C, (B) in the temperature programme from 600 to 700 °C, (C) in the temperature programme from 600 to 750 °C. The CH<sub>4</sub>/N<sub>2</sub> flow rate was 12 mL/min and 0.4 g sample mass.....72
- Figure 3-21** The XRD patterns for the post-reaction Landfill sample at different temperatures at 600 °C, from 600 to 700 °C and from 600 to 750 °C. ....73
- Figure 3-22** The TGA profiles for the post-reaction Landfill samples at different temperatures.(A) At 600 °C, (B) temperature programming from 600 to 700 °C and (C) temperature programming from 600 to 750 °C.....76
- Figure 3-23** SEM images of the post-reaction Landfill sample at 600 °C. (A) The remaining tubular morphology and (B) the appearance of a spherical morphology component. ....77
- Figure 3-24** SEM images of the post-reaction Landfill sample at the temperature programme from 600 to 700 °C. (A) The remaining tubular morphology and (B) the appearance of melted biogenic iron oxide tubes. ....78

- Figure 3-25** SEM images of the post-reaction Landfill sample at the temperature programme from 600 to 750 °C. (A) Low magnification image and (B) high magnification image. ....78
- Figure 3-26** TEM images of the post-reaction Landfill sample at different temperatures. (A) at 600 °C, (B) and (C) at the temperature programme from 600 to 700 °C. ....79
- Figure 3-27** TEM images of the post-reaction Landfill sample in the temperature programme from 600 to 750 °C. (A) the nanospheres graphitic structure and iron particles are encapsulated within graphitic layers and (B) the hollow nanosphere structure. ....80
- Figure 3-28** H<sub>2</sub>, CO and CO<sub>2</sub> formation rates as a function of TOS for CH<sub>4</sub> cracking over the synthetic 2-line ferrihydrites in the temperature programme from 600 to 800 °C. The CH<sub>4</sub>/N<sub>2</sub> flow rate was 12 mL/min and 0.4 g sample mass. ....82
- Figure 3-29** H<sub>2</sub> formation rates as a function of TOS for CH<sub>4</sub> cracking over the synthetic 2-line ferrihydrite and the natural 2-line ferrihydrites (the Landfill sample) in the temperature programme from 600 to 800 °C. The CH<sub>4</sub>/N<sub>2</sub> flow rate was 12 mL/min and 0.4 g sample mass. ....83
- Figure 3-30** The XRD patterns for the fresh and post-reaction synthetic 2-line ferrihydrite. ....84
- Figure 3-31** TGA profile for the post-reaction synthetic 2-line ferrihydrite samples. ....85
- Figure 3-32** SEM images for the fresh and post-reaction synthetic 2-line ferrihydrite sample. (A) The fresh synthetic 2-line ferrihydrite sample and (B) the post-reaction synthetic 2-line ferrihydrite sample. ....87
- Figure 3-33** *In situ* XRD patterns for the Landfill sample at room temperature, 500, 600 and 700 °C. ....88
- Figure 4-1** Powder X-ray diffraction patterns of the raw Landfill sample and calcined Landfill at different temperature. ....95
- Figure 4-2** Raman spectra of Landfill samples after being calcined at different temperature. ....96
- Figure 4-3** Powder X-ray diffraction patterns of the raw Factory sample and calcined Factory at different temperature; (♦) silica (SiO<sub>2</sub>) peaks. ....97
- Figure 4-4** SEM images of (A) Raw Landfill sample, (B) Landfill sample calcined at 300 °C, (C) Landfill sample calcined at 500 °C, (D) Landfill sample calcined at 700 °C and (E) Landfill sample calcined at 900 °C. ....100
- Figure 4-5** SEM images of (A) Raw Factory sample, (B) Factory sample calcined at 300 °C, (C) Factory sample calcined at 500 °C, (D) Factory sample calcined at 700 °C and (E) Factory sample calcined at 900 °C. ....101
- Figure 4-6** Hydrogen formation rates from 600 to 800 °C as a function of time on stream for CH<sub>4</sub> cracking over the raw Landfill sample and calcined Landfill samples. The CH<sub>4</sub>/N<sub>2</sub> flow rate was 12 mL/min and 0.4 g sample mass. ....103
- Figure 4-7** CO formation rates at 600 to 800 °C as a function of time on stream for CH<sub>4</sub> cracking over the non-calcined Landfill and calcined Landfill samples. The CH<sub>4</sub>/N<sub>2</sub> flow rate was 12 mL/min and 0.4 g sample mass. ....105
- Figure 4-8** CO<sub>2</sub> formation rates at 600 to 800 °C as a function of time on stream for CH<sub>4</sub> cracking over the non-calcined Landfill and calcined Landfill samples. The CH<sub>4</sub>/N<sub>2</sub> flow rate was 12 mL/min and 0.4 g sample mass. ....106

- Figure 4-9** Hydrogen formation rates at 600 to 800 °C as a function of time on stream for CH<sub>4</sub> cracking over the raw Factory sample and calcined Factory samples. The CH<sub>4</sub>/N<sub>2</sub> flow rate was 12 mL/min and 0.4 g sample mass.....107
- Figure 4-10** Powder x-ray diffraction patterns for post-reaction non-calcined and calcined Landfill samples at different temperature. ....109
- Figure 4-11** Powder x-ray diffraction patterns for post-reaction non-calcined and calcined Factory samples. 1: iron oxide (FeO); 2: iron carbide (Fe<sub>3</sub>C); 3: cohenite (Fe<sub>3</sub>C); 4: giniite FeFe<sub>4</sub>(PO<sub>4</sub>)<sub>4</sub>(OH)<sub>2</sub>.2H<sub>2</sub>O; 5: graphite (C); 6: quartz (SiO<sub>2</sub>). ....110
- Figure 4-12** TGA profiles for the post-reaction Landfill samples. ....113
- Figure 4-13** TGA profiles for the post-reaction non-calcined and calcined Landfill samples; (A) non-calcined and Landfill samples calcined at 300, 500 and 700 °C; (B) non-calcined and Landfill samples calcined at 900 °C. ....114
- Figure 4-14** TGA profiles for the post-reaction Factory samples. ....115
- Figure 4-15** TGA profiles for the post-reaction Factory samples. ....116
- Figure 4-16** SEM images for the post-reaction (A) non-calcined Landfill sample, (B) Landfill sample calcined at 300 °C, (C) Landfill sample calcined at 500 °C, (D) Landfill sample calcined at 700 °C and (E) Landfill sample calcined at 900 °C. ....119
- Figure 4-17** SEM images for the post-reaction (A) non-calcined Factory sample, (B) Factory sample calcined at 300 °C, (C) Factory sample calcined at 500 °C, (D) Factory sample calcined at 700 °C and (E,F) Factory sample calcined at 900 °C.....121
- Figure 4-18** Hydrogen formation rates at 600 to 800 °C as a function of time on stream for CH<sub>4</sub> cracking over the raw Landfill sample and Landfill sample treated with HCl. The CH<sub>4</sub>/N<sub>2</sub> flow rate was 12 mL/min and 0.4 g sample mass. ....123
- Figure 4-19** Hydrogen formation rates at 600 to 800 °C as a function of time on stream for CH<sub>4</sub> cracking over the raw Factory sample and Factory sample treated with HCl. The CH<sub>4</sub>/N<sub>2</sub> flow rate was 12 mL/min and 0.4 g sample mass. ....124
- Figure 4-20** Powder X-ray diffraction patterns for pre- and post-reaction HCl treated Landfill samples. 1: maghemite ( $\gamma$ -Fe<sub>2</sub>O<sub>3</sub>), 2: Clinoferrosillite (FeSiO<sub>3</sub>) 017-0548 and 3: Iron (Fe) 06-0696. ....126
- Figure 4-21** Powder X-ray diffraction patterns for pre- and post-reaction HCl treated Factory samples.1: Haematite ( $\alpha$ -Fe<sub>2</sub>O<sub>3</sub>) 24-0072, 2: Silica (SiO<sub>2</sub>) 42-1401, 3: Iron (Fe) 06-0696, 4: Iron carbide (Fe<sub>3</sub>C) 35-0772, 5: Silica (SiO<sub>2</sub>) 38-0360, 6: Graphite (C) 25-0284. ....127
- Figure 4-22** TGA profiles for the post-reaction HCl treated Landfill sample (A) and Factory samples (B). ....129
- Figure 4-23** SEM images of (A) raw Landfill sample, (B) pre-reaction treated Landfill sample, (C) raw Factory sample (D) pre-reaction treated Factory sample, (E) post-reaction treated Landfill sample, (F) post-reaction treated Factory sample. ....131
- Figure 4-24** Hydrogen formation rates at 600 to 800 °C as a function of time on stream for CH<sub>4</sub> cracking over the raw Landfill sample and 0.4 wt% Pd/Landfill. The CH<sub>4</sub>/N<sub>2</sub> flow rate was 12 mL/min and 0.4 g sample mass.....133
- Figure 4-25** CO formation rates at 600 to 800 °C as a function of time on stream for CH<sub>4</sub> cracking over the raw Landfill and 0.4 wt% Pd/Landfill samples. The CH<sub>4</sub>/N<sub>2</sub> flow rate was 12 mL/min and 0.4 g sample mass.....134

- Figure 4-26** CO<sub>2</sub> formation rates at 600 to 800 °C as a function of time on stream for CH<sub>4</sub> cracking over the raw Landfill and 0.4 wt% Pd/Landfill samples. The CH<sub>4</sub>/N<sub>2</sub> flow rate was 12 mL/min and 0.4 g sample mass.....135
- Figure 4-27** Hydrogen formation rates at 600 to 800 °C as a function of time on stream for CH<sub>4</sub> cracking over the raw Factory sample and 0.4 wt% Pd/Factory sample. The CH<sub>4</sub>/N<sub>2</sub> flow rate was 12 mL/min and 0.4 g sample mass. ....136
- Figure 4-28** CO formation rates at 600 to 800 °C as a function of time on stream for CH<sub>4</sub> cracking over the raw Factory and 0.4 wt% Pd/ Factory samples. The CH<sub>4</sub>/N<sub>2</sub> flow rate was 12 mL/min and 0.4 g sample mass.....137
- Figure 4-29** CO<sub>2</sub> formation rates at 600 to 800 °C as a function of time on stream for CH<sub>4</sub> cracking over the raw Factory and 0.4 wt% Pd/ Factory samples. The CH<sub>4</sub>/N<sub>2</sub> flow rate was 12 mL/min and 0.4 g sample mass.....138
- Figure 4-30** Powder X-ray diffraction patterns for the pre-reaction (A) and the post-reaction (B) 0.4 wt% Pd/Landfill sample.....139
- Figure 4-31** Powder X-ray diffraction patterns for pre-reaction (A) and post-reaction (B) 0.4 wt% Pd/Factory sample.....140
- Figure 4-32** TGA profiles for the post-reaction 0.4 wt% Pd/Landfill (A) and 0.4 wt% Pd/Factory samples (B). ....142
- Figure 4-33** SEM images of (A) raw Landfill sample, (B) pre-reaction 0.4 wt% Pd/Landfill sample, (C) post-reaction 0.4 wt% Pd/Landfill sample. ....144
- Figure 4-34** SEM images of (A) raw Factory sample, (B) pre-reaction 0.4 wt% Pd/Factory sample, (C) post-reaction 0.4 wt% Pd/Factory sample. ....145
- Figure 5-1** Hydrogen formation rates as a function of time on stream for methane cracking over 0.4 wt% Pd/H-ZSM-5 catalyst at different temperatures in the range of 600 to 900 °C, the methane flow rate was 12 mL/min and 0.4 g catalyst mass. ....152
- Figure 5-2** XRD patterns of 0.4 wt % Pd/H-ZSM-5 in the pre- and post-reaction forms run at different temperatures. ....153
- Figure 5-3** TGA profiles of post-reaction 0.4 wt % Pd/H-ZSM-5 catalyst at different reaction temperatures. ....155
- Figure 5-4** TGA profiles of post-reaction of 0.4 wt % Pd/H-ZSM-5 catalyst at different reaction temperatures. ....156
- Figure 5-5** SEM images of post-reaction 0.4 wt % Pd/H-ZSM-5 catalyst at different temperatures in the range from 600 to 900 °C. ....158
- Figure 5-6** TEM images of post-reaction 0.4 wt % Pd/H-ZSM-5 catalyst at different temperatures in the range from 650 to 750 °C. ....161
- Figure 5-7** TEM images of post-reaction 0.4 wt % Pd/H-ZSM-5 catalyst at reaction temperatures of 800 and 900 °C.....162
- Figure 5-8** Raman spectra for the post-reaction 0.4 wt % Pd/H-ZSM-5 catalyst at different reaction temperatures. ....164
- Figure 5-9** Hydrogen formation rates as a function of time on stream for 0.4 wt % Pd/H-ZSM-5 catalyst with varying flow rates at a reaction temperature of 800 °C and 0.4 g catalyst mass.....166
- Figure 5-10** XRD patterns of 0.4 wt % Pd/H-ZSM-5 in the pre- and post-reaction forms at different CH<sub>4</sub> flow rates. ....167

- Figure 5-11** TGA profiles for the post-reaction of 0.4 wt % Pd/H-ZSM-5 catalyst at different CH<sub>4</sub> flow rates. ....168
- Figure 5-12** TGA profiles for the post-reaction of 0.4 wt % Pd/H-ZSM-5 catalyst at different CH<sub>4</sub> flow rates. ....169
- Figure 5-13** Post-reaction SEM images for 0.4 wt% Pd/H-ZSM-5 catalyst at different CH<sub>4</sub> flow rates in the range from 12 to 48 mL/min. ....170
- Figure 5-14** Raman spectra for the post-reaction 0.4 wt % Pd/H-ZSM-5 catalyst at different CH<sub>4</sub> flow rates in the range of 12 to 48 mL/min. ....171
- Figure 5-15** Hydrogen formation rates as a function of time on stream for the parent 0.4 wt % Pd/H-ZSM-5 catalyst, and those doped with Fe<sup>3+</sup>, Ni<sup>2+</sup>, Cu<sup>2+</sup> and Co<sup>2+</sup> (dopant metal M/Pd atomic ratio of 0.25), the reaction temperature was 800 °C and 0.4 g catalyst mass. ....174
- Figure 5-16** Hydrogen formation rates as a function of time on stream for methane cracking over calcined H-ZSM-5, 0.1 wt % Fe/H-ZSM-5, 0.1 wt % Ni/H-ZSM-5, 0.1 wt % Co/H-ZSM-5 and 0.1 wt % Cu/H-ZSM-5 catalysts, the reaction temperature was 800 °C, the methane flow rate was 12 mL/min and 0.4 g catalyst mass. ....175
- Figure 5-17** XRD patterns of 0.4 wt % Pd/H-ZSM-5 and those doped with Fe, Ni, Co and Cu in the pre-reaction (A) forms, and post-reaction (B) forms, dopant metal M/Pd atomic ratio of 0.25. ....178
- Figure 5-18** TGA profiles of post-reaction 0.4 wt % Pd/H-ZSM-5 and those doped with Fe, Ni, Co and Cu (dopant metal M/Pd atomic ratio of 0.25). ....179
- Figure 5-19** TGA profiles for the post-reaction 0.4 wt % Pd/H-ZSM-5 and those doped with Fe, Ni, Co and Cu (dopant metal M/Pd atomic ratio of 0.25). ....180
- Figure 5-20** SEM images of post-reaction (A) non-doped catalyst 0.4 wt % Pd/H-ZSM-5, (B) doped with Fe<sup>3+</sup>, (C) doped with Ni<sup>2+</sup>, (D) doped with Co<sup>2+</sup> and (E) doped with Cu<sup>2+</sup> (dopant metal M/Pd atomic ratio of 0.25). ....183
- Figure 5-21** SEM image of post-reaction Pd-Ni/H-ZSM-5 (dopant metal Ni/Pd atomic ratio of 0.25). ....184
- Figure 5-22** Hydrogen formation rates as a function of time on stream for methane cracking over 0.4 wt % Pd/H-ZSM-5 catalyst prepared from different palladium precursors, the reaction temperature of 800 °C, the methane flow rate was 12 mL/min and 0.4 g catalyst mass. ....186
- Figure 5-23** XRD patterns of 0.4 wt % Pd/H-ZSM-5 in the pre-reaction (A) and post-reaction (B) forms that prepared from different Pd precursors. ....188
- Figure 5-24** TGA profiles of post-reaction 0.4 wt% Pd/H-ZSM-5 catalysts prepared from different Pd precursors. ....190
- Figure 5-25** TGA profiles for the post-reaction 0.4 wt% Pd/H-ZSM-5 catalysts prepared from different Pd precursors. ....191
- Figure 5-26** SEM images of post-reaction 0.4 wt % Pd/H-ZSM-5 catalysts prepared from different Pd precursors. ....193
- Figure 5-27** Raman spectra of post-reaction 0.4 wt% Pd/H-ZSM-5 catalyst prepared from different Pd precursors. ....194
- Figure 5-28** Hydrogen formation rates as a function of time on stream for 0.4 wt% Pd/H-ZSM-5, 0.4 wt% Pd/SiO<sub>2</sub> and 0.4 wt% Pd/γ-Al<sub>2</sub>O<sub>3</sub>, the reaction temperature was 800 °C, the methane flow rate was 12 mL/min and 0.4 g catalyst mass. ....197

<b>Figure 5-29</b> XRD pattern of 0.4 wt% Pd/SiO <sub>2</sub> in the pre- and post-reaction forms.....	199
<b>Figure 5-30</b> XRD pattern of 0.4 wt% Pd/ $\gamma$ -Al <sub>2</sub> O <sub>3</sub> in the pre- and post-reaction forms.....	200
<b>Figure 5-31</b> TGA profiles for the post-reaction 0.4 wt% Pd/H-ZSM-5, 0.4 wt% Pd/SiO <sub>2</sub> and 0.4 wt% Pd/ $\gamma$ -Al <sub>2</sub> O <sub>3</sub> catalysts.....	201
<b>Figure 5-32</b> TGA profiles for the post-reaction 0.4 wt% Pd/H-ZSM-5, 0.4 wt% Pd/SiO <sub>2</sub> and 0.4 wt% Pd/ $\gamma$ -Al <sub>2</sub> O <sub>3</sub> catalysts.....	202
<b>Figure 5-33</b> SEM images of post-reaction (A,B) 0.4 wt% Pd/H-ZSM-5, (C,D) 0.4 wt% Pd/SiO <sub>2</sub> and (E,F) 0.4 wt% Pd/ $\gamma$ -Al <sub>2</sub> O <sub>3</sub> catalysts.....	204
<b>Figure 5-34</b> Raman spectra for the post-reaction 0.4 wt% Pd/H-ZSM-5, 0.4 wt% Pd/SiO <sub>2</sub> and 0.4 wt% Pd/ $\gamma$ -Al <sub>2</sub> O <sub>3</sub> catalysts.....	205
<b>Figure 6-1</b> Hydrogen formation rates as a function of time on stream for 0.4 wt% Ni/H-ZSM-5, 0.4 wt% Pd/H-ZSM-5 and Pd-Ni/H-ZSM-5 catalysts (dopant metal Pd/Ni atomic ratio of 0.25), the reaction temperature of 800 °C, the methane flow rate was 12 mL/min and 0.4 g catalyst mass.....	212
<b>Figure 6-2</b> XRD patterns of 0.4 wt% Ni/HZSM-5, 0.4 wt% Pd/H-ZSM-5 and the 0.4 wt% Ni/HZSM-5 doped with Pd in the pre-reaction (A) forms, and post-reaction (B) forms...	214
<b>Figure 6-3</b> TGA profiles for the post-reaction of 0.4 wt% Ni/HZSM-5, 0.4 wt% Pd/H-ZSM-5 and the 0.4 wt% Ni/HZSM-5 doped with Pd (dopant metal Pd/Ni atomic ratio of 0.25). .....	215
<b>Figure 6-4</b> TGA profiles for the post-reaction of 0.4 wt% Ni/HZSM-5, 0.4 wt% Pd/H-ZSM-5 and the 0.4 wt% Ni/HZSM-5 doped with Pd (dopant metal Pd/Ni atomic ratio of 0.25), .....	216
<b>Figure 6-5</b> SEM images for the post-reaction 0.4 wt% Ni/HZSM-5 (A), 0.4 wt% Pd/H-ZSM-5 (B), and the 0.4 wt% Ni/HZSM-5 doped with Pd (C).....	218
<b>Figure 6-6</b> Hydrogen formation rates as a function of time on stream for methane cracking over 0.4 wt% Ni/H-ZSM-5 catalyst at different temperatures in range of 600 to 900 °C, the methane flow rate is 12 mL/min and 0.4 g catalyst mass. ....	220
<b>Figure 6-7</b> XRD pattern of 0.4 wt% Ni/H-ZSM-5 in the pre- and post-reaction forms at run different temperatures. ....	221
<b>Figure 6-8</b> TGA profiles for the post-reaction of 0.4 wt% Ni/H-ZSM-5 catalyst run at different reaction temperatures. ....	222
<b>Figure 6-9</b> TGA profiles for the post-reaction of 0.4 wt% Ni/H-ZSM-5 catalyst run at different reaction temperatures. ....	223
<b>Figure 6-10</b> SEM images of the post-reaction 0.4 wt% Ni/H-ZSM-5 catalyst run at different reaction temperatures. ....	225
<b>Figure 6-11</b> Hydrogen formation rates as a function of time on stream for methane cracking over Ni/H-ZSM-5 catalysts loaded with different amounts of Ni: 0.4, 4 and 8 wt%, the reaction temperature of 800 °C, the methane flow rate was 12 mL/min. ....	228
<b>Figure 6-12</b> XRD patterns of the pre- (A) and post-reaction (B) Ni/H-ZSM-5 catalysts loaded with different amounts of Ni: 0.4, 4 and 8 wt%. ....	229
<b>Figure 6-13</b> TGA profiles of the post-reaction Ni/H-ZSM-5 catalysts loaded with different amounts of Ni: 0.4, 4 and 8 wt%. ....	231
<b>Figure 6-14</b> TGA profiles of the post-reaction Ni/H-ZSM-5 catalysts loaded with different amounts of Ni: 0.4, 4 and 8 wt%. ....	232

- Figure 6-15** SEM images of the post-reaction 0.4 wt% Ni/H-ZSM-5 catalyst (A), 4 wt% Ni/H-ZSM-5 catalyst (B) and 8 wt% Ni/H-ZSM-5 catalyst (C).....233
- Figure 6-16** Hydrogen formation rates as a function of time on stream for 0.4 wt% Ni/H-ZSM-5, 0.4 wt% Ni/SiO<sub>2</sub>, 0.4 wt% Ni/ $\gamma$ -Al<sub>2</sub>O<sub>3</sub> and 0.4 wt% Ni/SiO<sub>2</sub>.xH<sub>2</sub>O (silicic acid), the reaction temperature of 800 °C, the methane flow rate was 12 mL/min and 0.4 g catalyst mass.....235
- Figure 6-17** XRD patterns of the pre- and post-reaction 0.4 wt% Ni/SiO<sub>2</sub>, 0.4 wt% Ni/SiO<sub>2</sub>.xH<sub>2</sub>O and 0.4 wt% Ni/ $\gamma$ -Al<sub>2</sub>O<sub>3</sub> catalysts. ....238
- Figure 6-18** TGA profiles of the post-reaction 0.4 wt% Ni/H-ZSM-5, 0.4 wt% Ni/SiO<sub>2</sub>, 0.4 wt% Ni/SiO<sub>2</sub>.xH<sub>2</sub>O and 0.4 wt% Ni/ $\gamma$ -Al<sub>2</sub>O<sub>3</sub> catalysts. ....240
- Figure 6-19** TGA profiles of the post-reaction 0.4 wt% Ni/H-ZSM-5, 0.4 wt% Ni/SiO<sub>2</sub>, 0.4 wt% Ni/SiO<sub>2</sub>.xH<sub>2</sub>O and 0.4 wt% Ni/ $\gamma$ -Al<sub>2</sub>O<sub>3</sub> catalysts. ....241
- Figure 6-20** SEM images of the post-reaction (A) 0.4 wt% Ni/H-ZSM-5, (B) 0.4 wt% Ni/SiO<sub>2</sub>, (C) 0.4 wt% Ni/SiO<sub>2</sub>.xH<sub>2</sub>O and (D) 0.4 wt% Ni/ $\gamma$ -Al<sub>2</sub>O<sub>3</sub> catalysts.....242
- Figure 6-21** Hydrogen formation rates as a function of time on stream for 0.4 wt% Cu/H-ZSM-5 and 0.4 wt% Ni/H-ZSM-5, the reaction temperature of 800 °C, the methane flow rate was 12 mL/min and 0.4 g catalyst mass.....245
- Figure 6-22** XRD patterns of the pre- and post-reaction 0.4 wt% Cu/HZSM-5 catalysts.246
- Figure 6-23** TGA profiles of the post-reaction 0.4 wt% Cu/H-ZSM-5 and 0.4 wt% Ni/H-ZSM-5. ....247
- Figure 6-24** TGA profiles of the post-reaction 0.4 wt% Cu/H-ZSM-5 and 0.4 wt% Ni/H-ZSM-5. ....248
- Figure 6-25** Post-reaction SEM images of 0.4 wt% Cu/H-ZSM-5 catalyst.....249
- Figure 8-1** Methane conversion as a function of TOS for CH<sub>4</sub> cracking over the Landfill, Factory and RM samples in the temperature programme from 600 to 800 °C. The CH<sub>4</sub>/N<sub>2</sub> flow rate was 12 mL/min and 0.4 g sample mass. These conversions correspond to hydrogen formation rates in Figure 3-7. ....259
- Figure 8-2** Methane conversion as a function of TOS for cracking of CH<sub>4</sub> over the Landfill sample at different temperatures. (A) At 600 °C, (B) in the temperature programme from 600 to 700 °C, (C) in the temperature programme from 600 to 750 °C. The CH<sub>4</sub>/N<sub>2</sub> flow rate was 12 mL/min and 0.4 g sample mass. These conversions are corresponding to hydrogen formation rates in Figure 3-20. ....260
- Figure 8-3** Methane conversion as a function of TOS for CH<sub>4</sub> cracking over the synthetic 2-line ferrihydrite and the natural 2-line ferrihydrites (the Landfill sample) in the temperature programme from 600 to 800 °C. The CH<sub>4</sub>/N<sub>2</sub> flow rate was 12 mL/min and 0.4 g sample mass. These conversions are corresponding to hydrogen formation rates in Figure 3-29.....261
- Figure 8-4** Methane conversion as a function of TOS for CH<sub>4</sub> cracking over the raw Landfill sample and calcined Landfill samples in the temperature programme from 600 to 800 °C. The CH<sub>4</sub>/N<sub>2</sub> flow rate was 12 mL/min and 0.4 g sample mass. These conversions correspond to hydrogen formation rates in Figure 4-6.....261
- Figure 8-5** Methane conversion as a function of TOS for CH<sub>4</sub> cracking over the raw Factory sample and calcined Factory samples in the temperature programme from 600 to 800 °C. The CH<sub>4</sub>/N<sub>2</sub> flow rate was 12 mL/min and 0.4 g sample mass. These conversions correspond to hydrogen formation rates in Figure 4-9.....262

- Figure 8-6** Methane conversion as a function of TOS for CH<sub>4</sub> cracking over the raw Landfill sample and the Landfill sample treated with HCl in the temperature programme from 600 to 800 °C. The CH<sub>4</sub>/N<sub>2</sub> flow rate was 12 mL/min and 0.4 g sample mass. These conversions correspond to hydrogen formation rates in Figure 4-18. ....262
- Figure 8-7** Methane conversion as a function of TOS for CH<sub>4</sub> cracking over the raw Factory sample and the Factory sample treated with HCl in the temperature programme from 600 to 800 °C. The CH<sub>4</sub>/N<sub>2</sub> flow rate was 12 mL/min and 0.4 g sample mass. These conversions correspond to hydrogen formation rates in Figure 4-19. ....263
- Figure 8-8** Methane conversion as a function of TOS for CH<sub>4</sub> cracking over the raw Landfill sample and 0.4 wt% Pd/ Landfill sample in the temperature programme from 600 to 800 °C. The CH<sub>4</sub>/N<sub>2</sub> flow rate was 12 mL/min and 0.4 g sample mass. These conversions correspond to hydrogen formation rates in Figure 4-24. ....263
- Figure 8-9** Methane conversion as a function of TOS for CH<sub>4</sub> cracking over the raw Factory sample and 0.4 wt% Pd/ Factory sample in the temperature programme from 600 to 800 °C. The CH<sub>4</sub>/N<sub>2</sub> flow rate was 12 mL/min and 0.4 g sample mass. These conversions correspond to hydrogen formation rates in Figure 4-27. ....264
- Figure 8-10** Methane conversion as a function of time on stream for methane cracking over 0.4 wt% Pd/H-ZSM-5 catalyst at different temperatures in the range of 600 to 900 °C, the methane flow rate was 12 mL/min and 0.4 g catalyst mass. These conversions correspond to hydrogen formation rates in Figure 5-1.....264
- Figure 8-11** Methane conversion as a function of time on stream for methane cracking over 0.4 wt % Pd/H-ZSM-5 catalyst with varying flow rates at a reaction temperature of 800 °C and 0.4 g catalyst mass. These conversions correspond to hydrogen formation rates in Figure 5-9.....265
- Figure 8-12** Methane conversion as a function of time on stream for CH<sub>4</sub> cracking over the parent 0.4 wt % Pd/H-ZSM-5 catalyst, and those doped with Fe<sup>3+</sup>, Ni<sup>2+</sup>, Cu<sup>2+</sup> and Co<sup>2+</sup> (dopant metal M/Pd atomic ratio of 0.25), the reaction temperature was 800 °C and 0.4 g catalyst mass. These conversions correspond to hydrogen formation rates in Figure 5-15. ....265
- Figure 8-13** Methane conversion as a function of time on stream for methane cracking over 0.4 wt % Pd/H-ZSM-5 catalyst prepared from different palladium precursors, the reaction temperature of 800 °C, the methane flow rate was 12 mL/min and 0.4 g catalyst mass.. These conversions correspond to hydrogen formation rates in Figure 5-22.....266
- Figure 8-14** Methane conversion as a function of time on stream for methane cracking over 0.4 wt% Pd/H-ZSM-5, 0.4 wt% Pd/SiO<sub>2</sub> and 0.4 wt% Pd/γ-Al<sub>2</sub>O<sub>3</sub>, the reaction temperature was 800 °C, the methane flow rate was 12 mL/min and 0.4 g catalyst mass.. These conversions correspond to hydrogen formation rates in Figure 5-28.....266
- Figure 8-15** Methane conversion as a function of time on stream for methane cracking over 0.4 wt% Ni/H-ZSM-5, 0.4 wt% Pd/H-ZSM-5 and Pd-Ni/H-ZSM-5 catalysts (dopant metal Pd/Ni atomic ratio of 0.25), the reaction temperature of 800 °C, the methane flow rate was 12 mL/min and 0.4 g catalyst mass. These conversions correspond to hydrogen formation rates in Figure 6-1.....267
- Figure 8-16** Methane conversion as a function of time on stream for methane cracking over 0.4 wt% Ni/H-ZSM-5 catalyst at different temperatures in range of 600 to 900 °C, the methane flow rate is 12 mL/min and 0.4 g catalyst mass. These conversions correspond to hydrogen formation rates in Figure 6-6. ....267

**Figure 8-17** Methane conversion as a function of time on stream for methane cracking over Ni/H-ZSM-5 catalysts loaded with different amounts of Ni: 0.4, 4 and 8 wt%, the reaction temperature of 800 °C, the methane flow rate was 12 mL/min. These conversions correspond to hydrogen formation rates in Figure 6-11.....268

**Figure 8-18** Methane conversion as a function of time on stream for methane cracking over 0.4 wt% Ni/H-ZSM-5, 0.4 wt% Ni/SiO<sub>2</sub>, 0.4 wt% Ni/γ-Al<sub>2</sub>O<sub>3</sub> and 0.4 wt% Ni/SiO<sub>2</sub>.xH<sub>2</sub>O (silicic acid), the reaction temperature of 800 °C, the methane flow rate was 12 mL/min and 0.4 g catalyst mass. These conversions correspond to hydrogen formation rates in Figure 6-16. ....268

**Figure 8-19** Methane conversion as a function of time on stream for methane cracking over 0.4 wt% Cu/H-ZSM-5 and 0.4 wt% Ni/H-ZSM-5, the reaction temperature of 800 °C, the methane flow rate was 12 mL/min and 0.4 g catalyst mass. These conversions correspond to hydrogen formation rates in Figure 6-21.....269

## List of tables

<b>Table 1-1</b> The capacity of world hydrogen production from different sources [13, 16].....	3
<b>Table 1-2</b> The major iron oxide and oxyhydroxide phases [132]. .....	23
<b>Table 2-1</b> the precursors and quantities of materials used in the preparation of 2 g of 0.4 % Pd/H-ZSM-5 catalyst, and those impregnated with Fe <sup>3+</sup> , Ni <sup>2+</sup> , Cu <sup>2+</sup> and Co <sup>2+</sup> .....	36
<b>Table 2-2</b> The quantities of materials used in the preparation of 0.4 % Pd/ H-ZSM-5 catalyst by different precursors. ....	36
<b>Table 2-3</b> The quantities of materials used in the preparation of 0.4 % Pd/ $\gamma$ -Al <sub>2</sub> O <sub>3</sub> and 0.4 % Pd/SiO <sub>2</sub> catalyst.....	37
<b>Table 2-4</b> The quantities of materials used in the preparation of Ni/HZSM-5 with different Ni loading, 0.4 % Ni-Pd/HZSM-5 and 0.4 % Cu/HZSM-5 catalyst.....	37
<b>Table 2-5</b> The quantities of materials used in the preparation of 0.4 wt% Ni/ $\gamma$ -Al <sub>2</sub> O <sub>3</sub> , 0.4 wt% Ni/SiO <sub>2</sub> and 0.4 wt% Ni/SiO <sub>2</sub> .xH <sub>2</sub> O catalyst. ....	38
<b>Table 3-1</b> ICP-OES analysis for elemental content of the raw Landfill, Factory and RM samples.....	50
<b>Table 3-2</b> CHN analysis for raw Landfill, Factory and RM samples.....	51
<b>Table 3-3</b> BET surface area analysis of raw Landfill, Factory and RM samples.....	55
<b>Table 3-4</b> Post-reaction CHN analysis of the Landfill, Factory and RM samples .....	64
<b>Table 3-5</b> BET surface area analysis of post-reaction Landfill, Factory and RM samples.....	67
<b>Table 3-6</b> CHN analysis for the post-reaction Landfill sample at different temperatures ..	75
<b>Table 3-7</b> Analysis of surface area for the Landfill sample both before and after exposure to methane at different temperatures.....	81
<b>Table 3-8</b> BET surface area analysis for the fresh and post-reaction synthetic 2-line ferrihydrite.....	86
<b>Table 4-1</b> CHN analysis for raw and calcined Landfill and Factory samples at 300, 500, 700 and 900 °C.....	97
<b>Table 4-2</b> BET surface area analysis for raw Landfill and Factory samples and those calcined at 300, 500, 700 and 900 °C. ....	98
<b>Table 4-3</b> CHN analyses for the post-reaction non-calcined and calcined Landfill and Factory samples at 300, 500, 700 and 900 °C.....	111
<b>Table 4-4</b> BET surface area analysis for the pre-reaction and post-reaction non-calcined and calcined Landfill and Factory samples at different temperature of 300, 500, 700 and 900 °C. ....	117
<b>Table 4-5</b> ICP-OES analysis for elemental content of the raw Landfill and Factory samples and Landfill and Factory samples treated with HCl.....	125
<b>Table 4-6</b> CHN analysis for the Non-treated Landfill and Factory samples and their post-reaction form and Pre-reaction treated Landfill and Factory sample with HCl and their post-reaction form. ....	128
<b>Table 4-7</b> BET surface area analysis for the pre- and post-reaction raw and treated Landfill and Factory samples. ....	130

<b>Table 4-8</b> CHN analysis for the pre- and post-reaction 0.4 wt% Pd/Landfill and 0.4 wt% Pd/Factory samples and the pre- and post-reaction raw Landfill and Factory samples.....	141
<b>Table 4-9</b> BET surface area analysis of raw Landfill and Factory samples and those doped with Pd. ....	143
<b>Table 5-1</b> CHN analysis for the post-reaction 0.4 wt% Pd/H-ZSM-5 catalyst at different reaction temperature.....	154
<b>Table 5-2</b> The result of intensity ratio $I_D/I_G$ for the D band and G band from Raman spectra for carbon produced at different reaction temperatures. ....	164
<b>Table 5-3</b> CHN analysis for the post-reaction of 0.4 wt % Pd/H-ZSM-5 catalyst at different CH <sub>4</sub> flow rates. ....	168
<b>Table 5-4</b> The result of intensity ratio $I_D/I_G$ for the D and G bands from Raman spectra for carbon produced at different CH <sub>4</sub> flow rates in the range from 12 to 48 mL/min.....	171
<b>Table 5-5</b> CHN analysis for the post-reaction 0.4 wt % Pd/H-ZSM-5 catalyst and those doped with Fe, Ni, Co and Cu (dopant metal M/Pd atomic ratio of 0.25). ....	179
<b>Table 5-6</b> CHN analysis for the post-reaction 0.4 wt% Pd/H-ZSM-5 catalyst prepared from different Pd precursors. ....	189
<b>Table 5-7</b> The result of intensity ratio $I_D/I_G$ for the D and G bands from Raman spectra for carbon produced by 0.4 wt% Pd/H-ZSM-5 catalysts prepared from different Pd precursors. ....	195
<b>Table 5-8</b> BET surface area analysis of 0.4 wt% Pd/H-ZSM-5, 0.4 wt% Pd/SiO <sub>2</sub> and 0.4 wt% Pd/ $\gamma$ -Al <sub>2</sub> O <sub>3</sub> samples.....	198
<b>Table 5-9</b> CHN analysis for the post-reaction 0.4 wt% Pd/H-ZSM-5, 0.4 wt% Pd/SiO <sub>2</sub> and 0.4 wt% Pd/ $\gamma$ -Al <sub>2</sub> O <sub>3</sub> catalysts.....	201
<b>Table 5-10</b> $I_D/I_G$ ratios for the D band and G band from Raman spectra for carbon produced by 0.4 wt% Pd/H-ZSM-5, 0.4 % Pd/SiO <sub>2</sub> and 0.4 % Pd/ $\gamma$ -Al <sub>2</sub> O <sub>3</sub> catalysts. ....	205
<b>Table 6-1</b> CHN analysis for the post-reaction 0.4 wt% Ni/H-ZSM-5, 0.4 wt% Pd/H-ZSM-5 and Pd-Ni/H-ZSM-5 catalysts.....	215
<b>Table 6-2</b> CHN analysis for the post-reaction 0.4 wt% Ni/H-ZSM-5 catalyst at different reaction temperatures. ....	222
<b>Table 6-3</b> CHN analyses of the post-reaction Ni/H-ZSM-5 catalysts loaded with different amounts of Ni: 0.4, 4 and 8 wt%.....	230
<b>Table 6-4</b> BET surface area analyses of Ni/H-ZSM-5, Ni/SiO <sub>2</sub> , Ni/ $\gamma$ -Al <sub>2</sub> O <sub>3</sub> and 0.4 wt% Ni/SiO <sub>2</sub> .xH <sub>2</sub> O samples. ....	236
<b>Table 6-5</b> CHN analyses of the post-reaction 0.4 wt % Ni/H-ZSM-5, 0.4 wt % Ni/SiO <sub>2</sub> , 0.4 wt % Ni/ $\gamma$ -Al <sub>2</sub> O <sub>3</sub> and 0.4 wt % Ni/SiO <sub>2</sub> .xH <sub>2</sub> O catalysts. ....	239
<b>Table 6-6</b> CHN analysis for the post-reaction 0.4 wt% Cu/H-ZSM-5 and 0.4 wt% Ni/H-ZSM-5. ....	247
<b>Table 7-1</b> the behaviour of the iron-containing wastes materials, in the temperature programme from 600 to 800 °C. The CH <sub>4</sub> /N <sub>2</sub> flow rate was 12 mL/min and 0.4 g sample mass.....	255
<b>Table 7-2</b> the behaviour of prepared catalysts, the reaction temperature was 800 °C, the methane flow rate was 12 mL/min, time on stream was 300 minutes and 0.4 g catalyst mass.....	256

## Publication

- Abdulrahman Alharthi, Ross A. Blackley, T. Hugh Flowers, Justin S. J. Hargreaves, Ian D. Pulford, James Wigzell and Wuzong Zhou, " Iron ochre – a pre-catalyst for the cracking of methane" , Journal of Chemical Technology & Biotechnology (2014), accepted for publication.

## Acknowledgements

I would like to express my sincere thanks and appreciation to all people who were involved directly or indirectly in helping me to complete this thesis. First and foremost, I would like to thank my supervisor Dr Justin Hargreaves for all the help, guidance, knowledge, encouragement and enthusiasm that he has given me during my PhD study. It was really a great experience to study under his supervision.

I would like to thank Mr Ron Spence for his help with the design and construction of the reactor system and Raman spectroscopy analyses. I would also like to thank Mr Andy Monaghan for all his help especially with XRD and TGA analyses. A big thanks to Mr Jim Gallagher for his kind assistance with the SEM analyses. A special thanks to Mrs Kim Wilson for her help in performing CHN analyses. I also extend my thanks to Mr Ross Blackley, University of St. Andrews, with his kind assistance in performing TEM analyses.

I would also like to express my appreciation to Prof. Rafiq Siddiqui for his advice and help when I was looking for a PhD position and for introducing me to Dr Justin Hargreaves group.

I would like to acknowledge my colleagues in the department of chemistry, Alexander Munnoch, Liam France, Muhammad Bilal, Javed Ali, Matar Al Shalwi, Abbas Lafta, Mohanad Al-Hachamii and Feras Alshehri, who assisted me at many points throughout my study.

My gratitude extends to my friends Mshari Alotaibi, Abdulsalam Alkhalidi, Mohammed Albarrati, Adel Alharf and Mohammed Alwashih and Faleh Alanzi, for making life in UK enjoyable and productive and also for their assistance and support about some personal issues.

My massive thanks and love goes to my parents, sisters and brothers for their support and encouragement. A special acknowledgement must go to my wife and children for their patience and sacrifice during my life and my study.

Finally, I am grateful to Salman bin Abdulaziz University, and the Saudi Cultural Bureau in London for generously providing funding.

**Author's declaration**

The work contained in this thesis, submitted for the degree of doctor of philosophy, is my own original work, except where due reference is made to others. No material within has been previously submitted for a degree at this or any other university.

# 1. Introduction

## 1.1. General introduction

Energy is the basis of numerous aspects of modern life. This has led to high demand. Hence, researchers have tried to develop various energy sources [1]. The energy derived from the fossil fuel (coal, petroleum and natural gas) has been associated with some major challenges such as sustainability and environmental influences. Fossil fuels are finite non-renewable sources of energy which may run out in the medium term future due to the rapid increase in demand and the limited reserves in the earth. The combustion of fossil fuels releases CO<sub>2</sub>, CO, NO<sub>x</sub>, and SO<sub>2</sub> into the atmosphere, which result in the damage to the Earth's climate and environment [2, 3]. However, the use of renewable energy sources, such as wind, solar, and biomass will not be the main energy sources in the near term due to their high cost and immature technology. Although nuclear energy provides an alternative energy source it is also not universally acceptable [4].

The use of hydrogen as an alternative fuel is more acceptable environmentally than hydrocarbons. Hydrogen has many environmental advantages over hydrocarbons, for example it is a source of clean energy and it can be produced using various methods and from a number of available materials. In addition, it has many potential uses that include powering of non-polluting vehicles, heating homes and fuelling cleaner aircraft. Other examples of hydrogen's uses are: a) the petroleum industry, b) the production of ammonia, c) the hydrogenation of fats and oils, d) fuel for rockets and e) fuel cells. It is expected that hydrogen will be the main source of energy in the future [5-7]. However, attention needs to be directed towards the sources and means of production of hydrogen to ensure that they are not more environmentally damaging than direct application of hydrocarbons and that they are sufficiently efficient.

One of the most important potential applications for H<sub>2</sub> is to operate fuel cells. Fuel cells are electrochemical devices in which convert chemical energy into electrical energy with high efficiencies and very low environmental impact. In addition, they demonstrate roughly two to three times greater efficiency than internal combustion engines in converting fuel to electricity [8, 9].

Fuel cells can be sub-divided into two main types; high temperature and low temperature. All fuel cells possess the same basic operating principle [8]. The proton exchange membrane (PEM) fuel cell is a low temperature fuel cell which requires relatively pure hydrogen as a fuel and cannot operate for any significant time in the presence of CO concentrations greater than 20 ppm [9]. Figure 1-1 presents a diagrammatic representation of a proton exchange membrane (PEM) fuel cell.

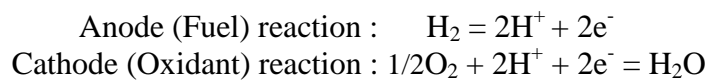
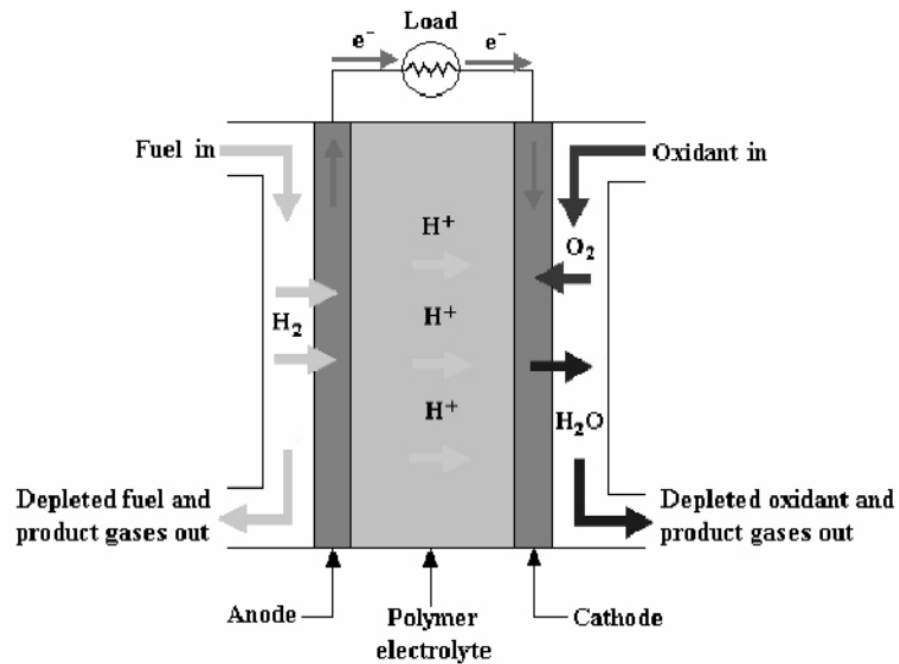


**Figure 1-1** Diagrammatic representation of an individual PEM fuel cell [10].

The fuel, hydrogen, and an oxidant, such as air, can be supplied to the device from external sources. On one side of the cell, hydrogen is passed over the anode plate where it is catalytically split into protons and electrons. On the other side of the cell, oxygen passes over the cathode plate. The negatively charged electrons, travel along an external circuit to the cathode plate to create an electrical current, while the positively charged protons pass through the polymer electrolyte membrane (PEM) to the cathode plate. At the cathode, the electrons, protons and oxygen molecules combine to produce pure water as the only reaction product, which passes out of the cell [8, 10].

Due to the growing interest in proton exchange membrane (PEM) fuel cells as alternatives to internal combustion engines, it is estimated that the demand for hydrogen production will be increased [11, 12].

## 1.2. Hydrogen production

Hydrogen is the simplest element and the most common gas in the universe. It is never naturally uncombined on Earth and is always combined with other elements such as oxygen, to form water, or carbon, to form hydrocarbons. Therefore, it has to be especially produced and for this reason it is not considered a primary source of energy. Hydrogen can be produced from many hydrogen-containing sources such as water, hydrocarbons and even biological materials. Additionally, it can be easily produced from synthesised hydrogen carriers such as methanol and ammonia [13].

Hydrogen is presently produced in several different ways, mainly from water, biomass and fossil fuels. Hydrogen can be produced from water by electrolysis, but this method is costly. Pyrolysis or gasification of biomass can produce hydrogen with mixture gases, such as CH<sub>4</sub>, CO<sub>2</sub>, CO and N<sub>2</sub>, which requires their removal. Hydrogen may be generated from fossil fuels (oil and natural gas) *via* various methods, for instance steam reforming of natural gas, coal gasification, partial oxidation of hydrocarbons and thermal cracking of natural gas [13-15]. Approximately half (48 %) of the used hydrogen in the world is produced from steam reforming (SR) of natural gas which is considered the most economical route from hydrocarbon feedstocks [13]. Other contributions to the production of hydrogen are based mainly on partial oxidation of refinery oil (roughly 30 %) and coal gasification (18 %), whereas the water electrolysis only contributes 4 % of the produced hydrogen. Table 1-1 summarises the contributions of the various sources for hydrogen production to the present worldwide.

<b>Raw material</b>	<b>Technology</b>	<b>%</b>
<b>Natural gas</b>	Catalytic steam reforming	48
<b>Refinery oil</b>	Partial oxidation	30
<b>Coal</b>	Gasification	18
<b>Water</b>	Electrolysis	4

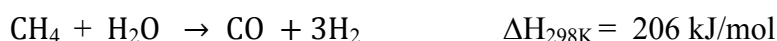
### 1.2.1 Hydrogen production from methane

Fossil fuels, particularly natural gas, will continue to dominate as a source for hydrogen production in the near-middle term [17]. Natural gas is abundant and it is found in gaseous form or as a mixture with oil in natural underground reserves all over the world. The major component of natural gas is methane (> 80 % CH<sub>4</sub> by volume) [18].

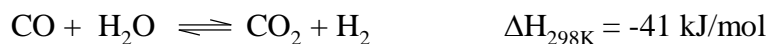
Due to the abundance of methane and its high H/C ratio, which is of course the highest among all hydrocarbons, it is an obvious source of hydrogen [19]. Three types of primary techniques used to produce hydrogen from hydrocarbon fuels are, steam reforming, partial oxidation (POX), and autothermal reforming (ATR) [20-22]. In this section, the main industrial methods for reforming of methane will be described.

### 1.2.2 Steam methane reforming (SMR)

Currently, hydrogen is mainly produced by steam reforming of natural gas. The process of steam methane reforming (SMR) for hydrogen production passes through several stages [5, 23-26]. The first stage includes primary purification of feedstock, while the second stage is the highly endothermic catalytic reforming of methane, which is run at high temperatures in range of 800 to 900 °C over Ni-based catalysts:



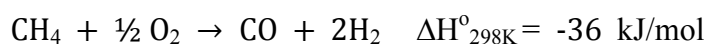
The third stage is the water-gas shift (WGS) reaction which is employed to reduce the concentration of carbon monoxide (CO) and further increase the amount of hydrogen:



The final stage is the purification of the H<sub>2</sub> by removal of CO<sub>2</sub> from the product by using a pressure swing adsorption (PSA) unit. This process requires other additional steps, for instance a desulfurisation unit and a steam generation section. Steam methane reforming (SMR) is a complex process because it has multiple stages. Also, it is not environmentally friendly due to the production of CO<sub>2</sub> [27, 28].

### 1.2.3 Partial oxidation of methane (POM)

Partial oxidation of methane (POM) to form synthesis gas (CO and H<sub>2</sub>) can be performed under non-catalytic conditions; methane is mixed with excess O<sub>2</sub> and then ignited, but it needs to be at a high temperature, usually above 1100 °C and pressures of 50 – 70 atm to achieve large conversion.



In contrast, the employment of a catalyst in this reaction promotes it so that it can be operated at lower temperatures. The catalysts used for POM are classified into three groups: Ni, Co and Fe; noble metals; and early transition metal carbides [29-31]. Amongst these catalysts, Ni/MgO has been considered fairly effective. However, there are some problems associated with POM, such as risk of explosion and deactivation of the catalyst.

### 1.2.4 Autothermal reforming of methane (ATR)

Autothermal reforming (ATR) has been utilised for industrial synthesis gas production since the late 1950s [32]. ATR is a combination of steam reforming and partial oxidation reactions in a single reactor. The autothermal reactor consists from two zones; the upper zone is combustion chamber, while the lower zone is catalyst bed. The produced gases are passed through the catalyst bed. As the temperature exiting the combustion zone is roughly 1200 - 1250 °C a high thermal stability catalyst is required. A Ni/MgAl<sub>2</sub>O<sub>4</sub> catalyst has shown high stability and activity for ATR reactors. The temperature exiting the catalyst bed is roughly 870 - 955 °C, and the produced synthesis gas is completely soot free [30].

However, all the hydrogen production processes described above result in CO and CO<sub>2</sub> products, which are potentially harmful to the environment and/or the performance of fuel cells [33]. Therefore, for application as a fuel source for fuel cells, separation and purification are necessary which are complex.

### 1.2.5 Direct cracking of methane

An alternative approach is the direct cracking of methane to produce hydrogen and solid carbon, as shown in the equation below. The process can produce “CO<sub>x</sub>-free hydrogen”. In addition the process is simple. It is probable that direct cracking of methane could reduce

the cost of hydrogen production and it is thus a good alternative to other hydrogen production processes for PEM fuel cell applications [25, 34, 35].



Moreover, unreacted methane from this reaction can be separated easily from the product by application of an absorbent or membrane to produce streams of 99 % by volume hydrogen [17, 36].

Direct cracking of methane can be classified into two major types, thermal cracking and thermal catalytic cracking. Thermal cracking of methane conducted in the absence of a catalyst requires high temperature, above 1200 °C to achieve a reasonable yield [37]. However, this process is not economical for commercial production of hydrogen because of this. To overcome this problem, the use of a catalyst is required to reduce the high temperature required for methane thermal cracking. The catalytic cracking of methane is a moderately endothermic reaction; the thermal energy requirement per mole of hydrogen produced is only 37.5 kJ/mol H<sub>2</sub> compared to 68.70 kJ/mol H<sub>2</sub> for steam methane reforming (SMR). Different supported transition metal catalysts were used to reduce the elevated temperature of methane thermal decomposition to: 500-700 °C for nickel-based catalysts, 700-950 °C for Fe-based catalysts and 700-1000 °C for Co, Pd, Pt, Cr, Ru, Mo, W catalysts [36]. These temperatures are much lower than that required by the non-catalytic process. Figure 1-2 presents summary of the available data from the literature on the catalysts and the preferred reaction temperature range for thermal catalytic cracking of methane.

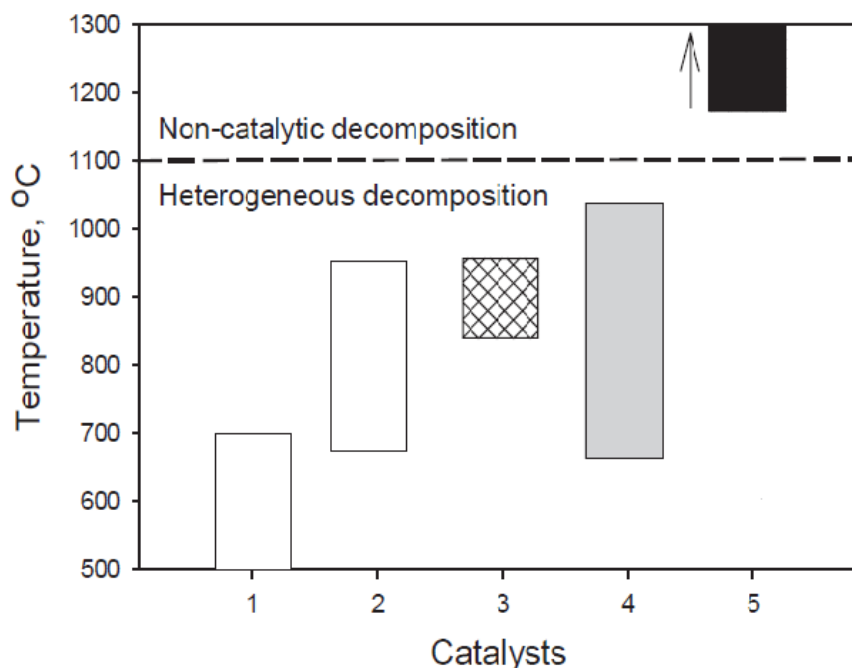


**Figure 1-2** Diagrammatic representation of the bulk of literature, preferred reaction temperature range for thermal catalytic cracking of methane reaction. Catalysts: 1 – Ni-based, 2 – Fe-based, 3 – carbon-based, 4 – summary of data related to Co, Ni, Fe, Pd, Pt, Cr, Ru, Mo, W catalysts, 5 – non-catalytic cracking [36].

Furthermore, not only is hydrogen gas produced the co-produced carbon is also potentially valuable. Filamentous carbons (carbon nanotubes and/or carbon nanofibres) are usually formed during the reaction of methane cracking over metal supported catalysts. They possess excellent properties such as high surface area, high mechanical strength, high electric conductivity and high resistance to strong acids and bases. These properties lead to many industrial applications. Filamentous carbon (carbon nanotubes and carbon nanofibres), can be employed as an adsorbent agent, catalyst, catalyst support, hydrogen storage medium and nano-electronic and nano-mechanical devices [38-40].

The direct catalytic cracking of methane to hydrogen and carbon is studied in this project.

### 1.2.5.1 Methane cracking over metal catalysts

A number of catalysts have been investigated for methane cracking. This area has been the subject of several recent reviews [4, 41-43]. Almost all transition metals show catalytic activity to some extent, and some presented remarkably high activity. However, there is no general agreement among different groups of researchers regarding the choice of the most efficient metal catalyst. For example, it has been reported that the rate of methane

activation in the presence of transition metals followed the order: Co, Ru, Ni, Rh > Pt, Re, Ir > Pd, Cu, W, Fe, Mo [44]. Whereas others have observed that Pd is the most active catalyst [25, 45-47], Ni has been reported by some to be the catalyst of choice [48-50], and in some papers Fe has been reported to be active [46, 51, 52]. Although cobalt catalysts have rarely been employed for methane decomposition because of their lower activity (compared to nickel), high toxicity and high price [53], they have occasionally been used as a catalyst for methane cracking [54-56].

Most studies have focused on nickel, iron and cobalt. Fe, Ni and Co are well known to have partially filled 3d orbitals, which can facilitate the dissociation of the hydrocarbon molecules by accepting electrons. This interaction along with “back-donation” from the metal into the unoccupied orbital in the hydrocarbon molecule changes the electronic structure of the adsorbed molecule, thus the dissociation of the molecule can occur [57].

A number of factors affecting the performance of metal catalysts for methane cracking have been identified. These factors included active components, support type, promoters or additives and preparation method [48, 52, 58-63]. In addition, the reaction conditions of methane cracking such as flow rate of methane gas and reaction temperature have also investigated [40, 47, 49, 58, 64].

The deactivation of metal catalysts in the reaction of methane cracking is the major challenge in this process. The carbons produced play a significant role in the decline of metal catalyst performance.

### **1.2.5.2 Catalyst deactivation**

Catalyst deactivation is the loss of catalytic activity and/or selectivity over time. The deactivation of catalyst can occur by different routes, both chemical and physical in nature. Poisoning, coking or fouling (carbon deposition), thermal degradation (sintering and/or evaporation of active phase) usually happen at high temperatures and phase transformations are also common causes of catalyst deactivation [65-67].

Sintering is generally a thermally induced process and is physical in nature. It is defined as the loss of catalyst active surface because of growth of the active phase or support material components. In the case of supported metal catalysts, decrease of the active surface area occurs *via* agglomeration and coalescence of small metal crystallites to form larger ones

[65, 66]. As shown in Figure 1-3, two principal mechanisms of metal crystallite growth have been proposed: (A) atomic migration and (B) crystallite migration. Atomic migration includes detachment of metal atoms from crystallites, migration of these atoms over the support surface and ultimately capture by larger crystallites. Crystallite migration includes the migration of whole crystallites over the support followed by collision and coalescence [67].

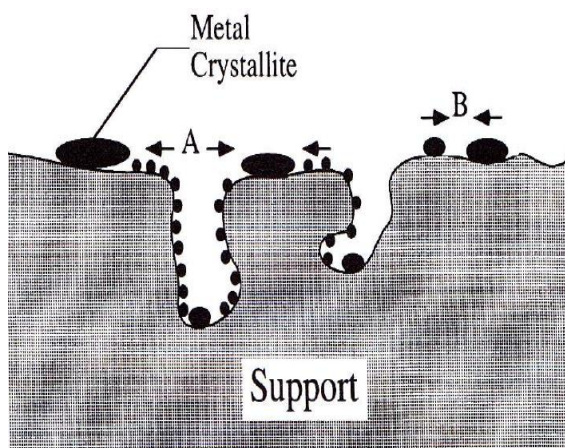


**Figure 1-3** Two theoretical models for crystallite growth due to sintering by (A) atomic migration or (B) crystallite migration [67].

The sintering process is strongly dependent upon temperature. Its mechanism is directly correlated to the temperature of the melting point of the catalyst metal and is defined by the so-called Hüttig and Tamman temperatures, which are indicative for the temperature at which sintering related processes are initiated. The semi-empirical relationships for the Hüttig and Tamman temperatures are shown below [66]:

$$T_{Hüttig} = 0.3T_{melting}$$

$$T_{Tamman} = 0.5T_{melting}$$

When the temperature reaches the Hüttig temperature, metal atoms at defects will become mobile and when the temperature reaches to the level of the Tamman temperature, metal atoms from the bulk display mobility. At the melting point temperature, the mobility of metal atoms will be very high where liquid-phase behaviour is noted [66].

Sintering is an important factor which leads to catalyst deactivation in hydrocarbon cracking due to the relatively high temperatures employed. As mentioned previously, the

metal catalysts used for the catalytic cracking of methane require the temperatures in range of 500 to 1000 °C depending on the type of metal used. In this range of temperatures, most of the metals used in this reaction achieve their Hüttig and Tamman temperatures [66]. Hence, the sintering process is expected to occur.

Despite this, it is considered that the main reason for the catalyst deactivation during catalytic cracking of methane is the deposition of carbon (coke formation) on the active surface of the catalyst [49, 68]. Coke formation is the physical deposition of carbonaceous species from the reacting species on the surface of catalyst. In addition, the deposition of coke interferes in several ways, such as blocking access to the active sites on the catalyst surface, encapsulation of the active metal particles, plugging the pores of the catalyst and accumulation of carbon filaments, which can cause disintegration of catalyst particles and plugging of reactor voids. The carbon species formed in catalytic processes vary depending upon the catalyst type, reaction type and reaction conditions [67, 69]. Figure 1-4 shows the possible impact of the carbon deposition on the supported metal catalysts.

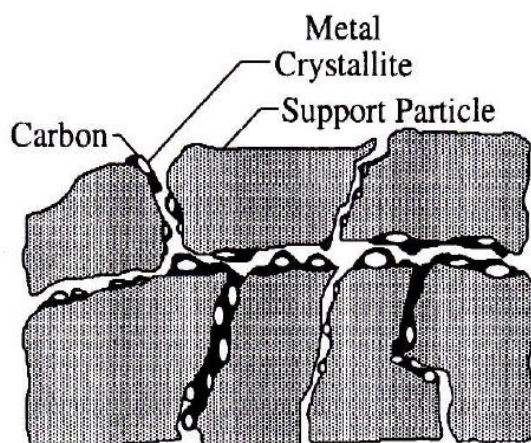


**Figure 1-4** Theoretical model of fouling, crystallite encapsulation and pore plugging of a supported metal catalyst due to carbon deposition [67].

Catalyst deactivation has been studied extensively. For example, Fajardo and co-workers [70] suggested that the deactivation of the Co/Al<sub>2</sub>O<sub>3</sub> catalyst during the catalytic decomposition of methane was due to the rate of carbon diffusion through the metal catalyst particle being slower than the rate of formation of carbon at the surface Co sites. Under these circumstances, carbon builds up on the surface of the catalyst and then encapsulates the metal particles causing a decrease in activity.

Goodman and co-workers [19, 71] showed that the reason for the rapid deactivation of the Ni/HZSM-5 catalyst during the decomposition of methane was the formation of

encapsulating carbon on the catalyst particles, which obstructed the reactant molecules. Figure 1-5 presents a micrograph taken from this study.

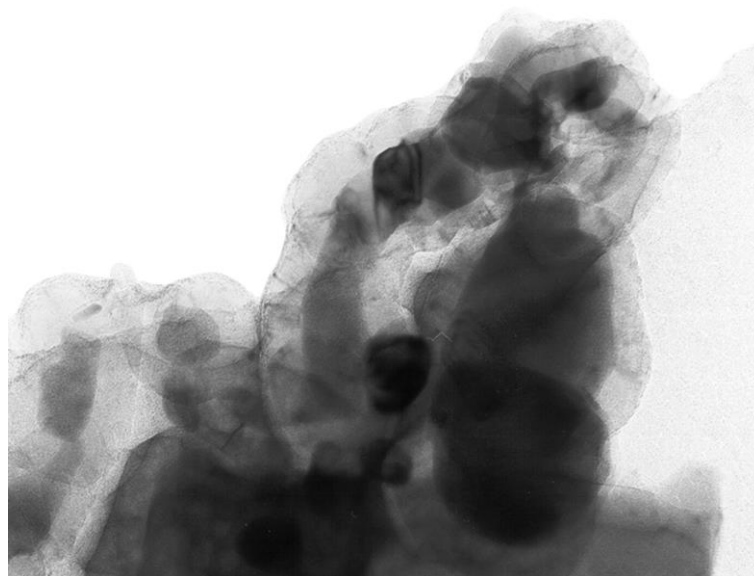


**Figure 1-5** TEM image of the post-reaction Ni/HZSM-5 catalyst applied to methane decomposition at 700 °C [71].

Zhang and Amiridis [72] studied the catalytic decomposition of methane using Ni/SiO<sub>2</sub>. Characterisation of the post-reaction catalyst by SEM and TEM showed that the carbon deposited on the catalyst was in the form of filaments. They suggested that the deactivation of catalyst occurred because of space limitations; the formed filaments started to interfere with each other and the silica surface, preventing the deposition of more carbon atoms in filamentous form.

Shah *et al.* [46] studied methane decomposition using a 0.5 % Mo-4.5 % Fe/Al<sub>2</sub>O<sub>3</sub> catalyst at 700 °C and showed the catalytic deactivation for a 1 g catalyst bed to be due to the detachment of metallic particles from the support and ultimate encapsulation of the metallic particles by a graphitic layer.

### **1.3. Carbon deposition**

As mentioned previously, carbon is one of the two major products for methane cracking. The carbon produced from the cracking of methane process is a pure product, which could be marketed in 1996 at a selling price of \$300/ton or more. For instance, as a high quality alternative for petroleum coke, it could have probably been sold for \$310–460/ton, the price-range for high purity petroleum coke. The forms of filamentous carbon are presently of much greater value. Hence, the value of the carbon produced can contribute to the

economics of hydrogen production. Carbon can be used in numerous application areas such as structural materials, power generation, soil amendment and environmental remediation [36].

It has been reported that there are three main types of carbon formed during the cracking of hydrocarbons (especially methane) over supported metal catalysts: amorphous, filamentous and graphitic. The structure and morphologies of the deposited carbons depend upon the reaction conditions and the type of catalyst [73, 74]. Amorphous carbon is a highly disordered network of carbon atoms, mostly in the form of rings or olefinic chains, as shown in Figure 1-6 (A) [75, 76]. Graphite has a layered hexagonal planar structure. The layers (sheets) are held together by van der Waals forces, as shown in Figure 1-6 (B) [75, 77]. Filamentous carbons can be classified into two main categories, carbon nanotubes (CNTs) (both single-walled (SWCNTs) and multi-walled (MWCNTs) which have a hollow cavity) and carbon nanofibres (CNFs) [78].

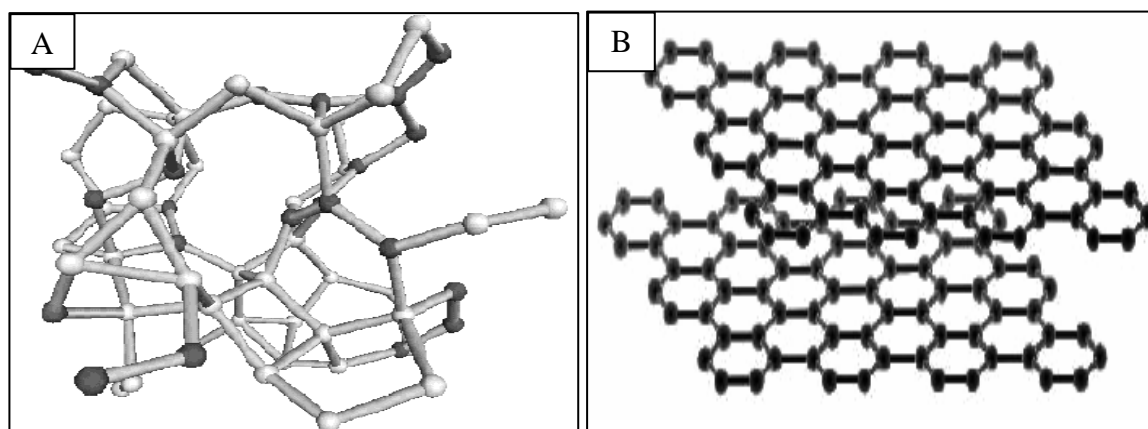


**Figure 1-6** Schematic representation of an amorphous carbon structure (A) [79], and a graphitic carbon structure (B) [80].

In the literature it can be seen that a lot of effort has been focused on the study of graphitic carbon nanostructures. Examples in the catalytic cracking of methane include carbon nanotubes (CNTs) [52, 81-86], carbon nanofibers (CNFs) [40, 87-90] and carbon nanoions [91, 92]. The following sections present some details about these types of carbon nanostructures.

### 1.3.1 Carbon nanotubes (CNTs)

Before the invention of transmission electron microscope (TEM), there were early studies, which considered the possibility of forming filamentous carbon from thermal decomposition of hydrocarbons [93]. Unfortunately, because of the low resolution of the

available microscopic techniques, it was hard to detail the filaments produced. Following, the first commercial TEM, which was produced by Siemens in 1939; there have been many reports concerning the formation of tubular structures similar to CNTs. It is believed that the first evidence of the formation of tubular nano-sized carbon filaments by TEM technique was published in 1952 by Radushkevich and Lukyanovich [93]. In 1976, Oberlin *et al.* [94] also showed similar images for the formation of tubular nano-sized carbon filaments as a result of pyrolysis of a mixture of benzene and hydrogen. In 1991, Ijima [95] presented the first unambiguous evidence of growing multi-walled carbon nanotubes (MWCNTs). Also, Ijima *et al.* [96] published the first clear report in 1993 about the formation of single-walled carbon nanotubes (SWCNTs). CNTs have since then become one of the most active fields of nano-science and nano-technology because of their unique properties that make them appropriate for several potential applications such as polymer reinforcements for composites or breakthrough materials for energy storage as well potential applications in electronics and catalysis [97].

As mentioned previously, the carbon nanotubes (CNTs), can be classified into two major types: single-walled (SWCNTs) and multi-walled (MWCNTs). Carbon nanotubes have structures similar to graphene sheets rolled up into cylindrical forms. SWCNTs comprise, as the name suggests, single graphene sheets whereas MWCNTs comprise a number of graphene sheet layers [78]. Figure 1-14 illustrates single-wall carbon nanotube (SWCNTs) and multi-wall carbon nanotube (MWCNTs) structures.

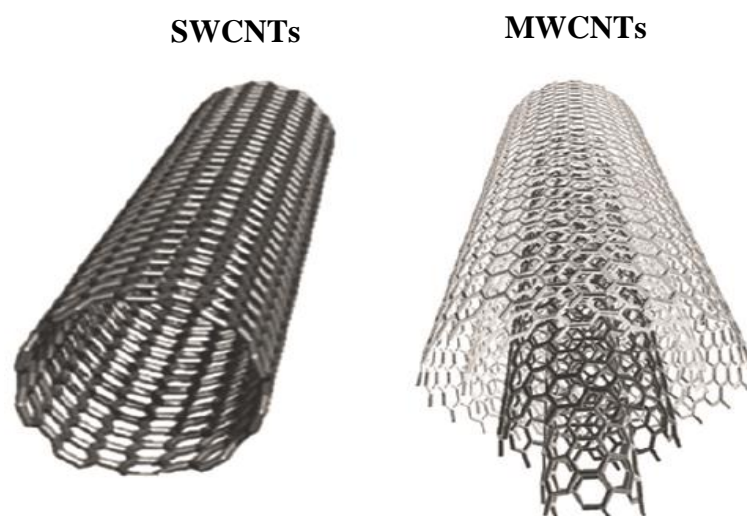


**Figure 1-7** Schematic diagrams of single-wall carbon nanotube (SWCNTs) and multi-wall carbon nanotube (MWCNTs) structures [98].

Li and co-workers [99] synthesised high quality carbon nanotubes through methane catalytic decomposition over the Fe/MgO catalysts at 800 °C. They showed that both single-walled and multi-walled carbon nanotubes were formed, as presented in Figure 1-8.

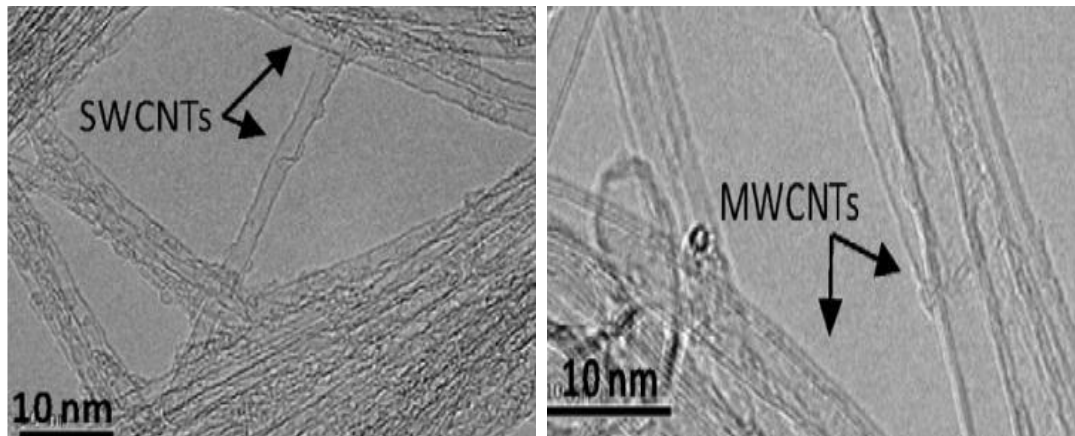


**Figure 1-8** HRTEM images for the carbon materials deposited on the Fe/MgO catalysts at 800 °C [99].

Catalytic decomposition of hydrocarbons, arc discharge and laser ablation are common techniques to produce carbon nanotubes. The limitation of the arc discharge and laser ablation techniques are that they cannot be applied to continuous synthesis of CNTs, which makes the catalytic decomposition of hydrocarbons a promising technique [100]. Catalytic decomposition of different hydrocarbons (acetylene, ethylene, propylene, acetone, n-pentane, methanol, toluene, and methane) as feedstocks were studied in a continuous process for the high volume and economic production of CNTs [101]. The employment of methane in the process of catalytic decomposition is reported to be the most suitable compared to the other hydrocarbons because of the fact that it is a cheaper carbon source [102].

### 1.3.1.1 The growth mechanism of carbon nanotubes

There are two main growth mechanisms for CNTs which have been suggested by researchers based on their observation of the location of catalyst metal particles. The “tip growth mechanism” was suggested when the metal particle is found to be located at the tip of carbon nanotubes, whereas the “base growth mechanism” is proposed when the metal particles are located at the base of the carbon nanotubes.

The tip growth mechanism is the most commonly suggested mechanism [73, 103-107]. It was proposed by Baker *et al.* in 1972, who proposed the growth of carbon filaments by

catalytic decomposition of the hydrocarbon and bulk diffusion of carbon [104]. The tip growth mechanism proposes that carbons produced from the cracking of hydrocarbon are deposited on the front-exposed surface of catalyst metal particles dissolving into the particle at the gas side followed by diffusion through the bulk of the metallic particle to the rear surface of the metallic particle, the support side. The carbon precipitation, consisting of graphite, at the rear of the particle builds up a deposit of carbon which forces the particle to move away from the support, as shown in Figure 1-9. Moreover, if the carbon deposited does not move from the surface of metallic particle to form filament walls rapidly enough, then the metal surface becomes encapsulated by the carbon and catalyst deactivation occurs.

The base growth mechanism is similar to the tip growth mechanism with the exception of the metallic particle which is located at the base of the carbon nanotube, the support side, as shown in Figure 1-9. The growth of carbon nanotube is caused by the metallic particle which remains in contact with the catalyst support. This mechanism supposes that the metallic particle has a strong interaction with the support and cannot be easily detached by the graphitic layer formed at the metal/support interface. Consequently, if the metal support interaction (MSI) is strong, the growth of carbon nanotubes should follow the base growth mechanism. In contrast, the presence of weak MSI during the formation of carbon nanotubes on supported metal catalyst will favour the tip growth mechanism [57, 73, 108, 109].

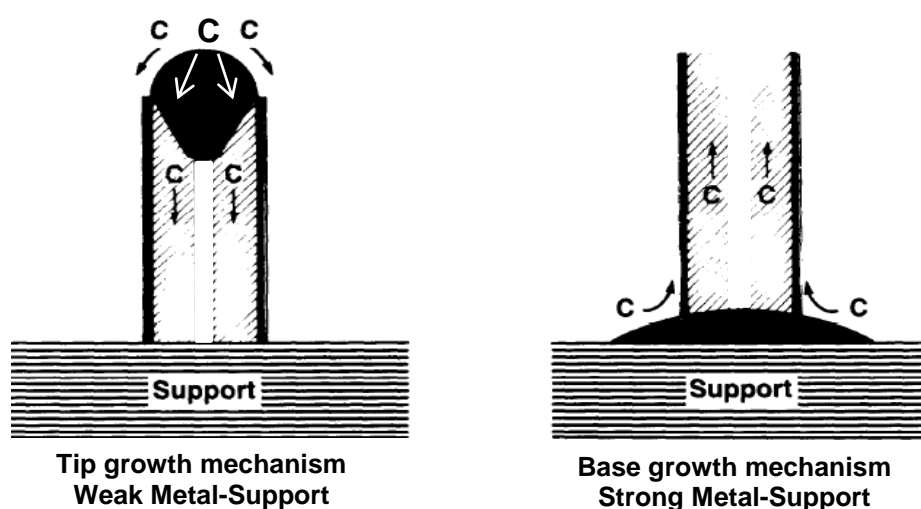


**Figure 1-9** Schematic representation of the two main growth mechanisms of carbon nanotubes [73].

Takenaka *et al.* [40] studied the decomposition of methane into hydrogen and carbon filaments over a 70 wt % Ni/SiO<sub>2</sub> catalyst. They analysed the post-reaction catalyst by scanning electron microscopy (SEM) and found that the carbon deposited in the form of filamentous carbon with the Ni metal particles present at the tip of the filaments, as illustrated in Figure 1-10.

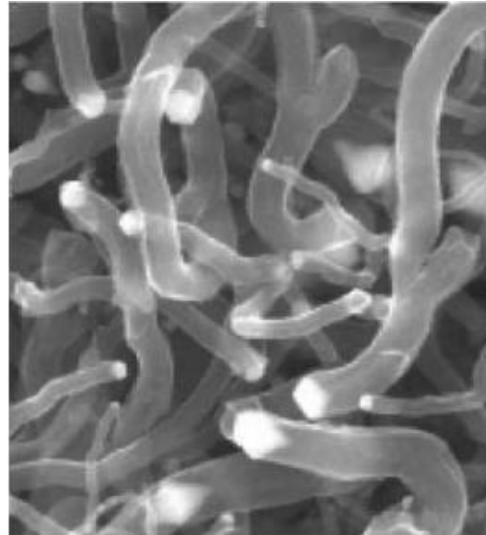


**Figure 1-10** SEM image for the post-reaction 70 wt % Ni/SiO<sub>2</sub> catalyst after reaction at 500 °C, bright spots represent the Ni metal particles located at the tip of the filaments [40].

Chen *et al.* [110] synthesised carbon nanotubes (CNTs) on a Ni film-coated Si substrate *via* decomposition of ethylene (C<sub>2</sub>H<sub>4</sub>) at *ca.* 700 °C using a hot-filament chemical vapor deposition (CVD) method and SEM images of the post-reaction material revealed that the CNTs were formed by base growth mechanism, as presented in Figure 1-11.

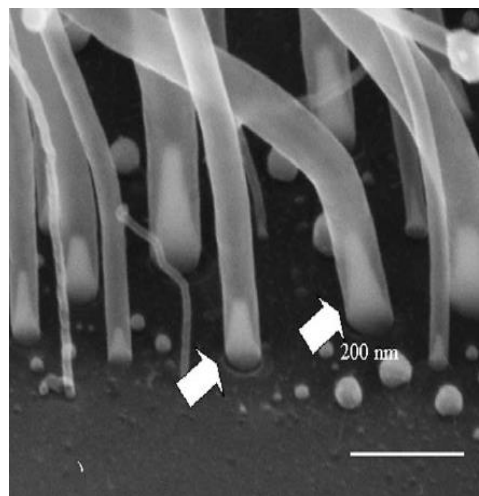


**Figure 1-11** SEM image for the post-reaction Ni-Si material at 700 °C, conical-shaped metallic nanoparticles are encapsulated at the base ends of the CNTs, as marked with arrows [110].

### 1.3.2 Carbon nanofibres (CNFs)

Carbon nanofibres are another type of graphitic filamentous structure, which differ from carbon nanotubes in the orientation of the graphite monolayer planes. In carbon nanotubes (CNTs), the planes of graphene-like layers are parallel to the axis of the tube, as shown in Figure 1-8, whereas in carbon nanofibres (CNFs), the graphite planes are arranged perpendicular to the axis of fibre (stacked form) or at an angle to the axis (herringbone form), which result in a non-hollow structure [111]. Stacked forms of carbon nanofibres are built up with graphite layers stacked as piles of “plates”, i.e. oriented along the vertical axis of the nanofibres, as illustrated in Figure 1-12. In the case of the herringbone form, the stacked graphite layers are bent similar to a bowl-shape and the nanofibre displays graphite layers making an oblique angle with respect to the vertical axis of nanofibre whilst leaving no internal cavity, as illustrated in Figure 1-13. Therefore, the value of angle  $\alpha$  between the graphite layers plays a significant role in the classification of CNFs. If the value of angle  $\alpha$  is close to  $180^\circ$ , the CNFs will be in the stacked form, whereas if it is between  $30^\circ$  and  $150^\circ$  it will be in the herringbone form [112]. The properties of carbon nanofibres such as high strength has made them an attractive material for the development of high performance composite structures [113].

#### Stacked form

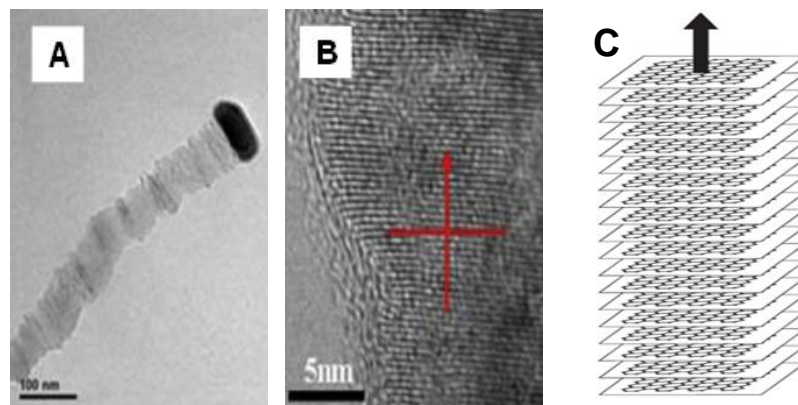


**Figure 1-12** HRTEM images of CNFs (stacked form), A) a single CNF at low magnification and B) at high magnification (arrows and lines in image (B) represent the direction of fibre axis and graphene layer of carbon nanofibres, respectively [114]). C) Schematic representation that shows the arrangement of graphite layers to the axis of fibre [111].

### Herringbone form

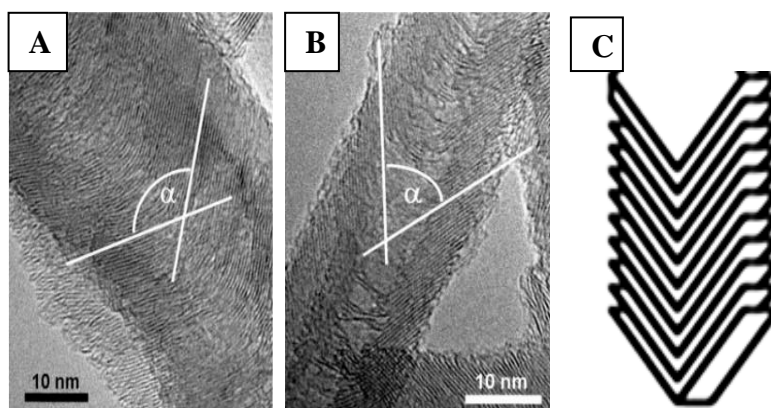


**Figure 1-13** TEM images of CNFs (herringbone form), (A) and (B) show single CNFs with different angles between the graphite layers [112], C) schematic representation that shows the arrangement of graphite layers with a specific angle to the axis of fibre [115].

The structure and properties of the fibres can be affected by different parameters such as the nature of the metal surface, the composition of the reactant gas and the temperature of synthesis [115]. The growth mechanism of carbon nanofibres is similar to that for CNTs when gaseous hydrocarbons contact catalyst particles at high temperature. The only difference between the growth mechanism of CNTs and CNFs is the existence of an intermediate stage, which determines the formation of CNTs and/or CNFs. However, it is believed that the operating conditions (especially the reaction temperature) play an important role in determining the type of carbon filaments formed [103]. At low reaction temperatures, the rate of carbon nucleation/precipitation over the metal/carbon interface is lower than the rate of carbon diffusion through the metallic particle. This nucleation leads to the formation of uniform carbon layers over the whole metal/support interface. When the layers of carbon are continuously excreted *via* carbon nucleation, the metallic particle can be lifted up from the support to form carbon nanofibres with solid core. At high temperature, the nucleation rate of carbon layers is much higher than the rate of carbon diffusion through the metallic particle. As a result, the path of carbon diffusion at metal/gas interface is shorter than that at metal/support interface. Hence, the nucleation will occur at the area close to the metal/gas interface. As soon as the excretion of carbon starts close to metal/gas interface, the carbon concentration in the metallic particle declines sharply to the saturation concentration of carbon. Consequently, no driving force is present any longer for nucleation at places with high diffusional path lengths, centre of metal/support. Carbon excretion will not take place at this central part, therefore, hollow structure carbon

nanotubes, are formed [103]. Figure 1-14 displays the growth mechanism of the carbon nanofibres and carbon nanotubes.

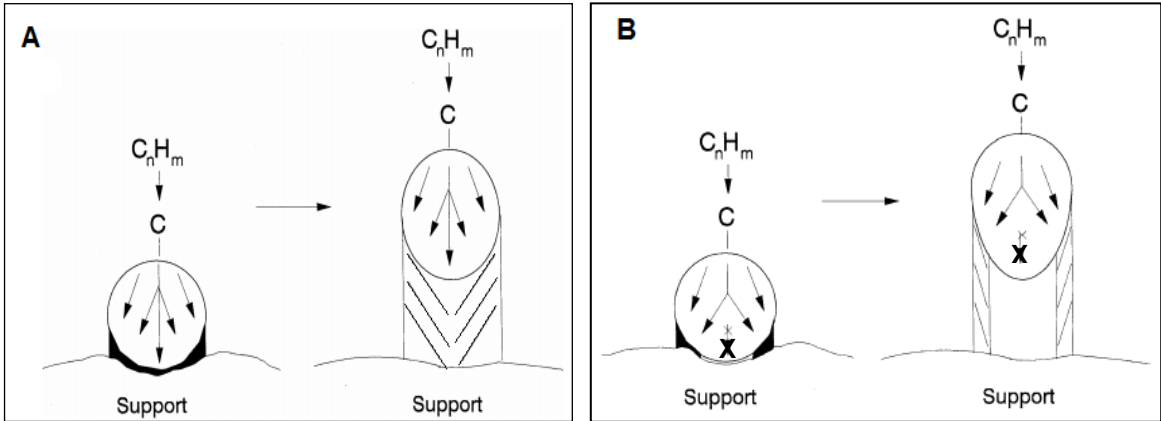


**Figure 1-14** Schematic representation of the growth mechanisms of carbon nanofibres (A) and carbon nanotubes (B) [103].

However, herringbone–bamboo nanotubes are type of carbon filaments, which have structures between those of carbon nanotubes and nanofibres. The structure of these filaments consists of a hollow core, which is not continuous but is sequentially closed by graphite layers and oriented vertical to the axis tube [112]. The structure of the bamboo form comprises a periodical repetition of hollow cores, which can be formed by periodical movement of metal particles inside the carbon filament [4] as illustrated in Figure 1-15.

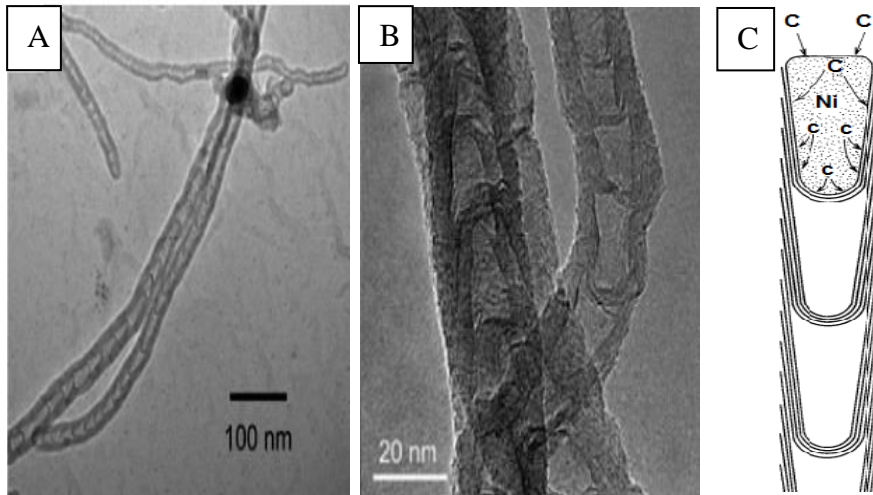


**Figure 1-15** TEM images of bamboo-structured carbon nanotubes observed after methane decomposition over 10 wt % Cu/MgO and 5 wt % Mo/MgO at 850 °C for 1 h, A) low magnification and B) high magnification [116], C) schematic diagram of the growth model of a bamboo tube with a Ni-based catalyst [117].

Numerous reports have been made concerning the formation of bamboo-shaped CNFs during methane decomposition [116, 118-121]. Chen *et al.* [119] demonstrated the formation of bamboo-shaped carbon filaments during decomposition with a feed of  $\text{CH}_4/\text{H}_2$  (1:2) over a Ni–Cu/ $\text{Al}_2\text{O}_3$  catalyst at 720–830 °C. Moreover, they proposed a growth mechanism for the bamboo structure. In their proposal, there are two types of movement of the metal particle inside the carbon filament, which can contribute to the formation of bamboo-shaped CNTs. The first mechanism includes a smooth movement in which the metal particle is pushed by the insertion of new layers of carbon at the carbon–metal interface, resulting in the continuous formation of uniform walls and cavities. The second mechanism involves jumping of the metal particle at regular periods of time. This movement is only possible when the metal particle is in the quasi-liquid state and has a low wetting ability with the surface of the graphitic carbon formed. During the formation of new layers of carbon, a depressing force is applied on the metal particle towards its axis and in the direction of growth. This stress accumulates as the insertion continues. When the stress is larger than the combined force of carbon and metal, a jump of the metal particle occurs. This mechanism is more defined than that proposed earlier by Saito [117], who suggested that it is not obvious if the Ni particle at the tip of tube was in state of liquid or solid during tube growth and concluded that the cone-shaped Ni was always at the tip of tube where it was absorbing carbon. The dissolved carbon diffused to the rear side of the Ni particle, and carbon segregated as graphite at the bottom and then into the side of the particle. After the formation of graphitic layers (about 20 layers) the Ni particle jumped out of the graphitic sheath to locate at the top of the tube. The force of pushing out the Ni particle could be stress accumulated in the graphitic sheath because of the segregation of carbon from the inside of the sheath, as presented in Figure 1-15 (C).

### 1.3.3 Carbon nano-onions

The onion-like carbon nanosphere is a graphite structured material. It comprises a spherical multilayer graphene-based shell and a hollow or metal particle-filled core. A report of onion-like carbon material on the surface of graphite electrodes was made in 1980 by Iijima [122]. Although carbon nanotubes and carbon fibres have received great attention due to their important potential applications, onion-like graphite structures have also found to have potential applications in electromagnetic devices for field emission, and as solid lubricants [123, 124]. There have been a number of successful attempts to synthesise onion-like graphite structures. For example, Zhao *et al.* [91] synthesised carbon nano-

onion structures *via* catalytic decomposition of methane over an Ni/Al catalyst at a relatively low temperature (600 °C). Figure 1-16 (A and B) illustrates two TEM images for two types of onion-like carbon nanospheres, a hollow or metal particle-filled core. From the image in Figure 1-16 (A), it is clear that the core of the carbon nano-onion is filled with metal particles, while the onion shown in Figure 1-16 (B) is completely empty.

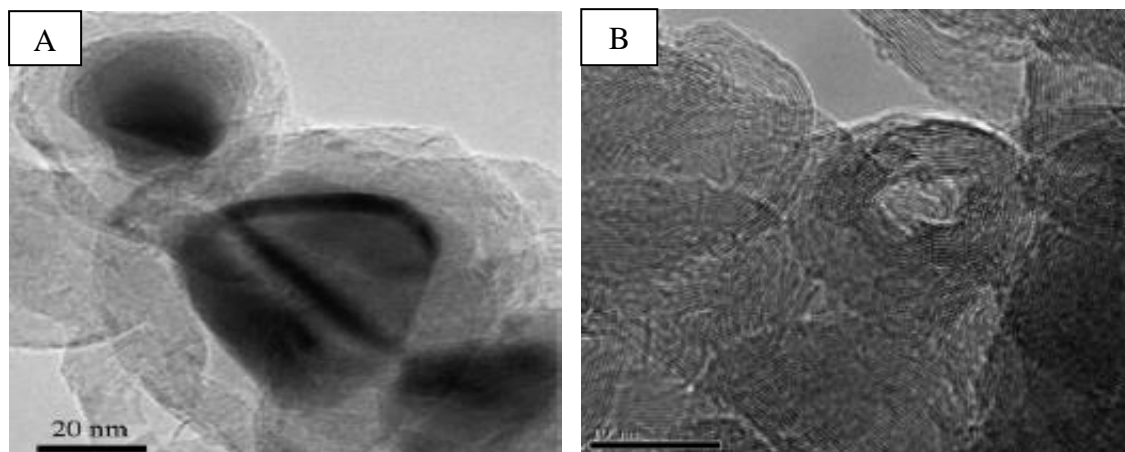


**Figure 1-16** HRTEM images of the carbon onions formed from methane decomposition over Ni/Al catalyst, (A) HRTEM image of the carbon nano-onions with nickel particle encapsulated, (B) HRTEM image of carbon nano-onions with hollow cores [92].

The mechanism of growth of carbon nano-onions was proposed by Zhao and co-workers [92]. Formation of carbon nano-onions begins with: formation of solid metal particles, adsorption of carbon-containing feed, the deposition of carbon from cracking, formation of graphitic layers around the metal particle until it is fully encapsulated. In case of carbon nano-onions with empty cores an additional step occurs, where the metal particle evaporates due to the high localised temperature within the nano-onion.

This mechanism is in good agreement with that suggested by Kanga *et al.* [125]. They objected only to the proposal of the formation of the empty core where they proposed that the presence of metal particle in the core of the carbon onion-like spheres is under pressure because of the building layers of graphite around it, which ultimately force it to eject leaving an empty core. Figure 1-17 displays the two different proposed growth mechanisms for the formation of two different carbon nano-onions.

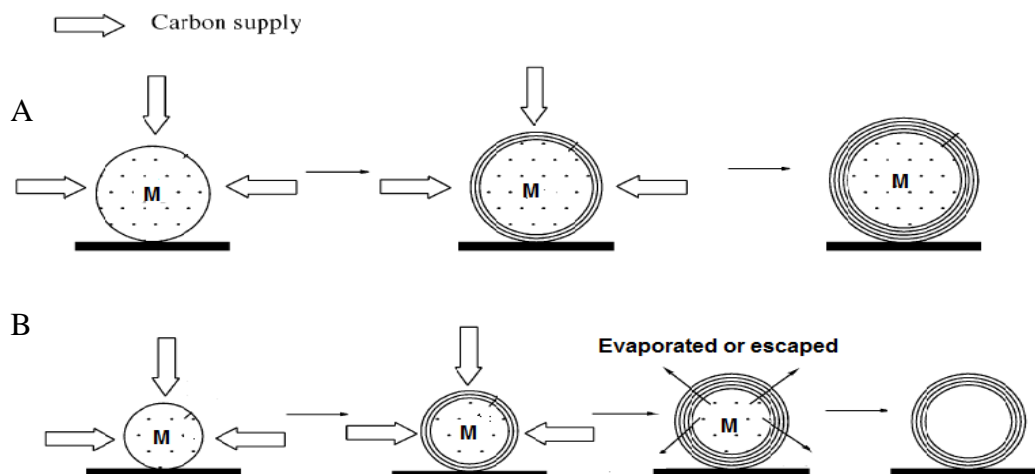


**Figure 1-17** Schematic representation of the growth mechanism of onion-like carbon nanosphere formation, (A) the carbon nano-onion with metal particle filled core, (B) the carbon nano-onion with an empty core [92].

## 1.4. Biogenic iron oxide

This section has been added to provide an overview of biogenic iron oxide. In this thesis, biogenic iron oxide has been studied as a pre-catalyst for the catalytic cracking of methane. Biogenic iron oxide can be a component of iron ochres which can interfere with water management. In such circumstances it requires dredging. Therefore biogenic iron oxide forms a disposable and low cost material for methane cracking. Hence, it is appropriate to present some information about biogenic iron oxide in general.

Iron is one of the transition metals widely used in catalysis. It is known to be active for the decomposition of hydrocarbons, especially methane [46, 51, 52, 126-129].

The occurrence of iron oxides is widespread in nature. They are found in soils and rocks, lakes and rivers, on the seafloor and in organisms [130]. There are many types of iron oxide. Table 1-2 shows the major iron oxides and oxyhydroxides. Some of these have been synthesised artificially and others are known to be produced not only synthetically but also biologically. Many organisms such as bacteria have the ability to produce iron oxides from the environment in which they live [131, 132]. These bacteria generally termed as iron oxidising bacteria, producing biogenic iron oxide [131, 133-135].

<b>Table 1-2</b> The major iron oxide and oxyhydroxide phases [132].			
<b>Oxyhydroxides</b>		<b>Oxides</b>	
<b>Formula</b>	<b>Mineral</b>	<b>Formula</b>	<b>Mineral</b>
Fe <sub>5</sub> HO <sub>8</sub> .4H <sub>2</sub> O	Ferrihydrite	α- Fe <sub>2</sub> O <sub>3</sub>	Haematite
α- FeOOH	Goethite	γ- Fe <sub>2</sub> O <sub>3</sub>	Maghemite
β- FeOOH	Akaganeite	Fe <sub>3</sub> O <sub>4</sub>	Magnetite
γ- FeOOH	Lepidocrocite		
δ- FeOOH	Feroxyhyte		

Iron represents the fourth most abundant element in the earth's crust [136] where iron cycling depends upon redox reactions, which frequently result in precipitation and dissolution of Fe-rich minerals. Also, microbial activity contributes to iron cycling, through carbon fixation, respiration and the reactions of passive sorption. Iron oxides formed in conjunction with bacteria, either as internal or external precipitates, are denoted as biogenic minerals. They can be formed in different types of environments on earth such as in freshwater, in marine systems, in aquifers, in soils and in mining impacted systems. Biogenic iron oxides generally occur as nano-crystals and display a large range of morphologies and mineralogies. These minerals can be produced as a result of the direct metabolic activity of bacteria or as a result of passive sorption and nucleation reactions. The oxidation of iron during the metabolic activity of acidophilic and neutrophilic bacteria in oxygen-rich waters promotes the oxidation of Fe<sup>2+</sup> to Fe<sup>3+</sup> and the precipitation of biogenic iron oxides as extracellular precipitates close to or onto the bacterial cells. In addition, the oxidation of iron in oxygen-deficient waters can also occur as a result of the activity of photoautotrophic bacteria using Fe<sup>2+</sup> as an electron donor. However, passive Fe sorption and nucleation onto bacterial cell walls is another important mechanism, leading to the formation of iron oxide. The bacterial surface under environmental pH conditions is net negatively charged, which results in the binding of soluble iron, ultimately leading to the precipitation of iron oxides under saturation conditions. Extracellular bacterial cell polymers can be produced, which act as a matrix for iron sorption and the nucleation of iron oxide. There are different types of bacteria cells in which iron oxides are formed within the cell. This intracellular biogenic mineral results in magnetotactic bacteria [133].

It is believed that the bacteria which form extracellular iron oxides obtain energy by oxidising soluble Fe<sup>2+</sup> ions into insoluble Fe<sup>3+</sup> ions and then precipitate iron oxide with unique structures such as twisted stalks and tube-like sheaths [131, 132]. There are many

groups of microorganisms, which can be identified and differentiated upon the morphology of the iron-containing phase(s) produced. *Gallionella ferruginea* which forms twisted stalks, and *Leptothrix ochracea* which forms hollow micro-tubes or sheaths, are the most commonly noted bacteria in association with biogenic iron oxides in neutral pH environments [131-133, 137] Figure 1-18 (A) demonstrates morphologies of biogenic iron oxides produced according to these bacteria.

Biogenic iron oxide, formed by *Leptothrix ochracea*, is the material used in this project as a pre-catalyst. *Leptothrix ochracea* was among the first microorganisms to be defined by researchers in the late 1700s and was likely termed after the orange ochreous deposits of Fe oxides visible within bodies of slowly moving freshwater [138]. The shape of *Leptothrix ochracea* cells is straight rods, which form straight tubular sheaths that surround single cells, as shown in Figure 1-18 (B). The production of sheaths is by excretion of fibrillar polymer, which are cross-linked to form a mesh-like fabric closely fitting to the cells for iron sorption and the nucleation of iron oxide [139]. Moreover, it has been suggested that the formation of sheaths is an effective strategy for such bacteria, which provide them with physical protection from external aggressions such as bacterial predators [139].

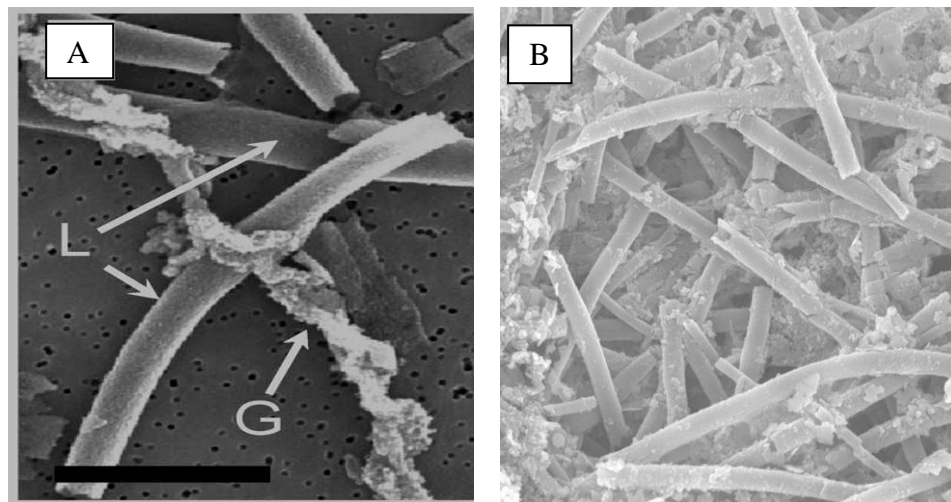


**Figure 1-18** Scanning electron micrographs demonstrating two morphologies of biogenic iron oxide. A) L shows the shape of hollow micro-tubes or sheaths associated with *Leptothrix ochracea*, G illustrates the shape of twisted stalks with *Gallionella ferruginea* [137], B) hollow micro tubes, sheaths, associated with *Leptothrix ochracea* [138].

*Leptothrix ochracea* is widely distributed in the environment and can easily exist at sites which are characterised by a neutral pH, an oxygen gradient and a source of reduced iron

minerals. Typical habitats comprise iron seeps of freshwater wetland areas, forest ponds, iron springs, the upper layers of sediments and even domestic water systems. At appropriate sites, the large growth of these organisms can be easily noted by the naked eye as masses of ocherous forms developing as surface films, as solid mats or fluffy and dispersed material with varied colour from yellowish-orange to dark brown [139]. Figure 1-19 illustrates photographs for some sites of the accumulation of biogenic iron oxide formed by *Leptothrix ochracea*.

Several studies have been demonstrated that the deposited iron oxide on the surface of *Leptothrix ochracea* cells is poorly ordered (amorphous) iron oxyhydroxide corresponding to 2-line ferrihydrite ( $\text{Fe}_5\text{HO}_8 \cdot 4\text{H}_2\text{O}$ ) [131, 140-142]. It was suggested that such a poorly ordered phase, is due to the rapid rates of oxidation and precipitation caused by the bacteria [140].

Biogenic iron oxide, can also find application for water treatment such as removal of phosphorus and heavy metals from contaminated water [143-146].



**Figure 1-19** photographs for some sites of the accumulations of biogenic iron oxide, which are formed by *Leptothrix ochracea* [147].

## 1.5. Zeolites

This section has been included since H-ZSM-5 zeolite has been used as a catalyst support in this thesis. Hence, it is appropriate to present general information about zeolites.

Zeolites are crystalline microporous aluminosilicates which are often termed molecular sieves. Zeolites can be natural or synthetic in origin, possess a variety of pore structures and properties [148] and can often be designed with these parameters in mind. The first description of zeolites was in 1756 by Axel Cronstedt, who heated an unknown silicate mineral and observed that steam evolved upon heating. This finding led him to term minerals that acted in this manner zeolites, derived from the Greek words “zeolithos”, which means “boiling stone” [149, 150]. The first synthetic zeolites that did not have a natural counterpart were reported by Barrer in the 1948 [149].

### 1.5.1 Zeolite Structure and properties

Zeolites are well-defined crystalline aluminosilicates comprising channels and cavities. The framework of a zeolite is composed of primary building units of  $\text{SiO}_4$  and  $\text{AlO}_4$  tetrahedra linked together by oxygen atoms resulting in inorganic macromolecules with structurally distinct three-dimensional frameworks. However, linking of  $\text{SiO}_4$  and  $\text{AlO}_4$  tetrahedra creates an electrical imbalance and one negative charge is associated with the aluminium centre due to the difference of valence between the  $(\text{SiO}_4)^{4-}$  and  $(\text{AlO}_4)^{5-}$  tetrahedral. This charge is balanced by extra-framework cations. The general formula for zeolites is [148, 150]:



where cations M of valence  $n$  neutralise the negative charge of the aluminosilicate framework,  $m$  is the number of water molecules per unit cell, and  $x$  and  $y$  are the numbers of Al and Si tetrahedra respectively per unit cell.

The primary building units,  $\text{SiO}_4$  and  $\text{AlO}_4$ , contribute to the formation of so-called secondary building units (SBUs) by joining together to form a wide variety of rings and cages. Repeating secondary building units (SBUs) can be linked to each other by atoms of oxygen to build extended networks of channels, channel intersections and cavities with molecular dimensions that characterise the zeolites structure and provide a high surface area, which is a desirable property for catalysis. The zeolite structures are determined, to a large extent, by the SBUs from which they are comprised [148, 150, 151]. In addition, the important feature of zeolites structure is the network of connected cavities or pores forming a system of channels throughout the structure. These cavities are of molecular dimensions and can adsorb species small enough to have access into them. The pore size of

the zeolite structures depend on the number of tetrahedra forming the pore, *i.e.* the ring size. For example, the zeolite Faujasite determined by 12-membered ring of corner-sharing tetrahedra with pore dimensions of 0.74 nm, while zeolite ZSM-5 determined by a 10-membered ring of corner-sharing tetrahedra with pore dimensions of 0.51 x 0.55 nm. The pore dimensions of zeolites lie in the range 0.35-0.75 nm. These dimensions allow zeolites to be employed in different applications such as in gas filtration, ion exchange, selective catalysis, desiccant applications, and cracking of hydrocarbons [150, 152]. Figure 1-20 illustrates the primary and secondary building units of zeolites and the structures of four selected zeolites with their micropore systems and dimensions are presented. In addition to the zeolite pore dimensions, the Si/Al ratio is important. Stability of the crystal framework increases with increasing Si/Al ratio.

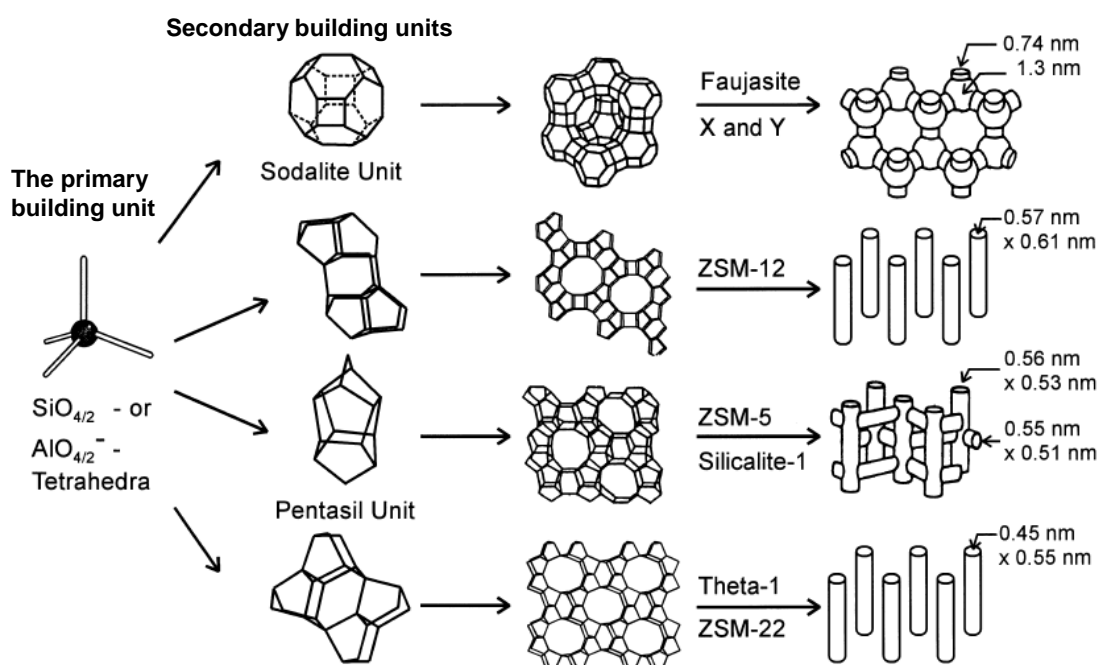


**Figure 1-20** Structures of four selected zeolites (from top to bottom: faujasite or zeolites X, Y; zeolite ZSM-12; zeolite ZSM-5 or silicalite-1; zeolite Theta-1 or ZSM-22) and their micropore systems and dimensions [148].

The acidity of zeolites is one of their most important properties, which is beneficial for many chemical reactions. The presence of acidic sites arise from the  $[\text{AlO}_4]$  tetrahedral units in the framework. These acid sites can be Brønsted or Lewis acid sites, or both depending on zeolite preparation conditions. Brønsted sites can be converted into Lewis sites by heating zeolites at temperatures above 500 °C [150]. Figure 1-21 shows a scheme for the formation of Brønsted and Lewis acid sites in a zeolite framework by thermal dehydration. Dehydration and steaming can also lead to extraframework aluminium production which can impact upon material performance [153].

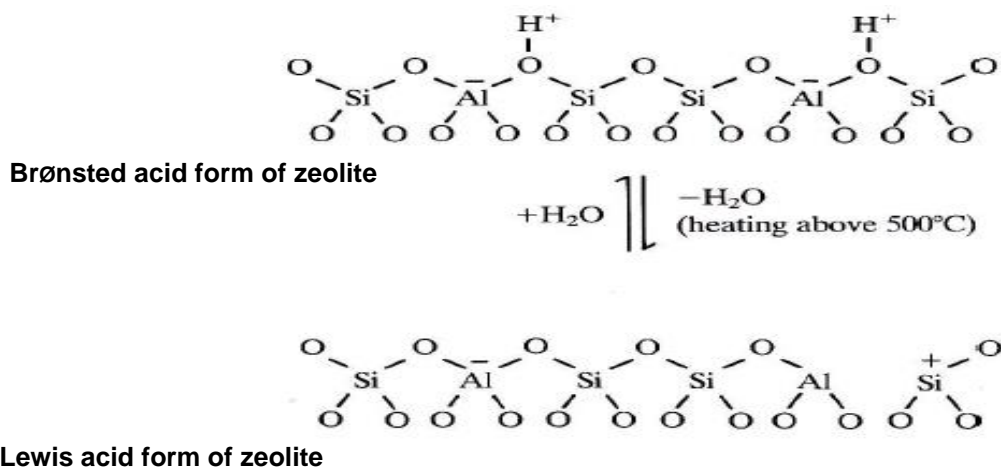


**Figure 1-21** Scheme for the thermal interconversion of Brønsted to Lewis acid sites in a zeolite framework [150].

## 1.5.2 H-ZSM-5

H-ZSM-5 zeolite is of particular interest in this thesis because it has been applied as a support for methane cracking.

The first published report concerning the synthesis of zeolite ZSM-5 (Zeolite Socony Mobil Five) was in 1972 by the Mobil Oil Corporation [154]. Although there are several types of zeolites available, ZSM-5 is one of the most recognised and widely applied zeolites in catalysis. It has been widely applied because of its unique channel structure, thermal stability, acidity, shape-selective property as a catalyst and sorbent, and it has been especially applied in petrochemical processing, fine chemical production and liquid and gas separation [155].

ZSM-5 is built from the pentasil secondary building unit, and is a medium pore zeolite composed of ten tetrahedral rings, which possesses a three dimensional porous network. It contains intersecting systems of pores, one being comprised straight channels with diameter 0.53 x 0.56 nm, which are perpendicular to zigzag/sinusoidal channels of diameter of 0.51 x 0.55 nm [148, 150, 156]. Figure 1-20 (line 3) shows the detailed structure of ZSM-5.

### 1.5.3 Catalysis by zeolites

Zeolites possess numerous significant catalytic properties since they have many catalytic sites with high temperature stability [152]. Moreover, zeolites can offer further features such as regular and well defined micropore structures and large specific surface areas [157]. Zeolites can be used as a catalyst support for transition metals and high dispersion of these metals can be achieved [150].

Zeolitic materials are widely applied in the petrochemical industry. In 1962, zeolite catalysis was introduced on an industrial scale for the catalytic cracking of heavy petroleum distillates, one of the most important chemical processes worldwide. The use of zeolite in these processes resulted in a significant increase in the selectivity/yield of gasoline, the most valuable product [67, 148]. Crude petroleum is initially separated by distillation into fractions, and these fractions, heavier gas-oil, are cracked on a zeolite to produce petrol (gasoline) [150]. In 1986, the addition of ZSM-5 zeolite was a significant development as an octane enhancer for gasoline production from gas oil cracking. Cracking of hydrocarbons is an acid-catalysed process which involves C-C bond dissociation *via* formation of carbocations (carbenium and carbonium ions), catalysed by Brønsted and Lewis acid sites of zeolites [67].

#### 1.5.3.1 Deactivation of zeolite catalysts (Coke formation)

Deactivation of zeolites can occur by deposition of carbonaceous (coke) species in two main ways, namely coverage of active site (i.e. the active sites are poisoned by coke adsorption) or blockage of pores (i.e. when the reactants cannot access the active sites) [158]. Coke may form on the external surfaces of zeolite crystals as well as in internal pores [159].

The structure of coke varies depending upon conditions, but basically consists of undefined polyaromatic compounds. The formation of coke on zeolites is believed to be a shape-selective process. For example, under similar conditions, the deposition of coke is much more slow on medium-pore zeolites such as H-ZSM-5 than on larger pore zeolites such as H-Y zeolite. This has been attributed to the suggestion that the space available at the channel intersections in ZSM-5 are insufficient to accommodate polyaromatic structures in contrast to the larger cavities of H-Y [159]. Moreover, reaction sensitivity to coking is

more severe with mono-directional than with three-dimensional zeolite pore system. With the former, blockage of a channel may obstruct the access to numerous active sites, whereas with the latter the sites remain potentially accessible from other pathways [158], as shown in Figure 1-22 (A). This concept can be extended to highlight the greater extent of pore blockage required to lower accessibility in the three dimensional pore network, Figure 1-22.

Figure 1-22 presents two modes of deactivation, coverage of active site and blockage of pores. In Figure 1-22 (A), coke is formed and trapped at the channel intersections restricting access. In this case, reactants can still access the rest of the pore system. This may reduce the zeolite activity by reducing the number of accessible active sites without drastically affecting the accessible surface area. Figure 1-22 (B) presents a schematic of deactivation by pore blockage [160]. This would affect both the number of accessible active sites and surface area.

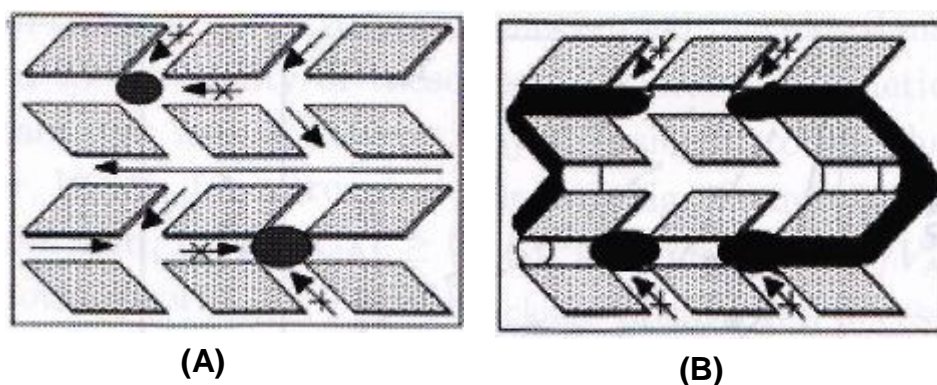


**Figure 1-22** Schematic representation of coke distribution in zeolite [160].

## 1.6. Objectives

The overall objective of this project was to investigate the direct catalytic cracking of methane into hydrogen and carbon. In this study, two major products, hydrogen and carbon, were evaluated and characterised. The objectives of the project were the following:

- To evaluate and characterise cheap and disposable iron-containing waste materials (as catalysts) for the direct catalytic cracking of methane.
- To explore optimisation of these waste materials for the direct catalytic cracking of methane.
- To study the effect of different parameters (such as reaction temperature, the flow rate of the feed gas, the addition of dopants, palladium precursor and the support type) and the nature of the carbon produced.
- To study and compare the activity of Ni/H-ZSM-5, Pd/H-ZSM-5 and Cu/H-ZSM-5 catalyst for the direct catalytic cracking of methane and evaluate and characterise the carbon deposited on them. Zeolite-supported catalysts were examined because of their potential further application for dehydroaromatisation of methane to valuable aromatics and higher hydrocarbons and selective poisoning of highly active catalysts could prove a novel route towards methane dehydroaromatisation catalysts.

## **2. Experimental**

### **2.1. Introduction**

The details of experimental techniques used in this study are presented in four separate sections: waste materials containing iron as catalysts, catalyst preparation, catalytic testing, and catalyst characterisation.

### **2.2. Waste materials containing iron as catalysts**

Three iron containing waste materials (Landfill sample, Factory sample and Red Mud sample) have been employed as catalysts for the direct catalytic cracking of methane into hydrogen and carbon. These materials have been procured from three different locations. Landfill and Factory samples have been named according to where the samples have been collected whereas Red Mud is a known waste material [161]. The following sections will present more details about these samples.

#### **2.2.1 Landfill and Factory samples**

The Landfill sample was collected from the River Allander in Milngavie, a town close to Glasgow in the United Kingdom. Figure 2-1 is a photograph of the site from which it was obtained. From the photograph, a clearly orange/red colouration associated with ochre is observable on the river bank. The Landfill sample was collected from the river at this location. This area was once used for Landfill dumping, as such it is expected that a part of the leachate originated from the Landfill waste.

The Factory sample was procured from a residue from a historic manufacturing site, Lennoxton Nail Works. Lennoxton is a town near to Glasgow in the United Kingdom. Figure 2-2 is a photograph of the site in the Lennoxton Nail Works from where the Factory sample was obtained.

Prior to receiving these samples they were washed with distilled water to removal of debris such as twigs and then dried in a laboratory oven at 110 °C. These procedures were kindly performed by Drs Pulford and Flower's groups at the University of Glasgow.



**Figure 2-1** The site in the River Allander from where the Landfill sample was obtained.



**Figure 2-2** The site in the Lennoxton Nail Works from where the Factory sample was obtained.

As will be shown in Chapter 3, the Landfill sample is in the form of biogenic iron oxide, originating from *Leptothrix* bacteria in the river, whereas the Factory sample is a heterogeneous mixture of phases. These samples were used as received and also following calcination, acid washing and palladium doping.

## **2.2.2 Red Mud sample (RM)**

Red Mud is a waste product of the aluminium industry, originating from bauxite processing using the Bayer Process. It is known that the major component of the Red Mud is iron oxide. The Red Mud sample used in this study was collected from a site in Southern India in 2008. This sample was employed as received without further modification. The Red Mud sample was kindly provided by Dr. Batra at the Centre for Energy and Environment, TERI, India.

## **2.2.3 Modification of Landfill and Factory sample**

As previously mentioned, the Landfill and Factory samples were employed in both as received and modified forms. The purpose of the modifications was to attempt to enhance catalyst activity for the methane cracking reaction. These modifications included calcination at different temperatures, washing with hydrochloric acid and palladium doping.

### **2.2.3.1 Calcination of iron-containing waste materials**

The Landfill and Factory samples were calcined in static air at temperatures of 300, 500, 700 and 900 °C for 5 hours applying a heating ramp rate of 10 °C/min. Approximately 0.6 g of sample was placed in a quartz boat, and was then calcined inside a tube furnace (Carbolite MTF 10/25/130). The calcined samples were stored in glass vials.

### **2.2.3.2 Acid washing of iron-containing waste materials**

After the initial treatment, the Landfill and Factory samples were washed with hydrochloric acid (37 %, Sigma-Aldrich). Approximately 1.5 g of the samples were immersed in 50 mL of 0.5 M hydrochloric acid. The resulting mixture was stirred for 30 minutes at room temperature. The obtained mixture was filtered and the residue was washed with distilled water several times. The samples were dried overnight at 100 °C and then calcined in static air at 500 °C for 5 hours applying a heating ramp rate of 10 °C/min. The treated samples were stored in glass vials.

### 2.2.3.3 Palladium addition to iron-containing waste materials

The Landfill and Factory samples were doped with palladium. Approximately 0.4 wt% Pd loadings were prepared by incipient wetness impregnation. An aqueous solution of palladium (II) nitrate hydrate (Aldrich,  $\text{Pd}(\text{NO}_3)_2 \cdot x\text{H}_2\text{O}$ ) containing the 0.01 g of  $\text{Pd}(\text{NO}_3)_2 \cdot x\text{H}_2\text{O}$  dissolved in deionised water was added to 1 g of the samples. The impregnated sample was dried at 100 °C for 24 hours and calcined in air at 500 °C for 16 hours applying a heating ramp rate of 10 °C/min.

## 2.3. Catalyst preparation

A number of different catalysts were prepared for the second part of this project. Pd, Ni, Cu, Fe and Co were loaded onto zeolite H-ZSM-5.

Different modifications of the Pd/H-ZSM-5 and Ni/H-ZSM-5 catalysts were performed to determine their effect upon performance. These modifications consisted of doping with other transitional metals and altering the loading of nickel. Pd and Ni utilising different supports were also investigated.

### 2.3.1 Preparation of Pd/H-ZSM-5 catalyst and its doping

The approximately 0.4 wt% Pd/HZSM-5 catalyst utilised in this work was prepared by incipient wetness impregnation of zeolite HZSM-5 (Catal, Si/Al ratio = 23) in powder form. Aqueous solutions of palladium nitrate ( $\text{Pd}(\text{NO}_3)_2 \cdot x\text{H}_2\text{O}$ ) were utilised as the palladium precursor. The impregnated sample was dried at 80 °C for 24 hours and calcined in static air at 500 °C for 16 hours. Care was taken to minimise the potential effects of deep bed steaming - materials were calcined as shallow beds in a quartz calcination boat.

The preparation of *ca.* 0.4 wt% Pd/HZSM-5 materials comprising additional metal cations were prepared by consecutive stages of impregnation. The first stage involved the initial incorporation of the palladium component onto the zeolite as previously mentioned. In the next stage additional impregnation of the zeolite with the second metal precursor salt was undertaken. After every stage, the resulting slurry was dried at 80 °C for 24 hours before undergoing calcination in static air at 500 °C for 16 hours. The 0.4 wt% Pd/H-ZSM-5 catalyst was doped with  $\text{Fe}^{3+}$ ,  $\text{Ni}^{2+}$ ,  $\text{Co}^{2+}$  and  $\text{Cu}^{2+}$ . The molar ratio of the dopant metal (M) added to Pd/H-ZSM-5 was *ca.* 0.25 (M/Pd).

Table 2-1 presents the precursors and quantities of materials used in the preparation for *ca.* 2 g of each catalyst. The quantities of these materials were arranged in the table depending upon the quantity of catalyst required.

<b>Table 2-1</b> the precursors and quantities of materials used in the preparation of 2 g of 0.4 % Pd/H-ZSM-5 catalyst, and those impregnated with Fe <sup>3+</sup> , Ni <sup>2+</sup> , Cu <sup>2+</sup> and Co <sup>2+</sup> .			
<b>Catalyst</b>	<b>Precursors</b>	<b>Quantity (g)</b>	<b>ZSM-5 Quantity(g)</b>
<b>0.4 % Pd/HZSM-5</b>	<b>Pd(NO<sub>3</sub>)<sub>2</sub>.xH<sub>2</sub>O (Aldrich)</b>	<b>0.019</b>	<b>2.000</b>
<b>0.4 % Pd-Ni/HZSM-5*</b>	<b>Pd(NO<sub>3</sub>)<sub>2</sub>.xH<sub>2</sub>O (Aldrich), Ni(NO<sub>3</sub>)<sub>2</sub>.6H<sub>2</sub>O (98.5, Aldrich)</b>	<b>0.019 0.010</b>	<b>2.000</b>
<b>0.4 % Pd-Fe/HZSM-5*</b>	<b>Pd(NO<sub>3</sub>)<sub>2</sub>.xH<sub>2</sub>O (Aldrich), Fe(NO<sub>3</sub>)<sub>3</sub>.9H<sub>2</sub>O (99 %, Janssen)</b>	<b>0.019 0.015</b>	<b>2.000</b>
<b>0.4 % Pd-Co/HZSM-5*</b>	<b>Pd(NO<sub>3</sub>)<sub>2</sub>.xH<sub>2</sub>O (Aldrich), Co(NO<sub>3</sub>)<sub>2</sub>.6H<sub>2</sub>O (98 %, Aldrich)</b>	<b>0.019 0.010</b>	<b>2.000</b>
<b>0.4 % Pd-Cu/HZSM-5*</b>	<b>Pd(NO<sub>3</sub>)<sub>2</sub>.xH<sub>2</sub>O (Aldrich), Cu(NO<sub>3</sub>)<sub>2</sub>.3H<sub>2</sub>O (99.5 %,Analar)</b>	<b>0.019 0.008</b>	<b>2.000</b>

\*dopant metal ion/Pd molar ratio of 0.25

### 2.3.2 Preparation of Pd/H-ZSM-5 catalyst by different precursors

Three palladium precursors were applied for preparation of 0.4 wt% Pd/HZSM-5 catalysts by incipient wetness impregnation using the drying and calcination conditions shown in Section 2.3.1. Palladium nitrate (Pd(NO<sub>3</sub>)<sub>2</sub>), palladium chloride (PdCl<sub>2</sub>) and palladium acetylacetonate Pd(C<sub>5</sub>H<sub>7</sub>O<sub>2</sub>)<sub>2</sub> were employed as palladium sources for the preparation of the 0.4 wt% Pd/H-ZSM-5 catalysts. The catalysts prepared from palladium nitrate and chloride were obtained by zeolite impregnation with aqueous solutions of these salts, while the sample prepared from palladium acetylacetonate was obtained by zeolite impregnation with a benzene solution of this precursor. The quantities of materials employed in the preparation for 2 g of each catalyst are presented in Table 2-2.

<b>Table 2-2</b> The quantities of materials used in the preparation of 0.4 % Pd/ H-ZSM-5 catalyst by different precursors.			
<b>Catalyst</b>	<b>Precursors</b>	<b>Quantity (g)</b>	<b>ZSM-5 Quantity(g)</b>
<b>0.4 % Pd/HZSM-5</b>	<b>Pd(NO<sub>3</sub>)<sub>2</sub>.xH<sub>2</sub>O (Aldrich)</b>	<b>0.019</b>	<b>2.000</b>
<b>0.4 % Pd/HZSM-5</b>	<b>PdCl<sub>2</sub> (JMO)</b>	<b>0.014</b>	<b>2.000</b>
<b>0.4 % Pd/HZSM-5</b>	<b>Pd(C<sub>5</sub>H<sub>7</sub>O<sub>2</sub>)<sub>2</sub> (99 %, Strem chemicals)</b>	<b>0.024</b>	<b>2.000</b>

### 2.3.3 Preparation of Pd based catalyst on non-zeolite supports

0.4 wt% Pd supported on  $\gamma$ -Al<sub>2</sub>O<sub>3</sub> and SiO<sub>2</sub> (Aldrich) were separately prepared by using the incipient wetness impregnation technique with the same conditions of drying and calcination as described in Section 2.3.1. It should be mentioned that the  $\gamma$ -Al<sub>2</sub>O<sub>3</sub> was prepared by calcination of boehmite (HiQ-30) at 500 °C for 5 hours. The  $\gamma$ -Al<sub>2</sub>O<sub>3</sub> phase was confirmed by XRD powder diffraction as will be shown in Chapters 5 and 6. The quantities of materials employed in the preparation for 2 g of each catalyst are presented in Table 2-3.

Catalyst	Precursors	Quantity (g)	Support	
			Type	Quantity(g)
0.4 wt% Pd/ $\gamma$ -Al <sub>2</sub> O <sub>3</sub>	Pd(NO <sub>3</sub> ) <sub>2</sub> .xH <sub>2</sub> O (Aldrich)	0.019	$\gamma$ -Al <sub>2</sub> O <sub>3</sub>	2.000
0.4 wt% Pd/SiO <sub>2</sub>	Pd(NO <sub>3</sub> ) <sub>2</sub> .xH <sub>2</sub> O (Aldrich)	0.019	SiO <sub>2</sub>	2.000

### 2.3.4 Preparation of Cu/H-ZSM-5, Ni/H-ZSM-5 with different Ni loadings and doping Ni/H-ZSM-5 with Pd

The preparation of Ni/HZSM-5 catalyst with different Ni loadings of 0.4, 4 and 8 wt% was carried out. Doping of 0.4 wt% Ni/HZSM-5 catalyst with Pd as a second metal (dopant Pd ion/Ni molar ratio of 0.25) was undertaken and 0.4 wt% Cu/HZSM-5 catalysts were also prepared. These catalysts were prepared using incipient wetness impregnation as detailed in Section 2.3.1. Table 2-4 presents the quantities of materials employed in the preparation for *ca.* 2 g of each catalyst.

Catalyst	Precursors	Quantity (g)	ZSM-5 Quantity(g)
0.4 wt % Ni/HZSM-5	Ni(NO <sub>3</sub> ) <sub>2</sub> .6H <sub>2</sub> O (98.5 %, Aldrich)	0.040	2.000
4 wt % Ni/HZSM-5	Ni(NO <sub>3</sub> ) <sub>2</sub> .6H <sub>2</sub> O (98.5 %, Aldrich)	0.400	2.000
8 wt % Ni/HZSM-5	Ni(NO <sub>3</sub> ) <sub>2</sub> .6H <sub>2</sub> O (98.5 %, Aldrich)	0.800	2.000
0.4 wt % Ni-Pd/HZSM-5*	Ni(NO <sub>3</sub> ) <sub>2</sub> .6H <sub>2</sub> O (98.5 %, Aldrich) Pd(NO <sub>3</sub> ) <sub>2</sub> .xH <sub>2</sub> O (Aldrich)	0.040 0.005	2.000
0.4 wt % Cu/HZSM-5	Cu(NO <sub>3</sub> ) <sub>2</sub> .3H <sub>2</sub> O (99.5 %, Analar)	0.031	2.000

\* dopant Pd ion/Ni molar ratio of 0.25

### 2.3.5 Preparation of Ni based catalyst on non-zeolite supports

In this work, 0.4 % Ni supported on  $\gamma$ -Al<sub>2</sub>O<sub>3</sub>, SiO<sub>2</sub> (Aldrich) and silicic acid (SiO<sub>2</sub>.xH<sub>2</sub>O, Mallinckrodt) were separately prepared and tested. The preparation technique used as detailed in Section 2.3.1. The quantities of materials employed in the preparation for *ca.* 2g of each catalyst are presented in Table 2-5.

<b>Table 2-5</b> The quantities of materials used in the preparation of 0.4 wt% Ni/ $\gamma$ -Al <sub>2</sub> O <sub>3</sub> , 0.4 wt% Ni/SiO <sub>2</sub> and 0.4 wt% Ni/SiO <sub>2</sub> .xH <sub>2</sub> O catalyst.				
Catalyst	Precursors	Quantity (g)	Support	
			Type	Quantity (g)
0.4 wt% Ni/ $\gamma$ -Al <sub>2</sub> O <sub>3</sub>	Ni(NO <sub>3</sub> ) <sub>2</sub> .6H <sub>2</sub> O (98.5 %, Aldrich)	0.040	$\gamma$ -Al <sub>2</sub> O <sub>3</sub>	2.000
0.4 wt% Ni/SiO <sub>2</sub>	Ni(NO <sub>3</sub> ) <sub>2</sub> .6H <sub>2</sub> O (98.5 %, Aldrich)	0.040	SiO <sub>2</sub>	2.000
0.4 wt% Ni/SiO <sub>2</sub> .xH <sub>2</sub> O	Ni(NO <sub>3</sub> ) <sub>2</sub> .6H <sub>2</sub> O (98.5 %, Aldrich)	0.040	SiO <sub>2</sub> .xH <sub>2</sub> O	2.000

### 2.3.6 Synthesis of 2-line ferrihydrite

Approximately 330 mL of 1 M KOH ( $\geq$ 85 %, Aldrich) solution was added to 500 mL of 0.1 M Fe(NO<sub>3</sub>)<sub>3</sub>.9H<sub>2</sub>O (99 %, Janssen) solution with stirring to bring the pH to 7-8, with the last few mL of KOH being added slowly in order not to exceed this pH. The resultant suspension was centrifuged and washed with distilled water several times. The solid product was collected and cooled in an ice bath for 1 day and was then left at room temperature for drying. The sample was stored in glass vials. The method of this synthesis is derived from the literature [130, 132].

## 2.4. Catalytic testing

A schematic of the micro-reactor applied for the methane cracking experiments, which was designed, built and commissioned is shown in Figure 2-3.

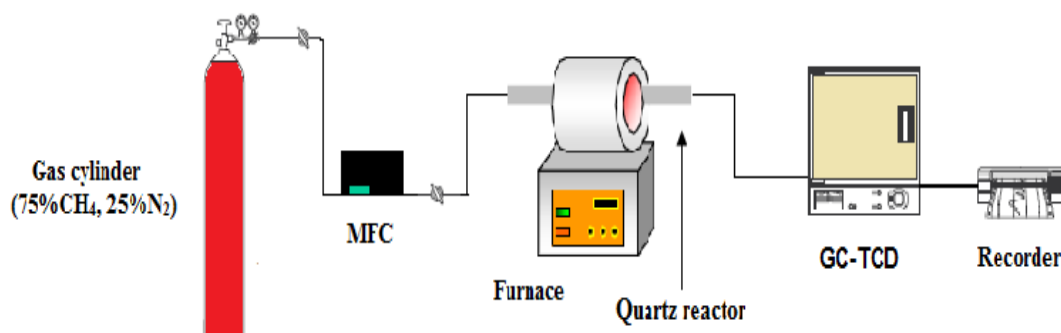


**Figure 2-3** Schematic representation of the reactor system.

The quartz reactor (33 cm length and 1cm internal diameter) was suitably designed for methane cracking in the absence of a gas-phase oxidant as shown in Figure 2-3. The iron-containing waste, zeolite, alumina and silica catalysts were each used in the form of powders. Each was charged centrally within the heated zone of a quartz micro-reactor between quartz wool plugs.

The reactions were performed at various temperatures under ambient pressure. A K-type thermocouple was attached to the exterior surface of the quartz micro-reactor tube, at the catalyst bed position, to measure the temperature of the reaction at the reactor wall. Although, in an ideal situation, the measurement of temperature within the catalyst bed is desirable, the non-inert nature of the thermocouple can affect the reaction and/or sample behaviour. Therefore, the appropriate compromise was the attachment of the thermocouple on the reactor wall.

The feed gas composition applied was a mixture of 75 % methane and 25 % nitrogen (BOC, 99.98 %) which was passed over a *ca.* 0.4 g of the sample at a total flow rate of 12 mL/min resulting in gas hourly space velocity (GHSV) typically of 720 h<sup>-1</sup>. Product

analysis was performed by on-line Hewlett Packard 5890A GC. For H<sub>2</sub> quantification a Molecular Sieve 13X packed column of 12 feet in length and TCD were employed. The GC carrier gas employed was argon (BOC).

The GC set-up, however, was not configured to detect carbon oxides. When required, to measure the CO<sub>x</sub> formation, offline FTIR spectroscopy was used. CO<sub>x</sub> quantification was measured by FTIR analysis of aliquots of the effluent reactor stream which were sampled by passage through a gas-phase FTIR cell. FTIR Spectrum was analysed using a Jasco 4100 FTIR Spectrometer operating in the 400–4000 cm<sup>-1</sup> spectral range acquiring 64 scans for each spectrum at a resolution of 4 cm<sup>-1</sup> following background subtraction. This method is limited, because of CO<sub>2</sub> background subtraction complications.

### **2.4.1 Gas calibrations**

Hydrogen is the main product in these studies. Hence, the calibration of hydrogen was carried out to obtain the response factor for hydrogen. Gas mixtures of different compositions were analysed and the arithmetic mean of six consistent measurements for each data point was taken. A line of correlation between the GC area counts and concentration was found from which a response factor was determined. The response factor of hydrogen was then used for the subsequent calculation of GC data.

Calibration of CO and CO<sub>2</sub> also was performed. A transmission IR cell (12 cm path length) was thoroughly flushed then filled with a known concentration of CO and CO<sub>2</sub>, using a gas mixture which consisted of 10 % H<sub>2</sub>, 10 % CH<sub>4</sub>, 10 % CO, 10 % CO<sub>2</sub> and 60 % argon (BOC). The IR spectra obtained were then employed as a standard reference, since both the intensity of the bands (2360 cm<sup>-1</sup> for CO<sub>2</sub> and 2170 cm<sup>-1</sup> for CO) and the concentration of CO and CO<sub>2</sub> are known. Therefore, the concentration of CO and CO<sub>2</sub> produced during the reaction could be calculated.

### **2.4.2 Catalytic testing procedure**

A quartz reactor tube with 1 cm internal diameter was charged with 0.4 g of the sample (waste samples containing iron or catalysts prepared), which was placed between plugs of quartz wool. Initial studies on the effect of reaction temperature were carried out with a temperature programme from 600 to 900 °C. Catalytic testing of waste materials was

carried out using a temperature programme from 600 to 800 °C. All zeolite, alumina and silica catalysts were examined isothermally at 800 °C. A mixture of 75 % methane and 25 % nitrogen (BOC, 99.98 %) was introduced into the reactor at 12 mL/min flow rate by using a calibrated Brooks Model 5878 mass flow controller. Nitrogen was used as an internal standard. The tail gas was sampled periodically and analysed through the gas chromatograph.

### **2.4.3 Manipulation of GC Data**

In this work, reaction data was reported in terms of specific formation rates of products (hydrogen or carbon oxides). This approach has been applied because, at generally low levels of conversion, the measurement of a small difference in the GC data may be subjected to a relative large degree of random error. This is a particular concern in the present study because the reaction never attains steady state, it is generally either in activation or deactivation phase. Based on the literature, expressing data for this reaction as formation rates is a fairly common practice, for example [51, 161, 162]. Appendix 1 shows the equations used for the calculation of reaction data. Methane conversion data for all catalysts were evaluated. The plots are presented in Appendix 2.

## **2.5. Characterisation of the catalyst**

The catalyst was characterised using different methods as described in the following subsections.

### **2.5.1 X-ray powder diffraction (XRD)**

Powder X-ray diffraction was performed on a Siemens D5000 diffractometer using Cu K $\alpha$  radiation. Data were collected over a range of  $2\theta$  values from 5 to 85 ° using a step size of 0.02 ° and a counting rate of 2 seconds per step. Samples were prepared by compaction into silicon sample holders.

### **2.5.2 Hot stage X-ray powder diffraction (XRD)**

Hot stage XRD analyses was also performed on the Siemens D5000 diffractometer using an Anton-Paar XRK reaction cell. The samples were heated *in situ* from room temperature

at a rate of 10 °C/min under a 20 mL/min flow rate of a mixture of 75 % methane and 25 % nitrogen (BOC, 99.98 %). Cu K $\alpha$  radiation was employed and the data were investigated over a range of 2 $\theta$  values from 10 to 85 ° using a step size of 0.02 ° and a counting rate of 2 s/step. Scans were taken at room temperature, 500, 600 and 700 °C. At each temperature increment the sample was held for 1 hour.

### **2.5.3 Thermal gravimetric analysis (TGA)**

TGA was carried out on a TA Instruments TGA Q500 series instrument under air. The catalyst charge was 8 mg and the flow rate of air used was 50 mL/min. The catalyst was heated from room temperature to 1000 °C in an air stream applying a ramp rate of 10 °C/min.

### **2.5.4 Elemental analysis (CHN)**

CHN analyses were performed by combustion using a CE-440 elemental analyser. Mrs. Kim Wilson, University of Glasgow, kindly performed these analyses.

### **2.5.5 N<sub>2</sub>-physisorption**

N<sub>2</sub>-physisorption measurements were undertaken at -196 °C on a Micromeritics Gemini III 2375 Surface Area Analyser. The resulting adsorption isotherms were analysed using the BET equation to determine the specific surface area of each sample. Prior to analysis, a known mass of sample, roughly 0.05 g, was degassed overnight under a flow of N<sub>2</sub> at 110 °C.

### **2.5.6 Raman Spectroscopy**

Raman spectra of post-reaction samples were carried out using a Horiba Jobin Yvon LabRAM High Resolution spectrometer. A Kimmon IK series He-Cd 532.17 nm laser was used as the excitation source for the laser. Laser light was focused for 10 seconds using a 50x objective lens and a grating of 600. The scattered light was collected in a back scattering configuration and was detected using a CCD detector. The spectral range examined was in the region of 500 to 3000 cm<sup>-1</sup>.

### **2.5.7 Scanning Electron Microscopy (SEM)**

SEM images of the pre- and post-reaction samples were taken using a Philips XL30 ESEM tungsten filament operating at 25 kV and secondary electron detector. The samples were dispersed on adhesive carbon stubs and the samples were then coated using a Polaron SC7640 Auto high resolution sputter coater with a gold / palladium target to improve image quality. In addition, the SEM system was equipped with an energy dispersive X-ray spectroscopy (EDXS) device, Oxford Instruments X-Act 10 mm<sup>2</sup>, for chemical elemental analyses.

### **2.5.8 High resolution transmission Electron Microscopy (HRTEM)**

HRTEM was carried out on samples using a Jeol JEM 2011 fitted with a LaB<sub>6</sub> filament and a resolution of 1.8 Å. Samples were prepared for TEM by dispersed in acetone and dropped onto holey carbon grids and allowed to dry. Mr. Ross Blackley, University of St. Andrews, kindly performed this analysis.

### **2.5.9 Inductively coupled plasma optical emission spectroscopy (ICP-OES)**

ICP optical emission spectroscopy (ICP-OES) was used to obtain information regarding the elemental composition of the waste samples containing iron oxide. The ICP-OES instrument used in this work was a ICPS-7000 SHIMADZU. Approximately 0.3 g of the sample as well as certified reference material, Soil IAEA 7, were placed in a Teflon pressure vessel and 6 mL nitric acid (65 % extra pure, Riedel-Deltaën) and 4 mL hydrofluoric acid (40%, Qualikems) were added. The vessels were capped, sealed and heated following the digestion method cycles reported elsewhere with some modification [163], then the vessels were cooled down for 2 hours. The aqua regia solution was used to complete the digestion, where 12 mL of aqua regia was added to samples. Each vessel was sealed and heated which followed the above procedure. After digestion, the samples were transferred to a volumetric flask and diluted with deionised water to 100 mL. Mr. Matar Al-shalwi, King Saud University, kindly performed these measurements.

### **2.5.10 Fourier Transform Infrared spectroscopy (FTIR)**

FTIR spectra of a side product produced from the reaction of methane cracking over the Factory sample was recorded by using a Fourier Transform Infrared Spectrometer (FTIR-8400S, Shimadzu). The spectrum was collected at a spectral resolution of  $2\text{ cm}^{-1}$ , with 35 scans over the range of  $600\text{--}4000\text{ cm}^{-1}$  being made. Background subtraction was applied.

### **2.5.11 NMR spectroscopy**

$^1\text{H}$  NMR and  $^{13}\text{C}$  NMR spectra were recorded in  $\text{CDCl}_3$  solutions for also a side product produced from the reaction of methane cracking over the Factory sample at room temperature using Bruker DPX 400 spectrometer. These measurements were kindly performed by the group of Professor Graeme Cooke at the University of Glasgow.

## Results

### 3. Waste iron oxides as catalysts for hydrogen production *via* direct cracking of methane

#### 3.1. General introduction

As discussed in Chapter 1, the direct cracking of methane is one of the methods used for hydrogen production and also one of the most promising technologies in this field. The process is technologically simple and involves one step ( $\text{CH}_4 \rightarrow 2\text{H}_2 + \text{C}$ ). Moreover, this process is environmentally friendly and does not produce harmful gases such as CO and  $\text{CO}_2$ , whereas traditional hydrogen production methods tend to pollute the environment and contribute to the greenhouse effect. However, non-catalytic thermal cracking of methane requires high temperatures of over 1200 °C for complete conversion. Therefore, an alternative approach is to employ a catalyst which can contribute to reducing the operating temperatures of the process and increase the rate of methane decomposition, thereby increasing the hydrogen yield. This greatly improves the economics of the process. Metal catalysts for direct cracking of methane are usually based on Ni, Co and Fe, which are well-known active catalysts for hydrocarbon decomposition. Catalysts based on Ni and Fe have been revealed to be the most effective [164, 165]. In addition, the reaction of catalysts based on a combination of metals has been studied previously, including Co/Mo/ $\text{Al}_2\text{O}_3$  or Ni/Cu/ $\text{Al}_2\text{O}_3$  [166] and Ni/ $\text{Al}_2\text{O}_3$  or Ni/Cu/ $\text{Al}_2\text{O}_3$  [167].

Noble metals and metal oxides are popular catalyst components for numerous industrial applications. However, their high price is one of the economic problems facing industrialists. Therefore, the use of waste materials as catalysts is encouraged for environmental and economic reasons. The use of either natural or industrial solid wastes that contain metals with catalytic properties as alternative sources for commercial catalysts can enable a reduction in the cost of production [168, 169], although this may involve a compromise in terms of performance. There would also be less of an economic penalty for disposal of deactivated materials obtained from such sources.

It is possible that the employment of waste materials with catalytic properties for the direct cracking of methane will drastically reduce the cost of hydrogen production as well as help

the environment and contribute to sustainability by providing an alternative use for unused waste.

A publication by Hargreaves and co-workers [161] was the first study on the direct cracking of methane over Red Mud, a waste product of the aluminium industry. They demonstrated that Red Mud possessed significant activity for the cracking of methane, producing hydrogen and a carbon containing magnetic material. This study has been followed by the same researchers to study the nature of carbon deposited during methane decomposition over Red Mud and the phase transformation sequences of Red Mud during the catalytic reaction [162]. Their study addressed some important aspects, such as the large surface area of the Red Mud sample having significant carbon growth, the evaluation of the formation of CO and CO<sub>2</sub> associated with hydrogen production in the initial phase of sample reduction and the observation of different carbon morphologies including nanospheres and multiwalled nanotubes (MWNT).

This chapter details and discusses the potential of using new waste materials for direct catalytic cracking of methane into hydrogen and carbon. These materials are iron-containing wastes procured from three locations—the leachate from a former Landfill site, residue from an old nail Factory and a waste product of the aluminium industry. As outlined in Chapter 2, these materials are named "Landfill sample", "Factory sample" (residue from an old nail Factory) and "RM" (a waste product of the aluminium industry, Red Mud) according to the place where they have been collected from or as per the known name of the waste. It must be noted that the Landfill sample is a biogenic iron oxide, which is formed by bacteria, while the other samples are merely industrial waste. A review of existing literature reveals that biogenic iron oxide does not appear to have been used before as a catalyst for direct decomposition of methane. As mentioned above, RM has been studied previously [161, 162], but it is used in this study for comparison with Landfill and Factory samples.

In the following sections, the characterisation of raw materials, reaction data and characterisation of post-reaction samples are presented and discussed. Moreover, an iron oxide compound that exhibits a similar phase composition to the Landfill sample has been prepared to test and compare with the Landfill sample. *In situ* XRD studies and the effect of reaction temperature on the Landfill sample have been applied to investigate the phase transformation sequences of the raw Landfill sample.

## 3.2. Results and discussion

### 3.2.1. Characterisation of raw Red Mud, Landfill and Factory samples

Characterisation of raw Landfill, Factory and RM samples have been made to identify those properties that are correlated with their catalytic performance. Many techniques such as XRD, ICP, TGA, CHN elements analysis, BET surface area, HRTEM and SEM have been used. The characterisation of these materials is described below.

#### 3.2.1.1. XRD patterns

Powder X-ray diffraction was performed on raw Landfill, Factory and RM samples and the results are illustrated in Figures 3-1 to 3-3. The XRD pattern of the raw Landfill sample exhibits an amorphous pattern with two very broad reflections, which is similar to 2-line ferrihydrite ( $\text{Fe}_5\text{HO}_8 \cdot 4\text{H}_2\text{O}$ ), as illustrated in Figure 3-1 [132, 170]. Figure 3-2 depicts the XRD pattern of the raw Factory sample. It is evident that it is more crystalline than the Landfill sample and it is apparent that it possesses a number of different phases as a result of a combination of precipitated iron and other minerals. This pattern was matched using the database of the Joint Committee on Powder Diffraction Standards (JCPDS) and the results showed that it is probably a mixture of several phases such as quartz ( $\text{SiO}_2$ ), haematite ( $\text{Fe}_2\text{O}_3$ ), clinoferrosilite ( $\text{FeSiO}_3$ ), aluminium oxide ( $\text{Al}_2\text{O}_3$ ) and iron oxide phosphate ( $\text{Fe}_9\text{O}_8\text{PO}_4$ ).

Figure 3-3 presents the powder X-ray diffraction of raw RM. It is evident that the RM is highly crystalline and contains numerous phases. These phases can be matched to goethite ( $\text{FeOOH}$ ), haematite ( $\text{Fe}_2\text{O}_3$ ), gibbsite ( $\text{Al}(\text{OH})_3$ ) and quartz ( $\text{SiO}_2$ ). This result is in good agreement with the result obtained by Hargreaves and co-workers [161], who used the same RM and studied its composition using powder X-ray diffraction.

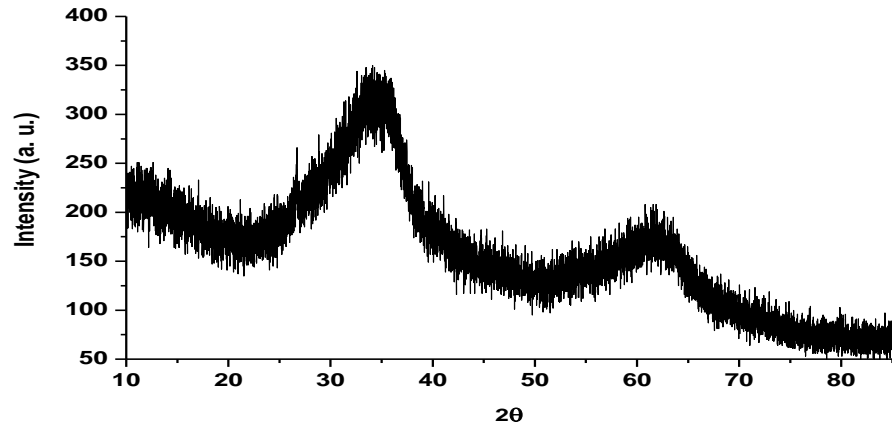


**Figure 3-1** Powder X-ray diffraction pattern of the raw Landfill sample which is consistent with the 2-line ferrihydrite structure  $\text{Fe}_5\text{HO}_8 \cdot 4\text{H}_2\text{O}$ .

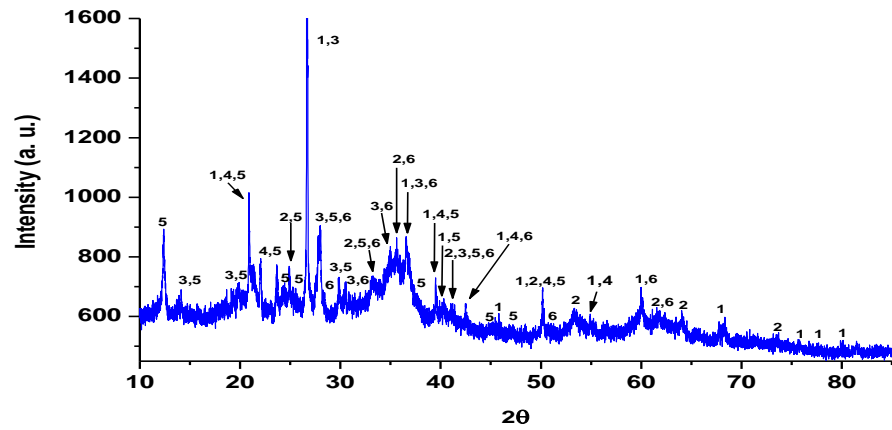


**Figure 3-2** Powder X-ray diffraction pattern of the raw Factory samples. 1: quartz ( $\text{SiO}_2$ ) 33-1161; 2: haematite ( $\text{Fe}_2\text{O}_3$ ) 33-0664; 3: clinoferrosilite ( $\text{FeSiO}_3$ ) 17-0548; 4: silicon oxide ( $\text{SiO}_2$ ) 43-0596; 5: aluminium oxide ( $\text{Al}_2\text{O}_3$ ) 31-0026; 6: iron oxide phosphate ( $\text{Fe}_9\text{O}_8\text{PO}_4$ ) 38-0031.

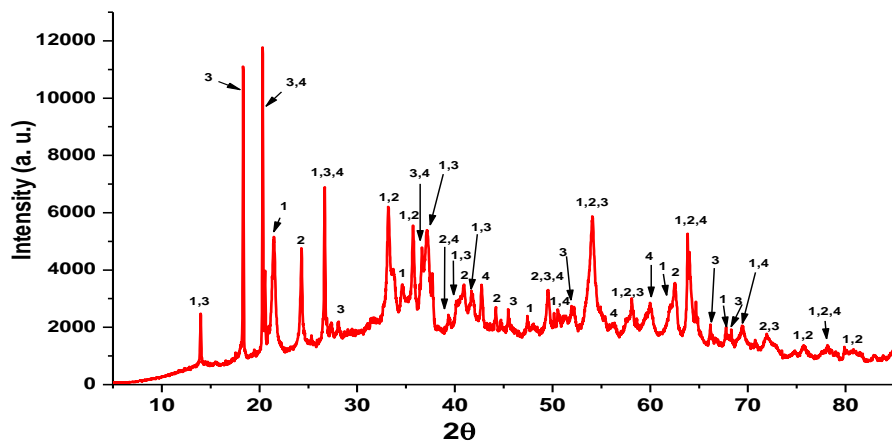


**Figure 3-3** Powder X-ray diffraction patterns of the raw RM samples. 1: goethite ( $\text{FeOOH}$ ) 17-0536; 2: haematite ( $\text{Fe}_2\text{O}_3$ ) 13-0534; 3: gibbsite ( $\text{Al}(\text{OH})_3$ ) 29-0041; 4: quartz ( $\alpha\text{-SiO}_2$ ) 05-0490.

### 3.2.1.2. ICP analysis of raw Landfill, Factory and Red Mud samples

Table 3-1 presents the elemental composition of the raw Landfill, Factory and RM samples as analysed using ICP-OES, as described in Chapter 2. As they are new materials, a wide scan of the raw Landfill and Factory samples was undertaken. A more restricted analysis of the RM sample was undertaken as the elemental composition of the used RM sample in this study was previously reported by Hargreaves and co-workers [161]. The elemental composition was determined by ICP. The researchers assumed that the elements are present in the form of pure oxides as is common for this material. They observed that iron, aluminium and silicon compounds are major components. Additionally, Ti, Ca, Mg, Na, K, P and Mn were found to be present. The results obtained here are similar to the values that they obtained if we assume that elements are present in the form of pure oxides. In addition, it is noteworthy that the total weight percentages for the Landfill and Factory samples do not total 100%. This may be because some unstable components may have been lost under the harsh chemical digestion method, thereby resulting in a change in the mass of samples.

It has been reported that the major elements of RM include iron, aluminium, silicon and titanium [171] and that their relative concentration depends on the geographical location of the source of the Red Mud. In addition, RM contains a range of alkali and alkaline earth compounds such as those containing sodium and calcium [161]. It is evident that the Landfill sample contains the highest weight percentage of iron (36.00 wt%), while the amount of iron in the Factory and RM samples are comparable to one another (22.70 and 25.00 wt%, respectively). Furthermore, the results reveal that the weight percentage of aluminium is the highest in the RM sample at 10.00 wt%, followed by the Factory sample at 3.80 wt% and the least in the Landfill sample at 1.20 wt%. It is not surprising that the RM sample contains the largest value of aluminium because it is a waste product of the aluminium industry and is generated from bauxite ore from which aluminium extraction is incomplete. It must be noted that the Landfill, Factory and RM samples contain a high proportion of silicon—17.30 wt%, 24.00 wt%, 9.50 wt%, respectively. In addition, the Landfill and Factory samples contain small amounts of a wide range of alkali metals, alkaline earth metals and transition metals.

<b>Table 3-1</b> ICP-OES analysis for elemental content of the raw Landfill, Factory and RM samples.			
<b>Element</b>	<b>Landfill sample</b>	<b>Factory sample</b>	<b>RM sample</b>
	<b>wt (%)</b>	<b>wt (%)</b>	<b>wt (%)</b>
Fe	36.00	22.70	25.00
Al	1.20	3.80	10.00
Si	17.30	24.00	9.50
Ca	2.50	1.44	1.60
Na	3.95	4.80	6.10
K	0.70	1.25	0.36
Mg	0.09	1.20	-
Mn	0.40	0.47	-
Ti	0.02	0.30	-
B	1.90	2.70	-
Co	0.001	0.004	-
Ni	0.001	0.005	-
Cu	0.001	0.006	-
Zn	0.020	0.040	-
V	0.002	0.020	-
Cd	0.004	0.002	-
Mo	0.001	0.001	-
Cr	0.002	0.005	-

### 3.2.1.3. CHN analysis of raw Landfill, Factory and Red Mud samples

CHN analysis for raw Landfill, Factory and Red Mud samples was conducted. The results are presented in Table 3-2. It is evident that all raw materials contain carbon. As mentioned earlier, the Landfill sample is biogenic iron oxide and as such may contain bacterial residue. Hence, the carbon content of the Landfill sample can be attributed to the presence of bacterial residue although it should be noted that the level of N was below the detection limit. In two separate studies, Emerson and Ghiorse [172, 173] investigated the ultrastructure and chemical composition of biogenic iron oxide sheaths, which were formed by *Leptothrix* bacteria. They found that these structures contain a protein and some sugars. Therefore, it is probable that this carbon is found due to the existence of sugars or organic sediments. In the case of the Factory sample, it is observed that there is a larger amount of carbon which may possibly arise from carbonate phases. The lowest carbon content was noted in the RM which may arise from carbonate phases.

<b>Table 3-2 CHN analysis for raw Landfill, Factory and RM samples</b>			
<b>Sample Code</b>	<b>Mean value, wt%</b>		
	<b>C</b>	<b>H</b>	<b>N</b>
<b>Raw Landfill</b>	<b>4.52 ± 0.02</b>	<b>1.29 ± 0.00</b>	-
<b>Raw Factory</b>	<b>10.70 ± 0.01</b>	<b>1.70 ± 0.05</b>	-
<b>Raw RM</b>	<b>1.00 ± 0.10</b>	<b>1.30 ± 0.01</b>	-

#### **3.2.1.4. SEM, EDX spectroscopy and HRTEM analysis of the raw Landfill, Factory and Red Mud samples**

SEM, HRTEM and EDX spectroscopic analyses of samples have been undertaken. SEM images of raw Landfill, Factory and RM samples are presented in Figure 3-4. It is evident from the image that there are differences in the morphology of the three samples. From the image in Figure 3-4 (A), it is evident that the Landfill sample comprises a component with an unusual morphology, which are either tubes or sheaths of iron oxide. It is believed that these hollow tubes of iron oxides have been formed by *Leptothrix* bacteria, whose single cells assume the shape of straight rods and it is considered that these tubes sheath these cells. It has been suggested that bacteria can gain energy through biotic reactions, which include the microbial oxidation of soluble Fe (II) to insoluble Fe (III) with extracellular precipitation of iron oxide sheaths with tube structures [131, 132]. In addition, it has been assumed that these sheaths serve various functions for the cells; for example, sheaths can provide physical protection for bacterial cells and play an important role in their nutrition system [133, 174]. Thus, micro-organisms can create attractive materials with unique morphologies and nanostructures which cannot be synthesised artificially. Figure 3-4 (B) depicts an image of the Landfill sample that reveals the inner and outer diameters of these tubes. According to the number of tubes in this image, the average outer diameter is 1.30  $\mu\text{m}$ , while the inner one is 663 nm. These dimensions are consistent with bacterial size ranges. Moreover, it is observed that the Landfill sample does not contain only tubes of iron oxides, but also aggregations of a poorly crystallised agglomeration as well. Takada *et al.* [131] studied some features of iron oxide sheaths formed by *Leptothrix* bacteria. Their

characterisation showed that the sheath was formed by hollow tubes whose average inner and outer diameters were found to be 1.1 and 1.4  $\mu\text{m}$ , respectively.

The morphology of the raw Factory and RM samples is somewhat similar to one another. From the images presented in Figure 3-4 (C) and (D), irregularly shaped aggregates and various particles of different sizes and shapes have been observed in both cases. Generally, the accumulation of irregular particles is found to be the dominant in all these samples; the exception being the Landfill sample, which is also comprises the tubular morphology component.

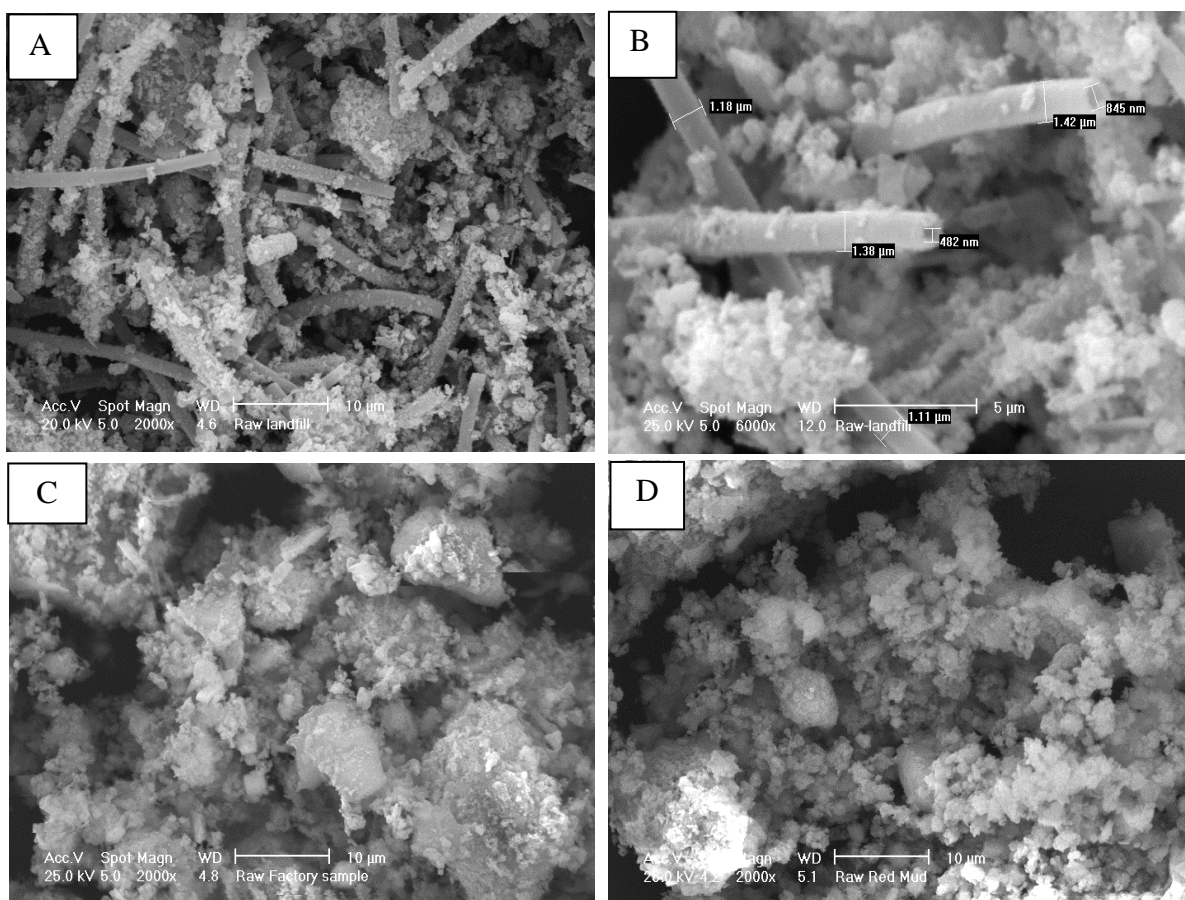


**Figure 3-4** SEM images of (A) raw Landfill sample, (B) a scanned image of the raw Landfill sample to reveal the inner and outer diameters of the tubes, (C) raw Factory sample and (D) raw RM sample.

Since the Landfill sample has two types of morphology, tubular and non-tubular, an EDX spectroscopic analysis was employed to conduct a detailed investigation of the composition of the different regions of the sample. Figure 3-5 demonstrates the SEM images of the raw Landfill sample with EDX spectra of selected spots from the two areas (as indicated by squares). It is evident that the EDX spectra for both morphologies are similar except for the different relative intensity of the peaks. Further, the major elements

that can be detected in these regions are Fe, Si, and Ca. It should be mentioned that Au and Pd peaks in spectra arise as a consequence of the sample coating undertaken to reduce the charge of sample during their analysis. In Figure 3-5 (A,B), the EDX spectra shows the chemical composition of the selected tube. The chemical composition was determined to be approximately Fe:Si:Ca = 92.80:4.10:3.10 (O, C, Au and Pd are not included in this analysis). The chemical composition of non-tubular region selected was determined to be Fe:Si:Ca = 94.55:3.30:2.15, (again excluding O, C, Au and Pd).

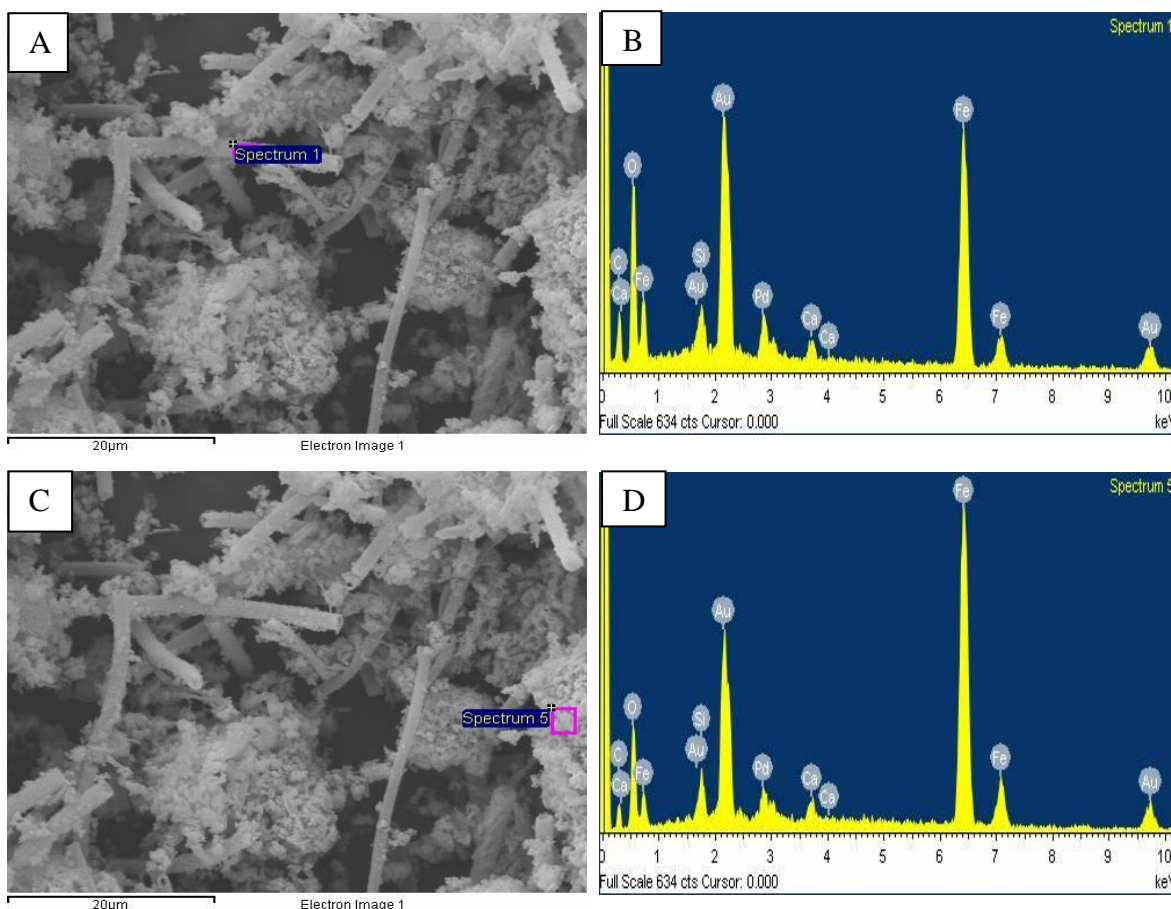


**Figure 3-5** SEM images and EDX analysis for the raw Landfill sample. (A) SEM images indicated by a square for the tubular shape. (B) EDX analysis for the selected spot indicated by the square in the SEM image (A). (C) SEM image that is indicated by a square for the non-tubular shape. (D) EDX analysis for the selected spot indicated by a square in the SEM image (C).

HRTEM images for raw Landfill and Factory samples are presented in Figure 3-6. The image in Figure 3-6 (A) illustrates both tubular and non-tubular components of the Landfill sample. In addition, there are dark areas which can be attributed to sample thickness effects. A high magnification image of the tube wall is presented in Figure 3-6 (B). The morphology was observed to be irregular.

Figure 3-6 (C and D) presents the HRTEM images of the Factory sample with different magnification. It is evident from these images that the sample particles are aggregated. In general, the Landfill sample was composed of smaller particles than the Factory sample. This difference in dispersion may play an important role in the surface area of the samples in addition to their catalytic activity.

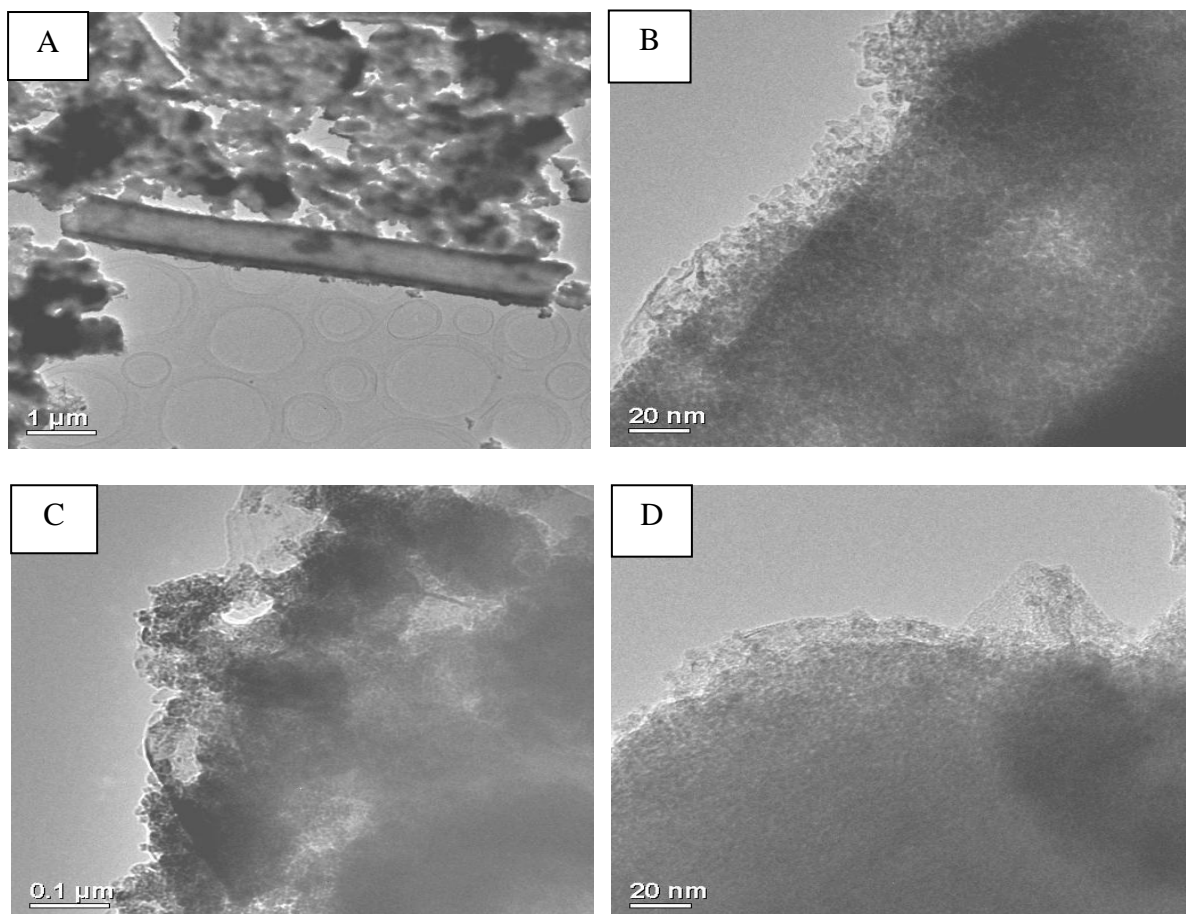


**Figure 3-6** HRTEM images of raw Landfill and Factory samples. (A) Low magnification image of the raw Landfill sample, (B) high magnification image of the raw Landfill sample, the sheath surface, (C) low magnification image of the raw Factory sample and (D) high magnification image of the raw Factory sample.

### 3.2.1.5. BET surface area measurements

The surface areas for raw Landfill, Factory and RM samples were measured. Table 3-3 presents the surface areas of the raw materials. It is evident that the surface area of the raw Landfill sample is significantly larger than that of other samples, whereas the RM sample has the smallest surface area. These results are consistent with the observation reported in

the previous section for the Landfill and Factory samples and that in the literature for RM [161].

<b>Table 3-3 BET surface area analysis of raw Landfill, Factory and RM samples</b>	
<b>Sample Code</b>	<b>BET surface area, m<sup>2</sup>/g</b>
<b>Landfill</b>	<b>254</b>
<b>Factory</b>	<b>43</b>
<b>RM</b>	<b>20</b>

### 3.3. Reaction data

The direct cracking of methane over the Landfill, Factory and RM samples under similar reaction conditions was conducted. The samples were used as obtained, without additional modification. These samples were not exposed to reduction or calcination processes prior to the reaction. During reaction, methane acted as a reductant for the iron oxide phases in these samples, and oxygen was removed by the formation of CO, CO<sub>2</sub> and H<sub>2</sub>O. Hence, all the hydrogen observed represents net production since in many studies reported in the literature more hydrogen is used in the preparation of reduced active phases than is recovered by methane cracking. This leads to the achievement of an important objective of this study, which is the valorisation of two waste materials. However, few researchers have employed this approach in their study; for example, Hargreaves *et al.* [161] studied the direct cracking of methane over Red Mud while Otsuka *et al.* [51] and Muradov [175] studied supported Fe<sub>2</sub>O<sub>3</sub> systems.

The results of the hydrogen formation rate against time-on-stream for the Landfill, Factory and RM samples are presented in Figure 3-7. The methane cracking experiments over the Landfill and Factory samples were conducted at least three times, while those for the RM sample were conducted twice to confirm the reproducibility of the experimental spread of data results. Temperature-programmed reactions were conducted in which the temperature was increased from 600 to 800 °C. It is apparent that all these samples are active for the direct decomposition of methane, and that at 600 °C, all samples produced a small amount of hydrogen. Furthermore, it is observed that for each stage of temperature increase —650, 700 and 750 °C—there was an increase in the hydrogen formation rate followed by a

gradual decrease. In the temperature range of 600 to 750 °C, and even in the initial phase of reaction at 800 °C, the RM sample exhibited the lowest hydrogen production. The hydrogen formation in the Landfill and Factory samples was rather similar in the temperature range of 600 to 700 °C, while at 750 °C the Factory sample had the highest hydrogen formation rate compared with the other samples. Moreover, in the first hour of the time-on-stream at 800 °C, the Factory sample had the highest hydrogen formation rate among other samples. However, beyond this point, the activity of the Landfill sample was significantly superior to the RM and Factory samples. In addition, the deactivation period was not observed in all samples and activity was apparently increasing for all samples at the point at which reaction was stopped although this could be related to the development of reactor blockage.

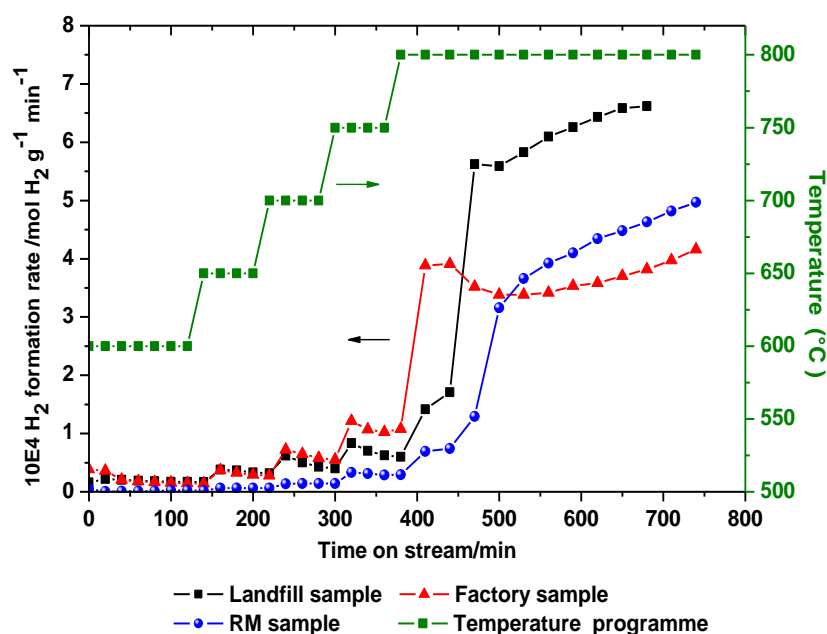


**Figure 3-7** Hydrogen formation rates as a function of TOS for CH<sub>4</sub> cracking over the Landfill, Factory and RM samples in the temperature programme from 600 to 800 °C. The CH<sub>4</sub>/N<sub>2</sub> flow rate was 12 mL/min and 0.4 g sample mass.

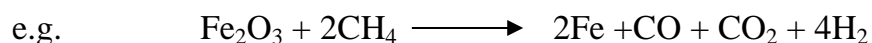
It is evident that the composition and surface area of these materials play a role in their activity. The results of the ICP analyses presented in Table 3-1 indicates the quantities of iron in these samples, active phase, where were found to be 36.00, 25.00 and 22.70 wt% for the Landfill, RM and Factory samples, respectively. The relative order of maximum hydrogen formation rate at 800 °C corresponds to the relative order of iron content. In addition, the BET surface area of these samples, as shown in Table 3-3, were found to be 254, 43 and 20 m<sup>2</sup>/g for the Landfill, Factory and RM samples, respectively. Therefore, the

apparent high activity of the Landfill sample at 800 °C can be attributed to the amount of iron and its surface area, while the delay in the reduction and activity of the RM could be due to its low surface area. However, the difference in the amount of iron between the Factory and RM samples is not large, as shown in Table 3-1; moreover, it is suggested that the high amount of carbon in the raw Factory sample, shown in Table 3-2, potentially had a negative impact on its activity.

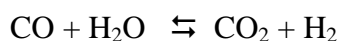
Alkali metals are known to be poisons for the decomposition of methane [161, 176]. Despite their presence, all materials were observed to be active and no direct relationship could be discerned between their concentration and catalytic efficacy.

Hargreaves *et al.* [161] studied hydrogen production from the direct decomposition of methane over three RM samples denoted RM4, RM6 and RM7. These samples were analysed by ICP and BET surface area and were used without modification at 800 °C and 60 mL/min flow of a mixture of 80% CH<sub>4</sub> and 20% N<sub>2</sub>. Their ICP result revealed that the RM4 contains a higher concentration of iron, whereas the concentration of iron in RM6 and RM7 is similar and lower than that in RM4. Additionally, the concentration of alkali metals and TiO<sub>2</sub> in RM6 was higher than that in other samples. Moreover, the BET surfaces areas for these samples were low and almost similar in the range from 8–15 m<sup>2</sup>/g. They found that RM4 was the most active sample, followed by RM7 and then RM6. They attributed the higher activity of the RM4 sample to high iron content and a lower concentration of alkali metal, while the activity of RM7 was ascribed to the low iron content. They also proposed that the RM6 sample was less active due to the high concentration of TiO<sub>2</sub>, which may have led to a strong metal-support interaction effect.

The carbon monoxide and carbon dioxide formation rates against time-on-stream for the Landfill and Factory samples are presented in Figure 3-8 and 3-9. Production of carbon monoxide and carbon dioxide which are associated with hydrogen formation is a result of reduction procedures, as shown in the following equation:



Possible further secondary reactions may occur, such as the water gas shift reaction:



Moreover, the production of carbon monoxide is noted throughout the reaction and clearly implies that the reduction process was not completed.

It was observed that the formation rates of carbon monoxide and carbon dioxide increase with the increase in temperature up to 800 °C and then drop significantly, particularly in the case of carbon dioxide. This indicates that 800 °C is the temperature at which reduction occurs. The formation rates of CO and CO<sub>2</sub> are higher in the Landfill sample. This may be due to the presence of a larger proportion of oxidic phases, particularly iron oxides, compared with the Factory sample. It must be noted that the formation rates of CO and CO<sub>2</sub> were studied using infrared spectroscopy; however, this method is limited because it is not sensitive at low levels of CO<sub>2</sub> below those used for background subtraction. It should be noted that the time on stream for the reaction of the Landfill sample is shorter than that of another samples. The Landfill sample was on stream for 680 minutes whereas the Factory and RM samples were on stream for 740 minutes. This is due to pressure-drop effects as a result of carbon deposition on the Landfill sample, while it was not noted in the Factory and RM samples.

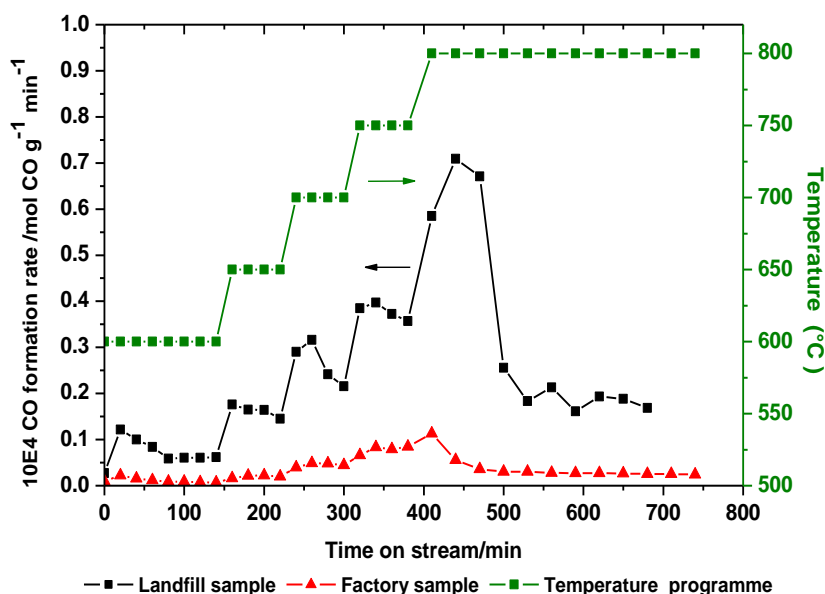


**Figure 3-8** CO formation rates as a function of TOS for CH<sub>4</sub> cracking over the Landfill and Factory samples in the temperature programme from 600 to 800 °C. The CH<sub>4</sub>/N<sub>2</sub> flow rate was 12 mL/min and 0.4 g sample mass.

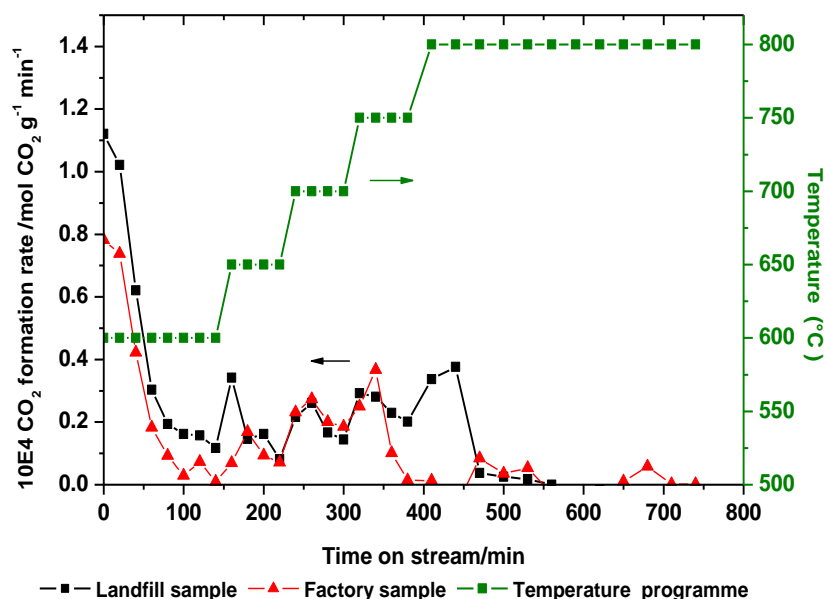


**Figure 3-9** CO<sub>2</sub> formation rates as a function of TOS for CH<sub>4</sub> cracking over the Landfill and Factory samples in the temperature programme from 600 to 800 °C. The CH<sub>4</sub>/N<sub>2</sub> flow rate was 12 mL/min and 0.4 g sample mass.

It is interesting that there is formation of a side product during the reaction of methane cracking over the Factory sample in the temperature range from 600 to 650 °C. This was observed only for the Factory sample and not for the other samples. The side product was evident on the walls of the reactor, as depicted in Figure 3-10. It was an oily light brown liquid. It is difficult to definitively attribute the production of this product from the reaction of methane with the Factory sample because it may be produced due to the heating of sample, particularly since this sample is a waste material for which there is little understanding of all its components and it has a high pre-reaction carbon content.

To reveal the identity of the side product, FTIR and NMR analyses were undertaken. Figure 3-11 (A–C) presents the results of these investigations. However, it was difficult to establish its identity. The IR spectrum showed the presence of a strong absorption band that at 2924 cm<sup>-1</sup> which can be attributed to C-H stretching and the bands at 1456, 1377 and 735 cm<sup>-1</sup> could be from the bending vibration of C-H. Moreover, it showed a characteristic absorption band at 2361 cm<sup>-1</sup>, corresponding to CO<sub>2</sub> stretching. The NMR spectra clearly indicated that the product is aliphatic in which no aromatic protons or carbons were observed. The <sup>1</sup>H NMR spectrum showed different types of protons that resonated within the region of 0.75–2.75 ppm. Also, the <sup>13</sup>C NMR spectrum of the product

showed the presence of aliphatic carbons that resonated between 15 and 32 ppm. Due to its liquid-state the side product was not submitted to CHN analysis.

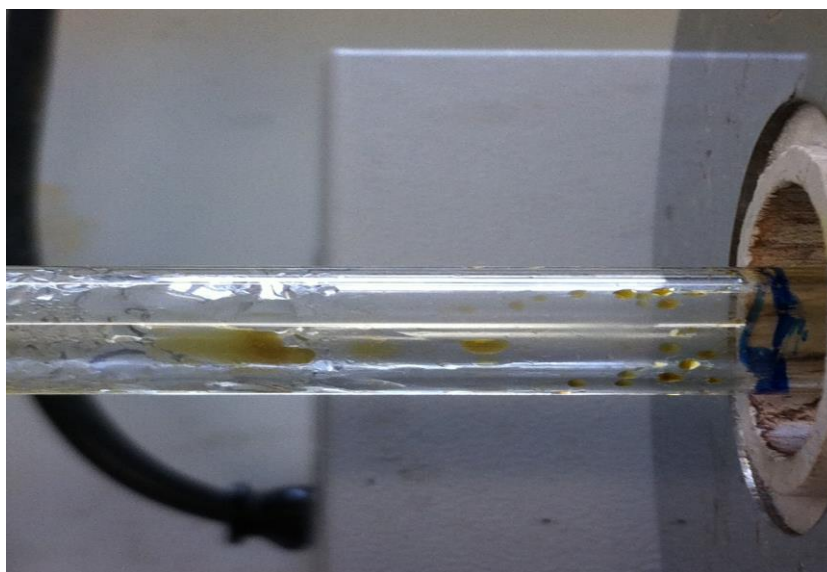


**Figure 3-10** The side product on the walls of the reactor in the temperature range of 600 to 650 °C.

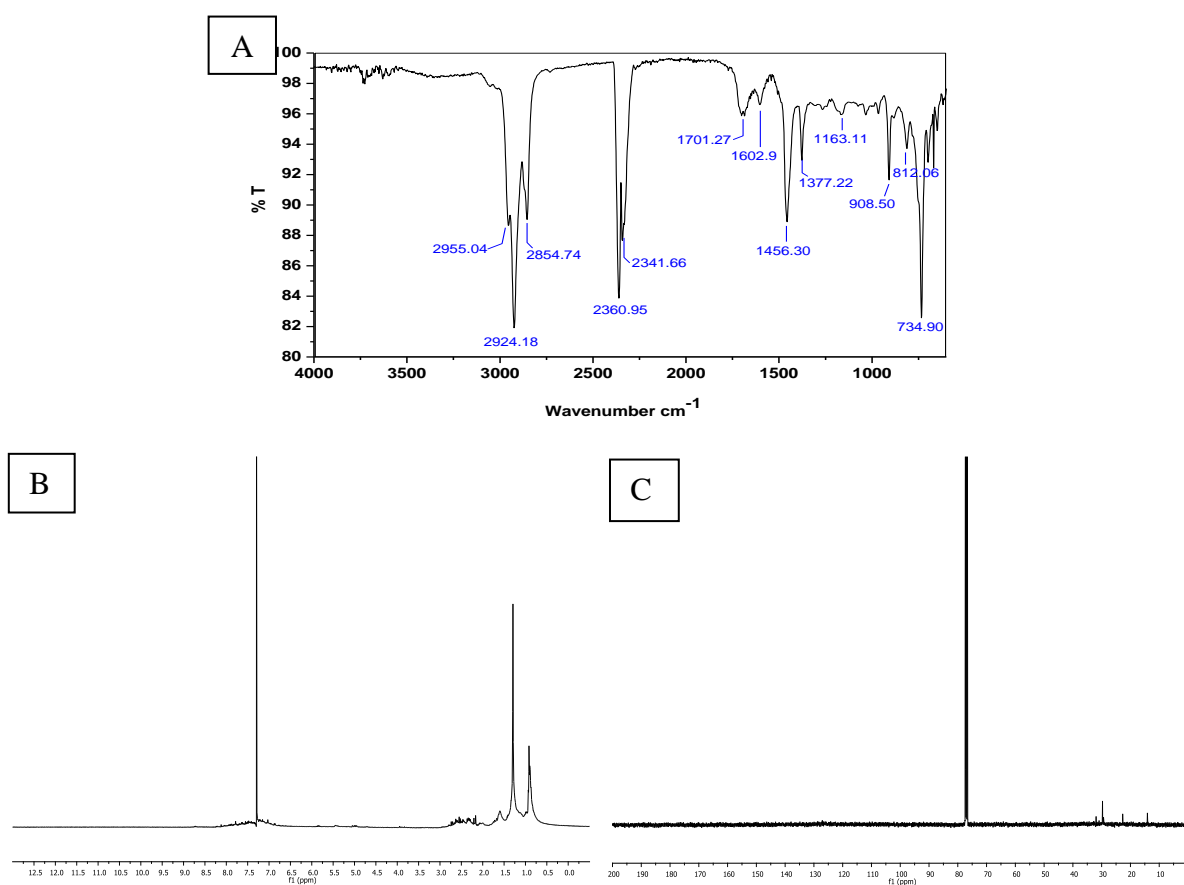


**Figure 3-11** The results of spectral analysis for the side product. (A) The FTIR spectrum, (B) the  $^1\text{H}$  NMR spectrum and (C) the  $^{13}\text{C}$  NMR spectrum.

### 3.3.1. Characterisation of post-reaction for the Landfill, Factory and Red Mud samples

The post-reaction of the Landfill, Factory and RM samples were characterised to observe the changes that occurred in these materials upon reaction. The characterisation was performed using different techniques such as XRD, TGA, CHN elemental analysis, BET surface area measurements, HRTEM and SEM.

#### 3.3.1.1. XRD patterns

Post-reaction XRD patterns of the Landfill, Factory and RM samples are presented in Figures 3-12 to 3-14. It is evident from Figure 3-12 that the direct cracking of methane over raw Landfill under the employed reaction conditions has strongly altered the initial amorphous phase of 2-line ferrihydrite  $\text{Fe}_5\text{HO}_8 \cdot 4\text{H}_2\text{O}$ , as shown in Figure 3-1, and transformed it into other phases with sharp reflections which match the positions of Fe,  $\text{Fe}_3\text{C}$  and graphite. The resultant XRD pattern when methane is decomposed over the Factory sample is shown in Figure 3-13. It is evident that the phases of the raw Factory sample—as shown in Figure 3-2—have changed to FeO,  $\text{Fe}_3\text{C}$ ,  $\text{FeFe}_4(\text{PO}_4)_4(\text{OH})_2 \cdot 2\text{H}_2\text{O}$ ,  $\text{SiO}_2$  and graphite upon reaction. Figure 3-14 shows that the major reflections of the post-reaction in the RM sample are Fe,  $\text{Fe}_3\text{C}$ ,  $\text{SiO}_2$  and graphite as reported previously [161].

It should be noted that there is a degree of similarity among the post-reaction samples in terms of the component phases. Fe,  $\text{Fe}_3\text{C}$  and graphite is present in the Landfill and RM samples, while the metallic Fe is not visible in the Factory sample. Moreover, FeO can be observed in the XRD pattern of the post-reaction Factory sample, suggesting that it was not completely reduced. This result is another possible reason for the relatively low catalytic activity of the Factory sample in comparison with the other two samples, where it may be assumed that the low catalytic activity for the Factory sample may be related to the low amount of iron in the sample. It may be that the presence of the large amount of carbon in the pre-reaction Factory sample, as shown in Table 3-2, may have led to the apparent suppression in the reduction.

The formation of  $\text{Fe}_3\text{C}$  and Fe has been widely reported in existing literature related to the decomposition of methane over iron-based materials. For example, Hargreaves *et al.* [161] studied the direct decomposition of methane over three types of RM samples. They

demonstrated that the reflections of post-reaction X-ray diffraction for all RM samples correspond to Fe and Fe<sub>3</sub>C as well as graphite, quartz and alumina. Otsuka *et al.* [51] investigated the decomposition of methane over 77 wt% Fe/Al<sub>2</sub>O<sub>3</sub> at 800 °C, and they reported that the XRD patterns of the post-reaction catalyst reveal the existence of Fe metal and Fe<sub>3</sub>C phases after 60 minutes of time-on-stream. Murata *et al.* [177] conducted the decomposition of methane over 10 wt% Fe/Al<sub>2</sub>O<sub>3</sub> at 600 °C for 5h and their XRD analysis for post-reaction catalyst evidenced the formation of Fe and Fe<sub>3</sub>C.

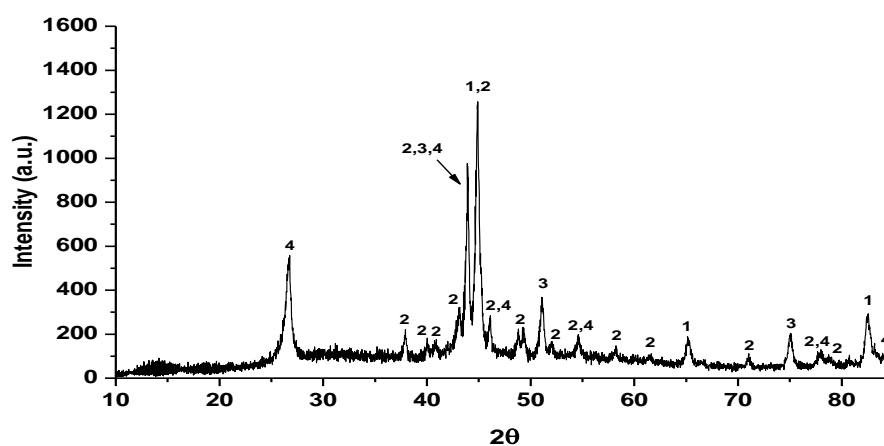


**Figure 3-12** X-ray pattern for post-reaction Landfill sample. 1: iron (Fe) 06-0696; 2: cohenite (Fe<sub>3</sub>C) 34-0001; 3: iron (Fe) 31-0619; 4: graphite-3R 26-1079.

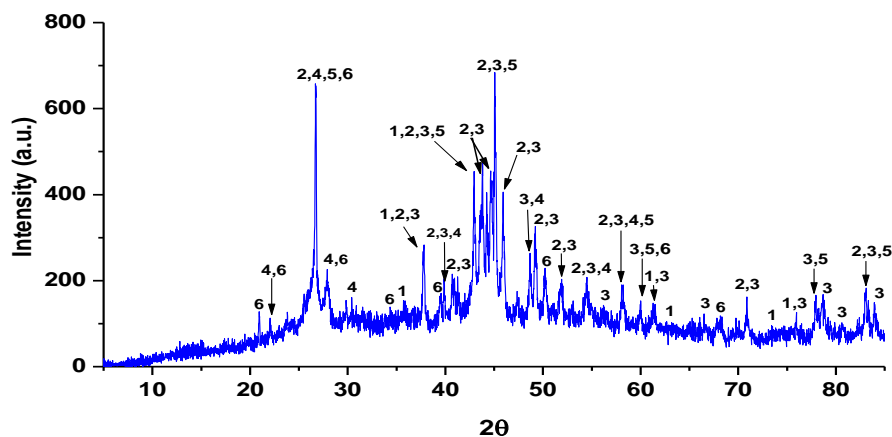


**Figure 3-13** X-ray pattern for post-reaction Factory sample. 1: iron oxide (FeO) 39-1088; 2: iron carbide (Fe<sub>3</sub>C) 03-0989; 3: cohenite (Fe<sub>3</sub>C) 35-0772; 4: giniite (FeFe<sub>4</sub>(PO<sub>4</sub>)<sub>4</sub>(OH)<sub>2</sub>·2H<sub>2</sub>O); 5: graphite (C) 23-0064; 6: quartz (SiO<sub>2</sub>) 33-1161.

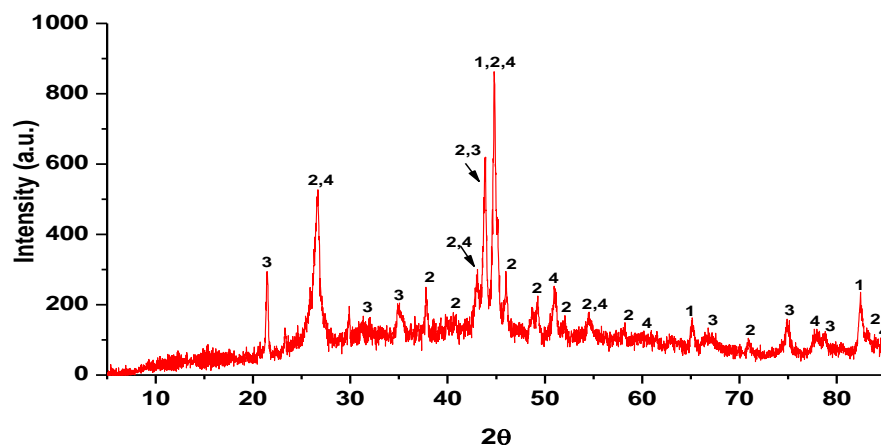


**Figure 3-14** X-ray pattern for post-reaction RM sample. 1: iron (Fe) 06-0696; 2: iron carbide ( $\text{Fe}_3\text{C}$ ) 03-0989; 3: quartz ( $\text{SiO}_2$ ) 04-0359; 4: graphite (C) 25-0284

As previously mentioned in relation to the reaction data, no deactivation period was observed for the samples. From the resultant XRD patterns of post-reaction materials, as illustrated above, it is probable that the metallic Fe and  $\text{Fe}_3\text{C}$  species played a significant role in the activity of these samples because they are catalytically active for methane cracking. Otsuka *et al.* [51] investigated the direct decomposition of methane over 77 wt%  $\text{Fe}_2\text{O}_3/\text{Al}_2\text{O}_3$  catalysts. They suggested that  $\text{Fe}_3\text{C}$  and Fe are the catalytically active phases for methane decomposition. In addition, they suggested that iron carbide decomposes to metallic iron and carbon to form filamentous carbons. In a related study, Muradov [175] studied the thermocatalytic decomposition of methane over 10 wt%  $\text{Fe}_2\text{O}_3/\text{Al}_2\text{O}_3$  and attributed the high catalytic activity to the presence of metallic iron and iron carbide phases.

### 3.3.1.2. Post-reaction CHN and TGA analysis

The post-reaction CHN analysis of the Landfill, Factory and RM samples are presented in Table 3-4. It is evident from the results that there is significant deposition of carbon in all samples as a result of their reaction with methane. The largest amount of carbon deposition was observed for the Landfill sample, whereas that for the Factory sample was much lower. In the case of RM sample, the quantity of carbon deposited was higher than that in the Factory sample and lower than that in Landfill sample.

<b>Table 3-4</b> Post-reaction CHN analysis of the Landfill, Factory and RM samples			
<b>Sample Code</b>	<b>Mean value, wt%</b>		
	<b>C</b>	<b>H</b>	<b>N</b>
<b>Landfill</b>	64.91 ± 0.90	-	-
<b>Factory</b>	41.60 ± 0.20	-	-
<b>RM</b>	48.40 ± 0.10	-	-

Figure 3-15 and 3-16 depict the TGA oxidation profiles under air and corresponding first-derivative profiles of the post-reaction samples. It is evident from Figure 3-15 that there is an initial weight increase between 350 and 500 °C, followed by a decrease up to 700 °C. The weight increase that occurred could be attributed to oxidation reactions for the reduced iron phases, iron carbide, metallic iron and/or even FeO. The weight loss can be ascribed to the combustion of carbon, which is consistent with the post-reaction CHN analysis. It is evident from the TGA profiles in Figure 3-15 that the weight loss, which represents the amount of deposited carbon, is almost 58, 31 and 42 wt% for the Landfill, Factory and RM samples, respectively. These carbon content values are less than their counterparts, obtained by the CHN analysis, as illustrated in Table 3-4. It would be anticipated that the general trend in the amount of carbon deposited on these samples is the same for the post-reaction CHN analysis and TGA profiles. It is possible that these results from a combination of sample inhomogeneity and the small amount of material required to implement these post-reaction techniques. The contribution of oxidation should also be taken into account.

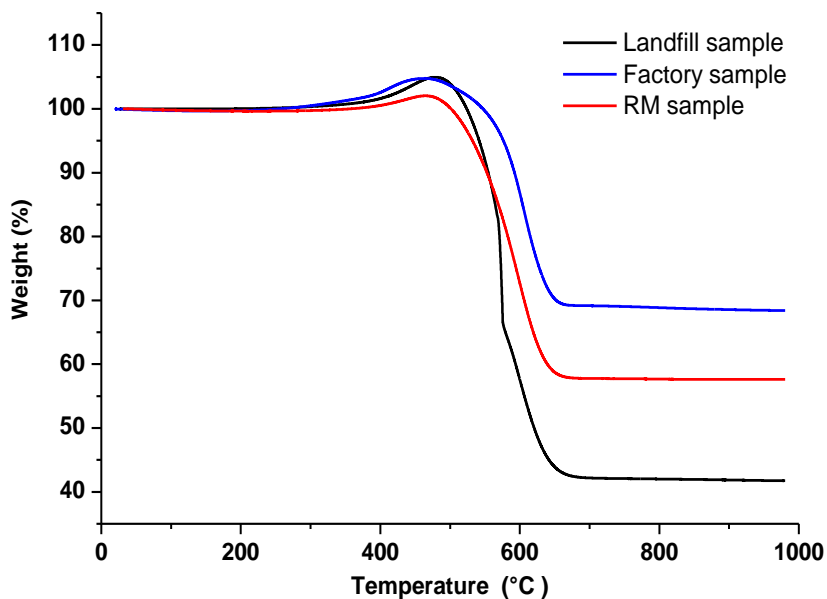


**Figure 3-15** TGA profiles for the post-reaction Landfill, Factory and RM samples.

It should be observed that the inflection in the mass loss profile for the Landfill sample, as shown in Figure 3-15, is reproducible and may be due to a high quantity of carbon species within a narrow reactivity distribution, which lead to a "high-burst" of carbon combustion at *ca.* 580 °C. TGA analysis of these samples was conducted three times to confirm the reproducibility of these results.

The proposed interpretation of these results may be supported by the first-derivative weight changes profiles of the post-reaction samples, as illustrated in Figure 3-16. From these profiles, the differences between the samples are more obvious than those in Figure 3-15. It is evident that the post-reaction Landfill showed two mass loss areas—that is, low and high temperature combustion of carbon at *ca.* 580 and 600 °C, respectively. The appearance of an intense peak at 580 °C can be ascribed to a narrow distribution of carbon species. However, there are two mass loss peaks in the Factory sample, at *ca.* 480 and 600 °C, which indicate the presence of two different forms of carbon. In the case of the RM sample, there is only one broad peak, at approximately 600 °C, which could be attributed to a wide distribution in the nature of the carbonaceous species. Furthermore, it should be born in mind that the components of the sample may function as oxidation catalysts. It must be noted that all species three samples demonstrated a similar mass loss peak, at approximately 600 °C.

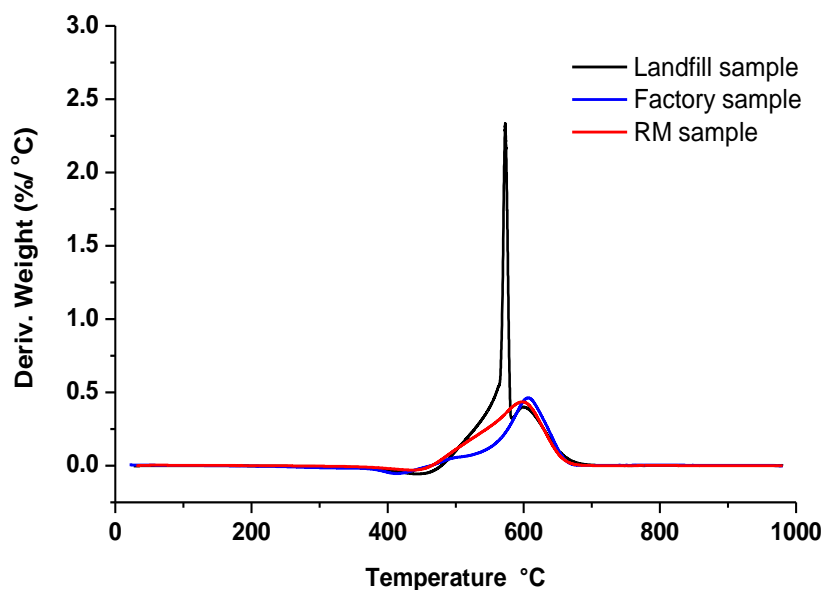


**Figure 3-16** TGA profiles for the post-reaction Landfill, Factory and RM samples

### 3.3.1.3. Post-reaction BET surface area measurements

The surface areas of the post-reaction Landfill, Factory and RM samples were measured. From Table 3-5, it is evident that the post-reaction surface area of the Landfill sample decreased significantly from 254 to 41 m<sup>2</sup>/g. In contrast, it increased significantly for the post-reaction Factory sample from 43 to 152 m<sup>2</sup>/g and the RM sample demonstrated a slight increase in surface area from 20 to 28 m<sup>2</sup>/g. It seems possible that the destruction of the morphology of the Landfill sample and deposition of a large amount of carbon caused a decrease in the surface area. Moreover, it is proposed that the increase in the surface area of the latter two samples can be due to mass normalisation effects and the relative density of carbon. Batra *et al.* [162] found that the surface area of three different types of RM samples increased after direct exposure to methane in *in situ* XRD studies. Gao *et al.* [178] also studied the cracking of CH<sub>4</sub> over synthesised La<sub>2</sub>NiO<sub>4</sub> catalyst on a stainless steel mesh and they reported that the carbon deposited on the catalyst as a result of methane cracking increases the surface area of the catalyst.

<b>Table 3-5</b> BET surface area analysis of post-reaction Landfill, Factory and RM samples	
<b>Sample Code</b>	<b>BET surface area, m<sup>2</sup>/g</b>
<b>Landfill</b>	<b>41</b>
<b>Factory</b>	<b>152</b>
<b>RM</b>	<b>28</b>

### 3.3.1.4. Post-reaction SEM and HRTEM images

The SEM images of the post-reaction Landfill, Factory and RM samples are reproduced in Figure 3-17. Figure 3-17 (A, B) depicts two images of the post-reaction Landfill sample. These images are taken from two different areas of the sample. It is evident from Figure 3-17 (A) that filamentous carbon is present in the sample, but it was not dense and not all over the sample. This may be due to the accumulation or/and interference between the carbon and the components of the sample. Such a structure has also been reported by Pinilla *et al.* [179] when they studied the production of hydrogen and filamentous carbon in the decomposition of methane over Fe/MgO at 800 °C. However, a significant observation of this analysis is that remnants of tubular morphology, or tubes of iron oxides, are found in the sample and these are not affected by the reaction conditions, as shown in Figure 3-17 (B). It must be mentioned that the existence of these iron oxide tubes was not commonly observed throughout the sample. This observation is consistent with the proposal that the reduction process was not completed, as previously mentioned.

However, the SEM images of the post-reaction Factory sample exhibited negligible apparent growth of any carbon structures, as depicted in Figure 3-17 (C). Figure 3-17 (D) depicts the SEM image of the deposited carbon in the RM sample after the reaction. It is evident that the RM sample can form filamentous carbon. This result supports the results of previous research, which showed that the cracking of methane over Red Mud leads to the formation of filamentous carbon [162].

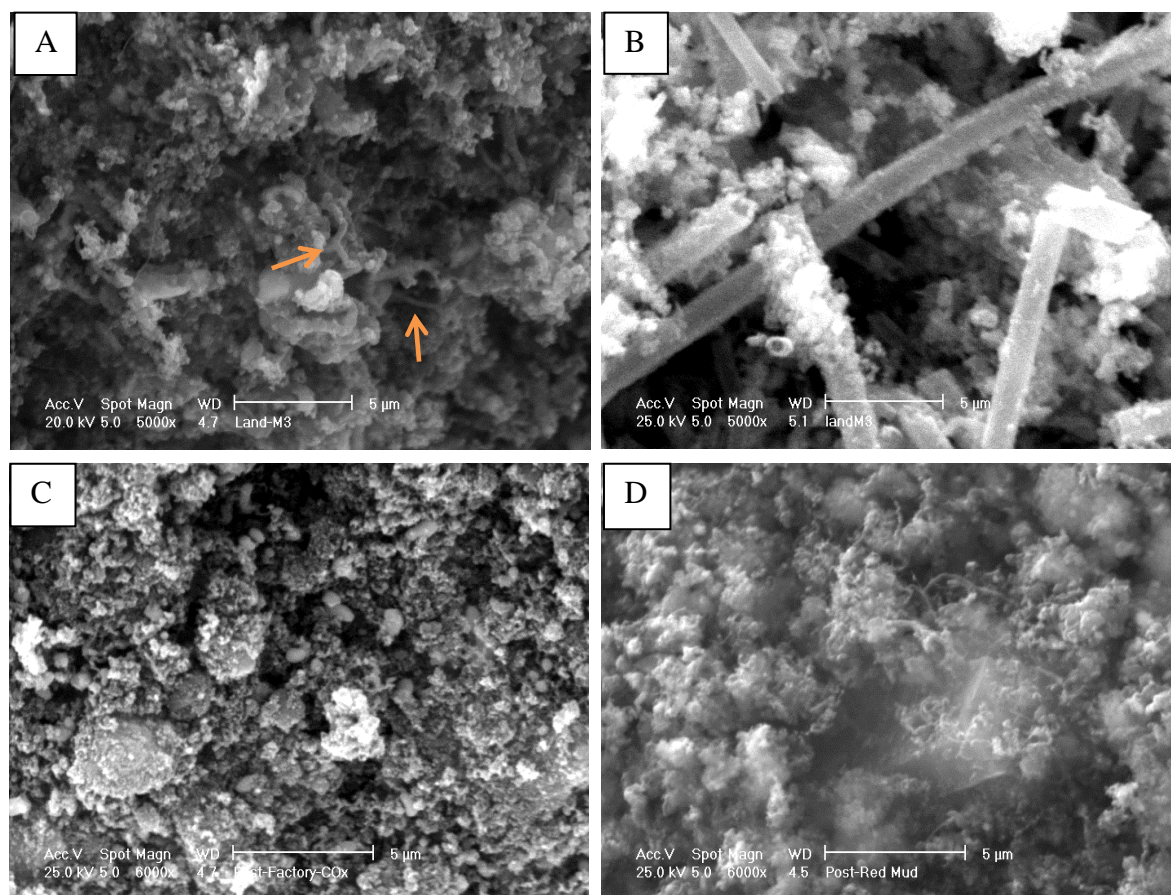


**Figure 3-17** SEM images of the post-reaction Landfill, Factory and RM sample. (A) The post-reaction Landfill sample shows the formation of carbon filaments, indicated by arrows, (B) the post-reaction Landfill sample shows the remnants of the tubular morphology in the sample, (C) the post-reaction Factory sample and (D) the post-reaction RM sample shows the presence of carbon filaments.

The TEM images of the post-reaction Landfill and Factory samples are presented in Figures 3-18 and 3-19, respectively. It is evident from the images in Figure 3-18 that several nanocarbon structures have been formed over the Landfill sample during the methane decomposition. Figure 3-18 (A) indicates that the formation of chain-like carbon fibres and iron metal (as indicated by regions of high contrast) could be found in the centre of the carbon fibres. In addition, an encapsulating type of carbon was observed. Further, it is evident from Figure 3-18 (B and C) that there are various shapes and sizes of onion-like carbon nanospheres that are comprised by graphitic layers. This type of carbon deposited was observed with some findings in other studies. For example, Batra *et al.* [162] analysed the deposited carbon on the RM as a result of the cracking of methane by HRTEM. They noted that the deposited carbon was in the form of carbon nanospheres and straight-chain bamboo-like nanotubes. In another study, Otsuka *et al.* [51] studied the direct cracking of

methane over  $\text{Fe}_2\text{O}_3/\text{Al}_2\text{O}_3$  and  $\text{Fe}_2\text{O}_3/\text{SiO}_2$ . They revealed that the deposited carbon had various structures such as chain-like carbon fibres and spherical carbon units.

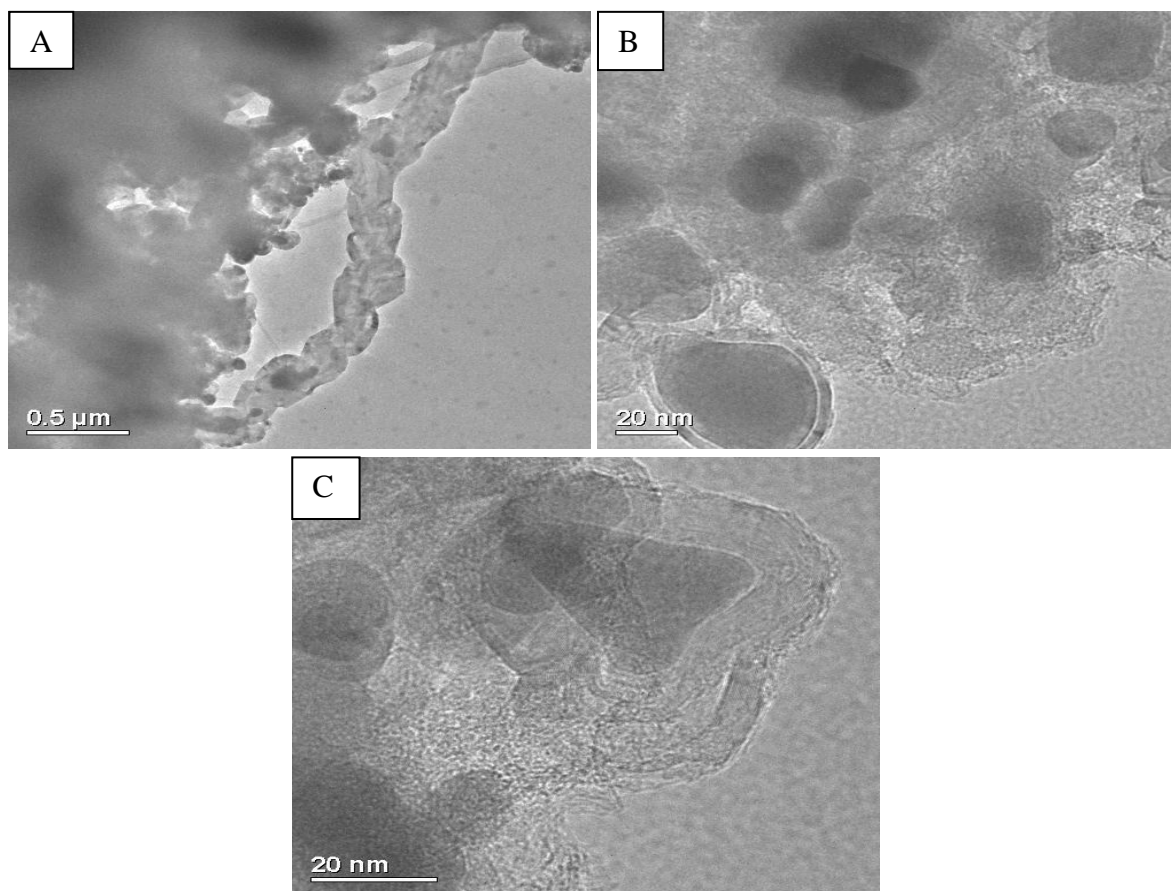


**Figure 3-18** TEM images of the post-reaction Landfill sample. (A) The post-reaction Landfill sample shows that the formation of chain-like carbon fibres and iron metal could be found at the centre of the carbon fibres (B) and (C) onion-like carbon nanospheres.

On the contrary, the HRTEM images of the post-reaction Factory sample did not present any significant formation of carbon nanostructures, as illustrated in Figure 3-19. It is evident from Figure 3-19 (A-B) that there was sintering, aggregation of metals and encapsulation by carbon. This result may help to identify another reason for the low activity in the Factory sample at 800 °C, which leads to suppression of the reduction process of the Factory sample, as shown in the XRD analysis in Figure 3-13 where the presence of iron metal was not observed.

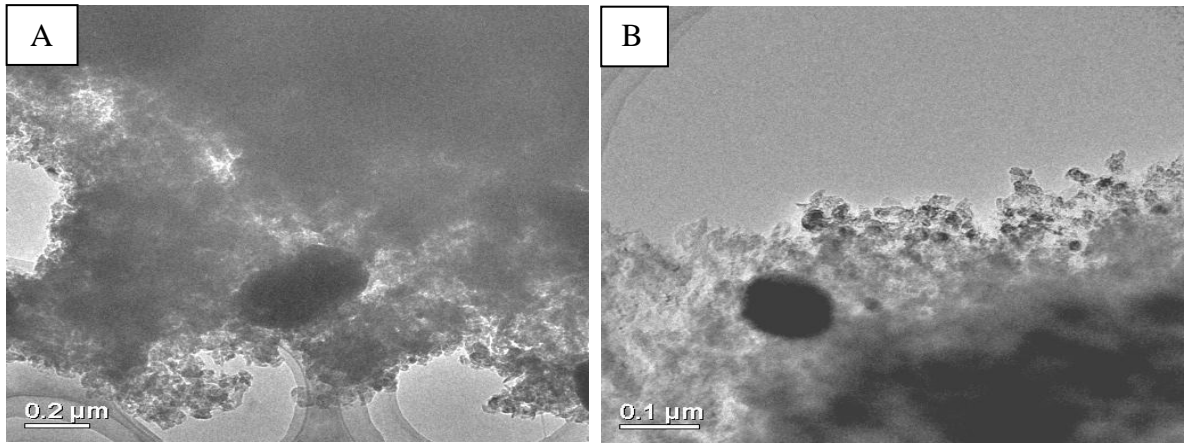


**Figure 3-19** TEM images of the post-reaction Factory sample. A and B depict the sintering, aggregation of metals and encapsulation of carbon.

### 3.4. Effect of reaction temperature on methane cracking over the Landfill sample

#### 3.4.1. Reaction data

The effect of reaction temperature on the activity of Landfill sample for the direct cracking of methane into hydrogen and carbon was studied. The temperature employed in this study was 600 °C, a temperature programme from 600 to 700 °C and a temperature programme from 600 to 750 °C. The results of the hydrogen formation rates against time-on-stream for the Landfill sample at different temperatures are presented in Figure 3-20. It appears from Figure 3-20 (A) that the hydrogen formation rate at 600 °C is low. In addition, there is an initial burst of hydrogen formation followed by a gradual decline in the production with time-on-stream. The maximum in hydrogen formation rate at 600 °C is  $0.28 \times 10^{-4}$  mol H<sub>2</sub> g<sup>-1</sup> min<sup>-1</sup>. Figure 3-20 (B) depicts the hydrogen formation rate in the temperature programme from 600 to 700 °C. It is evident that the hydrogen formation rate increased with each increase in temperature. When the temperature reached 700 °C, there was a sharp rise in the hydrogen formation rate, followed by rapid decline in the production with time-on-stream. In addition, it is apparent that the maximum in hydrogen formation rate was noted at 700 °C where is  $0.64 \times 10^{-4}$  mol H<sub>2</sub> g<sup>-1</sup> min<sup>-1</sup>.

It is evident from Figure 3-20 (C) that the Landfill sample exhibited the highest activity and hydrogen formation rate ( $7.70 \times 10^{-4}$  mol H<sub>2</sub> g<sup>-1</sup> min<sup>-1</sup> in maximum) at 750 °C, which is close to the result from the reaction at 800 °C, as illustrated in Figure 3-7 and 3-29. Moreover, it should be observed that the activation time of the Landfill sample at 750 °C is longer than that at 800 °C, as shown Figure 3-7 and 3-29. It seems that the temperature of 800 °C accelerated the activation of sample by the reduction of iron oxides. However, the reaction was stopped after 750 minutes on stream due to the pressure-drop effects as a result of carbon deposition, which was observed. Based on the results obtained, it can be suggested that the reaction temperatures beyond 700 °C are appropriate to activate the Landfill sample.

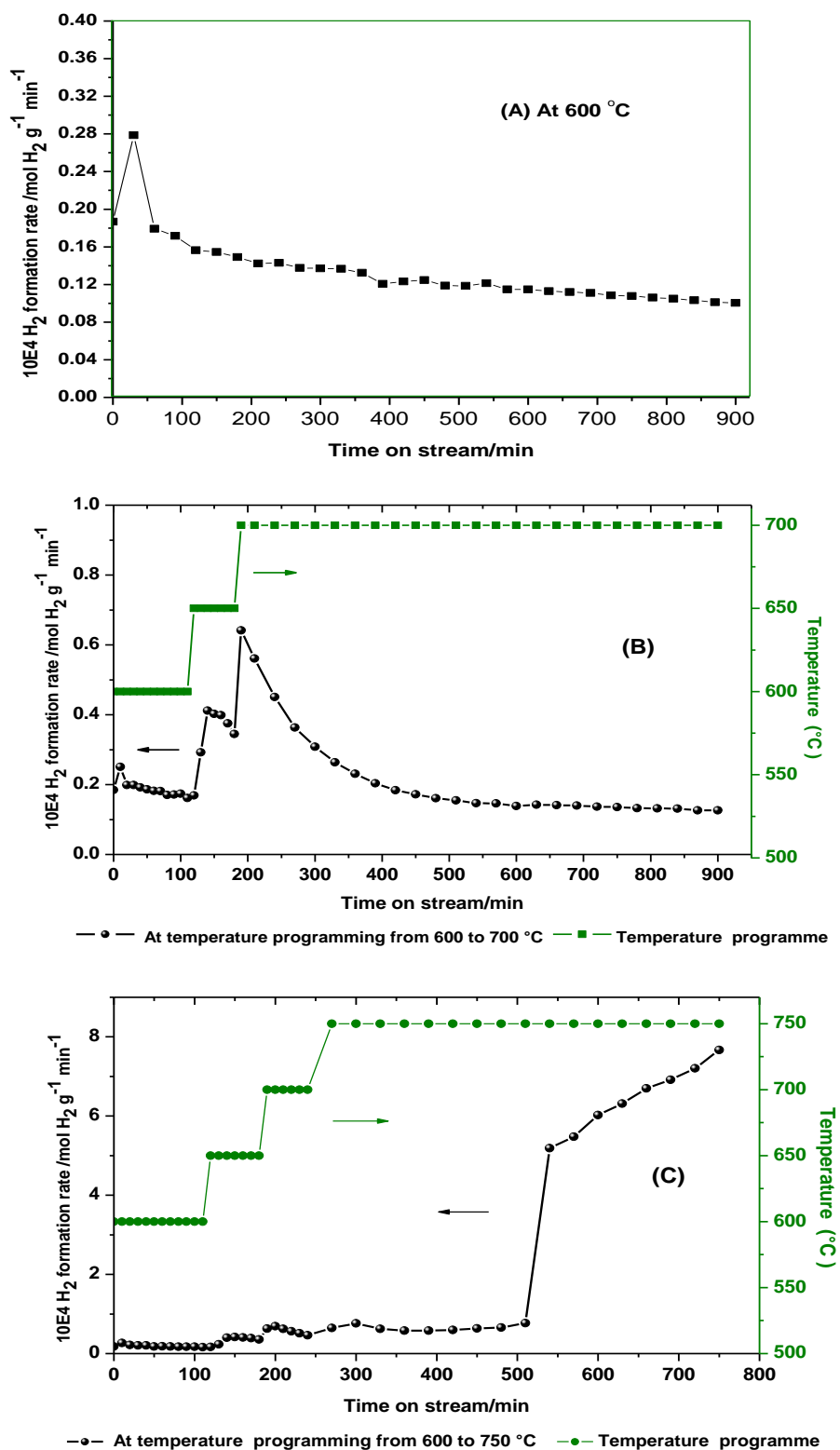


**Figure 3-20**  $H_2$  formation rate as a function of TOS for cracking of  $CH_4$  over the Landfill sample at different temperatures. (A) At 600  $^{\circ}\text{C}$ , (B) in the temperature programme from 600 to 700  $^{\circ}\text{C}$ , (C) in the temperature programme from 600 to 750  $^{\circ}\text{C}$ . The  $CH_4/N_2$  flow rate was 12 mL/min and 0.4 g sample mass.

### 3.4.2. XRD studies

The powder X-ray diffraction patterns for the post-reaction Landfill samples after reaction at different reaction temperatures have been recorded. Figure 3-21 shows the XRD patterns for raw and post-reaction Landfill samples as a function of reaction temperature. As described earlier, the powder X-ray diffraction of the raw Landfill sample is consistent with 2-line ferrihydrite ( $\text{Fe}_5\text{HO}_8 \cdot 4\text{H}_2\text{O}$ ), a poorly crystalline iron oxide/hydroxide with two very broad reflections apparent in its powder XRD pattern. It is evident from Figure 3-21 that the reaction temperature played a significant role in the phase transformations in ferrihydrite. The XRD pattern of the post-reaction Landfill sample at 600 °C shows that the ferrihydrite has transformed to wustite ( $\text{FeO}$ ). However, the XRD pattern of post-reaction Landfill sample in temperature programming regime from 600 to 700 °C demonstrates transformation of the ferrihydrite phase into wustite ( $\text{FeO}$ ) and metallic iron. In the case of the post-reaction Landfill sample in the run from 600 to 750 °C, the XRD pattern shows that the 2-line ferrihydrite phase exposed to the complete reduction process led to the disappearance of wustite and formation of other phases including graphitic carbon, metallic iron ( $\text{Fe}$ ) and iron carbide ( $\text{Fe}_3\text{C}$ ).

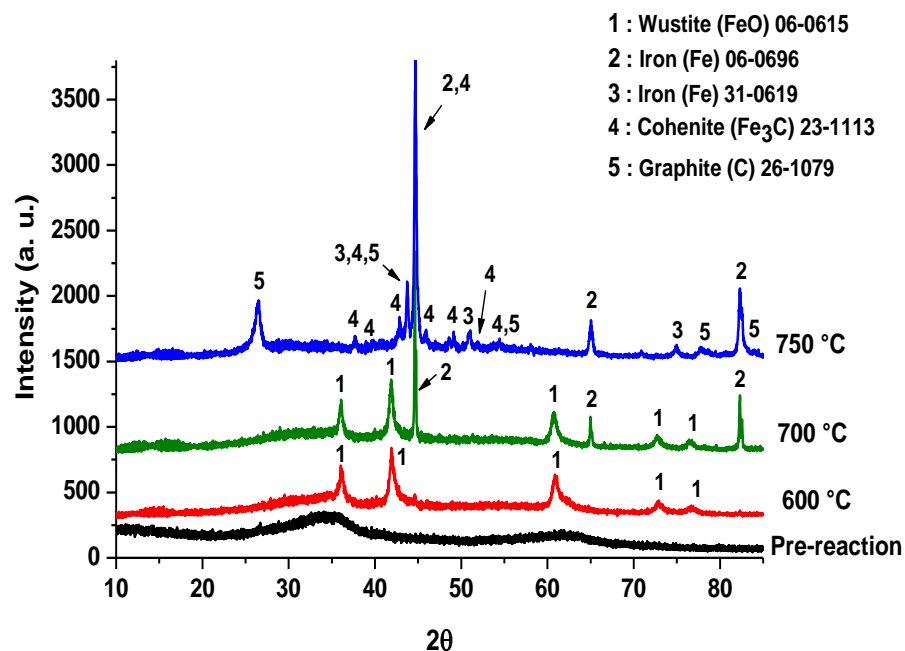


**Figure 3-21** The XRD patterns for the post-reaction Landfill sample at different temperatures at 600 °C, from 600 to 700 °C and from 600 to 750 °C.

The appearance of metallic Fe and Fe<sub>3</sub>C species in the post-reaction Landfill sample after the 600 to 750 °C temperature programme regime explains the high activity of the Landfill sample because these species have a catalytic effect in methane cracking [51, 175]. The latter result is similar with that found in the XRD pattern of the post-reaction Landfill sample in the temperature programme from 600 to 800 °C in terms of the high activity of the hydrogen production and the appearance of the same phases, as illustrated in Figure 3-12; there are differences in the intensity of peaks where they are higher at 800 °C and this is expected due to the increased reduction process and a higher crystallinity of the reduced phases. This indicates that 750 °C is the appropriate temperature for reducing the Landfill sample with methane to transform iron oxide to its active iron phase.

### 3.4.3. CHN and TGA analysis

CHN analysis and TGA studies for the post-reaction Landfill sample run under different reaction temperature regimes have been undertaken. Table 3-6 illustrates the results of CHN analyses. From this data, it is evident that the amount of carbon in the post-reaction sample at 600 °C and in the temperature programme from 600 to 700 °C is low and almost the same. This result is not surprising as the hydrogen formation rate was low and the results of the XRD patterns revealed no presence of carbon containing phases such as Fe<sub>3</sub>C and graphite. It can be assumed that the carbon produced in the cracking of methane is consumed in reaction with oxygen in the components of the Landfill sample to produce carbon dioxide and carbon monoxide during the reduction procedure. Methane itself is a reductant when it is applied directly [51, 161, 175]. However, the amount of deposited carbon at 750 °C after temperature programming from 600 to 750 °C is very large compared to the other results. This is due to the high activity in the Landfill sample for methane decomposition after completing the reduction process at this temperature range, as is depicted in Figure 3-20 (C). In addition, carbon containing phases in the XRD pattern are clearly present in the sample components, as illustrated in Figure 3-21. It is worth noting that the amount of deposited carbon on the sample in the temperature programme from 600 to 750 °C is similar to that at 800 °C, after temperature programming from 600 to 800 °C, as shown in Table 3-4; however, it must be noted that the time-on-stream at 750 °C is longer than that at 800 °C.

<b>Table 3-6</b> CHN analysis for the post-reaction Landfill sample at different temperatures			
Sample Code	Mean value, wt%		
	C	H	N
Post-reaction 600 °C	3.30 ± 0.10	-	-
Post-reaction temperature programme from 600 to 700 °C	3.80 ± 0.08	-	-
Post-reaction temperature programme from 600 to 750 °C	62.40 ± 0.03	-	-

TGA studies in the presence of air have been carried out for spent Landfill samples at different temperatures to estimate the amount of carbon formed in the Landfill sample and to determine its reactivity profile with respect to air. Figure 3-22 depicts the TGA profiles of the post-reaction Landfill samples. It is evident from the TGA result of the post-reaction Landfill sample at 600 °C, as shown in Figure 3-22 (A), that there is a slight initial decrease in weight probably as a result of water loss followed by weight gain in the region of 200 °C. For this, it is possible to link the results of the TGA analysis with those of the XRD analysis because the increase in weight implies the oxidation of wustite (FeO), as observed in XRD patterns in Figure 3-21. The observed weight gain was followed by a decrease in the weight in temperatures beyond 400 °C, which is identical to the amount of carbon obtained from the CHN analysis. Figure 3-22 (B) depicts the TGA profile of the post-reaction Landfill sample after temperature programming from 600 to 700 °C. It must be noted that the weight of the sample increased significantly in two regions at *ca.* 200 and 500 °C and there was no decrease in weight. Further, the XRD analysis demonstrated that the phases present in the post-reaction Landfill sample at a temperature programme from 600 to 700 °C are wustite (FeO) and metallic iron. These phases are strongly subject to oxidation reactions. The comparison between the TGA profile for the post-reaction Landfill sample at 600 °C, Figure 3-22 (A), and the TGA profile for the post-reaction Landfill at a temperature programme from 600 to 700 °C reveals that the weight increase at *ca.* 200 °C is attributable to the oxidation of wustite (FeO), while at *ca.* 500 °C is attributable to the oxidation of metallic iron. In addition, the absence of weight loss due to the burning of carbon, which is observed in the result of the CHN analysis, may be due to the dominance of the iron oxidation reaction.

Figure 3-22 (C) illustrates the TGA profile of the post-reaction Landfill sample after temperature programming from 600 to 750 °C. It is obvious from the TGA result that there

is an initial weight increase between 400 and 500 °C, followed by a decrease in the weight at a temperature of up to 700 °C. The increase in weight is assumed to be due to the oxidation reactions for the metallic iron and iron carbide phases, which are present in the XRD pattern in Figure 3-21. In addition, the estimated amount of carbon from the TGA analysis is almost 50 wt %, which is again lower than that measured in the CHN analysis.

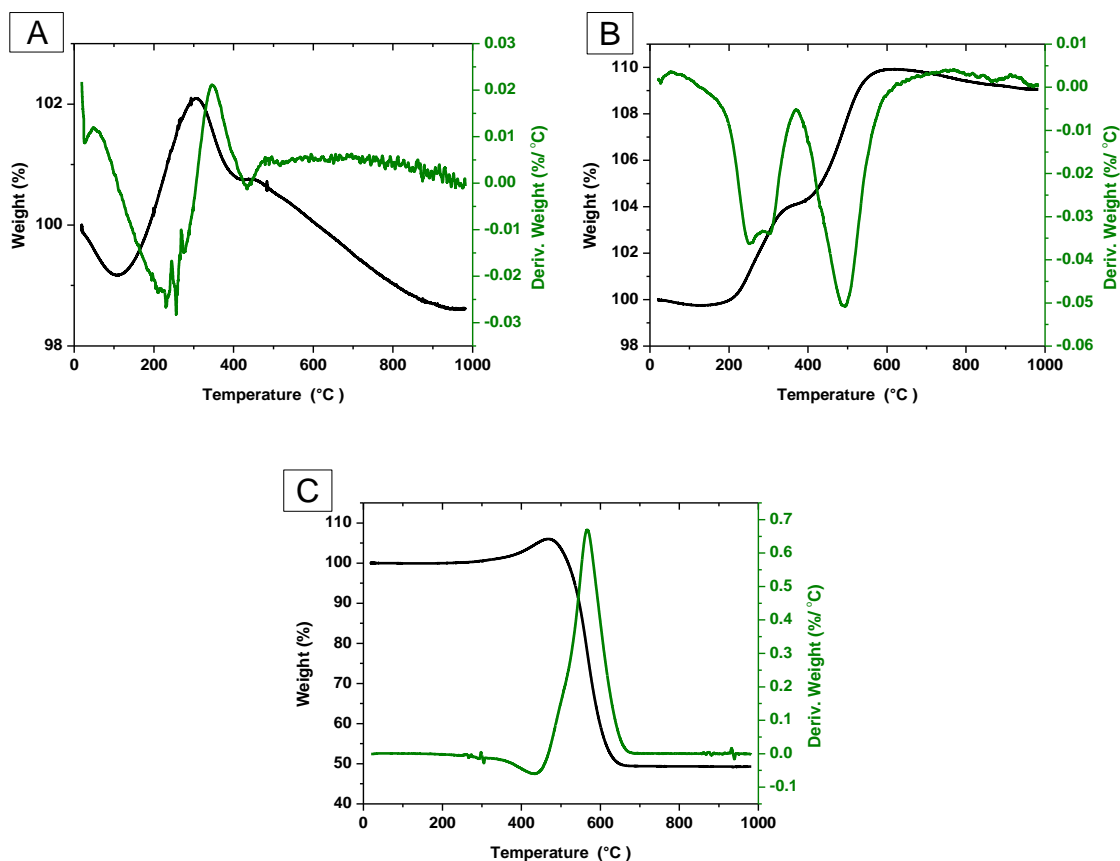


**Figure 3-22** The TGA profiles for the post-reaction Landfill samples at different temperatures.(A) At 600 °C, (B) temperature programming from 600 to 700 °C and (C) temperature programming from 600 to 750 °C.

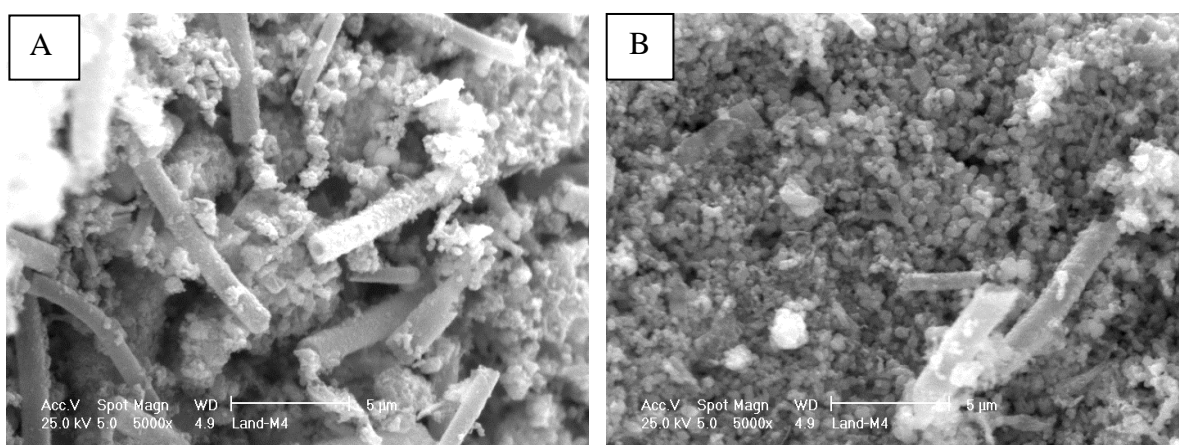
#### 3.4.4. SEM and HRTEM images

Post-reaction SEM and HRTEM images of the Landfill sample run under different temperature regimes are presented in Figures 3-23 to 3-25. The SEM images for the post-reaction Landfill sample at 600 °C are depicted in Figure 3-23 (A, B). It is obvious that the tubes of biogenic iron oxide remain in all parts of the sample and they were not affected by the temperature. In addition, the associated residues with the raw sample—non-tubular

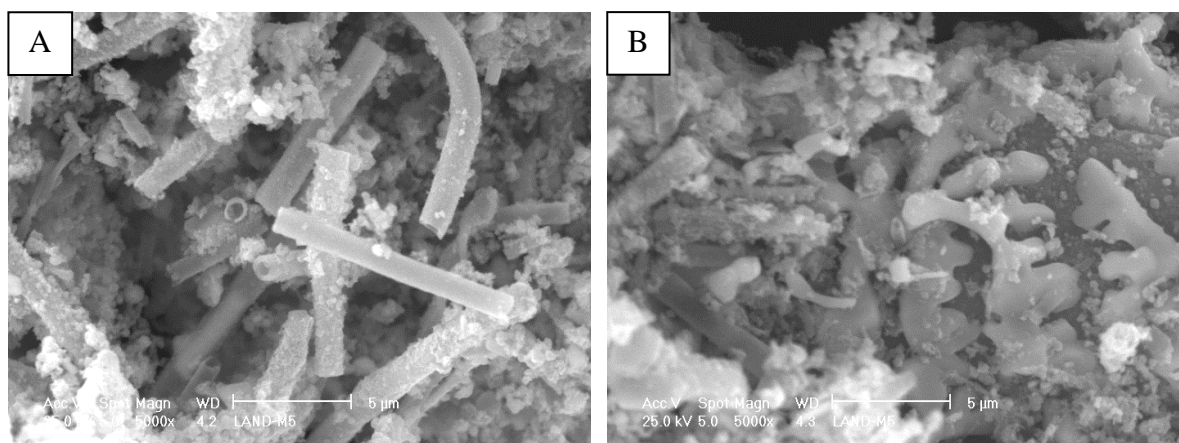
morphology—became agglomerated and spherical, as shown in Figure 3-23 (B). It is suggested that the appearance of spherical morphology clearly in the sample is related to the appearance of the wustite (FeO) phase in the post-reaction Landfill sample at 600 °C, as seen in the XRD pattern presented in Figure 3-21.

Figure 3-24 (A and B) shows the SEM images of the post-reaction Landfill sample after the temperature programme from 600 to 700 °C. It is evident that the temperature regime applied played a significant role in the morphology of sample. Figure 3-24 (A) shows that the tubes of biogenic iron oxide are still remaining. In addition, they began to melt and formed a magma like-shape or molten wax like-shape, as illustrated in Figure 3-24 (B). This suggests that the temperature of 700 °C led to the beginning of the destruction of biogenic iron oxide tubes. It can be assumed that the appearance of the "molten" tubes led to the emergence of the metallic iron phase in the XRD pattern, as depicted in Figure 3-21.

The post-reaction SEM images of the Landfill sample after temperature programming from 600 to 750 °C are shown in Figure 3-25 (A and B). The images are presented at different magnification to enable better visibility. It is evident that the shapes of the hollow tubes have disappeared and the carbon deposited was in the form of filamentous structures which were lumpy, convoluted and interlaced. Thus, the activity of the Landfill sample at 750 and 800 °C is associated with the collapse of the hollow tubes of biogenic iron oxide and their merger with non-tubular morphology, which could lead to re-dispersion and then facilitate the reduction process to form the active phases of iron, metallic iron and iron carbide.



**Figure 3-23** SEM images of the post-reaction Landfill sample at 600 °C. (A) The remaining tubular morphology and (B) the appearance of a spherical morphology component.



**Figure 3-24** SEM images of the post-reaction Landfill sample at the temperature programme from 600 to 700 °C. (A) The remaining tubular morphology and (B) the appearance of melted biogenic iron oxide tubes.

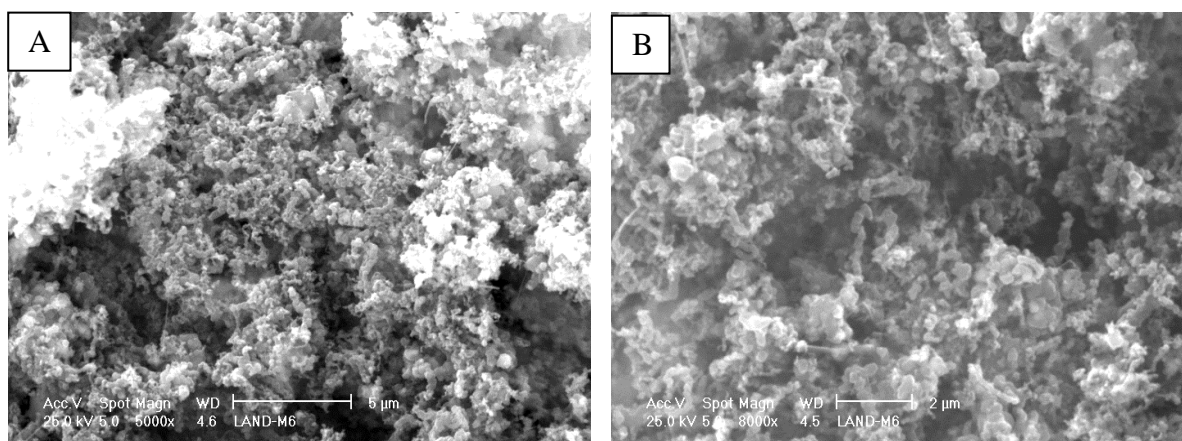


**Figure 3-25** SEM images of the post-reaction Landfill sample at the temperature programme from 600 to 750 °C. (A) Low magnification image and (B) high magnification image.

Post-reaction HRTEM images of the Landfill sample after different temperature regimes are presented in Figures 3-26 and 3-27. The image of the post-reaction Landfill sample at 600 °C is shown in Figure 3-26 (A). It can be seen that the tubular and non-tubular morphology are still present. It is obvious the non-tubular morphology in the case of accumulation and agglomeration.

Figure 3-26 (B-C) depicts the TEM images for the post-reaction Landfill sample after temperature programming from 600 to 700 °C. The image in Figure 3-26 (B) illustrates the collapse of the tube structure and dispersion of iron on the surface (as evident from sample contrast), whereas Figure 3-26 (C) exhibits a very dense area. It is observed from the SEM image in Figure 3-24 (B) that a part of the iron oxide tubes is "molten" at the temperature

programme from 600 to 700 °C. Thus, this dense area could be related to this "molten" morphology.

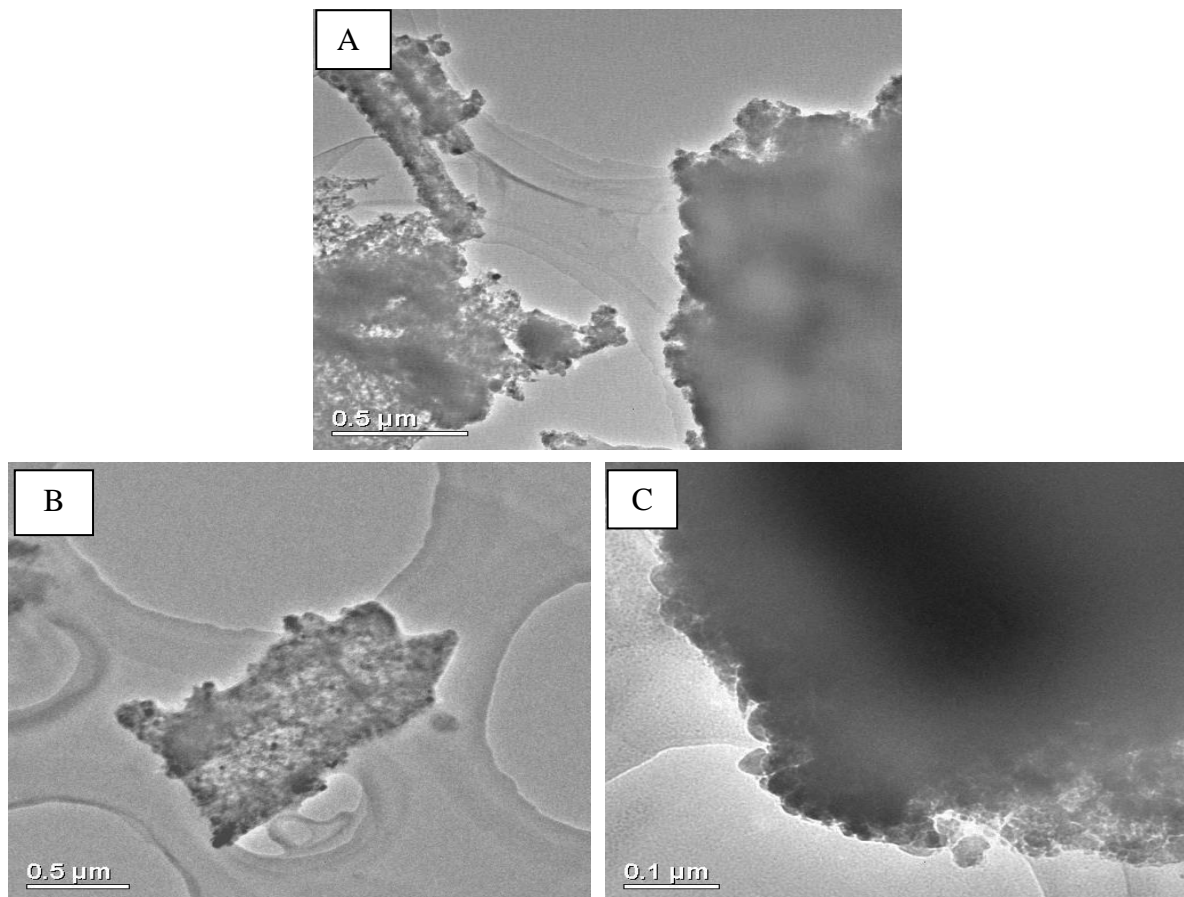


**Figure 3-26** TEM images of the post-reaction Landfill sample at different temperatures. (A) at 600 °C, (B) and (C) at the temperature programme from 600 to 700 °C.

The deposited carbon on the post-reaction Landfill sample in the temperature programme from 600 to 750 °C is different from that observed in the previous cases and similar to that in the post-reaction Landfill sample in the temperature programme from 600 to 800 °C, as shown in Figure 3-18. Figure 3-27 depicts the TEM images of the post-reaction Landfill sample after the temperature programme from 600 to 750 °C at different magnification. It is evident from Figure 3-27 (A) that a graphitic structure is present. The formation of nanospheres with a graphitic structure, either hollow or filled with metal particles (encapsulated within graphitic layers), was commonly observed in the sample.

Figure 3-27 (B) depicts a hollow nanosphere structure. It has been proposed that the metal particles in the core of the nanospheres experience pressure as a result of the accumulation of layers of carbon graphite and are forced to escape, leaving an empty core [125].

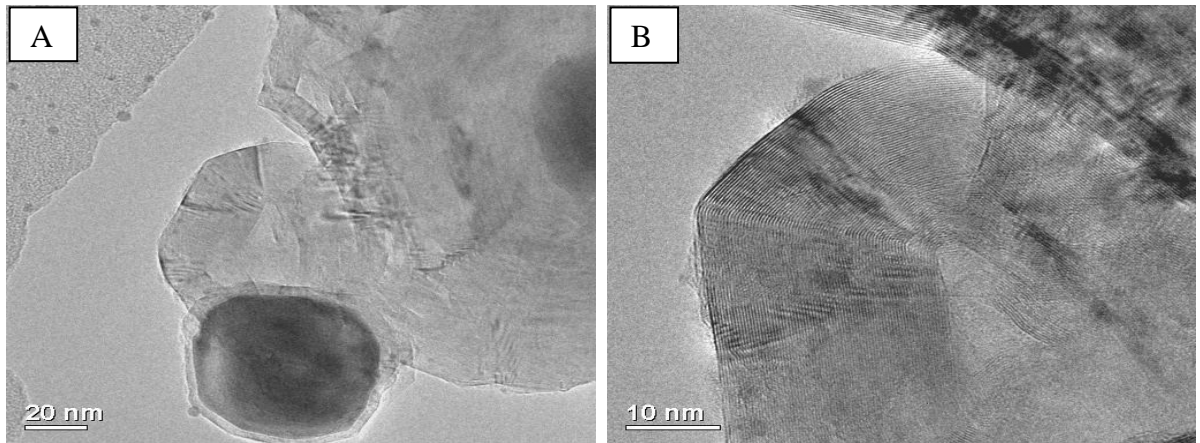


**Figure 3-27** TEM images of the post-reaction Landfill sample in the temperature programme from 600 to 750 °C. (A) the nanospheres graphitic structure and iron particles are encapsulated within graphitic layers and (B) the hollow nanosphere structure.

### 3.4.5. BET surface area

The surface areas for the post-reaction Landfill samples at different temperatures have been measured. Table 3-7 presents the surface areas for the raw and post-reaction samples. It is evident that the surface area of the Landfill sample decreased at all reaction temperatures employed. Although only a small amount of carbon was deposited on the sample at 600 and 700 °C, as evident from the CHN analysis in Table 3-6, the surface area was also considerably lowered. This suggests that a change occurred in the morphology of the post-reaction samples, thereby resulting in a low surface area. It should be noted that the surface area after the temperature programme from 600 to 700 °C was the lowest. The BET value is correlated to the total surface area of the particles, with a high surface area indicating a small particle size [180]. Hence, it could be that the particle size of the Landfill sample increased with the increasing temperature of the reaction. However, it also could be that the beginning of the fusion of the iron oxide tubes at 700 °C—as shown in the SEM images in Figure 3-24 (B)—increased the particle size of the sample, which led to the lowest surface area at this temperature, before it increased again at higher temperature due to increasing carbon deposition.

<b>Table 3-7</b> Analysis of surface area for the Landfill sample both before and after exposure to methane at different temperatures			
<b>Sample Code</b>	<b>BET surface area, m<sup>2</sup>/g</b>		
	<b>Temperature °C</b>	<b>Pre-reaction</b>	<b>Post-reaction</b>
<b>Landfill</b>	<b>600 °C</b>	<b>254</b>	<b>53</b>
	<b>Temperature programming from 600 to 700 °C</b>		<b>33</b>
	<b>Temperature programming from 600 to 750 °C</b>		<b>47</b>

### **3.5. Direct cracking of methane over synthesised 2-line ferrihydrite for hydrogen production**

#### **3.5.1. Introduction**

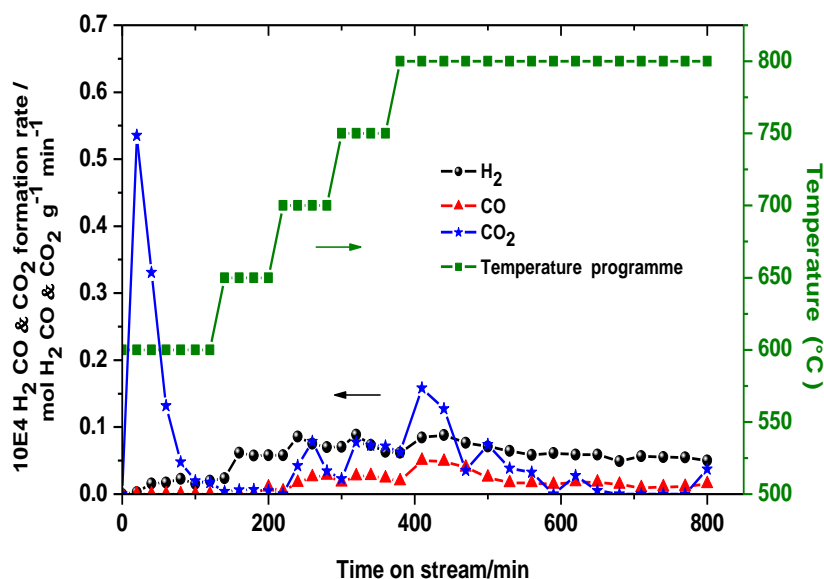
Ferrihydrite,  $\text{Fe}_5\text{HO}_8 \cdot 4\text{H}_2\text{O}$ , a reddish-brown mineral is widespread in surface environments. It is characterised by poor crystallinity and low stability. It is regarded as one of the main types of iron oxide/oxyhydroxide. Ferrihydrite can be formed in the natural environment and can be easily synthesised in the laboratory. It is classified into two types based on the order of the crystalline structure; 2-line ferrihydrite and six-line ferrihydrite. The XRD analysis of the 2-line ferrihydrite shows an amorphous structure with only two broad peaks, while the six-line ferrihydrite shows six broad peaks as structural order increases [132, 181]. Natural ferrihydrites usually contain significant amounts of Si. The presence of silica in the ferrihydrite component increases its stability. It is proposed that the existence of silica in ferrihydrite crystals may poison the surface and prevent further development or that silica substitutes the iron, which may lead to distortions in the structure and then to limited transformation. Natural and synthetic 2-line ferrihydrite containing silica is generally very poorly crystalline [170, 182]. Chukhrov *et al.* [181] found that synthesised ferrihydrite transformed to hematite after two weeks storage at 60 °C, whereas natural ferrihydrite containing 6 %  $\text{SiO}_2$  did not change under the same conditions. They concluded that the presence of silica in the ferrihydrite structure reduces the rate of structural transformation.

Previously, as discussed, the XRD analysis of the raw Landfill sample demonstrated that it contains natural 2-line ferrihydrite. Therefore, a 2-line ferrihydrite comparison material has been prepared in the lab, as described in Chapter 2, and tested under similar conditions.

### 3.5.2. Results and discussion

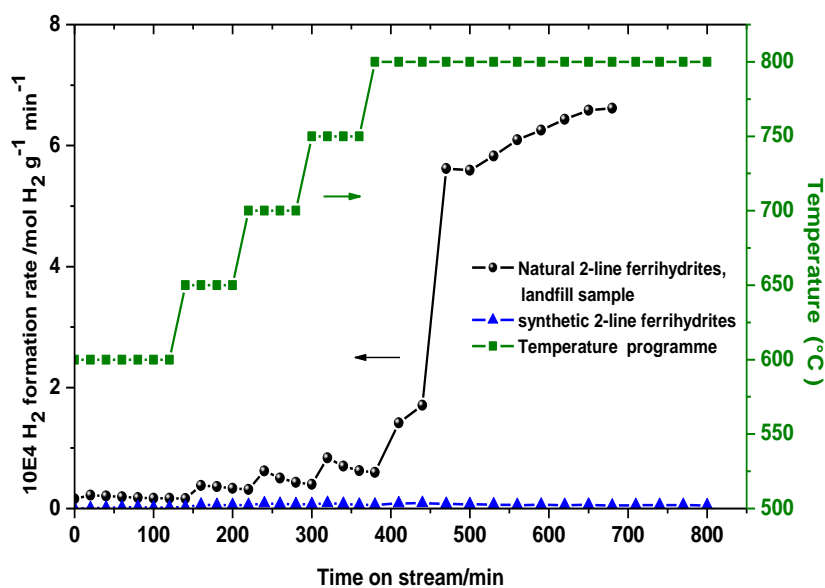
#### 3.5.2.1. Reaction data

Figure 3-28 presents the hydrogen, carbon monoxide and carbon dioxide formation rates against time-on-stream in the temperature programme from 600 to 800 °C as a result of the direct cracking of methane over synthetic 2-line ferrihydrite. It is evident that the hydrogen formation rate is at a very low level and is close to the associated formation rates of CO and CO<sub>2</sub>. Moreover, the hydrogen formation rate is almost steady from 650 to 800 °C with a slight increase in the rate when the temperature was increased. In addition, the CO formation rate is lower than the hydrogen production rate and has similar behaviour. It is evident that there is an initial burst in CO<sub>2</sub> formation. This "burst" is apparent at each increase in temperature and is followed by a reduction in the formation rate.



**Figure 3-28** H<sub>2</sub>, CO and CO<sub>2</sub> formation rates as a function of TOS for CH<sub>4</sub> cracking over the synthetic 2-line ferrihydrites in the temperature programme from 600 to 800 °C. The CH<sub>4</sub>/N<sub>2</sub> flow rate was 12 mL/min and 0.4 g sample mass.

However, Figure 3-29 depicts the comparison of the activity between the synthetic 2-line ferrihydrite and the natural 2-line ferrihydrites (the Landfill sample) for direct cracking of methane and hydrogen production under the same conditions. It is evident that there is significant difference in their activity. Natural 2-line ferrihydrites display a high level of hydrogen production, whereas the synthetic 2-line ferrihydrite possesses very low activity. Moreover, the CO and CO<sub>2</sub> formation rates are higher in natural 2-line ferrihydrites, as depicted in Figures 3-8 and 3-9, compared to those in the synthetic 2-line ferrihydrite.



**Figure 3-29** H<sub>2</sub> formation rates as a function of TOS for CH<sub>4</sub> cracking over the synthetic 2-line ferrihydrite and the natural 2-line ferrihydrites (the Landfill sample) in the temperature programme from 600 to 800 °C. The CH<sub>4</sub>/N<sub>2</sub> flow rate was 12 mL/min and 0.4 g sample mass.

The low activity of the synthetic 2-line ferrihydrite can probably be attributed to the presence of potassium in the sample component. KOH was added to Fe(NO<sub>3</sub>)<sub>3</sub>·9H<sub>2</sub>O during the preparation of the 2-line ferrihydrite, as reported in Chapter 2. Alkali metals elements are known to function as poisons in the decomposition of methane [161, 176]. Therefore, the presence of potassium in the component can play an important role in the deactivation of the synthetic 2-line ferrihydrite, particularly if the amount added is high. Valenzuela *et al.* [183] studied the effect of calcium and potassium addition on the activity of 30 wt% Ni/SiO<sub>2</sub> at 580 °C and they found that the presence of 3 wt% Ca and 3 wt% K in the catalyst composition lead to low activity. However, the result of the ICP

analysis, presented in Table 3-1, illustrated that the Landfill sample (natural 2-line ferrihydrites) contains many of the elements that may have played a role in the activity.

### 3.5.2.2. XRD studies

The XRD patterns of the synthetic 2-line ferrihydrite in the fresh and post-reaction forms are depicted in Figure 3-30. It is evident that the XRD pattern of the fresh synthetic 2-line ferrihydrite is consistent with the structure of the 2-line ferrihydrite ( $\text{Fe}_5\text{HO}_8 \cdot 4\text{H}_2\text{O}$ ), as reported in the literature [132, 170, 184]. Moreover, it is evident that the structure of the synthetic 2-line ferrihydrite has been transformed to a more crystalline phase after reaction. The XRD pattern of the post-reaction synthetic 2-line ferrihydrite shows that the structure of the 2-line ferrihydrite transformed into wustite ( $\text{FeO}$ ). From this result, it is apparent that the reduction process was not complete and metallic iron was not observed in the XRD analysis, explaining the low rate of hydrogen production observed.

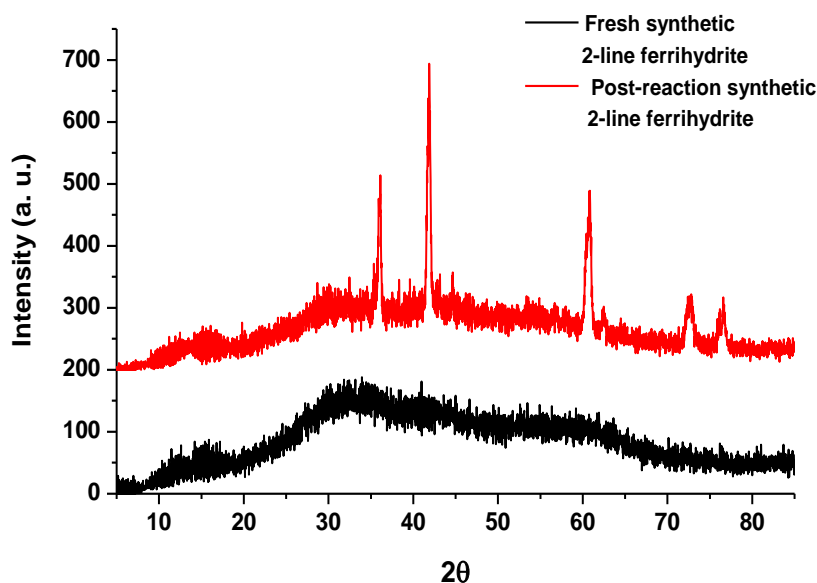


**Figure 3-30** The XRD patterns for the fresh and post-reaction synthetic 2-line ferrihydrite.

Although the reaction conditions employed are similar, the natural 2-line ferrihydrite in the Landfill sample was reduced and showed high activity for methane cracking, while the synthetic 2-line ferrihydrite sample has not been completely reduced and did not show any noticeable activity. Thus, it is suggested that the presence of potassium ions around the iron oxide suppress reduction leading to low activity for the methane cracking. It is possible that a high reaction temperature of over 800 °C is required to reduce the synthetic

2-line ferrihydrite sample. Shah *et al.* [46] studied hydrogen production by catalytic decomposition of methane over 5 % Fe/Al<sub>2</sub>O<sub>3</sub> catalyst at different reactor temperatures. In their study, ferrihydrite was employed as precursor for preparation of 5 % Fe/Al<sub>2</sub>O<sub>3</sub> catalyst. In addition, they assumed that the 5 % Fe/Al<sub>2</sub>O<sub>3</sub> catalyst requires high temperature (1000 °C) to reduce the catalyst to a metallic state and claimed that the catalyst pre-reduced at lower temperatures (700 or 850 °C) is not completely reduced and, so was not as effective in methane decomposition at lower reactor temperatures.

### 3.5.2.3. Post-reaction CHN and TGA analysis

CHN and TGA analyses for the post-reaction synthetic 2-line ferrihydrite have been undertaken. The CHN analyses revealed that the post-reaction sample does not contain carbon. TGA analysis of the post-reaction synthetic 2-line ferrihydrite is illustrated in Figure 3-31. It is evident that the weight of the sample gradually increased from 200 to 1000 °C. This is due to the oxidation of the sample which leads to an increase in the weight. This result is in good agreement with both XRD and CHN analyses which revealed that there is no carbon deposited on the sample. Upon oxidation wustite transforms to other iron oxides, such as magnetite (Fe<sub>3</sub>O<sub>4</sub>) [185].

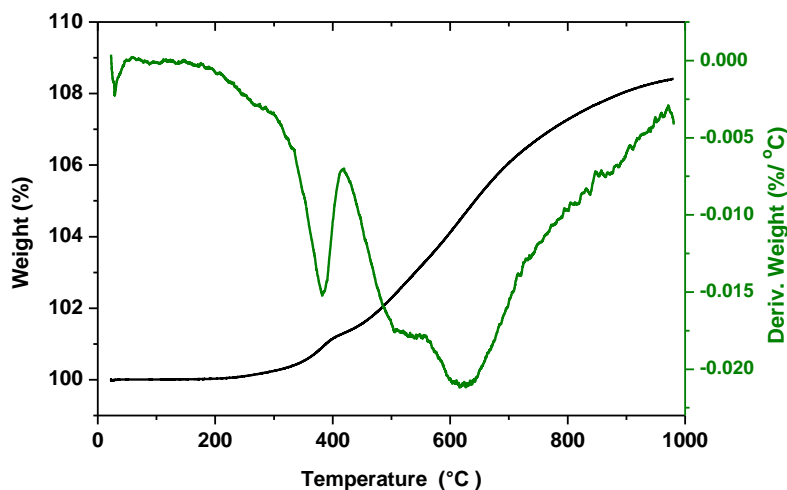


**Figure 3-31** TGA profile for the post-reaction synthetic 2-line ferrihydrite samples.

### 3.5.2.4. BET surface area measurements

The BET surface area of the synthetic 2-line ferrihydrite was measured for fresh and post-reaction and the data are presented in Table 3-8. It can be noted that the BET results demonstrate that the surface area of the fresh synthetic 2-line ferrihydrite is slightly higher than the natural 2-line ferrihydrite (Table 3-3). Surface areas in the range 200 to 400 m<sup>2</sup>/g are commonly reported for natural ferrihydrites [132]. Weidler [186] prepared 2-line ferrihydrite and measured its BET area as 277 m<sup>2</sup>/g, in close agreement with the value in Table 3-8. Although the synthetic 2-line ferrihydrite had a slightly higher surface area than that of the natural 2-line ferrihydrite, the raw Landfill sample, it did not display any noticeable activity and this did not facilitate complete reduction. The BET surface area of the post-reaction synthetic 2-line ferrihydrite is significantly decreased. However, the CHN and TGA analyses do not reveal any deposited carbon that affect the surface area, thereby suggesting that the loss of surface area can be attributed to sintering and/or the loss of porosity.

<b>Table 3-8</b> BET surface area analysis for the fresh and post-reaction synthetic 2-line ferrihydrite		
<b>Sample Code</b>	<b>BET surface area, m<sup>2</sup>/g</b>	
	<b>Pre-reaction</b>	<b>Post-reaction</b>
<b>Synthetic 2-line ferrihydrite</b>	<b>273</b>	<b>11</b>

### 3.5.2.5. SEM images

Figure 3-32 depicts the SEM images for the fresh and post-reaction synthetic 2-line ferrihydrite sample. It is evident from the images that there is a significant change in the morphology. The SEM image of the fresh synthetic 2-line ferrihydrite sample, Figure 3-32 (A), reveals various particles with different sizes and shapes. In contrast, the SEM image of the post-reaction synthetic 2-line ferrihydrite sample, Figure 3-32 (B), demonstrates that the vast majority of particles are uniform with similar shapes and sizes, and are contiguous and coherent. This may indicate the occurrence of sintering, which may have led to a series of observed effects such as delays in reduction, low surface area and then low activity.

This was not observed for the post-reaction Landfill sample, as illustrated in Figure 3-17 (A and B).

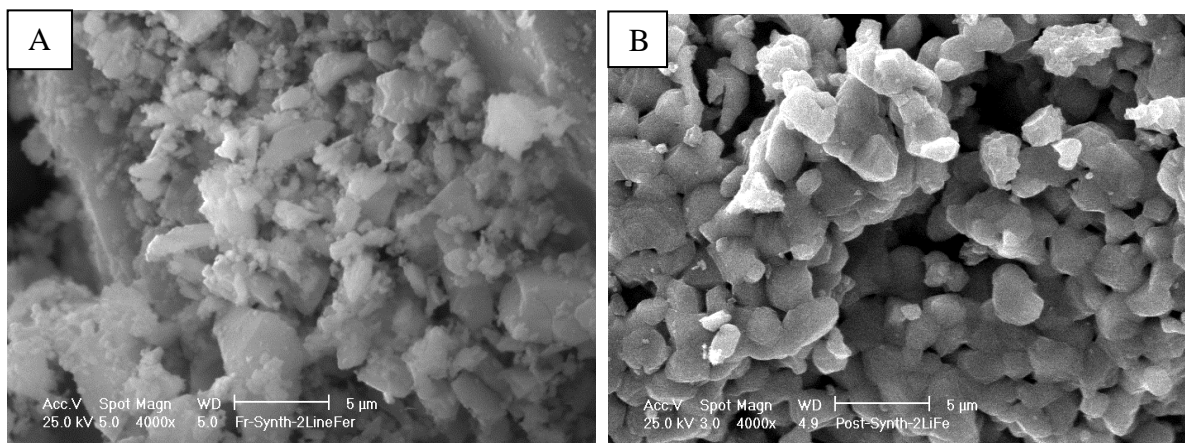


**Figure 3-32** SEM images for the fresh and post-reaction synthetic 2-line ferrihydrite sample. (A) The fresh synthetic 2-line ferrihydrite sample and (B) the post-reaction synthetic 2-line ferrihydrite sample.

### 3.5.3. *In situ* XRD studies and the reaction pathway over the Landfill sample

*In situ* XRD was conducted to investigate the phase transformation sequences of the raw Landfill sample during the reaction with methane. The reaction cell was charged by the raw Landfill sample and heated from room temperature to 700 °C, at a rate of 10 °C/min under a 20 mL/min flow of a mixture of 75 % CH<sub>4</sub> and 25 % N<sub>2</sub>. The employed feed gas was the same gas that was used in all the experiments in this research. Scans were taken at room temperature, 500 , 600 and 700 °C. At each temperature, the sample was held for 1h before the scan was taken. The results of *in situ* XRD patterns are shown in Figure 3-33.

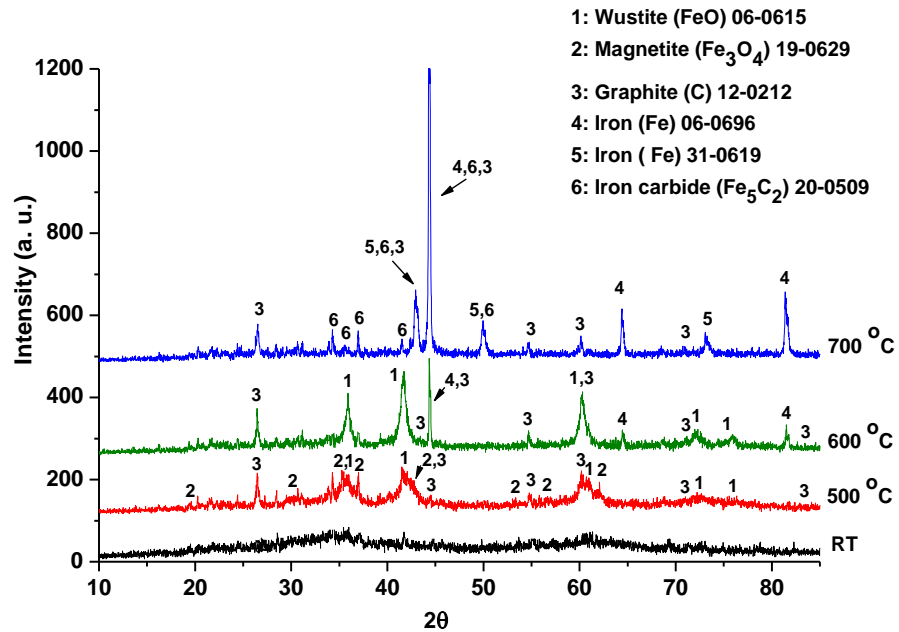


**Figure 3-33** *In situ* XRD patterns for the Landfill sample at room temperature, 500, 600 and 700 °C.

It is evident that the pattern of the raw Landfill sample recorded *in situ* under the CH<sub>4</sub> atmosphere at room temperature corresponds to 2-line ferrihydrite. A transformation of the structure at 500 °C is evident with the appearance of reflections which match wustite (FeO), magnetite (Fe<sub>3</sub>O<sub>4</sub>) and graphitic carbon. At 600 °C, the peaks due to magnetite phase are no-longer clear, while the metallic iron peaks began to appear. In addition, wustite (FeO) and graphitic carbon phases are also evident along with metallic iron. As the wustite (FeO) peaks became more intense, the XRD pattern at 700 °C revealed the complete disappearance of iron oxide phases and the appearance of new phases of metallic iron, iron carbide and graphite.

Methane was applied directly to reduce iron oxides in this sample. As mentioned previously, methane itself is a reductant and the initial decomposition of methane is responsible for the reduction of iron oxide where oxygen is eliminated by the formation of CO, CO<sub>2</sub> and H<sub>2</sub>O. However, a few studies have employed this approach and suggested the pathway of methane decomposition over iron oxides. Otsuka *et al.* [51] used X-ray powder diffraction to study the phase transformation sequences of 77 wt% Fe<sub>2</sub>O<sub>3</sub>/Al<sub>2</sub>O<sub>3</sub> catalyst during the direct decomposition of methane at 800 °C. They found that the XRD pattern of

fresh iron oxide based on alumina reveals the haematite ( $\text{Fe}_2\text{O}_3$ ) phase. After a few minutes of the reaction, they found that the  $\text{Fe}_2\text{O}_3$  phase disappeared and the magnetite ( $\text{Fe}_3\text{O}_4$ ) phase became apparent. When the time-on-stream continued for between 27 and 40 minutes, there was a reduction in the peaks of  $\text{Fe}_3\text{O}_4$  and the wustite ( $\text{FeO}$ ) and Fe metal phases began appearing. After 60 minutes of time-on-stream, the  $\text{FeO}$  phase disappeared completely and they observed the appearance of new phases which matched metallic Fe and iron carbide ( $\text{Fe}_3\text{C}$ ). From these results, it is evident that researchers have demonstrated that the haematite ( $\text{Fe}_2\text{O}_3$ ) phase in the fresh catalyst is reduced stepwise by methane during the reaction in the following manner:



In a related study, Batra *et al.* [162] investigated the phase transformation sequences of Red Mud during the direct cracking of methane. Their investigation was performed by *in situ* XRD in the temperature range from 100 to 500 °C. The haematite ( $\text{Fe}_2\text{O}_3$ ) was the main phase identified in the Red Mud sample. They revealed that the haematite ( $\text{Fe}_2\text{O}_3$ ) was reduced to produce the magnetite ( $\text{Fe}_3\text{O}_4$ ) phase at 400 °C. Additionally, small peaks of wustite ( $\text{FeO}$ ) were observed. Iron and iron carbide began appearing at 400 °C, but their peaks were not very intense at this stage. At 500 °C, graphite was also clearly present along with  $\text{Fe}_2\text{O}_3$ , Fe metal and  $\text{Fe}_3\text{C}$ .

In another major study, Gemmi *et al.* [187] studied the anaerobic combustion of methane over a 28 wt%  $\text{Fe}_2\text{O}_3/\text{CeO}_2$  catalyst using *in situ* time-resolved synchrotron X-ray powder diffraction and mass spectrometry measurements. Before the reaction, methane was employed as a reductant for 28 wt%  $\text{Fe}_2\text{O}_3/\text{CeO}_2$  at 920 °C and the phase transformation sequences during the reduction process were evident. They claimed that the initial main products of the reaction are  $\text{CO}_2$ ,  $\text{H}_2\text{O}$  and magnetite ( $\text{Fe}_3\text{O}_4$ ), according to the following reaction:

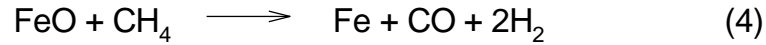


After the occurrence of the above reaction, a further reduction begins and wustite ( $\text{FeO}$ ) is formed as well as  $\text{CO}_2$ ,  $\text{CO}$ ,  $\text{H}_2$  and  $\text{H}_2\text{O}$ , as indicated below:



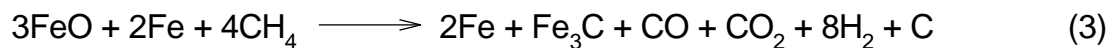


The reduction process continues with the wustite to form metallic Fe, in the following reaction:



They noted that when metallic Fe was formed, the decomposition of CH<sub>4</sub> to H<sub>2</sub> and C begins to occur. The mass spectrometry revealed a high production of H<sub>2</sub>, with a simultaneous decrease in the outgoing CH<sub>4</sub> flow. It was observed that the continuation of this reaction led to formation of iron carbides. This finding is in good agreement with the results of Otsuka [51].

The majority of studies that have been conducted for this type of reaction used haematite ( $\alpha\text{-Fe}_2\text{O}_3$ ), as precursor of Fe-based catalysts. In our study, the phase of the Landfill sample is 2-line ferrihydrite ( $\text{Fe}_5\text{HO}_8.4\text{H}_2\text{O}$ ). Therefore, according to previous studies and based on our results obtained from the effect of the reaction temperature and *in situ* XRD studies, it can be suggested that the following reaction pathway occurs with the Landfill sample:



### 3.6. Summary

The objective of this chapter was to investigate the possibility of using various waste materials containing oxidic iron components as catalysts to produce hydrogen from the direct cracking of methane. Three types of waste material were used, which were procured from three places—the leachate from Landfill (Landfill sample), residue from an old nail Factory (Factory sample) and a waste product of the aluminium industry (Red Mud sample, RM). The characterisation of raw materials demonstrated that the Landfill sample possess distinctive properties. The XRD patterns revealed that Landfill contains one phase—2-line ferrihydrite—while the Factory and RM samples comprise multiple phases. The ICP analysis revealed that the amount of iron in the Landfill sample is larger than that in other samples. Further, SEM images illustrated a unique morphology which was tubular in structure, and the surface area of the Landfill sample was greater than that of the other samples.

The reaction data demonstrated that the hydrogen formation rate as a result of methane cracking was higher in the Landfill sample, followed by the RM sample and then the Factory sample, respectively.

Characterisation of post-reaction materials was undertaken. The XRD patterns showed that the phase raw materials transformed to form Fe metal, iron carbide and graphitic carbon, except for the Factory sample which was not completely reduced and iron oxide and non-metallic iron remained. The CHN analyses revealed a large amount of deposited carbon on the post-reaction samples, particularly for the Landfill sample. The cracking of methane and the large amount of deposited carbon and led to a reduction in the BET surface area. The SEM and HRTEM images of the post-reaction materials illustrated the formation of carbon nanostructures in the Landfill and RM samples, whereas this was not observed in the Factory sample.

2-Line ferrihydrite, the main phase of the Landfill sample, was synthesised to simulate the Landfill sample and tested under the same reaction conditions that were employed for those materials. The reaction data demonstrated that the activity of synthesised 2-line ferrihydrite is very poor compared to the natural Landfill sample. Further, characterisation of the fresh and post-reaction synthesised 2-line ferrihydrite was undertaken to elucidate

some of the expected reasons for the low performance and this was related to sintering and/or the presence of potassium containing residues.

The influence of the reaction temperature on the performance of the Landfill sample has been studied. At 600 °C and the temperature programme from 600 to 700 °C, there was no significant activity and the performance was very poor, while it was very active in the temperature programme from 600 to 750 °C as well as in the temperature programme from 600 to 800 °C. In addition, XRD, SEM, HRTEM, BET, CHN, and TGA analyses were undertaken. SEM images of the post-reaction Landfill sample illustrated that the tubular morphology was not altered at 600 °C, whereas the tubes began melting at 700 °C. The XRD patterns revealed that the Landfill sample was not completely reduced at 600 °C and in the temperature programme from 600 to 700 °C. All characterisation of the post-reaction Landfill sample after the temperature programme regime from 600 to 750 °C showed significant similarity with that in the temperature programme regime from 600 to 800 °C.

*In situ* XRD was conducted to investigate the phase transformation sequences in the Landfill sample during the reaction. Scans were taken at room temperature, 500, 600 and 700 °C. At 500 °C, the phase of 2-line ferrihydrite ( $\text{Fe}_5\text{HO}_8 \cdot 4\text{H}_2\text{O}$ ) was transformed to wustite (FeO), magnetite ( $\text{Fe}_3\text{O}_4$ ) and graphitic carbon. When the temperature was increased to 600 °C, the metallic iron phase appeared along with the wustite (FeO) and graphitic carbon. At 700 °C, new phases of metallic iron, iron carbide and graphite were appeared. Based on the results of the XRD patterns of the post-reaction Landfill sample at different temperatures and the result of *in situ* XRD patterns, a reaction pathway over the Landfill sample has been proposed.

## 4. Modification of Landfill and Factory samples for hydrogen production from direct cracking of methane

### 4.1. Introduction

As shown in Chapter 3, the Landfill and Factory samples were used as obtained for direct cracking of methane to produce hydrogen and carbon. These samples revealed high catalytic activity, especially the Landfill sample. CHN analysis for raw samples showed that the Landfill and Factory samples contained 4.52 and 10.70 wt % carbon, respectively. In addition, ICP analysis for the components of raw Landfill and Factory samples illustrated that these samples contain alkali and alkaline earth metals such as  $\text{Na}^+$ ,  $\text{K}^+$ ,  $\text{Li}^+$ ,  $\text{Mg}^{2+}$  and  $\text{Ca}^{2+}$ . These elements are known to be poisons for the methane decomposition reaction [127, 176]. Valenzuela *et al.* [183] studied the effect of  $\text{Ca}^{2+}$ , and  $\text{K}^+$  addition on the activity of 30 wt% Ni/SiO<sub>2</sub> at 580 °C and confirmed that their presence led to low activity.

Calcination and acid washing of the waste iron based samples may improve their catalytic properties. The purpose of calcination is to decompose and remove unwanted components in the samples [188]. Moreover, washing with acids may enhance the catalytic activity by removal of poisonous metal cations *via* cation exchange. For example, one of the most popular chemical modifications of clays is their acid activation. This comprises the treatment of clay with acid solution, usually HCl or H<sub>2</sub>SO<sub>4</sub>. The main purpose is to obtain a high specific surface area, porosity and surface acidity [189].

On the other hand, Pd catalysts display unique performance for methane decomposition [45, 83]. Shah and co-workers [46] studied the catalytic decomposition of methane into hydrogen and carbon using 5 % Fe/Al<sub>2</sub>O<sub>3</sub> and binary 0.5 % Pd-4.5 % Fe/Al<sub>2</sub>O<sub>3</sub> catalysts at 700 °C. They observed that the loading of Pd as second metal into Fe/Al<sub>2</sub>O<sub>3</sub> catalyst improved the catalyst activity resulting in a high concentration of hydrogen. In a similar study, Ogihara *et al.* [63] investigated the formation of hydrogen through methane decomposition over Pd-based alloy catalysts supported on alumina. In their study, they noted that a Pd-based alloy containing Fe increased the methane conversion at 700 °C from *ca.* 15 % for Pd/Al<sub>2</sub>O<sub>3</sub>, to *ca.* 23 % for Pd-Fe/Al<sub>2</sub>O<sub>3</sub>, as well as extending the lifetime of the catalyst.

Based on the above studies, the Landfill and Factory samples were subjected to modification in an attempt to improve their performance for hydrogen production from direct cracking of methane. These modifications included the effect of calcination at different temperatures, washing by acids and Pd addition.

## **4.2. Results and discussion- Effect of calcination temperature on Landfill and Factory samples**

### **4.2.1 Characterisation of calcined Landfill and Factory samples**

The raw Landfill and Factory samples have been calcined in static air at different 300, 500, 700 and 900 °C. Characterisation of calcined samples was undertaken to determine the changes that occurred. A range of techniques including XRD, CHN elemental analysis, BET surface area and SEM have been used. The characterisation of these materials is described below.

#### **4.2.1.1 XRD patterns and Raman spectroscopy**

Figure 4-1 shows the powder XRD patterns of the raw Landfill and Landfill samples calcined at 300, 500, 700 and 900 °C. It can be seen that calcination results in a phase change from the 2-line ferrihydrite of the raw material. At 300 and 500 °C, the 2-line ferrihydrite structure transformed to maghemite ( $\gamma\text{-Fe}_2\text{O}_3$ ), while at 700 and 900 °C, it transformed to haematite ( $\alpha\text{-Fe}_2\text{O}_3$ ). It is observed that in the range of 300 - 500 °C maghemite with a similar degree of crystallinity is formed. In addition, the haematite formed at 700 °C is fairly amorphous and its crystallisation increased dramatically at 900 °C. It should be noted that 2-line ferrihydrite ( $\text{Fe}_5\text{HO}_8\cdot 4\text{H}_2\text{O}$ ) is an oxyhydroxide whereas maghemite and haematite are oxides. This clearly implies that dehydration reaction took place during calcination as expected. Maghemite can be synthesised in the laboratory by several methods. One of these methods involves heating of ferrihydrite in air at 450 °C [132].

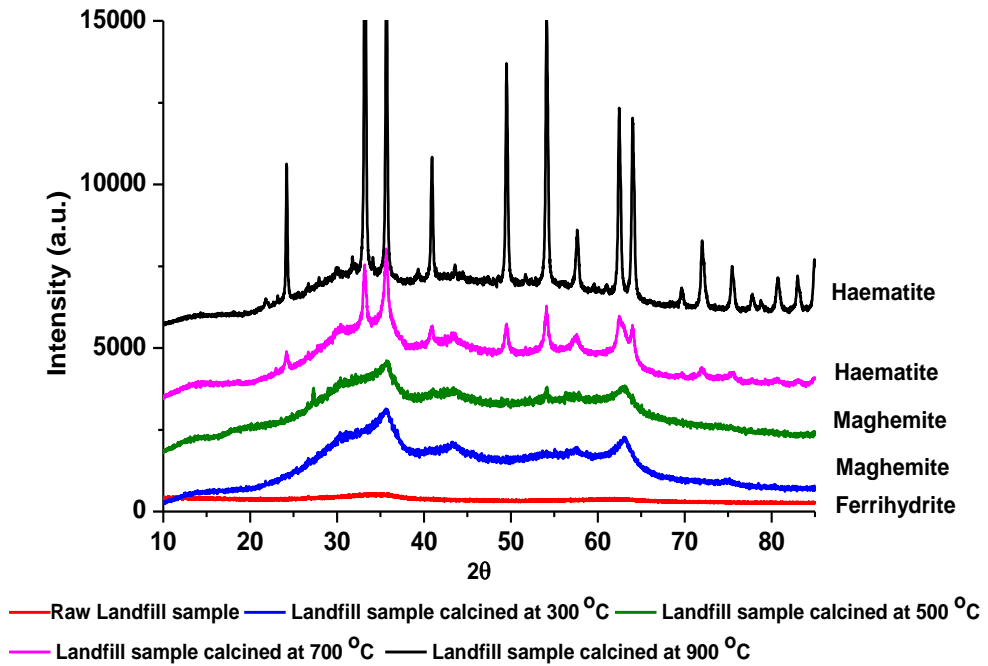


**Figure 4-1** Powder X-ray diffraction patterns of the raw Landfill sample and calcined Landfill at different temperature.

Moreover, the results of the XRD studies, Figure 4-1, for the phase transformation sequence of the raw Landfill sample, 2-line ferrihydrite, is in agreement with a number of studies which revealed that maghemite is an intermediate phase in the thermal transformation between ferrihydrite and haematite. Barron and Torrent [190], studied the effect of time on the phase transformation sequences of 2-line ferrihydrite at 150 °C. Their XRD results showed that the ferrihydrite phase changed to maghemite after 3 days and the phase then lasted for 14 days. After 90 days, they observed that the ferrihydrite was then converted into a mixture of maghemite, haematite and residue of ferrihydrite. Pure haematite was apparently formed after 120 days.

Although, X-ray diffraction is important for the identification and characterisation of iron oxide phases, the identification of magnetite ( $\text{Fe}_3\text{O}_4$ ) and maghemite ( $\gamma\text{-Fe}_2\text{O}_3$ ) phases by X-ray diffraction is quite complicated, because both phases possess a similar spinel structure and almost identical lattice parameters [191]. Therefore, Raman spectroscopy has been used to distinguish between maghemite and magnetite and to confirm the maghemite structure. Figure 4-2 illustrates the Raman spectrum for the Landfill samples calcined at different temperatures. It is reported that maghemite shows broad bands around 350, 500, and 700  $\text{cm}^{-1}$  whereas magnetite has a main band centred at around 670  $\text{cm}^{-1}$ . In addition, the position of the bands for haematite are at 225, 247, 293, 299, 412, 498 and 613  $\text{cm}^{-1}$

[132, 192-194]. From Figure 4-2, it can be seen that the Raman spectra for the Landfill samples calcined at 300 and 500 °C are assigned only to the maghemite phase. The XRD pattern of the calcined Landfill sample at 700 °C in Figure 4-1 revealed the presence of haematite and an amorphous component. The Raman spectrum for this sample indicates that it is in fact, a mixture of maghemite and haematite. The Raman spectrum of Landfill sample calcined at 900 °C confirms the formation of haematite.

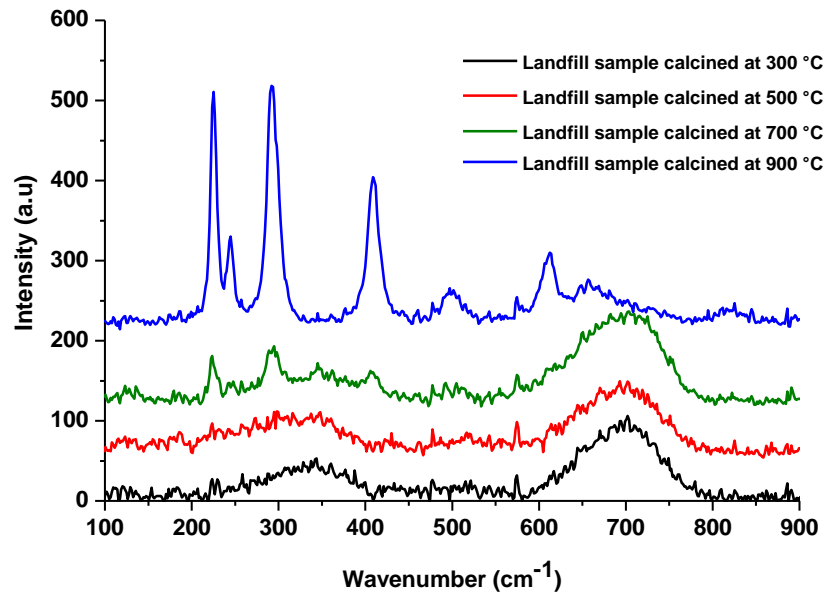


**Figure 4-2** Raman spectra of Landfill samples after being calcined at different temperature.

The powder XRD patterns of the raw Factory and calcined Factory samples at 300, 500, 700 and 900 °C are presented in Figure 4-3. As described in Chapter 3, haematite ( $\alpha$ -Fe<sub>2</sub>O<sub>3</sub>) and silica (SiO<sub>2</sub>) are the main phases of the raw Factory sample. From Figure 4-3, it can be seen that the calcination temperature did not affect the phase composition for the Factory sample, although it apparently played a significant role in increasing the sample crystallinity. Under oxidising conditions, haematite is thermodynamically the most stable compound and it is often the end phase for many transformation routes of iron oxides [132]. It can be observed from the XRD patterns in Figure 4-3 that silica was present in the raw and calcined samples. This is expected, especially as the Factory sample contains a relatively high amount of silicon, as shown in Chapter 3 using ICP elemental analysis. In addition, the intensity of the SiO<sub>2</sub> reflections relatively increased from raw sample to calcined sample at 500 °C and then decreased relatively at 700 and 900 °C. The haematite phase was of low crystallinity in the raw sample and samples calcined at 300 and 500 °C, but became more pronounced and crystalline at 700 and 900 °C.

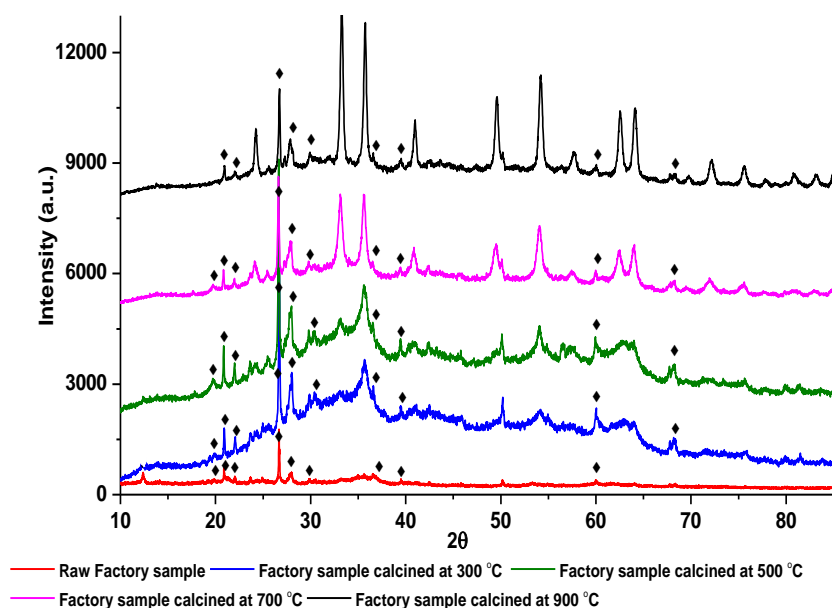


**Figure 4-3** Powder X-ray diffraction patterns of the raw Factory sample and calcined Factory at different temperature; (♦) silica ( $\text{SiO}_2$ ) peaks.

#### 4.2.1.2 CHN elemental analysis

Table 4-1 presents the CHN analyses of the raw and calcined Landfill and Factory samples. It is clear that the calcination of raw samples at different temperatures led to a reduction of the carbon and hydrogen content due to “burn off” and dehydration. This loss in the amount of carbon and hydrogen was reduced gradually with increasing temperature of calcination. It is observed that the carbon in Landfill sample was completely lost at 900 °C while it is completely lost in the Factory sample by 500 °C.

<b>Table 4-1</b> CHN analysis for raw and calcined Landfill and Factory samples at 300, 500, 700 and 900 °C.						
<b>Calcination temperature</b>	<b>Mean value, wt% for Landfill sample</b>			<b>Mean value, wt% for Factory sample</b>		
	<b>C</b>	<b>H</b>	<b>N</b>	<b>C</b>	<b>H</b>	<b>N</b>
<b>Raw sample</b>	<b>4.52 ± 0.02</b>	<b>1.29 ± 0.00</b>	-	<b>10.70 ± 0.01</b>	<b>1.70 ± 0.05</b>	-
<b>At 300 °C</b>	<b>0.78 ± 0.08</b>	<b>0.36 ± 0.01</b>	-	<b>2.34 ± 0.03</b>	<b>0.34 ± 0.05</b>	-
<b>At 500 °C</b>	<b>0.75 ± 0.04</b>	-	-	-	-	-
<b>At 700 °C</b>	<b>0.65 ± 0.07</b>	-	-	-	-	-
<b>At 900 °C</b>	-	-	-	-	-	-

### 4.2.1.3 BET surface area measurements

The surface areas of the various raw and calcined Landfill and Factory samples were measured. Table 4-2 presents the results. It can be observed that calcination caused a decrease in the surface area of the Landfill samples. The surface areas, after calcination at 300 or 500 °C, are quite similar and are about half of the surface area of the raw sample. The surface areas of calcined Landfill sample at 700 and 900 °C reduced to 67 and 14 m<sup>2</sup>/g, respectively. The BET value can be related to the total surface area of the particles, with high surface area corresponding to small particle size [180]. Hence, it is possible that the particle size of Landfill sample increased with the increasing calcination temperature as a result of sintering. However, from previous characterisation, it is noted that the calcined Landfill sample at 300 or 500 °C possessed similar characteristics.

<b>Table 4-2</b> BET surface area analysis for raw Landfill and Factory samples and those calcined at 300, 500, 700 and 900 °C.		
<b>Calcination temperature</b>	<b>BET surface area, m<sup>2</sup>/g</b>	
	<b>Landfill sample</b>	<b>Factory sample</b>
<b>Non-calcined sample</b>	<b>254</b>	<b>43</b>
<b>At 300 °C</b>	<b>128</b>	<b>88</b>
<b>At 500 °C</b>	<b>126</b>	<b>80</b>
<b>At 700 °C</b>	<b>67</b>	<b>50</b>
<b>At 900 °C</b>	<b>14</b>	<b>14</b>

The surface area of the raw Factory sample increased from 43 to 88 m<sup>2</sup>/g at a calcination temperature of 300 °C. It seems that there are changes occurred in the sample component led to this increase in surface area. The results of the CHN analyses, Table 4-1, showed the quantity of carbon in this sample dropped sharply at 300 °C and was completely removed by 500 °C. At 500 °C it is noted that the surface area began to decline gradually reaching 14 m<sup>2</sup>/g at 900 °C. Interestingly, it observed that the surface areas of the Landfill and Factory samples calcined at 900 °C are quite similar.

#### 4.2.1.4 SEM images

Figure 4-4 presents SEM micrographs of raw and calcined Landfill samples. The image (A) in Figure 4-4 shows the raw Landfill sample whereas the images (B, C) illustrate the samples calcined at 300 and 500 °C, respectively. It is clear that the tubular morphology of the Landfill sample was not affected by calcination at 300 and 500 °C. However, the morphology of the Landfill samples calcined at 300 and 500 °C are somewhat similar which supports the previous characterisation and suggests that the sample has stability in this range of calcination temperature.

The image in Figure 4-4 (D) illustrates the effect of calcination temperature on Landfill sample at 700 °C, where it can be seen that the tubes apparently started to melt and merge. This is in good agreement with the result obtained during the study of the effect of reaction temperature on methane cracking over the Landfill sample at 700 °C, as shown in Chapter 3, where the SEM images of post-reaction Landfill sample also showed that the tubes of iron oxides began to melt at this temperature indicating that this is effect of temperature rather than reaction atmosphere. The fusion between the components led to large particle size which is consistent with the reduced surface area as noted in Table 4-2.

A significant change can be observed in the Landfill sample calcined at 900 °C, Figure 4-4(E). It can be seen that the sample morphology completely changed. Moreover, the image reveals large agglomerates of spherical particles and a very few remnants of the tubular morphology component.

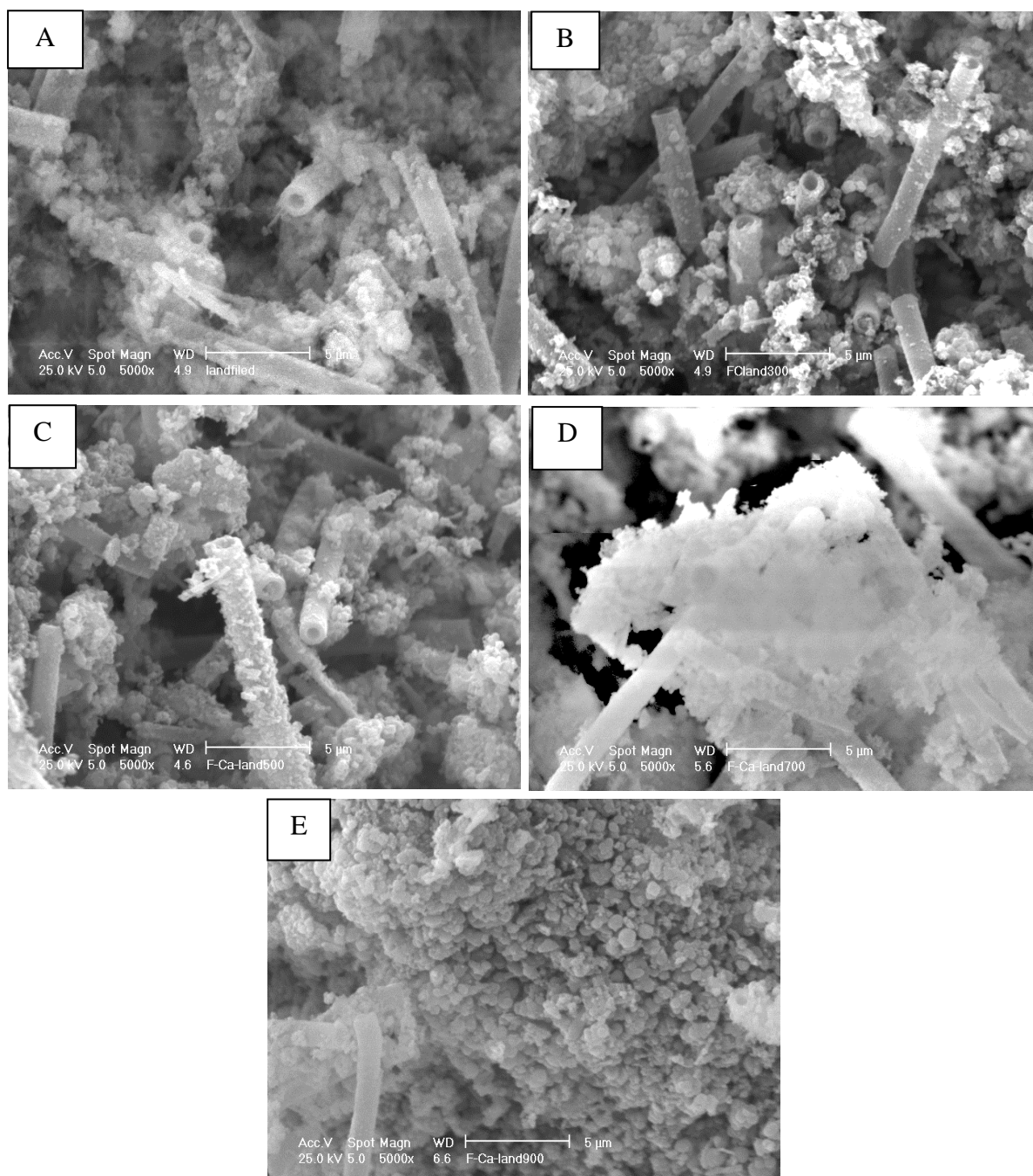


**Figure 4-4** SEM images of (A) Raw Landfill sample, (B) Landfill sample calcined at 300 °C, (C) Landfill sample calcined at 500 °C, (D) Landfill sample calcined at 700 °C and (E) Landfill sample calcined at 900 °C.

The SEM images of the Factory samples are shown in Figure 4-5. From image (A), it can be seen that the raw or non-calcined Factory sample possess bulky particles which may correspond to its relatively low surface area. Due to agglomeration of particles, it is difficult to estimate the particle size but it can be observed the changes occur upon calcination. It can be observed that the morphology of the raw Factory sample changed after calcination at 300 °C to yield smaller particles and agglomerates, as illustrated in Figure 4-5(B). The image in Figure 4-5 (C) shows the calcined Factory sample at 500 °C. It can be observed that the particles of Factory sample have agglomerated more than in the

300 °C calcined samples. As the calcination temperature was increased to 700 °C the particles increased further in size as shown in Figure 4-5(D). From the image in Figure 4-5(E), it can be seen that the calcination temperature of 900 °C produced smaller particles with large agglomeration, which may explain the sharp decline of the surface area.

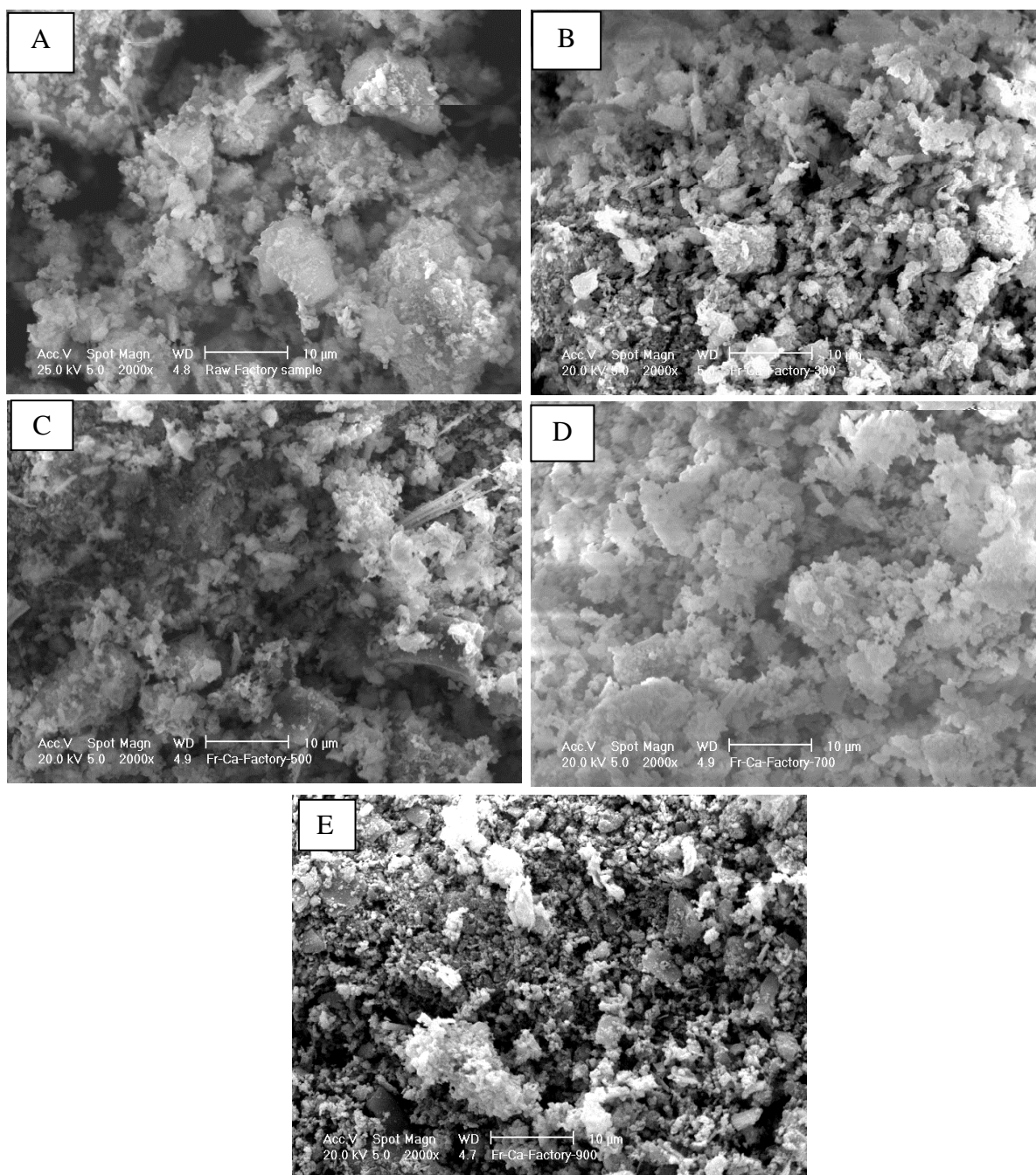


**Figure 4-5** SEM images of (A) Raw Factory sample, (B) Factory sample calcined at 300 °C, (C) Factory sample calcined at 500 °C, (D) Factory sample calcined at 700 °C and (E) Factory sample calcined at 900 °C.

## 4.2.2 Reaction data

### 4.2.2.1 Effect of calcination temperature on the Landfill sample

Figure 4-6 presents the hydrogen formation rates against time on stream for a temperature programmed reaction from 600 to 800 °C as a result of direct cracking of methane for the raw and calcined Landfill samples. In addition, the formation rates of carbon monoxide and carbon dioxide associated with the hydrogen production were studied and are presented in Figures 4-7 and 4-8, respectively. From Figure 4-6, it can be seen that the calcination temperature played significant role in the performance of the Landfill sample. Both non-calcined and calcined Landfill samples showed high levels of hydrogen formation, but the calcined Landfill samples demonstrated a delay in the onset of maximum hydrogen formation rate compared to the non-calcined sample. Moreover, the hydrogen formation rate for all calcined Landfill samples is low and quite similar in the temperature range from 600 to 750 °C and in the initial phase of reaction at 800 °C whereas the non-calcined sample showed a higher hydrogen formation rate. Also, it is observed that the hydrogen formation rate with the non-calcined Landfill sample was increased by each temperature increase, at 650, 700 and 750 °C, and followed by a gradual decrease. It increased sharply when the temperature was increased to 800 °C. This sharp increase in the hydrogen formation rate preceded increases for the other samples. However, it is notable that the hydrogen formation rates for all calcined Landfill samples are low and steady in the temperature range from 600 to 700 °C, but they increased slightly when the temperature rose to 750 °C and remained steady without a gradual decrease at this temperature. When the temperature was increased again at 800 °C, the hydrogen formation rates for these samples slightly increased and remained steady up to 600 minutes of time on stream followed by a dramatic increase in the hydrogen formation rates. It is clear that amongst these samples, the sample calcined at 900 °C demonstrated the highest hydrogen formation rate, whilst the calcined Landfill sample at 300, 500 and 700 °C demonstrated a similar activity and lower hydrogen formation rates. All the samples did not show any deactivation and the hydrogen formation rates were still increasing at the end of each experiment. It is likely that they will show high rates of hydrogen formation at prolonged time on stream. The activity of calcined Landfill sample at 500 °C is close to that the calcined Landfill sample at 300 °C as can be anticipated from their similar characteristics. It should be noted that the pressure drop effects due to carbon deposition are observed after 680 minutes on stream for the non-calcined sample as well as beyond 740 minutes on

stream for the sample calcined at 900 °C. In contrast, such effects were not observed for the remainder of the calcined samples.

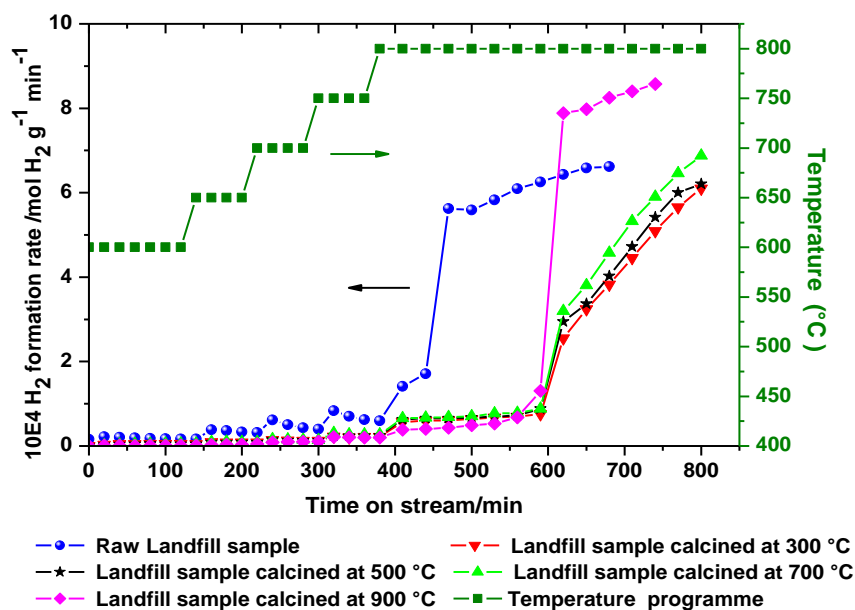


**Figure 4-6** Hydrogen formation rates from 600 to 800 °C as a function of time on stream for CH<sub>4</sub> cracking over the raw Landfill sample and calcined Landfill samples. The CH<sub>4</sub>/N<sub>2</sub> flow rate was 12 mL/min and 0.4 g sample mass.

It can be suggested that the delay in activity of the calcined samples results from their relatively small surface area, unlike the non-calcined sample that has a high surface area, as evident in Table 4-2. Although, the initial performance of non-calcined sample was high it did not show a maximum hydrogen formation rate as high as the sample calcined 900 °C. It may be that the early activity of non-calcined sample led to early carbon deposition, which suppresses its performance.

The SEM images presented in Figure 4-4 illustrate the changes in the sample morphology as a result of calcination. It was noted that the morphology of Landfill samples calcined at 700 and, particularly, 900 °C differ from the remainder of the samples. It may be that the collapse of the tubular morphology and its integration with the non-tubular component to form a new morphology plays a role in the enhanced performance of the 900 °C calcined sample.

The carbon monoxide and carbon dioxide formation rates against time on stream for the Landfill samples are shown in Figures 4-7 and 4-8, respectively. Production of carbon

monoxide and carbon dioxide are associated with the hydrogen formation as a result of reduction procedures, as mentioned previously in Chapter 3.

From Figure 4-7, it can be seen that the production of carbon monoxide for all samples occurred throughout the reaction, which possibly indicates the on-going occurrence of reduction processes. The non-calcined Landfill sample revealed the highest carbon monoxide formation rate in the temperature range from 600 to 750 °C. It increased at each stage of the temperature increase and was followed by a gradual decrease, but increased sharply after 60 minutes of time on stream at 800 °C followed by sharp decline. This can be associated with the observed hydrogen formation. However, all calcined Landfill samples demonstrated lower CO formation rates than the non-calcined Landfill sample in the temperature range from 600 to 800 °C, except the Landfill sample calcined at 900 °C, which showed the highest carbon monoxide formation rate among all samples at 800 °C and time on stream 620 minutes, which corresponds to the apparent burst in hydrogen formation rate as shown in Figure 4-6. Moreover, the carbon monoxide formation rates for the Landfill samples calcined at 300, 500 and 700 °C are somewhat similar. They increase and remain steady with temperature increase, but they dropped after 230 minutes of time on stream at 800 °C. Again, it can be observed that there is a relationship between the carbon oxides formation rates and the hydrogen formation rates. However, the carbon monoxide formation rates for all samples declined at 800 °C in opposition to the increase in the hydrogen formation rates, as shown in Figures 4-6 and 4-7. This may be the consequence of the interplay between the reduction process and the formation of active sites.

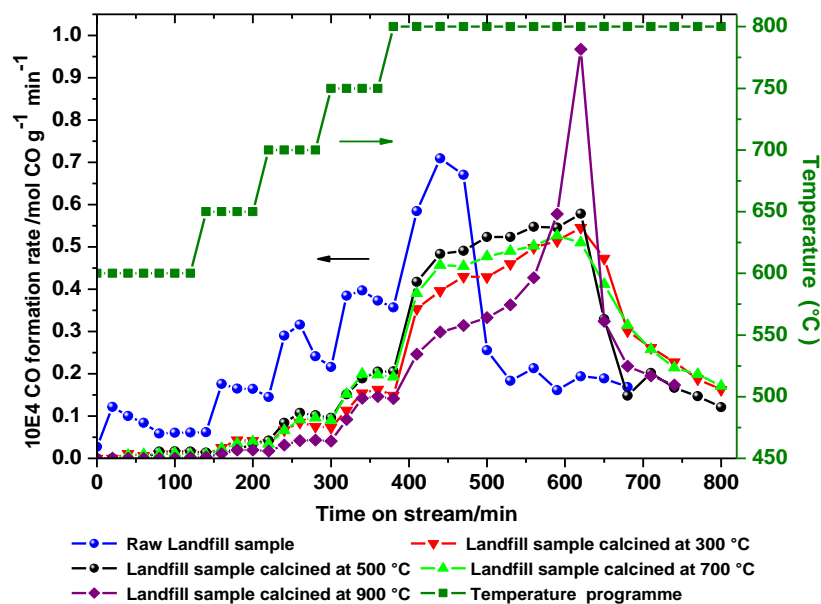


**Figure 4-7** CO formation rates at 600 to 800 °C as a function of time on stream for CH<sub>4</sub> cracking over the non-calcined Landfill and calcined Landfill samples. The CH<sub>4</sub>/N<sub>2</sub> flow rate was 12 mL/min and 0.4 g sample mass.

Figure 4-8 illustrates the carbon dioxide formation rates for all the samples tested in the temperature range from 600 to 800 °C. It can be noted that there is an initial burst in the CO<sub>2</sub> formation rate at 600 °C, except for the Landfill sample calcined at 900 °C, which showed the lowest initial CO<sub>2</sub> formation rate. It is observed that the CO<sub>2</sub> formation rates for all samples increased with temperature increase and were followed by a gradual decrease. The non-calcined Landfill sample demonstrated a rapid drop in the CO<sub>2</sub> formation rate at 800 °C, which almost corresponds to the lowering CO formation rate at 800 °C. This reveals that the non-calcined Landfill sample has rapid reduction compared to calcined samples. The samples calcined at 300, 500 and 700 °C displayed similar rates of carbon dioxide formation, which is also similar to their carbon monoxide production behaviour.

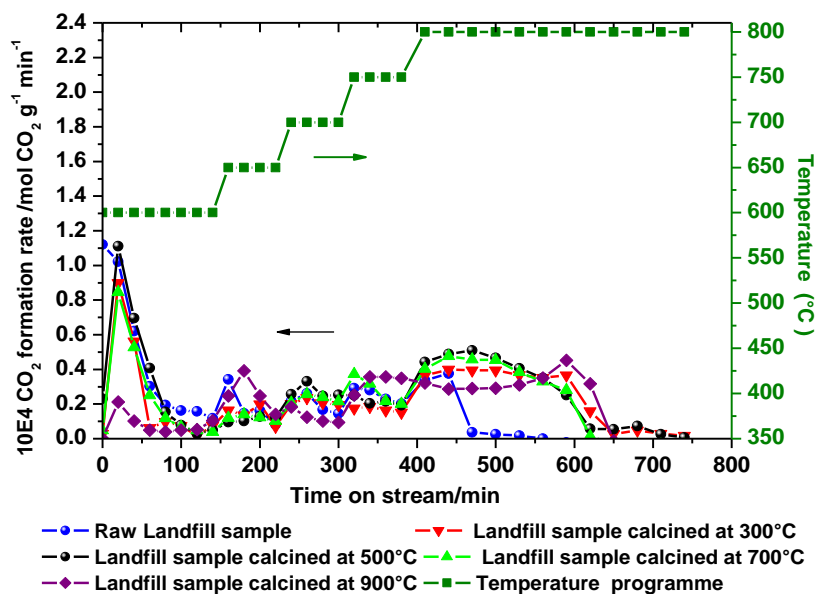


**Figure 4-8** CO<sub>2</sub> formation rates at 600 to 800 °C as a function of time on stream for CH<sub>4</sub> cracking over the non-calcined Landfill and calcined Landfill samples. The CH<sub>4</sub>/N<sub>2</sub> flow rate was 12 mL/min and 0.4 g sample mass.

#### 4.2.2.2 Effect of calcination temperature on the Factory sample

The hydrogen formation rates against time on stream at temperatures from 600 to 800 °C as a result of the direct cracking of methane over non-calcined and calcined Factory samples are presented in Figure 4-9. It can be seen from the profile of the non-calcined sample that it behaves differently from the calcined samples. It is noted that calcination at 300, 500 and 700 °C did not display any beneficial effects and all these samples showed low hydrogen formation rates. In addition, it is observed that the Factory sample calcined at 500 °C exhibits the lowest hydrogen formation rate. It can be observed that the non-calcined sample generally showed the highest hydrogen formation rate in the temperature range from 600 to 800 °C and throughout the reaction run. In the case of the Factory sample calcined at 900 °C, its behaviour was similar to the samples calcined at 300, 500 and 700 °C in the temperature range from 600 to 750 °C, but it exhibited superior activity and indeed the highest hydrogen formation rate of all samples after 60 minutes when the reaction temperature increased to 800 °C. Moreover, it was observed that the hydrogen formation rates for all samples rose with each temperature increase and then gradually decreased in the temperature range from 600 to 750 °C. It should be noted that the effects of pressure drop from carbon deposition were observed after 650 minutes on stream for the

Factory sample calcined at 900 °C. Although calcination at 300, 500 and 700 °C increased the surface area of samples as shown in Table 4-2, their performances were low. It is possible that the calcination at these temperatures retarded the reduction process of the samples more than non-calcined sample and the sample calcined at 900 °C. The SEM images in Figure 4-5 illustrated that the particles of Factory sample gradually agglomerated upon calcination from 300 to 700 °C and they became more ordered at 900 °C. Hence, it can be proposed that the morphology of these samples played a role in the reduction process and consequently their performance.

It should be mentioned that the formation rates of CO and CO<sub>2</sub> were not studied for technical reasons.

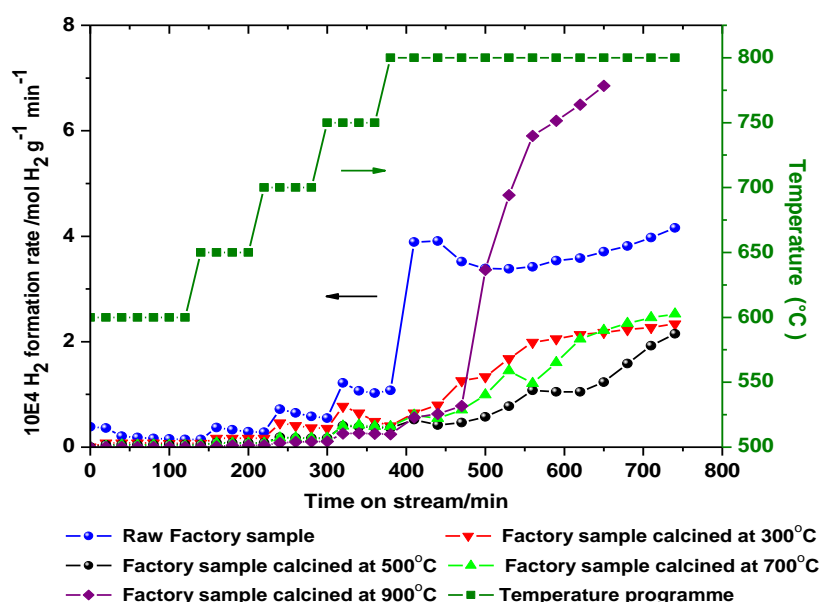


**Figure 4-9** Hydrogen formation rates at 600 to 800 °C as a function of time on stream for CH<sub>4</sub> cracking over the raw Factory sample and calcined Factory samples. The CH<sub>4</sub>/N<sub>2</sub> flow rate was 12 mL/min and 0.4 g sample mass.

For both the Landfill and Factory samples calcination at 900 °C resulted in the highest hydrogen formation rates. These samples are similar in some respects, for example, the XRD patterns, BET surface area and CHN analyses. The powder XRD patterns for these samples displayed that haematite ( $\alpha$ -Fe<sub>2</sub>O<sub>3</sub>) is the major phase, as illustrated in Figures 4-1 and 4-3. It is hard to attribute the high activity solely to the haematite phase, because haematite is also evident in many of the other samples. Although haematite is the major phase in the raw Factory sample and that calcined at 300, 500 and 700 °C, they did not show high activity for methane decomposition.

### 4.2.3 Characterisation of post-reaction calcined Landfill and Factory samples

Post-reaction samples were characterised. Various techniques such as XRD, CHN elemental analysis, TGA, BET surface area and SEM have been employed.

#### 4.2.3.1 XRD patterns

Post-reaction XRD patterns for the non-calcined and calcined Landfill and Factory samples are presented in Figures 4-10 and 4-11, respectively. Previously, it has been shown that the pre-reaction Landfill samples contain various iron oxides. The XRD patterns in Figure 4-1, showed that the raw or non-calcined Landfill samples comprises 2-line ferrihydrite ( $\text{Fe}_5\text{HO}_8 \cdot 4\text{H}_2\text{O}$ ), the calcined Landfill samples at 300 and 500 °C are maghemite ( $\gamma\text{-Fe}_2\text{O}_3$ ) and the Landfill samples calcined at 700 and 900 °C are haematite ( $\alpha\text{-Fe}_2\text{O}_3$ ).

In Figure 4-10, the XRD patterns of the post-reaction non-calcined and calcined Landfill samples at 300, 500 and 700 °C show reflections indicative of metallic iron (Fe), iron carbide ( $\text{Fe}_3\text{C}$ ) and graphite, while the post-reaction calcined Landfill samples at 900 °C can be matched to metallic iron and graphite. These phases have been marked on the patterns. It is clear that these phases have been formed as a result of the reduction of iron oxides by methane at the conditions employed. According to the results obtained on Chapter 3 and literature, the reduction processes of iron oxides are stepwise as follows [51]:



However, it has reported [51] that metallic iron (Fe) and iron carbide ( $\text{Fe}_3\text{C}$ ) are active phases for methane decomposition. At the end of reaction, the samples did not show any deactivation and rather the hydrogen formation rates were still increasing, as shown in Figure 4-6. It is observed that the peak intensity of iron carbide ( $\text{Fe}_3\text{C}$ ) in the post-reaction non-calcined Landfill sample is higher than post-reaction Landfill samples calcined at 300, 500 and 700 °C and the reflection intensity of metallic iron (Fe) is lower compared to the same samples and calcined samples at 900 °C. It could be that the delay in the reduction process for these samples led to a delay in the appearance of  $\text{Fe}_3\text{C}$  phase. It was observed from the formation rates of carbon monoxide in Figure 4-7 that the non-calcined Landfill sample showed early the highest carbon monoxide formation rate, whereas the Landfill

sample calcined at 900 °C revealed the lowest formation rate of carbon monoxide, except in the narrow area of time on stream (between 600 to 650 minutes at 800 °C) that showed the highest carbon monoxide formation rate amongst all samples. Also, the CO<sub>2</sub> formation rate for this sample, Figure 4-8, was low compared to other samples, which indicate the delay in the reduction process and delay in the formation of Fe<sub>3</sub>C phase.

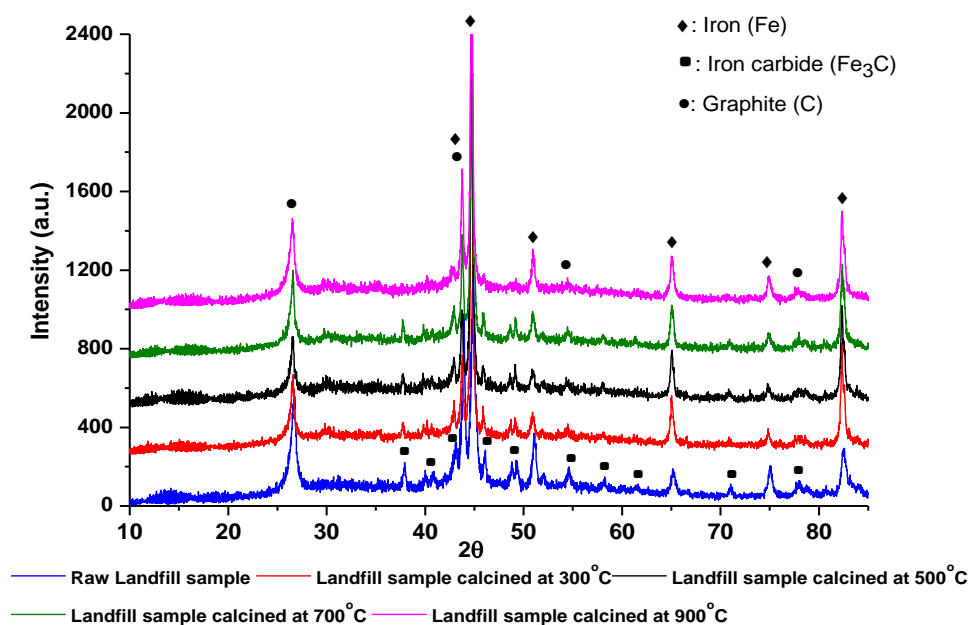


**Figure 4-10** Powder x-ray diffraction patterns for post-reaction non-calcined and calcined Landfill samples at different temperature.

Figure 4-11 illustrates the XRD patterns of the post-reaction non-calcined and calcined Factory samples. It can be seen that the XRD patterns of the post-reaction non-calcined Factory sample and those calcined at 300, 500 and 700 °C are quite similar. As shown and discussed in Chapter 3, the XRD pattern of the post-reaction raw Factory sample showed reflections indicative of FeO, Fe<sub>3</sub>C, FeFe<sub>4</sub>(PO<sub>4</sub>)<sub>4</sub>(OH)<sub>2</sub>·2H<sub>2</sub>O, SiO<sub>2</sub> and graphite.

However, the XRD pattern for the post-reaction Factory sample calcined at 900 °C shows completely different phase composition than the rest of the other samples. It can be observed that the metallic iron (Fe), quartz (SiO<sub>2</sub>) and graphite, as have been marked on the pattern, are the only phases in this sample. It is apparent from this result that the non-calcined Factory sample and those calcined at 300, 500 and 700 °C have not completed the process of reduction, whereas the Factory sample calcined at 900 °C is more fully reduced. This may explain the higher activity of the 900 °C calcined sample.

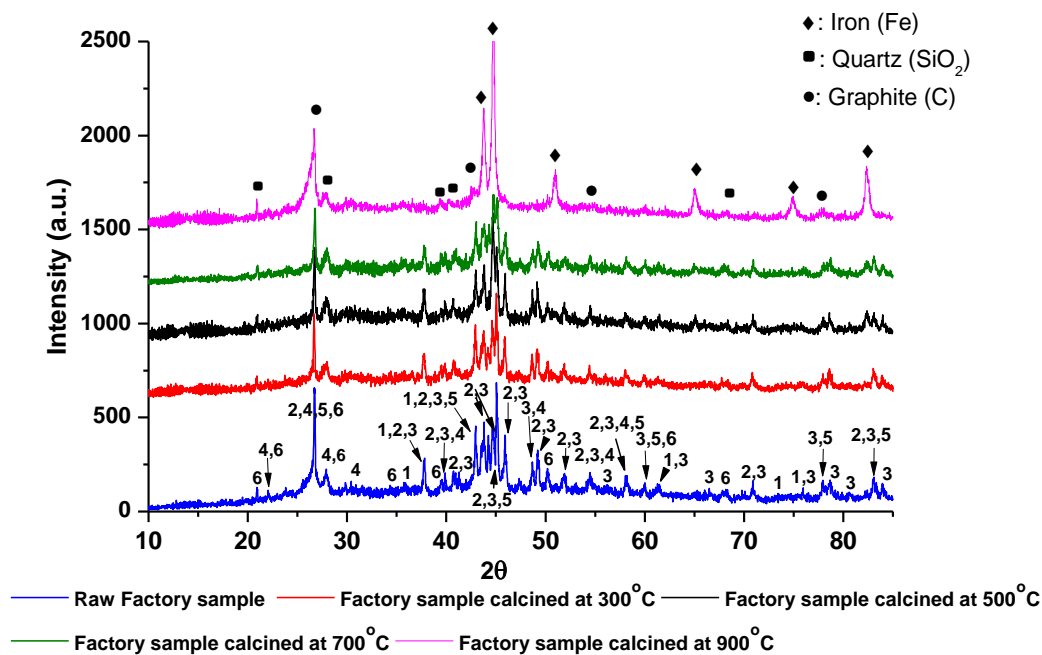


**Figure 4-11** Powder x-ray diffraction patterns for post-reaction non-calcined and calcined Factory samples. 1: iron oxide (FeO); 2: iron carbide (Fe<sub>3</sub>C); 3: cohenite (Fe<sub>3</sub>C); 4: giniite FeFe<sub>4</sub>(PO<sub>4</sub>)<sub>4</sub>(OH)<sub>2</sub>·2H<sub>2</sub>O; 5: graphite (C); 6: quartz (SiO<sub>2</sub>).

#### 4.2.3.2 Post-reaction CHN and TGA analysis

The post-reaction CHN analyses of non-calcined and calcined Landfill and Factory samples are shown in Table 4-3. From this data, it is clear that the non-calcined Landfill sample has the largest amount of carbon deposited on it (64.91 wt%) after the reaction and the calcined Landfill sample at 300 °C has the lowest amount of carbon (45.10 wt%). It is observed that the amount of carbon deposited on the calcined Landfill samples gradually increases with calcination temperature. This result parallels the results of the catalytic tests for the calcined Landfill samples, Figure 4-6, where the catalytic activity for methane decomposition over the calcined Landfill samples gradually increases with pre-calcination temperature.

<b>Table 4-3</b> CHN analyses for the post-reaction non-calcined and calcined Landfill and Factory samples at 300, 500, 700 and 900 °C.						
<b>Calcination temperature</b>	<b>Mean value, wt% for Landfill sample</b>			<b>Mean value, wt% for Factory sample</b>		
	<b>C</b>	<b>H</b>	<b>N</b>	<b>C</b>	<b>H</b>	<b>N</b>
<b>Raw sample</b>	<b>64.91 ± 0.90</b>	-	-	<b>41.60 ± 0.20</b>	-	-
<b>At 300 °C</b>	<b>45.10 ± 0.09</b>	-	-	<b>20.60 ± 0.15</b>	-	-
<b>At 500 °C</b>	<b>49.50 ± 1.98</b>	-	-	<b>8.60 ± 0.10</b>	-	-
<b>At 700 °C</b>	<b>50.83 ± 1.8</b>	-	-	<b>15.00 ± 0.11</b>	-	-
<b>At 900 °C</b>	<b>59.70 ± 0.51</b>	-	-	<b>47.10 ± 0.60</b>	-	-

Although the performance of non-calcined Landfill sample was not the highest and the time on stream was the shortest because of pressure drop effects as a result of rapid carbon deposition (64.91 wt%). The early onset of activity for this sample at temperatures below 800 °C may explain the reason of the largest amount of carbon deposited. Although the calcined Landfill sample at 900 °C displayed the highest hydrogen formation rate, the amount of carbon deposited (59.70 wt %) is lower than the amount of carbon deposited on the non-calcined Landfill sample. This can be attributed to the delay in its activity and the fact that its highest activity only occurred over a short reaction time. The CHN analysis for the post-reaction non-calcined and calcined Factory sample is also shown in Table 4-3. It can be seen that non-calcined and calcined Factory samples at 900 °C have a significant deposition of carbon being 41.60 and 47.10 wt% for the non-calcined and 900 °C calcined samples, respectively. Further, the Factory sample calcined at 500 °C has the lowest amount of carbon deposited (8.60 wt%). The amount of carbon deposited on the calcined Factory samples at 300 and 700 °C are 20.60 and 15.00 wt%, respectively. These quantities of carbon deposited are in agreement with those of reaction rates in Figure 4-9. For non-calcined sample and Factory samples calcined at 300, 500 and 700 °C, the amounts of carbon deposited is present in the form of iron carbide ( $\text{Fe}_3\text{C}$ ) and graphitic carbon whilst it is only graphitic carbon in the calcined Factory samples at 900 °C as shown by the XRD studies presented in Figure 4-11.

TGA studies in the presence of air have been performed for the post-reaction Landfill and Factory samples to estimate the amount of carbon deposited on them and to determine their reactivity profile with respect to air. Figure 4-12 presents the TGA profiles for the post-reaction Landfill samples. It is clear that there is an initial weight increase in the region of

450 °C, followed by weight loss within the region of 600 °C. The weight increase that occurred could be attributed to oxidation reactions for the reduced iron phases, iron carbide and metallic iron, which are observed in the XRD analyses, Figure 4-10. The weight loss can be ascribed to the combustion of carbon. In addition, it is apparent from the TGA profiles in Figure 4-12 that the weight loss, which represents the amount of carbon deposited, is roughly 57.50, 24.00, 30.00, 33.00 and 48.00 wt% for the non-calcined Landfill, Landfill calcined at 300 °C, Landfill calcined at 500 °C, Landfill calcined at 700 °C and Landfill calcined at 900 °C samples, respectively. These carbon content values are lower than those determined by CHN analyses, as illustrated in Table 4-3. It should be noted that the general trend in the amount of carbon deposited on these samples is the same for the post-reaction CHN analysis and TGA profiles. As discussed in Chapter 3, it is possible that this is due to the small amount of material required to carry out these post-reaction techniques. This suggests that there could be a degree of inhomogeneity in the dispersion of carbon in the samples. It may also be a consequence of the off-set of the mass gain and mass loss processes.

A study of the direct decomposition of methane over three types of Red Mud sample reported post-reaction sample XRD reflections to correspond to Fe and Fe<sub>3</sub>C as well as graphite, quartz and alumina [161]. In addition, TGA analyses for the post-reaction samples showed an initial mass increase between 350-550 °C followed by a decrease which extends beyond 800 °C. They attributed this increase in mass to the oxidation of the reduced Fe<sub>3</sub>C and/or Fe phases and the mass decrease to oxidation of carbon.

However, it should be noted that the inflection in the weight loss profile for the non-calcined Landfill and calcined Landfill samples at 900 °C, as shown in Figure 4-12, may be due to the high intensity of carbon species within a narrow distribution, which lead to a "high-burst" of carbon combustion at *ca.* 580 °C (it is more evident by the first-derivative weight change profiles as depicted in Figure 4-13). TGA analysis of these samples was conducted three times to confirm the reproducibility of these results.

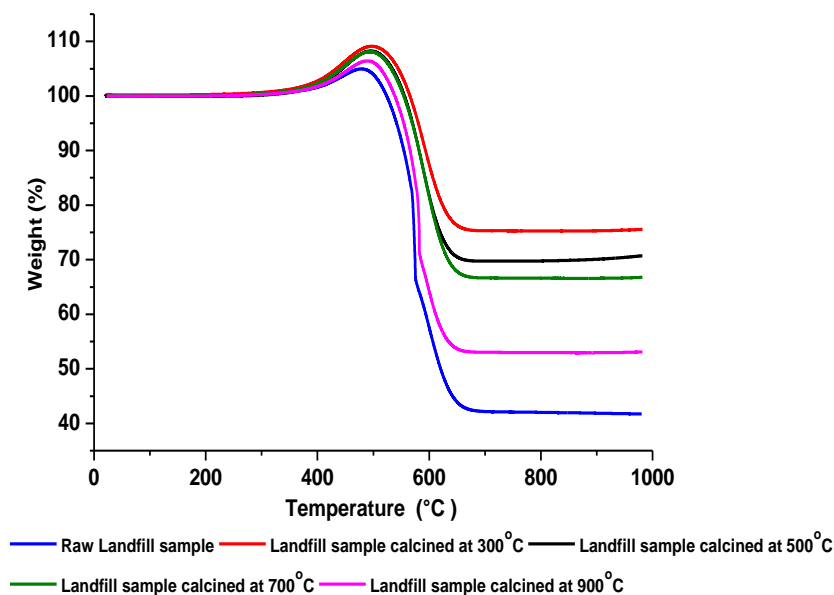


**Figure 4-12** TGA profiles for the post-reaction Landfill samples.

The first-derivative weight change profiles for the post-reaction Landfill samples are also presented in Figure 4-13. From these profiles, the differences between the samples will be clearer than those shown in Figure 4-12. From Figure 4-13 (A), it can be seen that the post-reaction non-calcined has two mass loss regions that is, “low” and “high” temperature combustion of carbon at *ca.* 570 and 600 °C, respectively. The intense peak at 570 °C occurring in the non-calcined sample can be ascribed to a narrow distribution in the nature of carbon species present. Landfill samples calcined at 300, 500 and 700 °C demonstrated only one mass loss region at 580 °C, corresponding to the “high” temperature combustion region. The general similarity of the profiles denotes that the deposited carbon species have similar reactivity. The TGA profiles in Figure 4-13 (B) show the post-reaction non-calcined and 900 °C calcined Landfill samples have the same two mass loss regions that is, “low” and “high” temperature combustion of carbon at *ca.* 570 and 600 °C, respectively. This indicates that these two samples have a similar form of carbon deposited with the main apparent difference being the amount of narrow distribution of carbon species at *ca.* 570 °C.

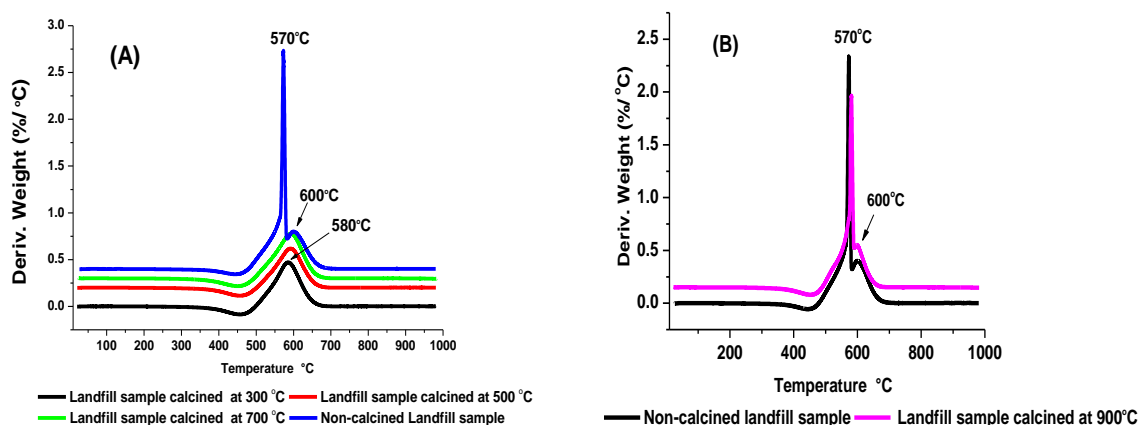


**Figure 4-13** TGA profiles for the post-reaction non-calcined and calcined Landfill samples; (A) non-calcined and Landfill samples calcined at 300, 500 and 700 °C; (B) non-calcined and Landfill samples calcined at 900 °C.

The TGA profiles for the post-reaction Factory samples are presented in Figure 4-14. It is obvious that there is an initial weight increase in the region of 400 °C, followed by weight loss within the region 500 to 660 °C. The weight increase that occurred could be ascribed to oxidation reactions for the iron phases, iron carbide and FeO, which corresponding to the XRD patterns displayed in Figure 4-11. Moreover, the initial weight increase is greater with the post-reaction Factory samples calcined at 300, 500 and 700 °C than those observed for the non-calcined and Factory sample calcined at 900 °C. It seems that there is a greater presence of more easily oxidised phases in 300, 500 and 700 °C samples than for the non-calcined and Factory sample calcined at 900 °C. Previously, the results of CHN analysis, Table 4-3, for the post-reaction Factory samples calcined at 300, 500 and 700 °C have shown that these samples have a low amount of carbon deposited, whereas the non-calcined sample and Factory calcined sample at 900 °C have the largest amounts of carbon deposited. Also, XRD results have demonstrated the presence of iron oxide phase (FeO) in the post-reaction non-calcined and calcined Factory samples at 300, 500 and 700 °C.

However, the carbon content values for all Factory samples are less than those obtained in the analysis of the CHN, as illustrated in Table 4-3.

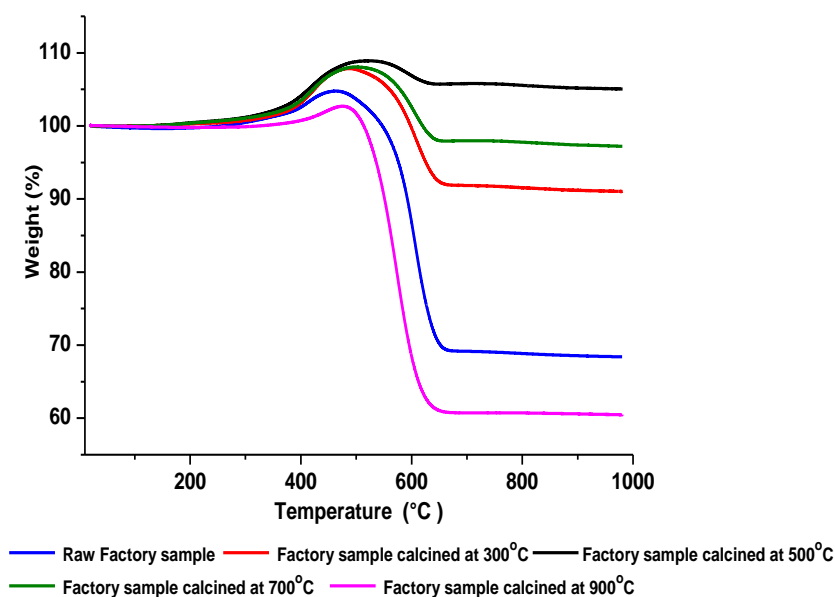


**Figure 4-14** TGA profiles for the post-reaction Factory samples.

Figure 4-15 shows the first-derivative weight change profiles for the post-reaction non-calcined and Factory samples calcined at different temperatures. It can be seen that the post-reaction non-calcined and Factory samples calcined at 300, 500 and 700 °C have two weight loss regions that is, “low” and “high” temperature combustion of carbon at *ca.* 500 and 620 °C, respectively. In addition, the weight increase is at *ca.* 430 °C is pronounced. These profiles are similar in terms of appearance, but their intensity is different due to the amount of carbon deposited on them. This is not surprising, since these samples showed similar phase composition, Figure 4-11. In the case of the post-reaction Factory sample calcined at 900 °C, the TGA profile is different. It showed to have one weight loss region at 570 °C, which was not observed with another samples. This refers to the formation of a different form of carbon species over this sample compared to other samples.

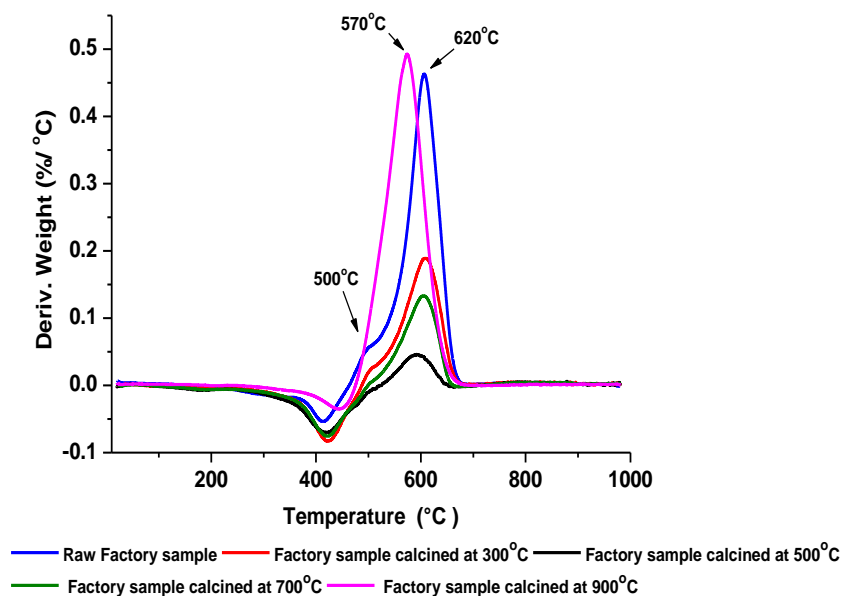


Figure 4-15 TGA profiles for the post-reaction Factory samples.

#### 4.2.3.3 BET surface area measurements

Table 4-4 shows the surface areas for the pre-reaction and post-reaction non-calcined and calcined Landfill and Factory samples. It is obvious that the post-reaction surface area of all Landfill samples, decreased significantly except for the Landfill sample calcined at 900 °C. It seems possible that the deposition of a large amount of carbon, as shown from CHN analysis in Table 4-3, on the surface areas of the sample caused a decrease in the surface area. Han *et al.* [195] studied the decomposition of methane over carbon black at different temperatures. They demonstrated that the specific surface area decreased as the amount of deposited carbon increased. However, the surface areas of the post-reaction Factory samples show a greater degree in variation. In the case of non-calcined and Factory sample calcined at 900 °C, a significant increase in the surface area is noted from 43 to 152 m<sup>2</sup>/g and from 14 to 40 m<sup>2</sup>/g, respectively. The increase in the surface area for post-reaction Factory samples calcined at 700 °C is smaller. These increases in the surface area of the post-reaction may be due to the presence of carbon species. Thus, this may be an additional reason, which reveals the high activity of these samples, especially for those non-calcined and Factory samples calcined at 900 °C. In addition, the surface areas for calcined Factory samples at 300 and 500 °C are decreased from 88 to 68 m<sup>2</sup>/g and from 80 to 33 m<sup>2</sup>/g, respectively. It was observed that the amount of carbon deposited on the post-reaction

Factory samples calcined at 300 and 500 °C were the lowest amount compared to other samples. In addition the results of the TGA showed that the nature of the carbon deposited on these samples is similar to the non-calcined and Factory samples calcined at 700 °C except for the Factory samples calcined at 900 °C. This indicates that the amount and nature of the deposited carbon may have not played a role in the decrease of surface area of Factory samples calcined at 300 and 500 °C. Hence, it can be suggested that there is a high agglomeration of sample particles during the reaction, which caused to low surface area and then low reaction rates.

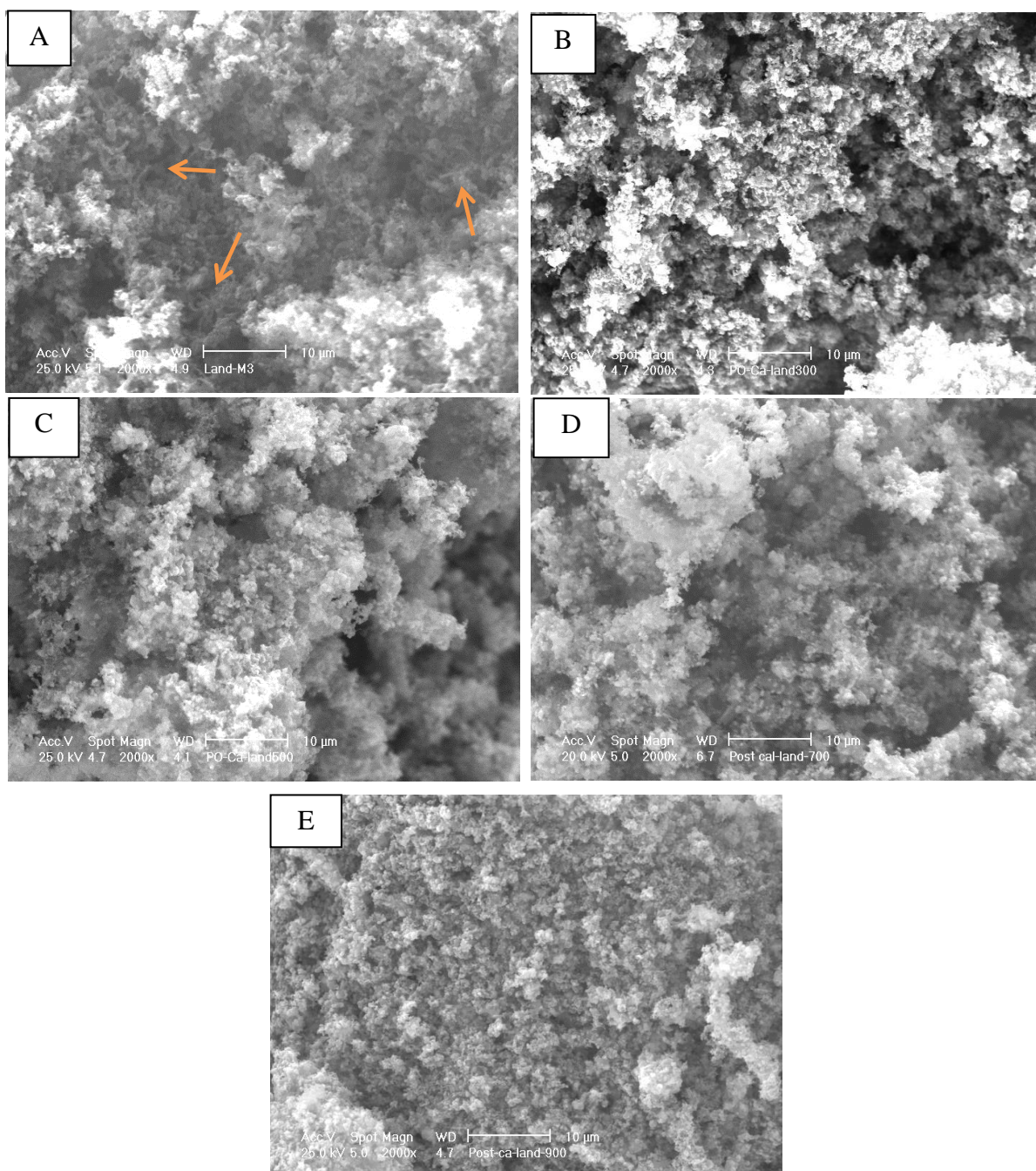
<b>Table 4-4</b> BET surface area analysis for the pre-reaction and post-reaction non-calcined and calcined Landfill and Factory samples at different temperature of 300, 500, 700 and 900 °C.				
<b>Calcination temperature</b>	<b>BET surface area, m<sup>2</sup>/g</b>			
	<b>Landfill sample</b>		<b>Factory sample</b>	
	<b>Pre-reaction</b>	<b>Post-reaction</b>	<b>Pre-reaction</b>	<b>Post-reaction</b>
<b>Non-calcined sample</b>	<b>254</b>	<b>41</b>	<b>43</b>	<b>152</b>
<b>At 300 °C</b>	<b>128</b>	<b>10</b>	<b>88</b>	<b>68</b>
<b>At 500 °C</b>	<b>126</b>	<b>15</b>	<b>80</b>	<b>33</b>
<b>At 700 °C</b>	<b>67</b>	<b>9</b>	<b>50</b>	<b>56</b>
<b>At 900 °C</b>	<b>14</b>	<b>16</b>	<b>14</b>	<b>40</b>

#### 4.2.3.4 SEM images

Figure 4-16 and 4-17 present the images for the post-reaction non-calcined and calcined Landfill and Factory samples. From the images in Figure 4-16, it is clear that the tubular morphology of the Landfill sample, which was observed in the pre-reaction non-calcined and calcined Landfill samples has been lost upon reaction. Moreover, it can be noted that carbon filaments were not formed over the calcined Landfill samples during the reaction conditions employed, while they are observed on the non-calcined Landfill sample, as marked with arrows in Figure 4-16 (A). As shown and discussed in Chapter 3, the non-calcined Landfill sample demonstrated the formation of carbon filaments. The high magnification SEM and TEM images confirmed their presence.

However, it can be seen that the morphology for the post-reaction calcined samples is similar particularly for those calcined at 500 and 700 °C. In addition, it can be noted that particle size of the samples became larger than that in non-calcined sample as a result of the agglomeration or/and sintering of the particles during the calcination process and under reaction conditions.

It is reported in the literature that the catalyst performance and the formation of carbon filaments is strongly dependent on the catalyst particle size in the decomposition of methane. Beyond a certain size range, being either too small or too big, metal particles will be inappropriate for filament growth. As a result it may be that the particle size of the calcined Landfill samples is not appropriate for carbon filamentous formation. Chen and co-workers [39] studied the influence of the crystal size of Ni on the growth of carbon nanofibres during the decomposition of methane. They revealed that small Ni crystals result in a low growth rate, whereas large Ni crystals reduce the growth rate because of their low surface area. In addition, they demonstrated that the optimum growth rate and yield of carbon nanofibres can be achieved on optimally sized Ni crystals of *ca.* 34 nm diameter. Lazaro *et al.* [196] investigated the effect of the preparation method and calcination temperature (450, 600, 800, and 1000 °C) on the activity of Ni–TiO<sub>2</sub> and Ni–Cu–TiO<sub>2</sub> catalysts in the catalytic decomposition of methane at 700 °C. They found that the increase of the calcination temperature increases the particle size and that they observed that the largest Ni particles did not promote the formation of carbon filaments.



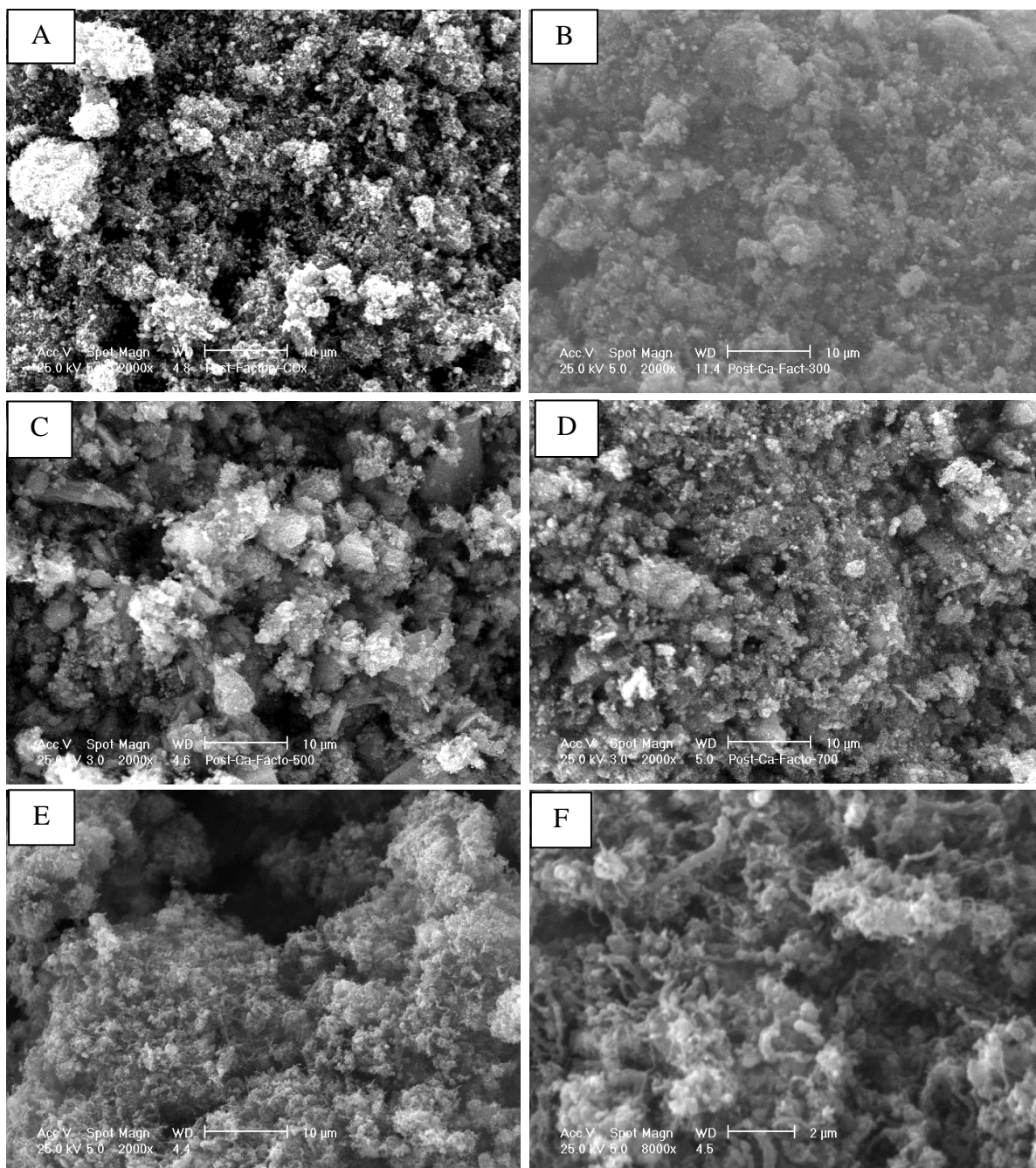
**Figure 4-16** SEM images for the post-reaction (A) non-calcined Landfill sample, (B) Landfill sample calcined at 300 °C, (C) Landfill sample calcined at 500 °C, (D) Landfill sample calcined at 700 °C and (E) Landfill sample calcined at 900 °C.

Figure 4-17 presents the images for post-reaction non-calcined and calcined Factory samples. It can be seen that there is a difference among the morphology of the samples in terms of particle agglomeration and size. The images of all samples have been taken at same magnification except for one image for the Factory sample calcined at 900 °C where high magnification is used for clarification the surface of this sample. From these images, it is noted that the carbon filaments were not formed over the non-calcined and Factory samples calcined at 300, 500 and 700 °C, while they are clearly present in Factory sample calcined at 900 °C, as shown in Figure 4-17 (E, F).

Comparison between the images displayed in Figure 4-17 (A-D), indicates an increase of agglomeration of particles. Previously, it has been noted that the calcination of raw Factory sample at different temperatures led to agglomeration of sample particles, as presented in Figure 4-5. Therefore, the employed reaction conditions seemed to result in further sintering. It should be mentioned that it is difficult to determine the exact particle size but it can be observed the changes that have taken place.

By looking at the image (C) in Figure 4-17, it appears that the post-reaction Factory sample calcined at 500 °C possess the largest particle size. This may be a reason for the fact that this sample exhibits the lowest activity of all the samples. Echegoyen *et al.* [197] studied the effect of three different methods of preparation on the methane decomposition over Ni–Mg catalysts at 700 °C. They noted that the activity of these catalysts is different. The variation in the performance of these catalysts was attributed to the particle size of spent catalysts. They claimed that the highest particle size of Ni led to the lowest hydrogen production and the smallest particle size of Ni results in the highest hydrogen yield.

However, image (E) in Figure 4-17 illustrates the morphology of post-reaction the Factory sample calcined at 900 °C. It is clear that the morphology of this sample has a “fluffy cotton” like shape, resulting from formation of filamentous carbon. The high magnification image in Figure 4-17 (F), shows filamentous carbon on the surface of the post-reaction sample. It suggests that calcination at high temperatures (900 °C) for this sample and the reaction condition produced a suitable morphology and particle size for the formation of these filaments in addition to the high activity of this sample as observed in Figure 4-9. However, further investigation is required to define the most suitable morphology and particle size.



**Figure 4-17** SEM images for the post-reaction (A) non-calcined Factory sample, (B) Factory sample calcined at 300 °C, (C) Factory sample calcined at 500 °C, (D) Factory sample calcined at 700 °C and (E,F) Factory sample calcined at 900 °C.

### **4.3. Effect of acid treatment on Landfill and Factory samples**

#### **4.3.1 Introduction**

By analogy to the treatment of clays, Landfill and Factory samples were treated with hydrochloric acid in an attempt to improve their catalytic performance. The treatment of clays with acids is one of the most common methods to activate them as catalysts that by improving their physical and chemical properties. There are many published studies that showed the activation of clay for catalytic purposes by acids, for example, Sivasankar and co-workers [198] studied the cracking of cumene over two types of clay activated with hydrochloric acid. They treated these materials with different concentrations of HCl and revealed that this treatment led to leaching out of the exchangeable cations and some amount of aluminium without seriously disrupting the clay structure. Also, they found that the surface area and the acidity increase with increase in the concentration of acid. The conversion of cumene to other hydrocarbons was found to increase linearly as a function of acidity for these samples of clay.

As outlined in Chapter 2, 50 mL of 0.5 M HCl was added to 1.5 g of as obtained Landfill and Factory samples. The resulting solution was stirred for 30 minutes at room temperature. The obtained solution was filtered and the residue was washed with distilled water several times. The samples were dried at 100 °C for overnight and calcined in air at 500 °C for 5 h. The characterisation of pre-reaction treated samples, reaction data and the characterisation of post-reaction for treated samples are presented below. A number of characterisation techniques such as XRD, ICP, TGA, CHN elemental analysis, BET surface area measurement and SEM have been applied.

#### **4.3.2 Reaction data**

Figures 4-18 and 4-19 present the hydrogen formation rates against time-on-stream in the temperature programme from 600 to 800 °C as a result of the direct cracking of methane over the raw and HCl treated samples. In Figure 4-18, it can be seen that the treatment of Landfill sample with HCl led to a significant decline in the activity. For both untreated and treated samples, it is observed that for each stage of temperature increase there was an increase in the hydrogen formation rate. At 800 °C, it is clear that the raw Landfill sample showed superior performance whereas the treated sample showed only a modest initial activity increase followed by a gradual decrease.

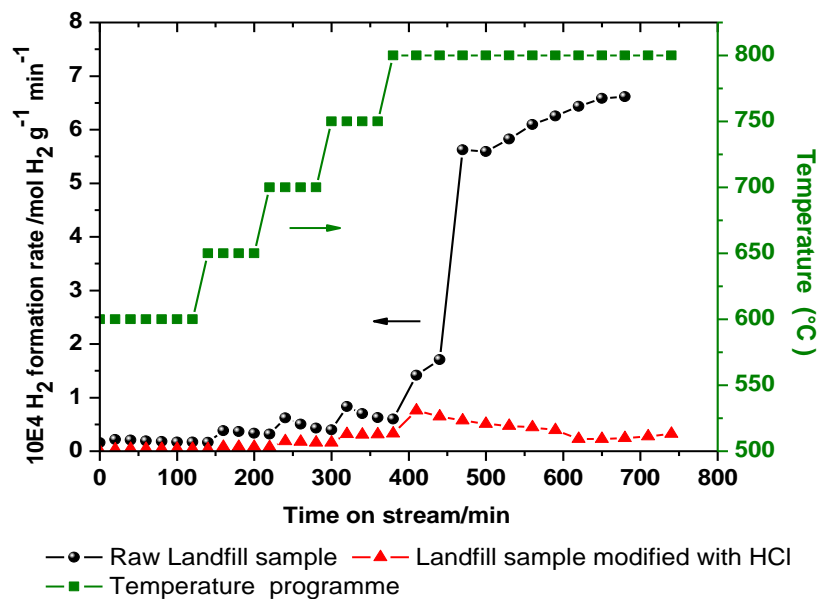


**Figure 4-18** Hydrogen formation rates at 600 to 800 °C as a function of time on stream for CH<sub>4</sub> cracking over the raw Landfill sample and Landfill sample treated with HCl. The CH<sub>4</sub>/N<sub>2</sub> flow rate was 12 mL/min and 0.4 g sample mass.

Figure 4-19 presents the formation rate data for hydrogen production against time-on-stream in the temperature programme from 600 to 800 °C as a result of the direct cracking of methane over the raw Factory sample and Factory samples treated with HCl. It can be seen from Figure 4-19 that the treatment of Factory sample with HCl decreased the activity of the raw Factory sample. It is noted for both untreated and treated samples that for each stage of temperature increase there was an increase in the hydrogen formation rate. At 800 °C, it is evident that raw Factory sample showed higher performance while the treated sample with HCl showed a more gradual increase for hydrogen production. In addition, no deactivation was observed for either sample. It may be possible that the treated sample with HCl shows high performance beyond 750 minutes and no deactivation was noted.

From comparison between the performance of the Factory sample calcined at 500 °C (no treatment with HCl) as shown in Figure 4-9, and Factory samples treated with HCl, it is evident that the performance of treated Factory samples with HCl is higher at 800 °C. This indicates that the sample composition has altered to be more active than the Factory sample calcined at 500 °C for methane cracking reaction.

The characterisation of pre-reaction and post-reaction samples may shed light upon the reasons which affected the activity of these samples.

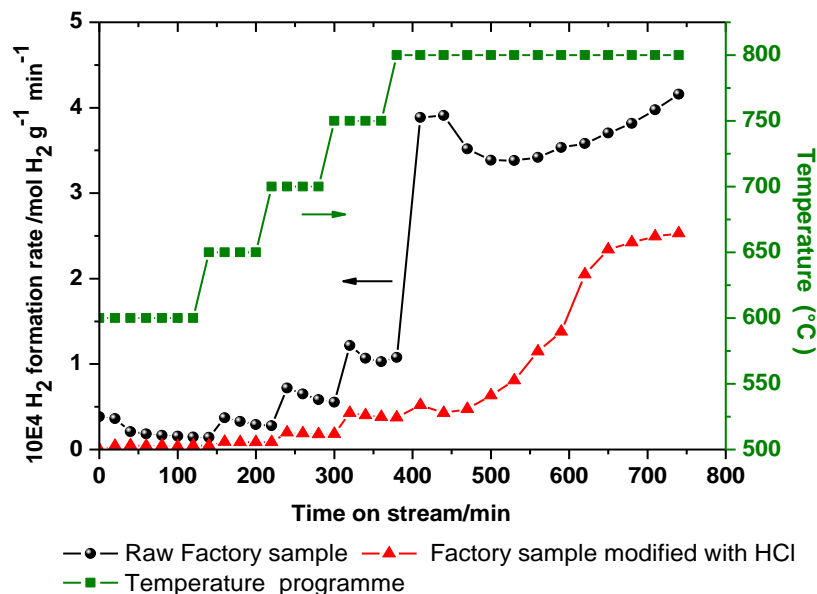


**Figure 4-19** Hydrogen formation rates at 600 to 800 °C as a function of time on stream for CH<sub>4</sub> cracking over the raw Factory sample and Factory sample treated with HCl. The CH<sub>4</sub>/N<sub>2</sub> flow rate was 12 mL/min and 0.4 g sample mass.

### 4.3.3 ICP analysis of Landfill and Factory samples treated with HCl

Table 4-5 presents the results of ICP-OES analyses for some elements of the Landfill and Factory samples to observe the changes that have occurred on the components of these samples upon HCl treatment. For the samples treated with HCl, the weight percentages of Fe, Al, Si, Ca, Na, K and Mg were measured. Also the weight percentage of these elements in the raw samples is presented for comparison. It can be seen that the amount of iron in both samples increased after treatment with acid. This indicates that some components of the samples were removed and that the acid may not have affected the iron component or may have a very limited relative impact upon it. The weight percentage of Fe increased from 36.00 to 58.00 wt% for the Landfill sample, whereas it increased from 22.70 to 32.20 wt% for the Factory sample. It is observed that the amount of aluminium in the treated samples slightly decreased compared to the raw sample counterparts. For silicon, it is clear that its amount dramatically decreased from 17.30 to 7.00 wt% for the Landfill sample, whereas it increased from 24.00 to 35.00 wt% for Factory sample. This suggests that the silicon in Landfill sample is less acid-stable than that of the Factory sample.

**Table 4-5** ICP-OES analysis for elemental content of the raw Landfill and Factory samples and Landfill and Factory samples treated with HCl.

Element	Raw Landfill sample	Landfill sample after treatment with HCl	Raw Factory sample	Factory sample after treatment with HCl
	wt (%)	wt (%)	wt (%)	wt (%)
Fe	36.00	58.00	22.70	32.20
Al	1.20	0.82	3.80	3.51
Si	17.30	7.00	24.00	35.00
Ca	2.50	0.72	1.44	1.24
Na	3.95	5.16	4.80	2.23
K	0.70	0.18	1.25	0.89
Mg	0.09	0.04	1.20	0.97

Moreover, it is noted the amount of Ca, K and Mg in the treated sample decreased compared to raw samples. The amount of Na in the treated Landfill sample increased from 3.95 to 5.16 wt%, whereas it decreased from 4.80 to 2.23 wt% in the treated Factory sample. It is possible that sodium species are different in both samples where it is non-soluble or has low solubility in HCl in Landfill sample whilst it is dissolved in the Factory sample.

However, from the ICP results in Table 4-5, it was noted that the amount of Fe and Na increased whereas the amount of Si decreased. Thus, the low activity of the treated Landfill sample could be attributed to the increase in the relative amount of Na (Na is an alkali metal, which is known to function as poison in the decomposition of methane).

Although the results of the ICP analysis for the HCl treated Factory sample apparently favourably improve the performance of the sample, it was limited. Therefore, it could be the morphology or particle size of the treated sample played a role in the low performance.

#### 4.3.4 XRD patterns

The XRD patterns of the pre- and post-reaction forms of the HCl treated Landfill and Factory samples are shown in Figures 4-20 and 4-21, respectively. From Figure 4-20, it is obvious that the treatment of Landfill sample transforms the 2-line ferrihydrite phase ( $\text{Fe}_5\text{HO}_8 \cdot 4\text{H}_2\text{O}$ ) to amorphous maghemite ( $\gamma\text{-Fe}_2\text{O}_3$ ) and clinoferrosillite ( $\text{FeSiO}_3$ ). However, the XRD pattern of the post-reaction treated Landfill sample shows that the iron

oxide phases have transformed to metallic iron (Fe). This indicates that the sample is completely reduced to metallic iron. Although metallic iron is an active phase for methane cracking the sample does not appear to possess any significant activity. Also, iron carbide, which is proposed to be an active phase for methane cracking did not form. This suggests that the sample is completely reduced to metallic iron and the narrow reflections observed indicate the iron particles sintered.

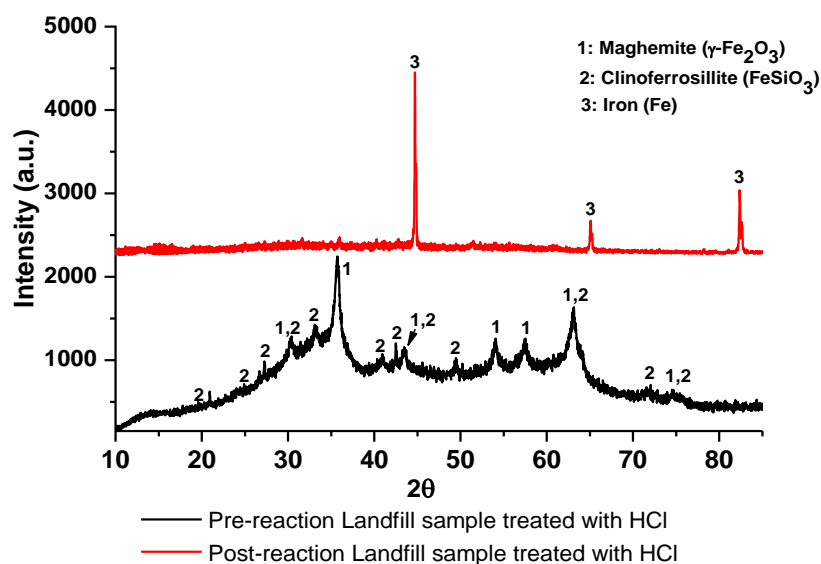


**Figure 4-20** Powder X-ray diffraction patterns for pre- and post-reaction HCl treated Landfill samples. 1: maghemite ( $\gamma\text{-Fe}_2\text{O}_3$ ), 2: Clinoferrosillite ( $\text{FeSiO}_3$ ) 017-0548 and 3: Iron (Fe) 06-0696.

The XRD patterns of the pre- and post-reaction treated Factory samples are presented in Figure 4-21. It can be observed that the XRD pattern of the pre-reaction treated Factory sample is similar to those for the Factory samples calcined at 300 and 500 °C, as shown in Figure 4-3, which match to haematite ( $\alpha\text{-Fe}_2\text{O}_3$ ) and silica ( $\text{SiO}_2$ ). This indicates that the Factory sample is not much affected by acid treatment, but it was affected by the calcination process despite the change of element ratio. However, the XRD pattern of the post-reaction treated Factory sample displays the formation of many phases including metallic iron (Fe), iron carbide ( $\text{Fe}_3\text{C}$ ), silica ( $\text{SiO}_2$ ) and graphite (C). This suggests that the treated Factory sample reduced substantially upon reaction. This behaviour was not observed in the patterns of the post-reaction raw Factory sample and the Factory samples calcined at 300, 500 and 700 °C, which demonstrated the formation of  $\text{FeO}$ ,  $\text{Fe}_3\text{C}$ ,  $\text{FeFe}_4(\text{PO}_4)_4(\text{OH})_2 \cdot 2\text{H}_2\text{O}$ ,  $\text{SiO}_2$  and graphite, as previously shown in Figure 4-11. Therefore, it can be concluded that the treatment of the Factory sample with HCl assists in

the reduction of the Factory sample during the reaction run. It is difficult to find a clear reason from the results of XRD patterns for the apparent low performance of treated Factory sample compared to the raw Factory sample as the ICP and XRD analyses would suggest that improved activity may be expected.

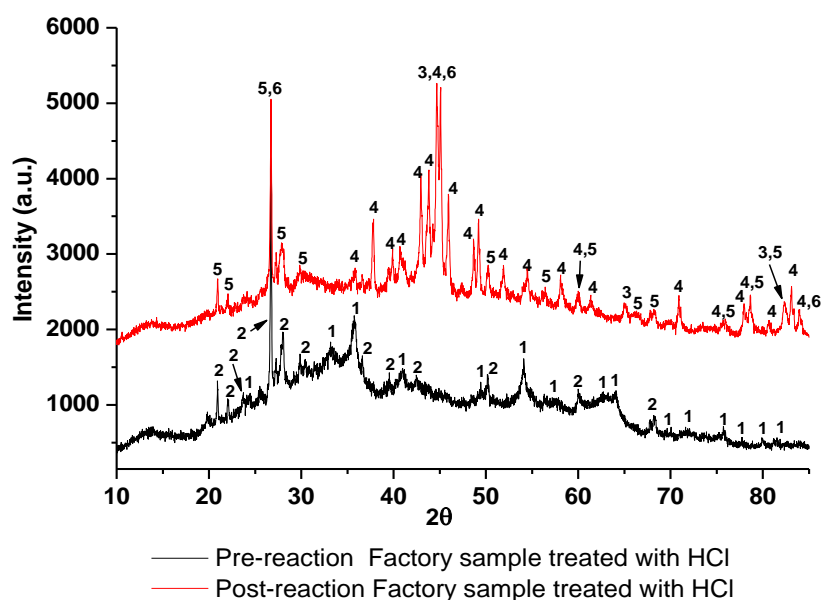


**Figure 4-21** Powder X-ray diffraction patterns for pre- and post-reaction HCl treated Factory samples. 1: Haematite ( $\alpha$ - $\text{Fe}_2\text{O}_3$ ) 24-0072, 2: Silica ( $\text{SiO}_2$ ) 42-1401, 3: Iron ( $\text{Fe}$ ) 06-0696, 4: Iron carbide ( $\text{Fe}_3\text{C}$ ) 35-0772, 5: Silica ( $\text{SiO}_2$ ) 38-0360, 6: Graphite ( $\text{C}$ ) 25-0284.

#### 4.3.5 CHN and TGA analysis

CHN analyses for the pre- and post-reaction HCl treated Landfill and Factory samples are presented in Table 4-6. The data for the corresponding non-treated samples are also presented for comparison. It can be seen that the treatment of these samples led to loss of the carbon and hydrogen from the Landfill and Factory raw samples. It is observed that the post-reaction HCl treated Landfill sample does not contain carbon is due to its low reaction performance. XRD patterns support this result where the peaks of iron carbide or/and graphite were not observed, as shown in Figure 4-20. The post-reaction treated Factory sample contains 13.53 wt% carbon but this is still lower than the post-reaction non-treated Factory sample. Again, this can be related to its low reaction performance compared to raw Factory sample. For comparison between the amount of carbon deposited on treated Factory sample and on calcined Factory sample at 500 °C (as shown in Table 4-1), it can

be noted that the amount of carbon deposited on the treated Factory sample is larger than the amount of carbon deposited on the Factory sample calcined at 500 °C being 13.53 and 8.60 wt%, respectively. This is also due to the poorer reaction performance of the calcined Factory sample calcined at 500 °C.

<b>Table 4-6</b> CHN analysis for the Non-treated Landfill and Factory samples and their post-reaction form and Pre-reaction treated Landfill and Factory sample with HCl and their post-reaction form.			
<b>Sample</b>	<b>Mean value, wt%</b>		
	<b>C</b>	<b>H</b>	<b>N</b>
<b>Non-treated Landfill sample</b>	<b>4.52 ± 0.02</b>	<b>1.29 ± 0.00</b>	-
<b>Pre-reaction HCl-treated Landfill sample</b>	-	-	-
<b>Post-reaction Non-treated Landfill sample</b>	<b>64.91 ± 0.90</b>	-	-
<b>Post-reaction HCl-treated Landfill sample</b>	-	-	-
<b>Non-treated Factory sample</b>	<b>10.70 ± 0.01</b>	<b>1.70 ± 0.05</b>	-
<b>Pre-reaction HCl-treated Factory sample</b>	-	-	-
<b>Post-reaction Non-treated Factory sample</b>	<b>41.60 ± 0.20</b>	-	-
<b>Post-reaction HCl-treated Factory sample</b>	<b>13.53 ± 0.25</b>	-	-

TGA studies in the presence of air have been performed for the post-reaction treated Landfill and Factory samples to evaluate the amount of carbon formed in both samples and to determine their reactivity profiles with respect to air. Figure 4-22 (A and B) presents the TGA profiles for the post-reaction treated Landfill and Factory samples. From Figure 4-22 (A), it can be seen that the weight of the post-reaction treated Landfill sample gradually increased in the region from 200 to 750 °C followed by no further increase up to 1000 °C. It was noted from XRD pattern of this sample that metallic iron is the main phase and it is the only phase apparent, as shown in Figure 4-20. Therefore, the increase of weight can be attributed to the oxidation of metallic iron. Furthermore, it is noted that there is no loss in weight, in good agreement with the CHN data. The TGA profile in Figure 4-22 (B) of the post-reaction treated Factory sample exhibits an initial weight increase of *ca.* 7 wt%, followed by a decrease in the weight of the sample in temperatures beyond 480 °C. The weight increase can be attributed to the oxidation of the metallic Fe and/or Fe<sub>3</sub>C phases, as

observed in the XRD pattern in Figure 4-21. In addition, the weight decrease can be ascribed to the burning off carbon deposited on the sample, which is about 8 wt%.

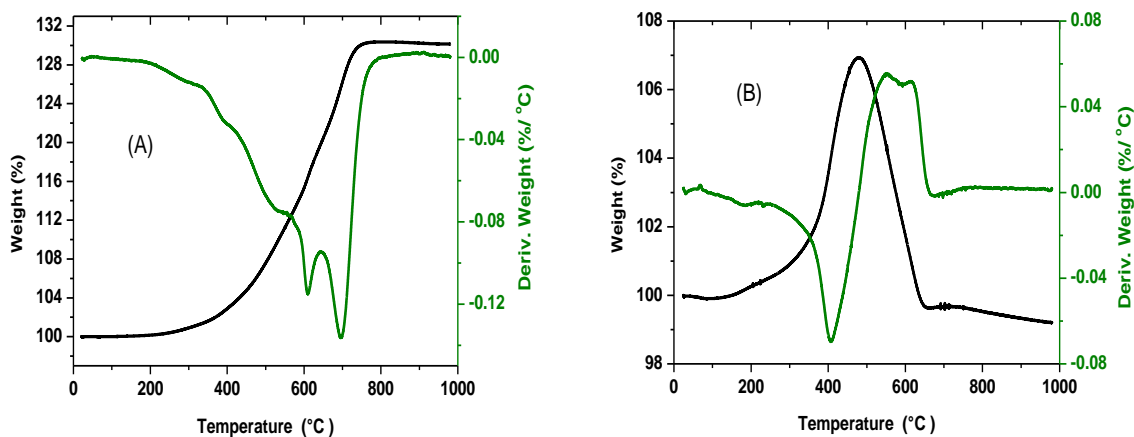


**Figure 4-22** TGA profiles for the post-reaction HCl treated Landfill sample (A) and Factory samples (B).

#### 4.3.6 BET surface area measurements

Table 4-7 presents the surface areas of the pre-and post-reaction HCl treated Landfill and Factory samples. Their non-treated counterparts are included for ease of comparison. From the data, it can be seen that the surface area of the Landfill sample reduced from 254 to 140  $\text{m}^2/\text{g}$  as a result of the treatment process, while the surface area of the Factory sample increased from 43 to 81  $\text{m}^2/\text{g}$ . However, it can be noted that the surface areas of post-reaction raw and treated Landfill samples dropped to 41 and 14  $\text{m}^2/\text{g}$ , respectively. The decrease in the surface area of the post-reaction raw Landfill sample was attributed to the large amount of carbon deposited. The post-reaction treated Landfill sample did not show the presence of any deposited carbon although a decrease in the surface area of the post-reaction treated Landfill sample was observed. Based on this result, this may be the major reason of decline in the performance of this sample.

However, it can be observed that the surface area of the post-reaction raw Factory sample increased from 43 to 152  $\text{m}^2/\text{g}$ , whilst the surface area of the post-reaction treated Factory sample decreased from 81 to 43  $\text{m}^2/\text{g}$ . The increase in the surface area of post-reaction non-treated Factory samples was attributed to mass normalisation effects and the density of the carbon deposited, while the decrease in the surface area of the post-reaction treated Factory sample could be ascribed to sintering.

<b>Table 4-7</b> BET surface area analysis for the pre- and post-reaction raw and treated Landfill and Factory samples.				
<b>BET surface area, m<sup>2</sup>/g</b>				
<b>Sample</b>	<b>Raw Landfill sample</b>	<b>Landfill sample treated with HCl</b>	<b>Raw Factory sample</b>	<b>Factory sample treated with HCl</b>
<b>Pre-reaction</b>	254	140	43	81
<b>Post-reaction</b>	41	4	152	43

### 4.3.7 SEM images

Figure 4-23 presents the SEM images of the pre- and post-reaction treated Landfill and Factory samples in addition to the SEM images of raw Landfill and Factory samples. The images (A and B) in Figure 4-23 show the morphology of the raw Landfill sample and the pre-reaction treated Landfill sample, respectively. It can be observed that the treatment process of Landfill sample results to reduce the occurrence of the tubular morphology phase and increases sample agglomeration, which may reduce the surface area of the treated Landfill, as shown in Table 4-7. The image (E) shows the morphology of the post-reaction treated Landfill sample. From this image, it can be seen that the tubular morphology completely disappeared and the agglomeration of the sample particles increased to generate much larger particles.

The images (C and D) in Figure 4-23 present the morphology of raw and pre-reaction treated Factory samples, respectively. From these images, it can be observed that the treatment of Factory sample produced a slightly smaller particle size compared to the raw Factory sample, despite the morphology of both samples being generally similar. The formation of small particle size for the treated Factory sample may be the reason for the increase in the surface area of the sample, as shown in Table 4-7. The image (F) illustrates the morphology of the post-reaction treated Factory sample. This image shows that no filamentous carbon is formed and the particles size appears to be smaller and agglomerated compared to the pre-reaction treated Factory sample.

It should be mentioned that all characterisation, which has been made for the pre-reaction and post-reaction treated Factory sample, shows that the chemical and physical properties of this sample have been modified, but its performance remains lower than that of raw sample. This cannot at present be explained.

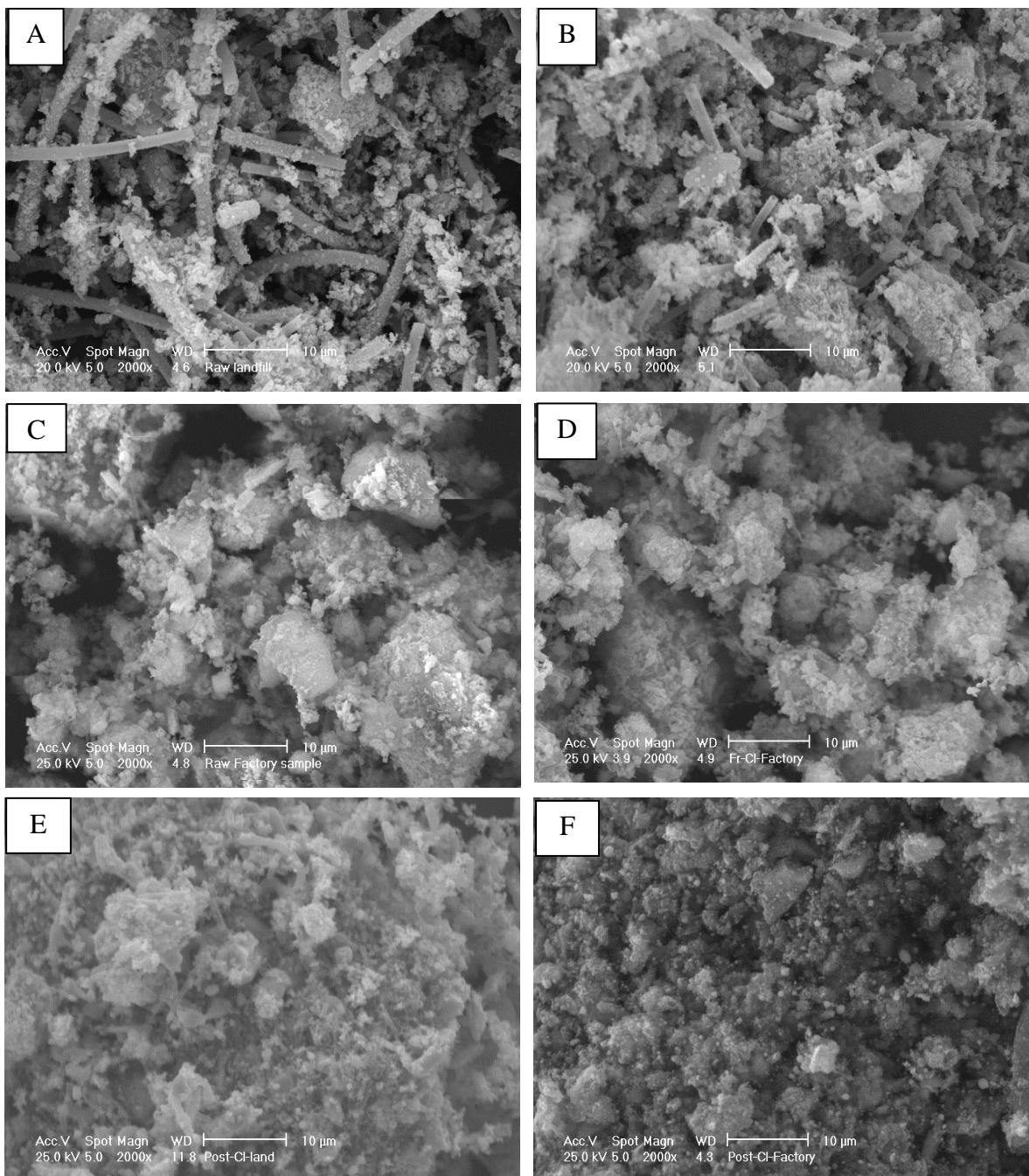


**Figure 4-23** SEM images of (A) raw Landfill sample, (B) pre-reaction treated Landfill sample, (C) raw Factory sample (D) pre-reaction treated Factory sample, (E) post-reaction treated Landfill sample, (F) post-reaction treated Factory sample.

## 4.4. Effect of palladium dopant on the Landfill and Factory samples

### 4.4.1 Introduction

The major metal in the Landfill and Factory samples is iron and as mentioned in the introduction of this chapter, palladium based catalysts have high activity for the methane cracking reaction. In addition, palladium has been used as promoter for Fe based catalysts. Ogihara and co-workers [63] studied the methane decomposition for hydrogen production over Pd-based alloy catalysts supported on alumina. They found that the hydrogen yield increased 5x following Pd addition at 700 °C respectively. Shah *et al.* [46] also investigated the effect of Pd addition to Fe/Al<sub>2</sub>O<sub>3</sub> catalyst for methane decomposition and hydrogen production as a function of increasing temperature. They found that Pd-Fe/Al<sub>2</sub>O<sub>3</sub> catalyst showed a higher activity than Fe/Al<sub>2</sub>O<sub>3</sub> catalyst. Therefore, palladium has been used as promoter for the Landfill and Factory samples in an attempt to enhance their catalytic activity.

As outlined in Chapter 2, 0.4 wt% Pd/Landfill and 0.4 wt% Pd/Factory samples were prepared by incipient wetness impregnation of Landfill and Factory samples. An aqueous solution of palladium nitrate (Pd (NO<sub>3</sub>)<sub>2</sub>.xH<sub>2</sub>O) containing the required amount of Pd was added to Landfill and Factory samples. The impregnated sample was dried at 100 °C for 24 h and calcined in air at 500 °C for 16 h. The 0.4 wt% Pd/Landfill and 0.4 wt% Pd/Factory samples were subjected to the same reaction conditions applied to the raw and modified Landfill and Factory samples. The characterisation of pre-reaction and post-reaction 0.4 wt% Pd/Landfill and 0.4 wt% Pd/Factory samples has been undertaken.

### 4.4.2 Reaction data

The hydrogen, carbon monoxide and carbon dioxide formation rates against time-on-stream in the temperature range from 600 to 800 °C for the 0.4 wt% Pd/Landfill and 0.4 wt% Pd/Factory samples are shown in Figures 4-24 to 4-28. The data for the raw Landfill and Factory samples is also shown for comparison. From Figure 4-24, it is evident that the 0.4 wt% Pd/Landfill sample demonstrated a low level of the hydrogen formation rate in the temperature range from 600 to 750 °C and even in the initial stage of temperature at 800 °C, being lower than that in raw Landfill sample. In addition, it is observed that the hydrogen formation rate with 0.4 wt% Pd/Landfill sample increased at each stage of

temperature increase and remained steady. This is different from the raw sample for which an increase with the temperature increase was followed by a gradual decrease observed after each temperature increment. When the temperature was increased to 800 °C, the hydrogen formation rate with raw Landfill sample gradually increased along with the temperature increase to achieve a maximum of  $6.61 \times 10^{-4}$  mol H<sub>2</sub> g<sup>-1</sup> min<sup>-1</sup>, while the hydrogen formation rate with 0.4 wt% Pd/Landfill sample increased slightly and remained steady around 150 minutes followed by a sharp increase to achieve roughly  $7.5 \times 10^{-4}$  mol H<sub>2</sub> g<sup>-1</sup> min<sup>-1</sup>, which is higher than that in the raw sample. It should be noted that the activation time of 0.4 wt% Pd/Landfill sample at 800 °C is longer than for the raw sample. Also, deactivation was not observed and both reactions were stopped due to the reactor blockage as a result of carbon deposition and an increased pressure drop through the fixed bed.

It can be suggested that the low performance of 0.4 wt% Pd/Landfill sample at temperatures below 800 °C and the delay of the high performance of the sample at 800 °C is attributed to the delay of the reduction process to form active sites for the cracking reaction.

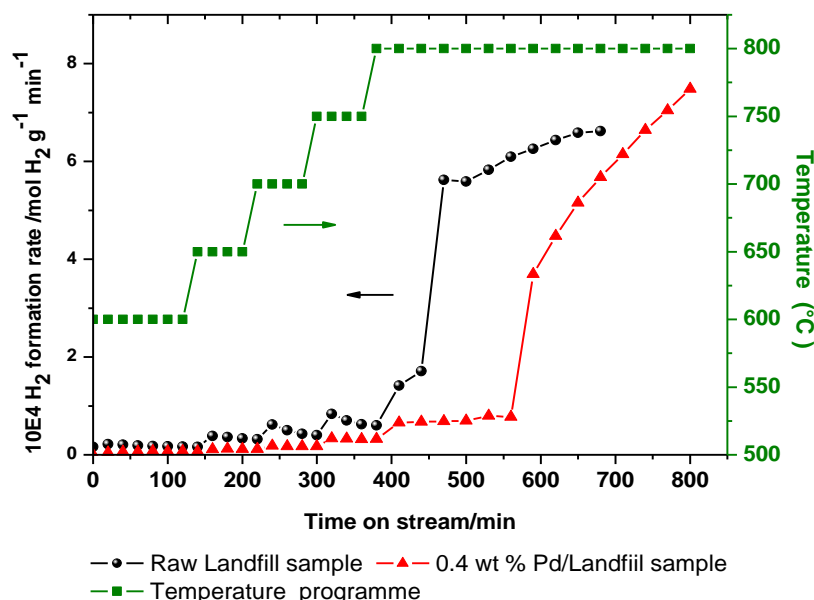


**Figure 4-24** Hydrogen formation rates at 600 to 800 °C as a function of time on stream for CH<sub>4</sub> cracking over the raw Landfill sample and 0.4 wt% Pd/Landfill. The CH<sub>4</sub>/N<sub>2</sub> flow rate was 12 mL/min and 0.4 g sample mass.

Figures 4-25 and 4-26 illustrate the carbon monoxide and carbon dioxide formation rates for the raw and Pd doped Landfill samples in the temperature range from 600 to 800 °C, respectively. As mentioned in Chapter 3, production of carbon monoxide and carbon

dioxide are associated with hydrogen production, which is a result of reduction of the metal oxides, particularly iron. It can be seen from Figure 4-25 that the formation rate of CO for the raw Landfill sample is higher than the formation rate of CO for the 0.4 wt% Pd/Landfill sample. Also, the CO formation rates for both samples increased for each temperature increment. However, the stability at each isothermal step varied between raw and Pd-promoted samples where the raw sample showed evidence of decrease during each step and the Pd-promoted sample only clearly decreased at 800 °C. The maximum and the sharp drop of CO formation rate was observed at 800 °C and *ca.* 450 minutes of time on stream for the raw Landfill sample, while it occurs at *ca.* 600 minutes time on stream for the 0.4 wt% Pd/Landfill sample.

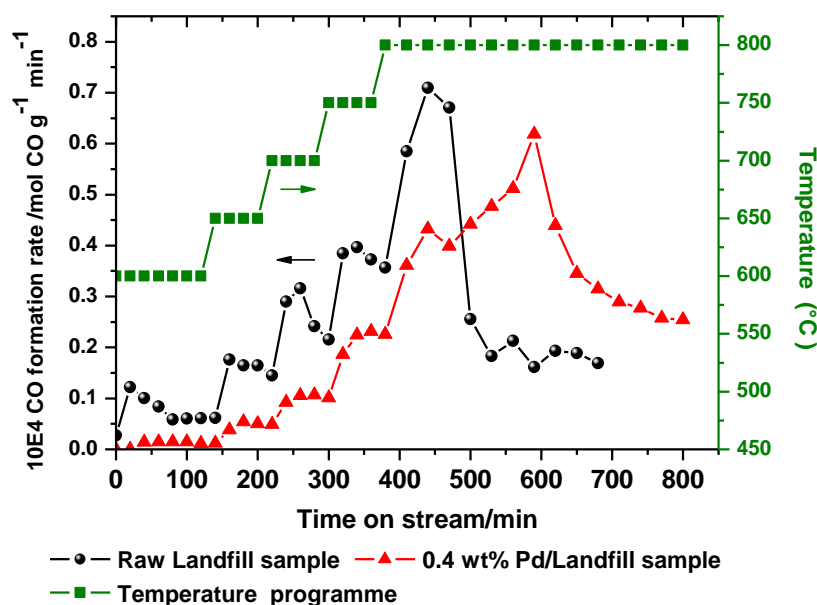


**Figure 4-25** CO formation rates at 600 to 800 °C as a function of time on stream for CH<sub>4</sub> cracking over the raw Landfill and 0.4 wt% Pd/Landfill samples. The CH<sub>4</sub>/N<sub>2</sub> flow rate was 12 mL/min and 0.4 g sample mass.

However, the raw Landfill sample demonstrated a high initial CO<sub>2</sub> formation rate at 600 °C compared to 0.4 wt% Pd/Landfill sample and at 650 °C, as shown Figure 4-26. Similar values of CO<sub>2</sub> formation rate at 700 and 750 °C occurred for both samples. Again the CO<sub>2</sub> formation rates for both samples were increased at each temperature increment followed by a gradual decrease. Moreover, a sharp drop of the CO<sub>2</sub> formation rate was observed at 800 °C and *ca.* 450 minutes of time on stream for the raw Landfill sample, while it is noted at *ca.* 570 minutes of time on stream for the 0.4 wt% Pd/Landfill sample.

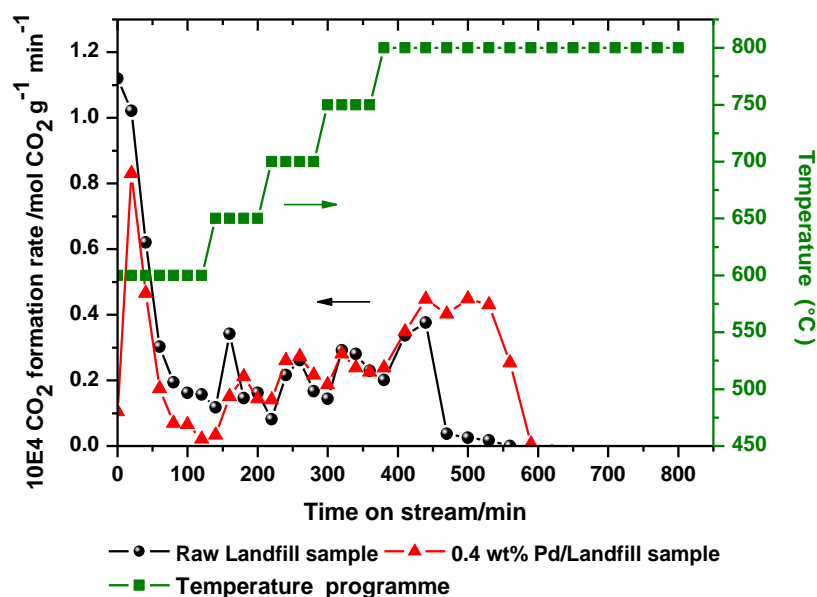


**Figure 4-26** CO<sub>2</sub> formation rates at 600 to 800 °C as a function of time on stream for CH<sub>4</sub> cracking over the raw Landfill and 0.4 wt% Pd/Landfill samples. The CH<sub>4</sub>/N<sub>2</sub> flow rate was 12 mL/min and 0.4 g sample mass.

Since the CO formation rate over Pd/Landfill sample is lower than that the raw Landfill sample and the formation rate of CO and CO<sub>2</sub> dropped at a later time on stream, it seems that the Pd/Landfill sample is reduced more slowly, which may be resulted in the delay of the high performance of this sample at 800 °C. In addition, for both samples, when the CO and CO<sub>2</sub> formation rates increased to their maximum values and then sharply dropped, the hydrogen formation rates increased.

Figure 4-27 shows the hydrogen formation rate *versus* time on stream in the temperature range from 600 to 800 °C for the raw and Pd doped Factory samples. From Figure 4-27, it is evident that the performance of 0.4 wt% Pd/Factory was very low compared to the raw Factory sample. In addition, it is lower than those calcined Factory sample at 500 °C and Factory samples treated with HCl, as illustrated in Figures 4-9 and 4-19.

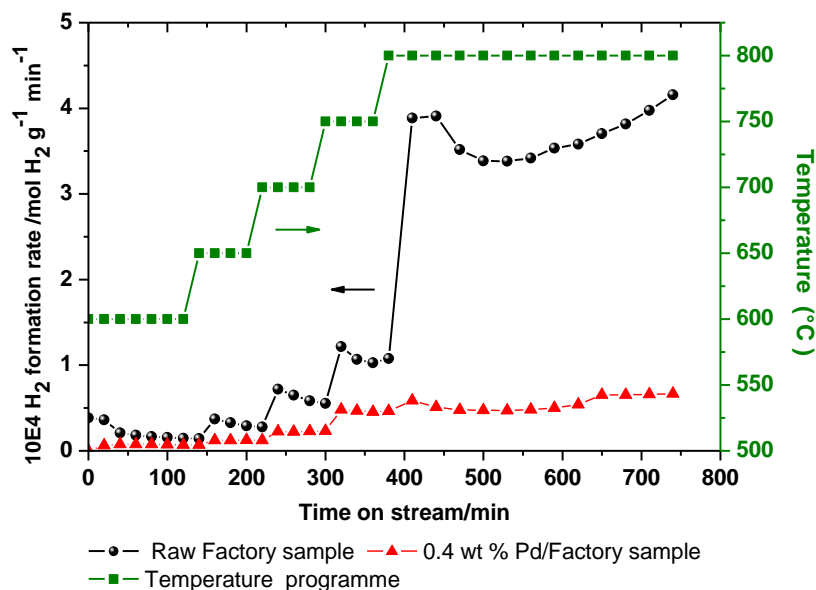


**Figure 4-27** Hydrogen formation rates at 600 to 800 °C as a function of time on stream for CH<sub>4</sub> cracking over the raw Factory sample and 0.4 wt% Pd/Factory sample. The CH<sub>4</sub>/N<sub>2</sub> flow rate was 12 mL/min and 0.4 g sample mass.

It is surprising that the addition of palladium into Factory sample acted as a poison, especially since palladium is such an active metal for methane cracking. However the addition of palladium sample enhanced the Landfill performance at 800 °C. Moreover, a few studies have revealed that the addition of palladium to iron based catalysts or *vice versa*, enhance their activity. During the procedure of modification of the Factory sample with Pd, it may be an undesirable component may have formed or some other effect occurred, which is not clear, particularly as this sample is a waste material for which there is incomplete understanding of all its components.

Figures 4-28 and 4-29 present the carbon monoxide and carbon dioxide formation rates for the raw Factory and Pd doped Factory samples in the temperature range from 600 to 800 °C, respectively. It can be observed from Figure 4-28 that the formation rate of CO for the Pd/Factory sample is higher than for the raw Factory sample especially in the temperature range from 650 to 800 °C. Also, it is noted that the CO formation rates for both samples are quite similar at temperature 600 °C, followed by increased differences at each stage of the temperature increase.

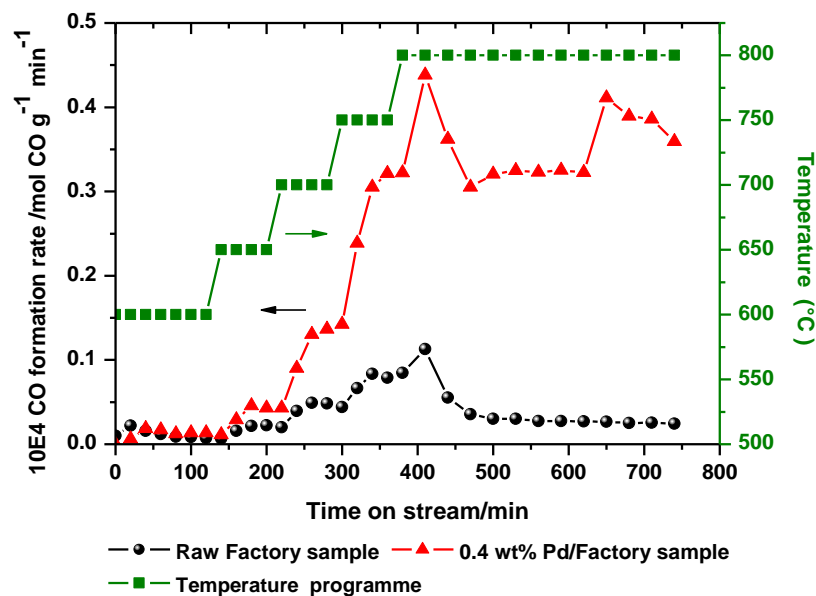


**Figure 4-28** CO formation rates at 600 to 800 °C as a function of time on stream for CH<sub>4</sub> cracking over the raw Factory and 0.4 wt% Pd/Factory samples. The CH<sub>4</sub>/N<sub>2</sub> flow rate was 12 mL/min and 0.4 g sample mass.

Figure 4-29 illustrates the CO<sub>2</sub> formation rates for the raw and Pd doped Factory samples in the temperature programme range from 600 to 800 °C. It can be observed that both samples showed an initial high CO<sub>2</sub> formation rate at 600 °C, followed by a sharp decline. The CO<sub>2</sub> formation rates for two samples were quite similar in the temperature range from 600 to 750 °C. Also, their behaviour was quite similar where they were increased in each stage of the temperature increase and followed by a gradual decrease. Moreover, it was noted that the CO<sub>2</sub> formation rate for the raw Factory sample sharply dropped after 60 minutes of time on stream at 750 °C, while it was sharply declined after 30 minutes of time on stream at 800 °C for the Pd doped Factory sample.

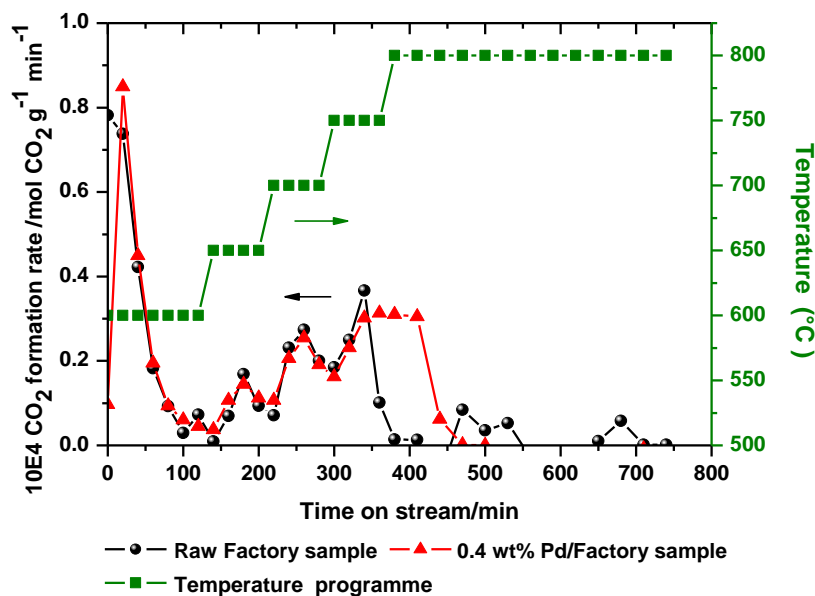


**Figure 4-29** CO<sub>2</sub> formation rates at 600 to 800 °C as a function of time on stream for CH<sub>4</sub> cracking over the raw Factory and 0.4 wt% Pd/ Factory samples. The CH<sub>4</sub>/N<sub>2</sub> flow rate was 12 mL/min and 0.4 g sample mass.

Again, the production of CO and CO<sub>2</sub> are a result of reduction procedures of the sample. Therefore, it would seem from the data in Figure 4-28 and 4-29 that the 0.4 wt% Pd/Factory sample is more reducible than raw Factory sample. This finding is unexpected; especially the 0.4 wt% Pd/Factory sample did not show high activity. The characterisation of pre-reaction and post-reaction for these modified samples could lead to elucidation of the reasons.

#### 4.4.3 XRD patterns

Figures 4-30 and 4-31 present the XRD patterns of the pre- and post-reaction 0.4 wt% Pd/Landfill, respectively. From Figure 4-30 (A), it is evident that the addition of Pd to the Landfill sample results in transformation the 2-line ferrihydrite phase (Fe<sub>5</sub>HO<sub>8</sub>.4H<sub>2</sub>O) to maghemite (γ-Fe<sub>2</sub>O<sub>3</sub>) a significant amorphous component. The palladium added into the Landfill sample was not detected suggesting that the Pd containing component remains in a highly dispersed form. This XRD pattern of the pre-reaction 0.4 wt% Pd/Landfill sample is similar to those XRD patterns of Landfill samples calcined at 300 and 500 °C as well as the Landfill sample treated with HCl. This suggests that calcination at 500 °C in these samples played an important role in the similarity of these phases.

However, the XRD pattern for the post-reaction 0.4 wt% Pd/Landfill sample shows the formation of iron (Fe), iron carbide ( $\text{Fe}_3\text{C}$ ) and graphite phases, as marked on the pattern. This indicates that the sample is reduced during reaction. This result is in a good agreement with the phases that formed during cracking of methane over the raw and calcined Landfill samples. As mentioned in Chapter 3, the metallic Fe and  $\text{Fe}_3\text{C}$  species have a catalytic effect in methane cracking and when these phases are formed in Landfill sample, the high activity appears. Although these phases were noted in the post-reaction 0.4 wt% Pd/Landfill sample, the raw Landfill sample and Landfill sample calcined at 500 °C, the 0.4 wt% Pd/Landfill sample showed the highest maximum  $\text{H}_2$  formation rate amongst them. Hence, it is suggested that the palladium addition to Landfill sample increased the activity of Landfill sample, although an extended time on stream was necessary.

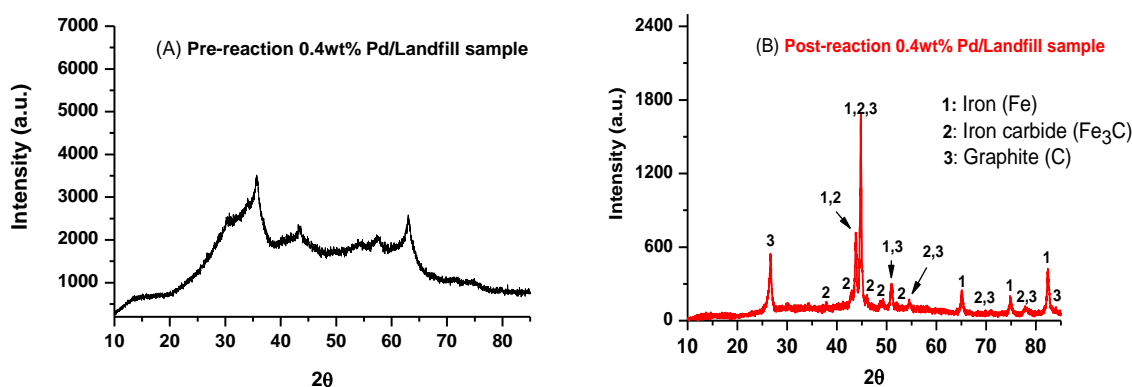


**Figure 4-30** Powder X-ray diffraction patterns for the pre-reaction (A) and the post-reaction (B) 0.4 wt% Pd/Landfill sample.

Figure 4-31 presents the XRD patterns of the pre- and post-reaction 0.4 wt% Pd/Factory samples. From Figure 4-31 (A), it can be noted that the XRD pattern of the pre-reaction 0.4 wt% Pd/Factory sample is similar to those for the pre-reaction Factory sample calcined at 500 °C and Factory sample treated with HCl, as shown in Figure 4-3 and 4-21, which can be matched with the haematite ( $\alpha\text{-Fe}_2\text{O}_3$ ) and silica ( $\text{SiO}_2$ ). Furthermore, the palladium component was not detected. This indicates that the Factory sample is not much affected by the palladium addition.

The XRD pattern of the post-reaction for 0.4 wt% Pd/Factory sample is shown in Figure 4-31 (B). It can be observed that the positions of reflections correspond to metallic Fe and  $\text{SiO}_2$  phases, as marked on the pattern. This reveals that the haematite ( $\alpha\text{-Fe}_2\text{O}_3$ ) phase in the pre-reaction 0.4 wt% Pd/Factory sample has been reduced and transformed to metallic iron (Fe) and the silica ( $\text{SiO}_2$ ) phase still remaining. This finding could lead to

understanding the cause of the low performance of the 0.4 wt% Pd/Factory sample. Since the iron carbide phase is absent and the metallic iron is formed, this indicates that the sample was completely reduced and the severe sintering may have occurred. In addition, iron carbide is active phase for methane cracking and its absence in the sample could lead to lose a part of its activity.

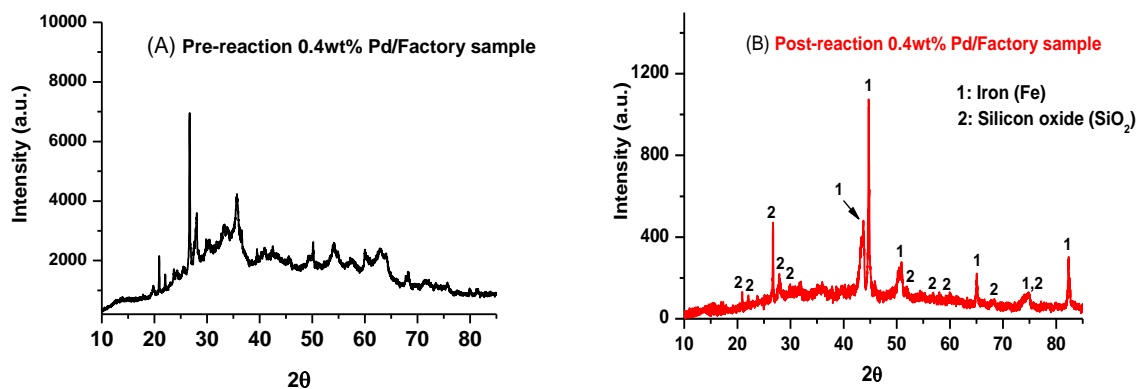


**Figure 4-31** Powder X-ray diffraction patterns for pre-reaction (A) and post-reaction (B) 0.4 wt% Pd/Factory sample.

It is somewhat surprising that the modified Factory sample in three cases (calcined at 500 °C, treated with HCl and Pd doped) have a quite similar resemblance in their pre-reaction phases, but their post-reaction phases are different. For example, the XRD pattern of the post-reaction Factory sample calcined at 500 °C shows that the sample was not completely reduced and iron oxide (FeO) was still present, in addition to the presence of iron carbide (Fe<sub>3</sub>C) and silica (SiO<sub>2</sub>), whereas the post-reaction HCl treated Factory sample showed that the sample was completely reduced and metallic iron, iron carbide (Fe<sub>3</sub>C) and silica (SiO<sub>2</sub>) were formed. In case of the 0.4 wt% Pd/Factory sample, only metallic iron (Fe) and silicon oxide (SiO<sub>2</sub>) were apparent.

#### 4.4.4 CHN and TGA analysis

Table 4-8 presents the CHN analyses for the pre- and post-reaction 0.4 wt% Pd/Landfill and 0.4 wt% Pd/Factory samples. The data for the pre- and post-reaction raw Landfill and Factory samples is also presented for comparison. It can be observed that the modification procedures of Landfill sample with Pd results in a reduction of the amount of carbon and hydrogen from 4.52 to 0.28 wt% and from 1.29 to 0.26 wt%, respectively. However, it is noted that the modification of the Factory sample with Pd led to the loss of all the carbon and hydrogen content.

CHN data for the the post-reaction 0.4 wt% Pd/Landfill sample shows that the amount of carbon deposited is 61.53 wt%. This value is marginally lower than amount of carbon deposited on the post-reaction raw Landfill sample, which is 64.91 wt%. Despite the reaction rate of 0.4 wt% Pd/Landfill sample being higher than that raw Landfill sample at 800 °C, the amount of carbon deposited is lower. The high amount of carbon deposited on the post-reaction raw Landfill sample can be attributed to its high reaction rate during the temperature programme from 600 to 750 °C and even in the first stage of reaction at 800 °C, as shown Figure 4-24. The post-reaction CHN analysis of the 0.4 wt% Pd/Factory sample shows a very low amount of carbon deposited, which is 1.48 wt%. This is expected as the overall reaction rate was very low for this sample.

<b>Table 4-8</b> CHN analysis for the pre- and post-reaction 0.4 wt% Pd/Landfill and 0.4 wt% Pd/Factory samples and the pre- and post-reaction raw Landfill and Factory samples.			
Sample	Mean value, wt%		
	C	H	N
Raw Landfill sample	4.52 ± 0.02	1.29 ± 0.00	-
Pre-reaction 0.4 wt% Pd/Landfill sample	0.28 ± 0.08	0.26 ± 0.03	-
Post-reaction raw Landfill sample	64.91 ± 0.90	-	-
Post-reaction 0.4 wt% Pd/Landfill sample	61.53 ± 0.30	-	-
Raw Factory sample	10.70 ± 0.01	1.70 ± 0.05	-
Pre-reaction 0.4 wt% Pd/Factory sample	-	-	-
Post-reaction raw Factory sample	41.60 ± 0.20	-	-
Post-reaction 0.4 wt% Pd/Factory sample	1.48 ± 0.08	-	-

TGA studies in air have been carried out for the post-reaction 0.4 wt% Pd/Landfill and 0.4 wt% Pd/Factory samples to estimate the amount of carbon deposited upon them and to determine their reactivity profiles with respect to air. Figure 4-32 (A, B) depict the TGA oxidation profiles for the post-reaction 0.4 wt% Pd/Landfill and 0.4 wt% Pd/Factory samples. Figure 4-32 (A) illustrates the TGA profile for the post-reaction 0.4 wt%

Pd/Landfill sample. It is obvious that there is an initial weight increase between 400 and 500 °C, followed by a decrease up to 700 °C as for other samples, the weight increase that occurred could be ascribed to oxidation reactions for the metallic iron and iron carbide phases, which have been observed in the XRD pattern reproduced in Figure 4-30. In addition, the weight loss can be attributed to the oxidation of carbon. The value of the estimated carbon from the TGA result is almost 52 wt%. This value is lower than that in the CHN analysis. This difference may relate to the reasons described earlier. Figure 4-32 (B) illustrates the TGA profile for the post-reaction 0.4 wt% Pd/Factory sample. It can be observed that the sample weight increases sharply in the region from 200 to 700 °C followed by a gradual weight decrease up to 1000 °C. It was observed in the XRD pattern of this sample that metallic iron and silica are the main phases, as shown in Figure 4-31. Therefore, the weight increase can be ascribed to the oxidation of metallic iron in air. Additionally, it is observed that there is slightly weight decrease in the region beyond 700 °C, which may be due to the burning of small amount of carbon that have been observed in the result of CHN analyses.

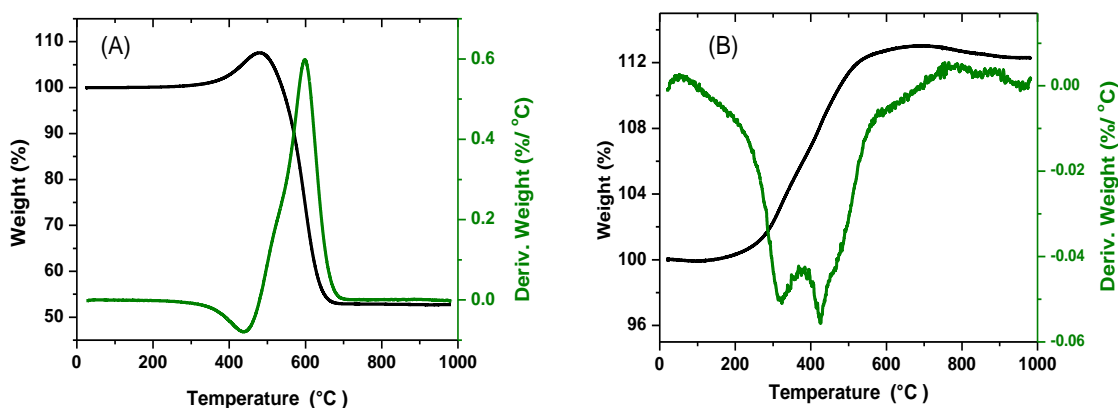


**Figure 4-32** TGA profiles for the post-reaction 0.4 wt% Pd/Landfill (A) and 0.4 wt% Pd/Factory samples (B).

#### 4.4.5 BET surface area measurements.

Table 4-9 shows the surface areas for the pre- and post-reaction 0.4 wt% Pd/Landfill and 0.4 wt% Pd/Factory samples. The data for the pre- and post-reaction raw Landfill and Factory samples is also shown for comparison. It can be noted that the Pd addition to Landfill sample decreases the surface area of the raw Landfill sample from 257 to 99 m<sup>2</sup>/g.

It can be assumed that the decrease in the surface area is due to the calcination process during modification the Landfill sample with Pd. In the previous section; it was observed that the surface area of the Landfill sample decreased with the calcination temperature increase; this was attributed to the sintering process and concomitant increase in particle size. It can be suggested that the low activity for the 0.4 wt% Pd/Landfill sample in the temperature range from 600 to 750 °C and even at an early stage at 800 °C is due to the decrease in the surface area, which played a role in the delay the reduction process. However, The BET surface areas for the post-reaction raw Landfill and 0.4 wt% Pd/Landfill samples dropped to 41 and 19 m<sup>2</sup>/g, respectively. It seems possible that the decrease in the surface area of these samples is due to the large amount of carbon deposited on them.

The BET surface area of the Factory sample was enhanced after modification with Pd and increased from 43 to 75 m<sup>2</sup>/g. Although the surface area of the 0.4 wt% Pd/Factory sample is higher than the raw Factory sample it showed very low performance and a low hydrogen production rate. However, The BET surface area for the post-reaction raw Factory sample significantly increased from 43 to 152 m<sup>2</sup>/g. As shown and discussed in Chapter 3, this increase was attributed to mass normalisation effects and the density of carbon deposited. In addition, it is observed that the surface area for the post-reaction 0.4 wt% Pd/Factory sample decreased from 75 to 5 m<sup>2</sup>/g, although it did not show a large amount of carbon deposited. In fact the amount of carbon deposited on it was very low, around 1.48 wt%. A possible explanation for this might be that the sintering has occurred, which may have played an important role in the low activity of the 0.4 wt% Pd/Factory sample.

<b>Table 4-9</b> BET surface area analysis of raw Landfill and Factory samples and those doped with Pd.				
<b>BET surface area, m<sup>2</sup>/g</b>				
<b>Sample</b>	<b>Raw Landfill sample</b>	<b>0.4 wt% Pd/Landfill sample</b>	<b>Raw Factory sample</b>	<b>0.4 wt% Pd/Factory sample</b>
<b>Pre-reaction</b>	254	99	43	75
<b>Post-reaction</b>	41	19	152	5

#### 4.4.6 SEM images

Figures 4-33 and 4-34 present the SEM images for the pre- and post-reaction 0.4 wt% Pd/Landfill and 0.4 wt% Pd/Factory samples, in addition to the SEM images of raw Landfill and Factory samples which are presented for comparison. The images (A and B) in Figure 4-33 show the morphology of raw Landfill sample and the pre-reaction 0.4 wt% Pd/Landfill sample, respectively. It can be noted from the image of pre-reaction 0.4 wt% Pd/Landfill sample that the tubular morphology is retained and the morphology of tubular and non-tubular component may have become more agglomerated, which may result in a reduction of the surface area of the 0.4 wt% Pd/Landfill sample, as shown in Table 4-9. From the image (C) in Figure 4-33, it can be seen that the tubular morphology completely disappeared and no filamentous carbon is observed in the sample. In addition, it is noted that there are some bright spots, which may be due to the aggregation of metallic iron or metallic Pd.

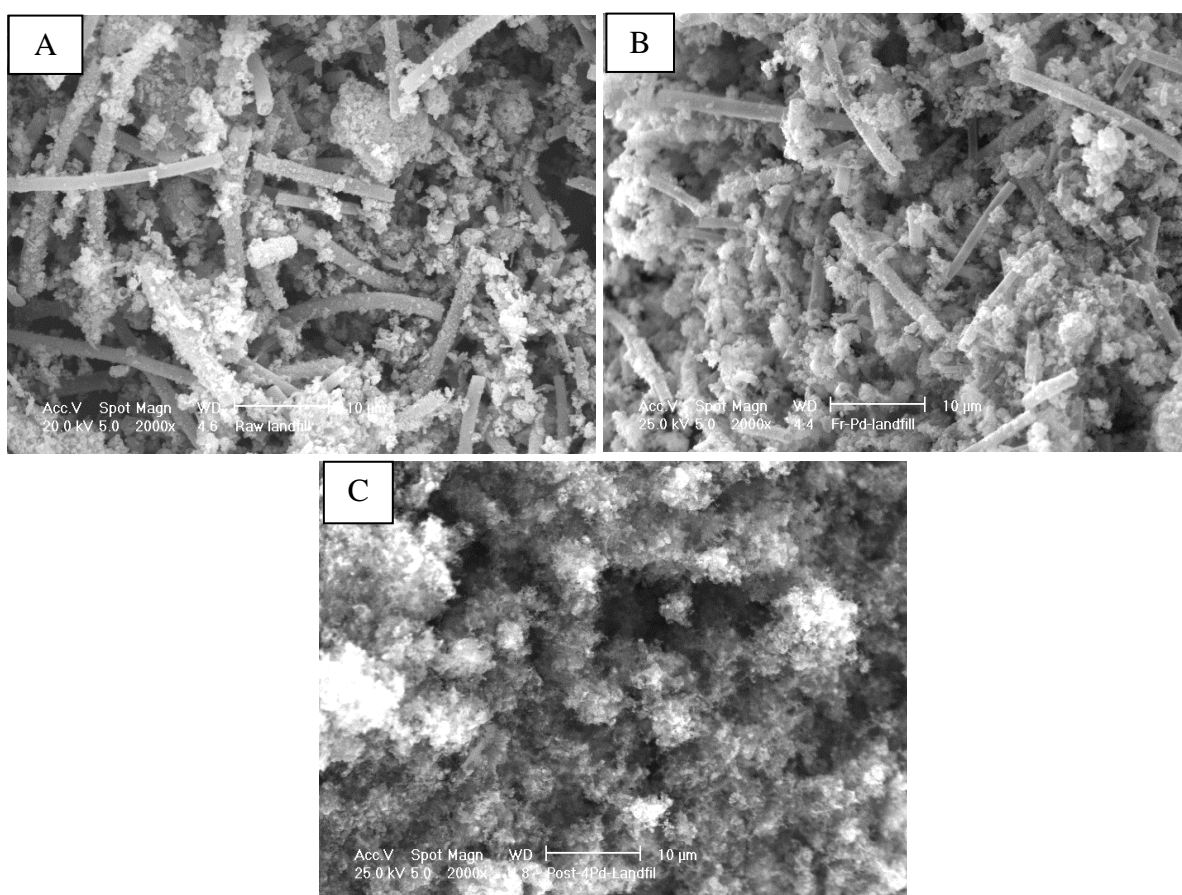


**Figure 4-33** SEM images of (A) raw Landfill sample, (B) pre-reaction 0.4 wt% Pd/Landfill sample, (C) post-reaction 0.4 wt% Pd/Landfill sample.

Figure 4-34 presents the SEM images for the raw Factory sample and pre-reaction 0.4 wt% Pd/ Factory. From the image (B), it appears that the particle size of pre-reaction 0.4 wt% Pd/Factory sample may be smaller than the raw Factory sample as a result of the procedure of Pd addition to the Factory sample. Hence, the increase of surface area of the pre-reaction 0.4 wt% Pd/ Factory sample, as shown in Table 4-9, can be attributed to the smaller particle size. However, Figure 4-34 (C) presents the image the post-reaction 0.4 wt% Pd/Factory sample. From this image, it can be seen that the particle size of the post-reaction 0.4 wt% Pd/Factory sample is agglomerated and stacked compared to the pre-reaction sample. This may have led to the decline of the surface area of the sample and hence to low activity. Moreover, it is clear that most of the sample surface is bright, which suggests that most of the sample component is metallic iron as well as metallic Pd. This supports the XRD result, as illustrated in Figure 4-31, which demonstrated that the metallic Fe and SiO<sub>2</sub> are two major phases.

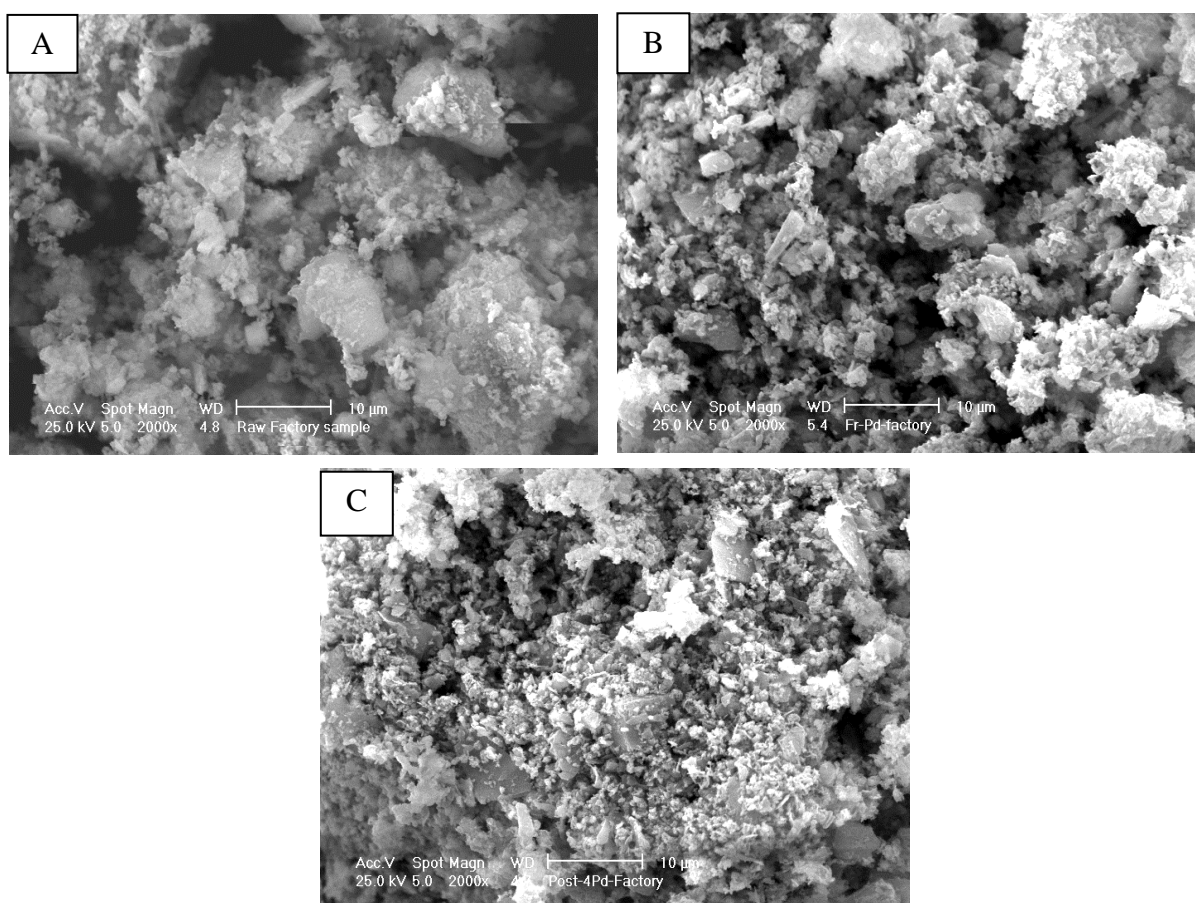


**Figure 4-34** SEM images of (A) raw Factory sample, (B) pre-reaction 0.4 wt% Pd/Factory sample, (C) post-reaction 0.4 wt% Pd/Factory sample.

## 4.5. Summary

The present study was designed to investigate the effect of some modifications on behaviour of the Landfill and Factory samples for hydrogen production from the direct cracking of methane. The effect of calcination temperature, acid treatment and palladium addition for both samples were studied. Both Landfill and Factory samples were calcined at 300, 500, 700 and 900 °C. The main phase of the Landfill sample, 2-line ferrihydrite, transformed to maghemite ( $\gamma\text{-Fe}_2\text{O}_3$ ) at calcination temperatures of 300 and 500 °C, while it transformed to haematite ( $\alpha\text{-Fe}_2\text{O}_3$ ) at 700 and 900 °C. These phases were confirmed by Raman spectroscopy. The calcination temperature did not affect the phase transformation of the Factory sample (haematite,  $\alpha\text{-Fe}_2\text{O}_3$ , and silica,  $\text{SiO}_2$ ), but it played significant role in increasing the sample crystallinity. Moreover, the calcination temperature caused the removal of carbon content, which was observed in the raw samples. In addition, the surface area of the Landfill sample was decreased gradually with increase in calcination temperature. In contrast, it was increased for the Factory sample. SEM images for the calcined Landfill sample showed that the increase of the calcination temperature led to the agglomeration of tubular and non-tubular morphology at 300 and 500 °C which started to merge with each other at 700 °C. At 900 °C, the tubular morphology disappeared. The SEM images of Factory samples calcined at 300 and 500 °C illustrated that their particle sizes are smaller than for the raw Factory sample and they begin to agglomerate and increase in size beyond 700 °C.

The reaction data showed that the hydrogen formation rates for all calcined Landfill samples are lower than the non-calcined Landfill sample in the temperature range from 600 to 750 °C. At 800 °C, the non-calcined Landfill sample showed a rapid increase in the hydrogen formation rate, while the other calcined Landfill samples demonstrated a delay in the high hydrogen formation rate. Among all Landfill samples, the Landfill sample calcined at 900 °C showed the highest hydrogen formation rate. However, it was found that the Factory samples calcined at 300, 500 and 700 °C demonstrated the lowest hydrogen formation rates, whereas the Factory sample calcined at 900 °C exhibited the highest hydrogen formation rate observed. Generally, the calcination temperature of 900 °C enhanced the performance of Landfill and Factory samples and they displayed the highest hydrogen formation rates among all samples.

Characterisation of post-reaction calcined Landfill and Factory samples was undertaken. The XRD patterns for post-reaction calcined Landfill samples showed that the phases are

metallic iron (Fe), iron carbide ( $\text{Fe}_3\text{C}$ ) and graphite, whereas FeO,  $\text{Fe}_3\text{C}$ ,  $\text{FeFe}_4(\text{PO}_4)_4(\text{OH})_2 \cdot 2\text{H}_2\text{O}$ ,  $\text{SiO}_2$  and graphite occurred for the post-reaction Factory samples calcined at 300, 500 and 700 °C. Metallic iron (Fe), silica ( $\text{SiO}_2$ ) and graphite were the only phases detected in the post-reaction Factory sample calcined at 900 °C. The CHN analysis revealed the amount of deposited carbon for the post-reaction calcined Landfill samples, which is in the range from 45 to 65 wt%, whilst it is in the range from 8 to 47 wt% for the post-reaction calcined Factory samples. The SEM images of the post-reaction calcined Landfill samples illustrated that the carbon filaments were not formed over samples calcined at 300, 500, 700 and 900 °C. The SEM images of the post-reaction calcined Factory sample illustrated that there is not significant carbon deposition on Factory samples calcined at 300, 500 and 700 °C, while the carbon filaments were observed over the Factory sample calcined at 900 °C.

Landfill and Factory samples were treated with HCl. The purpose of this study was to attempt to enhance their catalytic activity. The characterisation of pre-reaction treated samples was undertaken. ICP analyses showed that the acidic treatment process caused an increase in the amount of relative iron in both samples, while the amounts of some other elements decreased. The XRD patterns showed that the phases present in the pre-reaction treated Landfill sample are maghemite ( $\gamma\text{-Fe}_2\text{O}_3$ ) and  $\text{FeSiO}_3$ . However, the haematite ( $\alpha\text{-Fe}_2\text{O}_3$ ) and silica ( $\text{SiO}_2$ ) phases were observed in the pre-reaction treated Factory sample. CHN analysis demonstrated that the acid pre-treatment process removed the carbon content. Moreover, the acidic treatment process reduced the surface area of the Landfill sample, whereas it increased the surface area of Factory sample. The SEM images of the treated Landfill sample showed that the tubular morphology fraction decreased and the agglomeration of sample particles increased. The SEM images of the treated Factory sample suggested that particle sizes are slightly smaller compared to the raw Factory sample.

Reaction data showed that this attempt was not successful for enhancing the activity of these samples. Both treated Landfill and treated Factory samples exhibited low hydrogen formation rates compared to their raw counterparts.

Characterisation of post-reaction treated samples was conducted. The XRD patterns showed that the phase formed for the post-reaction treated Landfill sample is only metallic iron (Fe). However, Fe,  $\text{Fe}_3\text{C}$ ,  $\text{SiO}_2$  and graphite phases were evident in the post-reaction treated Factory sample. CHN analysis revealed that no carbon was deposited on the post-

reaction treated Landfill sample, whereas 13.53 wt% was deposited on the post-reaction treated Factory samples. Moreover, the surface area for the post-reaction treated Landfill and Factory samples were decreased. The SEM images for the post-reaction treated Landfill sample illustrated that the tubular morphology completely disappeared and manifestations of sintering are clear. The SEM images for the post-reaction treated Factory sample showed the absence of filamentous carbon.

This chapter has also described the effect of palladium dopant on the Landfill and Factory samples. The characterisation of the pre-reaction doped samples was conducted. The XRD pattern for the pre-reaction 0.4 wt% Pd/Landfill sample revealed the formation of an amorphous maghemite ( $\gamma\text{-Fe}_2\text{O}_3$ ) containing phase. However, haematite ( $\alpha\text{-Fe}_2\text{O}_3$ ) and silica ( $\text{SiO}_2$ ) were detected in the pre-reaction 0.4 wt% Pd/Factory sample. In addition, the reflections of palladium were not detected in both samples. CHN analyses revealed that the procedures of palladium addition removed carbon content. Moreover, the preparation procedures reduced the surface area of Landfill sample, while increasing the surface area of the Factory sample. In addition, the SEM images for the pre-reaction 0.4 wt% Pd/Landfill sample showed that the tubular morphology was still retained and the both tubular and non-tubular morphologies became more agglomerated. In the case of the pre-reaction 0.4 wt% Pd/Factory sample, the SEM images revealed that its particle size was smaller than that for the raw Factory sample. These prepared samples were applied to the direct cracking of methane. The reaction data showed that the addition of palladium into the Landfill sample reduced its performance in the temperature range from 600 to 750 °C, while it enhanced the performance at 800 °C. However, the addition of palladium into the Factory sample led to deactivation of the Factory sample and showed only low levels of hydrogen production.

The characterisation of post-reaction Pd doped samples has been undertaken. The XRD pattern for the post-reaction 0.4 wt% Pd/Landfill sample showed the presence of iron (Fe), iron carbide ( $\text{Fe}_3\text{C}$ ) and graphite phases, whereas it showed metallic iron (Fe) and silica ( $\text{SiO}_2$ ) for the post-reaction 0.4 wt% Pd/Factory sample. CHN analysis demonstrated a large amount of carbon deposited on the post-reaction Pd/Landfill sample, whereas the amount of carbon deposited on the post-reaction 0.4 wt% Pd/Factory sample was very low, which is 1.48 wt%. Furthermore, the surface area of the post-reaction 0.4 wt% Pd/Landfill sample and 0.4 wt% Pd/Factory samples were decreased. The SEM images for the post-reaction 0.4 wt% Pd/Landfill sample demonstrated that the tubular morphology completely disappeared and that no filamentous carbon was formed. The SEM images for the post-

reaction 0.4 wt% Pd/Factory sample illustrated the agglomeration of particles and sintering.

Generally, the calcination temperature of 900 °C for both Landfill and Factory sample enhanced the performance of these samples for hydrogen production from methane cracking. The treatment of Landfill and Factory samples with HCl resulted in low hydrogen formation rates compared to their raw counterparts. The palladium dopant on the Landfill and Factory samples caused to enhance the activity of Landfill sample at 800 °C, while it led to the deactivation of the Factory sample and showed only low levels of hydrogen production.

## 5. Cracking of methane over Pd based catalysts for the production of hydrogen and carbon nanostructures

### 5.1. Introduction

From reviewing the literature, it can be seen that the Pd/H-ZSM-5 has been widely applied for the catalytic combustion of methane as well as nitric oxide reduction [199-203]. Moreover, few studies in the literature have reported the decomposition of methane over the Pd/H-ZSM-5 catalyst. Liu and co-workers [83] investigated the decomposition of methane over a plasma reduced Pd/H-ZSM-5 at 700 °C. They demonstrated that carbon nanotubes (CNTs) were formed and that metal particles were located on the tips of the carbon nanotubes. In addition, their study included the decomposition of methane over the hydrogen reduced Pd/H-ZSM-5 catalyst to compare the effectiveness of CNT growth with plasma reduced Pd/H-ZSM-5 catalyst.

Hargreaves and co-workers [45] studied the direct cracking of methane into hydrogen and carbon over a 3 % Pd/H-ZSM-5 catalyst at 700 °C. They showed that the Pd/H-ZSM-5 catalyst showed very high activity initially where hydrogen formation rate was roughly  $77 \times 10^{-7} \text{ molH}_2 \text{ g}^{-1} \text{ s}^{-1}$ . Also, TEM images of post-reaction 3 % Pd/H-ZSM-5 catalyst illustrated that carbon nanotubes were formed.

Due to the relative lack of studies conducted on Pd/H-ZSM-5, this chapter presents and discusses the effect of many parameters on the activity of Pd/H-ZSM-5. The effects of palladium precursor, the reaction temperature, the flow rate of the feed gas, the addition of dopants and the support type were all studied.

It is worth mentioning, the system of reaction in this study is perhaps related to those catalytic systems in which methane can be converted to aromatic hydrocarbons, mainly C<sub>6</sub>H<sub>6</sub>. Recently, the direct conversion of methane under non-oxidative conditions into aromatics has received a lot of attention [204, 205]. It was found that zeolites support, notably ZSM-5, ZSM-8 and ZSM-11, are the best supports for transition metal ions especially Mo for methane dehydroaromatisation [206]. Therefore, interest in this catalyst (Pd/H-ZSM-5) may extend towards methane dehydroaromatisation where the zeolite support may improve aromatics selectivity.

## 5.2. Effects of reaction temperature on direct cracking of methane over 0.4 wt% Pd/H-ZSM-5 catalyst

### 5.2.1 Introduction

As previously mentioned, Pd/HZSM-5 has been little explored for methane cracking [45, 83]. However, a lot of studies have focused on the use of nickel. These studies have been concerned with the optimisation of the catalyst formulation by varying the composition, the type of textural promoter and the concentration of various additives [40, 48, 62, 207-209]. Studies of reaction conditions are fewer despite the crucial role they play in methane conversion, the deactivation of catalyst and the nature of the deposited carbon. In order to make the process of catalytic methane decomposition economically feasible, a complete understanding of these determinant parameters is necessary. For example from reviewing the literature, it does not appear that the Pd/H-ZSM-5 catalyst has been studied for the direct cracking of methane at different reaction temperatures.

This study aims to address this omission for a 0.4 wt% Pd/H-ZSM-5 catalyst. The flow rate of methane was fixed at 12 mL/min and catalyst mass was held at 0.4 g. The catalysts were characterised using techniques such as XRD, CHN, TGA, SEM, TEM and Raman spectroscopy to observe any changes in the catalyst and to characterise carbon deposited on them. However, it should be pointed out that the time on stream for the experiments described in this section is longer than those applied in other sections.

## 5.3. Results and discussion

### 5.3.1 Reaction data

Figure 5-1 shows the hydrogen formation rates against time on stream for 0.4 wt% Pd/H-ZSM-5 catalysts run at different reaction temperatures in the range from 600 to 900 °C. It can be seen that the hydrogen formation rates generally increased with increase of reaction temperature as would be expected. It appears that the lowest hydrogen formation rate is observed at 600 °C where it is *ca.*  $0.5 \times 10^{-4}$  mol H<sub>2</sub> g<sup>-1</sup> min<sup>-1</sup>, while the highest peak formation rate is noted at 750 °C where it is *ca.*  $3.5 \times 10^{-4}$  mol H<sub>2</sub> g<sup>-1</sup> min<sup>-1</sup>. Moreover, it is clear that the hydrogen formation rate sequentially increases from 600 to 750 °C. In addition, the hydrogen formation rates gradually increased with time on stream and deactivation was not observed in this range of temperature. At 800 °C, the catalyst showed

the highest initial hydrogen formation rate at 30 minutes of time on stream, after which the hydrogen formation rate dropped within *ca.* 80 minutes and then remained almost steady. The behaviour of the catalyst at 900 °C, resembled the runs at 700 and 750 °C where the hydrogen formation rate gradually increased up to *ca.*  $2.5 \times 10^{-4}$  mol H<sub>2</sub> g<sup>-1</sup> min<sup>-1</sup> at 120 minutes followed by relative stability in the hydrogen formation rate until *ca.* 240 minutes of time on stream after which it slowly decreased for the rest of the run. It should be noted that the time on stream for the reaction at 700 and 750 °C is shorter than the other reactions. The reason for this is that the reaction was stopped due to a pressure drop effect which was observed. Solymosi *et al* [47] studied the hydrogen production from methane decomposition over 5 % Pd/SiO<sub>2</sub> at reaction temperatures in the range from 200 to 330 °C. They observed that at 200 °C, methane was decomposed and with increase the temperature the hydrogen formation rate increased.

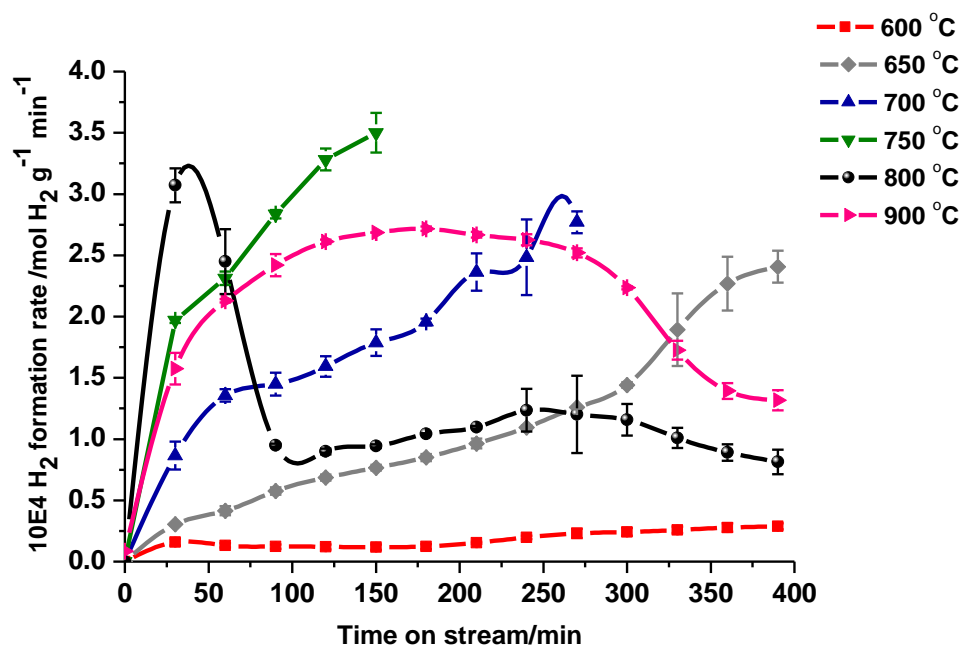


**Figure 5-1** Hydrogen formation rates as a function of time on stream for methane cracking over 0.4 wt% Pd/H-ZSM-5 catalyst at different temperatures in the range of 600 to 900 °C, the methane flow rate was 12 mL/min and 0.4 g catalyst mass.

The rapid deactivation of the catalyst at 800 °C can be attributed to the rapid deposition of carbon on the catalyst surface and the nature of carbon deposited, which may be an encapsulating type of carbon. Furthermore, it is possible that sintering of palladium has occurred beyond 750 °C. SEM and TEM images for the post-reaction catalysts are presented later in this chapter in relation to these suggestions.

### 5.3.2 XRD patterns

Figure 5-2 presents the XRD patterns for the pre and post-reaction 0.4 wt % Pd/H-ZSM-5 samples. The pattern for the pre-reaction 0.4 wt % Pd/H-ZSM-5 displays the characteristic reflections of H-ZSM-5 with the main  $2\theta$  values of *ca.* 8°, 9° and 23-25°. No palladium-containing phases were apparent.

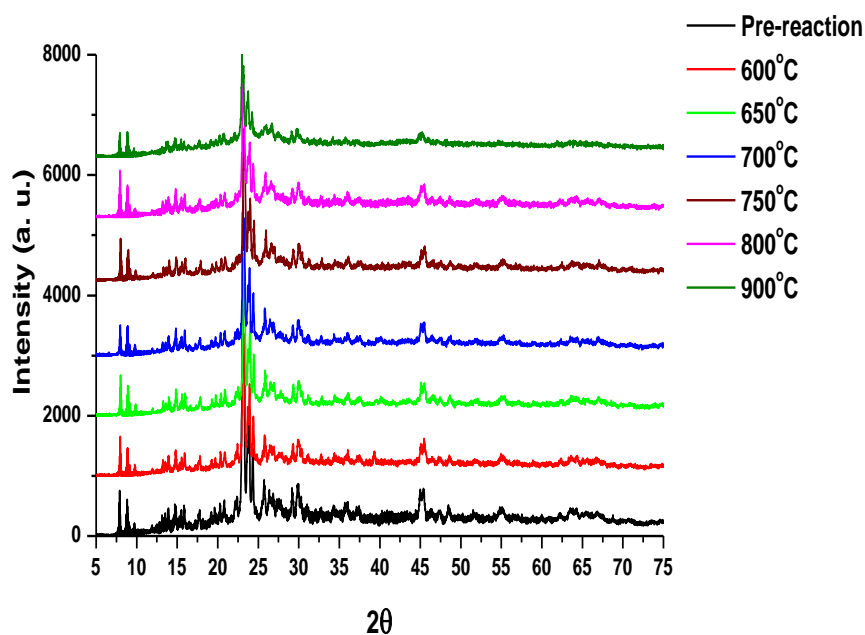


**Figure 5-2** XRD patterns of 0.4 wt % Pd/H-ZSM-5 in the pre- and post-reaction forms run at different temperatures.

The XRD patterns of the post-reaction catalysts confirm that the zeolite framework remains intact even at high reaction temperatures. The only obvious change among the patterns is that the post-reaction catalysts appear to show lower crystallinity as the peaks are slightly less intense, which may be as consequence of carbon deposited on the catalysts.

### 5.3.3 Post-reaction carbon and TGA analysis

The post-reaction carbon analysis and TGA profiles for the 0.4 wt % Pd/H-ZSM-5 catalyst at different reaction temperature are shown in Table 5-1, Figures 5-3 and 5-4, respectively. It should be noted that these catalysts did not have similar periods of time on stream. It was observed that the time on stream for the reactions at 700 and 750 °C were shorter than

other reactions. From the data in Table 5-1, it can be seen that the lowest amount of carbon deposited is observed on the catalyst at reaction temperature of 600 °C (1.25 wt %), whereas the largest is at the reaction temperature of 900 °C (21.12 wt %). Although the time on stream was less at 700 and 750 °C due to the pressure drop, the catalyst produced a relatively large amount of carbon compared to other temperatures, which are 15.75 and 14.20 wt%, respectively. This is not surprising because the catalyst displayed a high rate of reaction at these temperatures. However, the amount of carbon deposited on the catalyst at reaction temperature of 650 and 800 °C is quite similar where they are 11.76 and 11.25 wt %, respectively. It could be that the observed drop in the reaction rate at *ca.* 50 minutes of time on stream for the reaction at 800 °C led to low amount of carbon produced, while the reaction rate was gradually increases at 650 °C.

<b>Table 5-1</b> CHN analysis for the post-reaction 0.4 wt% Pd/H-ZSM-5 catalyst at different reaction temperature.				
<b>Catalyst</b>	<b>Reaction Temperature (°C)</b>	<b>C wt%</b>	<b>H wt%</b>	<b>N wt%</b>
<b>0.4 wt% Pd/H-ZSM-5</b>	<b>600</b>	<b>1.25 ± 0.09</b>	<b>0.57 ± 0.04</b>	-
	<b>650</b>	<b>11.76 ± 0.01</b>	<b>0.49 ± 0.06</b>	-
	<b>700</b>	<b>15.75 ± 0.05</b>	<b>0.59 ± 0.09</b>	-
	<b>750</b>	<b>14.20 ± 0.07</b>	<b>0.45 ± 0.01</b>	-
	<b>800</b>	<b>11.25 ± 0.13</b>	<b>0.30 ± 0.01</b>	-
	<b>900</b>	<b>21.12 ± 0.11</b>	<b>0.30 ± 0.00</b>	-

TGA studies in the presence of air have been carried out for the post-reaction 0.4 wt% Pd/H-ZSM-5 catalysts to estimate the amount of carbon deposited on them and to determine their reactivity profile with respect to air. Figure 5-3 displays the TGA profiles. The total mass changes in these profiles are in good agreement with the carbon analyses. Furthermore, it can be seen that there is a small weight loss below 250 °C which can be ascribed to desorption of adsorbed water on the catalyst. This weight loss is more pronounced for catalysts run at lower reaction temperatures and it is not so clear in the post-reaction catalyst at 900 °C, but it is the highest in the post-reaction catalyst at 600 °C. This could be associated with increasing hydrophobicity and decreasing available pore volume as a function of increasing carbon content. The weight loss that is apparent between *ca.* 550 and 760 °C is due to burning off coke that has been formed on the catalyst.

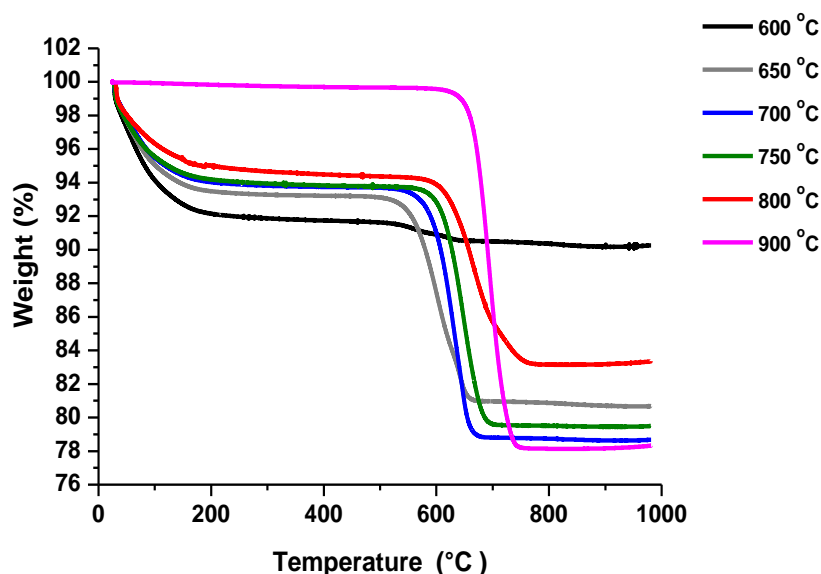


**Figure 5-3** TGA profiles of post-reaction 0.4 wt % Pd/H-ZSM-5 catalyst at different reaction temperatures.

The first-derivative weight change profiles from 250 °C onwards for the post-reaction 0.4 wt% Pd/H-ZSM-5 catalysts are presented in Figure 5-4. From these profiles, the differences between the samples are more apparent than those in Figure 5-3. It can be observed that the post-reaction 0.4 wt% Pd/H-ZSM-5 which were run at 600, 650, 700 and 800 °C have two mass loss regions, while those run at 750 and 900 °C have only one mass loss region. Moreover, the position of the oxidation peaks has gradually shifted to higher oxidation temperature with increase in reaction temperature from 600 to 900 °C. This indicates the formation of different species of carbon deposited. Whilst it may be possible that the amount and density of the carbon deposited led to the high oxidation temperature it is possible that e.g. the carbon is becoming more graphitic at higher reaction temperature. It is known that the carbon formed from the catalytic decomposition of methane can include amorphous carbon and filamentous carbons, which comprise single-walled carbon nanotubes (SWCNTs), multi-walled carbon nanotubes (MWCNTs) and carbon nanofibres (CNFs) [49, 52, 84]. The nature of the carbon deposited on the catalyst is generally complex and its reactivity depends on the formation conditions and mechanism. The carbon materials possess characteristic weight loss temperatures, when submitted to TGA in an oxidising atmosphere. It has been reported that the oxidation temperature is about 330 °C for amorphous carbon, 500-600 °C for SWCNTs and around 700 °C for MWCNTs [85]. Carbon nanofibres (no hollow cavity) have been found to be resistant to temperatures in the range 500–600 °C under an oxidising atmosphere [87, 210]. In addition, the

oxidation of graphitic carbon can occur at high temperatures of around 700 °C or beyond [211]. The weight loss can be also shifted towards the high oxidation temperature region as a result of the increased amount of carbon deposited on the catalyst [212]. However, the presence of residual metal in the sample can catalyse the oxidation of the carbon species may lower the temperature at which the maximum oxidation rate occurs [97, 211].

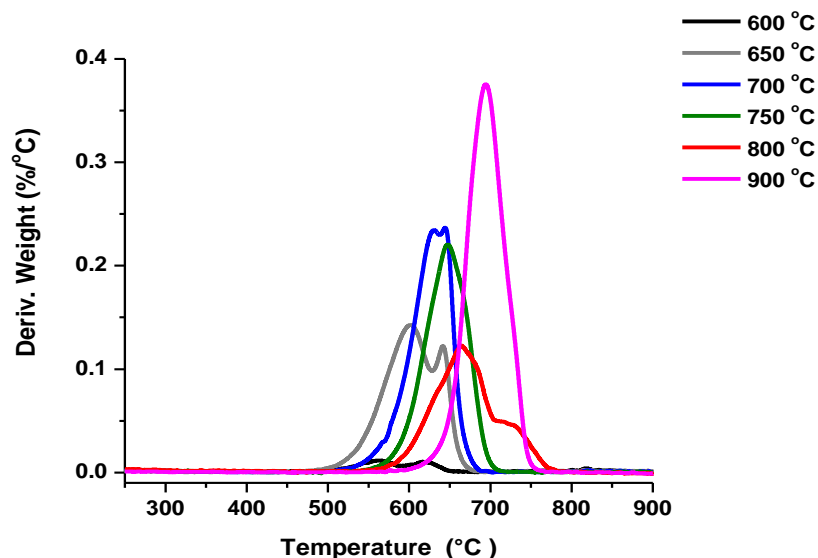


**Figure 5-4** TGA profiles of post-reaction of 0.4 wt % Pd/H-ZSM-5 catalyst at different reaction temperatures.

Based on the discussion above and from derivative weight changes profiles in Figure 5-4, it can be suggested that amorphous carbon was not formed, while MWCNTs and carbon nanofibres can be present in all post-reaction samples. Also, the post-reaction samples run at 750, 800 and 900 °C can be contained graphitic carbon. In general, it is possible that a mixture of carbon species have formed on each sample, which depends on the reaction temperature employed. SEM and TEM images for the carbon deposited on these samples (will be shown and discussed later) may support this finding.

### 5.3.4 Post-reaction SEM and HRTEM images

SEM and HRTEM studies of the post-reaction 0.4 wt% Pd/H-ZSM-5 catalyst have been undertaken. Figure 5-5 presents the SEM images of the 0.4 wt% Pd/H-ZSM-5 catalyst run at different reaction temperatures. From these images, no deposited carbon is observed at 600 °C and the sample surface seems bright possibly as a result of the very low amount of carbon deposited. For the post-reaction 0.4 wt% Pd/H-ZSM-5 catalyst samples run at temperatures in the range from 650 to 900 °C, it is clear that carbon filaments (CFs) were

formed over the catalysts. In addition, the carbon filaments formed on the catalysts, run at reaction temperatures from 650 to 800 °C are more pronounced than those formed on the catalyst run at 900 °C. Therefore, higher magnification studies of the post-900 °C catalyst were taken.

Moreover, it can be seen from these images that the palladium particles are located at the tip of the grown CF and they are clearly visible in the CF formed on catalyst at temperatures in range from 650 to 750 °C. This is evident from the images where the filaments have bright tips. This indicates that the carbon filaments have formed by the tip-growth mechanism.

Although the carbon filaments formed over the catalyst run at 800 °C were dense and location of palladium particles on the tip of the CF appears very limited. Due to the low presence of CF in the catalyst carried out at 900 °C, it is hard to determine the location of palladium particles.

The mechanism of carbon filament formation resulting from the decomposition of hydrocarbons over metal catalysts has been extensively investigated and two mechanisms have been proposed: the “tip-growth” and “base-growth” mechanisms [104, 109, 213, 214]. Where the tip-growth mechanism involves the catalyst particle being lifted up by the growing CF and continues to promote CF growth at its tip. The hydrocarbon decomposition at the gas–metal interface is followed by dissolution of carbon into the metal and diffusion through the particle. The carbon then precipitates at the metal–support interface, detaching the metal particle from the support and forming a filament with an exposed metal particle at its tip. The rate-determining step of this process is believed to be the diffusion of carbon through the metal particle. This mode of carbon accumulation allows the catalyst to maintain its activity for an extended period of time without deactivation [215].

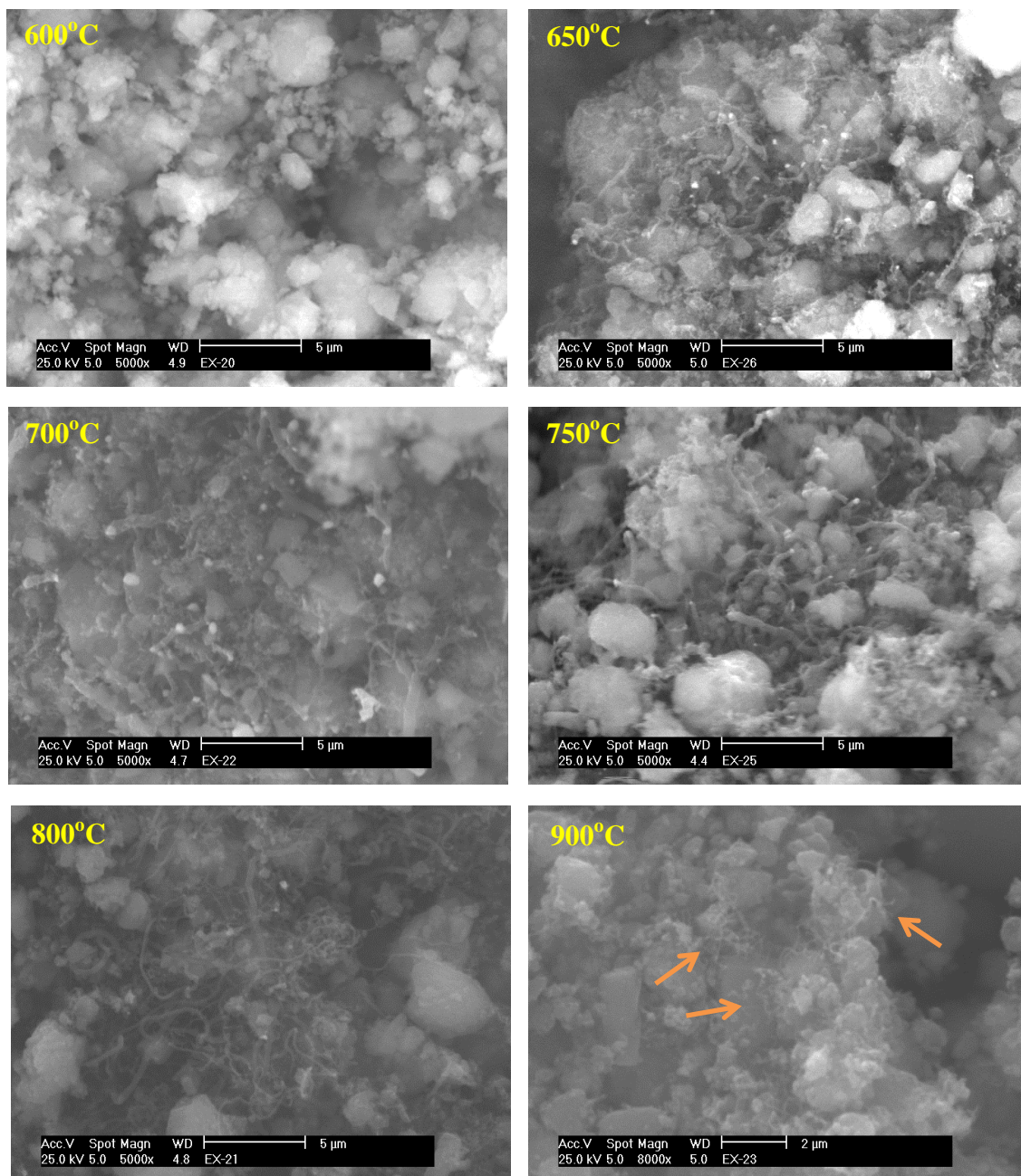


**Figure 5-5** SEM images of post-reaction 0.4 wt % Pd/H-ZSM-5 catalyst at different temperatures in the range from 600 to 900 °C.

Zhang and Amiridis [72] studied hydrogen production *via* the direct cracking of methane over Ni/SiO<sub>2</sub> catalysts. Their SEM and TEM characterisation for the spent catalyst showed that carbon deposits were present on the catalyst in the form of hollow cylindrical filamentous, with a nickel particle located on the tip of each filament. They revealed that the catalyst deactivation was not caused by the formation of carbon filaments *per se*, but it was because these filaments began to entwine with each other and the silica surface, due to the spatial limitations of the pore structure of the catalyst.

Zabidi *et al.* [58] studied the production of hydrogen from catalytic decomposition of methane over Ni/M-based (M= Mn, Fe, Co, and Cu) catalysts at 725 °C. They demonstrated that Ni/Mn catalyst showed high activity and stability without deactivation compared to other catalysts. In their study, TEM images were presented. Based on this, they attributed the Ni/Mn catalyst stability to the presence of Ni particles at the tip of the carbon filaments. They found that the other catalysts have produced encapsulating type of carbon, which led to their deactivation.

The presence of the metal particles at the tips of the carbon filaments contributes to the high and stable methane conversion as metal particles continually interact with incoming methane molecules.

Based on the SEM images and the above discussion, the activity of 0.4 wt % Pd/H-ZSM-5 catalyst at different reaction temperatures can be interpreted. It was observed that the catalyst was active, no deactivation period is observed, at reaction temperatures of 650, 700 and 750 °C. These activities can be ascribed to the presence of Pd particles on the tip of filaments. The rapid deactivation of the catalyst at 800 °C could be attributed to the formation of encapsulating type of carbon, *i.e.* Pd particles encapsulated within carbon filaments or other types of encapsulating carbon. At 900 °C, it can be suggested that there is a sintering process or re-dispersion of palladium, which could lead to the high activity and a low growth of carbon filaments. Chena and co-workers [39] investigated the effect of the crystal size of Ni on the growth of carbon nanofibres (CNFs) during the decomposition of methane. They found that small Ni crystals result a low growth rate, while large Ni crystals reduce the rate of growth due to low surface area. Furthermore, they argued that the optimum growth rate and yield of carbon nanofibres can be achieved on optimally sized Ni crystals, about 34 nm. Noda *et al.* [86] studied the methane decomposition over 1 wt% Ni/SiO<sub>2</sub> and 5 wt% Ni/SiO<sub>2</sub> catalysts at different reaction temperature from 625 to 800 °C in a fixed bed quartz tube reactor for the formation of CNT. They found that the amount of CNT decreased at high temperature for both catalysts due to sintering.

Figure 5-6 presents the TEM images for the post-reaction 0.4 wt% Pd/H-ZSM-5 catalyst at reaction temperatures of 650, 700 and 750 °C, while Figure 5-7 presents the TEM images for the post-reaction catalyst at 800 and 900 °C. From these images, the particles size can be seen to vary with each sample *i.e.* a large and small size are visible for each sample, but it is generally observed that the particles size tends to increase with increasing

reaction temperature although caution must be exercised in such a conclusion due to the statistical limitations of the technique (*i.e.* only a very small fraction of sample is imaged). It may be possible that the sintering process is different between the surface and the channels of the H-ZSM-5 zeolite support. Moreover, the large particle size is responsible for the growth of carbon filaments. However, it can be seen that the type of carbon filaments formed on all post-reaction catalyst is nanofibres (CNFs). Carbon nanofibres (CNFs) are graphitic filamentous structures which differ from nanotubes in the orientation of the graphite monolayer planes. In nanotubes (CNTs), the graphite monolayer planes are parallel to the tube axis, while in nanofibres, the layers of graphite are arranged vertical to the fibre axis, stacked form, or at an angle to the axis, herringbone form [111].

The TEM image in Figure 5-6 for the post-reaction catalyst at 650 °C illustrates the formation of carbon nanofibres, as indicated with the palladium particle located at the tip of the CNF as marked by the arrow. Also, it is noted that the shape of fibre is irregular; its diameter being roughly 33 nm. However, the TEM image in Figure 5-6 for the post-reaction catalyst at 700 °C shows the presence of two types of carbon nanofibres, marked by numbers 1 and 2. The CNF number of 1 is free of Pd particles and is close-ended. This suggests that this CNF is formed by a “base-growth” mechanism. So, it could be that not all CNFs formed with “tip-growth” mechanisms, although most are. In addition, it is observed that the shape is irregular; the average diameter being around 41 nm. The CNF number of 2 shows a smaller diameter, 12 nm, and there is a Pd particle at the tip.

Two TEM images (750 °C A and 750 °C B) for the post-reaction catalyst at 750 °C are presented in Figure 5-6. It can be seen from the image (750 °C A) that the CNFs are present in both the stacked (marked with the orange arrow) and the herringbone–bamboo nanotube (marked with the red arrow) form. Also, it is noted that the tip of stacked form of CNFs have a central empty core surrounded by graphite layers. This suggests that the CNF grow to a certain extent then stop growing and then form closed hollow nano-spheres of carbon layers. This may indicate that the growth mechanism is “tip-growth”. It has been reported that the metal particle present in the core of the nano-sphere is under pressure and is forced to escape leaving an empty core [162]. The loss of palladium particles from the core of the nano-spheres may lead to the emergence new catalytically active surfaces. This may explain that the activity of the catalyst at this temperature is highest as well as the presence of palladium particles at the tip of CNF as illustrated in SEM images. The TEM image of 750 °C (B) in Figure 5-6 is an addition image for the post-reaction 750 °C

catalyst, which demonstrates the stacked form of CNF and a Pd particle at the tip of the filament.

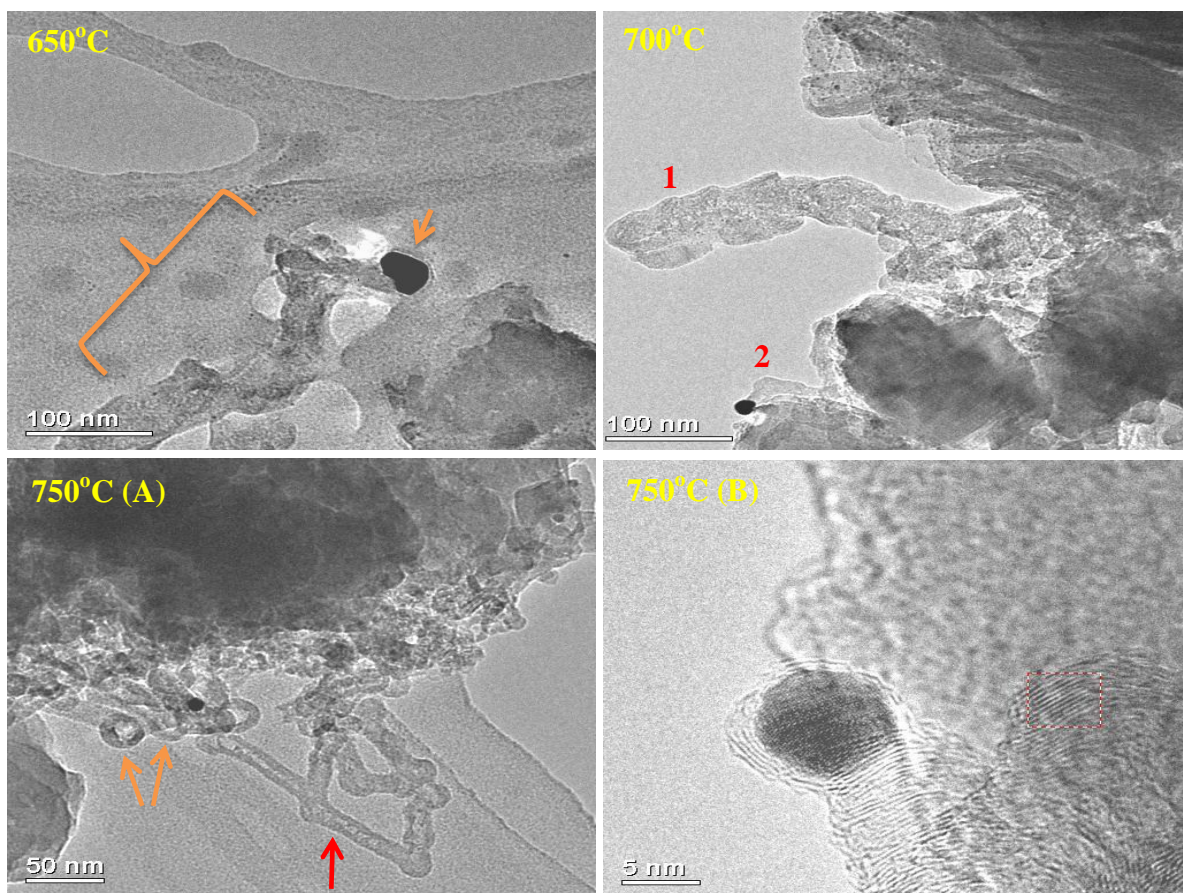


**Figure 5-6** TEM images of post-reaction 0.4 wt % Pd/H-ZSM-5 catalyst at different temperatures in the range from 650 to 750 °C.

Figure 5-7 illustrates the TEM images for the post-reaction 0.4 wt % Pd/H-ZSM-5 catalyst run at 800 and 900 °C. The TEM images of 800 °C (A) and 800 °C (B) show the presence of carbon deposited on the catalyst. It can be seen that the carbon nanofibres (herringbone–bamboo nanotube form) are formed. It is hard to determine their growth mechanisms due to the absence of Pd particles in their structure. Based on the SEM images, Figure 5-5, and TEM images, it can be suggested that their formation mechanisms are “base-growth”. The diameter average of CNFs is 17 nm. Furthermore, it can be observed from the image of 800 °C (A) that the Pd particles, black dots, seem that they are covered by encapsulating carbon. Also, it can be seen from TEM image of 800 °C (B) that the Pd particles have sintered and are encapsulated by layers of graphitic carbon. The encapsulation of the catalyst particles leads to the prevention of the catalyst particles contacting CH<sub>4</sub> molecules, resulting in deactivation. Therefore, the observed rapid deactivation of the catalyst at a temperature of 800 °C can be attributed to the occurrence of carbon encapsulation.

Choudhary *et al.* [19] investigated the effect of various supports on the catalytic activity of Ni. The supports were HY, HZSM-5 and SiO<sub>2</sub>. The results of their study indicated that Ni/SiO<sub>2</sub> and Ni/HY catalysts have superior catalytic activity and a longer lifetime than an Ni/HZSM-5 catalyst, which deactivated rapidly. TEM images revealed the reason for the rapid deactivation of the Ni/HZSM-5 catalyst, showing that encapsulating carbon formation on the catalyst particles obstructs the reactant molecules access to the active sites, while in the case of Ni/SiO<sub>2</sub> and Ni/HY catalysts the carbon forms in filaments. The researchers suggested that the presence Ni particles at the tip of the filaments acted to increase the lifetime of the catalyst.

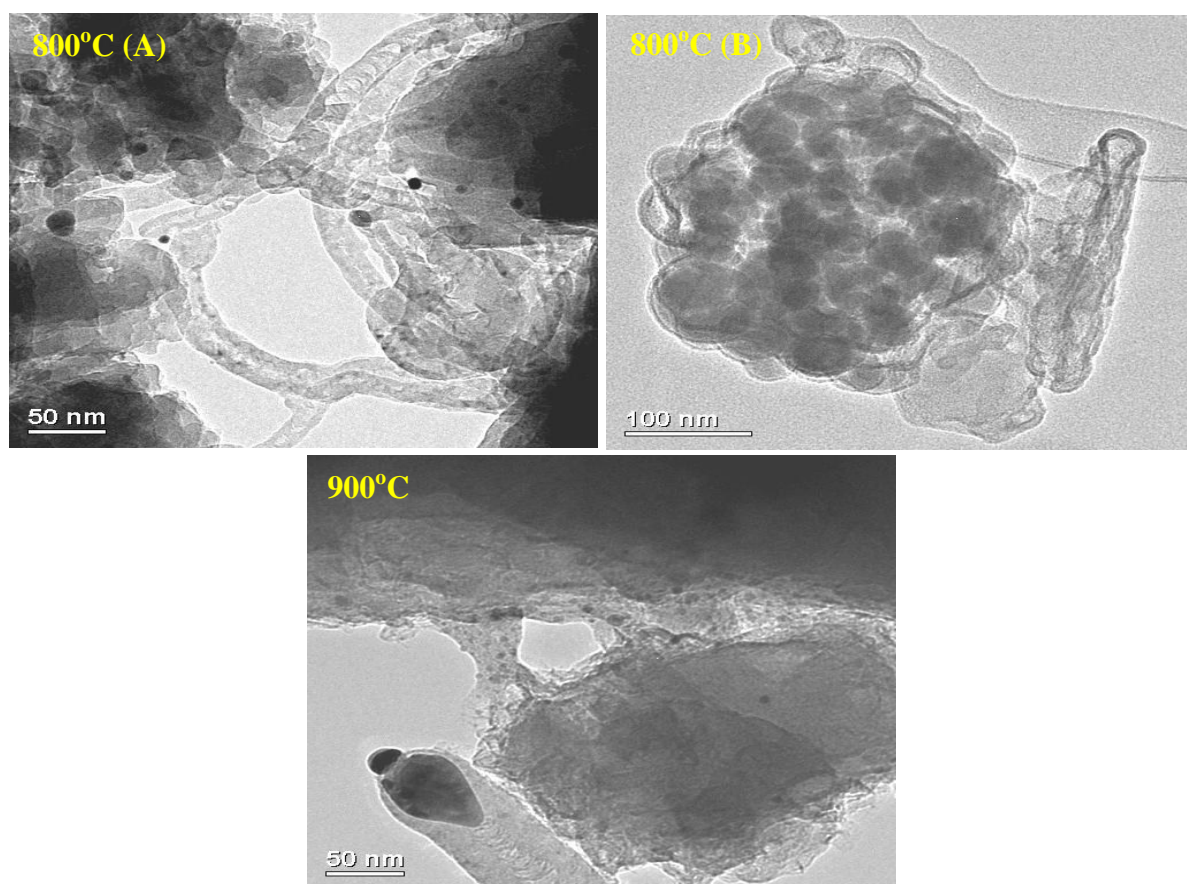


**Figure 5-7** TEM images of post-reaction 0.4 wt % Pd/H-ZSM-5 catalyst at reaction temperatures of 800 and 900 °C.

It is observed from the TEM image of 900 °C in Figure 5-7 that the carbon nanofibres (herringbone–bamboo nanotube form) are produced with large diameter, 57 nm, and the Pd particle is located at the tips of the CNFs. Also, it can be noted that the particles size of Pd are varying, large size is at the tip of CNF and small size are dispersed on the surface of zeolite. Moreover, the small Pd particles sizes appear to be non-encapsulated with a layer of carbon. The presence of the Pd particle at the tip of the CNF and the apparent lack of

encapsulating carbon may explain the high activity of catalyst at 900 °C compared to the activity of catalyst at 800 °C.

It should be mentioned that the structure of the CNFs observed in this study are analogous to the structures of CNFs prepared by Hargreaves and co-workers [45] and Liu and co-workers [83] when they studied the decomposition of methane over Pd/H-ZSM-5 despite difference in the preparation of catalyst and the reaction conditions.

### 5.3.5 Raman spectroscopy

Raman spectroscopy has played an significant role in the characterisation of structural graphitic materials and has been widely applied in the last four decades to characterise graphitic systems, such as carbon fibres, glassy carbon and carbon nanotubes [216]. The Raman spectra of graphitic materials usually comprise two significant bands. These bands are the so-called G and D bands. The G band appears at around 1582  $\text{cm}^{-1}$  and is attributed to the vibration of  $\text{sp}^2$  bonded carbon atoms in the ordered carbon graphite and carbon nanotubes, while the D band at about 1350  $\text{cm}^{-1}$  is assigned to the vibration of the carbon atoms with dangling bonds in plane terminations of disordered structures. The intensity ratio  $I_D/I_G$  for the D band and G band is widely used for characterising the defect quantity in graphitic materials. The larger value of intensity ratio reveals the more defects in graphitic structure [216, 217].

Raman spectroscopy was used to investigate the graphitisation degree in the carbon produced during methane decomposition over 0.4 % Pd/H-ZSM-5 catalyst run at different reaction temperatures. Figure 5-8 presents the Raman spectra for the post-reaction 0.4 % Pd/H-ZSM-5 catalyst run at the different reaction temperatures (except for that at 600 °C due to the bands not being visible for this sample). From the Raman spectra, the two main bands at 1352  $\text{cm}^{-1}$  (D band) and at 1590  $\text{cm}^{-1}$  (G band) are observed.

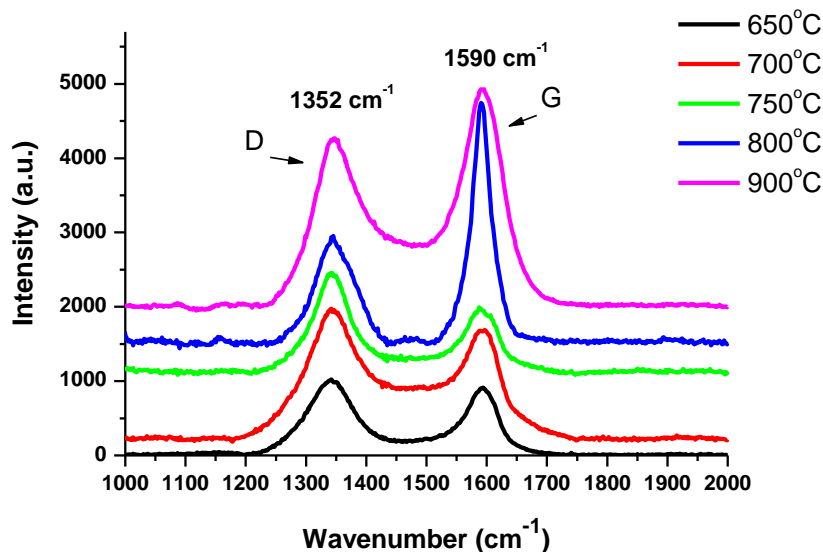


**Figure 5-8** Raman spectra for the post-reaction 0.4 wt % Pd/H-ZSM-5 catalyst at different reaction temperatures.

Table 5-2 shows the intensity ratio  $I_D/I_G$  for the D band and G band from Raman spectra for carbon produced at different reaction temperatures. It should be mentioned that the intensity ratio  $I_D/I_G$  was calculated based on the band areas. From the data in Table 5-2, the highest  $I_D/I_G$  value was observed after reaction at 750 °C ( $I_D/I_G=1.51$ ), indicating that the structure of graphitic carbon is the most disordered, while the lowest value was observed after reaction at 800 °C ( $I_D/I_G=0.76$ ), which indicates the lowest disordered.

<b>Table 5-2</b> The result of intensity ratio $I_D/I_G$ for the D band and G band from Raman spectra for carbon produced at different reaction temperatures.		
<b>Catalyst</b>	<b>Reaction temperature (°C)</b>	<b>Peak area ratio (<math>I_D/I_G</math>)</b>
0.4 % Pd/H-ZSM-5	650	1.34
	700	1.41
	750	1.51
	800	0.76
	900	0.93

## 5.4. Effect of feed gas flow rate on direct cracking of methane over 0.4 wt% Pd/H-ZSM-5 catalyst

### 5.4.1 Introduction

Flow rate is an important parameter that plays a role in catalyst activity due to its impact on the gas residence time in the reactor. Therefore, the effect of flow rate on hydrogen production and the nature of the carbon deposited from direct cracking of methane over 0.4 wt% Pd/H-ZSM-5 catalyst were studied.

Methane flow rates of 12, 24, 36, and 48 mL/min were employed at reaction temperature of 800 °C and time on stream of 300 minutes using a constant catalyst mass of 0.4 g. It should be noted that the time on stream in this section is shorter than that in the previous section. The catalysts were characterised using the same techniques.

### 5.4.2 Reaction data

Figure 5-9 shows the results of the hydrogen formation rates against time on stream for 0.4 % Pd/H-ZSM-5 catalysts at different flow rates of feed gas (75 % CH<sub>4</sub>+25 %N<sub>2</sub>). The employed reaction temperature is 800 °C. It can be seen that the increasing the flow rate increases the initial hydrogen formation rates at the beginning of the reaction. In addition, the increase of flow rate of gas feed leads to rapid deactivation of catalyst in the following order: 48 > 36 > 24 > 12 mL/min. The lowest peak hydrogen formation rate is observed at 12 mL/min, while the highest hydrogen peak formation rate is at 36 mL/min. Furthermore, it is obvious that the behaviour of catalyst at 12 mL/min differs from the behaviour of the catalyst at other flow rates. At 12 mL/min there is a delayed burst of hydrogen formation rate followed by a gradual decline until the end of run. At 24, 36 and 48 mL/min the catalyst displayed similar behaviour with the peak high hydrogen formation occurred initially and then dramatically declined up to 60 minutes of time on stream, after which it remained steady for the rest of the run. After 60 minutes of time on stream, the highest hydrogen formation rate is exhibited at 12 mL/min, whereas the lowest hydrogen formation rate is at 48 mL/min. In general, increase of flow rate results in deactivation of catalyst decreasing the hydrogen production. A plausible explanation is the deposition of carbonaceous species on the catalyst leading to active site blockage.

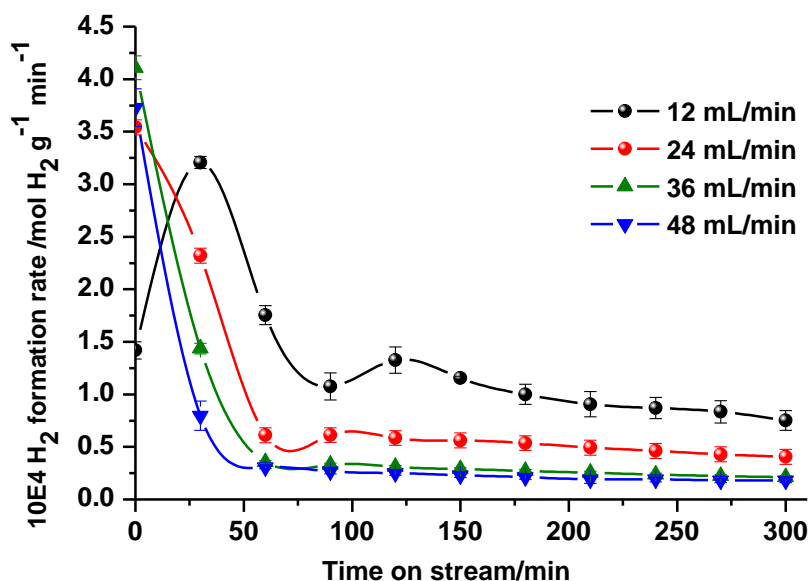


**Figure 5-9** Hydrogen formation rates as a function of time on stream for 0.4 wt % Pd/H-ZSM-5 catalyst with varying flow rates at a reaction temperature of 800 °C and 0.4 g catalyst mass.

A number of studies in the literature are consistent with this result. For example, Suelves *et al.* [49] studied the effect of the CH<sub>4</sub> flow rate on the hydrogen production and CH<sub>4</sub> conversion over 65 wt% Ni/SiO<sub>2</sub>-Al<sub>2</sub>O<sub>3</sub> catalyst at reaction temperature of 700 °C. They reported enhanced deactivation at higher flow rate.

Zabidi *et al.*[58] studied the effects of CH<sub>4</sub> flow rate on the Ni/Mn based catalyst for methane decomposition to hydrogen. Their results showed that by increasing the flow rate the yield of hydrogen decreased. They attributed the low yield of hydrogen to short contact time between the methane molecule and catalyst.

### 5.4.3 XRD patterns

XRD powder diffraction studies of the 0.4 % Pd/H-ZSM-5 catalysts were undertaken. Figure 5-10 displays the XRD patterns for all runs. It can be seen that the zeolite structure is maintained. However, there is a slight possible decrease in the intensity of the characteristic peaks of ZSM-5, between 23 and 25° 2θ, suggesting a decrease in the crystallinity of the catalyst as a result of the carbon deposited on the catalysts. The palladium content was not apparent.

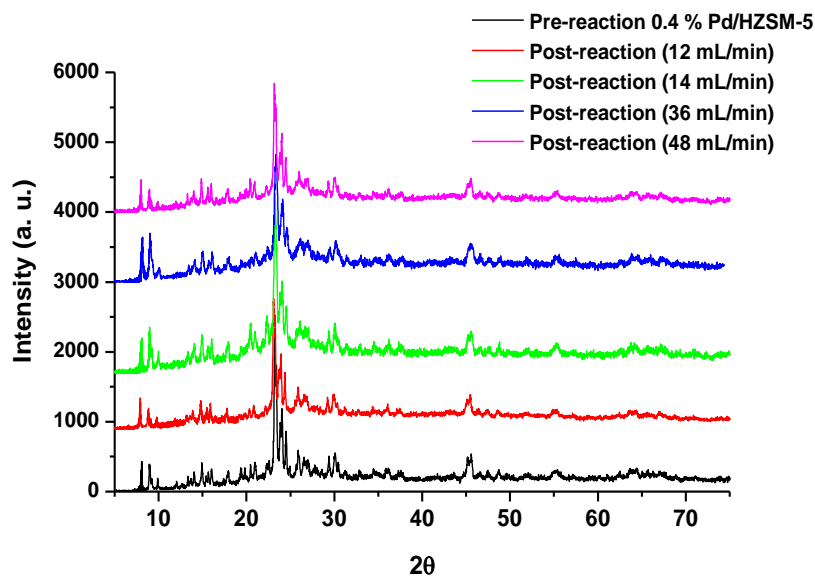


**Figure 5-10** XRD patterns of 0.4 wt % Pd/H-ZSM-5 in the pre- and post-reaction forms at different CH<sub>4</sub> flow rates.

#### 5.4.4 Post-reaction CHN and TGA analysis

The post-reaction CHN analysis of the 0.4 wt% Pd/H-ZSM-5 run at different flow rates is presented in Table 5-3. It can be observed that the amount of carbon deposited is increased with increasing flow rate. The lowest amount of carbon deposited is 10.80 wt% at 12 mL/min, while the largest amount of carbon deposited is 14.92 wt% at 48 mL/min. Also, the amount of carbon deposited at flow rate 24 and 36 mL/min are 13.29 and 14.52 wt%, respectively. Although the increase in the flow rate of CH<sub>4</sub> resulted in catalyst deactivation, it is observed that the amounts of carbon increased with increasing the flow rate. It was observed from the profiles of hydrogen formation rate in Figure 5-9 that increasing of flow rate led to a significant increase in the initial reaction rate followed by a dramatic decline. Hence, it could be that the greatest total amount of deposited carbon was attained before the catalyst deactivated. Moreover, it could be the cause of the deactivation of the catalysts.

These findings of the current study are consistent with those of Suelves *et al.* [218] who investigated the effect of space velocity on the evolution of the hydrogen concentration and the properties of carbon deposited from the decomposition of methane in a fixed bed reactor using a NiCuAl catalyst at 700 °C. They demonstrated that increasing space

velocity lead to increasing methane decomposition reaction rate and caused an increase in the rate of catalyst deactivation. Also, the amount of carbon deposited was increased with increasing space velocity. They attributed these increases to increases in the initial reaction rate. There are other studies which indicate that increasing methane flow rate increases the amount of carbon deposited [219, 220].

<b>Table 5-3</b> CHN analysis for the post-reaction of 0.4 wt % Pd/H-ZSM-5 catalyst at different CH <sub>4</sub> flow rates.				
<b>Catalyst</b>	<b>Flow rate (mL/min)</b>	<b>Mean value, wt%</b>		
		<b>C</b>	<b>H</b>	<b>N</b>
<b>0.4 % Pd/H-ZSM-5</b>	<b>12</b>	<b>10.80 ± 0.10</b>	<b>0.50 ± 0.04</b>	<b>-</b>
	<b>24</b>	<b>13.29 ± 0.00</b>	<b>0.30 ± 0.00</b>	<b>-</b>
	<b>36</b>	<b>14.52 ± 1.60</b>	<b>0.35 ± 0.04</b>	<b>-</b>
	<b>48</b>	<b>14.92 ± 1.45</b>	<b>0.31 ± 0.01</b>	<b>-</b>

TGA studies in the presence of air have been performed for the post-reaction 0.4 % Pd/H-ZSM-5 catalysts. Figures 5-11 and 5-12 show the TGA profiles. From Figure 5-11, it can be seen that there is a weight loss before 250 °C, which is attributed to desorption of water. In addition, the weight loss in the region between 600 to 700 °C resulting from the loss of deposited carbon. Once again, it can be observed that the results of TGA and CHN analysis are in good agreement.

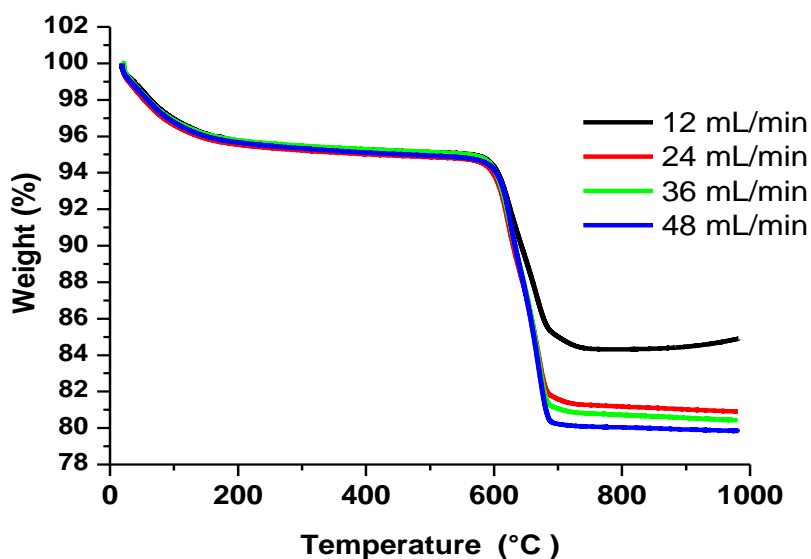


**Figure 5-11** TGA profiles for the post-reaction of 0.4 wt % Pd/H-ZSM-5 catalyst at different CH<sub>4</sub> flow rates.

Figure 5-12 displays the first-derivative weight changes profiles for the post-reaction 0.4 % Pd/H-ZSM-5 catalysts at different CH<sub>4</sub> flow rate. These profiles illustrate the differences between the samples more clearly. It can be seen that there are three peaks in the burning-off-coke region at *ca.* 615, 665 and 715 °C, suggesting that different types of carbonaceous species were deposited. Also, it can be noted that all samples have the same types of carbon species except for the catalyst run at the highest flow rate where there are only two regions of coke loss, 615 and 665 °C. Furthermore, it is observed that the area of the peaks at 615 and 665 °C gradually increased with increasing flow rate as a result of the amount of carbon deposited, whilst the peak at 715 °C gradually decreased with increasing the flow rate from 12 to 36 mL/min and completely disappeared at the flow rate of 48 mL/min. It was mentioned in previous section that the region between 500 to 700 °C related to filamentous carbons and graphitic carbon. However, SEM images (will be showed and discussed later) suggested that the amount of filamentous carbons formed gradually decreased with increasing flow rate.

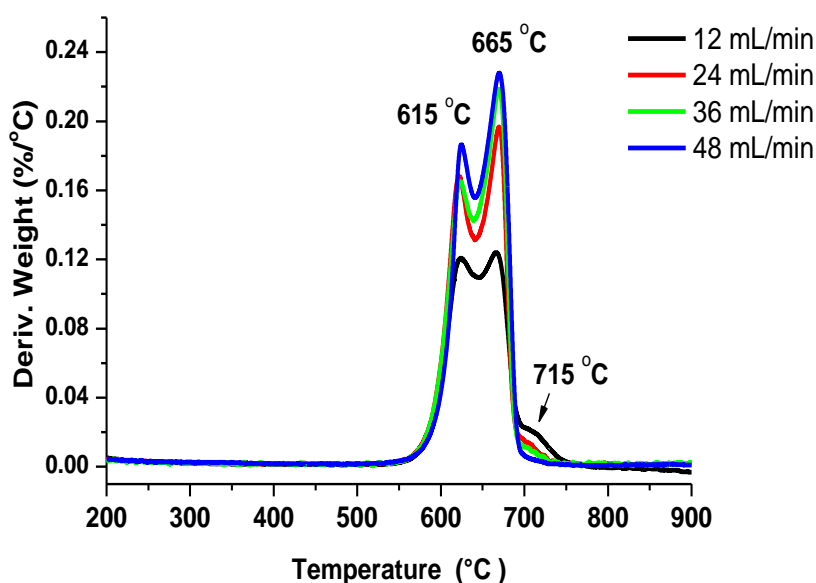


**Figure 5-12** TGA profiles for the post-reaction of 0.4 wt % Pd/H-ZSM-5 catalyst at different CH<sub>4</sub> flow rates.

#### 5.4.5 Post-reaction SEM images

Figure 5-13 illustrates the SEM images of carbons deposited on 0.4 wt % Pd/H-ZSM-5 catalyst at different CH<sub>4</sub> flow rates at 800 °C. From these images, it can be seen that the variation of the CH<sub>4</sub> flow rate seemed to play a role in the growth rate and density of

carbon filaments. It is observed that the growth of carbon filaments decreased with increasing methane flow rate. The significant growth of carbon filaments with different diameters is observed at 12 mL/min, whilst low growth of carbon filaments is noted at 48 mL/min. At 24 mL/min, it can be seen that the density of carbon filaments is apparently lower than that at 12 mL/min. Also, the diameter of filamentous carbon seems smaller and more uniform. The filamentous carbon formed at 36 mL/min is less dense compared to that formed at 24 mL/min. Moreover, the image for post-reaction 0.4 wt% Pd/H-ZSM-5 catalyst at 48 mL/min showed a high reduction in the filamentous carbon growth. It can be suggested that the increase of flow rate led to the rapid deposition of carbon on the catalyst surface, which covered the active sites. As a result, hydrogen production and the growth rate of filamentous carbon are reduced. In addition, it may be possible that the high flow rate favours encapsulation type carbon for active particles by formed graphene layers, which deactivated hydrogen production and the growth of filamentous carbon.

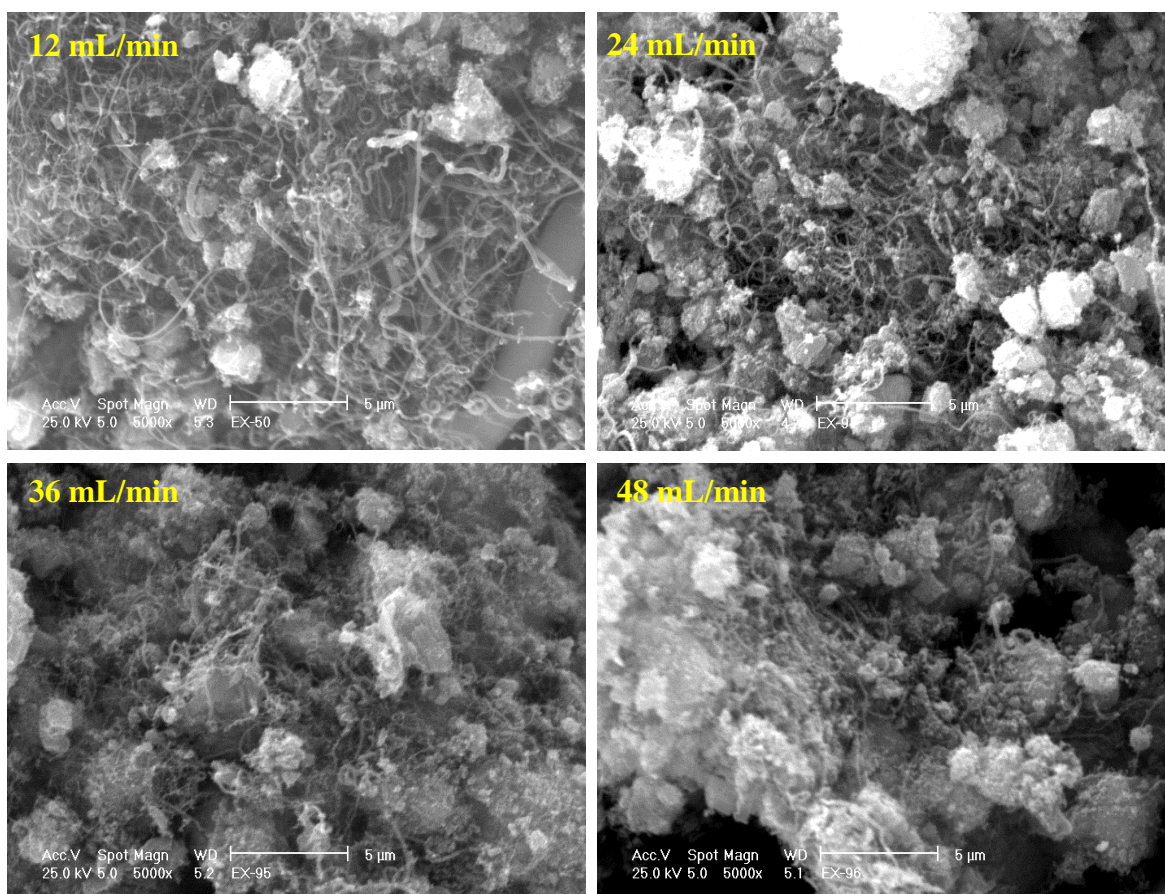


**Figure 5-13** Post-reaction SEM images for 0.4 wt% Pd/H-ZSM-5 catalyst at different CH<sub>4</sub> flow rates in the range from 12 to 48 mL/min.

### 5.4.6 Raman spectroscopy

The Raman spectra for the post-reaction 0.4 wt % Pd/H-ZSM-5 catalysts were measured. The Raman spectra are shown in Figure 5-14. It can be seen that there are two main bands at  $1350\text{ cm}^{-1}$  (D band) and at  $1596\text{ cm}^{-1}$  (G band), which reveals the presence of graphitic structural carbon.

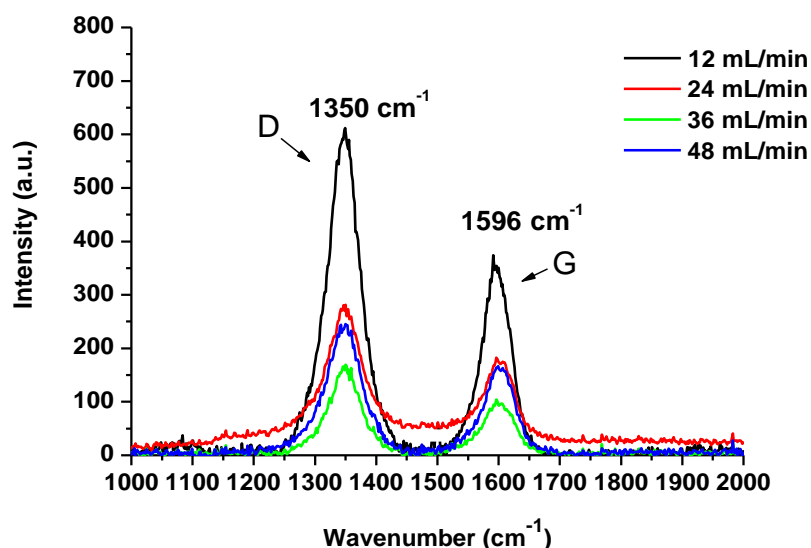


**Figure 5-14** Raman spectra for the post-reaction 0.4 wt % Pd/H-ZSM-5 catalyst at different  $\text{CH}_4$  flow rates in the range of 12 to 48 mL/min.

The intensity ratios  $I_D/I_G$  of the D band and G band are presented in Table 5-4. Again the intensity ratio  $I_D/I_G$  calculated based on the bands area. It can be seen from the data in Table 5-4 that the highest  $I_D/I_G$  value was noted after reaction at flow rate of 12 mL/min ( $I_D/I_G=1.97$ ), indicating that the graphitisation degree is the most disordered, while the lowest value was observed after reaction at flow rate of 24 mL/min ( $I_D/I_G=1.50$ ), which indicates the lowest apparent degree of disorder amongst all samples.

**Table 5-4** The result of intensity ratio  $I_D/I_G$  for the D and G bands from Raman spectra for carbon produced at different  $\text{CH}_4$  flow rates in the range from 12 to 48 mL/min.

Catalyst	Flow rate (mL/min)	Peak area ratio ( $I_D/I_G$ )
0.4 wt% Pd/H-ZSM-5	12	1.97
	24	1.50
	36	1.68
	48	1.70

## 5.5. Effects of dopants on the activity of 0.4 wt% Pd/H-ZSM-5 catalyst for direct cracking of methane

### 5.5.1 Introduction

Promotion of activity involves the enhancement of at least one of the catalyst properties, with respect to product formation, by the addition of a minor component. These properties are conversion improvement, selectivity enhancement and increased catalyst lifetime.

Generally, it has been reported in many studies that the presence of a second metal in the catalyst systems can have a significant influence on activity. However, for methane decomposition over Pd-based catalysts, very few studies of this have been reported. Ogihara *et al.* [63] studied the effect of doping with Ni, Cu, Co, Fe, Ag and Rh on the activity of Pd /Al<sub>2</sub>O<sub>3</sub> catalyst for hydrogen production from methane decomposition at 973 K. They found that all metals added to the Pd/Al<sub>2</sub>O<sub>3</sub> catalyst led to high activity and long life time except for the addition of Ag which led to deactivation.

On the other hand, palladium has been found to be a good dopant for other catalyst systems for the methane decomposition reaction. For example, it was found that the addition of Pd to Fe/Al<sub>2</sub>O<sub>3</sub> catalyst enhanced its activity [46]. Also, it was reported that the introduction of Pd into the Ni/SiO<sub>2</sub> catalyst improved significantly the catalytic life and hydrogen yield [221].

From the results of the effect of the reaction temperature study (the first section of this chapter) on the activity of 0.4 wt% Pd/H-ZSM-5, it was observed that the temperature of 800 °C resulted in the highest initial burst of hydrogen which was followed by a sharp decline in hydrogen production. This behaviour was not observed for the other reaction temperatures, which showed a gradual increase in the hydrogen production rate, as shown in Figure 5-1.

In an attempt to enhance the performance and stability of 0.4 wt% Pd/H-ZSM-5 catalyst at 800 °C, the catalyst was modified by addition of other metal species. Transition metals such as Fe, Ni and Co are known to possess the highest activity for methane cracking in general [40, 51, 55, 56, 126, 179, 222]. Hence, Fe<sup>3+</sup>, Ni<sup>2+</sup>, Co<sup>2+</sup> and Cu<sup>2+</sup> were added to the 0.4 wt% Pd/H-ZSM-5 catalyst as dopants. The choice of copper metal as promoter in this study was based upon a number of studies which demonstrated the role of copper in

improving the performance and stability of nickel-based catalysts for the methane decomposition reaction [60, 223, 224].

It should be mentioned that the molar ratio of the dopant metal added ( $M = \text{Fe}^{3+}$ ,  $\text{Ni}^{2+}$ ,  $\text{Co}^{2+}$  and  $\text{Cu}^{2+}$ ) to Pd/H-ZSM-5 was 0.25 (M/Pd). A number of characterisation techniques such as XRD, TGA, CHN elemental analysis and SEM have been applied to characterise the resultant pre- and post-reaction catalysts.

### 5.5.2 Reaction data

The effect of the addition of  $\text{Fe}^{3+}$ ,  $\text{Ni}^{2+}$ ,  $\text{Co}^{2+}$  and  $\text{Cu}^{2+}$  dopants on the activity 0.4 wt% Pd/H-ZSM-5 catalyst was investigated. Figure 5-15 shows the hydrogen formation rates as a function of time on stream for methane cracking over 0.4 wt% Pd/H-ZSM-5 catalyst and those doped with  $\text{Fe}^{3+}$ ,  $\text{Ni}^{2+}$ ,  $\text{Co}^{2+}$  and  $\text{Cu}^{2+}$ . The molar ratio of the dopant metal (M) added to Pd/H-ZSM-5 was 0.25 (M/Pd). From the hydrogen production profiles in Figure 5-15, it is observed that the addition of these dopants reduced the performance of 0.4 wt% Pd/H-ZSM-5 throughout the run. The  $\text{Cu}^{2+}$  doped 0.4 wt% Pd/H-ZSM-5 catalyst showed initially the lowest hydrogen formation rate compared to other catalysts, which gradually dropped and was similar to those doped with  $\text{Fe}^{3+}$ ,  $\text{Ni}^{2+}$ , and  $\text{Co}^{2+}$  at extended times on stream. In addition, the  $\text{Ni}^{2+}$  doped 0.4 wt% Pd/H-ZSM-5 catalyst displayed a high initial hydrogen formation rate, which is higher than Cu-Pd/H-ZSM-5 catalyst and lower than Fe-Pd/H-ZSM-5 and Co-Pd/H-ZSM-5.

However, it is noted that the behaviour of all doped catalysts is similar to the parent 0.4 wt% Pd/H-ZSM-5 catalyst where there was the initial burst in  $\text{H}_2$  formation followed by a sharp drop, except for the Cu-Pd/H-ZSM-5 catalyst which demonstrated a more gradual decrease. This may suggest that the presence of these dopants in the catalyst led to obstruction of part of the active sites of the palladium *i.e.* a part of the palladium content is still active whereas the other part is not due to obstruction. This finding is somewhat surprising especially these metals ( $\text{Fe}^{3+}$ ,  $\text{Ni}^{2+}$  and  $\text{Co}^{2+}$ ) are known to be active for methane cracking. As mentioned in the introduction of this section, it was found that the addition of Fe, Ni and Co into Pd/ $\text{Al}_2\text{O}_3$  catalyst enhanced its activity especially Pd-Ni/ $\text{Al}_2\text{O}_3$  and Pd-Co/ $\text{Al}_2\text{O}_3$  displayed the highest hydrogen yields from methane cracking [63]. Also, it was shown that the addition of Pd into Ni/ $\text{SiO}_2$  catalyst improved the catalytic performance for methane decomposition [221].

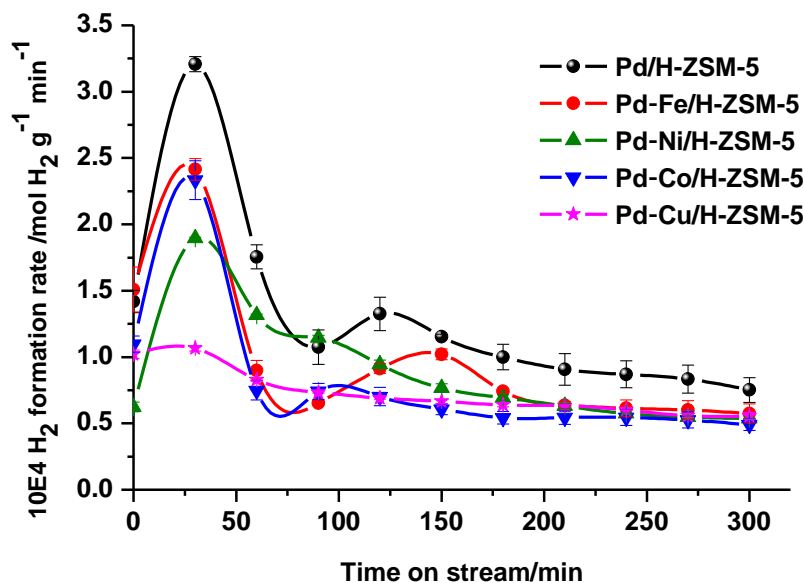


**Figure 5-15** Hydrogen formation rates as a function of time on stream for the parent 0.4 wt % Pd/H-ZSM-5 catalyst, and those doped with  $\text{Fe}^{3+}$ ,  $\text{Ni}^{2+}$ ,  $\text{Cu}^{2+}$  and  $\text{Co}^{2+}$  (dopant metal M/Pd atomic ratio of 0.25), the reaction temperature was 800 °C and 0.4 g catalyst mass.

It may be that these metals are inactive in the presence of the zeolite support and/or that access to the Pd metal is limited by coverage and/or pore blockage by the 1<sup>st</sup> row transition metal dopants. Therefore, Fe/H-ZSM-5, Ni/H-ZSM-5, Co/H-ZSM-5 and Cu/H-ZSM-5 catalysts were prepared to test their activity for methane cracking. Preparation of these catalysts employed the same method as for the parent catalyst and their loadings were equivalent to the parent catalysts.

Figure 5-16 displays the hydrogen formation rates as a function of time on stream for methane cracking over calcined H-ZSM-5 (support), 0.1 wt% Fe/H-ZSM-5, 0.1 wt% Ni/H-ZSM-5, 0.1 wt% Co/H-ZSM-5 and 0.1 wt% Cu/H-ZSM-5 catalysts. It can be seen that the activity of 0.1 wt% Fe/H-ZSM-5 and 0.1 wt% Co/H-ZSM-5 catalysts are low and quite similar to the support (calcined H-ZSM-5), while 0.1 wt% Ni/H-ZSM-5 and 0.1 wt% Cu/H-ZSM-5 catalysts had higher activities.

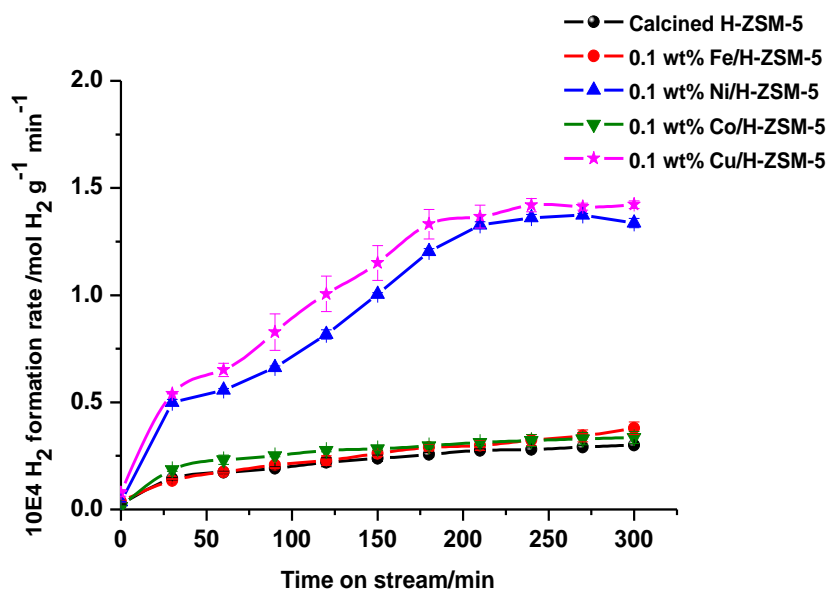


**Figure 5-16** Hydrogen formation rates as a function of time on stream for methane cracking over calcined H-ZSM-5, 0.1 wt % Fe/H-ZSM-5, 0.1 wt % Ni/H-ZSM-5, 0.1 wt % Co/H-ZSM-5 and 0.1 wt % Cu/H-ZSM-5 catalysts, the reaction temperature was 800 °C, the methane flow rate was 12 mL/min and 0.4 g catalyst mass.

From the results in Figure 5-16, it seems that there is a so-called strong metal-support interaction effect (SMSI) for 0.1 wt% Fe/H-ZSM-5 and 0.1 wt% Co/H-ZSM-5 *i.e.* there is strong interaction between the Fe and Co with the zeolite (support). The strong MSI may lead to the difficulty of reduction of the precursor oxide which may require higher temperatures or even be irreducible. Also, the strong MSI prevents metal mobility on the support [225, 226]. Therefore, it may be that SMSI resulted in the low activity of 0.1 wt% Fe/H-ZSM-5 and 0.1 wt% Co/H-ZSM-5 catalysts. On the other hand, this effect may be absent in the case of 0.1 wt% Ni/H-ZSM-5 and 0.1 wt% Cu/H-ZSM-5 catalysts, meaning that these metal ions were more easily reduced leading to enhanced activity. Furthermore, it could be that Ni and Cu possess mobility on the surface of zeolite.

From the above, it can be suggested that Fe and Co species are segregated in the 0.4 % Pd/H-ZSM-5 catalyst as a result of strong MSI and possibly deactivate a part of the Pd sites around where it is situated or blocked part of the Pd sites. It is pertinent to note that the addition of these metals is made after the addition of palladium into zeolite during the preparation procedures. If the additional metal located at the mouth of the channels, pore blockage could result limiting accessibility to the more active intra-channel dispersed Pd species. Another possible reason may be that there is the formation of a mixed phase such

as Fe-Pd and Co-Pd, which displays different behaviour from the Pd-alone containing phase.

It was reported that the formation of Ni carbides ( $\text{Ni}_3\text{C}$ ) during methane decomposition over Ni- based catalyst lead to the deactivation of the catalyst [227, 228]. Takenaka *et al.* [229] studied the methane decomposition into hydrogen and carbon nanofibres over Ni/SiO<sub>2</sub> and Pd-Ni/SiO<sub>2</sub> catalysts. They revealed that the addition of Pd into Ni/SiO<sub>2</sub> enhanced the catalytic activity and life for methane decomposition into hydrogen and carbon nanofibres. These catalysts was characterised by measuring the Ni and Pd K-edge XANES and EXAFS. The characterisation showed that Ni metal in the Ni/SiO<sub>2</sub> catalyst was transformed into Ni carbides at the deactivation period, while the Pd-Ni/SiO<sub>2</sub> catalyst did not show a change in the structure and average crystallite size during methane decomposition and it was resistant to phase transformation. It seems possible that the addition of Ni into Pd/H-ZSM-5 catalyst did not form Ni-Pd alloy, which is considered an active phase for methane decomposition. It may be that the support has played a role in the lack of Ni-Pd formation. Therefore, the effect of Ni and Cu can be explained considering mobility on the surface of zeolite. The higher mobility of Ni and Cu particles at reaction temperature of 800 °C may be caused the sintering or/and agglomeration of Ni or Cu particles and thus prevent methane molecules to contact with palladium particles (more active sites) or even may have led to the formation of carbides. In addition, it could be that there is a formation of a mixed phase of Cu-Pd, which may has low activity compared to the Pd containing phase alone.

Moreover, the nature of the carbon deposited should be considered where these dopants added to Pd/H-ZSM-5 may have led to the formation of encapsulation carbon resulting in the deactivation of catalyst. Further investigations are required to explain more about these negative effects.

### 5.5.3 XRD patterns

Figure 5-17 (A, B) presents the XRD patterns for the pre and post-reaction catalysts. All XRD patterns of the pre and post-reaction catalysts for the parent 0.4 wt% Pd/H-ZSM-5 and those doped with Fe, Ni, Co and Cu completely matched with the pattern of H-ZSM-5, which indicates that the reaction conditions and the modification procedures has no obvious effect on the zeolite structure. Palladium or dopant metal phases were not apparent.

It is observed that there are differences between the relative intensities of the reflections at  $8-9^\circ$  and  $23-25^\circ$   $2\theta$  between the pre-reaction and post-reaction catalysts. It can be seen that the intensities of peaks at  $8-9^\circ$   $2\theta$  in the post-reaction catalysts are higher than those in pre-reaction catalysts particularly in the post-reaction Cu-Pd/HZSM-5, Ni-Pd/HZSM-5 and Co-Pd/HZSM-5 catalysts. Also, it is noted that the intensities of these peaks in the post-reaction Cu-Pd/HZSM-5 is the highest among all catalysts.

It was reported that the intensities of peaks below  $10^\circ$   $2\theta$  in the pattern of ZSM-5 are sensitive to the presence of any species inside the channels where the intensities of peaks decrease when metals occupy the channels of zeolite [230]. Therefore, it can be suggested that the addition of these metals into the parent 0.4 wt% Pd/H-ZSM-5 catalyst lead to low dispersion of these metal as well as palladium on the zeolite channels and keep them on the external surface of zeolite crystals. This also suggests the occurrence of sintering or/and agglomeration of palladium with dopant metals on the external surface of zeolite. On the other hand, it may be that there is high dispersion and too small particle size of metals on the surface of the zeolite, which is inactive for methane cracking. As mentioned in the previous chapter, the catalyst performance in the methane cracking is highly dependent on the metal particle size and there is optimisation for the size of particles where too small or too big metal particles could be inappropriate.

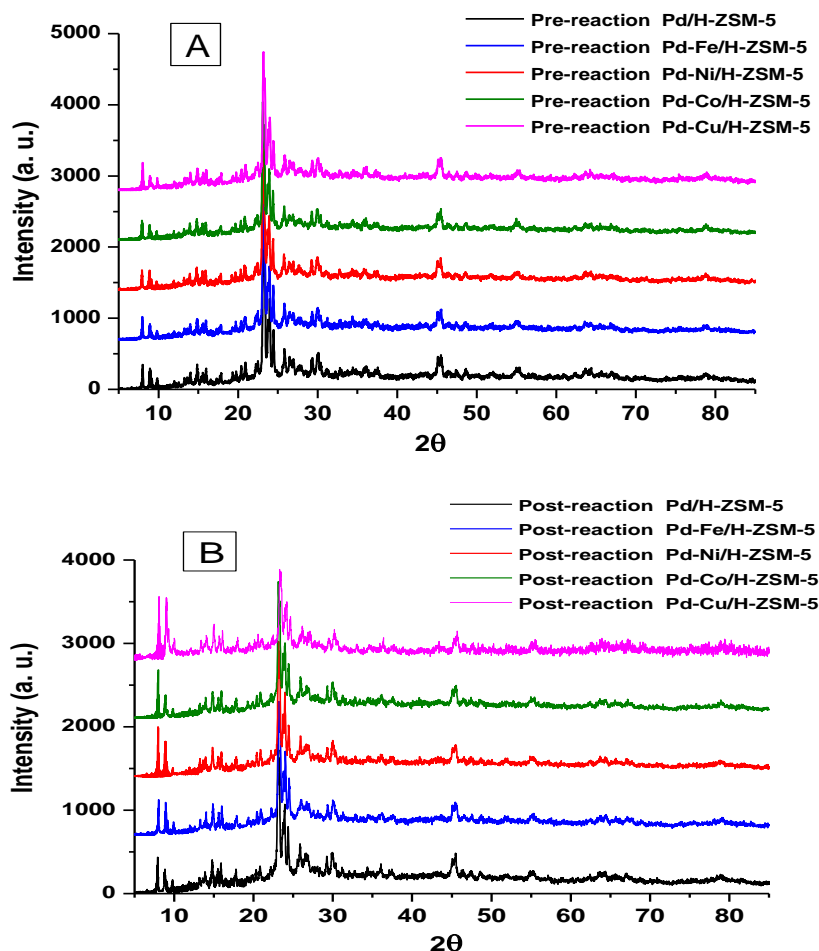


**Figure 5-17** XRD patterns of 0.4 wt % Pd/H-ZSM-5 and those doped with Fe, Ni, Co and Cu in the pre-reaction (A) forms, and post-reaction (B) forms, dopant metal M/Pd atomic ratio of 0.25.

### 5.5.4 Post-reaction CHN and TGA analysis

The post-reaction CHN analyses of the doped catalysts and the 0.4 wt% Pd/H-ZSM-5 catalyst are presented in Table 5-5. It is evident from the results that all doped catalysts show low quantities of carbon deposited on them compared to the non-doped parent catalyst, 0.4 wt% Pd/H-ZSM-5. It can be observed that the largest amount of carbon deposited was observed for the non-doped catalyst, 10.80 wt%, whereas the Cu<sup>2+</sup> doped catalyst has the lowest amount of carbon deposited, 4.25 wt%. The carbon content in the Fe and Ni doped catalyst is almost similar, which is *ca.* 8.20 wt%. The quantity of carbon deposited on the Co<sup>2+</sup> doped catalyst is *ca.* 6.05 wt%, which is smaller than the parent catalyst, 0.4 wt% Pd/H-ZSM-5, and those doped with the Fe and Ni. It seems that the catalyst activity can be correlated with the amount of carbon deposited.

**Table 5-5** CHN analysis for the post-reaction 0.4 wt % Pd/H-ZSM-5 catalyst and those doped with Fe, Ni, Co and Cu (dopant metal M/Pd atomic ratio of 0.25).

Catalyst	Mean value, wt%		
	C	H	N
0.4 wt % Pd/H-ZSM-5	10.80 ± 0.10	0.50 ± 0.04	-
Fe <sup>3+</sup> doped 0.4 wt % Pd/H-ZSM-5	8.17 ± 0.10	0.30 ± 0.00	-
Ni <sup>2+</sup> doped 0.4 wt % Pd/H-ZSM-5	8.20 ± 0.50	0.30 ± 0.00	-
Co <sup>2+</sup> doped 0.4 wt % Pd/H-ZSM-5	6.05 ± 0.16	0.30 ± 0.00	-
Cu <sup>2+</sup> doped 0.4 wt % Pd/H-ZSM-5	4.25 ± 0.10	0.41 ± 0.00	-

TGA studies of the oxidation of post-reaction carbon species have been carried out. The TGA profiles recorded for the 0.4 wt% Pd/H-ZSM-5 and those doped with Fe, Ni, Co and Cu are displayed in Figure 5-18.

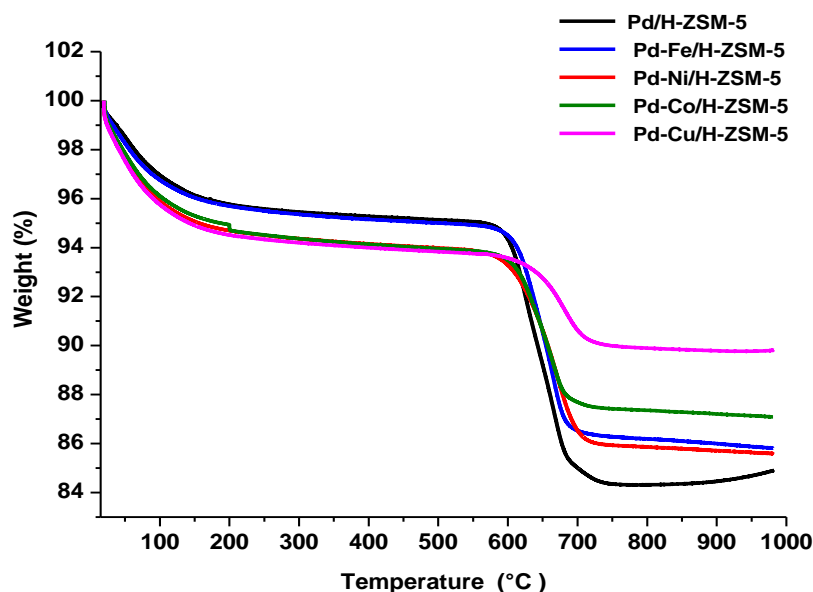


**Figure 5-18** TGA profiles of post-reaction 0.4 wt % Pd/H-ZSM-5 and those doped with Fe, Ni, Co and Cu (dopant metal M/Pd atomic ratio of 0.25).

As can be seen from the profiles in Figure 5-18, there is a low weight loss below 250 °C, which is ascribed to desorption of adsorbed water on the catalyst, while the major weight loss is that in the region from 600 to 750 °C resulting from the oxidation of carbon deposited. Furthermore, it can be observed that there is good agreement between the results of CHN and TGA analysis.

The first-derivative weight changes profiles for the post-reaction for the 0.4 wt% Pd/H-ZSM-5 and those doped with Fe, Ni, Co and Cu are also presented in Figure 5-19.

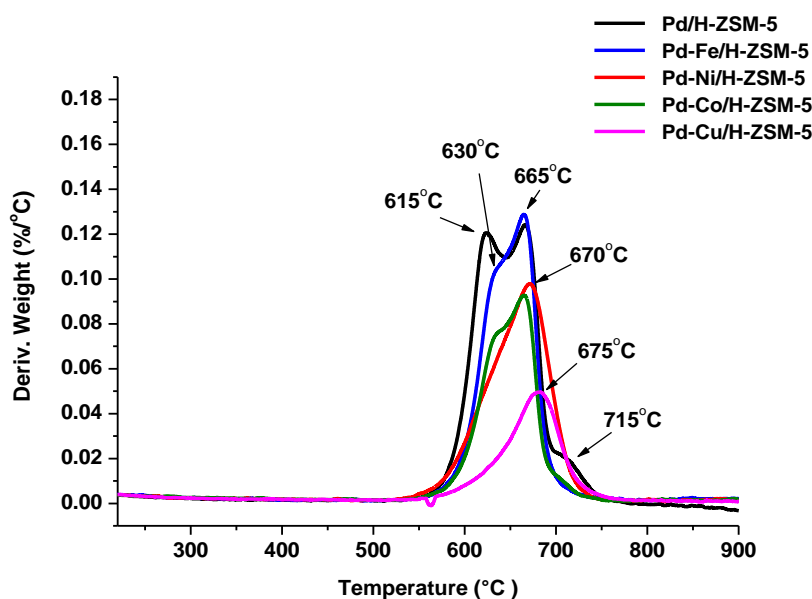


**Figure 5-19** TGA profiles for the post-reaction 0.4 wt % Pd/H-ZSM-5 and those doped with Fe, Ni, Co and Cu (dopant metal M/Pd atomic ratio of 0.25).

From Figure 5-19, it can be seen that there is a difference between the carbons deposited on these catalysts. The non-doped catalyst showed three regions of weight loss at roughly 615, 665 and 715 °C, which relates to different species of carbon deposited, possibly carbon nanotube, carbon nanofibre and/or graphitic carbon. As previously mentioned amorphous carbon is oxidised about 330 °C. Hence, it seems that it is not formed in these samples. However, the third oxidation region for the non-doped catalyst of 0.4 wt% Pd/H-ZSM-5 was missing in all doped catalysts. The catalysts doped with Fe<sup>3+</sup> and Co<sup>2+</sup> showed main peak oxidation at approximately 665 °C and a small shoulder to the main peak that was almost 630 °C. The main peak oxidation is corresponding to second oxidation region in the parent catalyst of 0.4 wt% Pd/H-ZSM-5, which indicates they may have one species of carbon. With respect to the catalysts doped with Ni<sup>2+</sup> and Cu<sup>2+</sup>, it is apparent that there is only one oxidation region at 670 and 675 °C, respectively.

One of the factors affecting on the nature of the carbon formed is the nature of active phase. From above, it was noted that there is a similarity in the nature of the carbon deposited on the parent catalyst of 0.4 wt% Pd/H-ZSM-5 and those doped with Fe<sup>3+</sup> and Co<sup>2+</sup>. In addition, it was observed that the non-doped catalyst and those doped with Fe<sup>3+</sup>

and  $\text{Co}^{2+}$  had similar profiles for hydrogen production regardless of their activity. Therefore, it can be suggested that the  $\text{Fe}^{3+}$  and  $\text{Co}^{2+}$  dopants had a lower effect on metallic Pd in the 0.4 wt% Pd/H-ZSM-5 catalyst resulting in an unaffected fraction of metallic Pd. The  $\text{Ni}^{2+}$  and  $\text{Cu}^{2+}$  dopants had a greater effect on metallic Pd in the parent catalyst, which led to different behaviour for hydrogen production and the formation of different species of carbon.

### 5.5.5 Post-reaction SEM images

Figure 5-20 (A-E) presents the SEM images for the post-reaction non-doped 0.4 wt% Pd/H-ZSM-5 catalyst (A) and those doped with Fe, Ni, Co and Cu (B-E). From the images, it can be seen that filamentous carbon was formed over all catalysts. It is hard to determine the growth mechanism of these filaments. However, it is observed that the doped catalysts showed filamentous carbons, which are possibly thinner than those in the non-doped 0.4 wt% Pd/H-ZSM-5 catalyst although caution must be exercised in view of the statistical limitations of this observation. From the SEM image in Figure 5-20 (E), it can be observed that the filamentous carbons formed on Pd-Cu/HZSM-5 are the thinnest and smallest compared to the filamentous carbon formed on all another catalysts.

The size of metal particle is believed to affect the diameters of the resulting filamentous carbon [231]. Many studies have been reported that the carbon nanotube (CNT) diameter is determined by the catalyst particle size [232-234]. Cheung *et al.* [235] used iron nanoclusters with average values of diameter of 3, 9 and 13 nm to define the diameters of carbon nanotubes grown by chemical vapor deposition (CVD). They found that the average diameters of carbon nanotubes produced are roughly 3, 7 and 12 nm, respectively, which is related to the diameters of the metal particles. Suelves and co-workers [236] studied the performance of a NiCu/MgO catalyst for catalytic methane decomposition reaction. They demonstrated that the type of carbon formed is nanofibre structure with diameters that correlated with the nickel particle size.

Wen *et al.* [237] prepared Pd/ZSM-5 and Pd-Fe/ZSM-5 by exchanging Pd from a dilute aqueous solution of  $[\text{Pd}(\text{NH}_3)_4](\text{NO}_3)_2$  into either H/ZSM-5 or Fe/ZSM-5. They found that there is a significant difference between Pd/ZSM-5 and Pd-Fe/ZSM-5 after calcination. The Pd in Pd/ZSM-5 is present as large PdO particles, but in Pd-Fe/ZSM-5 it is highly

dispersed over the zeolite. Also, the authors suggested that the Fe ions and/or Fe oxo ions act as very effective chemical anchors.

Ogura *et al.* [238] prepared Pd-Co/ZSM-5 catalyst by ion-exchange for reduction of nitric oxide (NO) with methane as a reductant. They showed that Pd and Co are well dispersed inside the zeolite when the concentrations of Pd and Co are less than 1 wt%. While the increase of Co loading causes aggregation of Pd on the ZSM-5.

According to the above and to our SEM images in Figure 5-20, it can be proposed that the addition of these metals (Fe, Ni, Co and Cu) into 0.4 wt% Pd/H-ZSM-5 catalyst led to increase the palladium dispersion. This effect would normally enhance the performance of doped catalysts but the opposite effect was observed. Therefore, the effect of the nature of the carbon deposited must be taken into account.

It was observed in the SEM images in Figure 5-20, that carbon filaments were formed over all post-reaction catalysts and it was difficult to determine their growth mechanism due to the metal particles not being apparent. Hence, a higher magnification image of 0.4 wt% Pd/H-ZSM-5 doped with Ni was studied. The image is illustrated in Figure 5-21. It can be seen from the image that there are bright spots, marked with arrows, in the middle of the filaments of carbon. This suggested that the metal particles are encapsulated inside the carbon filaments (penetration of metal atoms deep into the filament), which prevents access of the methane molecules. This type of deactivation by formation of the encapsulated carbon for the metal active sites is so-called intercalation or erosion [239].

In general, it may be that the addition of these metals into 0.4 wt% Pd/H-ZSM-5 catalyst formed encapsulated carbon for catalyst particles, which caused deactivation for the performance of the doped catalysts. HRTEM analysis would be required for more detailed investigation about the location of metal particles in the filamentous carbon and the zeolite.

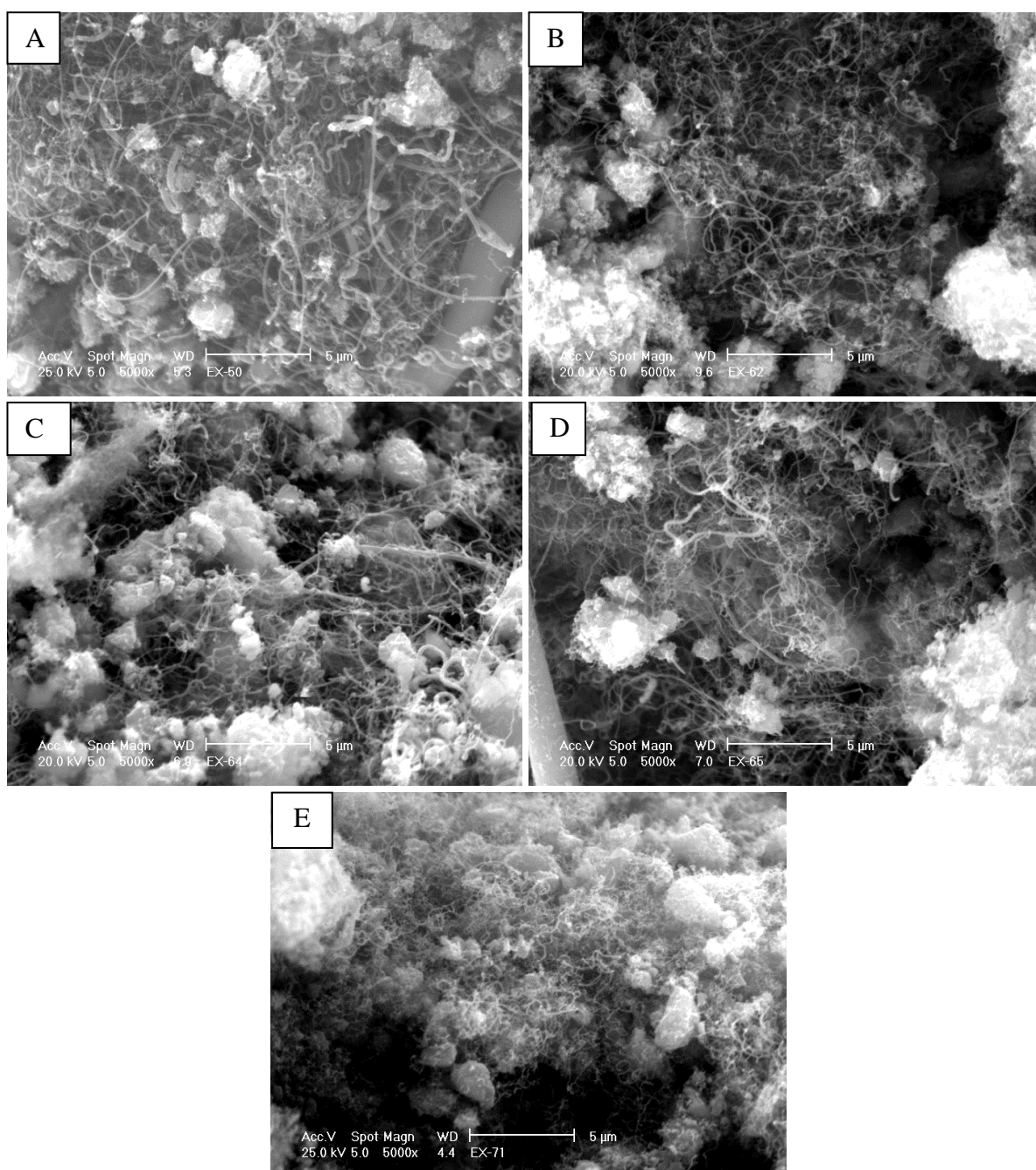


**Figure 5-20** SEM images of post-reaction (A) non-doped catalyst 0.4 wt % Pd/H-ZSM-5, (B) doped with  $\text{Fe}^{3+}$ , (C) doped with  $\text{Ni}^{2+}$ , (D) doped with  $\text{Co}^{2+}$  and (E) doped with  $\text{Cu}^{2+}$  (dopant metal M/Pd atomic ratio of 0.25).

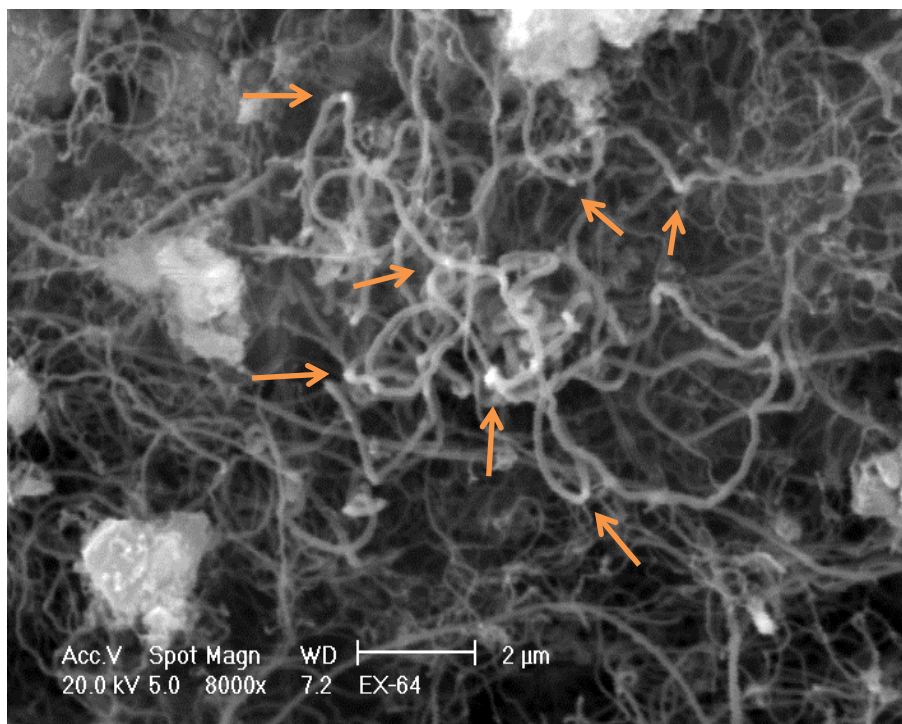


**Figure 5-21** SEM image of post-reaction Pd-Ni/H-ZSM-5 (dopant metal Ni/Pd atomic ratio of 0.25).

## 5.6. The effect of palladium precursor on the activity of 0.4 wt% Pd/H-ZSM-5 catalyst for direct cracking of methane

### 5.6.1 Introduction

The nature of the precursor salt plays a significant role in both the nature of the species present on the catalyst surface, and on its surface area. It was found that the type of the precursor employed can affect the dispersion of Pd and the form in which it occurs on the surface of supported catalyst [240, 241]. From reviewing the literature and regardless of the support type, it is apparent that the Pd precursor most frequently used for methane cracking into hydrogen and carbon is palladium chloride ( $\text{PdCl}_2$ ) [47, 63, 83, 221, 229] with a few studies emphasising palladium nitrate ( $\text{Pd}(\text{NO}_3)_2$ ) [45, 46]. Surveying the literature, it seems that the effect of precursor has not been addressed. Therefore, the effect of the type of the palladium precursor in the preparation of 0.4 wt% Pd/H-ZSM-5 catalysts on their catalytic activity was studied in this section.

Three palladium precursors have been employed. Palladium chloride ( $\text{PdCl}_2$ ), palladium nitrate ( $\text{Pd}(\text{NO}_3)_2$ ) and palladium acetylacetonate  $\text{Pd}(\text{C}_5\text{H}_7\text{O}_2)_2$  were used as palladium sources for the preparation of the 0.4 wt% Pd/H-ZSM-5 catalysts.

The samples prepared from palladium chloride and nitrate were obtained by zeolite impregnation with aqueous solutions of these salts, whereas the sample prepared from palladium acetylacetonate was obtained by zeolite impregnation with a benzene solution of this precursor. The samples were named 0.4 wt% Pd/H-ZSM-5 (Cl), 0.4 wt% Pd/H-ZSM-5 (NO) and 0.4 wt% Pd/H-ZSM-5 (AcAc) catalysts relating to ( $\text{PdCl}_2$ ), ( $\text{Pd}(\text{NO}_3)_2$ ) and  $\text{Pd}(\text{C}_5\text{H}_7\text{O}_2)_2$  precursors, respectively.

### 5.6.2 Reaction data

The effect of the type of palladium precursors on the catalyst activity of 0.4 wt% Pd/H-ZSM-5 catalyst for hydrogen production from direct cracking of methane was studied. Figure 5-22 presents the hydrogen formation rates as a function of time on stream for methane cracking. It can be seen that the palladium precursor has strong effect on the catalyst activity. It was observed that the catalyst prepared from palladium nitrate, 0.4 wt% Pd/H-ZSM-5 (NO), had the highest hydrogen formation rate, while the catalyst prepared from palladium chloride, 0.4 wt% Pd/H-ZSM-5 (Cl), showed the lowest hydrogen formation rate. The catalyst prepared from palladium acetylacetonate, 0.4 wt% Pd/H-ZSM-5 (AcAc), showed initially medium activity and then dropped to have a similar performance of 0.4 wt% Pd/H-ZSM-5 (Cl) catalyst. In general, the 0.4 wt% Pd/H-ZSM-5 (NO) catalyst demonstrated the highest hydrogen formation rate throughout the run, whereas 0.4 wt% Pd/H-ZSM-5 (Cl) and 0.4 wt% Pd/H-ZSM-5 (AcAc) catalysts had similar behaviour beyond 90 minutes of time on stream despite the differences in the activities at the beginning of reaction. Furthermore, it is observed that the 0.4 wt% Pd/H-ZSM-5 (NO) and 0.4 wt% Pd/H-ZSM-5 (AcAc) catalysts showed an initial burst of hydrogen formation followed by rapid decline, while the 0.4 wt% Pd/H-ZSM-5 (Cl) catalyst showed gradual increase in hydrogen formation rate up to 60 minutes of time on stream followed by gradual decrease.

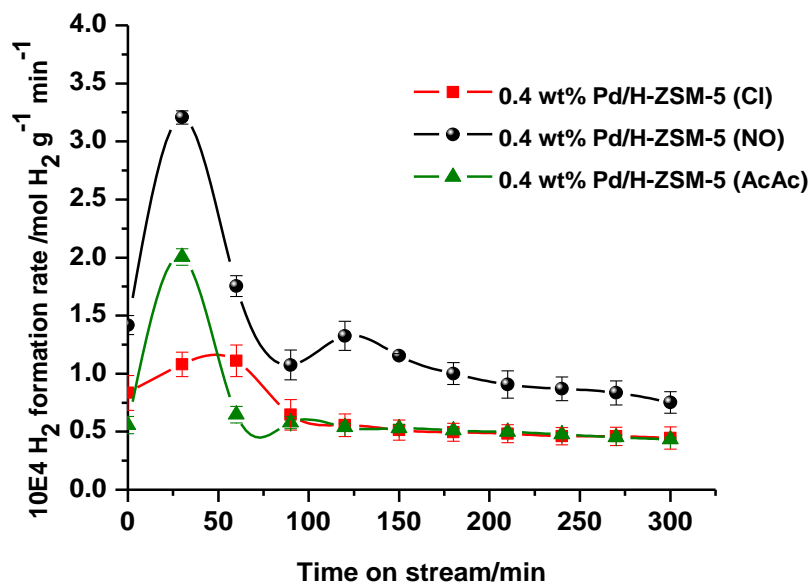


**Figure 5-22** Hydrogen formation rates as a function of time on stream for methane cracking over 0.4 wt % Pd/H-ZSM-5 catalyst prepared from different palladium precursors, the reaction temperature of 800 °C, the methane flow rate was 12 mL/min and 0.4 g catalyst mass.

Roth *et al.* [240] prepared a series of Pd/Al<sub>2</sub>O<sub>3</sub> catalysts by using several precursors (H<sub>2</sub>PdCl<sub>4</sub>, Pd(NO<sub>3</sub>)<sub>2</sub> and Pd(AcAc)<sub>2</sub>) for methane oxidation. Their characterisation showed that the highest Pd dispersions were obtained by using Pd(AcAc)<sub>2</sub> as a precursor, while the lowest dispersion was noted by using PdCl<sub>2</sub> as a precursor.

Andre *et al.* [242] used PdCl<sub>2</sub> and Pd(acac)<sub>2</sub> as a precursors for preparation of Pd/Al<sub>2</sub>O<sub>3</sub> and Pd/CeO<sub>2</sub>/Al<sub>2</sub>O<sub>3</sub> catalysts. They found that the dispersion of Pd in Pd/Al<sub>2</sub>O<sub>3</sub> catalyst was approximately equal for all precursors. Moreover, they observed that the dispersion of Pd in the Pd/CeO<sub>2</sub>/Al<sub>2</sub>O<sub>3</sub> catalyst became different where the PdCl<sub>2</sub> precursor led to low Pd dispersion.

Panpranot and co-workers [243] prepared a series of silica (SiO<sub>2</sub> and MCM-41)-supported Pd catalysts from different Pd precursors such as Pd(NO<sub>3</sub>)<sub>2</sub>, PdCl<sub>2</sub>, and palladium acetate (Pd(OOCCH<sub>3</sub>)<sub>2</sub>) for hydrogenation of 1-hexene reaction. They demonstrated that the use of PdCl<sub>2</sub> as a precursor for both SiO<sub>2</sub> and MCM-41 support resulted in smaller Pd particles and higher dispersion, while the other precursors showed close value of particle size and dispersion in all supports.

From above, it is possible to say that the type of the precursor plays an important role in the catalyst properties depending on the type of support used. Hence, on the basis of the literature cited, it could be suggested that the 0.4 wt% Pd/H-ZSM-5 catalyst prepared from the Pd(NO<sub>3</sub>)<sub>2</sub> precursor resulted in the highest dispersion and/or appropriate particle size for direct cracking of methane, whilst the 0.4 wt% Pd/H-ZSM-5 catalyst prepared from the PdCl<sub>2</sub> precursor resulted in the lowest dispersion and/or inappropriate particle size for the direct cracking of methane reaction.

Moreover, the size of these precursors may play an important role in the dispersion of palladium. Palladium chloride (PdCl<sub>2</sub>) has smaller size, which could lead to higher dispersion of palladium inside the zeolite channels. Blockage of channels can be occurred either by sintering of palladium or carbon deposition. As a result, this prevents the methane from access to the active sites, which result in low activity of catalyst. Palladium acetylacetonate Pd(C<sub>5</sub>H<sub>7</sub>O<sub>2</sub>)<sub>2</sub> has larger size, which may reduce or prevent the dispersion of palladium particles inside the zeolite channels and so it will probably remain on the outer surface of the zeolite. This can reduce the total dispersion of palladium on the support. In case of the palladium nitrate (Pd(NO<sub>3</sub>)<sub>2</sub>), it appears medium size, which can be dispersed in the channels and on the outer surface of the zeolite. This may explain the high performance of catalyst, prepared from palladium nitrate (Pd(NO<sub>3</sub>)<sub>2</sub>).

### 5.6.3 XRD patterns

Figure 5-23 (A, B) presents the XRD patterns for the pre and post-reaction 0.4 wt% Pd/H-ZSM-5 forms that prepared from different Pd precursors. From Figure 5-23 (A), it can be seen that the patterns of the pre-reaction catalysts display the characteristic reflections of H-ZSM-5 with the main 2θ values of *ca.* 8°, 9° and 23-25°. Again, no evidence of Pd-containing phases could be found. However, from these patterns, another different reason that might elucidate the different performance of catalysts can be investigated. As mentioned in the previous section, the intensities of peaks below 10° 2θ in the pattern of ZSM-5 are sensitive to the presence of any species inside the channels where the intensities of peaks decreases when metals occupy the channels of zeolite. Therefore, it is observed from the XRD patterns for the pre-reaction catalysts, Figure 5-23 (A), that the relative intensity of peaks at *ca.* 2θ 8° and 9° are higher in the order of Pd/H-ZSM-5 (AcAc) > Pd/H-ZSM-5 (NO) > Pd/H-ZSM-5 (Cl). This suggests that the palladium in Pd/H-ZSM-5 (Cl) catalyst is dispersed inside the channels of zeolite more than other catalysts, followed

by Pd/H-ZSM-5 (NO) catalyst. While the palladium in Pd/H-ZSM-5 (AcAc) is least dispersion inside the channels of zeolite. Hence, in case of Pd/H-ZSM-5 (Cl) catalyst, it may be the most of cracking of methane occurs inside zeolite channels, which may be trapped the palladium atoms in intersections of zeolite as result of carbon deposition and then preventing the access of methane molecules to the active site. Subsequently, the deactivation of catalyst occurs. Moreover, it seems that the Pd/H-ZSM-5 (NO) catalyst has highest deposition in both channels and outer surface of zeolite.

The patterns of the post-reaction catalysts are presented in Figure 5-23 (B). It can be observed that the reaction conditions and different palladium precursors did not affect on zeolite structure and they remain intact. In addition, the palladium crystals were not detected; it may be due to the reasons that mentioned earlier.

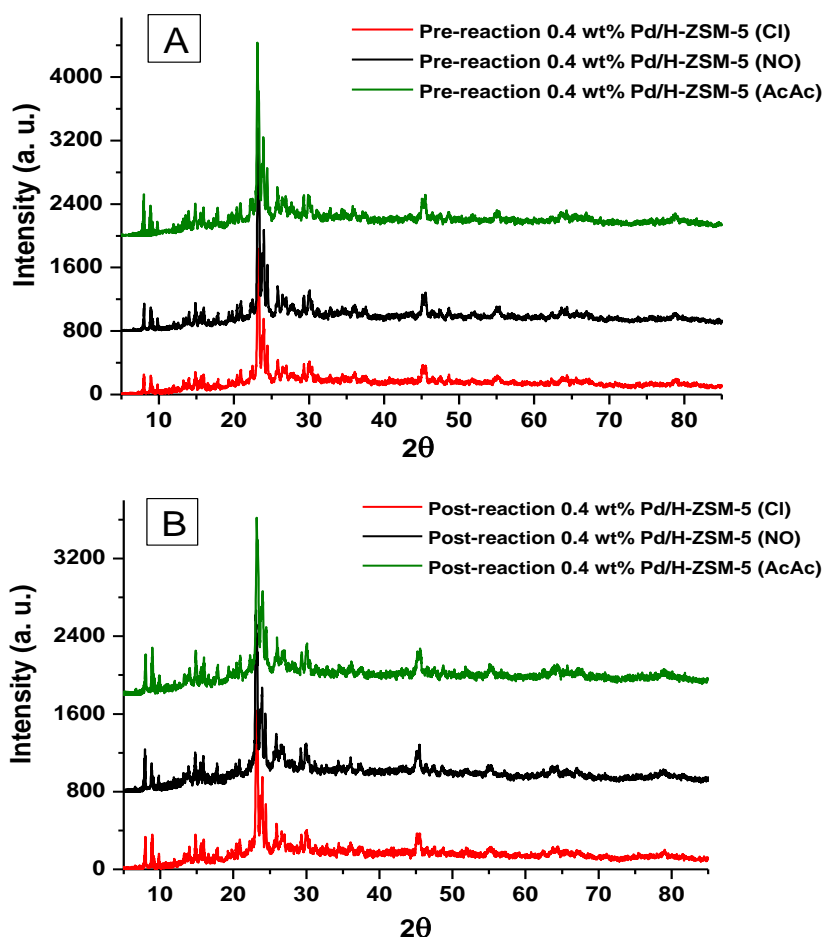


**Figure 5-23** XRD patterns of 0.4 wt % Pd/H-ZSM-5 in the pre-reaction (A) and post-reaction (B) forms that prepared from different Pd precursors.

### 5.6.4 Post-reaction CHN and TGA analysis

The post-reaction CHN analysis for the 0.4 wt% Pd/H-ZSM-5 catalysts prepared from different Pd precursors are presented in Table 5-6. It is evident from the results that there is a varying in the amount of carbon deposited on samples as a result of their reaction with methane. The largest amount of carbon deposition was observed for the 0.4 wt% Pd/H-ZSM-5 (NO) catalyst where it was 10.80 wt%, whereas that for the 0.4 wt% Pd/H-ZSM-5 (Cl) catalyst was much lower at 2.50 wt%. The amount of carbon deposited on the 0.4 wt% Pd/H-ZSM-5 (AcAc) was 6.10 wt%. Furthermore, these amounts of carbon deposited are in agreement with the reaction rates previously showed in Figure 5-22, *i.e.* the highest hydrogen formation rate was observed with the 0.4 wt% Pd/H-ZSM-5 (NO) catalyst, while the lowest hydrogen formation rate was observed with the 0.4 wt% Pd/H-ZSM-5 (Cl) catalyst.

<b>Table 5-6</b> CHN analysis for the post-reaction 0.4 wt% Pd/H-ZSM-5 catalyst prepared from different Pd precursors.			
<b>Catalysts</b>	<b>Mean value, wt%</b>		
	<b>C</b>	<b>H</b>	<b>N</b>
<b>0.4 wt% Pd/H-ZSM-5 (Cl)</b>	<b>2.50 ± 0.02</b>	<b>0.34 ± 0.04</b>	-
<b>0.4 wt% Pd/H-ZSM-5 (NO)</b>	<b>10.80 ± 0.10</b>	<b>0.50 ± 0.04</b>	-
<b>0.4 wt% Pd/H-ZSM-5 (AcAc)</b>	<b>6.10 ± 0.52</b>	<b>0.42 ± 0.01</b>	-

TGA studies in the presence of air were conducted for post-reaction samples that prepared from different Pd precursors. Figures 5-24 and 5-25 depict the TGA oxidation profiles under air and corresponding first-derivative profiles of the post-reaction samples, respectively.

It can be observed from Figure 5-24 that there is weight loss before 250 °C, which is attributed to desorption of adsorbed water. Additionally, the weight loss in the region between 600 to 700 °C resulting from the burning off carbon deposited is evident. There is a good agreement between the results of TGA and CHN analysis.

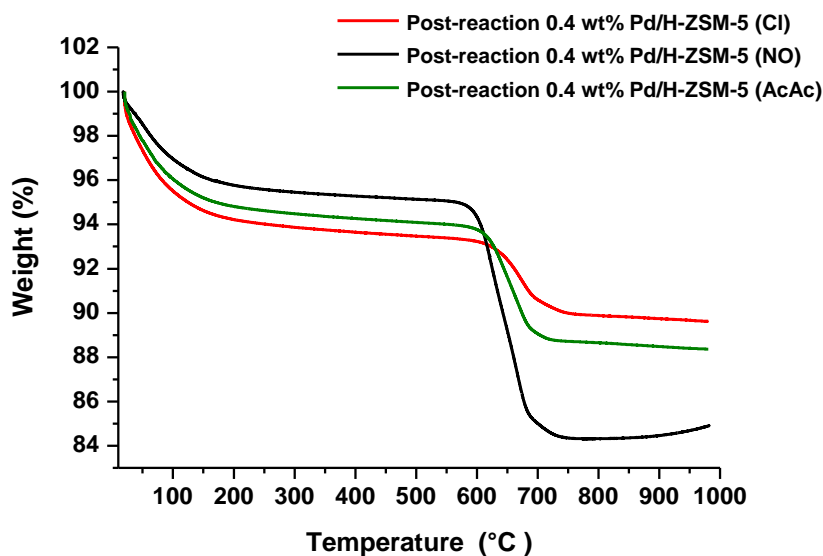


**Figure 5-24** TGA profiles of post-reaction 0.4 wt% Pd/H-ZSM-5 catalysts prepared from different Pd precursors.

Figure 5-25 depicts the first-derivative weight changes profiles for the post-reaction 0.4 wt% Pd/H-ZSM-5 catalysts that prepared from different Pd precursors. These profiles can reveal the differences between these samples more clearly. From Figure 5-25, it is obvious that there are differences among the TGA profiles. It can be seen that there are three peaks in the burning off coke region for the samples prepared from palladium acetylacetonate and nitrate. These regions are *ca.* 615, 665 and 715 °C for the samples prepared from palladium nitrate and *ca.* 640, 665 and 715 °C for the samples prepared from palladium acetylacetonate. The samples prepared from palladium chloride showed two oxidation peaks in the regions at *ca.* 665 and 730 °C. In addition, it is observed that all samples have similar oxidation region, which is at 665 °C as well as oxidation peak at the region beyond 700 °C. The difference between these samples is in the region before 650 °C where the first oxidation peak has slightly shifted to high region temperature for the sample prepared from palladium acetylacetonate and it is absent in the sample prepared from palladium chloride.

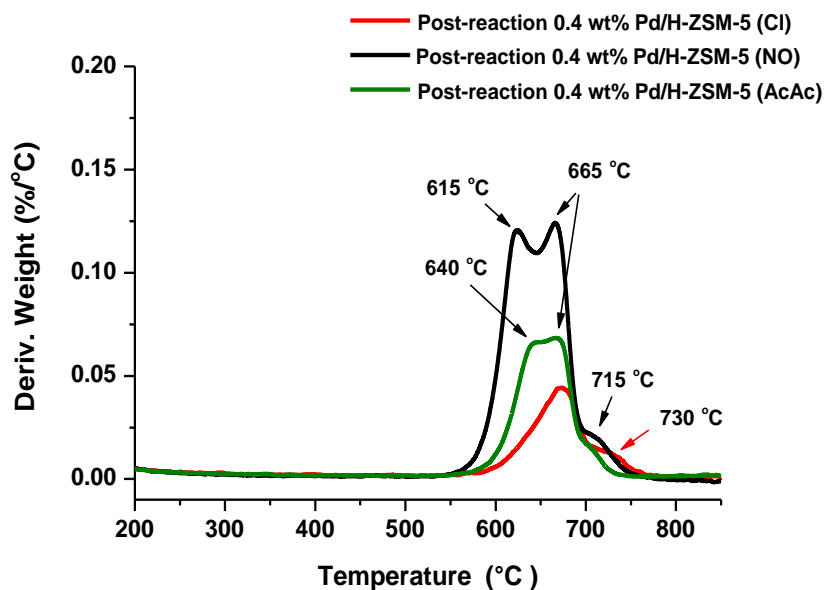


**Figure 5-25** TGA profiles for the post-reaction 0.4 wt% Pd/H-ZSM-5 catalysts prepared from different Pd precursors.

This suggests that these samples have similar carbonaceous species in the region 650 °C and the region beyond 700 °C, while they differ more significantly in the region before 650 °C. Previously, it was mentioned that the oxidation region beyond 500 °C is related to filamentous carbons (carbon nanofibres or nanotubes) and layers of graphitic carbon. However, SEM images (shown and discussed later) showed that the filamentous carbons were formed on all samples, but their amount in the sample prepared from palladium chloride seems to be low. Therefore, it is possible that the absence of a peak in the region of 615 °C is related to the filamentous carbons. From this, it can be suggested that the oxidation peak at 615 and 665 °C are attributed to filamentous carbons, whereas the oxidation peak beyond 700 °C is attributed to graphitic carbon.

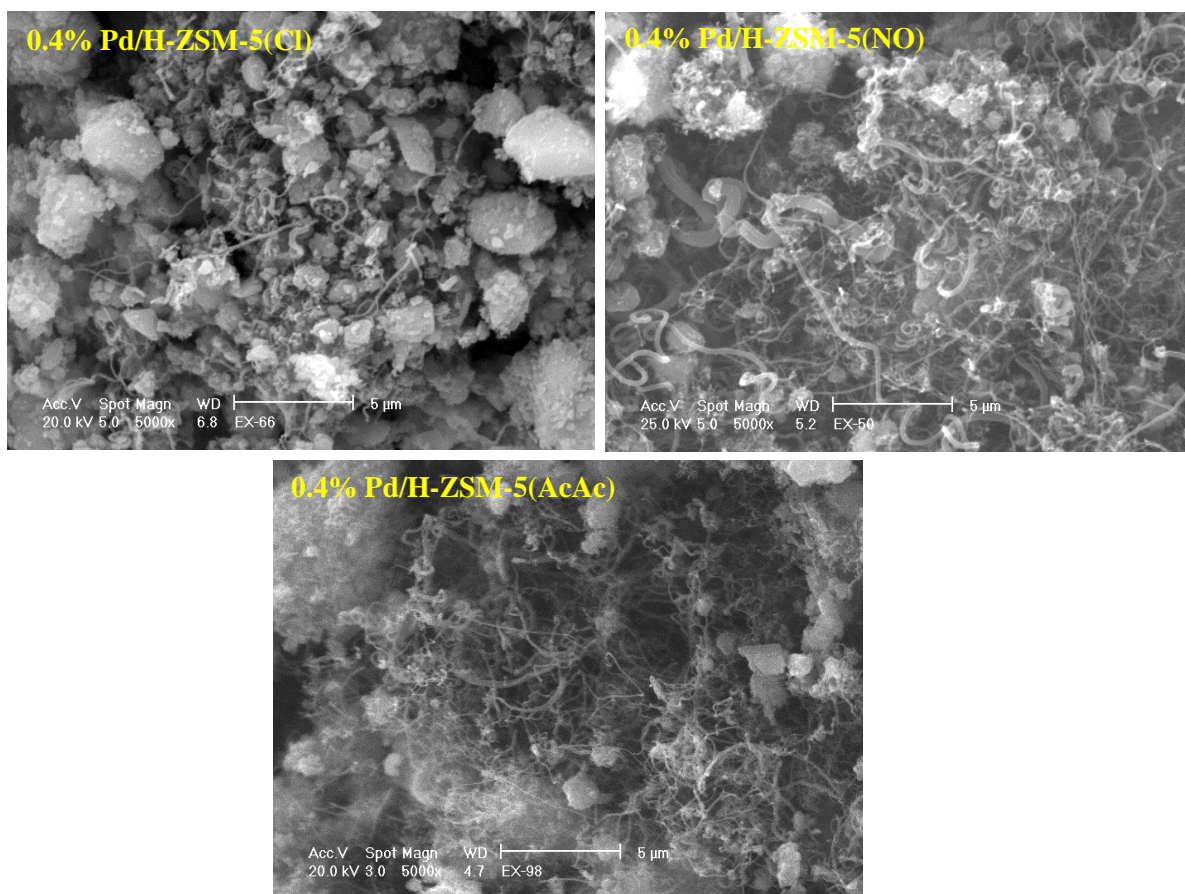
### 5.6.5 Post-reaction SEM images

Figure 5-26 presents SEM micrographs of the post-reaction 0.4 % Pd/H-ZSM-5 catalysts that prepared from different Pd precursors. From the images, it can be seen that the filamentous carbons were formed in all post-reaction samples. However, it is observed that there is a lower density of filamentous carbon formed on the 0.4 % Pd/H-ZSM-5 (Cl) catalyst and their diameters seem relatively small. The low amount of carbon filaments formed on the 0.4 % Pd/H-ZSM-5 (Cl) catalyst is consistent with the CHN results and TGA analysis, which showed a small amount of carbon deposited. In addition, the zeolite particles are clearly visible.

The SEM image for the 0.4 % Pd/H-ZSM-5 (NO) catalyst showed a large amount of filamentous carbon formed with filaments possessing a range of diameters. Also, it can be noted that the filamentous carbons are present on most of the catalyst surface. CHN and TGA analyses, Table 5-6 and Figure 5-24, demonstrated that the largest amount of carbon deposited was observed in the 0.4 % Pd/H-ZSM-5 (NO) catalyst. The SEM image suggests that the majority of this carbon deposited is from the filamentous carbon.

It can be seen from the SEM image for the 0.4 % Pd/H-ZSM-5 (AcAc) catalyst that there is a dense amount of filamentous carbons formed with thin diameter. Additionally, it is observed that the catalyst surface was covered by these filaments.

As previously mentioned, the diameter of the carbon fibres should be roughly equal to the diameters of the metal particles. Furthermore, it has been reported that small catalyst particles lead to a low growth rate and high initial reaction rates but fast deactivation, whereas catalysts with large particles have low initial activities and a short life. Therefore, it is apparent that there is an optimum particle size, for which maximum catalyst activity and carbon growth rate is exhibited [39, 207, 236].



**Figure 5-26** SEM images of post-reaction 0.4 wt % Pd/H-ZSM-5 catalysts prepared from different Pd precursors.

According to the above SEM images, it seems that the palladium precursors play a significant role in the dispersion and particles size of palladium, which affected the catalyst activity and formation of carbon. It can be assumed that the use of palladium chloride ( $\text{PdCl}_2$ ) as precursor produces a low dispersion on the outer surface of the zeolite. In addition, a few small particles can be present on the outer surface, which led to the formation of carbon filaments. However, the palladium acetylacetonate  $\text{Pd}(\text{C}_5\text{H}_7\text{O}_2)_2$  seems to have produced the smallest particles because the diameters of the carbon filaments are thinner. In case of catalyst prepared from palladium nitrate ( $\text{Pd}(\text{NO}_3)_2$ ) it seems that the diameters of the carbon filaments are thicker than the diameters of the carbon filaments formed from the catalyst prepared from palladium acetylacetonate  $\text{Pd}(\text{C}_5\text{H}_7\text{O}_2)_2$ , which indicates a larger particle size. Thus, it seems that the particle size of catalyst prepared from palladium nitrate ( $\text{Pd}(\text{NO}_3)_2$ ) is more effective compared with other catalysts *i.e.* they are not very small and not very large as well. Again, it seems that there is an optimum particle size of Pd leads to the high catalyst activity and high rate of carbon formation.

Further investigation is required to show the role of palladium precursors in the formation of various particle sizes and to determine the optimum particle size for catalyst activity.

### 5.6.6 Raman spectroscopy

Figure 5-27 presents the Raman spectra for the post-reaction 0.4 wt % Pd/H-ZSM-5 catalyst prepared from different Pd precursors. From the spectra, it can be seen that there are two main bands at  $1350\text{ cm}^{-1}$  (D band) and at  $1594\text{ cm}^{-1}$  (G band), which indicate the presence of graphitic carbon.

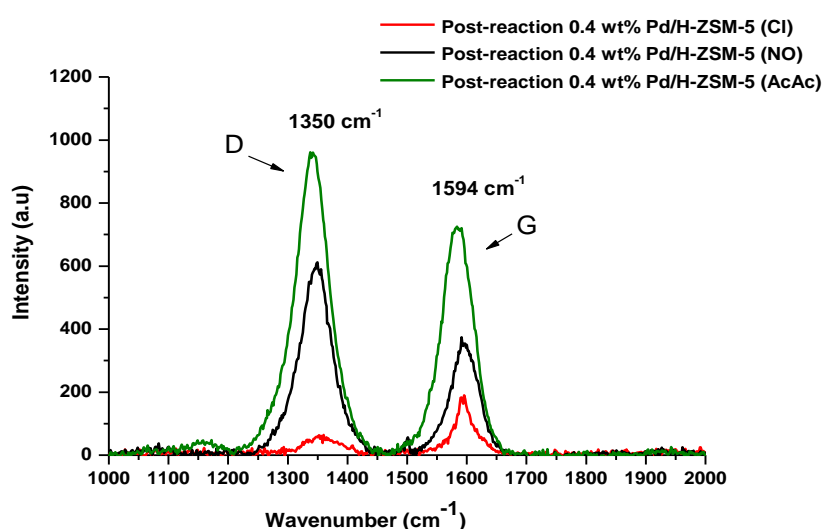


**Figure 5-27** Raman spectra of post-reaction 0.4 wt% Pd/H-ZSM-5 catalyst prepared from different Pd precursors.

Table 5-7 depicts the intensity ratio  $I_D/I_G$  for the D band and G band from Raman spectra for carbon produced by 0.4 wt% Pd/H-ZSM-5 catalyst prepared from different Pd precursors. From Table 5-7, it can be observed that the highest ratio of  $I_D/I_G$  is 1.97 for carbon produced by 0.4 wt% Pd/H-ZSM-5 catalyst prepared from palladium nitrate ( $\text{Pd}(\text{NO}_3)_2$ ), indicating that the graphitisation species are the most disordered, whereas the lowest ratio was noted with carbon formed by 0.4 wt% Pd/H-ZSM-5 catalyst prepared from palladium chloride ( $\text{PdCl}_2$ ) where it is 0.52, suggesting 0.4 % Pd/H-ZSM-5 (Cl) catalyst produces more organised carbon structures compared to another catalysts.

<b>Table 5-7</b> The result of intensity ratio $I_D/I_G$ for the D and G bands from Raman spectra for carbon produced by 0.4 wt% Pd/H-ZSM-5 catalysts prepared from different Pd precursors.	
<b>Catalyst</b>	<b>Peak area ratio (<math>I_D/I_G</math>)</b>
0.4 % Pd/H-ZSM-5 (Cl)	0.52
0.4 % Pd/H-ZSM-5 (NO)	1.97
0.4 % Pd/H-ZSM-5 (AcAc)	1.50

## 5.7. Effect of support on the activity of palladium catalysts for direct cracking of methane

### 5.7.1 Introduction

The support material plays an important role in the properties of catalysts, which directly affects methane conversion and the nature of carbon deposition. The most important factors affecting during metal-catalysed methane decomposition are the surface area, particle size, dispersion and stabilisation of the metallic catalyst particles, which can be controlled by selecting an appropriate support. Metal–support interaction (MSI) is important factor, which can influence the reduction of metal oxide precursors and dispersion of metal. A strong MSI inhibits the sintering or/and agglomeration of the metal particles on the support surface enhancing the dispersion of metal particles thus resulting in a high density of the catalytic sites [225, 226]. On the other hand, a strong MSI may lead to the difficulty of reduction of the precursor oxide which may require higher temperatures or even be irreducible. Furthermore, a suitable strength of MSI results in to prevent metal particles from aggregation and forming unwanted large particles.

It has been found that metal–support interaction (MSI) plays a role in the mechanism of carbon filaments growth. A weak MSI lead to a “tip-growth” mechanism, *i.e.* the catalyst particle is detached from the support and localised on the tip of carbon filaments, while strong interaction results in a “base-growth” mechanism, *i.e.* carbon filaments grows up with the catalyst particle rooted at its base [109].

A number of studies have investigated the effect of support on the hydrogen and carbon production from methane cracking. Solymosi *et al.* [47] studied the effect of support on Pd catalyst supported on TiO<sub>2</sub>, Al<sub>2</sub>O<sub>3</sub>, SiO<sub>2</sub> and MgO for methane decomposition. The

reaction data showed that the most effective catalyst for hydrogen formation was Pd/TiO<sub>2</sub> followed by Pd/Al<sub>2</sub>O<sub>3</sub>, Pd/SiO<sub>2</sub> and Pd/MgO. They believed that the reason for the variation in catalyst activity was due to the differences in crystal size of the Pd and/or with the ease of carbon migration from the Pd to the support, producing free Pd surface on the catalyst.

Takenaka *et al.* [62] studied the influence of different supports for Ni-based catalysts on the activity and stability of the methane decomposition reaction. The results of catalytic tests showed that Ni catalysts supported on SiO<sub>2</sub>, TiO<sub>2</sub> and graphite displayed high activities and long lifetimes for the reaction, while the catalysts supported on Al<sub>2</sub>O<sub>3</sub>, MgO and SiO<sub>2</sub>·MgO were inactive. Characterisation of the catalysts showed that Ni species in the active catalysts were present as crystallised Ni metal particles, while Ni species in the inactive catalysts were formed an oxide compound with the support. Moreover, the researchers studied the catalytic activity of the Ni catalysts supported on silicas with different specific surface areas and pore structures. They found that the silica support with no pore structure was found to enhance catalyst activity and lifetime. In another study from the same group [55], Co-based catalysts supported on various supports (MgO, Al<sub>2</sub>O<sub>3</sub>, SiO<sub>2</sub> and TiO<sub>2</sub>) were tested. The reaction results demonstrated that the activity of Co/Al<sub>2</sub>O<sub>3</sub> and Co/MgO were superior to those of Co/TiO<sub>2</sub> and Co/SiO<sub>2</sub> catalysts. They revealed that the activity of Co/Al<sub>2</sub>O<sub>3</sub> and Co/MgO catalysts is due to the small size of cobalt particles where they possessed diameters of 10–30 nm, whereas Co particles over 30 nm had no activity. In addition, they found that the diameter of Co metal particles, which were located at the tip of carbon nanofibres is similar to the diameter of the corresponding fibre.

In view of these studies, when metal species are loaded on different supports, it is generally accepted that the catalytic activity of metal species depends on the type of support due to its effect on the crystal size and the dispersion of the metal.

In this section, the effect of different supports on the catalytic activity of Pd based catalyst was studied for the cracking of methane. H-ZSM-5,  $\gamma$ -Al<sub>2</sub>O<sub>3</sub> and SiO<sub>2</sub> were employed as supports. The supported Pd catalysts used were prepared by impregnating the supports with aqueous solutions of Pd(NO<sub>3</sub>)<sub>2</sub>. The reactions were performed at similar conditions, 0.4 wt% loading, reaction temperature is 800 °C, at 12 mL/min flow rate and using a catalyst mass of 0.4 g.

## 5.7.2 Reaction data

Figure 5-28 shows the hydrogen formation rate profile as a result of methane cracking at 800 °C over Pd catalysts supported on various supports. The catalysts tested are 0.4 wt% Pd/H-ZSM-5, 0.4 wt% Pd/SiO<sub>2</sub> and 0.4 wt% Pd/ $\gamma$ -Al<sub>2</sub>O<sub>3</sub>. From Figure 5-28, it can be seen that the activity of catalysts at the initial period of reaction were higher in the order of Pd/ $\gamma$ -Al<sub>2</sub>O<sub>3</sub> > Pd/SiO<sub>2</sub> > Pd/H-ZSM-5. However, the 0.4 wt% Pd/ $\gamma$ -Al<sub>2</sub>O<sub>3</sub> catalyst showed superior activity and the highest peak hydrogen formation rate (*ca.*  $7.02 \times 10^{-4}$  mol H<sub>2</sub> g<sup>-1</sup> min<sup>-1</sup>) throughout the run conducted compared to other catalysts. Also, it is observed that hydrogen formation rate increased initially followed by a gradual decline as a result of deposited carbon. It should be noted that the time on stream is shorter than another catalysts because of reaction was stopped as a result of pressure drop effects. The peak hydrogen formation rate for 0.4 wt% Pd/H-ZSM-5 catalyst was *ca.*  $3.20 \times 10^{-4}$  mol H<sub>2</sub> g<sup>-1</sup> min<sup>-1</sup>, which consider as the lowest hydrogen formation rate among the catalysts. The 0.4 wt% Pd/SiO<sub>2</sub> catalyst demonstrated an initially high rate of hydrogen production (*ca.*  $4.40 \times 10^{-4}$  mol H<sub>2</sub> g<sup>-1</sup> min<sup>-1</sup>) then rapidly decline until 60 minutes of time on stream followed by a slow decline for the rest of the run. In addition, it is observed that the hydrogen formation rates for 0.4 wt% Pd/H-ZSM-5 and 0.4 wt% Pd/SiO<sub>2</sub> after 60 minutes of time on stream are comparable.

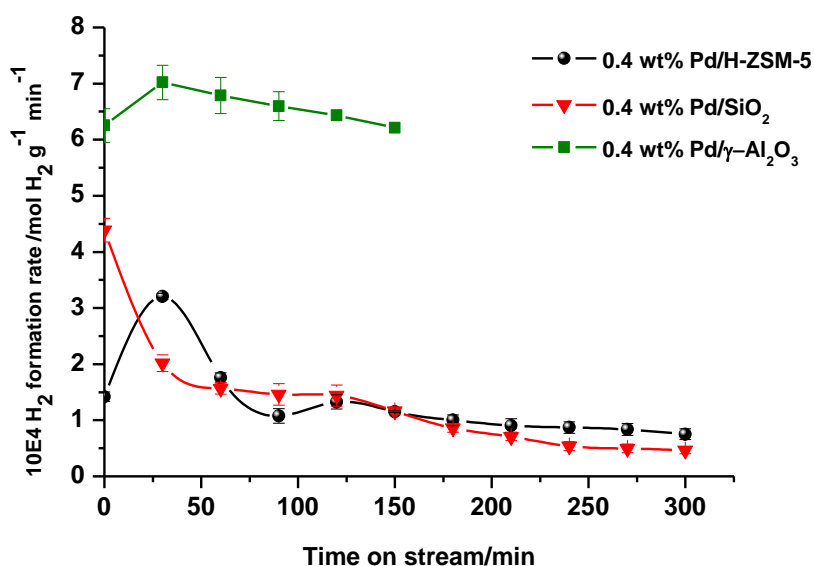


**Figure 5-28** Hydrogen formation rates as a function of time on stream for 0.4 wt% Pd/H-ZSM-5, 0.4 wt% Pd/SiO<sub>2</sub> and 0.4 wt% Pd/ $\gamma$ -Al<sub>2</sub>O<sub>3</sub>, the reaction temperature was 800 °C, the methane flow rate was 12 mL/min and 0.4 g catalyst mass.

From the result above, there are several possible explanations for these different activities. The ranking of catalyst activity as a function of support material does not correlate with support acidity because zeolites are generally considered more acidic than silica yet both supports provided similar activities. Surface areas of catalysts, dispersion and the particle size of palladium could play a role in the catalyst behaviour. The BET surface areas of the catalysts were measured. Table 5-8 presents the results. It is obvious that the surface area of the 0.4 wt% Pd/H-ZSM-5 catalyst is larger than that of other catalysts, whereas the 0.4 wt% Pd/SiO<sub>2</sub> catalyst has the smallest surface area. According to the BET results, it is evident that there is no correlation between surface area and the catalysts activity. It should also be noted that application of the BET method to the H-ZSM-5 catalyst is not strictly correct, so the absolute value of this surface area should be taken with caution.

<b>Table 5-8</b> BET surface area analysis of 0.4 wt% Pd/H-ZSM-5, 0.4 wt% Pd/SiO <sub>2</sub> and 0.4 wt% Pd/ $\gamma$ -Al <sub>2</sub> O <sub>3</sub> samples.	
<b>Sample Code</b>	<b>BET surface area, m<sup>2</sup>/g</b>
<b>4 % Pd/H-ZSM-5</b>	<b>251</b>
<b>0.4 % Pd/SiO<sub>2</sub></b>	<b>203</b>
<b>0.4 % Pd/<math>\gamma</math>-Al<sub>2</sub>O<sub>3</sub></b>	<b>210</b>

However, it seems that the dispersion and particle size of these catalysts may vary leading to the observed differences.

SEM for the carbon deposited on these catalysts, will be shown and discussed later, may assist in the interpretation of the cause of the variation of catalyst activity. It was noted that carbon filaments were formed on 0.4 wt% Pd/ $\gamma$ -Al<sub>2</sub>O<sub>3</sub> catalyst surface and they largely covered the surface of catalyst with very thin diameter filaments (they cannot be measured with certainty) compared to other catalysts. For the 0.4 wt% Pd/H-ZSM-5 and 0.4 wt% Pd/SiO<sub>2</sub> catalysts, the carbon filaments were also formed with similar diameters from *ca.* 145 to 436 nm. In addition, it was observed that some parts of the 0.4 wt% Pd/H-ZSM-5 catalyst had larger diameter of carbon filaments that reached 692 nm, which indicates larger Pd particle size. Moreover, it was noted that carbon filaments formed on 0.4 wt% Pd/SiO<sub>2</sub> catalysts developed in different parts of the sample, which implied low dispersion of Pd metal particles.

It can be concluded that the highest activity for 0.4 wt% Pd/ $\gamma$ -Al<sub>2</sub>O<sub>3</sub> is attributed to highest dispersion and smallest particle size of Pd, whilst 0.4 wt% Pd/H-ZSM-5 and 0.4 wt% Pd/SiO<sub>2</sub> showed larger diameter of carbon filaments as a result of large particle size. The apparently lowest activity of 0.4 wt% Pd/H-ZSM-5 catalyst may possibly be ascribed to it having the largest particle size. Also, it should be noted that the zeolite structure contains channels that may be blocked by the deposition of carbon, thus preventing the reactants from access to the active sites.

Moreover, the influence of nature of carbon deposited should be taken into account.

### 5.7.3 XRD patterns

Figures 5-29 and 5-30 present the XRD patterns of the pre- and post-reaction 0.4 wt % Pd/SiO<sub>2</sub> and 0.4 wt% Pd/ $\gamma$ -Al<sub>2</sub>O<sub>3</sub> catalysts, respectively. The XRD patterns of the pre- and post-reaction 0.4 wt% Pd/H-ZSM-5 catalysts were shown and discussed in a previous section, Figure 5-22, where it was seen that no change in zeolite structure for both pre- and post-reaction forms occurred.

From Figure 5-29, it can be seen that the XRD pattern of the pre and post-reaction 0.4 wt% Pd/SiO<sub>2</sub> catalyst shows only the reflections corresponding to amorphous silica. No palladium-containing phases were apparent. The only obvious visible change between the two patterns is that the post-reaction catalyst exhibits a small peak at 26°, which has been marked on the patterns and which matches to graphite.

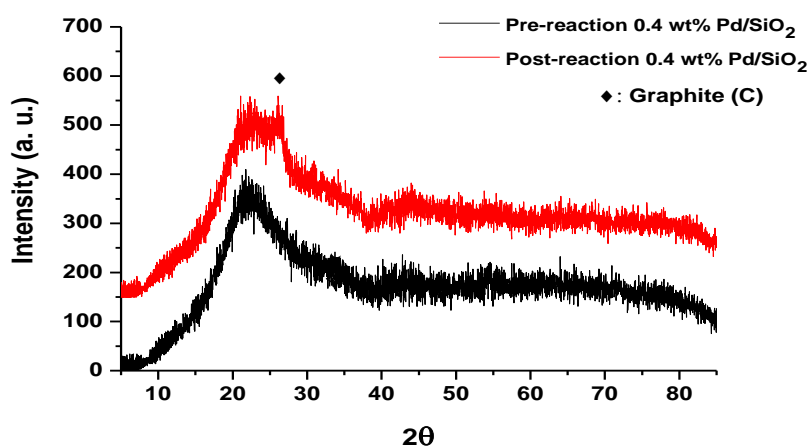


**Figure 5-29** XRD pattern of 0.4 wt% Pd/SiO<sub>2</sub> in the pre- and post-reaction forms.

The XRD patterns of the pre- and post-reaction 0.4 wt% Pd/ $\gamma$ -Al<sub>2</sub>O<sub>3</sub> catalysts are shown in Figure 5-30. The powder diffraction pattern of 0.4 wt% Pd/ $\gamma$ -Al<sub>2</sub>O<sub>3</sub> displays the characteristic reflections of the  $\gamma$ -Al<sub>2</sub>O<sub>3</sub> phase. The XRD pattern for the post-reaction 0.4 wt% Pd/ $\gamma$ -Al<sub>2</sub>O<sub>3</sub> catalyst again shows the appearance of high intensity peak at 26° 2 $\theta$  that can be assigned to graphite. The graphite reflection is wide that may indicate that the crystals of graphite carbon are small and/or disordered. Neither of the XRD patterns exhibited reflections indicative of any palladium phases, which imply to high dispersion of the palladium, with a particle size under the detection limit of XRD technique.

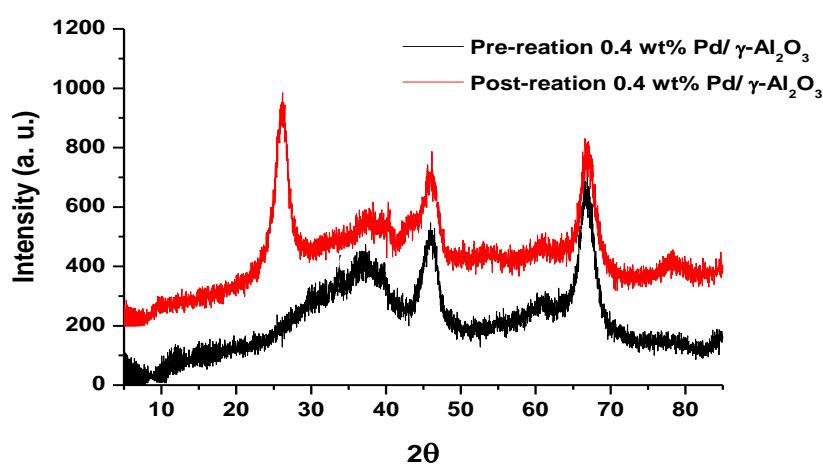


**Figure 5-30** XRD pattern of 0.4 wt% Pd/ $\gamma$ -Al<sub>2</sub>O<sub>3</sub> in the pre- and post-reaction forms.

#### 5.7.4 Post-reaction CHN and TGA analysis

CHN analysis and TGA studies for the post-reaction 0.4 % Pd/H-ZSM-5, 0.4 % Pd/SiO<sub>2</sub> and 0.4 % Pd/ $\gamma$ -Al<sub>2</sub>O<sub>3</sub> catalysts have been undertaken. Table 5-9 illustrates the results. From this data, it is obvious that the amount of carbon deposited on 0.4 % Pd/ $\gamma$ -Al<sub>2</sub>O<sub>3</sub> is by far the largest (43.8 wt%) compared to other samples. This result is not surprising as the hydrogen formation rate was the highest and the results of the XRD patterns showed the strong evidence for the presence of graphite. The amounts of carbon deposited on the 0.4 % Pd/H-ZSM-5 and 0.4 % Pd/SiO<sub>2</sub> catalysts are roughly similar.

<b>Table 5-9</b> CHN analysis for the post-reaction 0.4 wt% Pd/H-ZSM-5, 0.4 wt% Pd/SiO <sub>2</sub> and 0.4 wt% Pd/ $\gamma$ -Al <sub>2</sub> O <sub>3</sub> catalysts.			
Catalysts	Mean value, wt%		
	C	H	N
0.4 % Pd/H-ZSM-5	10.80 ± 0.10	0.50 ± 0.04	-
0.4 % Pd/SiO <sub>2</sub>	10.10 ± 0.30	-	-
0.4 % Pd/ $\gamma$ -Al <sub>2</sub> O <sub>3</sub>	43.80 ± 1.90	-	-

Figure 5-31 depicts the TGA oxidation profiles under air for the post-reaction catalysts. It is evident that the 0.4 % Pd/H-ZSM-5 and 0.4 % Pd/ $\gamma$ -Al<sub>2</sub>O<sub>3</sub> catalysts showed a degree of weight loss before 250 °C, which is ascribed to desorption of adsorbed water, while it is almost absent in the 0.4 % Pd/SiO<sub>2</sub>. In addition, there is weight loss in the region beyond 600 °C resulting from the burning off carbon formed on the samples. However, it is noted that there is reasonably good agreement between the results of TGA and CHN analysis.

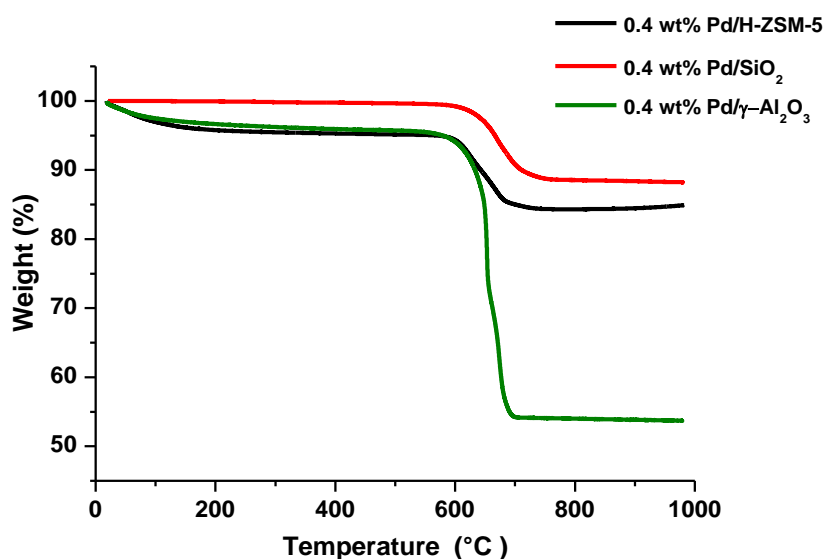


**Figure 5-31** TGA profiles for the post-reaction 0.4 wt% Pd/H-ZSM-5, 0.4 wt% Pd/SiO<sub>2</sub> and 0.4 wt% Pd/ $\gamma$ -Al<sub>2</sub>O<sub>3</sub> catalysts.

Figure 5-32 displays the first-derivative weight change profiles for the catalysts. From the profiles, it can be observed that the carbon deposited on 0.4 wt% Pd/SiO<sub>2</sub> and 0.4 wt% Pd/ $\gamma$ -Al<sub>2</sub>O<sub>3</sub> catalysts have two peaks in the coke burning off region at *ca.* 640 and 665 °C for 0.4 wt% Pd/ $\gamma$ -Al<sub>2</sub>O<sub>3</sub> catalyst, and at 665 and 700 °C for 0.4 wt% Pd/SiO<sub>2</sub> catalyst. As described and discussed in the previous section, the first-derivative weight changes profile

for the post-reaction 0.4 % Pd/H-ZSM-5 shows three peaks in the burning off coke region at *ca.* 615, 665 and 715 °C. These differences in the position of oxidation peaks for all samples indicate that there are different types of carbonaceous species deposited on the catalyst surfaces. Also, it can be seen that all samples have one common region of coke-burning-off at 665 °C, which may imply a similar species is formed for all samples. The TGA profile for 0.4 wt% Pd/ $\gamma$ -Al<sub>2</sub>O<sub>3</sub> catalysts demonstrate an intense peaks that can be ascribed to a narrow distribution of two types of carbon species.

However, SEM images (shown later) illustrated that all samples form carbon filaments. Therefore, it may be that these carbon filaments are different and that there is also graphitic carbon, resulting in the appearance of different regions of coke removal.

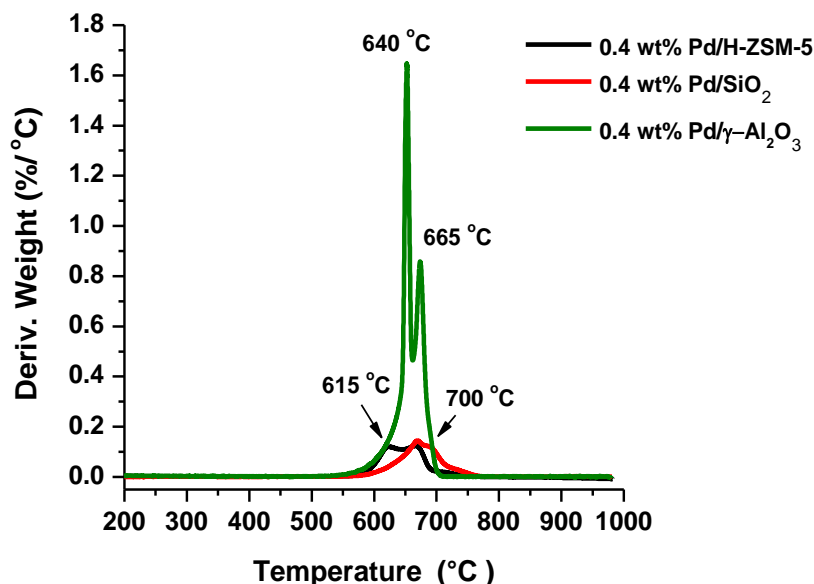


**Figure 5-32** TGA profiles for the post-reaction 0.4 wt% Pd/H-ZSM-5, 0.4 wt% Pd/SiO<sub>2</sub> and 0.4 wt% Pd/ $\gamma$ -Al<sub>2</sub>O<sub>3</sub> catalysts.

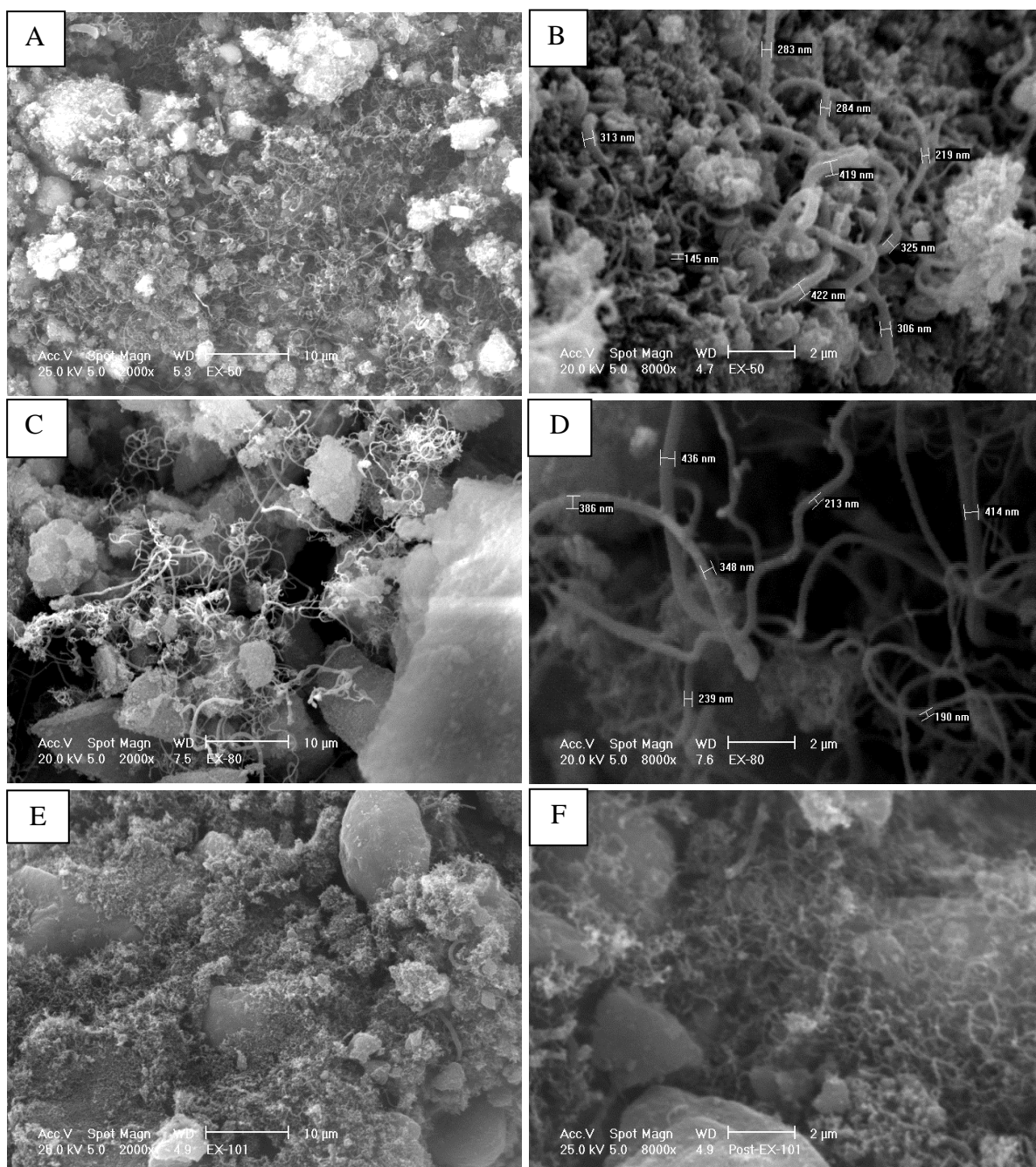
### 5.7.5 Post-reaction SEM images

Figure 5-33 presents the SEM images for the post-reaction 0.4 wt% Pd/H-ZSM-5, 0.4 wt% Pd/SiO<sub>2</sub> and 0.4 wt% Pd/ $\gamma$ -Al<sub>2</sub>O<sub>3</sub> catalysts. For each sample, there are two images corresponding to high and low magnification.

Figure 5-33 (A, B) depicts two images of the post-reaction 0.4 wt% Pd/H-ZSM-5 catalyst. From the low magnification image (A), it can be seen that the filamentous carbon is highly distributed on the surface of the catalyst. The high magnification image (B) illustrates carbon filaments with measured diameters. According to the measured diameters of the filamentous carbon, it is obvious that the diameters range from *ca.* 145 to 422 nm, which can be similar to the possible diameter of palladium particles.

Two images of the post-reaction 0.4 wt% Pd/SiO<sub>2</sub> catalyst are presented in Figure 5-33 (C, D). It can be observed from low magnification image (C) that the carbon filaments were not fully distributed on the surface of catalyst and they are clustered in different parts. This may indicate a low dispersion of palladium particles. The diameters of some of these filaments were measured and they are shown by high magnification in image (D). The diameters of these filamentous carbons are in the range from 195 to 436 nm, which could correspond to the diameters of the palladium particles from which they form.

Figure 5-33 (E, F) present low and high magnification images of the post-reaction 0.4 wt% Pd/ $\gamma$ -Al<sub>2</sub>O<sub>3</sub> catalyst, respectively. The image (E) shows the catalyst surface, it is noted that the surface of catalyst is covered highly with very small carbon filaments, denoting a high dispersion of palladium. The high magnification image (F) clearly shows the carbon filaments formed on the catalyst surface. It can be seen that these filaments are small and have very thin diameters that imply a small palladium particle size. This finding may be supportive of the XRD result where it was found that the peak of graphite structure was wide, which suggests small domains of graphite. It seems that the alumina support formed a small particle size and high dispersion of the palladium leading to the superior activity of this catalyst. Moreover, the images of samples did not show the particles of palladium to be at the tip of the carbon filaments, suggesting the occurrence of the “base-growth” mechanism.



**Figure 5-33** SEM images of post-reaction (A,B) 0.4 wt% Pd/H-ZSM-5, (C,D) 0.4 wt% Pd/SiO<sub>2</sub> and (E,F) 0.4 wt% Pd/γ-Al<sub>2</sub>O<sub>3</sub> catalysts.

### 5.7.6 Raman spectroscopy

The Raman spectra for the post-reaction 0.4 wt% Pd/H-ZSM-5, 0.4 wt% Pd/SiO<sub>2</sub> and 0.4 wt% Pd/γ-Al<sub>2</sub>O<sub>3</sub> catalysts is presented in Figure 5-34. The Raman spectra confirm the presence of graphitic structure with two main bands at 1350 cm<sup>-1</sup> (D band) and at 1595 cm<sup>-1</sup> (G band), being present.

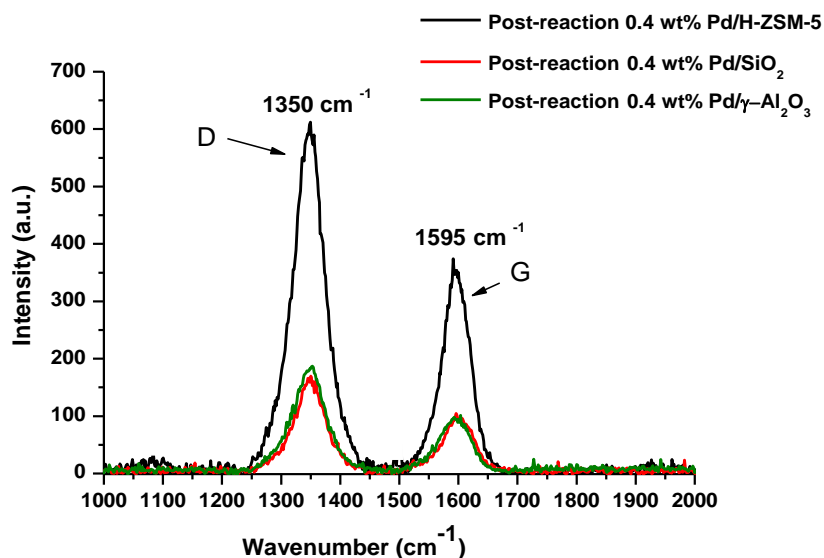


**Figure 5-34** Raman spectra for the post-reaction 0.4 wt% Pd/H-ZSM-5, 0.4 wt% Pd/SiO<sub>2</sub> and 0.4 wt% Pd/ $\gamma$ -Al<sub>2</sub>O<sub>3</sub> catalysts.

Table 5-10 presents the intensity ratio  $I_D/I_G$  for the D band and G band, calculated from the Raman spectra. It can be seen that the highest ratio of  $I_D/I_G$  is 2.00 for carbon formed by 0.4 % Pd/ $\gamma$ -Al<sub>2</sub>O<sub>3</sub> catalyst, indicating that the graphitisation degree is the most disordered, whereas the lowest ratio was noted with carbon formed by 0.4 % Pd/SiO<sub>2</sub> catalyst where it is 1.76, which suggests 0.4 % Pd/SiO<sub>2</sub> catalyst produces more organised carbon structures compared to another catalysts. The greater degree of disorder in the graphite produced in the Pd/ $\gamma$ -Al<sub>2</sub>O<sub>3</sub> catalyst may also be consistent with the broader reflection evident at *ca.* 26° 2 $\theta$ , as shown in Figure 5-30.

<b>Table 5-10</b> $I_D/I_G$ ratios for the D band and G band from Raman spectra for carbon produced by 0.4 wt% Pd/H-ZSM-5, 0.4 % Pd/SiO <sub>2</sub> and 0.4 % Pd/ $\gamma$ -Al <sub>2</sub> O <sub>3</sub> catalysts.	
<b>Catalyst</b>	<b>Peak area ratio (<math>I_D/I_G</math>)</b>
0.4 % Pd/H-ZSM-5	1.97
0.4 % Pd/SiO <sub>2</sub>	1.76
0.4 % Pd/ $\gamma$ -Al <sub>2</sub> O <sub>3</sub>	2.00

## 5.8. Summary

The purpose of this study was to determine the effect of some parameters on the activity of Pd/H-ZSM-5 catalyst for hydrogen and carbon production from the direct cracking of methane. The effects of reaction temperature, the flow rate of feed gas, the addition of dopants, the palladium precursor and the support type were investigated.

The results of reaction temperature effect on the activity of 0.4 wt% Pd/H-ZSM-5 catalyst in the range from 600 to 900 °C show that the hydrogen formation rate generally increased with increasing reaction temperature. The lowest peak hydrogen formation rate was observed at 600 °C, while the highest peak formation rate is noted at 750 °C. The behaviour of the catalyst at 650, 700, 750 and 900 °C was similar (the hydrogen formation rates gradually increased during the reaction) for the fact that deactivation was observed after 200 minutes of time on stream at 900 °C. At 800 °C, the catalyst showed different behaviour where there was a relatively high initial hydrogen formation rate at 30 minutes of time on stream, after which a sharp drop occurred within *ca.* 80 minutes of time on stream. CHN and TGA analysis demonstrated that the lowest amount of carbon deposited was observed for the sample run at 600 °C and the largest amount was noted for the sample run at 900 °C. SEM images for the post-reaction 0.4 % Pd/H-ZSM-5 catalyst at different temperatures illustrated the formation of filamentous carbon over the catalyst except at 600 °C. In addition, HRTEM images showed the types of carbon deposited.

The influence of methane flow rate on the performance of 0.4 wt% Pd/H-ZSM-5 catalyst at 800 °C was studied. The flow rates used were 12, 24, 36 and 48 mL/min. The reaction data displayed that increase of flow rate increased the initial peak hydrogen formation rate which was followed by a sharp decline. The CHN and TGA analyses revealed that the increase of flow rate increased the amount of carbon deposited from roughly 10 to 16 wt%. Moreover, SEM images showed that the increase of methane flow rate resulted in low growth of carbon filaments.

The effects of various dopants on the activity of 0.4 wt% Pd/H-ZSM-5 catalyst were studied. Fe<sup>3+</sup>, Ni<sup>2+</sup>, Co<sup>2+</sup> and Cu<sup>2+</sup> were employed as dopants. It was observed that these additives led to a reduction of catalyst activity, showing the palladium loaded on zeolite to be sensitive to these additives. The quantity of carbon deposited was determined by CHN and TGA analyses. All carbon produced from doped catalysts was less than that produced

on the non-doped catalyst. SEM images for the post-reaction doped 0.4 % Pd/H-ZSM-5 catalyst with  $\text{Fe}^{3+}$ ,  $\text{Ni}^{2+}$ ,  $\text{Co}^{2+}$  and  $\text{Cu}^{2+}$  demonstrated that carbon filaments were formed. The diameter of the carbon filaments formed over the doped catalyst is thinner than those formed on non-doped 0.4 % Pd/H-ZSM-5 catalyst.

Three types of palladium precursor were used to investigate activity for methane cracking. Palladium chloride ( $\text{PdCl}_2$ ), palladium nitrate ( $\text{Pd}(\text{NO}_3)_2$ ) and palladium acetylacetonate  $\text{Pd}(\text{C}_5\text{H}_7\text{O}_2)_2$  were used as palladium sources for the preparation of 0.4 wt% Pd/H-ZSM-5 catalysts. It was found that the catalyst prepared from palladium nitrate had the highest hydrogen formation rate, while the catalyst prepared from palladium chloride showed the lowest hydrogen formation rate. The CHN and TGA analyses revealed a large amount of deposited carbon was observed on catalyst prepared from palladium nitrate and the lowest amount was on the catalyst prepared from palladium chloride. SEM micrographs illustrated the formation of filamentous carbon on all post-reaction catalysts. The carbon filaments formed in the catalysts prepared from either palladium nitrate or palladium acetylacetonate was dense with differences in their diameters. Growth was negligible in the catalyst prepared from palladium chloride.

The performance of Pd catalyst supported on H-ZSM-5,  $\gamma\text{-Al}_2\text{O}_3$  and  $\text{SiO}_2$  for methane cracking was investigated. The initial hydrogen formation rates were in the order of  $\text{Pd}/\gamma\text{-Al}_2\text{O}_3 > \text{Pd}/\text{SiO}_2 > \text{Pd}/\text{H-ZSM-5}$ . The 0.4 wt%  $\text{Pd}/\gamma\text{-Al}_2\text{O}_3$  catalyst exhibited superior activity and the highest hydrogen formation rate throughout the run compared to 0.4 wt%  $\text{Pd}/\text{SiO}_2$  and 0.4 wt%  $\text{Pd}/\text{H-ZSM-5}$  catalysts. CHN and TGA analyses revealed that the quantity of carbon deposited on  $\text{Pd}/\gamma\text{-Al}_2\text{O}_3$  catalyst to be the largest with both  $\text{Pd}/\text{SiO}_2$  and  $\text{Pd}/\text{H-ZSM-5}$  catalysts exhibiting similar quantities of deposited carbon. SEM images for these catalysts after reaction showed that the filamentous carbon was formed over all catalysts.

In general, the results of this study show that the highest performance of 0.4 wt% Pd/H-ZSM-5 for hydrogen production from methane cracking was obtained at a temperature of 750 °C. The 0.4 % Pd/H-ZSM-5 catalyst showed good activity at 12 mL/min flow rate and a reaction temperature of 800 °C.  $\text{Fe}^{3+}$ ,  $\text{Ni}^{2+}$ ,  $\text{Co}^{2+}$  and  $\text{Cu}^{2+}$  dopants resulted in reduction of the performance of 0.4 % Pd/H-ZSM-5 catalyst at 800 °C and 12 mL/min. The use of palladium nitrate ( $\text{Pd}(\text{NO}_3)_2$ ) as a source of palladium for the preparation of 0.4 wt% Pd/H-ZSM-5 catalyst exhibited the highest activity for hydrogen production. The palladium

supported on  $\gamma\text{-Al}_2\text{O}_3$  displayed superior activity and the highest hydrogen formation rate compared to H-ZSM-5 and  $\text{SiO}_2$ .

## 6. Cracking of methane over Ni- and Cu-based catalysts for the production of hydrogen and carbon nanostructures

### 6.1. Introduction

In recent years, there has been an increasing interest in the cracking of methane into CO<sub>x</sub>-free hydrogen and carbon [161, 164, 179, 183, 224, 228]. The direct cracking of methane displays a promising alternative to the conventional hydrogen production methods such as methane steam reforming (MSR) and partial oxidation of methane (POM) because there is no further co-product except carbon [227].

Nickel is the most commonly used metal as a catalyst for methane cracking due to its high activity [19, 244]. The associated problem with Ni-based catalysts during methane cracking is the rapid deactivation of catalyst as a result of carbon deposition. The carbon deposited on the catalyst surface can cover the active sites or accumulate at the entrance of the pores to block further access of the reactants due to pore-mouth plugging [48]. In addition, the carbon deposited is in the form of carbon filaments or as encapsulating carbon and the latter form as well as catalyst sintering are believed to be the reasons of catalyst deactivation [19, 74].

Nickel catalysts are sensitive to the reaction conditions of methane cracking. It was reported that the operation stability of nickel catalysts is in the narrow temperature range of 500-550 °C [53]. Takenaka *et al.*[40] investigated the effect of reaction temperature on the performance of a 40 % Ni/SiO<sub>2</sub> catalyst. The range of temperature applied was from 500 to 700 °C. The reaction data showed that the increase of reaction temperatures led to the rapid deactivation of the catalyst whereas the reaction temperatures of 500 and 530 °C displayed the highest catalyst stability and high yields of hydrogen and carbon. In addition, SEM images showed the formation of carbon nanofibres on deactivated catalysts at all reaction temperatures. It was found that the average diameters of carbon nanofibres become smaller with increasing reaction temperature.

Croiset and co-workers [64] studied the influence of reaction temperature in the range from 500 to 650 °C on the activity of a 5 % Ni/ $\gamma$ -Al<sub>2</sub>O<sub>3</sub> catalyst. They found that the reaction can

be best carried out between 500 and 550 °C. Also, they observed that the density of the carbon filaments decreases with increasing reaction temperature.

Supported Ni catalysts are not generally employed at elevated temperatures for methane cracking reaction due to their rapid deactivation. The introduction of a second metal was found to enhance the activity and stability of Ni catalysts at high temperatures. Chen *et al.* [61] showed that the doping of Cu into a Ni/Al<sub>2</sub>O<sub>3</sub> catalyst improved the activity and stability of the Ni/Al<sub>2</sub>O<sub>3</sub> catalyst for methane decomposition to produce CO<sub>x</sub>-free hydrogen and nanocarbon materials at 740 °C. Takenaka *et al.* [221] studied the influence of the addition of different metals (Cu, Rh, Pd, Ir, and Pt) upon Ni/SiO<sub>2</sub> catalysts. They found that the addition of Pd significantly increased the catalytic lifetime and the accumulated yields of hydrogen and carbon at the complete deactivation of the catalyst, while the addition the other metals resulted in the decrease of yields compared to those for Ni/SiO<sub>2</sub>.

It was found that the support plays an important role in activity of Ni catalysts. Takenaka *et al.* [62] reported on the effect of the support for Ni catalysts at 500 °C. They studied the catalytic activity and the longevity of Ni catalysts with different supports (SiO<sub>2</sub>, TiO<sub>2</sub>, graphite, ZrO<sub>2</sub>, SiO<sub>2</sub>·Al<sub>2</sub>O<sub>3</sub>, Al<sub>2</sub>O<sub>3</sub>, MgO and MgO·SiO<sub>2</sub>). The Ni catalysts supported on SiO<sub>2</sub>, TiO<sub>2</sub> and graphite possessed the highest activity and longevity in the reaction, while the catalysts supported on Al<sub>2</sub>O<sub>3</sub>, MgO and MgO·SiO<sub>2</sub> did not show any worthy activity in the reaction. Characterisation demonstrated that the Ni species in the high activity catalysts were present in the metallic state whereas the Ni species on the inactive catalysts were mainly present as NiO, suggesting the formation of a compound oxide between Ni and the supports. Inaba and co-workers [245] studied the use of various types of zeolite as supports at 650 °C. They demonstrated that Ni-supported by a USY zeolite (Si/Al = 14,360) had a longer catalytic lifetime compared to other zeolite supports. The authors attributed this to the small diameter of the nickel particles, the lower amount of solid acid and the larger outer surface area. In addition, the SEM results showed that the carbon deposited on the catalyst was in the form of filaments.

The catalytic activity for hydrogen and carbon filaments depended strongly on the Ni loading. Venugopal *et al.* [48] studied the impact of Ni loading on the catalytic activity of Ni/SiO<sub>2</sub> at 600 °C. The Ni loading amounts ranged from 5 to 90 wt%. They found that a Ni loading of 30 wt% had good activity and longevity and resulted in the highest yield of hydrogen and carbon filaments. In addition, they suggested that the catalyst lifetime of 30

wt% Ni/SiO<sub>2</sub> for methane decomposition was dependent on the particle size of the Ni metal.

This chapter comprises a study of the effects of different parameters on the direct cracking of methane for hydrogen and carbon production over Ni-based catalysts. This study includes a comparison of 0.4 wt% Ni/H-ZSM-5 and 0.4 wt% Pd/H-ZSM-5 catalysts, the effect of the reaction temperature on 0.4 wt% Ni/H-ZSM-5 catalyst, the effect of Ni loading on Ni/H-ZSM-5 catalyst and the influence of the type of support will be presented and discussed. Additionally, 0.4 wt% Cu/H-ZSM-5 catalyst has been compared with the 0.4 wt% Ni/H-ZSM-5 and 0.4 wt% Pd/H-ZSM-5 catalysts.

## **6.2. Direct catalytic cracking of methane over 0.4 wt% Ni/HZSM-5, 0.4 wt% Pd/HZSM-5 and Pd-Ni/HZSM-5 catalysts for hydrogen and carbon production: comparative study**

### **6.2.1 Introduction**

In this section, a comparative study between the 0.4 wt% Ni/HZSM-5 and 0.4 wt% Pd/HZSM-5 catalysts for direct cracking of methane for hydrogen and carbon production is described. These catalysts were prepared by the same method, as outlined in Chapter 2. In addition, the 0.4 wt% Ni/HZSM-5 catalyst was doped with Pd to observe its promotional effect on the catalytic activity. The molar ratio of the dopant Pd added to Ni/H-ZSM-5 was 0.25 (Pd/Ni). It should be mentioned that these catalysts were calcined at 500 °C and they were not treated with hydrogen to reduce the metals loaded on zeolite.

### **6.2.2 Reaction data**

The direct cracking of methane over the 0.4 wt% Ni/HZSM-5, 0.4 wt% Pd/HZSM-5 and 0.4 wt% Ni/HZSM-5 Pd-doped catalysts under similar reaction conditions was conducted. Figure 6-1 shows their hydrogen formation rate against time on stream. It can be seen that the 0.4 wt% Pd/HZSM-5 catalyst showed a burst in hydrogen formation rate at the beginning of the reaction which was apparently the highest hydrogen formation rate among all catalysts and which was followed by a sharp drop to the lowest apparent hydrogen formation rate after 120 minutes of time on stream. On the contrary, 0.4 wt% Ni/HZSM-5

catalyst displayed a more gradual increase in the hydrogen formation rate, which became higher than 0.4 wt% Pd/HZSM-5 catalyst after 90 minutes of time on stream before gradually declining. In general, the 0.4 wt% Ni/HZSM-5 catalyst showed better performance than the 0.4 wt% Pd/HZSM-5 catalyst beyond 90 minutes time on stream until the end of run.

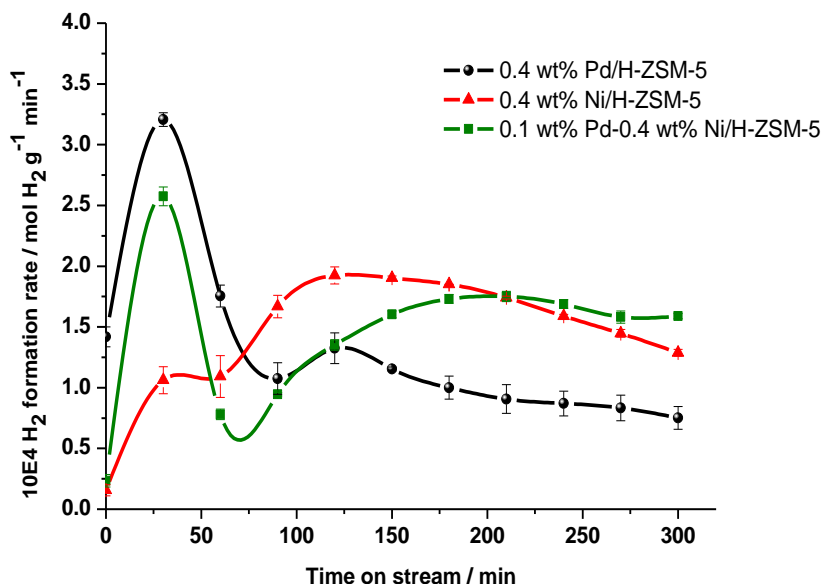


**Figure 6-1** Hydrogen formation rates as a function of time on stream for 0.4 wt% Ni/H-ZSM-5, 0.4 wt% Pd/H-ZSM-5 and Pd-Ni/H-ZSM-5 catalysts (dopant metal Pd/Ni atomic ratio of 0.25), the reaction temperature of 800 °C, the methane flow rate was 12 mL/min and 0.4 g catalyst mass.

As mentioned previously, these catalysts have not been treated with hydrogen to pre-reduce the metals loaded on the zeolite. Therefore, it could be that the reduction process played a role in the hydrogen production rates. According to some of the literature, the temperature-programmed reduction (TPR) of Ni/H-ZSM-5 and Pd/HZSM-5 catalysts revealed that there is a difference between Ni/H-ZSM-5 and Pd/HZSM-5 catalysts in the reduction temperature. It was reported that Ni/H-ZSM-5 may be reduced by 5 % H<sub>2</sub>-Ar in the temperature range of 550-600 °C under comparable conditions [246, 247], whereas Pd/H-ZSM-5 has been reported as being reducible by H<sub>2</sub> below 130 °C (ramp rate not specified) [248] and by CH<sub>4</sub> at approximately 325 °C under comparable conditions to those of references [246, 247]. Both indicate Pd to reduce more readily than Ni when supported by H-ZSM-5. As a result of the reduction temperature, it can be suggested that the 0.4 wt% Pd/HZSM-5 catalyst was reduced in the early phase of reaction, which explains its apparent high activity at the beginning of the reaction. However, it was shown in previous

chapter that the reason for the deactivation of Pd/HZSM-5 catalyst was due to the formation of encapsulating carbon on Pd particles. In the case of 0.4 wt% Ni/HZSM-5 catalyst, the gradual increase in performance could be attributed to a slow reduction process where complete reduction of the Ni particles only occurs at 90 minutes on stream. The gradual deactivation of the 0.4 wt% Ni/HZSM-5 catalyst beyond 90 minutes can be ascribed to the carbon deposited on the catalyst surface, as discussed in the introduction to this chapter. Moreover, consideration should be given to the relative atomic masses involved. 0.4 wt% of Ni in Ni/H-ZSM-5 contains a larger number of nickel atoms ( $12.10 \times 10^{13}$  atoms), in Ni/H-ZSM-5 catalyst, compared to Pd atoms in the 0.4 wt% Pd/H-ZSM-5 catalyst ( $6.36 \times 10^{13}$  atoms). This could provide an additional explanation for the activity of the Ni catalyst as well.

The effect of Pd doping of 0.4 wt% Ni/HZSM-5 catalyst was also presented in Figure 6-1. It can be observed that the Pd-Ni/HZSM-5 catalyst had similar traits to both Ni/H-ZSM-5 and Pd/H-ZSM-5 catalysts. It is clear that there is a burst in hydrogen formation rate at the beginning of the reaction which is similar to the behaviour of the 0.4 wt% Pd/H-ZSM-5 catalyst and the hydrogen formation rate was lower than that noted in the 0.4 wt% Pd/H-ZSM-5 catalyst – this could be due to the low amount of Pd doped in the 0.4 wt% Ni/HZSM-5 catalyst. In addition, the behaviour of the Pd-Ni/H-ZSM-5 catalyst after 60 minutes of time on stream was similar to the behaviour of the non-doped Ni/H-ZSM-5 catalyst. It seems that there is no evident synergy between the Ni and Pd from the beginning of the reaction to 240 minutes of time on stream. However, it can be noted after 240 minutes of time on stream that the catalyst showed greater stability. This may be because a phase change occurred at this stage of reaction and then enhanced the catalyst performance. Takenaka *et al.* [221] showed that Pd doping of the Ni/SiO<sub>2</sub> catalyst for methane decomposition into hydrogen and carbon at 550 °C led to improvement of the Ni/SiO<sub>2</sub> catalyst and an increase in its life time compared to the non-doped Ni/SiO<sub>2</sub>. It was observed in Chapter 5 that the addition of Ni into the 0.4 wt% Pd/H-ZSM-5 catalyst resulted in catalyst deactivation. It may be that the order of introduction of the precursors of these metals into the zeolite plays a role in the activity of the catalyst. Further investigations are required to clarify this expectation.

### 6.2.3 XRD patterns

Figure 6-2 (A, B) presents the XRD patterns for the pre- and post-reaction catalysts. All XRD patterns of the pre- and post-reaction catalysts for the 0.4 wt% Ni/HZSM-5, 0.4 wt% Pd/H-ZSM-5 and Pd-Ni/H-ZSM-5 catalysts matched with the pattern of H-ZSM-5. This indicates that the reaction conditions and the modification procedures of Pd-Ni/H-ZSM-5 catalyst did not affect on the zeolite structure and it remains intact.

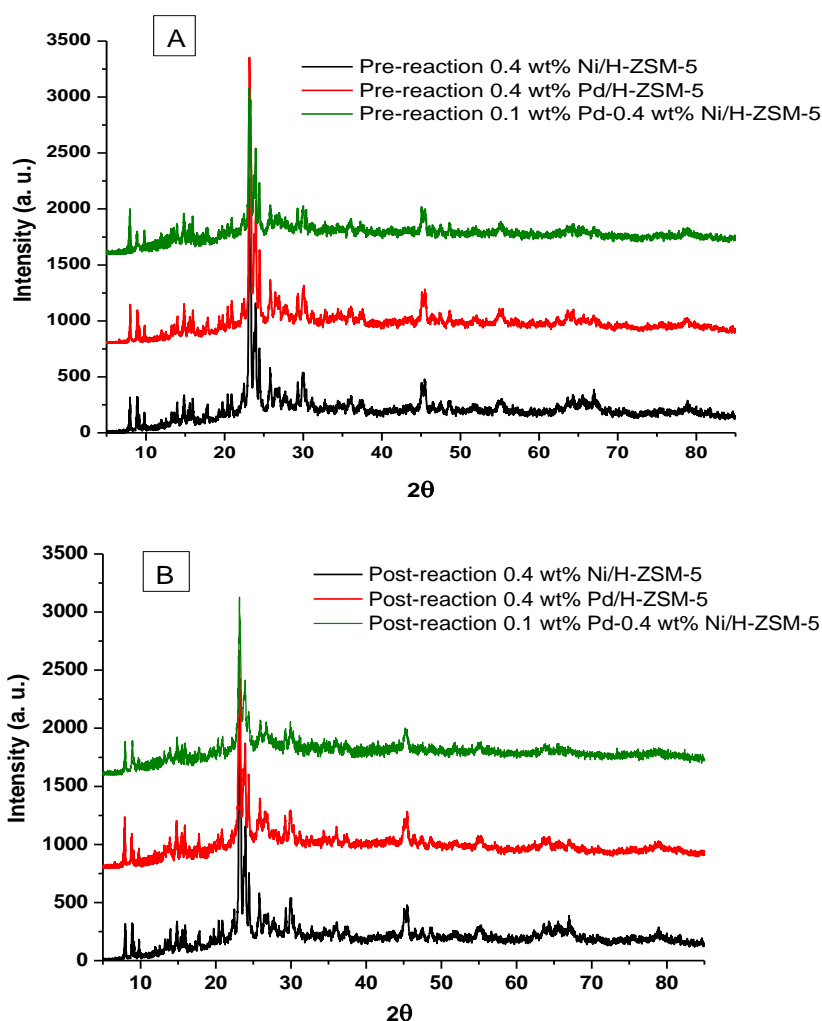


**Figure 6-2** XRD patterns of 0.4 wt% Ni/HZSM-5, 0.4 wt% Pd/H-ZSM-5 and the 0.4 wt% Ni/HZSM-5 doped with Pd in the pre-reaction (A) forms, and post-reaction (B) forms.

### 6.2.4 Post-reaction CHN and TGA analyses

CHN analysis and TGA studies for the post-reaction 0.4 wt% Ni/HZSM-5, 0.4 wt% Pd/H-ZSM-5 and Pd-Ni/H-ZSM-5 catalysts have been undertaken. Table 6-1 presents the results

of CHN analyses. From this data, it is evident that the amount of carbon deposited on the post-reaction catalysts is quite similar and is in the range of 10.20 to 10.80 wt%.

Catalyst	Mean value (wt%)		
	C	H	N
0.4 wt% Ni/H-ZSM-5	10.55 ± 0.15	-	-
0.4 wt% Pd/H-ZSM-5	10.80 ± 0.10	0.50 ± 0.04	-
0.1 wt% Pd-0.4 wt% Ni/H-ZSM-5	10.20 ± 0.10	-	-

TGA studies in the presence of air were performed for the post-reaction 0.4 wt% Ni/H-ZSM-5, 0.4 wt% Pd/H-ZSM-5 and Pd-Ni/H-ZSM-5 catalysts to estimate the amount of carbon deposited and to determine its reactivity profile with respect to air. Figure 6-3 shows the TGA profiles for the post-reaction 0.4 wt% Ni/H-ZSM-5, 0.4 wt% Pd/H-ZSM-5 and Pd-Ni/H-ZSM-5 catalysts. It is clear that there is a small weight loss below 250 °C, which is attributed to desorption of adsorbed water on the catalyst, with the weight loss in the region from 550 to 700 °C resulting from the burning off of deposited carbon. In addition, it can be observed that the results of CHN and TGA analyses are in good agreement.

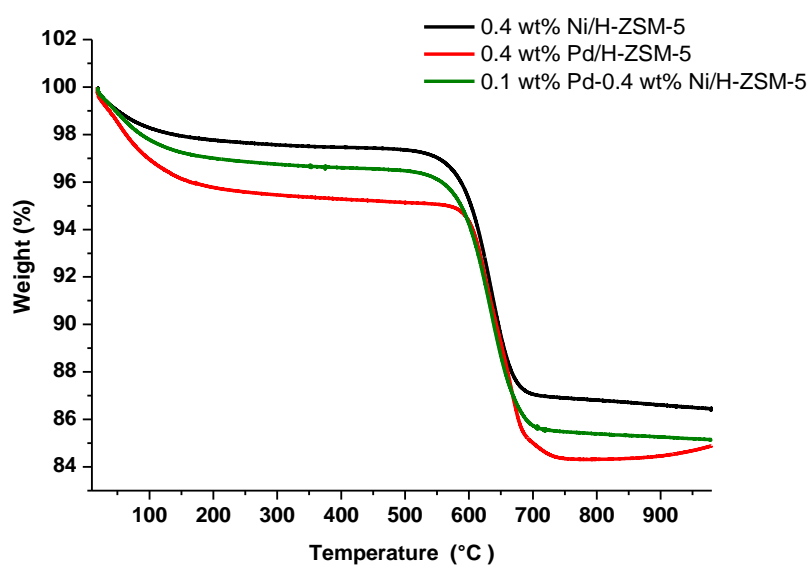


**Figure 6-3** TGA profiles for the post-reaction of 0.4 wt% Ni/HZSM-5, 0.4 wt% Pd/H-ZSM-5 and the 0.4 wt% Ni/HZSM-5 doped with Pd (dopant metal Pd/Ni atomic ratio of 0.25).

The first-derivative weight changes profiles for the post-reaction 0.4 wt% Ni/H-ZSM-5, 0.4 wt% Pd/H-ZSM-5 and Pd-Ni/H-ZSM-5 catalysts are presented in Figure 6-4. These profiles can indicate any differences in the nature of carbon deposited on the catalysts. From the profiles, it is evident that there is one peak in the burning off coke region at approximately 640 °C for the post-reaction 0.4 wt% Ni/H-ZSM-5 and Pd-Ni/H-ZSM-5 catalysts, whereas there were three peaks in the burning off coke region at approximately 615, 665 and 715 °C for the post-reaction 0.4 wt% Pd/H-ZSM-5 catalyst. This reveals that the carbonaceous species in 0.4 wt% Pd/H-ZSM-5 catalyst differs from those deposited on 0.4 wt% Ni/H-ZSM-5 and Pd-Ni/H-ZSM-5 catalysts although consideration has to be made of the catalytic effects of the metal components with respects to carbon oxidation. In addition, it seems apparent that the 0.4 wt% Ni/H-ZSM-5 and Pd-Ni/H-ZSM-5 catalysts had similar carbon species despite the differences in the composition of catalyst and reaction profile. This suggests that the Ni metal in the Pd-Ni/H-ZSM-5 catalyst may have played the major role for carbon deposition.

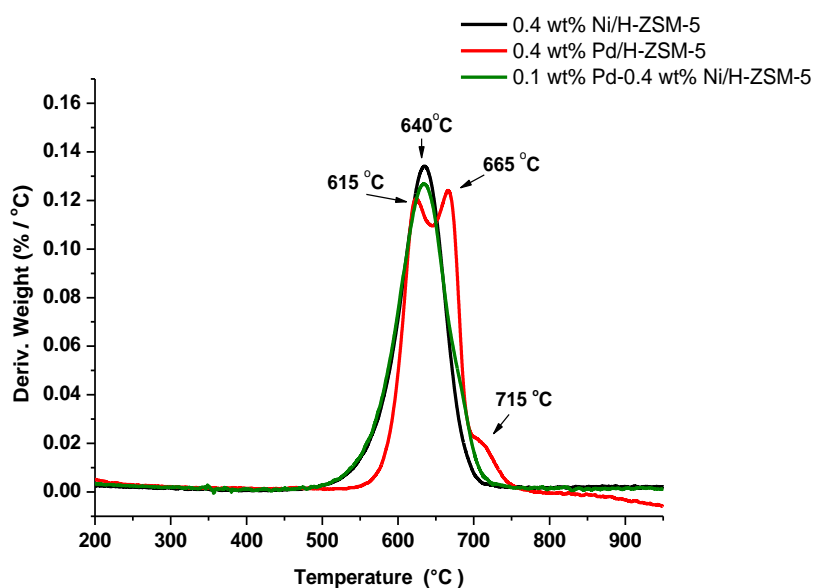


**Figure 6-4** TGA profiles for the post-reaction of 0.4 wt% Ni/HZSM-5, 0.4 wt% Pd/H-ZSM-5 and the 0.4 wt% Ni/HZSM-5 doped with Pd (dopant metal Pd/Ni atomic ratio of 0.25),.

### 6.2.5 Post-reaction SEM images

SEM images of the post-reaction 0.4 wt% Ni/H-ZSM-5, 0.4 wt% Pd/H-ZSM-5 and Pd-Ni/H-ZSM-5 catalysts are presented in Figure 6-5. From the image (A) it appears that carbon filaments were not formed over the 0.4 wt% Ni/H-ZSM-5 catalyst, while they

clearly formed over the 0.4 wt% Pd/H-ZSM-5 catalyst, as seen in image (B). The Pd-Ni/H-ZSM-5 catalyst showed very low formation of carbon filaments, which are marked with arrows. The formation of filamentous carbon in the Pd-Ni/H-ZSM-5 catalyst can be attributed to the palladium content in the catalyst.

Goodman and co-workers [19] studied hydrogen production *via* catalytic decomposition of methane over a 10 wt% Ni/H-ZSM-5 catalyst at reaction temperatures of 450 and 700 °C. They demonstrated that no filamentous carbon was observed on Ni/H-ZSM-5 catalyst at 700 °C, whereas they were formed at 450 °C. In addition, they stated that graphitic carbon was formed at high temperatures, which led to the deactivation of catalyst by encapsulation of Ni particles limiting the growth of filamentous carbon. This study conflicts with the finding by Chai *et al.* [249] who reported that carbon nanofibres were grown over a 10 wt% Ni/H-ZSM-5 catalyst at 550 and 700 °C.

Ziebro *et al.* [250] synthesised filamentous carbon over a 4 wt% Ni/ZSM-5 catalyst by the chemical vapour deposition of methane in the relatively low temperature range of 400–550 °C. The SEM and TEM micrographs showed that the formation of filamentous carbon occurred at temperature range 400–550 °C. Moreover, they claimed that methane decomposition at 400 °C mainly took place in the channels of the zeolite, while above 400 °C the carbon deposited was observed on the surface of the 4 wt% Ni/ZSM-5 catalyst.

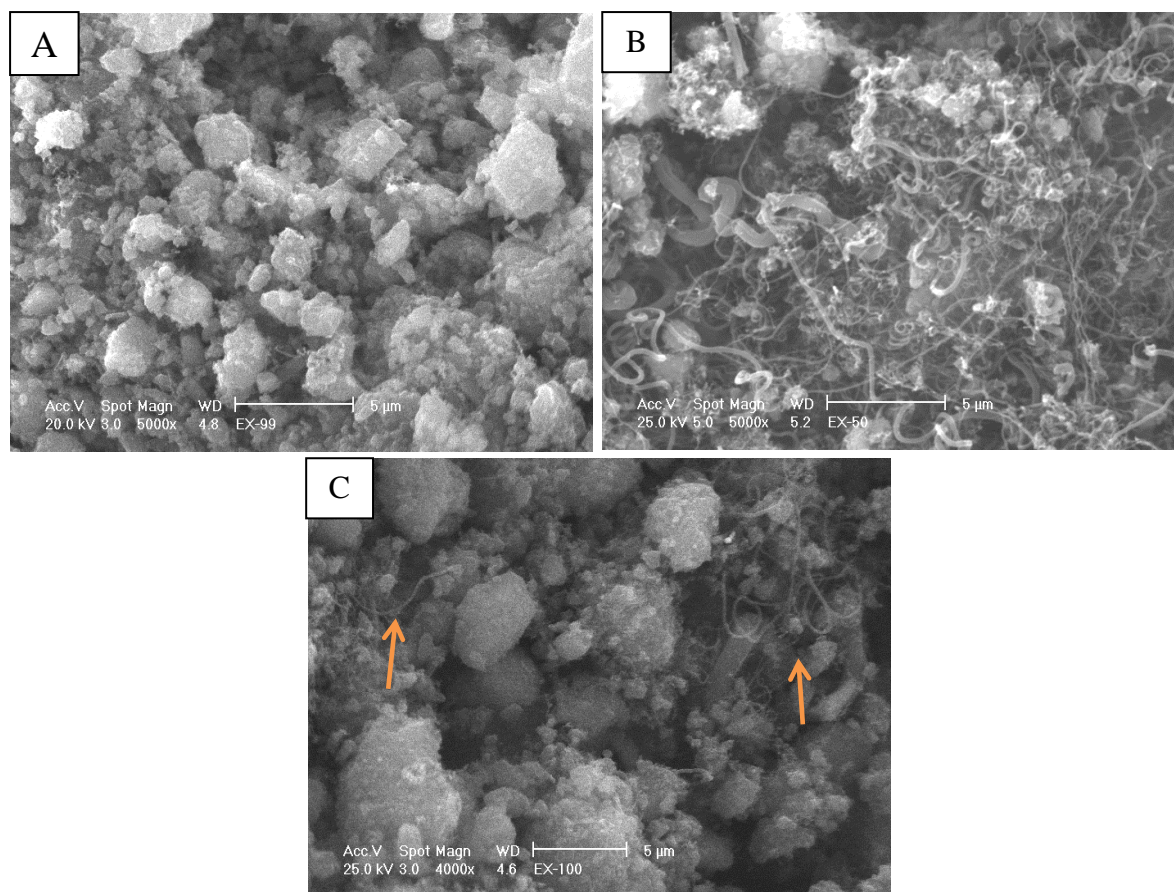


**Figure 6-5** SEM images for the post-reaction 0.4 wt% Ni/HZSM-5 (A), 0.4 wt% Pd/HZSM-5 (B), and the 0.4 wt% Ni/HZSM-5 doped with Pd (C).

At high temperature, it was suggested that Ni-based catalysts will appear in a quasi-liquid state where the catalyst particles may easily convert into small particles which are easily encapsulated by the carbon layers formed during methane decomposition, contributing to faster catalyst deactivation. On the contrary, at low temperature, the catalyst was proposed to remain in the solid state instead, remaining active during the catalysis process [61]. Moreover, the high reaction temperature above 700 °C caused sintering of Ni particles to form large Ni particles, which deactivate and reduce the formation of carbon filaments [86].

From the above studies, it seems that the temperature used in this work is not appropriate for formation of filamentous carbon over the 0.4 wt% Ni/ZSM-5 catalyst. In the next section, the effect of reaction temperature on the activity of the 0.4 wt% Ni/ZSM-5 catalyst for methane cracking into hydrogen and carbon will be described.

### **6.3. Effects of reaction temperature on the direct cracking of methane over the 0.4 wt% Ni/H-ZSM-5 catalyst**

#### **6.3.1 Introduction**

From reviewing the literature, the maximum temperature used for the cracking of methane over Ni/H-ZSM-5 catalysts was 700 °C [19, 249, 250]. In this study, different reaction temperatures were used in the range from 600 to 900 °C for methane cracking over the 0.4 wt% Ni/H-ZSM-5 catalyst. The flow rate of methane was fixed at 12 mL/min and catalyst mass at 0.4 g. The catalysts were characterised using different techniques such as XRD, CHN, TGA, SEM, to observe the occurred changes in catalysts and carbon deposited on them. However, it should be mentioned that the time on stream for the experiments detailed in this section is longer than for those in other sections.

#### **6.3.2 Reaction data**

The effect of the reaction temperature on the activity of 0.4 wt% Ni/H-ZSM-5 was studied. Figure 6-6 shows the data of the hydrogen formation rates against time on stream at different temperatures in range from 600 to 900 °C. It is apparent from the profile of hydrogen production that as expected hydrogen formation rates were increased by increasing reaction temperature. The performance of the catalyst was not significantly noticeable in the range of 600 to 700 °C while it was remarkable between 750 and 900 °C. However, catalyst deactivation rate is observed clearly and it is faster at the higher cracking temperatures whereas it is not observed at temperatures in the range from 600 to 750 °C. The rapid deactivation of the catalyst, which occurred at high temperatures, could be attributed to the production of large amounts of carbon in addition to other factors such as sintering and/or the formation of encapsulated carbon on the catalyst particles.

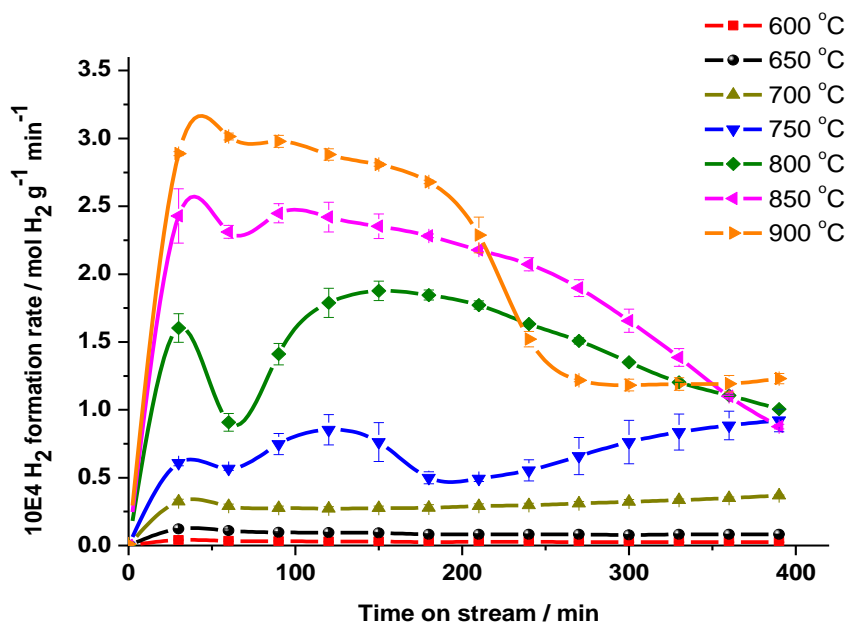


**Figure 6-6** Hydrogen formation rates as a function of time on stream for methane cracking over 0.4 wt% Ni/H-ZSM-5 catalyst at different temperatures in range of 600 to 900 °C, the methane flow rate is 12 mL/min and 0.4 g catalyst mass.

Inaba *et al.* [245] investigated the methane decomposition over nickel-based catalysts on different types of zeolite at 650 °C. They found that the 10 wt% Ni/H-ZSM-5 catalyst was completely deactivated after 4 h. Chai *et al.* [249] studied the direct decomposition of methane over 10 wt% Ni/H-ZSM-5 catalyst at 550 and 700 °C. They demonstrated that a 10 wt% Ni/H-ZSM-5 catalyst at 550 °C had good activity and stability throughout the experiment, while it showed high initial methane conversions (roughly 47 %) followed by rapid drop to be below 2 % at 700 °C.

In the current study, the 0.4 wt% Ni/H-ZSM-5 catalyst showed low activity and high stability at temperatures in range from 600 to 750 °C.

### 6.3.3 XRD patterns

Figure 6-7 presents the XRD patterns for the pre- and post-reaction 0.4 wt% Ni/HZSM-5 catalysts run at different reaction temperatures. It can be seen that no modification of phases is observed (except for a certain loss in the intensity of the principal diffraction lines of H-ZSM-5 which are at *ca.* 23-25° 2θ as a result of carbon deposited on the catalysts). However, the nickel contained in the catalyst was not detected by XRD. This suggests that Ni crystallites may remain in a highly dispersed form on the surface or in the

channels of the H-ZSM-5 zeolite or their amount is too small to be identified by the XRD technique.

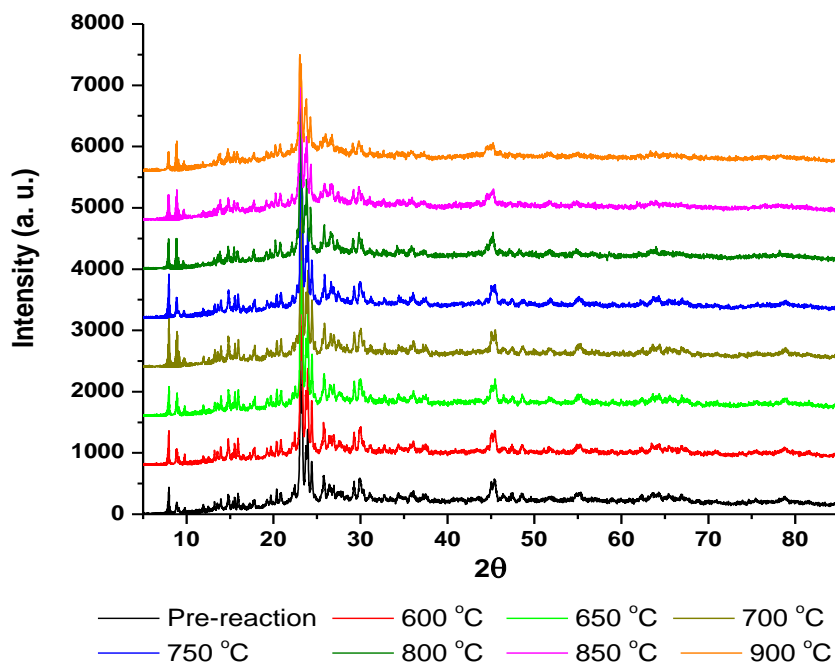


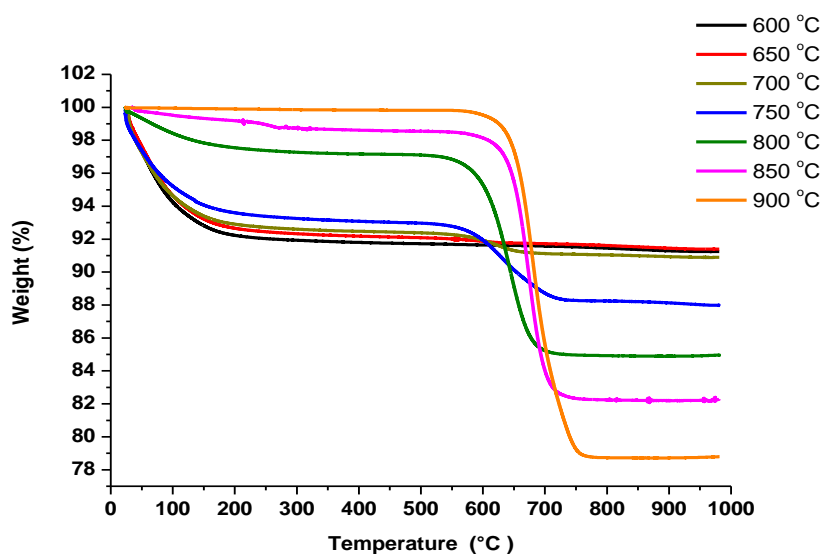
**Figure 6-7** XRD pattern of 0.4 wt% Ni/H-ZSM-5 in the pre- and post-reaction forms at run different temperatures.

### 6.3.4 Post-reaction CHN and TGA analyses

CHN and TGA analyses for the post-reaction 0.4 wt% Ni/H-ZSM-5 catalysts have been undertaken. Table 6-2 presents the results of the CHN analyses. It can be observed that no deposited carbon can be detected on the post-reaction catalyst at 600 and 650 °C. In addition, it can be noted that the amount of carbon deposited on the post-reaction 0.4 wt% Ni/H-ZSM-5 catalysts is increased with increasing reaction temperature from 700 to 900 °C. These increases in the amount of carbon deposited are consistent with the increase in the reaction rates observed in Figure 6-6.

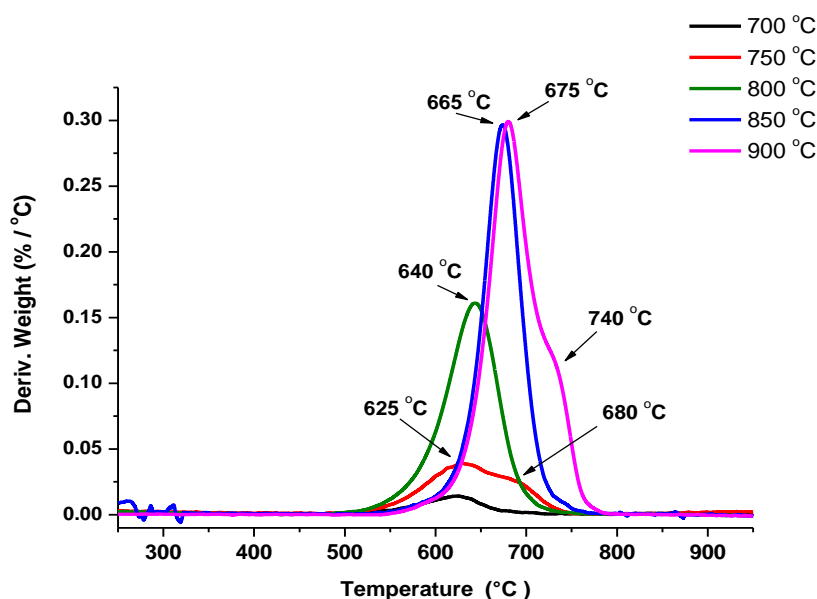
<b>Table 6-2</b> CHN analysis for the post-reaction 0.4 wt% Ni/H-ZSM-5 catalyst at different reaction temperatures.				
<b>Catalyst</b>	<b>Reaction Temperature (°C)</b>	<b>Mean value (wt%)</b>		
		<b>C</b>	<b>H</b>	<b>N</b>
<b>0.4 wt% Ni/H-ZSM-5</b>	<b>600</b>	-	<b>0.61 ± 0.03</b>	-
	<b>650</b>	-	<b>0.58 ± 0.02</b>	-
	<b>700</b>	<b>1.10 ± 0.10</b>	<b>0.53 ± 0.04</b>	-
	<b>750</b>	<b>5.00 ± 0.10</b>	<b>0.48 ± 0.01</b>	-
	<b>800</b>	<b>12.04 ± 0.16</b>	<b>0.47 ± 0.02</b>	-
	<b>850</b>	<b>16.32 ± 0.15</b>	<b>0.34 ± 0.02</b>	-
	<b>900</b>	<b>21.30 ± 0.13</b>	<b>0.48 ± 0.01</b>	-

Figure 6-8 shows their TGA oxidation profiles under air. From these profiles, it can be seen that a small weight loss below 250 °C occurs which can be ascribed to desorption of adsorbed water on the catalyst, whereas the weight loss between almost 550 and 780 °C is due to the burning off of coke that has been deposited on the catalyst. It is observed that there is a good agreement between the results of CHN and TGA analyses since the weight percentage of carbon deposited is increased with increasing temperature from 700 to 900 °C. Additionally, no weight loss beyond 250 °C is observed for the post-reaction catalysts at 600 and 650 °C.



**Figure 6-8** TGA profiles for the post-reaction of 0.4 wt% Ni/H-ZSM-5 catalyst run at different reaction temperatures.

The first-derivative weight change profiles are presented in Figure 6-9. From these profiles, the differences among the carbon deposited on catalysts are more apparent than those evident in Figure 6-8. It can be observed that the post-reaction 0.4 wt% Ni/H-ZSM-5 catalysts run at reaction temperatures of 700, 800 and 850 °C possess one oxidation peak, while at 750 and 900 °C there is an additional small shoulder to the main weight loss. Moreover, the position of the oxidation peaks has gradually shifted to the high oxidation temperature with increase reaction temperature from 700 to 900 °C. This possibly indicates the formation of different species of carbon deposited and/or due to increasing density of the carbon deposited. However, it can be observed that the post-reaction 0.4 wt% Ni/H-ZSM-5 catalysts at 700 to 800 °C have somewhat similar carbonaceous materials in the region 620 to 640 °C. Also, the post-reaction 0.4 wt% Ni/H-ZSM-5 catalyst at 750 °C showed a second oxidation peak at the higher temperature of 680 °C. For the post-reaction catalysts which were run at 850 and 900 °C, it can be seen that these two catalysts possessed similar carbonaceous materials in the region of 665 to 675 °C, apart from a small shoulder after the main peak at roughly 740 °C for the post-900 °C material.



**Figure 6-9** TGA profiles for the post-reaction of 0.4 wt% Ni/H-ZSM-5 catalyst run at different reaction temperatures.

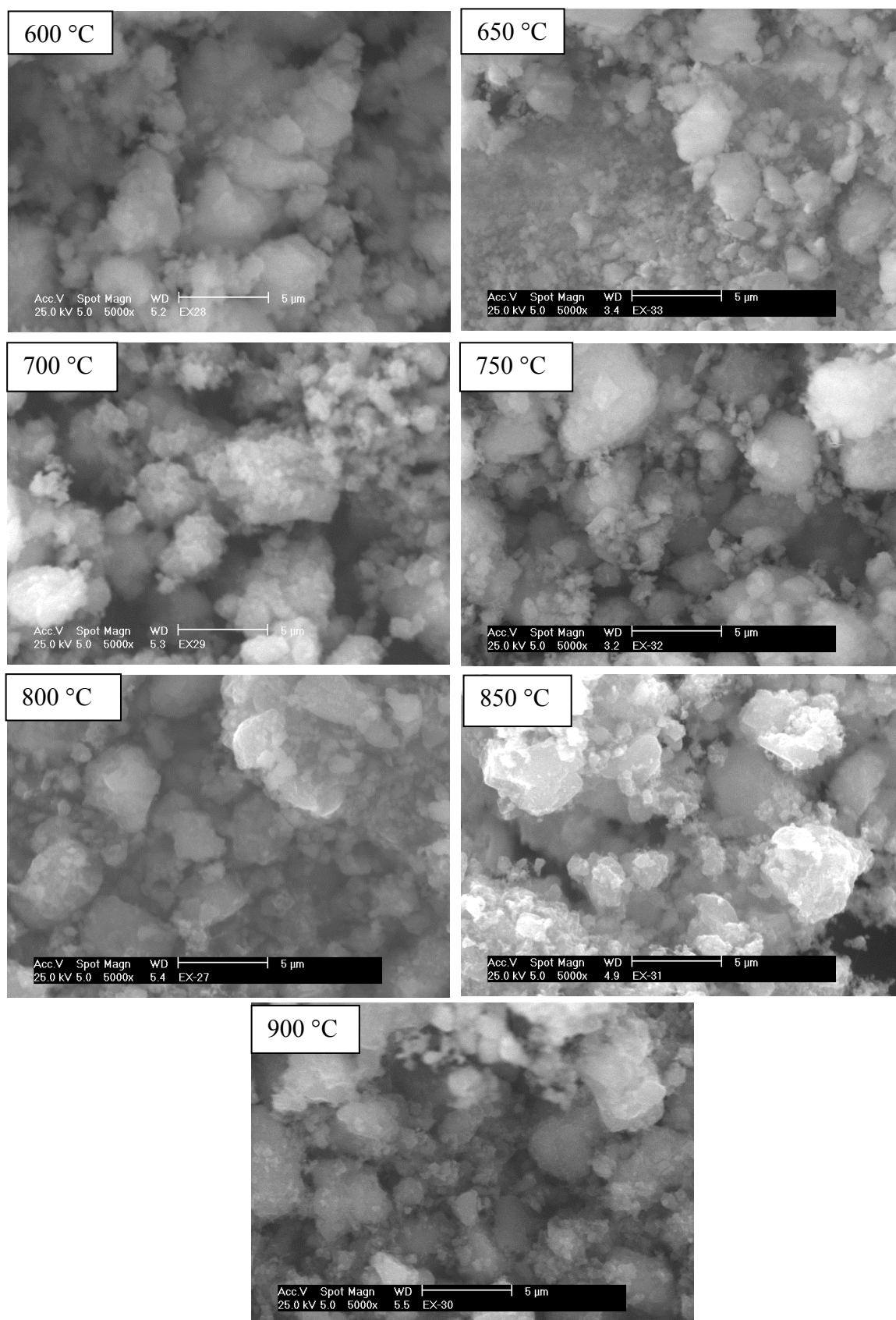
### 6.3.5 Post-reaction SEM images

Figure 6-10 presents SEM images of the post-reaction 0.4 wt% Ni/H-ZSM-5 catalysts. From these images it is clear that carbon filaments (CF) were not formed. Hence it seems that H-ZSM-5 supported nickel, at the loading employed, cannot be used to produce filamentous carbon. This is unlike palladium, which showed its potential for the production of carbon filaments under the same conditions.

Takenaka *et al.* [62] studied the decomposition of methane over Ni catalysts supported on silicas with different specific surface areas and pore structures. They found that the silica support with no pore structure was found to have the highest catalytic activity and the longest catalyst lifetime. They interpreted this finding as that the growth of carbon filaments in the pores of the silica supports has a high probability of the collision with other carbon filaments in the pores or with the inside walls of the supports, which may deactivate the catalyst and preventing extended growth of carbon filaments. Therefore, the non-porous silica was the most effective support.

It is known that the framework of H-ZSM-5 zeolite contains channels and pores. Also, the Ni loading in this study is low. Therefore, it can be suggested that nickel is highly dispersed and the majority of the methane cracking reaction occurs within the pore structure which limits the growth of carbon filaments on the surface of the zeolite. This is in contrast to palladium, which can be dispersed in the channels and on the outer surface of zeolite.

However, the amount of Ni loading on Ni/ZSM-5 catalyst in this study is low. Therefore, it may be that the low loading of Ni is not suitable to form filamentous carbon on Ni/ZSM-5 catalyst. In next section this aspect was further studied.



**Figure 6-10** SEM images of the post-reaction 0.4 wt% Ni/H-ZSM-5 catalyst run at different reaction temperatures.

## 6.4. Effect of nickel loading on the direct cracking of methane over the Ni/H-ZSM-5 catalyst

### 6.4.1 Introduction

In the previous two sections, it was observed that no carbon filaments were formed on the Ni/H-ZSM-5 catalyst. Also, as mentioned previously the Ni loading in previous experiments was low (0.4 wt %) which possibly plays a role in the apparent lack of formation of carbon filaments. Elsewhere, studies have showed the formation of filamentous carbon over Ni/H-ZSM-5 catalyst regardless of reaction temperature, at 4 wt% and 10 wt% Ni loadings [19, 249, 250].

Moreover, some of the studies that have examined the effect of the amount of nickel loaded on the support did not show and discuss the formation of carbon filaments at low loadings of nickel. For example, Venugopal *et al.* [48] studied the effect of Ni loading on the catalytic activity of Ni/SiO<sub>2</sub> for methane decomposition at 600 °C. The Ni loading amounts in the Ni/SiO<sub>2</sub> ranged from 5 to 90 wt%. They demonstrated the formation of filamentous carbon over 30 and 50 wt% Ni/SiO<sub>2</sub>, but they did not refer to the formation of carbon filaments over the catalyst with lower amounts of Ni. Takenaka and co-workers [40] also studied the impact of Ni loading on silica for hydrogen and carbon production from methane decomposition at 500 °C. The amount of Ni loading was in the range 1 to 90 wt%. They showed the formation of filamentous carbon over 13, 40 and 70 wt% Ni/SiO<sub>2</sub>, but they did not refer to the formation of carbon filaments over the lower amount of Ni loaded on the support.

However, Noda *et al.* [86] studied the effect of Ni loading and reaction temperature on the formation of carbon nanotubes from methane catalytic decomposition over Ni/SiO<sub>2</sub>. The amount of Ni loading was 1 and 5 wt%. They showed that a low loading of Ni (1 wt%) produced a low quantity of carbon nanotubes, while higher loading of Ni (5 wt%) produced a large quantity of carbon nanotubes. Also, they demonstrated that the amount of carbon nanotubes decreased with increasing the reaction temperature for both catalysts due to sintering effects.

The aim of the work described in this section was to investigate the formation of carbon filaments on the surface of Ni/H-ZSM-5 catalyst as a function of Ni loading.

Ni/H-ZSM-5 catalysts with Ni loadings of 0.4, 4 and 8 wt% were prepared as described in Chapter 2. These catalysts were calcined at 500 °C and they were not pre-treated with hydrogen to reduce the nickel loaded on zeolite.

### 6.4.2 Reaction data

Direct cracking of methane at 800 °C over Ni/H-ZSM-5 catalyst with different loadings was performed. Figure 6-11 displays the data of the hydrogen formation rates against time on stream. It can be seen that increasing the nickel loading increases the initial hydrogen formation rates at the beginning of the reaction. 8 wt% Ni/H-ZSM-5 showed the highest initial hydrogen formation rate followed by 4 wt% Ni/H-ZSM-5 catalyst. 0.4 wt% Ni/H-ZSM-5 catalyst demonstrated the lowest initial hydrogen formation rate. 8 wt% Ni/H-ZSM-5 and 4 wt% Ni/H-ZSM-5 catalysts showed initially a rapid decline in hydrogen formation rates, whereas the 0.4 wt% Ni/HZSM-5 catalyst displayed gradual increase in its hydrogen formation rate. After 50 minutes of time on stream, 0.4 wt% Ni/HZSM-5 and 4 wt% Ni/H-ZSM-5 catalysts had quite similar and hydrogen formation rates until the end of reaction. In contrast, 8 wt% Ni/H-ZSM-5 was the most active up to 60 minutes of time on stream and then gradually dropped to show the lowest hydrogen formation rate.

It seems that the increase of nickel loading (from 0.4 to 4 and 8 wt %) in the catalyst increases the nickel particle size on the support. As a result, reactions run at the high temperature of 800 °C could lead to accelerated sintering because the Tamman temperature of Ni is 590 °C [66, 251]. This may explain the reason for the rapid deactivation of the catalyst at the higher loading. Conversely, the presence of a low loading of Ni (0.4 wt %) in the catalyst may result in less sintering because the nickel particles are highly dispersed and spaced from each other. Hence, the deactivation period was not observed at the beginning of the reaction, but it was noted after 150 minutes of time on stream as a result of carbon deposited.

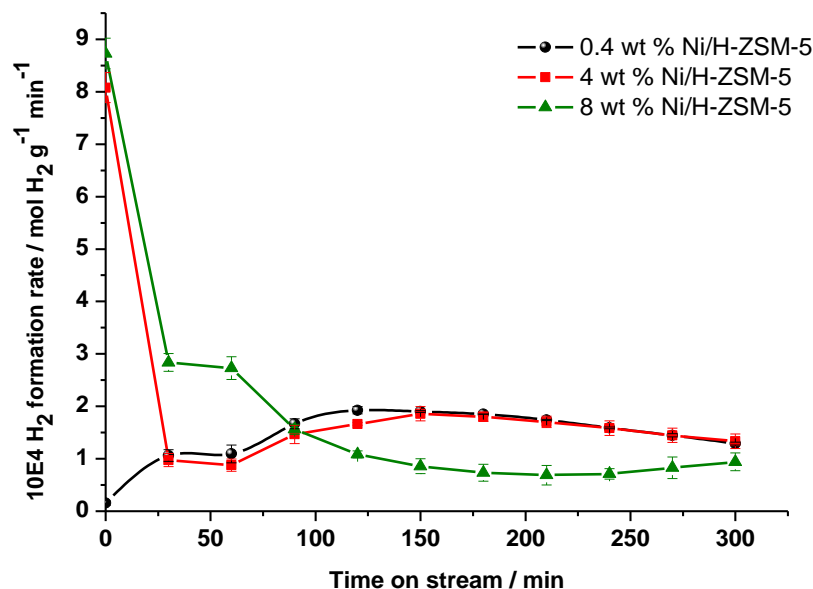


**Figure 6-11** Hydrogen formation rates as a function of time on stream for methane cracking over Ni/H-ZSM-5 catalysts loaded with different amounts of Ni: 0.4, 4 and 8 wt%, the reaction temperature of 800 °C, the methane flow rate was 12 mL/min.

### 6.4.3 XRD patterns

The XRD patterns for the pre- and post-reaction Ni/H-ZSM-5 catalysts are presented in Figure 6-12 (A, B). From Figure 6-12 (A), it can be seen that the XRD patterns of the pre-reaction 0.4 and 4 wt% Ni/H-ZSM-5 catalysts show the characteristic reflections of H-ZSM-5. In addition, the 8 wt% Ni/H-ZSM-5 catalyst displayed additional reflections at  $2\theta = 37.28^\circ, 43.30^\circ, 62.80^\circ, 75.30^\circ$  and  $79.40^\circ$ , which can be attributed to the NiO phase. Furthermore, it can be observed that the intensity of H-ZSM-5 reflections particular at  $2\theta$  of *ca.* 8, 9 reduced with increasing the amount of Ni loading from 0.4 to 8 wt%. This is possibly due to the increase of NiO in the channels of the H-ZSM-5 zeolite.

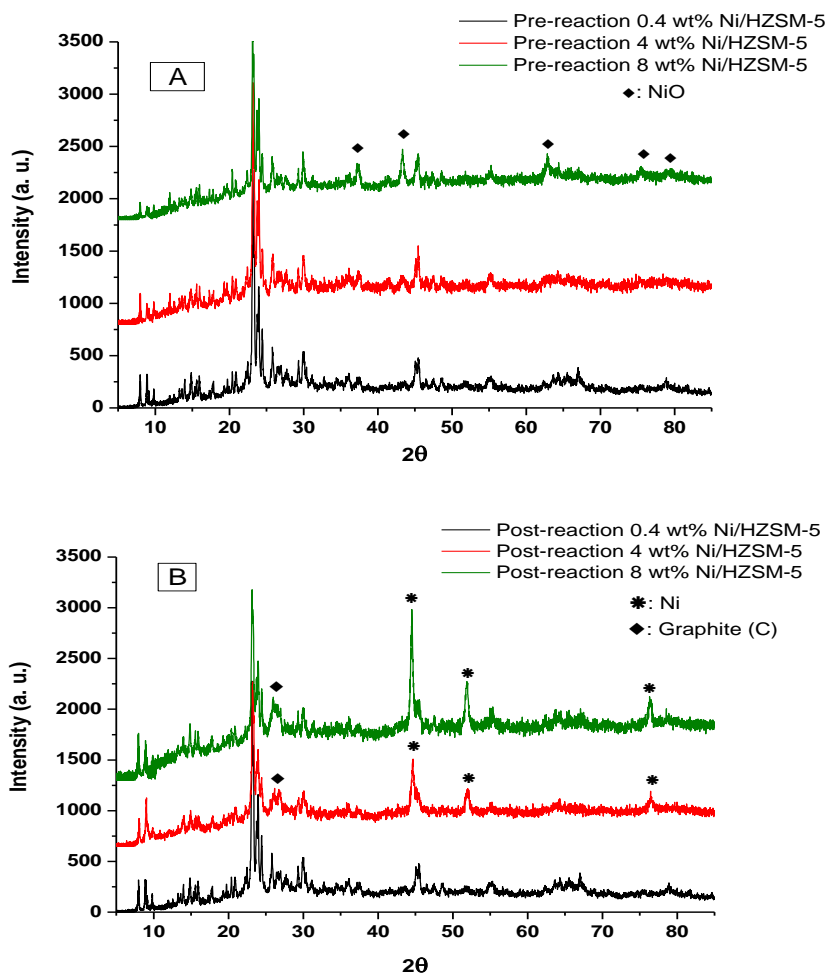


**Figure 6-12** XRD patterns of the pre- (A) and post-reaction (B) Ni/H-ZSM-5 catalysts loaded with different amounts of Ni: 0.4, 4 and 8 wt%.

Figure 6-12 (B) presents the XRD patterns for the post-reaction materials. It can be seen that the XRD pattern for the post-reaction 0.4 wt% Ni/HZSM-5 catalyst did not change corresponding to the XRD pattern for the pre-reaction 0.4 wt% Ni/HZSM-5 catalyst, which matches the pattern of H-ZSM-5. This indicates that nickel is still highly dispersed and/or its quantity is too small to be identified by the XRD technique. In case of 4 and 8 wt% Ni/H-ZSM-5 catalysts, the appearance of a new phase additional to H-ZSM-5 reflections is evident. This new phase matches metallic nickel at  $2\theta = 44.20^\circ$ ,  $51.70^\circ$  and  $76.40^\circ$ . The presence of metallic Ni in the post-reaction catalysts confirms reduction of the NiO phase to form metallic Ni during reaction.

Since the NiO phase in the 4 wt% precursor cannot be seen by XRD this suggests that the reaction conditions caused sintering or agglomeration process of Ni particles, increasing

their particle size. Therefore, it can be assumed that sintering is a deactivation route in addition to carbon deposition.

Also, it can be observed from the XRD patterns, Figure 6-12 (B), for the post-reaction 4 and 8 wt% Ni/H-ZSM-5 catalysts that there is change in the peak at  $2\theta = 26.10^\circ$  where the peak appeared to be somewhat more intense and broad. This indicates that graphitic carbon was formed in these two samples.

#### 6.4.4 Post-reaction CHN and TGA analyses

Table 6-3 displays the post-reaction CHN analysis for the post-reaction catalysts. It can be seen that the quantity of carbon deposited increased in the following order:  $10.80 < 12.90 < 14.71$  wt% with the increasing amount of Ni loading. Although the increases between these quantities are not large they may have affected the catalysts' activity, as shown in Figure 6-11.

<b>Table 6-3</b> CHN analyses of the post-reaction Ni/H-ZSM-5 catalysts loaded with different amounts of Ni: 0.4, 4 and 8 wt%.			
<b>Catalysts</b>	<b>Mean value (wt%)</b>		
	<b>C</b>	<b>H</b>	<b>N</b>
<b>0.4 wt% Ni/H-ZSM-5</b>	<b>10.55 ± 0.15</b>	-	-
<b>4 wt% Ni/H-ZSM-5</b>	<b>12.90 ± 0.50</b>	<b>0.33 ± 0.08</b>	-
<b>8 wt% Ni/H-ZSM-5</b>	<b>14.71 ± 0.40</b>	<b>0.30 ± 0.00</b>	-

Figure 6-13 shows the TGA oxidation analysis under air for the post-reaction catalysts. From the TGA profiles in Figure 6-13, it can be seen that again there are two main weight loss regions. The weight loss in the region below 250 °C is attributed to water loss, whereas the weight loss in the region between 500 to 700 °C is due to the burning off of the carbon deposited.

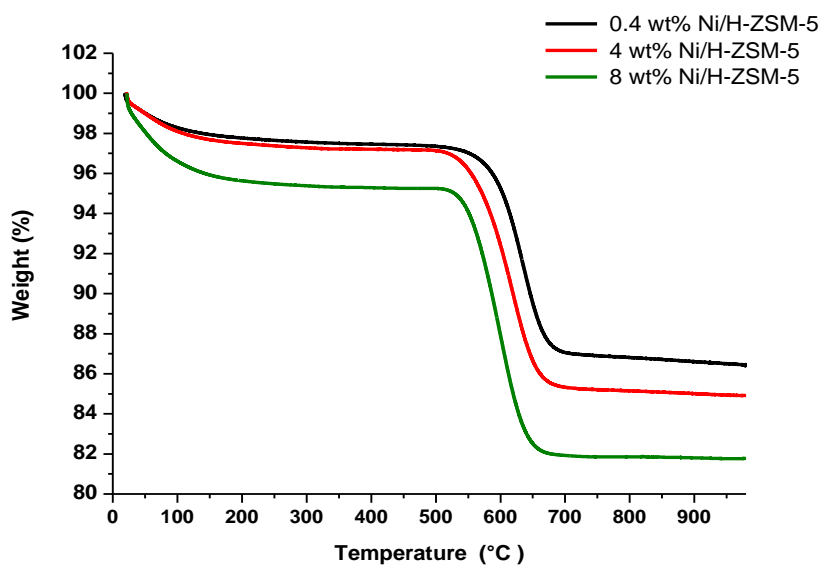


**Figure 6-13** TGA profiles of the post-reaction Ni/H-ZSM-5 catalysts loaded with different amounts of Ni: 0.4, 4 and 8 wt%.

The first-derivative weight changes profiles for the post-reaction materials are shown in Figure 6-14. It can be seen from these profiles that all post-reaction catalysts have one weight loss region between 500 to 700 °C. These weight loss regions are at roughly 635, 615 and 600 °C for the post-reaction 0.4 wt% Ni/H-ZSM-5, 4 wt% Ni/H-ZSM-5 and 8 wt% Ni/H-ZSM-5 catalysts, respectively. However, the difference among them is in the areas under the peaks, relating to the amount of carbon deposited, and also in the position of the oxidation peaks.

Furthermore, it is observed that the position of the oxidation peaks (weight loss regions) is shifted from 635 to 600 °C with increase the amount of Ni loading on catalyst. As mentioned in the previous chapter, the presence of residual metal in the sample can catalyse the oxidation of the carbon species and may lower the temperature at which the maximum oxidation rate occurs. As a result, an increase in the amount of nickel in the sample may promote the oxidation reaction of carbon at lower temperatures. Therefore, the burning off carbon deposited on the 8 wt% Ni/H-ZSM-5 catalyst showed a relatively low oxidation temperature at roughly 600 °C, while it occurred at a relatively high oxidation temperature of 635 °C for the 0.4 wt% Ni/H-ZSM-5 catalyst.

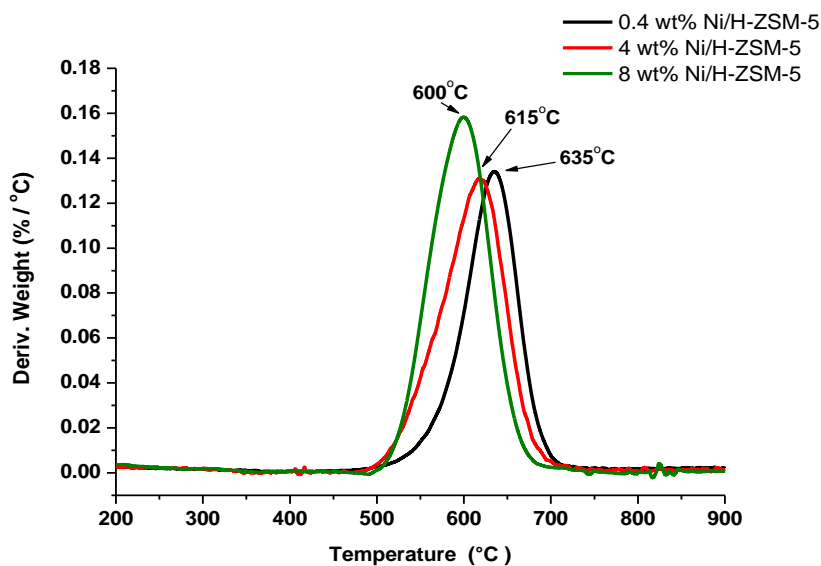


**Figure 6-14** TGA profiles of the post-reaction Ni/H-ZSM-5 catalysts loaded with different amounts of Ni: 0.4, 4 and 8 wt%.

### 6.4.5 Post-reaction SEM images

Figure 6-15 (A-C) presents SEM images for the post-reaction catalysts. In images B and C, it can be seen that carbon filaments were formed over the 4 and 8 wt% Ni/H-ZSM-5 catalysts, while they were not formed over the 0.4 wt% Ni/H-ZSM-5 catalyst (image A). However, it appears that the increase of Ni loading from 4 to 8 wt% led to an increase in the growth of filamentous carbon. This confirms that the Ni loading has a significant influence on carbon filament growth. It is possible that the increase of Ni loading led to an increased Ni content on the outer surface of zeolite and thus resulted in form the filamentous carbon over the catalyst. Indeed, the observation of NiO reflections suggests that particles  $> 30 \text{ \AA}$  were formed which would be too large to be accommodated within the ZSM-5 channel structure.

Moreover, it was reported that the particles size of Ni metal were increased gradually with the increase of Ni loading as a result of the agglomeration of Ni metal particles [48, 252]. Also, it was mentioned in Chapter 4 that the formation of carbon filaments is highly dependent on the catalyst particle size in the decomposition of methane. Beyond a certain size range, being either too small or too big, metal particles are inappropriate for filament growth [39, 196]. Hence, it can be suggested that the high loading of Ni, 4 and 8 wt%, over H-ZSM-5 support led to particles sizes of Ni metal appropriate for filament growth.

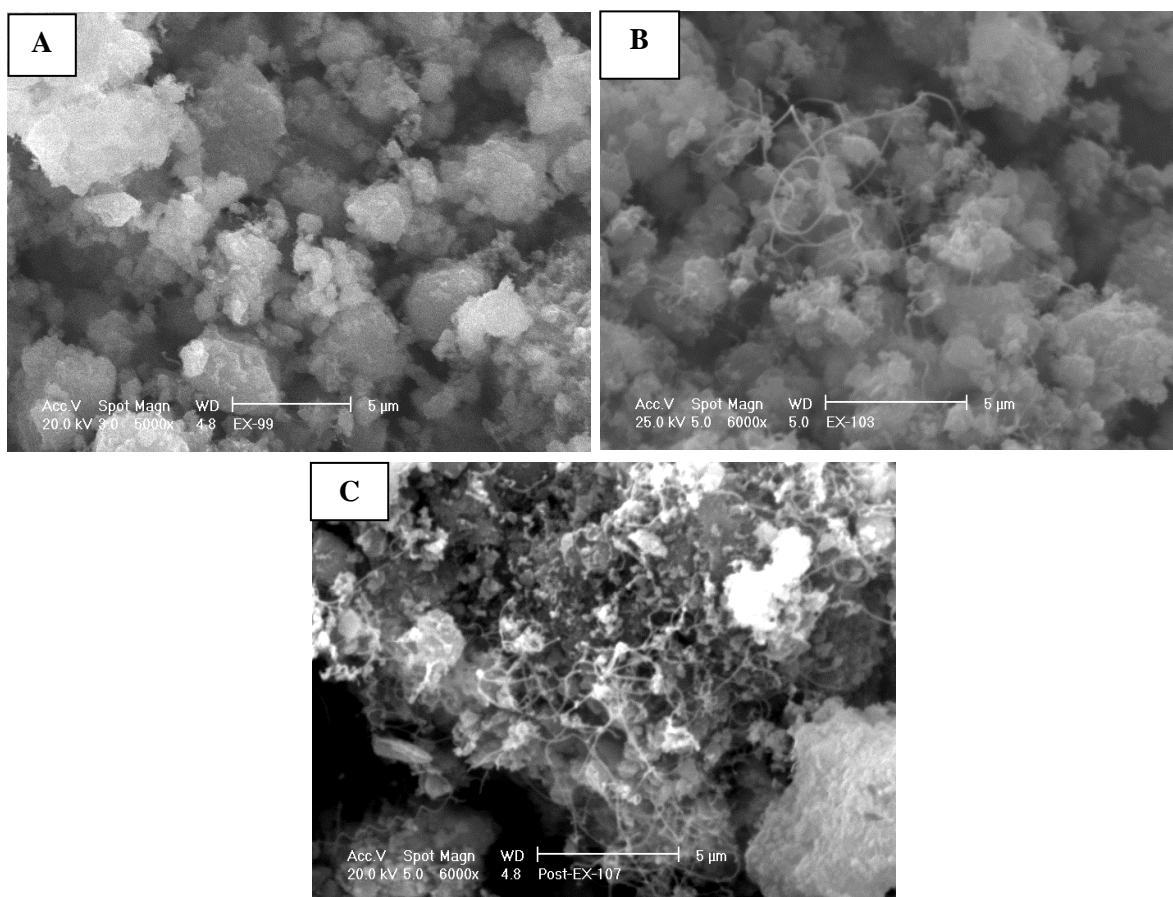


**Figure 6-15** SEM images of the post-reaction 0.4 wt% Ni/H-ZSM-5 catalyst (A), 4 wt% Ni/H-ZSM-5 catalyst (B) and 8 wt% Ni/H-ZSM-5 catalyst (C).

## 6.5. Effect of support on the activity of nickel catalysts for the direct cracking of methane

### 6.5.1 Introduction

As mentioned in the previous chapter, the support material can directly influence the methane cracking reaction by affecting the surface area of the loaded metal by stabilisation of the metallic catalyst particles and by influencing the metal's electronic state. Several supports have been used for preparation nickel-based catalysts such as  $\text{SiO}_2$ ,  $\text{TiO}_2$ ,  $\text{Al}_2\text{O}_3$ ,  $\text{MgO}$ ,  $\text{ZrO}_2$  and graphite for methane cracking [62, 207, 253]. Among these, silica-supported-Ni ( $\text{Ni}/\text{SiO}_2$ ) is well known to be one of the most effective catalysts [40, 48, 72, 86, 215]. Furthermore, different types of zeolite supports have been employed for nickel catalysts for methane cracking [59, 245, 249].

Goodman and co-workers [19] investigated the decomposition of methane on several Ni-supported catalysts at 550 °C.  $\text{SiO}_2$ , HY and H-ZSM-5 were used as supports. They

showed that the initial activity were comparable for all three catalysts. Complete deactivation was observed for the Ni/ZSM-5 catalyst after roughly 1 h while the Ni/SiO<sub>2</sub> and Ni/HY catalysts displayed catalytic activity for methane decomposition for more than 12 h. The authors attributed the rapid deactivation of the Ni/H-ZSM-5 catalyst to the formation of encapsulating graphitic carbon on the Ni particles. But in the cases of Ni/HY and Ni/SiO<sub>2</sub> catalysts, there was evidence for filamentous carbon formation which resulted in the longer lifetime of these catalysts.

Ashok *et al.* [59] studied hydrogen production by catalytic decomposition of methane over Ni supported on HY, USY, SiO<sub>2</sub> and SBA-15 at 550 °C. They found that the catalytic activity for these catalysts was in the order of HY > USY > SiO<sub>2</sub> > SBA-15. They attributed this activity to the particle size of Ni where HY and USY zeolite possessed the smallest particle size. Ni supported on HY zeolite and SiO<sub>2</sub> showed long life time compared to other supports.

Chai *et al.* [249] investigated the effect of various supports on the catalytic activity of 10 wt% Ni for direct decomposition of methane at 550 and 700 °C. The supports were SiO<sub>2</sub>, HZSM-5, CeO<sub>2</sub> and Al<sub>2</sub>O<sub>3</sub>. The results showed that the catalytic performance of supported-NiO catalysts decreased in the order of NiO/SiO<sub>2</sub> > NiO/HZSM-5 > NiO/CeO<sub>2</sub> > NiO/Al<sub>2</sub>O<sub>3</sub> at reaction temperatures of 550 and 700 °C. TEM images showed that the carbons deposited on these catalysts were in filamentous carbon form at both reaction temperatures.

In this study, the influence of H-ZSM-5,  $\gamma$ -Al<sub>2</sub>O<sub>3</sub> and SiO<sub>2</sub> supports for the Ni catalysts have been investigated and the range has been extended to include silicic acid (SiO<sub>2</sub>.xH<sub>2</sub>O). Ni-supported catalysts (0.4 wt%) were prepared by impregnating the supports with aqueous solutions of Ni(NO<sub>3</sub>)<sub>2</sub>.6H<sub>2</sub>O. The reactions were performed under comparable conditions in which the reaction temperature was 800 °C, the flow rate of feed gas was 12 mL/min and catalyst mass was 0.4g.

### 6.5.2 Reaction data

Figure 6-16 displays the hydrogen formation rate profile at 800 °C over Ni catalysts supported on different supports. The catalysts tested are 0.4 wt% Ni/H-ZSM-5, 0.4 wt% Ni/SiO<sub>2</sub>, 0.4 wt% Ni/ $\gamma$ -Al<sub>2</sub>O<sub>3</sub> and 0.4 wt% Ni/SiO<sub>2</sub>.xH<sub>2</sub>O (silicic acid). From Figure 6-16, it can be seen that the activity of 0.4 wt% Ni/SiO<sub>2</sub> catalyst at the initial period of reaction

was the highest followed by 0.4 wt% Ni/SiO<sub>2</sub>.xH<sub>2</sub>O. The peak hydrogen formation rate was *ca.* 8.00 x 10<sup>-4</sup> mol H<sub>2</sub> g<sup>-1</sup> min<sup>-1</sup> for 0.4 wt% Ni/SiO<sub>2</sub>, while it was *ca.* 6.40 x 10<sup>-4</sup> mol H<sub>2</sub> g<sup>-1</sup> min<sup>-1</sup> for 0.4 wt% Ni/SiO<sub>2</sub>.xH<sub>2</sub>O. These two catalysts showed initially high hydrogen formation rates at the beginning of the reaction, which dropped rapidly after 30 minutes of time on stream to be the lowest hydrogen formation rates, below *ca.* 0.5 x 10<sup>-4</sup> mol H<sub>2</sub> g<sup>-1</sup> min<sup>-1</sup>, among all catalysts for the rest of the run. Also, it is evident that the activity of these catalysts is similar after 30 minutes of time on stream. In contrast, 0.4 wt% Ni/H-ZSM-5 and 0.4 wt% Ni/γ-Al<sub>2</sub>O<sub>3</sub> catalysts showed lower apparent activity at the early stage of reaction. 0.4 wt% Ni/HZSM-5 catalyst exhibited gradual increase in the hydrogen formation rate up to 120 minutes of time on stream followed by a gradual decline until the end of reaction, whereas 0.4 wt% Ni/γ-Al<sub>2</sub>O<sub>3</sub> showed a gradual increase in the hydrogen formation rate up to 90 minutes of time on stream and then remained steady for the rest of the run. Moreover, it can be observed that the behaviour of 0.4 wt% Ni/SiO<sub>2</sub> and 0.4 wt% Ni/SiO<sub>2</sub>.xH<sub>2</sub>O is quite similar which is possibly not expected. Also, 0.4 wt% Ni/H-ZSM-5 and 0.4 wt% Ni/γ-Al<sub>2</sub>O<sub>3</sub> catalysts possessed similar behaviour.

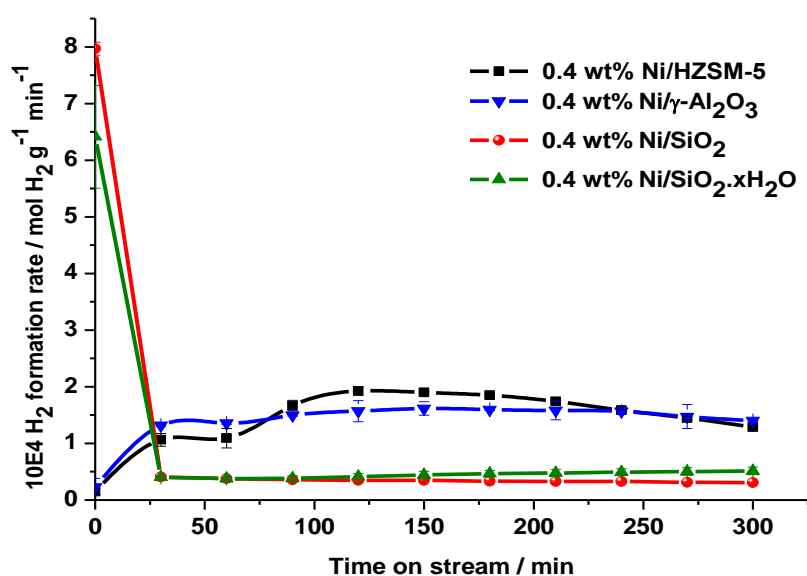


**Figure 6-16** Hydrogen formation rates as a function of time on stream for 0.4 wt% Ni/H-ZSM-5, 0.4 wt% Ni/SiO<sub>2</sub>, 0.4 wt% Ni/γ-Al<sub>2</sub>O<sub>3</sub> and 0.4 wt% Ni/SiO<sub>2</sub>.xH<sub>2</sub>O (silicic acid), the reaction temperature of 800 °C, the methane flow rate was 12 mL/min and 0.4 g catalyst mass.

From the above data, it is apparent that the support played a crucial role in activity. In an attempt to understand the differences in the activities of these catalysts, BET surface areas were determined. Table 6-4 shows the results. It is obvious that the surface area of the 0.4 wt% Ni/SiO<sub>2</sub>.xH<sub>2</sub>O catalyst is the highest, while the 0.4 wt% Ni/SiO<sub>2</sub> catalyst has the

lowest surface area. According to the BET results, it is obvious that there is no correlation between surface area and catalyst activity.

<b>Table 6-4</b> BET surface area analyses of Ni/H-ZSM-5, Ni/SiO <sub>2</sub> , Ni/γ-Al <sub>2</sub> O <sub>3</sub> and 0.4 wt% Ni/SiO <sub>2</sub> .xH <sub>2</sub> O samples.	
<b>Sample Code</b>	<b>BET surface area (m<sup>2</sup>/g)</b>
<b>0.4 wt% Ni/H-ZSM-5</b>	<b>271</b>
<b>0.4 wt% Ni/SiO<sub>2</sub></b>	<b>208</b>
<b>0.4 wt% Ni/SiO<sub>2</sub>.xH<sub>2</sub>O</b>	<b>290</b>
<b>0.4 wt% Ni/γ-Al<sub>2</sub>O<sub>3</sub></b>	<b>238</b>

As mentioned in Chapter 5, the support can affect with catalyst properties such as metal particle size and stability. In addition, the interaction between the metal and support depends on the type of support. A strong metal–support interaction (MSI) prevents the sintering or/and agglomeration of the metal particles on the support surface that enhance the dispersion of metal particles, while the catalyst with weak MSI leads to sintered metal particles. Also, a strong MSI may lead to the difficulty of reduction of the precursor oxide in catalyst. However, an appropriate strength of MSI is required to prevent metal particles from aggregation to form unwanted large particles and to maintain catalyst activity.

Silica-supported-Ni (Ni/SiO<sub>2</sub>) is well known to be one of the active catalysts for the decomposition of methane at low temperature reaction in range from 500 to 600 °C [48, 62, 244, 249]. The detachment of catalyst particles from the support and their localisation on the tip of carbon filaments results from a weak MSI. A number of studies have revealed that Ni metal particles were located at the tips of carbon nanofibres produced from methane cracking over Ni/SiO<sub>2</sub> at 500 °C [40, 62]. Also, it was found that the sintering process in Ni/SiO<sub>2</sub> occurred during methane decomposition at 750 °C and also catalyst regeneration forming large particles that reach up to 200 nm, which are inactive for methane decomposition [86, 254]. Takenaka and co-workers [40] studied the effect of temperature on the activity of Ni/SiO<sub>2</sub> in range from 500 to 700 °C. They observed that increase of reaction temperature accelerates the catalyst deactivation. Also, there was rapid drop in the catalyst activity at 700 °C noted at *ca.* 20 minutes time on stream.

From the above, it appears that the interaction between Ni and SiO<sub>2</sub> is weak, which can result in sintering of Ni particles especially at high reaction temperature. In this work, the

reaction temperature applied was 800 °C, which is a high reaction temperature particularly for Ni/SiO<sub>2</sub>. Therefore, a possible explanation for the rapid deactivation of 0.4 wt% Ni/SiO<sub>2</sub> and 0.4 wt% Ni/SiO<sub>2</sub>.xH<sub>2</sub>O catalysts may be that the severe aggregation of Ni particle has occurred at 800 °C and/or it may be that there is rapid deposition of carbon on the catalysts as a result of high initial reaction rate, as observed in the early phase of the reaction, Figure 6-16.

Chai *et al.* [249] prepared and tested the Ni/Al<sub>2</sub>O<sub>3</sub> (XRD pattern reported suggest  $\gamma$ -Al<sub>2</sub>O<sub>3</sub> but reflections are very weak) for methane decomposition. They showed that the activity was low at 500 and 700 °C. In addition, they emphasised that there is a strong metal–support interaction (MSI) between Ni and the Al<sub>2</sub>O<sub>3</sub> support, which leads to deactivation. Chen and co-workers [255] prepared NiO/ $\gamma$ -Al<sub>2</sub>O<sub>3</sub> catalyst with various nickel loadings. The reducibilities of NiO over these catalysts were examined by the temperature-programmed reduction (TPR) technique. They found that there is strong interaction between NiO and Al<sub>2</sub>O<sub>3</sub> especially at low nickel loadings. In relation to the strong metal–support interaction, there have been reports of nickel aluminate spinel formation which is difficult to reduce [50, 256, 257]. Hence, the initial low and gradually increasing activity of Ni/Al<sub>2</sub>O<sub>3</sub> catalyst in this study could be attributed to the strong metal–support interaction which led to more difficult, and hence prolonged, reduction of the nickel oxide in this catalyst.

In case of Ni/H-ZSM-5 catalyst, Zakaria *et al.* [247] demonstrated that Ni species can be dispersed in three positions of H-ZSM-5 – the outer surface of zeolite, nickel ions that are associated within the charge compensation sites of ZSM-5 and those inside the channels of H-ZSM-5 that are more difficult to reduce. Therefore, the low activity of the catalyst at the beginning of the reaction and gradual increase of the hydrogen production rate can be attributed to the dispersion of Ni particles inside the channels of zeolite. The possibly strong interaction between nickel and the aluminium sites/species of the zeolite may also impact upon the observed activity.

### 6.5.3 XRD patterns

Figure 6-17 (A-C) shows the XRD patterns of the pre- and post-reaction 0.4 wt% Ni/SiO<sub>2</sub>, 0.4 wt% Ni/SiO<sub>2</sub>.xH<sub>2</sub>O and 0.4 wt% Ni/ $\gamma$ -Al<sub>2</sub>O<sub>3</sub> catalyst. The XRD pattern of the pre- and post-reaction 0.4 wt% Ni/H-ZSM-5 catalyst was presented and discussed previously.

It can be seen from Figure 6-17 (A, B) that the 0.4 wt% Ni/SiO<sub>2</sub> and 0.4 wt% Ni/SiO<sub>2</sub>.xH<sub>2</sub>O possessed similar patterns for both pre- and post-reaction. In addition, it is observed that the XRD patterns of the pre-reaction 0.4 wt% Ni/SiO<sub>2</sub> and 0.4 wt% Ni/SiO<sub>2</sub>.xH<sub>2</sub>O are assigned only to amorphous silica (SiO<sub>2</sub>) additional nickel containing phases were not apparent. However, the XRD patterns of the post-reaction 0.4 wt% Ni/SiO<sub>2</sub> and 0.4 wt% Ni/SiO<sub>2</sub>.xH<sub>2</sub>O catalysts showed the appearance of low intensity metallic Ni peaks at  $2\theta = 44.20^\circ, 51.70^\circ$ , as marked on the patterns.

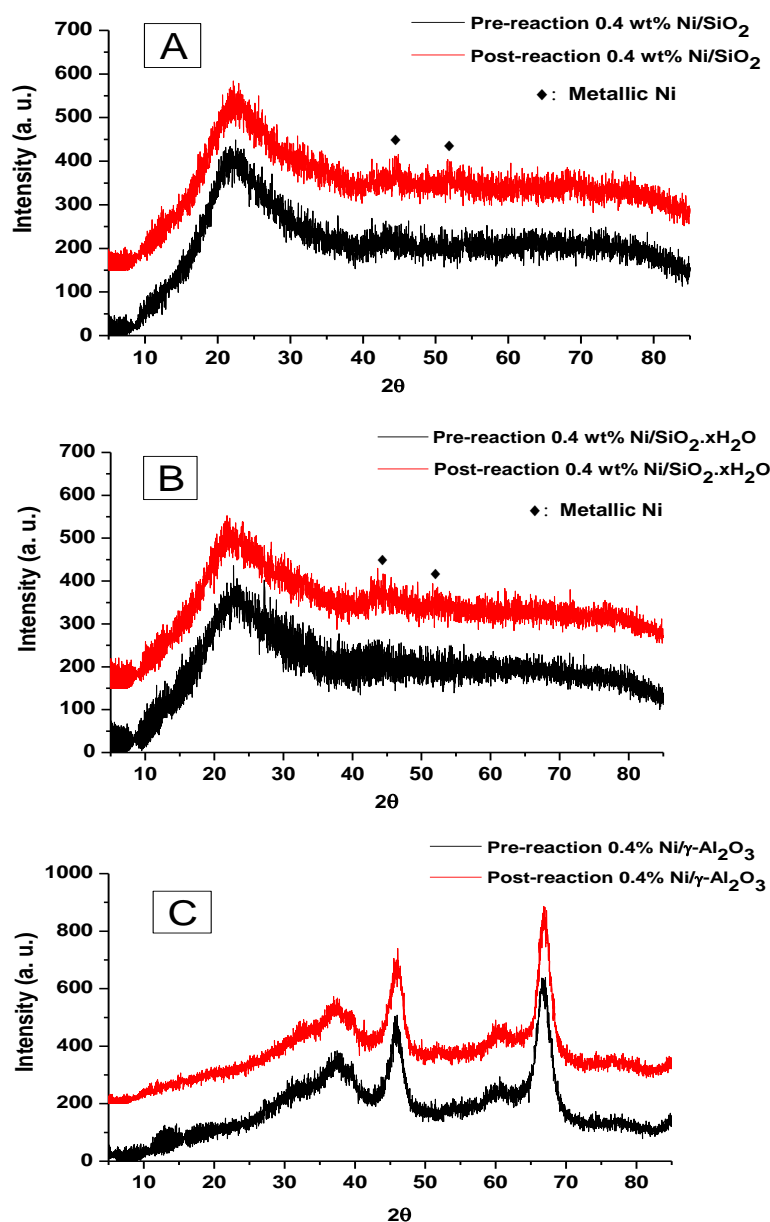


**Figure 6-17** XRD patterns of the pre- and post-reaction 0.4 wt% Ni/SiO<sub>2</sub>, 0.4 wt% Ni/SiO<sub>2</sub>.xH<sub>2</sub>O and 0.4 wt% Ni/ $\gamma$ -Al<sub>2</sub>O<sub>3</sub> catalysts.

Figure 6-17 (C) presents the XRD patterns of the pre- and post-reaction 0.4 wt% Ni/ $\gamma$ -Al<sub>2</sub>O<sub>3</sub> catalyst. It can be observed that these show only the characteristic reflections of the  $\gamma$ -Al<sub>2</sub>O<sub>3</sub> phase. Moreover, no evidence of the nickel crystallites containing could be observed in the post-reaction catalysts. This suggests that Ni crystals remained highly dispersed on the surface of alumina. Hence, this implies that there is a strong metal–support interaction (MSI) between Ni and the  $\gamma$ -Al<sub>2</sub>O<sub>3</sub> support, preventing sintering.

### 6.5.4 Post-reaction CHN and TGA analyses

The post-reaction CHN analyses of the post-reaction samples are presented in Table 6-5. It can be seen that the amount of carbon deposited on the 0.4 wt% Ni/H-ZSM-5 and 0.4 wt% Ni/ $\gamma$ -Al<sub>2</sub>O<sub>3</sub> catalysts is similar, in the range of 10.50 to 11.50 wt%, and larger than those deposited on 0.4 wt% Ni/SiO<sub>2</sub> and 0.4 wt% Ni/SiO<sub>2</sub>.xH<sub>2</sub>O catalysts. It can be observed also that the amount of carbon deposited on 0.4 wt% Ni/SiO<sub>2</sub> and 0.4 wt% Ni/SiO<sub>2</sub>.xH<sub>2</sub>O catalysts is quite similar, which is roughly 3.00 wt%. Although the quantity of carbon deposited on the 0.4 wt% Ni/SiO<sub>2</sub> and 0.4 wt% Ni/SiO<sub>2</sub>.xH<sub>2</sub>O catalysts is small compared to 0.4 wt% Ni/H-ZSM-5 and 0.4 wt% Ni/ $\gamma$ -Al<sub>2</sub>O<sub>3</sub> catalysts, the catalysts showed rapid deactivation. This suggested that the main reason for the rapid deactivation of 0.4 wt% Ni/SiO<sub>2</sub> and 0.4 wt% Ni/SiO<sub>2</sub>.xH<sub>2</sub>O catalysts is the sintering of Ni particles at the reaction temperature of 800 °C.

<b>Table 6-5</b> CHN analyses of the post-reaction 0.4 wt % Ni/H-ZSM-5, 0.4 wt % Ni/SiO <sub>2</sub> , 0.4 wt % Ni/ $\gamma$ -Al <sub>2</sub> O <sub>3</sub> and 0.4 wt % Ni/SiO <sub>2</sub> .xH <sub>2</sub> O catalysts.			
<b>Catalysts</b>	<b>Mean value (wt%)</b>		
	<b>C</b>	<b>H</b>	<b>N</b>
<b>0.4 wt% Ni/H-ZSM-5</b>	<b>10.55 ± 0.15</b>	-	-
<b>0.4 wt% Ni/SiO<sub>2</sub></b>	<b>3.00 ± 0.05</b>	-	-
<b>0.4 wt% Ni/SiO<sub>2</sub>.xH<sub>2</sub>O</b>	<b>3.10 ± 0.10</b>	-	-
<b>0.4 wt% Ni/<math>\gamma</math>-Al<sub>2</sub>O<sub>3</sub></b>	<b>11.21 ± 0.10</b>	-	-

Figure 6-18 shows the TGA oxidation profiles under air for the post-reaction 0.4 wt% Ni/H-ZSM-5, 0.4 wt% Ni/SiO<sub>2</sub>, 0.4 wt% Ni/SiO<sub>2</sub>.xH<sub>2</sub>O and 0.4 wt% Ni/ $\gamma$ -Al<sub>2</sub>O<sub>3</sub> catalysts. From these profiles, it is evident that the 0.4 wt% Ni/H-ZSM-5 and 0.4 wt% Ni/ $\gamma$ -Al<sub>2</sub>O<sub>3</sub> catalysts exhibited weight loss before 250 °C, which is attributed to the loss of adsorbed

water, while it is almost absent in the 0.4 wt% Ni/SiO<sub>2</sub> and 0.4 wt% Ni/SiO<sub>2</sub>.xH<sub>2</sub>O. Also, the weight loss in the region beyond 500 °C results from the burning off of the carbon formed on the samples. However, it is observed that there is an agreement between the results of TGA and CHN analyses.

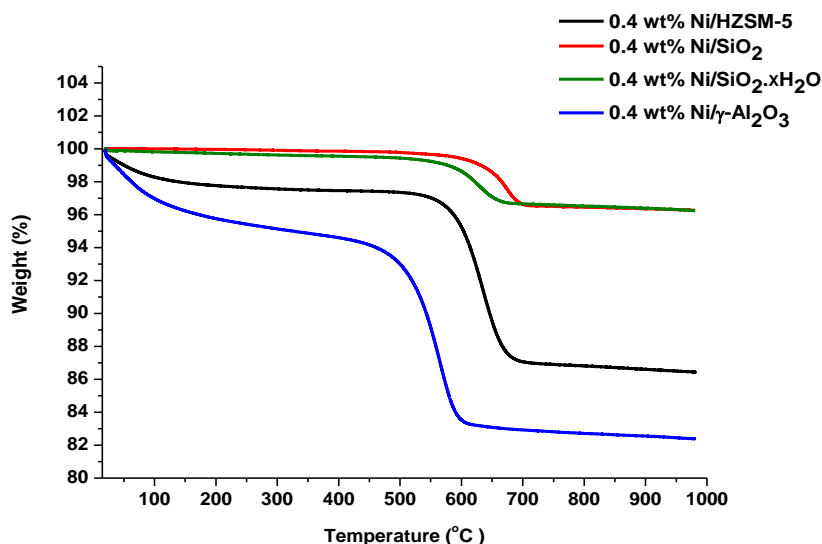


**Figure 6-18** TGA profiles of the post-reaction 0.4 wt% Ni/H-ZSM-5, 0.4 wt% Ni/SiO<sub>2</sub>, 0.4 wt% Ni/SiO<sub>2</sub>.xH<sub>2</sub>O and 0.4 wt% Ni/ $\gamma$ -Al<sub>2</sub>O<sub>3</sub> catalysts.

The first-derivative weight change profiles for the post-reaction catalysts are presented in Figure 6-19. It can be seen from these profiles that all post-reaction samples showed one weight loss region. This indicates that each sample contains homogeneous species of carbon. However, these weight loss regions are at approximately 570, 640, 630 and 675 °C for the post-reaction 0.4 wt% Ni/ $\gamma$ -Al<sub>2</sub>O<sub>3</sub>, 0.4 wt% Ni/H-ZSM-5, 0.4 wt% Ni/SiO<sub>2</sub>.xH<sub>2</sub>O and 0.4 wt% Ni/SiO<sub>2</sub>, respectively.

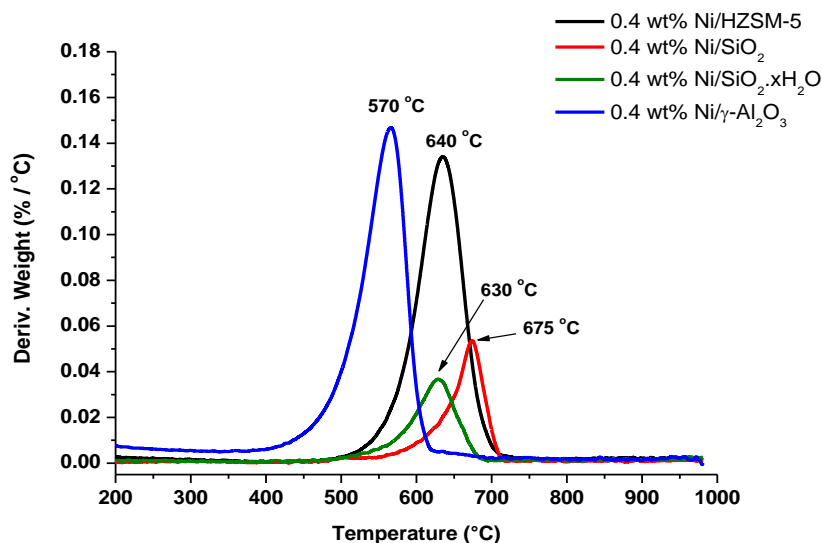


**Figure 6-19** TGA profiles of the post-reaction 0.4 wt% Ni/H-ZSM-5, 0.4 wt% Ni/SiO<sub>2</sub>, 0.4 wt% Ni/SiO<sub>2</sub>.xH<sub>2</sub>O and 0.4 wt% Ni/γ-Al<sub>2</sub>O<sub>3</sub> catalysts.

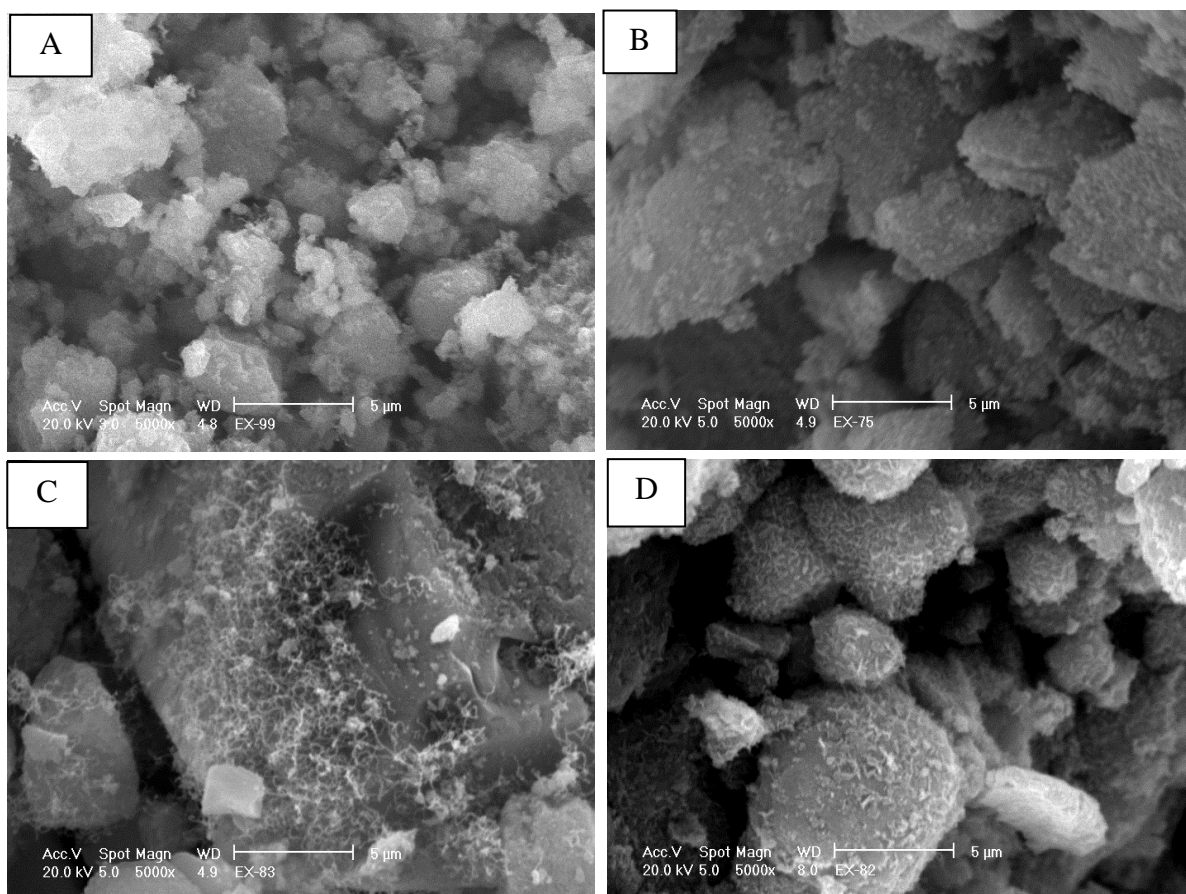
### 6.5.5 Post-reaction SEM images

Figure 6-20 (A-D) illustrates the SEM images of the post-reaction catalysts. It can be seen from the images (A,B,D) that carbon filaments were not formed on 0.4 wt% Ni/H-ZSM-5, 0.4 wt% Ni/SiO<sub>2</sub> and 0.4 wt% Ni/γ-Al<sub>2</sub>O<sub>3</sub>, respectively, while they can be observed in 0.4 wt% Ni/SiO<sub>2</sub>.xH<sub>2</sub>O catalyst (image (C)).

In the case of the Ni/H-ZSM-5 catalyst, it was found in the previous section that the amount of nickel loading played a role in the formation of carbon filaments. It was suggested that the dispersion of a low amount of nickel took place inside the zeolite channels which inhibited the formation of carbon filaments, whilst increasing the amount of nickel loaded on zeolites led to an increase in the quantity of nickel on the outer surface of the zeolite, which can produce the carbon filaments.

From image (B) in Figure 6-20, it can be seen that the carbon filaments were not formed on the 0.4 wt% Ni/SiO<sub>2</sub> catalyst. This result is in agreement with the study by Noda *et al.* [86]. They reported that no carbon filaments were formed over Ni/SiO<sub>2</sub> at reaction temperatures above 700 °C because of the particles size increase as a result of the sintering to form large particles in the range of 100 to 200 nm which are inappropriate for carbon filament formation. Also, they reported that low loadings of Ni (1 wt%) produced a small amount of carbon nanotubes in the reaction temperature range from 625 to 700 °C. As a

result, it could be that the reaction temperature of 800 °C led to sintering in the Ni/SiO<sub>2</sub> catalyst to form Ni particles of increased size, negatively impacting on the catalyst activity and the formation of carbon filaments.



**Figure 6-20** SEM images of the post-reaction (A) 0.4 wt% Ni/H-ZSM-5, (B) 0.4 wt% Ni/SiO<sub>2</sub>, (C) 0.4 wt% Ni/SiO<sub>2</sub>.xH<sub>2</sub>O and (D) 0.4 wt% Ni/γ-Al<sub>2</sub>O<sub>3</sub> catalysts.

It can be seen from image (C) in Figure 6-20 that carbon filaments were formed on the 0.4 wt% Ni/SiO<sub>2</sub>.xH<sub>2</sub>O catalyst. It should be mentioned that they were relatively sparse. A possible explanation for the apparent difference might be that the morphology of the silicic acid support (SiO<sub>2</sub>.xH<sub>2</sub>O) is different from the silica support (SiO<sub>2</sub>), which may have kept some of the nickel particles in a small and/or appropriate size to form the filamentous carbon. However, it was noted from the first-derivative weight change profiles in Figure 6-19 that there is a difference in the temperature of the weight loss region between the post-reaction 0.4 wt% Ni/SiO<sub>2</sub> and 0.4 wt% Ni/SiO<sub>2</sub>.xH<sub>2</sub>O catalysts. It may be that the presence of carbon filaments is the reason for this difference. Further, TEM analyses would be required to develop more understanding of this aspect.

As can be seen in image (D) of Figure 6-20, carbon filaments were not formed in the 0.4 wt% Ni/γ-Al<sub>2</sub>O<sub>3</sub> catalyst. However, it was reported that the carbon filaments can be formed

over Ni/Al<sub>2</sub>O<sub>3</sub> catalyst as a result of methane cracking at different reaction temperatures in the range from 500 to 800 °C [64, 89, 249, 258]. In these reports, the amount of Ni on Al<sub>2</sub>O<sub>3</sub> is between 5 and 10 wt%. Also, it was found that the increase of the amount of Ni loading on support led to an increase in the Ni particle size [48, 252]. Furthermore, it was shown that the small Ni particles yield a low growth of the carbon filaments and additionally the large particle size of Ni suppresses the growth of the carbon filaments. Thus, there is optimum particle size that can show the high carbon filament growth nickel [39, 256]. Therefore, it may be the case that the amount of Ni loading in 0.4 wt% Ni/ $\gamma$ -Al<sub>2</sub>O<sub>3</sub> catalyst is too low to form the suitable size of Ni particles necessary for the formation of carbon filaments. Also, it can be suggested that the strong metal–support interaction (MSI) between Ni and Al<sub>2</sub>O<sub>3</sub> support and nickel aluminate spinel formation prevent the formation of the appropriate particles size of nickel especially at the low loading thus lowering carbon filament formation. Further, TPR investigations on a range of supports may provide greater insight into this phenomenon.

In general, the low amount of Ni loaded may be played a role in the decline the growth rates of carbon filaments.

## 6.6. Direct catalytic cracking of methane over 0.4 wt% Cu/HZSM-5 catalyst for hydrogen and carbon production

### 6.6.1 Introduction

Copper has been used as a promoter for Ni-based catalysts. It was reported that the addition of a Cu component to the Ni-based catalysts enhances the performance of the catalyst [60, 61, 167]. However, only a few reports have demonstrated the possibility of using copper itself as a catalyst for methane cracking.

Matsukata *et al.* [259] studied the decomposition of methane over Ni/SiO<sub>2</sub> and Cu/SiO<sub>2</sub> catalysts using a fluidised bed at 600 and 750 °C. They reported that the activity and amount of hydrogen produced by the Cu/SiO<sub>2</sub> catalyst was very low compared to the Ni/SiO<sub>2</sub> catalyst.

Ammendola *et al.* [260] studied methane decomposition over Cu/Al<sub>2</sub>O<sub>3</sub> over a wide range of reaction temperatures. They observed that the rates of methane decomposition and of hydrogen production strongly increased at 600 °C and the maximum value of methane conversion (> 40 %) was reached at 800 °C which was followed by a rapid deactivation as a result of carbon deposition. In addition, they investigated the effect of copper loading in the range from 0.4 to 8.4 wt% and showed that 8.4 wt% Cu/Al<sub>2</sub>O<sub>3</sub> catalyst produced the highest amount of hydrogen.

From reviewing the literature, there do not seem to be any reports relating to the Cu supported on H-ZSM-5. Therefore, 0.4 wt% Cu/HZSM-5 catalyst was prepared and tested to investigate its activity and compare it with the 0.4 wt% Ni/HZSM-5 catalyst.

### 6.6.2 Reaction data

The hydrogen formation rate against time on stream for 0.4 wt% Cu/HZSM-5 is shown in Figure 6-21 and the data for the 0.4 wt% Ni/HZSM-5 catalyst, is also shown for comparison. From the hydrogen profile, it is evident that 0.4 wt% Cu/HZSM-5 behaves in a similar manner to 0.4 wt% Ni/HZSM-5 catalyst. Both Cu/HZSM-5 and Ni/HZSM-5 catalysts showed an apparent gradual increase in the hydrogen formation rate up to 90 minutes of time on stream for Cu/HZSM-5 and 120 minutes for Ni/HZSM-5 followed by a gradual decrease. It is interesting to observe that Cu/HZSM-5 showed relatively higher

activity between 30 and 90 minutes of time on stream compared to Ni/HZSM-5. After 120 minutes of time on stream, both Cu/HZSM-5 and Ni/HZSM-5 catalysts exhibited similar activity and hydrogen formation rate until the end of reaction.

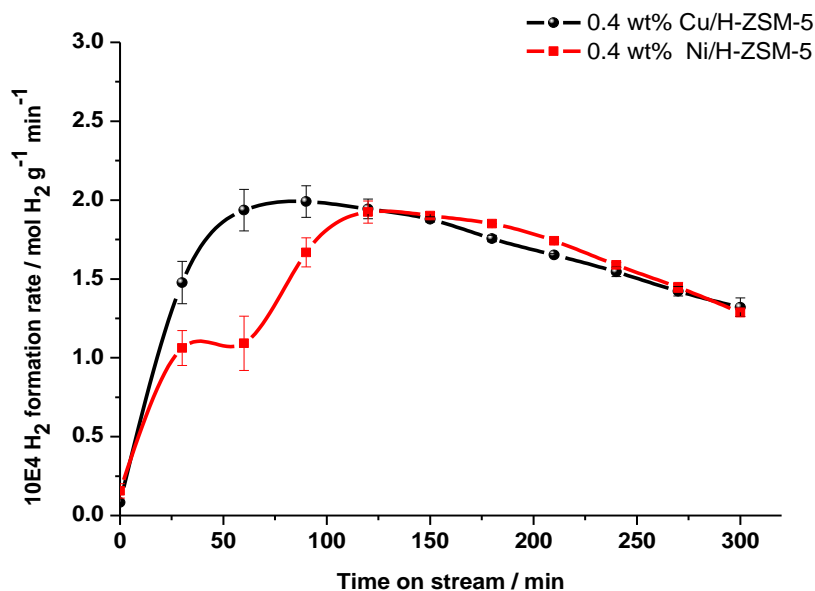


**Figure 6-21** Hydrogen formation rates as a function of time on stream for 0.4 wt% Cu/H-ZSM-5 and 0.4 wt% Ni/H-ZSM-5, the reaction temperature of 800 °C, the methane flow rate was 12 mL/min and 0.4 g catalyst mass.

In this work the materials were not pre-reduced and were readily reduced under reaction conditions. The difference in activity between Cu/H-ZSM-5 and Ni/H-ZSM-5 over 30-120 minutes time-on-stream, Figure 6-21, may be attributed to Cu/HZSM-5 reducing more readily than the Ni catalyst in the initial stage of reaction. It has been reported that the Cu/HZSM-5 catalyst can be reduced by 10% H<sub>2</sub>-N<sub>2</sub> with ramp rate of 10 °C/min and by 5 % H<sub>2</sub>-Ar with ramp rate of 5 °C/min in the temperature range of 230-250 °C [261, 262], whereas Ni/H-ZSM-5 was reported as being reducible by 5 % H<sub>2</sub>-Ar with ramp rate of 20 °C/min in the temperature range of 550-600 °C under comparable conditions [246, 247].

### 6.6.3 XRD patterns

Powder X-ray diffraction was performed on the pre- and post-reaction 0.4 wt% Cu/HZSM-5 catalysts and the results are presented in Figure 6-22. It can be seen from Figure 6-22 that the XRD pattern of the pre-reaction 0.4 wt% Cu/HZSM-5 catalyst matches the pattern of

H-ZSM-5 and there were no reflections indicative of any additional copper phases. The XRD pattern of the post-reaction 0.4 wt% Cu/HZSM-5 showed the appearance of a small reflection at  $43.6^\circ$ , which is marked with an arrow, which is consistent with metallic copper indicates that the copper oxide has been reduced to form metallic copper and the relatively narrow reflection width suggests this to comprise a large particle size.

The sintering process of copper can occur more readily than for nickel since that the Tamman temperature for copper is  $405^\circ\text{C}$ , while the Tamman temperature for nickel is  $590^\circ\text{C}$  [66]. However, the reaction temperature in this study is  $800^\circ\text{C}$ , significantly higher than both Tamman temperatures.

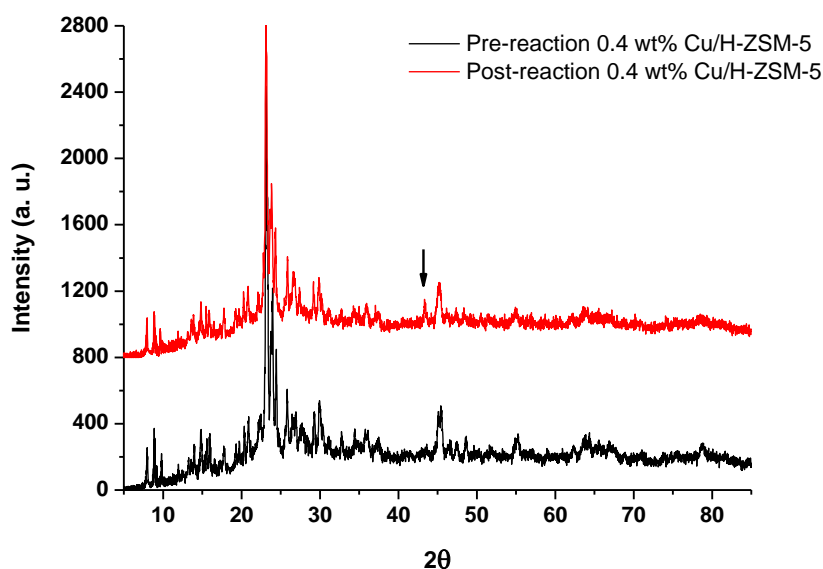


**Figure 6-22** XRD patterns of the pre- and post-reaction 0.4 wt% Cu/HZSM-5 catalysts.

#### 6.6.4 Post-reaction CHN and TGA analyses

Table 6-6 presents CHN analyses of the post-reaction 0.4 wt% Cu/H-ZSM-5 and 0.4 wt% Ni/H-ZSM-5 samples. From this data, it is evident that the amount of carbon deposited on the post-reaction catalysts is similar being in the range of 10.55 to 10.93 wt%. This is not a surprising since that the reaction profiles of both catalysts were similar.

<b>Table 6-6</b> CHN analysis for the post-reaction 0.4 wt% Cu/H-ZSM-5 and 0.4 wt% Ni/H-ZSM-5.			
<b>Catalyst</b>	<b>Mean value (wt%)</b>		
	<b>C</b>	<b>H</b>	<b>N</b>
0.4 wt% Cu/H-ZSM-5	10.93 ± 0.20	0.31 ± 0.01	
0.4 wt% Ni/H-ZSM-5	10.55 ± 0.15	-	-

TGA studies in the presence of air were carried out for the post-reaction 0.4 wt% Cu/H-ZSM-5 and 0.4 wt% Ni/H-ZSM-5 samples to evaluate the nature of the carbon deposited. Figure 6-23 displays the TGA profiles for the post-reaction 0.4 wt% Cu/H-ZSM-5 and 0.4 wt% Ni/H-ZSM-5 samples. It is obvious that there is a small weight loss below 250 °C that is ascribed to the loss of adsorbed water. The major weight loss is that in the region from 500 to 700 °C resulting from the combustion of the carbon deposited. Also, it can be observed that there is good agreement between the results of CHN and TGA analyses.

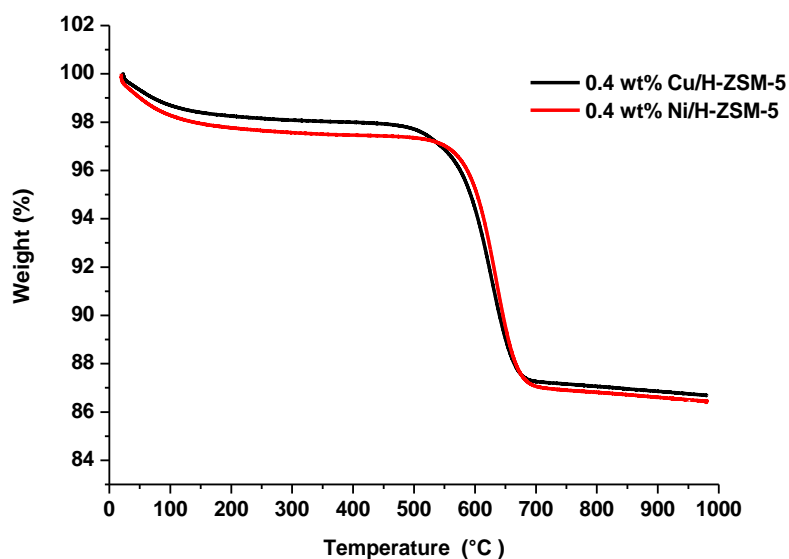


**Figure 6-23** TGA profiles of the post-reaction 0.4 wt% Cu/H-ZSM-5 and 0.4 wt% Ni/H-ZSM-5.

Figure 6-24 shows the first-derivative weight changes profiles for the post-reaction 0.4 wt% Cu/H-ZSM-5 and 0.4 wt% Ni/H-ZSM-5 samples. It can be observed that there is a slight difference between the carbons deposited on these catalysts. The 0.4 wt% Cu/H-ZSM-5 sample exhibited two weight loss regions at 525 and 625 °C, whereas the 0.4 wt% Ni/H-ZSM-5 sample displayed a single weight loss region at 640 °C. It was stated previously that the region between 500 to 700 °C is usually related to filamentous carbons

and graphitic carbon. In the previous sections of this chapter, SEM images demonstrated that the filamentous carbon was not formed on the 0.4 wt% Ni/H-ZSM-5 catalyst. Hence, it may be that the carbon deposited on this catalyst is graphitic. However, SEM images for the post-reaction 0.4 wt% Cu/H-ZSM-5 (as shown later) illustrated that the filamentous carbons were formed. Therefore, it could be that these two weight loss regions at 525 and 625 °C are attributed to filamentous carbons and graphitic carbon.

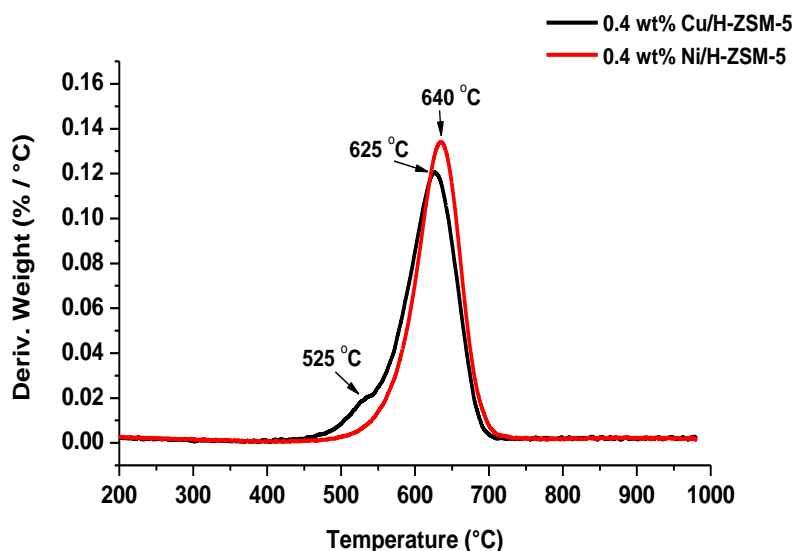


**Figure 6-24** TGA profiles of the post-reaction 0.4 wt% Cu/H-ZSM-5 and 0.4 wt% Ni/H-ZSM-5.

### 6.6.5 Post-reaction SEM images

Figure 6-25 presents the SEM images with high and low magnification for the post-reaction 0.4 wt% Cu/H-ZSM-5 catalyst. The SEM images for the post-reaction 0.4 wt% Ni/H-ZSM-5 were shown and discussed previously. It can be seen that the carbon filaments were formed over the 0.4 wt% Cu/H-ZSM-5 catalyst. In addition, the copper particles do not appear to be located on the tip of these filaments. This suggests that the growth mechanism of these filaments is “base-growth”. However, it should be mentioned that the formation of the filaments was not dense.

This result contrasts with the findings reported by Ammendola *et al.* [260] who studied the methane decomposition over a Cu/Al<sub>2</sub>O<sub>3</sub> catalyst and reported that no carbon fibres grew

on the catalyst surface up to 800 °C. The difference between their result and the result in this study can be possibly ascribed to the type of support.

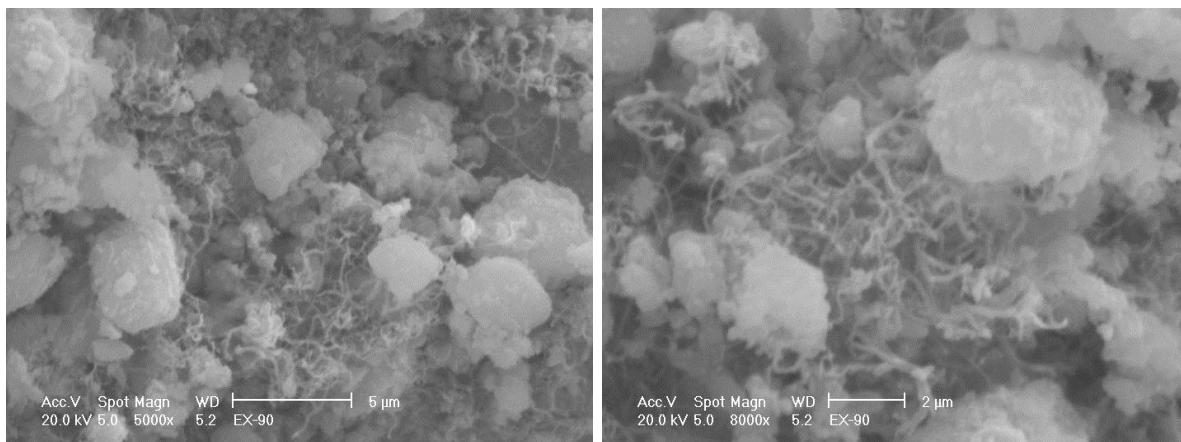


**Figure 6-25** Post-reaction SEM images of 0.4 wt% Cu/H-ZSM-5 catalyst.

Although the 0.4 wt% Ni/H-ZSM-5 and 0.4 wt% Cu/H-ZSM-5 had a similar behaviour and amount of carbon deposited it was noted that the filamentous carbons were not formed on 0.4 wt% Ni/H-ZSM-5. It seems that copper disperses on the outer surface of the zeolite whereas nickel does not. The apparently large Cu particle size, as indicated by the narrow Cu reflection in the XRD pattern of the post-reaction catalyst, is consistent with this suggestion. Also, it may be that the enhanced sintering process of copper led to the formation of a suitable particle size for the formation of carbons filaments.

## 6.7. Summary

This study set out to investigate the direct cracking of methane over Ni-based catalysts for the production of hydrogen and carbon. This study included a comparative study between the 0.4 wt% Ni/HZSM-5 and 0.4 wt% Pd/HZSM-5 catalysts, the effect of reaction temperature on the activity of 0.4 wt% Ni/HZSM-5 catalyst, the effect of the nickel loading and the effect of support. In addition, a comparative study between the 0.4 wt% Ni/HZSM-5 and 0.4 wt% Cu/HZSM-5 catalysts was presented.

The reaction data from the comparison study between the 0.4 wt% Ni/HZSM-5 and 0.4 wt% Pd/HZSM-5 catalysts showed that the 0.4 wt% Pd/HZSM-5 catalyst displayed an apparently high initial hydrogen formation rate followed with a sharp decline to be the lowest hydrogen formation rate after 120 minutes of time on stream. The 0.4 wt% Ni/HZSM-5 catalyst showed a gradual increase in the hydrogen formation rate with time

on stream, which became higher than the 0.4 wt% Pd/HZSM-5 catalyst after 90 minutes of time on stream and then exhibited a gradual decline. Moreover, palladium was added to 0.4 wt% Ni/HZSM-5 catalyst as promoter. The reaction data showed that palladium enhances the initial performance of the 0.4 wt% Ni/HZSM-5 catalyst. The results of CHN and TGA analyses revealed that the quantity of carbon deposited on the 0.4 wt% Ni/HZSM-5, 0.4 wt% Pd/HZSM-5 and Pd- Ni/HZSM-5 catalysts was somewhat similar. SEM images of post-reaction catalysts showed carbon filament growth over 0.4 wt% Pd/HZSM-5 and Pd-Ni/HZSM-5 catalysts but not over 0.4 wt% Ni/HZSM-5.

The effect of reaction temperature on the activity of the 0.4 wt% Ni/H-ZSM-5 catalyst in the range from 600 to 900 °C, demonstrated that the hydrogen formation rates increased with increasing reaction temperature as would be expected. In addition, it was observed that the increase of reaction temperature led to rapid deactivation of the catalyst. CHN and TGA analyses showed that the amount of carbon deposited also increased with increasing reaction temperature. SEM images of the post-reaction 0.4 wt% Ni/H-ZSM-5 catalyst, obtained at different reaction temperatures, illustrated that no filamentous carbon was formed with this material.

Different loadings of nickel on H-ZSM-5 zeolite were studied at 800 °C. The nickel loadings were 0.4, 4 and 8 wt%. It was observed that the increasing of nickel loading increases the initial hydrogen formation rates. 8 wt% Ni/H-ZSM-5 catalyst exhibited the highest initial hydrogen formation rate followed by 4 wt% Ni/H-ZSM-5 catalyst, while the 0.4 wt% Ni/H-ZSM-5 catalyst demonstrated the lowest initial hydrogen formation rate. Also, it was found that the increasing of nickel loading resulted in an enhanced decline in hydrogen formation rate and increased the quantity of carbon deposited. Furthermore, SEM images revealed that the filamentous carbon was formed at the higher loadings of nickel and their density increased with increasing loading.

The performance of 0.4 wt% Ni supported on H-ZSM-5,  $\gamma$ -Al<sub>2</sub>O<sub>3</sub>, SiO<sub>2</sub> and SiO<sub>2</sub>.xH<sub>2</sub>O for methane cracking at 800 °C was studied. The initial hydrogen formation rates were higher in the order of Ni/SiO<sub>2</sub> > Ni/SiO<sub>2</sub>.xH<sub>2</sub>O > Ni/H-ZSM-5  $\approx$  Ni/ $\gamma$ -Al<sub>2</sub>O<sub>3</sub>. The Ni/SiO<sub>2</sub> and Ni/SiO<sub>2</sub>.xH<sub>2</sub>O catalysts showed similar behaviour, which was a high hydrogen formation rate initially followed by a rapid drop after 30 minutes of time on stream to the lowest hydrogen formation rates, whereas the Ni/H-ZSM-5 and Ni/ $\gamma$ -Al<sub>2</sub>O<sub>3</sub> catalysts displayed initially lower activity followed by a gradual increase in hydrogen formation rates. The

results of CHN and TGA analyses demonstrated that the amount of carbon deposited on Ni/H-ZSM-5 and Ni/ $\gamma$ -Al<sub>2</sub>O<sub>3</sub> catalysts was larger than for Ni/SiO<sub>2</sub> and Ni/SiO<sub>2</sub>.xH<sub>2</sub>O. Moreover, SEM images illustrated that filamentous carbon was formed with Ni/SiO<sub>2</sub>.xH<sub>2</sub>O but not for the other catalysts.

The direct cracking of methane over 0.4 wt% Cu/H-ZSM-5 was studied. It was observed that 0.4 wt% Cu/HZSM-5 is active for hydrogen production and it behaves in a similar manner to 0.4 wt% Ni/HZSM-5. In addition, both Cu/HZSM-5 and Ni/HZSM-5 catalysts exhibited gradual increase in the hydrogen formation followed by gradual decrease in the rate of the hydrogen formation. CHN and TGA analyses showed that the quantity of carbon deposited on the post-reaction Cu/H-ZSM-5 and Ni/H-ZSM-5 catalysts was similar. Furthermore, SEM images for the post-reaction Cu/HZSM-5 catalyst showed that filamentous carbon was formed.

Generally, this study showed that the activity of Pd/HZSM-5 catalyst was higher than Ni/H-ZSM-5. The addition of palladium into Ni/HZSM-5 catalyst enhanced the initial performance of 0.4 wt% Ni/HZSM-5. Increasing reaction temperature increased the activity of 0.4 wt% Ni/HZSM-5 catalyst where the catalyst showed the highest performance at the highest reaction temperature of 900 °C. Increase of nickel loading led to an increase in the initial hydrogen formation rate and the formation of filamentous carbon. Nickel supported on SiO<sub>2</sub> and SiO<sub>2</sub>.xH<sub>2</sub>O displayed the highest hydrogen formation rate compared to H-ZSM-5 and  $\gamma$ -Al<sub>2</sub>O<sub>3</sub>. The filamentous carbons were not formed on Ni/SiO<sub>2</sub>, Ni/H-ZSM-5 and Ni/ $\gamma$ -Al<sub>2</sub>O<sub>3</sub>, whereas they were observed on Ni/SiO<sub>2</sub>.xH<sub>2</sub>O. The 0.4 wt% Cu/HZSM-5 catalyst was active for hydrogen production and exhibited similar behaviour to the 0.4 wt% Ni/HZSM-5 catalyst. In addition, it was observed that filamentous carbons were formed over Cu/HZSM-5.

## 7. Conclusions and Future work

This project was focused on the investigation of the catalytic cracking of methane into hydrogen and carbon. An extensive study was undertaken on two categories of materials, namely iron-containing wastes and prepared catalysts which include palladium-based catalysts, nickel-based catalysts and copper-based catalyst. The following conclusions are drawn from the investigations.

Three kinds of iron-containing wastes investigated, namely Landfill (biogenic iron oxide sample), Factory (residue from an old nail Factory) and Red Mud (a waste product of the aluminium industry) samples. Characterisation of these materials showed the variation in the properties of these materials. For example, SEM images of Landfill sample showed that this sample has unique tubular morphology and it also possessed the highest surface area and iron content compared to the other waste iron samples. The activity of these samples at reaction temperature of 800 °C was in the following order: Landfill > Red Mud > Factory, as would be expected on the basis of their iron content and surface area. Temperature programmed studies showed the Landfill sample to provide its highest activity after 700 °C associated with the loss of tubular morphology. Also, the carbon produced for all samples was in the form of filaments and encapsulating graphite. The CO and CO<sub>2</sub> produced with hydrogen production during the cracking of methane over Landfill and Factory samples was evaluated and the level of CO was found to be too high for direct application as a feed for PEM based fuel cells.

The effect of modification on Landfill and Factory samples has been studied. They were calcined at 300, 500, 700 and 900 °C. It was found that the calcination of these samples significantly affected properties such as surface area, phase and morphology. For Landfill sample, a calcination temperature of 300 and 500 °C resulted in more compact morphology. At 700 °C, the biogenic tubes began to merge with each other, while they were lost by 900 °C. The calcination of Landfill and Factory samples at 900 °C resulted in enhancement of their performance. Also, the highest observed hydrogen formation rate obtained from Landfill sample calcined at 900 °C was  $8.57 \times 10^{-4} \text{ molH}_2 \text{ g}^{-1} \text{ min}^{-1}$  compared to  $6.61 \times 10^{-4} \text{ molH}_2 \text{ g}^{-1} \text{ min}^{-1}$  for raw Landfill sample, whereas the highest hydrogen formation rate observed from Factory sample calcined at 900 °C was  $6.85 \times 10^{-4} \text{ molH}_2 \text{ g}^{-1} \text{ min}^{-1}$  compared to  $4.15 \times 10^{-4} \text{ molH}_2 \text{ g}^{-1} \text{ min}^{-1}$  for the raw Factory sample. The growth of carbon filaments were not observed in the case of post-reaction investigations on all

calcined Landfill samples, whereas they were formed for the Factory sample calcined at 900 °C.

Pre-treatment of the Landfill and Factory samples with HCl was conducted. Although this treatment increased the relative proportion of iron in both samples and the surface area of the Factory sample, resultant activity appeared to be poisoned. The modification of Landfill and Factory samples was extended doping with palladium. This reduced the performance of the Landfill sample below 800 °C, whereas it enhanced the performance at 800 °C. Pd-doping of the Factory sample was not beneficial to hydrogen production.

The peak hydrogen formation rates for different metal-zeolite containing were found to be in the following order: Pd/H-ZSM-5 > Cu/H-ZSM-5 > Ni/H-ZSM-5. In addition, it was noted that the quantity of carbon produced over these catalysts was similar. However, filamentous carbon was formed on Pd/H-ZSM-5 and Cu/H-ZSM-5 catalyst, whereas it was not observed on Ni/H-ZSM-5.

For both Pd/H-ZSM-5 and Ni/H-ZSM-5 catalysts, it was observed that the hydrogen formation rates and carbon deposited generally increased with increase of reaction temperature from 600 to 900 °C. The performance of Pd/H-ZSM-5 catalyst was higher than that Ni/H-ZSM-5 catalyst in range from 600 to 750 °C, while Ni/H-ZSM-5 catalyst showed high activity from 800 to 900 °C, but this was accompanied by rapid deactivation. The growth of carbon filaments was observed for Pd/H-ZSM-5 catalyst run between of 650 to 900 °C, but they were not formed over the Ni/H-ZSM-5 catalyst.

H-ZSM-5,  $\gamma$ -Al<sub>2</sub>O<sub>3</sub> and SiO<sub>2</sub> were used as supports for palladium. It was found that the initial hydrogen production rates were in the order of Pd/ $\gamma$ -Al<sub>2</sub>O<sub>3</sub> > Pd/SiO<sub>2</sub> > Pd/H-ZSM-5 for reactions at 800 °C. Moreover, Pd/ $\gamma$ -Al<sub>2</sub>O<sub>3</sub> catalyst showed the highest hydrogen formation rate and a superior performance throughout the reaction run compared to Pd/SiO<sub>2</sub> and Pd/H-ZSM-5 catalysts. The diameters of the carbon filaments produced by this catalyst were smaller than those from the other samples, possibly indicating there to be a higher Pd dispersion. Carbon filaments formed over all the catalysts.

Ni was supported on H-ZSM-5,  $\gamma$ -Al<sub>2</sub>O<sub>3</sub>, SiO<sub>2</sub> and SiO<sub>2</sub>.xH<sub>2</sub>O. It was found that the initial hydrogen formation rates were higher in the order of Ni/SiO<sub>2</sub> > Ni/SiO<sub>2</sub>.xH<sub>2</sub>O > Ni/H-ZSM-5  $\approx$  Ni/ $\gamma$ -Al<sub>2</sub>O<sub>3</sub>. Although the Ni/SiO<sub>2</sub> and Ni/SiO<sub>2</sub>.xH<sub>2</sub>O catalysts exhibited the

highest peak hydrogen formation rates initially, they rapidly deactivated. The Ni/H-ZSM-5 and Ni/ $\gamma$ -Al<sub>2</sub>O<sub>3</sub> catalysts possessed different behaviour, which were initially lower performance followed by a gradual increase in hydrogen formation rates. In addition, it was found that the quantity of carbon produced on Ni/H-ZSM-5 and Ni/ $\gamma$ -Al<sub>2</sub>O<sub>3</sub> catalysts was larger than for Ni/SiO<sub>2</sub> and Ni/SiO<sub>2</sub>.xH<sub>2</sub>O. Filamentous carbon was only formed over Ni/SiO<sub>2</sub>.xH<sub>2</sub>O.

Ni-doping of the Pd/H-ZSM-5 catalyst resulted in lowered hydrogen formation rate and carbon produced, while Pd-doping of the Ni/HZSM-5 catalyst enhanced the initial hydrogen formation rate and produced similar amount of carbon compared to parent catalyst. However, the addition of Pd into Ni/HZSM-5 catalyst led to the growth of carbon filaments.

It was observed that the phase of Pd precursor play a role in the performance of the Pd/H-ZSM-5 catalyst. The reaction data showed that the hydrogen formation rates and the quantity of carbon produced at 800 °C to follow the order: Pd(NO<sub>3</sub>)<sub>2</sub> > Pd(C<sub>5</sub>H<sub>7</sub>O<sub>2</sub>)<sub>2</sub> > PdCl<sub>2</sub>. Filamentous carbon were formed on all post-reaction catalysts with a difference in their growth intensity where their growth rate decreased in the following above order.

For Ni/H-ZSM-5 catalyst, it was found that the amount of Ni loading on zeolite plays a significant role in the formation of carbon filaments. It was observed that no carbon filaments was formed over 0.4 wt% Ni/H-ZSM-5, whereas they formed over 4 wt% Ni/H-ZSM-5 and 8 wt% Ni/H-ZSM-5 catalysts and their density increased with increasing loading, which suggest the increase of Ni dispersion over zeolite surface and formation of appropriate particles size for carbon filaments growth.

Tables 7-1 and 7-2 summarise the behaviour, under comparable reaction conditions (temperature, flow rate, mass of sample) of the iron-containing wastes materials and prepared catalysts, respectively, which were investigated in this thesis. Also, the quantity and morphology of carbon deposited are presented in these tables. The carbon morphology is inferred from SEM and/or TEM analyses. The deposited carbon on the surface of catalysts was in the filamentous or non-filamentous form. In most cases of the iron-containing wastes materials, no carbon nanostructure was observed. In raw Landfill sample, filamentous carbon and onion-like carbon nanospheres were observed, similarly in Red Mud sample and in Factory sample calcined at 900 °C filamentous carbon was

observed. In raw factory sample, encapsulating type of carbon was observed. However, in the case of prepared catalysts, more carbon filaments were observed compared to these samples.

Since H<sub>2</sub> formation is not monitored continuously, carbon deposition is perhaps a more reliable indicator of overall catalyst activity.

**Table 7-1 the behaviour of the iron-containing wastes materials, in the temperature programme from 600 to 800 °C. The CH<sub>4</sub>/N<sub>2</sub> flow rate was 12 mL/min and 0.4 g sample mass.**

Sample	Peak H <sub>2</sub> formation rate measured (mol H <sub>2</sub> g <sup>-1</sup> min <sup>-1</sup> )	Post-reaction carbon analyses (wt %)	Carbon morphology
Raw Landfill sample <sup>(a)</sup>	6.62	64.91	Filamentous Carbon and onion-like carbon nanospheres are formed
Raw Factory sample <sup>(b)</sup>	4.20	41.60	Encapsulating type of carbon was observed
Red Mud <sup>(b)</sup>	4.97	48.48	Filamentous Carbon was formed
Synthetic 2-line ferrihydrite <sup>(c)</sup>	0.09	NO carbon	No Carbon nanostructure was observed
Landfill sample calcined at 300 °C <sup>(c)</sup>	6.10	45.10	No Carbon nanostructure was observed
Landfill sample calcined at 500 °C <sup>(c)</sup>	6.21	49.50	No Carbon nanostructure was observed
Landfill sample calcined at 700 °C <sup>(c)</sup>	6.87	50.83	No Carbon nanostructure was observed
Landfill sample calcined at 900 °C <sup>(b)</sup>	8.57	59.70	No Carbon nanostructure was observed
Factory sample calcined at 300 °C <sup>(b)</sup>	2.34	20.60	No Carbon nanostructure was observed
Factory sample calcined at 500 °C <sup>(b)</sup>	2.15	8.60	No Carbon nanostructure was observed
Factory sample calcined at 700 °C <sup>(b)</sup>	2.52	15.00	No Carbon nanostructure was observed
Factory sample calcined at 900 °C <sup>(d)</sup>	6.85	47.10	Filamentous Carbon was formed.
HCl treated Landfill <sup>(b)</sup>	0.76	NO carbon	No Carbon nanostructure was observed
HCl treated Factory <sup>(b)</sup>	2.53	13.53	No Carbon nanostructure was observed
Pd/Landfill <sup>(c)</sup>	7.50	61.53	No Carbon nanostructure was observed
Pd/Factory <sup>(b)</sup>	0.70	1.48	No Carbon nanostructure was observed

(a) Time on stream is 680 minute (Pressure drop was observed)

(b) Time on stream is 740 minute (Pressure drop was observed with Landfill sample calcined at 900 °C )

(c) Time on stream is 800 minute.

(d) Time on stream is 650 minute (Pressure drop was observed).

**Table 7-2 the behaviour of prepared catalysts, the reaction temperature was 800 °C, the methane flow rate was 12 mL/min, time on stream was 300 minutes and 0.4 g catalyst mass.**

<b>Sample</b>	<b>Peak H<sub>2</sub> formation rate measured (mol H<sub>2</sub> g<sup>-1</sup> min<sup>-1</sup>)</b>	<b>Post-reaction carbon analyses (wt %)</b>	<b>Carbon morphology</b>
<b>Pd/H-ZSM-5</b>	<b>3.21</b>	<b>10.80</b>	<b>Filamentous Carbon was formed; carbon nanofibres type (herringbone–bamboo nanotube form)</b>
<b>Ni/H-ZSM-5</b>	<b>1.92</b>	<b>10.55</b>	<b>No Filamentous carbon was observed</b>
<b>Cu/H-ZSM-5</b>	<b>1.99</b>	<b>10.93</b>	<b>Filamentous Carbon was formed</b>
<b>Pd/SiO<sub>2</sub></b>	<b>4.39</b>	<b>10.10</b>	<b>Filamentous Carbon was formed</b>
<b>Pd/γ-Al<sub>2</sub>O<sub>3</sub></b>	<b>7.02</b>	<b>43.80</b>	<b>Filamentous Carbon was formed</b>
<b>Ni/SiO<sub>2</sub></b>	<b>7.97</b>	<b>3.00</b>	<b>No Filamentous Carbon was observed</b>
<b>Ni/γ-Al<sub>2</sub>O<sub>3</sub></b>	<b>1.61</b>	<b>11.21</b>	<b>No Filamentous carbon was observed</b>
<b>Ni/SiO<sub>2</sub>.xH<sub>2</sub>O</b>	<b>6.41</b>	<b>3.10</b>	<b>Filamentous Carbon was formed</b>

## 7.1. Future work

Although this work has showed a number of interesting results regarding the direct cracking of methane into hydrogen and carbon there still remains a number of ideas that may yet be explored:

- Investigation of the application of the post-reaction waste iron oxides samples to observe their performance for water treatment since these materials carbon containing composite which possess magnetic properties. The application of waste materials for methane cracking is also interesting from a viewpoint of their disposal upon deactivation.
- Further Pd EXAFS studies on the Fe, Ni, Co and Cu doped Pd/H-ZSM-5 catalysts to improve understanding of the nature and form of the metal component.
- Investigation of partial poisoning of the dehydrogenation components of the metal-zeolite catalysts components of catalyst (Pd/H-ZSM-5 catalyst) to try to promote selectivity switch towards methane dehydroaromatisation. This proposed work can be a new approach for the development of improved activity catalysts for benzene production from methane. In the literature, benzene production by the dehydroaromatisation of methane has attracted a lot of interest e.g. [204, 205]. It was reported that Mo/H-ZSM-5 catalyst is effective for the methane dehydroaromatisation reaction since that the Mo species and the Brønsted acid sites of the zeolite are necessary components of an active catalyst [45, 206]. Numerous studies with little success were carried out to improve the performance this catalyst. However, the partial poisoning of high activity catalysts for methane cracking (such as Pd/H-ZSM-5) may result in improved rate for benzene production compared to the conventional MoO<sub>3</sub>/ZSM-5 system which has low activity necessitating operation at low space velocities to approach equilibrium conversion.

## 8. Appendix

### 8.1. Appendix 1

Nitrogen was used as an internal standard, calculation of product formation rate is conducted taking into account the change in volume on reaction using the following expressions:

Hydrogen formation rate ( $\text{molH}_2 \text{ g}^{-1}\text{min}^{-1}$ )

$$= \left[ \frac{\% \text{H}_2 \left( \frac{\text{N}_2 \text{ in}}{\text{N}_2 \text{ out}} \right)}{100} \times \frac{\text{Flow rate (mLmin}^{-1})}{22400 \text{ (mL)}} \right] \div \text{mass of catalyst (g)}$$

CO or CO<sub>2</sub> formation rate ( $\text{molCO}_x \text{ g}^{-1}\text{min}^{-1}$ )

$$= \left[ \frac{\% \text{CO}_x \left( \frac{\text{N}_2 \text{ in}}{\text{N}_2 \text{ out}} \right)}{100} \times \frac{\text{Flow rate (mLmin}^{-1})}{22400 \text{ (mL)}} \right] \div \text{mass of catalyst (g)}$$

$$\text{Methane Conversion (\%)} = \left[ \frac{\text{CH}_4 \text{ (In)} - [\text{CH}_4 \text{ (Out)} \left( \frac{\text{N}_2 \text{ in}}{\text{N}_2 \text{ out}} \right)]}{\text{CH}_4 \text{ (In)}} \right] \times 100$$

## 8.2. Appendix 2

Methane conversion with time on stream for the cracking of methane over the samples (catalysts) used in this study for different reaction conditions, are presented from Figure 8-1 to 8-19. These data correspond to the hydrogen formation rates, which are presented throughout this thesis.

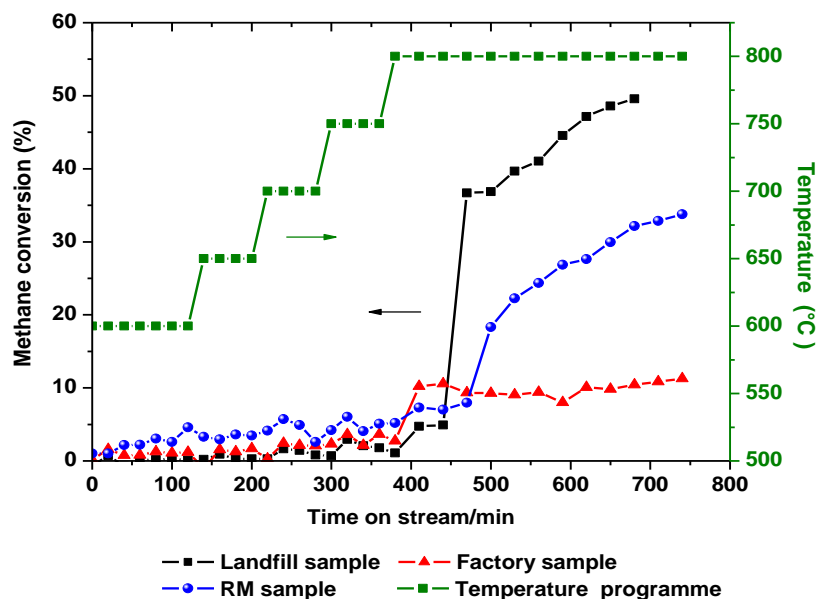


**Figure 8-1** Methane conversion as a function of TOS for CH<sub>4</sub> cracking over the Landfill, Factory and RM samples in the temperature programme from 600 to 800 °C. The CH<sub>4</sub>/N<sub>2</sub> flow rate was 12 mL/min and 0.4 g sample mass. These conversions correspond to hydrogen formation rates in Figure 3-7.

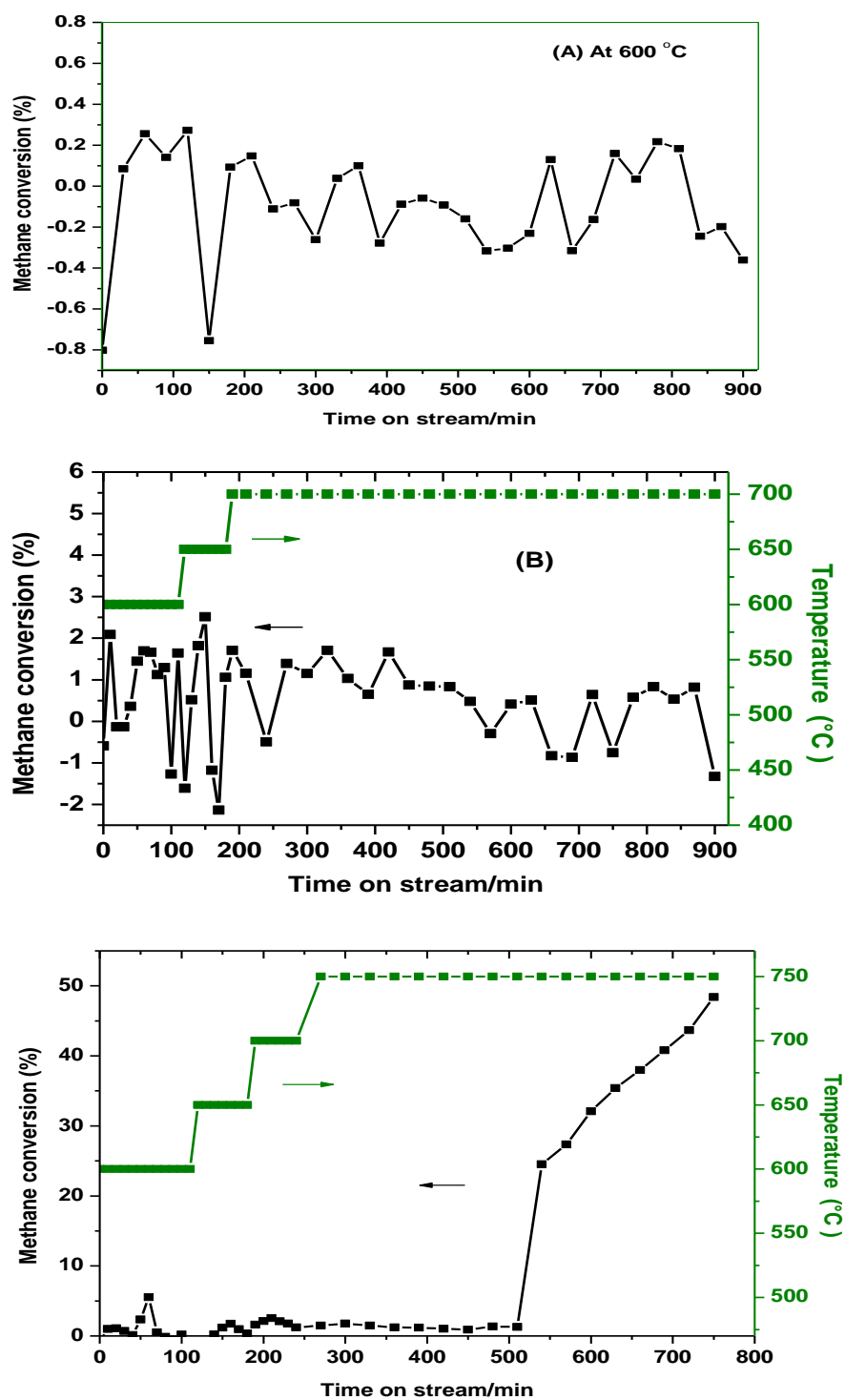


**Figure 8-2** Methane conversion as a function of TOS for cracking of CH<sub>4</sub> over the Landfill sample at different temperatures. (A) At 600 °C, (B) in the temperature programme from 600 to 700 °C, (C) in the temperature programme from 600 to 750 °C. The CH<sub>4</sub>/N<sub>2</sub> flow rate was 12 mL/min and 0.4 g sample mass. These conversions are corresponding to hydrogen formation rates in Figure 3-20.

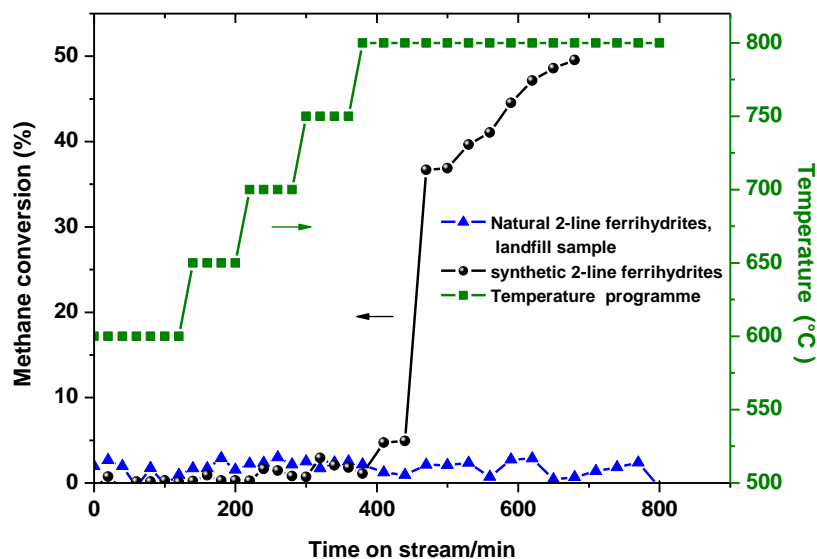


**Figure 8-3** Methane conversion as a function of TOS for CH<sub>4</sub> cracking over the synthetic 2-line ferrihydrite and the natural 2-line ferrihydrites (the Landfill sample) in the temperature programme from 600 to 800 °C. The CH<sub>4</sub>/N<sub>2</sub> flow rate was 12 mL/min and 0.4 g sample mass. These conversions are corresponding to hydrogen formation rates in Figure 3-29.

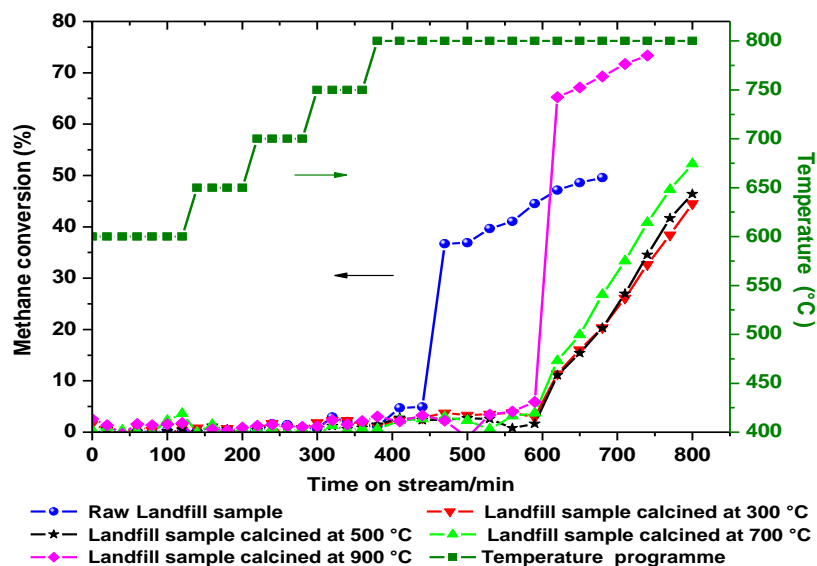


**Figure 8-4** Methane conversion as a function of TOS for CH<sub>4</sub> cracking over the raw Landfill sample and calcined Landfill samples in the temperature programme from 600 to 800 °C. The CH<sub>4</sub>/N<sub>2</sub> flow rate was 12 mL/min and 0.4 g sample mass. These conversions correspond to hydrogen formation rates in Figure 4-6.

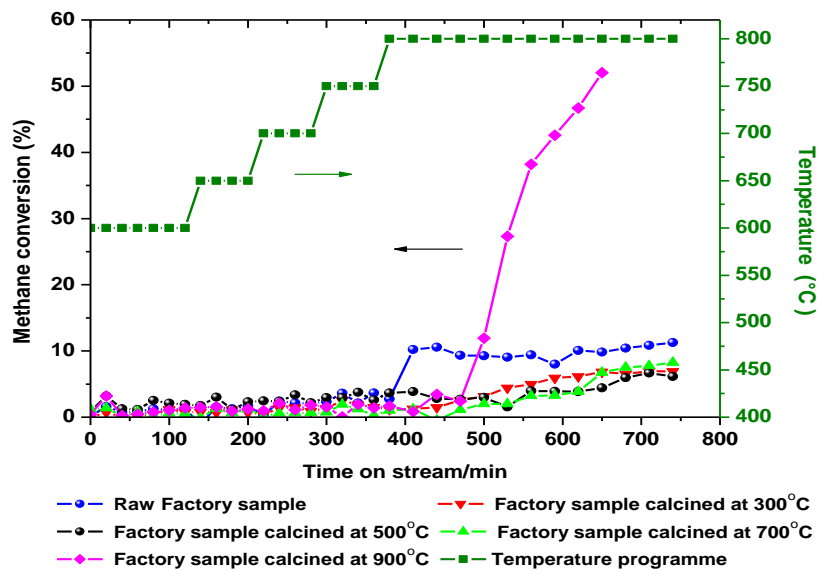


**Figure 8-5** Methane conversion as a function of TOS for CH<sub>4</sub> cracking over the raw Factory sample and calcined Factory samples in the temperature programme from 600 to 800 °C. The CH<sub>4</sub>/N<sub>2</sub> flow rate was 12 mL/min and 0.4 g sample mass. These conversions correspond to hydrogen formation rates in Figure 4-9.

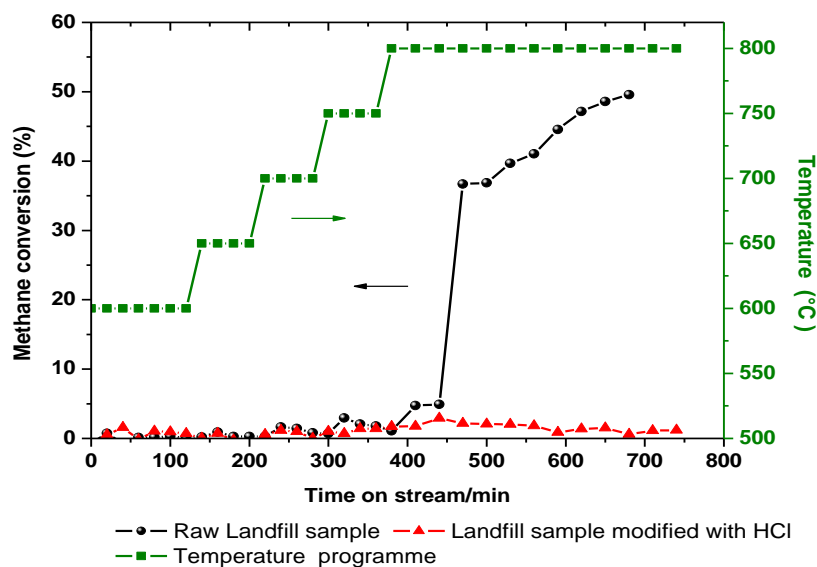


**Figure 8-6** Methane conversion as a function of TOS for CH<sub>4</sub> cracking over the raw Landfill sample and the Landfill sample treated with HCl in the temperature programme from 600 to 800 °C. The CH<sub>4</sub>/N<sub>2</sub> flow rate was 12 mL/min and 0.4 g sample mass. These conversions correspond to hydrogen formation rates in Figure 4-18.

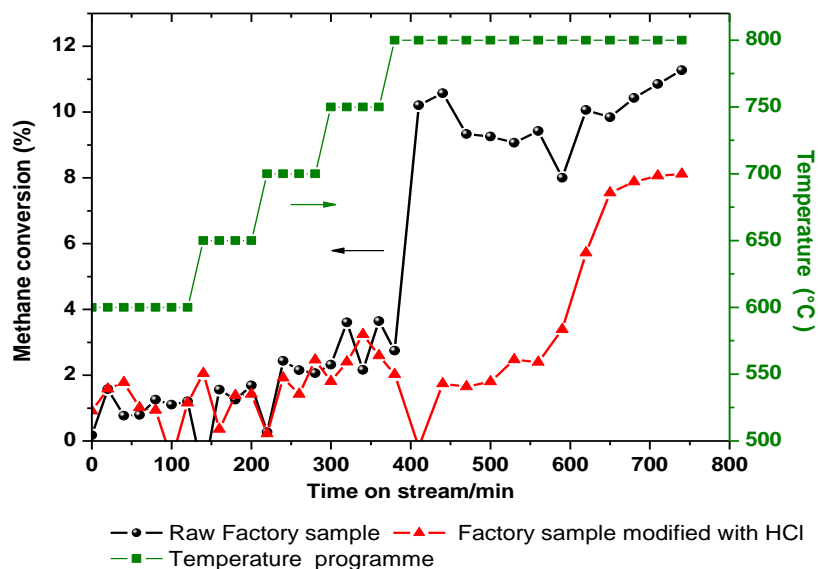


**Figure 8-7** Methane conversion as a function of TOS for CH<sub>4</sub> cracking over the raw Factory sample and the Factory sample treated with HCl in the temperature programme from 600 to 800 °C. The CH<sub>4</sub>/N<sub>2</sub> flow rate was 12 mL/min and 0.4 g sample mass. These conversions correspond to hydrogen formation rates in Figure 4-19.

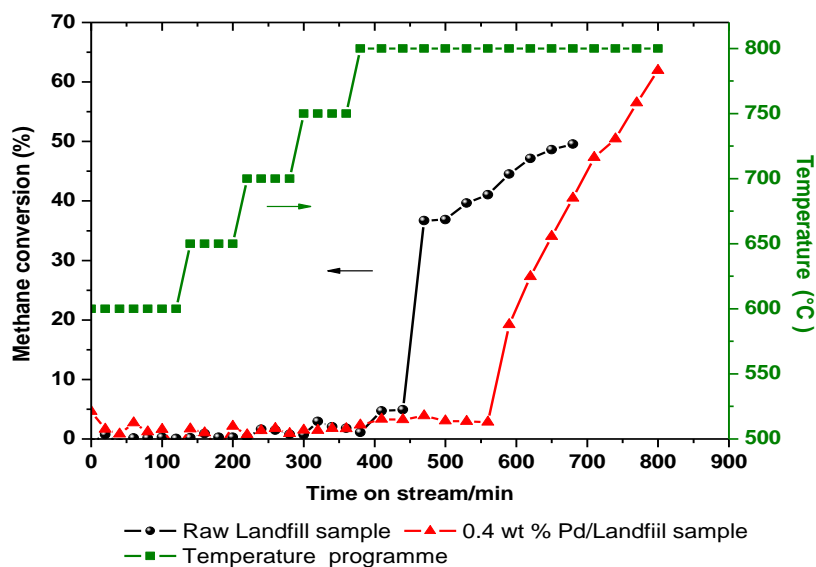


**Figure 8-8** Methane conversion as a function of TOS for CH<sub>4</sub> cracking over the raw Landfill sample and 0.4 wt% Pd/ Landfill sample in the temperature programme from 600 to 800 °C. The CH<sub>4</sub>/N<sub>2</sub> flow rate was 12 mL/min and 0.4 g sample mass. These conversions correspond to hydrogen formation rates in Figure 4-24.

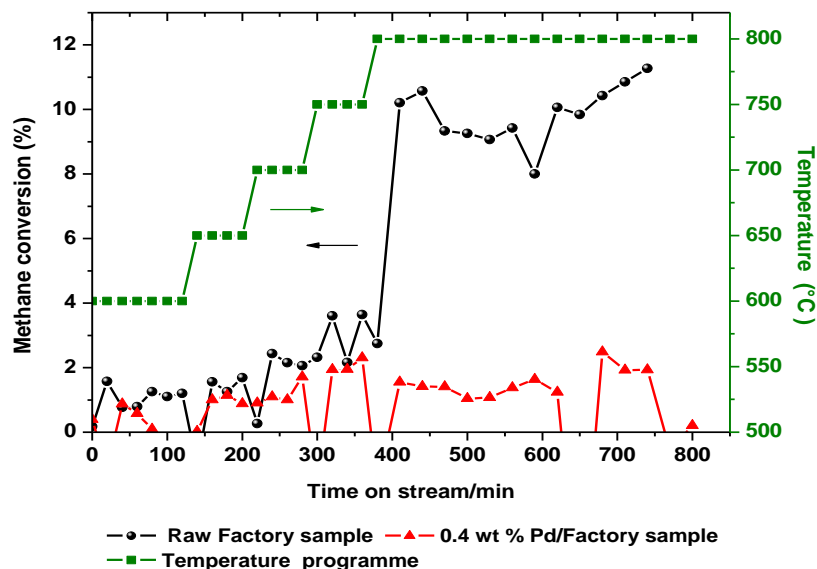


**Figure 8-9** Methane conversion as a function of TOS for CH<sub>4</sub> cracking over the raw Factory sample and 0.4 wt% Pd/ Factory sample in the temperature programme from 600 to 800 °C. The CH<sub>4</sub>/N<sub>2</sub> flow rate was 12 mL/min and 0.4 g sample mass. These conversions correspond to hydrogen formation rates in Figure 4-27.

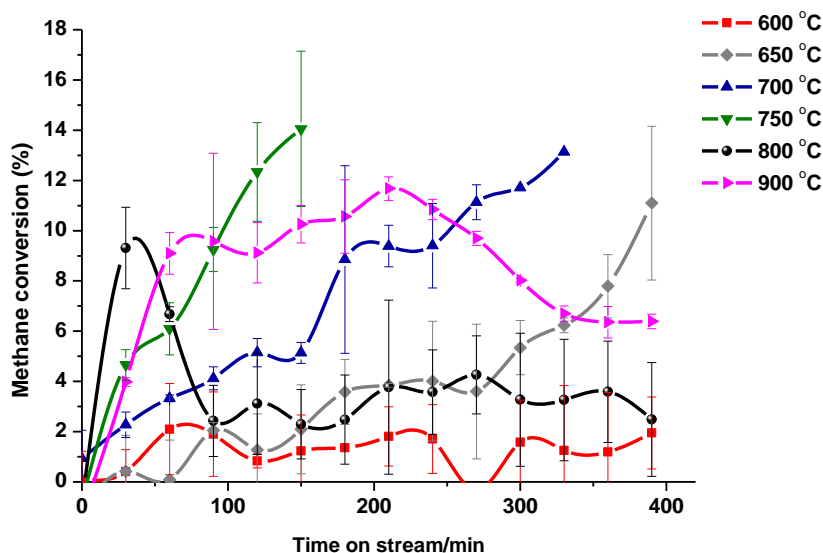


**Figure 8-10** Methane conversion as a function of time on stream for methane cracking over 0.4 wt% Pd/H-ZSM-5 catalyst at different temperatures in the range of 600 to 900 °C, the methane flow rate was 12 mL/min and 0.4 g catalyst mass. These conversions correspond to hydrogen formation rates in Figure 5-1.

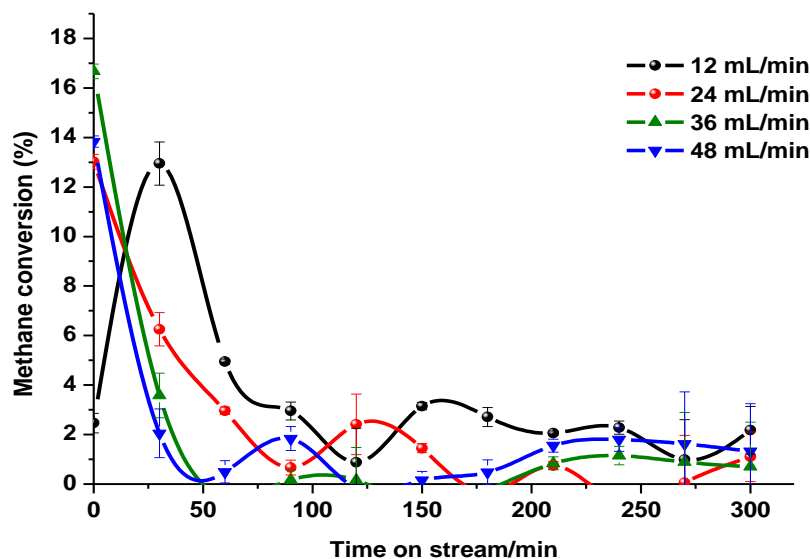


**Figure 8-11** Methane conversion as a function of time on stream for methane cracking over 0.4 wt % Pd/H-ZSM-5 catalyst with varying flow rates at a reaction temperature of 800 °C and 0.4 g catalyst mass. These conversions correspond to hydrogen formation rates in Figure 5-9.

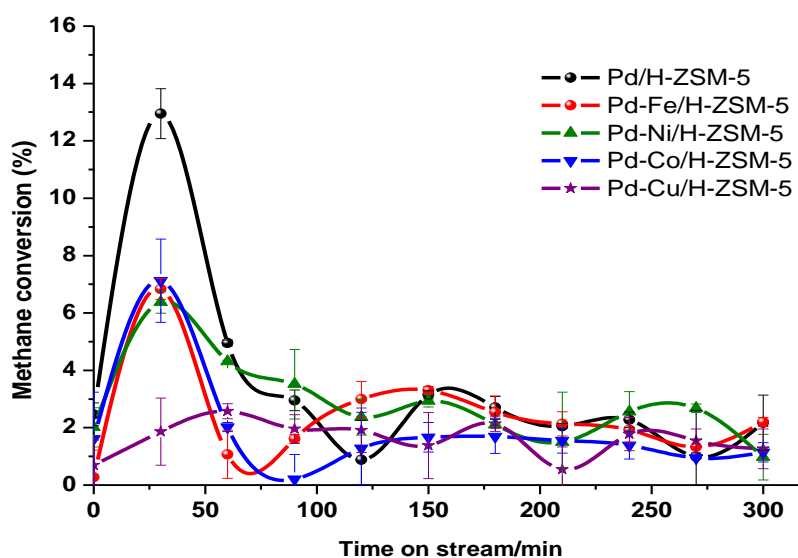


**Figure 8-12** Methane conversion as a function of time on stream for CH<sub>4</sub> cracking over the parent 0.4 wt % Pd/H-ZSM-5 catalyst, and those doped with Fe<sup>3+</sup>, Ni<sup>2+</sup>, Cu<sup>2+</sup> and Co<sup>2+</sup> (dopant metal M/Pd atomic ratio of 0.25), the reaction temperature was 800 °C and 0.4 g catalyst mass. These conversions correspond to hydrogen formation rates in Figure 5-15.

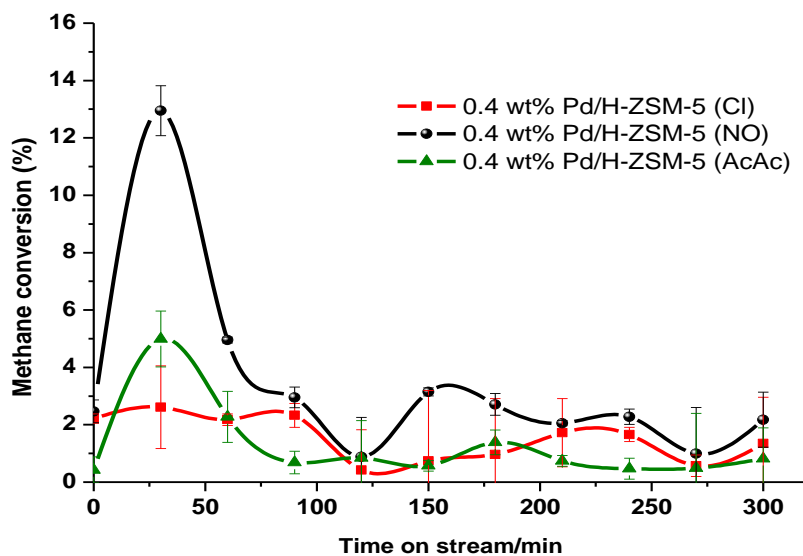


**Figure 8-13** Methane conversion as a function of time on stream for methane cracking over 0.4 wt % Pd/H-ZSM-5 catalyst prepared from different palladium precursors, the reaction temperature of 800 °C, the methane flow rate was 12 mL/min and 0.4 g catalyst mass.. These conversions correspond to hydrogen formation rates in Figure 5-22.

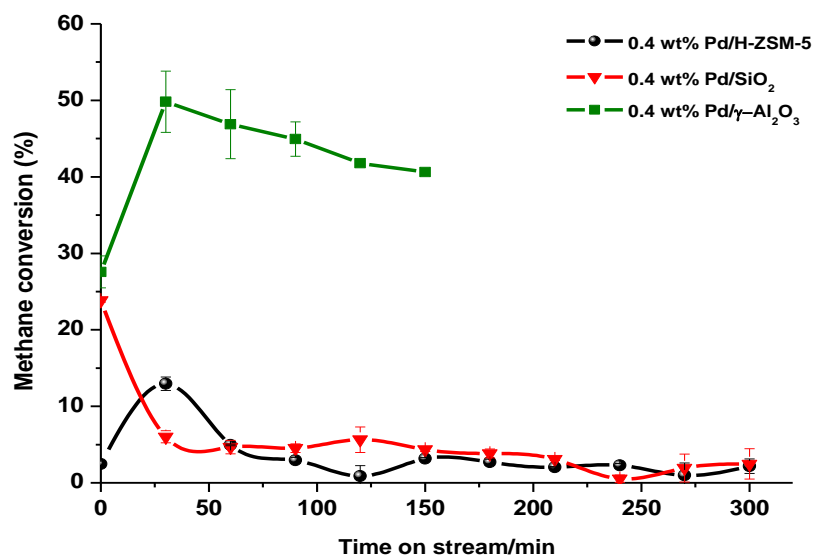


**Figure 8-14** Methane conversion as a function of time on stream for methane cracking over 0.4 wt% Pd/H-ZSM-5, 0.4 wt% Pd/SiO<sub>2</sub> and 0.4 wt% Pd/ $\gamma$ -Al<sub>2</sub>O<sub>3</sub>, the reaction temperature was 800 °C, the methane flow rate was 12 mL/min and 0.4 g catalyst mass.. These conversions correspond to hydrogen formation rates in Figure 5-28.

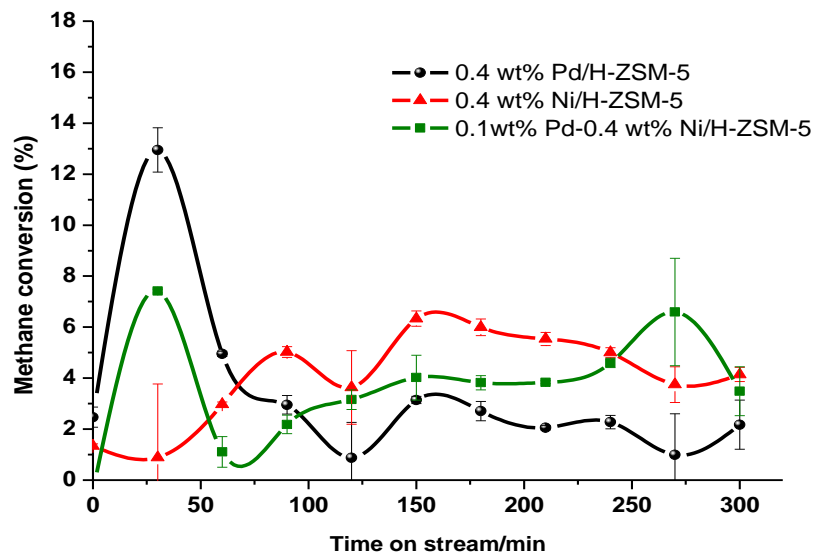


**Figure 8-15** Methane conversion as a function of time on stream for methane cracking over 0.4 wt% Ni/H-ZSM-5, 0.4 wt% Pd/H-ZSM-5 and Pd-Ni/H-ZSM-5 catalysts (dopant metal Pd/Ni atomic ratio of 0.25), the reaction temperature of 800 °C, the methane flow rate was 12 mL/min and 0.4 g catalyst mass. These conversions correspond to hydrogen formation rates in Figure 6-1.

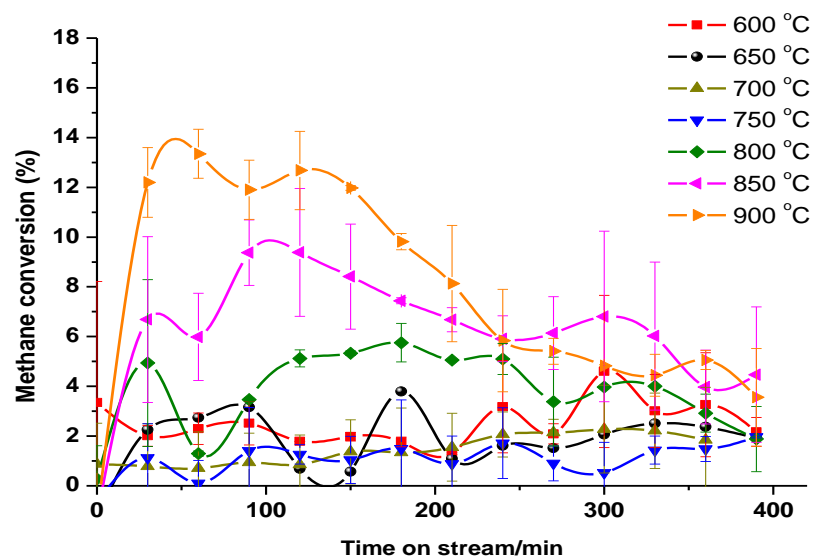


**Figure 8-16** Methane conversion as a function of time on stream for methane cracking over 0.4 wt% Ni/H-ZSM-5 catalyst at different temperatures in range of 600 to 900 °C, the methane flow rate is 12 mL/min and 0.4 g catalyst mass. These conversions correspond to hydrogen formation rates in Figure 6-6.

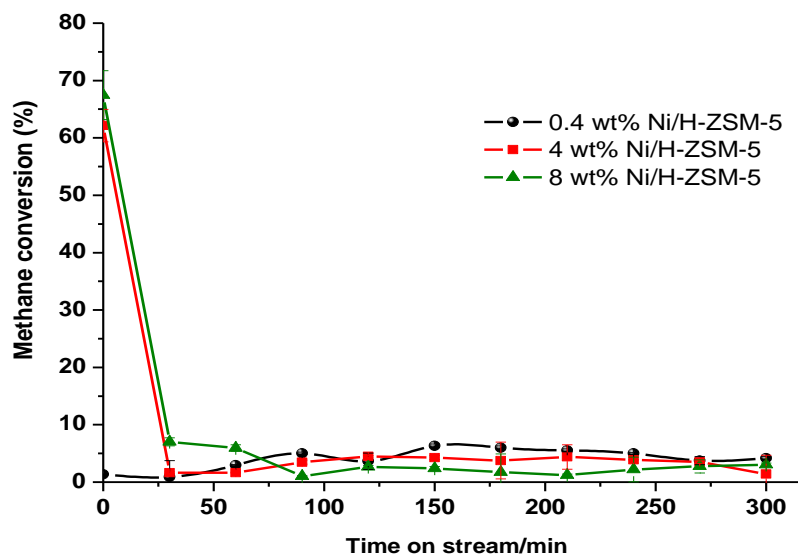


**Figure 8-17** Methane conversion as a function of time on stream for methane cracking over Ni/H-ZSM-5 catalysts loaded with different amounts of Ni: 0.4, 4 and 8 wt%, the reaction temperature of 800 °C, the methane flow rate was 12 mL/min. These conversions correspond to hydrogen formation rates in Figure 6-11.

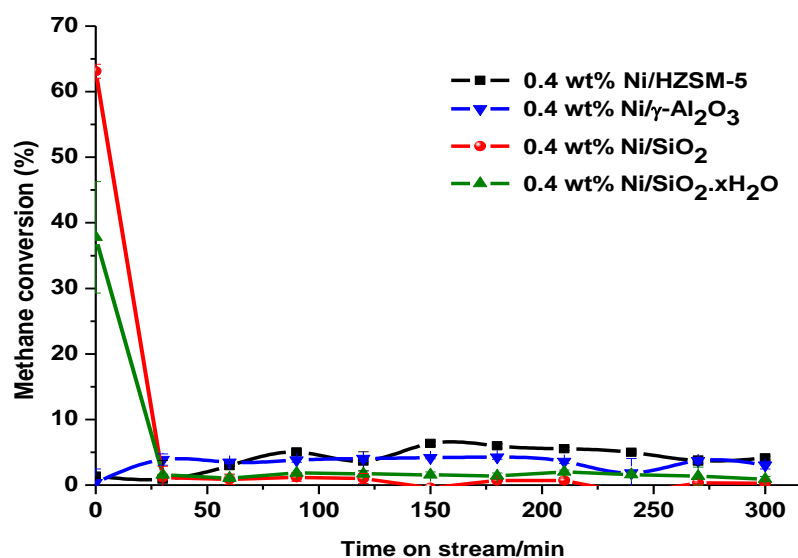


**Figure 8-18** Methane conversion as a function of time on stream for methane cracking over 0.4 wt% Ni/H-ZSM-5, 0.4 wt% Ni/SiO<sub>2</sub>, 0.4 wt% Ni/ $\gamma$ -Al<sub>2</sub>O<sub>3</sub> and 0.4 wt% Ni/SiO<sub>2</sub>.xH<sub>2</sub>O (silicic acid), the reaction temperature of 800 °C, the methane flow rate was 12 mL/min and 0.4 g catalyst mass. These conversions correspond to hydrogen formation rates in Figure 6-16.

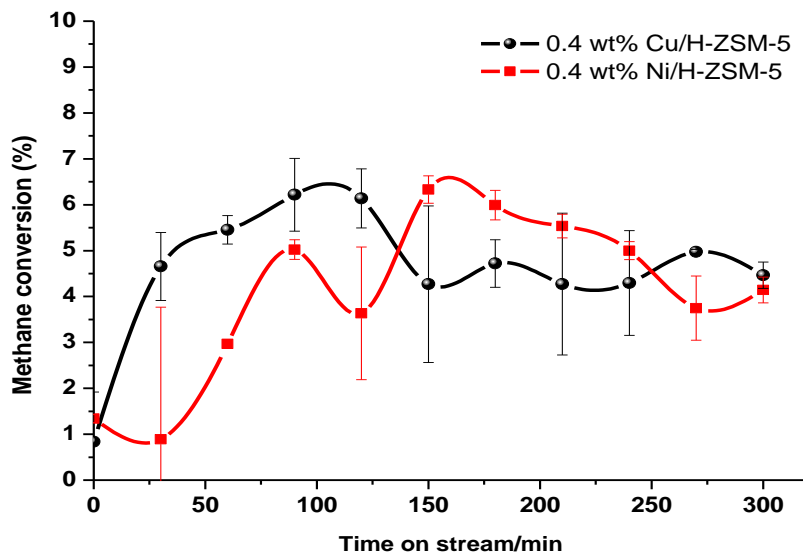


**Figure 8-19** Methane conversion as a function of time on stream for methane cracking over 0.4 wt% Cu/H-ZSM-5 and 0.4 wt% Ni/H-ZSM-5, the reaction temperature of 800 °C, the methane flow rate was 12 mL/min and 0.4 g catalyst mass. These conversions correspond to hydrogen formation rates in Figure 6-21.

## References

- [1] S. Jebaraj, S. Iniyan, *Renewable and Sustainable Energy Reviews*, 10 (2006) 281-311.
- [2] T. N. Veziroğlu, *International Journal of Hydrogen Energy*, 12 (1987) 99-129.
- [3] D.J. Wuebbles, A.K. Jain, *Fuel Processing Technology*, 71 (2001) 99-119.
- [4] Y. Li, D. Li, G. Wang, *Catalysis Today*, 162 (2011) 1-48.
- [5] C. Koroneos, A. Dompros, G. Roumbas, N. Moussiopoulos, *International Journal of Hydrogen Energy*, 29 (2004) 1443-1450.
- [6] T.N. Veziroğlu, *International Journal of Hydrogen Energy*, 20 (1995) 1-7.
- [7] R. Ramachandran, R.K. Menon, *International Journal of Hydrogen Energy*, 23 (1998) 593-598.
- [8] C. Song, *Catalysis Today*, 77 (2002) 17-49.
- [9] D. Shekhawat, J. J. Spivey, D.A. Berry, *Fuel cells: Technology For Fuel Cell Processing*, Elsevier, 2011, ISBN: 978-0-444-53563-4.
- [10] J. Zhang, *PEM Fuel Cell Electrocatalysts and Catalyst Layers*, Springer, 2008, ISBN: 978-1-84800-935-6.
- [11] Z. Chen, S.E.H. Elnashaie, *Chemical Engineering Science*, 59 (2004) 3965-3979.
- [12] N.Z. Muradov, T.N. Veziroğlu, *International Journal of Hydrogen Energy*, 33 (2008) 6804-6839.
- [13] P. Corbo, F. Migliardini, O. Veneri, *Hydrogen as Future Energy Carrier*, in: *Hydrogen Fuel Cells for Road Vehicles*, Springer London, 2011, pp. 33-70, ISBN:978-970-85729-85135-85726.
- [14] D. Das, T.N. Veziroğlu, *International Journal of Hydrogen Energy*, 26 (2001) 13-28.
- [15] R.M. Navarro, M.C. Sanchez-Sanchez, M.C. Alvarez-Galvan, F.d. Valle, J.L.G. Fierro, *Energy and Environmental Science*, 2 (2009) 35-54.
- [16] B. Gaudernack, *Hydrogen Production from Fossil Fuels*, in: T.O. Saetre (Ed.) *Hydrogen Power: Theoretical and Engineering Solutions*, Springer Netherlands, 1998, pp. 75-89, ISBN:978-990-481-5029-5028.
- [17] N.Z. Muradov, *International Journal of Hydrogen Energy*, 18 (1993) 211-215.
- [18] C. Guéret, M. Daroux, F. Billaud, *Chemical Engineering Science*, 52 (1997) 815-827.
- [19] T.V. Choudhary, C. Sivadinarayana, C.C. Chusuei, A. Klinghoffer, D.W. Goodman, *Journal of Catalysis*, 199 (2001) 9-18.
- [20] J.D. Holladay, J. Hu, D.L. King, Y. Wang, *Catalysis Today*, 139 (2009) 244-260.
- [21] R. Kothari, D. Buddhi, R.L. Sawhney, *Renewable and Sustainable Energy Reviews*, 12 (2008) 553-563.
- [22] Y. Jamal, M.L. Wyszynski, *International Journal of Hydrogen Energy*, 19 (1994) 557-572.
- [23] U. Izquierdo, V.L. Barrio, J.F. Cambra, J. Requies, M.B. Güemez, P.L. Arias, G. Kolb, R. Zapf, A.M. Gutiérrez, J.R. Arraibi, *International Journal of Hydrogen Energy*, 37 (2012) 7026-7033.
- [24] J.N. Armor, *Applied Catalysis A: General*, 176 (1999) 159-176.
- [25] M.G. Poirier, C. Sapundzhiev, *International Journal of Hydrogen Energy*, 22 (1997) 429-433.
- [26] D. Mogensen, J.D. Grunwaldt, P.V. Hendriksen, K. Dam-Johansen, J.U. Nielsen, *Journal of Power Sources*, 196 (2011) 25-38.
- [27] R.M. Navarro, M.A. Peña, J.L.G. Fierro, *Chemical Reviews*, 107 (2007) 3952-3991.
- [28] K. Otsuka, S. Takenaka, H. Ohtsuki, *Applied Catalysis A: General*, 273 (2004) 113-124.
- [29] Q. Zhu, X. Zhao, Y. Deng, *Journal of Natural Gas Chemistry*, 13 (2004) 191-203.
- [30] X. Song, Z. Guo, *Energy Conversion and Management*, 47 (2006) 560-569.
- [31] A.E. York, T. Xiao, M.H. Green, *Topics in Catalysis*, 22 (2003) 345-358.

- [32] K. Aasberg-Petersen, J.H. Bak Hansen, T.S. Christensen, I. Dybkjaer, P.S. Christensen, C. Stub Nielsen, S.E.L. Winter Madsen, J.R. Rostrup-Nielsen, *Applied Catalysis A: General*, 221 (2001) 379-387.
- [33] T.V. Choudhary, D.W. Goodman, *Catalysis Today*, 77 (2002) 65-78.
- [34] N. Muradov, *Catalysis Communications*, 2 (2001) 89-94.
- [35] N. Muradov, F. Smith, C. Huang, A. T-Raissi, *Catalysis Today*, 116 (2006) 281-288.
- [36] N.Z. Muradov, T.N. Veziroğlu, *International Journal of Hydrogen Energy*, 30 (2005) 225-237.
- [37] H.F. Abbas, W.M.A.W. Daud, *International Journal of Hydrogen Energy*, 35 (2010) 12268-12276.
- [38] J. Ashok, G. Raju, P.S. Reddy, M. Subrahmanyam, A. Venugopal, *Journal of Natural Gas Chemistry*, 17 (2008) 113-119.
- [39] D. Chen, K. O. Christensen, E. O. Fernández, Z. Yu, B. Tøtdal, N. Latorre, A. Monzón, A. Holmen, *Journal of Catalysis*, 229 (2005) 82-96.
- [40] S. Takenaka, S. Kobayashi, H. Ogihara, K. Otsuka, *Journal of Catalysis*, 217 (2003) 79-87.
- [41] S. Ahmed, A. Aitani, F. Rahman, A. Al-Dawood, F. Al-Muhaish, *Applied Catalysis A: General*, 359 (2009) 1-24.
- [42] H.F. Abbas, W.M.A. Wan Daud, *International Journal of Hydrogen Energy*, 35 (2010) 1160-1190.
- [43] A.M. Amin, E. Croiset, W. Epling, *International Journal of Hydrogen Energy*, 36 (2011) 2904-2935.
- [44] C.E.G. Padró, F. Lau, *Advances in Hydrogen Energy*, Springer, 2000, ISBN : 9780306464294.
- [45] S. Burns, J. G. Gallagher, J. S. J. Hargreaves, P. J. F. Harris, *Catalysis Letters*, 116 (2007) 122-127.
- [46] N. Shah, D. Panjala, G. P. Huffman, *Energy and Fuels*, 15 (2001) 1528-1534.
- [47] F. Solymosi, A. Erdohelyi, J. Cserenyi, A. Felvegi, *Journal of Catalysis*, 147 (1994) 272-278.
- [48] A. Venugopal, S. Naveen Kumar, J. Ashok, D. Hari Prasad, V. Durga Kumari, K.B.S. Prasad, M. Subrahmanyam, *International Journal of Hydrogen Energy*, 32 (2007) 1782-1788.
- [49] I. Suelves, M. J. Lázaro, R. Moliner, B. M. Corbella, J. M. Palacios, *International Journal of Hydrogen Energy*, 30 (2005) 1555-1567.
- [50] J.I. Villacampa, C. Royo, E. Romeo, J.A. Montoya, P. Del Angel, A. Monzón, *Applied Catalysis A: General*, 252 (2003) 363-383.
- [51] S. Takenaka, M. Serizawa, K. Otsuka, *Journal of Catalysis*, 222 (2004) 520-531.
- [52] L.B. Avdeeva, T.V. Reshetenko, Z.R. Ismagilov, V.A. Likhobov, *Applied Catalysis A: General*, 228 (2002) 53-63.
- [53] M.A. Ermakova, D.Y. Ermakov, G.G. Kuvshinov, *Applied Catalysis A: General*, 201 (2000) 61-70.
- [54] P. Jana, V.A. de la Peña O'Shea, J.M. Coronado, D.P. Serrano, *International Journal of Hydrogen Energy*, 37 (2012) 7034-7041.
- [55] S. Takenaka, M. Ishida, M. Serizawa, E. Tanabe, K. Otsuka, *The Journal of Physical Chemistry B*, 108 (2004) 11464-11472.
- [56] L.B. Avdeeva, D.I. Kochubey, S.K. Shaikhutdinov, *Applied Catalysis A: General*, 177 (1999) 43-51.
- [57] A. C. Dupuis, *Progress in Materials Science*, 50 (2005) 929-961.
- [58] N.A.M. Zabidi, S.H.S. Zein, A. Mohamed, *Universiti Teknologi Petronas. Platform*, 3 (2003) 3-9.
- [59] J. Ashok, S. Kumar, A. Venugopal, V. Durga Kumari, M. Subrahmanyam, *Journal of Power Sources*, 164 (2007) 809-814.

- [60] I. Suelves, M. Lázaro, R. Moliner, Y. Echegoyen, J. Palacios, *Catalysis Today*, 116 (2006) 271-280.
- [61] J. Chen, Y. Li, Z. Li, X. Zhang, *Applied Catalysis A: General*, 269 (2004) 179-186.
- [62] S. Takenaka, H. Ogihara, I. Yamanaka, K. Otsuka, *Applied Catalysis A: General*, 217 (2001) 101-110.
- [63] H. Ogihara, S. Takenaka, I. Yamanaka, E. Tanabe, A. Genseki, K. Otsuka, *Journal of Catalysis*, 238 (2006) 353-360.
- [64] M.S. Rahman, E. Croiset, R.R. Hudgins, *Topics in Catalysis*, 37 (2006) 137-145.
- [65] P. Forzatti, L. Lietti, *Catalysis Today*, 52 (1999) 165-181.
- [66] J.A. Moulijn, A.E. van Diepen, F. Kapteijn, *Applied Catalysis A: General*, 212 (2001) 3-16.
- [67] C.H. Bartholomew, R.J. Farrauto, *Fundamentals of Industrial Catalytic Processes*, 2nd ed., Wiley, 2006, ISBN:13 978-0-471-45713-8.
- [68] H.F. Abbas, W.M.A.W. Daud, *International Journal of Hydrogen Energy*, 35 (2010) 141-150.
- [69] C.H. Bartholomew, *Applied Catalysis A: General*, 212 (2001) 17-60.
- [70] G.B. Nuernberg, H.V. Fajardo, D.Z. Mezalira, T.J. Casarin, L.F.D. Probst, N.L.V. Carreño, *Fuel*, 87 (2008) 1698-1704.
- [71] T. V. Choudhary, D.W. Goodman, *Catalysis*, 19 (2006) 164-183.
- [72] T. Zhang, M. Amiridis, *Applied Catalysis A: General*, 167 (1998) 161-172.
- [73] R.T.K. Baker, *Carbon*, 27 (1989) 315-323.
- [74] J. Guo, H. Lou, X. Zheng, *Carbon*, 45 (2007) 1314-1321.
- [75] M.S. Dresselhaus, G. Dresselhaus, P.C. Eklund, *Science of Fullerenes and Carbon Nanotubes*, Elsevier Science, 1996, ISBN: 0-12-221820-5.
- [76] J.D. Carey, S.R. Silva, *Effects of Nanoscale Clustering in Amorphous Carbon*, in: G. Messina, S. Santangelo (Eds.) *Carbon*, Springer Berlin Heidelberg, 2006, pp. 137-152, ISBN:978-133-540-29531-29530.
- [77] B.T. Kelly, *Physics of graphite*, Applied Science, London, 1981, ISBN:0853349606-9780853349600.
- [78] D.M. Guldi, N. Martín, *Carbon Nanotubes and Related Structures: Synthesis, Characterization, Functionalization and Applications*, 2010, ISBN: 978-3-527-32406-4.
- [79] N. A. Marks, D. R. McKenzie, B.A. Pailthorpe, *Physical review letters*, 76 (1996) 768-771.
- [80] K. T. Lau, D. Hui, *Composites Part B: Engineering*, 33 (2002) 263-277.
- [81] L. Piao, Y. Li, J. Chen, L. Chang, J.Y.S. Lin, *Catalysis Today*, 74 (2002) 145-155.
- [82] A.R. Biris, Z. Li, E. Dervishi, D. Lupu, Y. Xu, V. Saini, F. Watanabe, A.S. Biris, *Physics Letters A*, 372 (2008) 3051-3057.
- [83] Y. Zhao, Y. X. Pan, L. Cui, C. J. Liu, *Diamond and Related Materials*, 16 (2007) 229-235.
- [84] A. Rashidi, R. Lotfi, E. Fakhrmosavi, M. Zare, *Journal of Natural Gas Chemistry*, 20 (2011) 372-376.
- [85] S. Tang, Z. Zhong, Z. Xiong, L. Sun, L. Liu, J. Lin, Z.X. Shen, K.L. Tan, *Chemical Physics Letters*, 350 (2001) 19-26.
- [86] L. Noda, N. Gonçalves, A. Valentini, L. Probst, R. Almeida, *Journal of Materials Science*, 42 (2007) 914-922.
- [87] R. Ravindra, B. Badekai Ramachandra, *Applied Nanoscience*, 1 (2011) 103-108.
- [88] Y. Li, J. Chen, L. Chang, *Applied Catalysis A: General*, 163 (1997) 45-57.
- [89] X. Zhu, D. Cheng, P. Kuai, *Energy and Fuels*, 22 (2008) 1480-1484.
- [90] T. Baird, J.R. Fryer, B. Grant, *Carbon*, 12 (1974) 591-602.
- [91] C. He, N. Zhao, X. Du, C. Shi, J. Ding, J. Li, Y. Li, *Scripta Materialia*, 54 (2006) 689-693.

- [92] C. He, N. Zhao, C. Shi, X. Du, J. Li, *Materials Chemistry and Physics*, 97 (2006) 109-115.
- [93] M. Monthioux, V.L. Kuznetsov, *Carbon*, 44 (2006) 1621-1623.
- [94] A. Oberlin, M. Endo, T. Koyama, *Journal of Crystal Growth*, 32 (1976) 335-349.
- [95] S. Iijima, *Nature*, 354 (1991) 56-58.
- [96] S. Iijima, T. Ichihashi, *Nature*, 363 (1993) 603-605.
- [97] P. Serp, M. Corrias, P. Kalck, *Applied Catalysis A: General*, 253 (2003) 337-358.
- [98] S. Yellampalli, *Carbon Nanotubes – Polymer Nanocomposites*, InTech, 2011, ISBN : 978-953-307-498-6.
- [99] Y. Jin, G. Wang, Y. Li, *Applied Catalysis A: General*, 445-446 (2012) 121-127.
- [100] R. Oriňáková, A. Oriňák, *Fuel*, 90 (2011) 3123-3140.
- [101] K. Hernadi, A. Fonseca, J.B. Nagy, A. Siska, I. Kiricsi, *Applied Catalysis A: General*, 199 (2000) 245-255.
- [102] B.C. Liu, S.C. Lyu, T.J. Lee, S.K. Choi, S.J. Eum, C.W. Yang, C.Y. Park, C.J. Lee, *Chemical Physics Letters*, 373 (2003) 475-479.
- [103] J.W. Snoeck, G.F. Froment, M. Fowles, *Journal of Catalysis*, 169 (1997) 240-249.
- [104] R.T.K. Baker, M.A. Barber, P.S. Harris, F.S. Feates, R.J. Waite, *Journal of Catalysis*, 26 (1972) 51-62.
- [105] R.T. Yang, J.P. Chen, *Journal of Catalysis*, 115 (1989) 52-64.
- [106] C. Pan, Y. Liu, F. Cao, J. Wang, Y. Ren, *Micron*, 35 (2004) 461-468.
- [107] M.L. Toebes, J.H. Bitter, A.J. van Dillen, K.P. de Jong, *Catalysis Today*, 76 (2002) 33-42.
- [108] S. Vm, A.R. Mohamed, A.Z. Abdullah, S.P. Chai, *Journal of Nanomaterials*, 2010 (2010) 1-11.
- [109] E. Lamouroux, P. Serp, P. Kalck, *Catalysis Reviews*, 49 (2007) 341-405.
- [110] X. Chen, R. Wang, J. Xu, D. Yu, *Micron*, 35 (2004) 455-460.
- [111] M. Bell, R. Lacerda, K.K. Teo, W. Milne, *Characterisation of the Growth Mechanism during PECVD of Multiwalled Carbon Nanotubes*, in: G. Messina, S. Santangelo (Eds.) *Carbon*, Springer Berlin Heidelberg, 2006, pp. 77-93, ISBN:978-973-540-29531-29530.
- [112] M. Monthioux, L. Noe, L. Dussault, J.C. Dupin, N. Latorre, T. Ubierto, E. Romeo, C. Royo, A. Monzon, C. Guimon, *Journal of Materials Chemistry*, 17 (2007) 4611-4618.
- [113] P. morgan, *Carbon Fibers and Their Composites*, CRC Press, 2005, ISBN: 0-8247-0983-7.
- [114] X. Duan, G. Qian, J. Zhou, X. Zhou, D. Chen, W. Yuan, *Catalysis Today*, 186 (2012) 48-53.
- [115] N.M. Rodriguez, A. Chambers, R.T.K. Baker, *Langmuir*, 11 (1995) 3862-3866.
- [116] Z. Li, J.A. Larsson, P. Larsson, R. Ahuja, J.M. Tobin, J. O'Byrne, M.A. Morris, G. Attard, J.D. Holmes, *The Journal of Physical Chemistry C*, 112 (2008) 12201-12206.
- [117] Y. Saito, *Carbon*, 33 (1995) 979-988.
- [118] Y. Li, J. Chen, Y. Ma, J. Zhao, Y. Qin, L. Chang, *Chemical Communications*, (1999) 1141-1142.
- [119] J. Chen, Y. Li, Y. Ma, Y. Qin, L. Chang, *Carbon*, 39 (2001) 1467-1475.
- [120] X.X. Zhang, Z.Q. Li, G.H. Wen, K.K. Fung, J. Chen, Y. Li, *Chemical Physics Letters*, 333 (2001) 509-514.
- [121] Z. Li, J. Chen, X. Zhang, Y. Li, K.K. Fung, *Carbon*, 40 (2002) 409-415.
- [122] S. Iijima, *Journal of Crystal Growth*, 50 (1980) 675-683.
- [123] Z. Qiao, J. Li, N. Zhao, C. Shi, P. Nash, *Scripta Materialia*, 54 (2006) 225-229.
- [124] S. P. Chai, W. M. Yeoh, K. Y. Lee, A. R. Mohamed, *Journal of Alloys and Compounds*, 488 (2009) 294-299.
- [125] J.L. Kang, J.J. Li, X.W. Du, C.S. Shi, N.Q. Zhao, L. Cui, P. Nash, *Journal of Alloys and Compounds*, 456 (2008) 290-296.

- [126] M.A. Ermakova, D.Y. Ermakov, *Catalysis Today*, 77 (2002) 225-235.
- [127] M. A. Ermakova, D. Y. Ermakov, A. L. Chuvilin, G. G. Kuvshinov, *Journal of Catalysis*, 201 (2001) 183-197.
- [128] K. Hernadi, A. Fonseca, J.B. Nagy, D. Bernaerts, A.A. Lucas, *Carbon*, 34 (1996) 1249-1257.
- [129] L. Tang, D. Yamaguchi, N. Burke, D. Trimm, K. Chiang, *Catalysis Communications*, 11 (2010) 1215-1219.
- [130] U. Schwertmann, R.M. Cornell, *Iron oxides in the Laboratory*, Wiley-VCH Verlag, 1991, ISBN: 3-527-26991-6.
- [131] H. Hashimoto, S. Yokoyama, H. Asaoka, Y. Kusano, Y. Ikeda, M. Seno, J. Takada, T. Fujii, M. Nakanishi, R. Murakami, *Journal of Magnetism and Magnetic Materials*, 310 (2007) 2405-2407.
- [132] R.M. Cornell, U. Schwertmann, *The Iron Oxides: Structure, Properties, Reactions, Occurrences and Uses*, Wiley, 1996, ISBN: 3527285768.
- [133] D. Fortin, S. Langley, *Earth-Science Reviews*, 72 (2005) 1-19.
- [134] T. W. Hodges, J.B. Olson, *Applied and Environmental Microbiology*, 75 (2009) 1650-1657.
- [135] T. Sakai, Y. Miyazaki, A. Murakami, N. Sakamoto, T. Ema, H. Hashimoto, M. Furutani, M. Nakanishi, T. Fujii, J. Takada, *Organic and Biomolecular Chemistry*, 8 (2010) 336-338.
- [136] K.L. Straub, M. Benz, B. Schink, *FEMS Microbiology Ecology*, 34 (2001) 181-186.
- [137] R.E. James, F.G. Ferris, *Chemical Geology*, 212 (2004) 301-311.
- [138] L. J. Florea, C. L. Stinson, J. Brewer, R. Fowler, J. B. Kearns, A.M. Greco, *International Journal of Speleology*, 40 (2011) 205-219.
- [139] M. Dworkin, S. Falkow, E. Rosenberg, K.H. Schleifer, E. Stackebrandt, *The Prokaryotes*, Springer New York, 2006, ISBN:978-0-387-25495-1.
- [140] C.B. Kennedy, S.D. Scott, F.G. Ferris, *Geomicrobiology Journal*, 20 (2003) 199-214.
- [141] H. Hashimoto, H. Asaoka, T. Nakano, Y. Kusano, H. Ishihara, Y. Ikeda, M. Nakanishi, T. Fujii, T. Yokoyama, N. Horiishi, T. Nanba, J. Takada, *Dyes and Pigments*, 95 (2012) 639-643.
- [142] T. Kasama, T. Murakami, *Chemical Geology*, 180 (2001) 117-128.
- [143] J.A. Rentz, I.P. Turner, J.L. Ullman, *Water Research*, 43 (2009) 2029-2035.
- [144] I. Takeda, H. Somura, Y. Mori, *Ecological Engineering*, 36 (2010) 1064-1069.
- [145] I. Katsoyiannis, A. Zouboulis, H. Althoff, H. Bartel, *Chemosphere*, 47 (2002) 325-332.
- [146] I. A. Katsoyiannis, A. I. Zouboulis, *Water Quality Research Journal of Canada*, 41 (2006) 117-129.
- [147] L.S. Isaacson, E.D. Burton, R.T. Bush, D.R.G. Mitchell, S.G. Johnston, B.C.T. Macdonald, L.A. Sullivan, I. White, *Applied Geochemistry*, 24 (2009) 1825-1834.
- [148] J. Weitkamp, *Solid State Ionics*, 131 (2000) 175-188.
- [149] M.E. Davis, R.F. Lobo, *Chemistry of Materials*, 4 (1992) 756-768.
- [150] L. Smart, E. Moore, *Solid State Chemistry*, Chapman and Hall, 1992, ISBN: 0-412-40040-5.
- [151] H. Van Bekkum, E. M. Flanigen, P. A. Jacobs, J.C. Jansen, *Introduction to Zeolite Science and Practice*, 2nd ed, Elsevier, 2001.
- [152] B.C. Gates, *Catalytic Chemistry*, John Wiley and Sons Incorporated, 1992, ISBN:9780471559146.
- [153] J. Jiao, J. Kanellopoulos, W. Wang, S.S. Ray, H. Foerster, D. Freude, M. Hunger, *Physical Chemistry Chemical Physics*, 7 (2005) 3221-3226.
- [154] R.J. Argauer, G.R. Landolt, *Crystalline Zeolite ZSM-5 and Method of Preparing the Same*, United States Patent Office 3702886, 1972.

- [155] S. Sang, F. Chang, Z. Liu, C. He, Y. He, L. Xu, *Catalysis Today*, 93–95 (2004) 729-734.
- [156] J. Jiang, C. Duanmu, Y. Yang, X. Gu, J. Chen, *Powder Technology*, 251 (2014) 9-14.
- [157] N. Rahimi, R. Karimzadeh, *Applied Catalysis A: General*, 398 (2011) 1-17.
- [158] S. Bhatia, J. Beltramini, D.D. Do, *Catalysis Reviews*, 31 (1989) 431-480.
- [159] C. N. Satterfield, *Heterogeneous Catalysis in Industrial Practice*, 2nd ed, 1991, ISBN:1-57524-002-5.
- [160] M. Guisnet, F.R. Ribeiro, *Deactivation and Regeneration of Zeolite Catalysts*, Imperial College Press, 2011, ISBN:9781848166370.
- [161] M. Balakrishnan, V. S. Batra, J. S. J. Hargreaves, A. Monaghan, I. D. Pulford, J. L. Rico, S. Sushil, *Green Chemistry*, 11 (2009) 42-47.
- [162] S. Sushil, A. M. Alabdulrahman, M. Balakrishnan, V. S. Batra, R. A. Blackley, J. Clapp, J. S. J. Hargreaves, A. Monaghan, I. D. Pulford, J. L. Rico, W. Zhou, *Journal of Hazardous Materials*, 180 (2010) 409-418.
- [163] S. Gaudino, C. Galas, M. Belli, S. Barbizzi, P. Zorzi, R. Jaćimović, Z. Jeran, A. Pati, U. Sansone, *Accred Qual Assur*, 12 (2007) 84-93.
- [164] A. Konieczny, K. Mondal, T. Wiltowski, P. Dydo, *International Journal of Hydrogen Energy*, 33 (2008) 264-272.
- [165] A. F.Cunha, J. J. M.Órfão, J. L. Figueiredo, *Applied Catalysis A: General*, 348 (2008) 103-112.
- [166] W. Qian, T. Liu, F. Wei, Z. Wang, Y. Li, *Applied Catalysis A: General*, 258 (2004) 121-124.
- [167] Y. Li, J. Chen, Y. Qin, L. Chang, *Energy and Fuels*, 14 (2000) 1188-1194.
- [168] S. Sushil, V. S. Batra, *Applied Catalysis B: Environmental*, 81 (2008) 64-77.
- [169] M. Balakrishnan, V. S. Batra, J. S. J. Hargreaves, I. D. Pulford, *Green Chemistry*, 13 (2011) 16-24.
- [170] R. A. Eggleton, R. W. Fitzpatrick, *Clays and Clay Minerals*, 36 (1988) 111-124.
- [171] S. Wang, H. M. Ang, M. O. Tadé, *Chemosphere*, 72 (2008) 1621-1635.
- [172] D. Emerson, W.C. Ghiorse, *Journal of Bacteriology*, 175 (1993) 7819-7827.
- [173] D. Emerson, W.C. Ghiorse, *Journal of Bacteriology*, 175 (1993) 7808-7818.
- [174] S. Spring, *The Genera Leptothrix and Sphaerotilus*, in: M. Dworkin, S. Falkow, E. Rosenberg, K. H. Schleifer, E. Stackebrandt (Eds.) *The Prokaryotes*, Springer, New York, 2006, pp. 758-777.
- [175] N. Z. Muradov, *Energy and Fuels*, 12 (1998) 41-48.
- [176] M. H. Kim, E. K. Lee, J. H. Jun, S. J. Kong, G. Y. Han, B. K. Lee, T. J. Lee, K. J. Yoon, *International Journal of Hydrogen Energy*, 29 (2004) 187-193.
- [177] K. Murata, M. Inaba, M. Saito, I. Takahara, N. Mimura, *Journal of the Japan Petroleum Institute* 46 (2003) 196-202.
- [178] L. Z. Gao, L. Kiwi-Minsker, A. Renken, *Surface and Coatings Technology*, 202 (2008) 3029-3042.
- [179] J. L. Pinilla, R. Utrilla, R. K. Karn, I. Suelves, M. J. Lázaro, R. Moliner, A. B. García, J. N. Rouzaud, *International Journal of Hydrogen Energy*, 36 (2011) 7832-7843.
- [180] I. Atribak, A. B. López, A. G. García, *Journal of Catalysis*, 259 (2008) 123-132.
- [181] F. V. Chukhrov, B. B. Zvyagin, L. P. Ermilova, A. I. Gorshkov, In Serratos, J.M. (ed.): *Proceedings of the 1972 International Clay Conference*. Division de Ciencias C.S.I.C., Madrid, (1973) 333-341.
- [182] F. V. Chukhov, B. B. Zvyagin, A. I. Gorshkov, L. P. Yermilova, V. V. Balashova, *International Geology Review*, 16 (1974) 1131-1143.
- [183] B. Zapata, M. A. Valenzuela, J. Palacios, E. T. Garcia, *International Journal of Hydrogen Energy*, 35 (2010) 12091-12097.

- [184] R.M.C. U. Schwertmann, Frontmatter, in: *Iron Oxides in the Laboratory*, Wiley-VCH Verlag GmbH, 2007, pp. i-xviii.
- [185] G. Garnaud, R. A. Rapp, *Oxidation of Metals*, 11 (1977) 193-198.
- [186] P. G. Weidler, *Journal of Porous Materials*, 4 (1997) 165-169.
- [187] M. Gemmi, M. Merlini, U. Cornaro, D. Ghisletti, G. Artioli, *Journal of Applied Crystallography*, 38 (2005) 353-360.
- [188] F. Pinna, *Catalysis Today*, 41 (1998) 129-137.
- [189] P. Komadel, J. Madejová, Chapter 7.1 Acid Activation of Clay Minerals, in: B.K.G.T. Faïza Bergaya, L. Gerhard (Eds.) *Developments in Clay Science*, Elsevier, 2006, pp. 263-287.
- [190] V. Barrn, J. Torrent, *Geochimica et Cosmochimica Acta*, 66 (2002) 2801-2806.
- [191] W. Kim, C.Y. Suh, S. W. Cho, K. M. Roh, H. Kwon, K. Song, I. J. Shon, *Talanta*, 94 (2012) 348-352.
- [192] N. Pinna, S. Grancharov, P. Beato, P. Bonville, M. Antonietti, M. Niederberger, *Chemistry of Materials*, 17 (2005) 3044-3049.
- [193] D. L. A. de Faria, S. V. Silva, M. T. de Oliveira, *Journal of Raman Spectroscopy*, 28 (1997) 873-878.
- [194] I. V. Chernyshova, M. F. Hochella Jr, A. S. Madden, *Physical Chemistry Chemical Physics*, 9 (2007) 1736-1750.
- [195] S. C. Lee, H. J. Seo, G. Y. Han, *Korean J. Chem. Eng.*, (2013) 1-6.
- [196] M. J. Lázaro, Y. Echegoyen, C. Alegre, I. Suelves, R. Moliner, J. M. Palacios, *International Journal of Hydrogen Energy*, 33 (2008) 3320-3329.
- [197] Y. Echegoyen, I. Suelves, M. J. Lázaro, M. L. Sanjuán, R. Moliner, *Applied Catalysis A: General*, 333 (2007) 229-237.
- [198] J. Ravichandran, C. M. Lakshmanan, B. Sivasankar, *Reaction Kinetics and Catalysis Letters*, 59 (1996) 301-308.
- [199] C.k. Shi, L.f. Yang, Z.C. Wang, X. He, J.X. Cai, G. Li, X.S. Wang, *Applied Catalysis A: General*, 243 (2003) 379-388.
- [200] C.j. Liu, K. Yu, Y.p. Zhang, X. Zhu, F. He, B. Eliasson, *Catalysis Communications*, 4 (2003) 303-307.
- [201] C. Shi, L. Yang, J. Cai, *Fuel*, 86 (2007) 106-112.
- [202] C.J. Loughran, D.E. Resasco, *Applied Catalysis B: Environmental*, 5 (1995) 351-365.
- [203] B.J. Adelman, W.M.H. Sachtler, *Applied Catalysis B: Environmental*, 14 (1997) 1-11.
- [204] T.V. Choudhary, E. Aksoylu, D. Wayne Goodman, *Catalysis Reviews*, 45 (2003) 151-203.
- [205] Y. Xu, X. Bao, L. Lin, *Journal of Catalysis*, 216 (2003) 386-395.
- [206] C. Zhang, S. Li, Y. Yuan, W.-X. Zhang, T.-H. Wu, L.-W. Lin, *Catal Lett*, 56 (1998) 207-213.
- [207] M. A. Ermakova, D. Y. Ermakov, G. G. Kuvshinov, L.M. Plyasova, *Journal of Catalysis*, 187 (1999) 77-84.
- [208] S. Takenaka, Y. Shigeta, K. Otsuka, *Chemistry Letters*, 32 (2003) 26-27.
- [209] V.V. Chesnokov, A.S. Chichkan, *International Journal of Hydrogen Energy*, 34 (2009) 2979-2985.
- [210] D. Sebastián, J.C. Calderón, J.A. González-Expósito, E. Pastor, M.V. Martínez-Huerta, I. Suelves, R. Moliner, M.J. Lázaro, *International Journal of Hydrogen Energy*, 35 (2010) 9934-9942.
- [211] B. Kitiyanan, W.E. Alvarez, J.H. Harwell, D.E. Resasco, *Chemical Physics Letters*, 317 (2000) 497-503.
- [212] J.G. McCarty, H. Wise, *Journal of Catalysis*, 57 (1979) 406-416.

- [213] S.B. Sinnott, R. Andrews, D. Qian, A.M. Rao, Z. Mao, E.C. Dickey, F. Derbyshire, *Chemical Physics Letters*, 315 (1999) 25-30.
- [214] J. Gavillet, A. Loiseau, F. Ducastelle, S. Thair, P. Bernier, O. Stéphan, J. Thibault, J.C. Charlier, *Carbon*, 40 (2002) 1649-1663.
- [215] R. Aiello, J. Fiscus, H. zur Loye, M. Amiridis, *Applied Catalysis A: General*, 192 (2000) 227-234.
- [216] M.A. Pimenta, G. Dresselhaus, M.S. Dresselhaus, L.G. Cancado, A. Jorio, R. Saito, *Physical Chemistry Chemical Physics*, 9 (2007) 1276-1290.
- [217] D. Yuan, J. Chen, X. Hu, J. Zeng, S. Tan, Y. Liu, *International Journal of Electrochemical Science*, 3 (2008) 1268 - 1276.
- [218] I. Suelves, J.L. Pinilla, M.J. Lázaro, R. Moliner, J.M. Palacios, *Journal of Power Sources*, 192 (2009) 35-42.
- [219] S. Zhan, Y. Tian, Y. Cui, H. Wu, Y. Wang, S. Ye, Y. Chen, *China Particuology*, 5 (2007) 213-219.
- [220] J.L. Pinilla, I. Suelves, M.J. Lázaro, R. Moliner, J.M. Palacios, *International Journal of Hydrogen Energy*, 35 (2010) 9801-9809.
- [221] S. Takenaka, Y. Shigeta, E. Tanabe, K. Otsuka, *Journal of Catalysis*, 220 (2003) 468-477.
- [222] J. Chen, X. Zhou, L. Cao, Y. Li, *Studies in Surface Science and Catalysis*, 147 (2004) 73-78.
- [223] J. Ashok, P.S. Reddy, G. Raju, M. Subrahmanyam, A. Venugopal, *Energy and Fuels*, 23 (2008) 5-13.
- [224] Y. Echegoyen, I. Suelves, M. J. Lázaro, R. Moliner, J. M. Palacios, *Journal of Power Sources*, 169 (2007) 150-157.
- [225] S.J. Tauster, S.C. Fung, R.T.K. Baker, J.A. Horsley, *Science*, 211 (1981) 1121-1125.
- [226] S.J. Tauster, *Accounts of Chemical Research*, 20 (1987) 389-394.
- [227] Z. Bai, H. Chen, B. Li, W. Li, *International Journal of Hydrogen Energy*, 32 (2007) 32-37.
- [228] F. A. L. Sy, L. C. Abella, T.G. Monroy, *International Journal of Chemical Engineering and Applications*, 3 (2012) 92-97.
- [229] S. Takenaka, Y. Shigeta, E. Tanabe, K. Otsuka, *The Journal of Physical Chemistry B*, 108 (2004) 7656-7664.
- [230] B. Li, S. Li, N. Li, H. Chen, W. Zhang, X. Bao, B. Lin, *Microporous and Mesoporous Materials*, 88 (2006) 244-253.
- [231] S. Sato, A. Kawabata, M. Nihei, Y. Awano, *Chemical Physics Letters*, 382 (2003) 361-366.
- [232] Y. Li, W. Kim, Y. Zhang, M. Rolandi, D. Wang, H. Dai, *The Journal of Physical Chemistry B*, 105 (2001) 11424-11431.
- [233] H. Dai, A.G. Rinzler, P. Nikolaev, A. Thess, D.T. Colbert, R.E. Smalley, *Chemical Physics Letters*, 260 (1996) 471-475.
- [234] Y. Zhang, Y. Li, W. Kim, D. Wang, H. Dai, *Applied Physics A*, 74 (2002) 325-328.
- [235] C.L. Cheung, A. Kurtz, H. Park, C.M. Lieber, *The Journal of Physical Chemistry B*, 106 (2002) 2429-2433.
- [236] J.L. Pinilla, I. Suelves, M.J. Lázaro, R. Moliner, J.M. Palacios, *Applied Catalysis A: General*, 363 (2009) 199-207.
- [237] B. Wen, J. Jia, W.M.H. Sachtler, *The Journal of Physical Chemistry B*, 106 (2002) 7520-7523.
- [238] M. Ogura, Y. Sugiura, M. Hayashi, E. Kikuchi, *Catalysis Letters*, 42 (1996) 185-189.
- [239] T.V. Reshetenko, L.B. Avdeeva, Z.R. Ismagilov, A.L. Chuvilin, V.A. Ushakov, *Applied Catalysis A: General*, 247 (2003) 51-63.
- [240] D. Roth, P. Gélin, A. Kaddouri, E. Garbowski, M. Primet, E. Tena, *Catalysis Today*, 112 (2006) 134-138.

- [241] M. Schmal, M.M.V.M. Souza, V.V. Alegre, M.A.P. da Silva, D.V. César, C.A.C. Perez, *Catalysis Today*, 118 (2006) 392-401.
- [242] A.L. Guimarães, L.C. Dieguez, M. Schmal, *Anais da Academia Brasileira de Ciências*, 76 (2004) 825-832.
- [243] J. Panpranot, O. Tangjitwattakorn, P. Praserthdam, J.G. Goodwin Jr, *Applied Catalysis A: General*, 292 (2005) 322-327.
- [244] K. Otsuka, S. Kobayashi, S. Takenaka, *Applied Catalysis A: General*, 190 (2000) 261-268.
- [245] M. Inaba, K. Murata, M. Saito, I. Takahara, N. Mimura, *Reaction Kinetics and Catalysis Letters*, 77 (2002) 109-115.
- [246] V. Mohan, C. Raghavendra, C.V. Pramod, B.D. Raju, K.S. Rama Rao, *RSC Advances*, 4 (2014) 9660-9668.
- [247] Z. Y. Zakaria, J. Linnekoski, N. S. Amin, *Chemical Engineering Journal*, 207-208 (2012) 803-813.
- [248] C.L. Luu, T.K.T. Dao, T. Nguyen, T.H. Bui, T.N.Y. Dang, M.N. Hoang, S.T. Ho, *Advances in Natural Sciences: Nanoscience and Nanotechnology*, 4 (2013) 045001.
- [249] S.P. Chai, S.S. Zein, A.R. Mohamed, *Diamond and Related Materials*, 16 (2007) 1656-1664.
- [250] J. Ziebro, I. Łukasiewicz, E. Borowiak-Palen, B. Michalkiewicz, *Nanotechnology*, 21 (2010) 145308.
- [251] H.M. Swaan, V.C.H. Kroll, G.A. Martin, C. Mirodatos, *Catalysis Today*, 21 (1994) 571-578.
- [252] J. Salmones, J.A. Wang, M.A. Valenzuela, E. Sánchez, A. Garcia, *Catalysis Today*, 148 (2009) 134-139.
- [253] S. H. Zein, A.R. Mohamed, *IIUM Engineering Journal*, 5 (2004) 13-23.
- [254] S. Takenaka, E. Kato, Y. Tomikubo, K. Otsuka, *Journal of Catalysis*, 219 (2003) 176-185.
- [255] C. Li, Y.-W. Chen, *Thermochimica Acta*, 256 (1995) 457-465.
- [256] S. Yunfei, S. Zhijun, Z. Jinghong, L. Ping, Z. Xinggui, C. De, *Asia-Pacific Journal of Chemical Engineering*, 4 (2009) 814-820.
- [257] G. Li, L. Hu, J.M. Hill, *Applied Catalysis A: General*, 301 (2006) 16-24.
- [258] S. Makvandi, S. Alavi, *Iranian Journal of Chemical Engineering*, 8 (2011) 24-33.
- [259] M. Matsukata, T. Matsushita, K. Ueyama, *Energy and Fuels*, 9 (1995) 822-828.
- [260] P. Ammendola, R. Chirone, L. Lisi, G. Ruoppolo, G. Russo, *Journal of Molecular Catalysis A: Chemical*, 266 (2007) 31-39.
- [261] M. Jia, W. Li, H. Xu, S. Hou, C. Yu, Q. Ge, *Catalysis Letters*, 84 (2002) 31-35.
- [262] C. Quincoces, A. Kikot, E. Basaldella, M. González, *Industrial and Engineering Chemistry Research*, 38 (1999) 4236-4240.